論文 / 著書情報
Article / Book Information

題目(和文)	
Title(English)	Microstructure Control and Fatigue Crack Growth Behavior of Wrought γ-based TiAl Alloys Containing β-Ti Phase
著者(和文)	SIGNORI Loris Jonathan
Author(English)	Loris Signori
出典(和文)	学位:博士(工学), 学位授与機関:東京工業大学, 報告番号:甲第10949号, 授与年月日:2018年9月20日, 学位の種別:課程博士, 審査員:竹山 雅夫,中村 吉男,藤居 俊之,村石 信二,小林 覚
Citation(English)	Degree:Doctor (Engineering), Conferring organization: Tokyo Institute of Technology, Report number:甲第10949号, Conferred date:2018/9/20, Degree Type:Course doctor, Examiner:,,,,
学位種別(和文)	博士論文
Type(English)	Doctoral Thesis

Doctor Thesis

Microstructure Control and Fatigue Crack Growth Behavior of Wrought γ-based TiAl Alloys Containing β-Ti Phase

By
Loris Signori

Supervised by
Prof. Masao Takeyama
Associate Prof. Satoru Kobayashi

Department of Metallurgy and Ceramics Science
Tokyo Institute of Technology
September 2018

Contents

Chapter 1

General Introduction

1.1 Context of the study

The air traffic or RPK, that represents the number of kilometers traveled by paying passengers, doubles every 15 years and leads to an increase in service aircrafts. **Figure 1-1** shows the world annual traffic between 1950 and 2012 that increase by 4.4% every year [1].

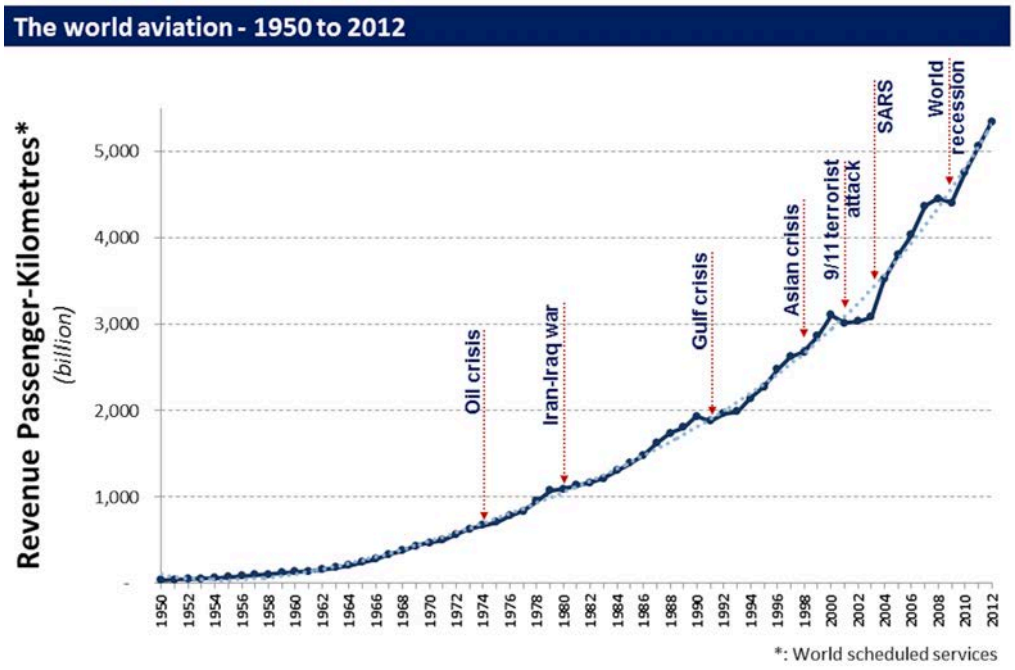

Fig. 1-1. World annual traffic between 1950 and 2012 [1].

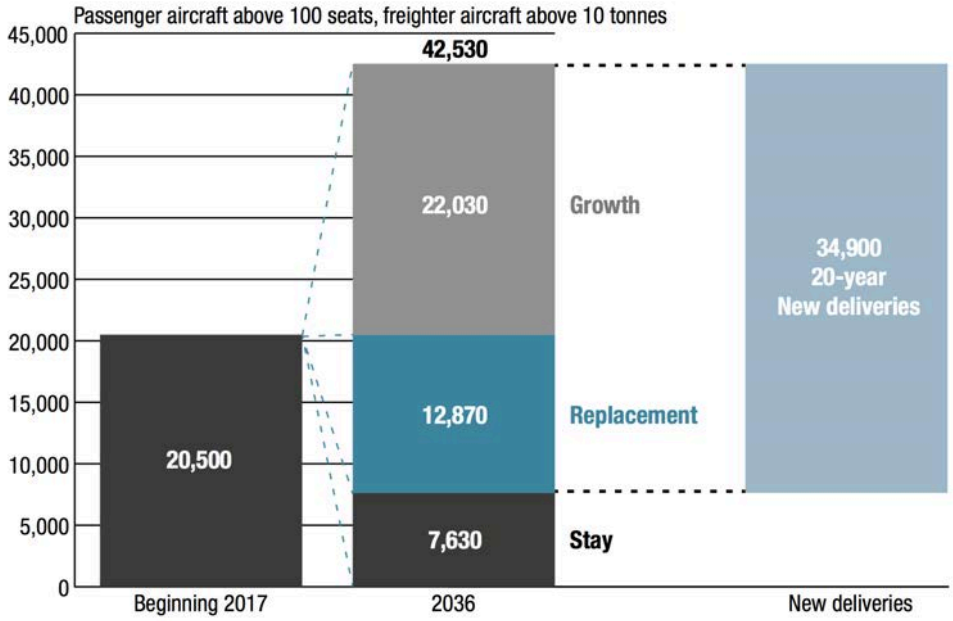

Fig. 1-2. Evolution of the fleet in service [2].

Two consequences stem from the air traffic growth. On one hand, the rise of the new aircrafts is needed to support this traffic as estimated by Airbus in **Figure 1-2**. The aircraft fleet will double in less than twenty years from 20,500 to 42,530 [2]. On the other hand, the increase of the civil fleet will release a large amount of CO_2 in atmosphere if no actions are employed as shown in **Figure 1-3**. The International Air Transport Association (IATA) detailed a CO_2 reduction roadmap based on new technology and the utilization of biofuel to reduce emission by 50% compare to 2005 [3]. Moreover, despite aviation was not included in 2015 Paris Agreement, during the general 39th session in October 2016, the member of the International Civil Aviation Organization (ICAO) decided to create a tool to limit the aviation CO_2 emission [4].

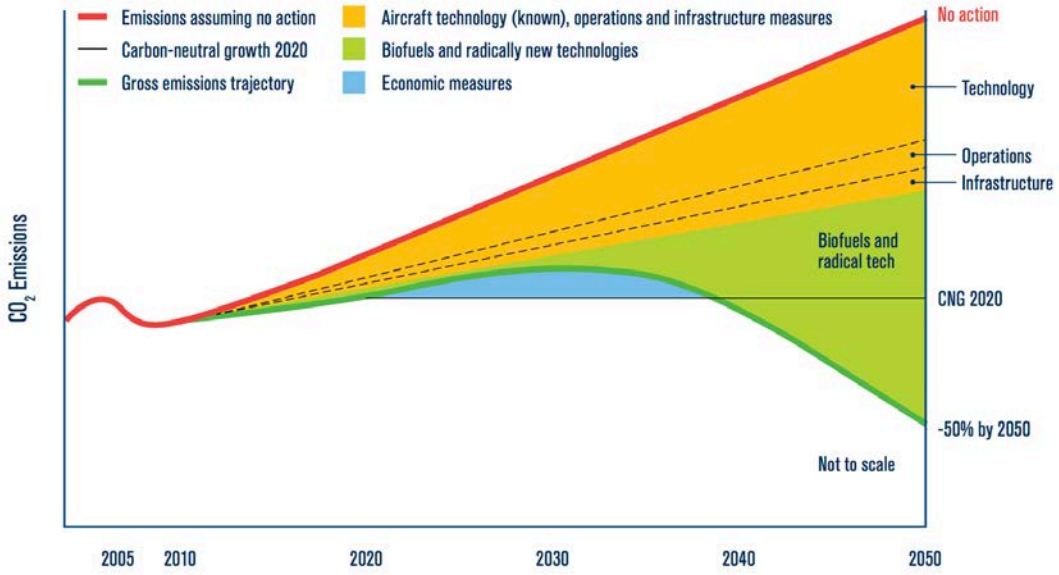

Fig. 1-3. Schematic CO_2 emissions reduction roadmap [3].

Furthermore, kerosene price represents one of the major expense of airline companies. With the continuous rise of kerosene price and despite the economic crisis in 2017 [5], engine maker's companies look ceaselessly for new solutions to improve the turbojet efficiency.

Improve the energy efficiency of turbojet engine is an important issue for saving fuel and reducing CO_2. The turbojet engine efficiency can be described by the following equation:

$$\text{Efficiency} \propto \frac{\text{thrust}}{\text{mass}} \tag{1-1}$$

Hence, two ways of research can be explored to optimize an efficient engine. One of the research way consist to increase the thrust, which mean increase the combustion chamber temperature. **Figure 1-4** shows the evolution of pressure and temperature through a turbojet engine [6]. Currently applied temperature in the chamber is already very high and reaches almost 1200°C. Therefore, the merge of progressions is very limited without technological breakthrough.

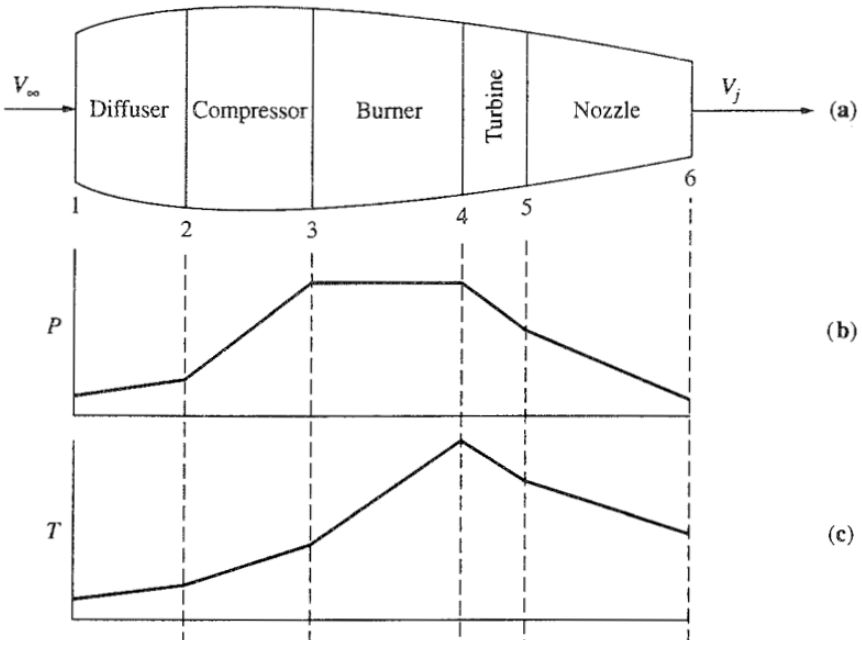

Fig. 1-4. Schematic illustration of the (a) component, (b) change in pressure and (c) change in temperature in turbojet engine [6].

The second way is to use light-weight materials in order to decrease the mass of engine. For example, turbofans were made from titanium alloy and have been replaced by lighter composite materials. Titanium aluminides (TiAl) alloys are also one of the promising materials for intermediate temperature' applications up to 800°C. Indeed, TiAl alloys show half density of conventional high temperature resisting alloys, especially nickel based superalloys with interesting mechanical properties. **Table 1-1** show a comparison between titanium, nickel and titanium aluminides alloys. TiAl alloys have been intensively investigated in order to replace the last stage of low pressure turbine (LPT) blades and possibly high pressure compressor (HPC) blades during the four last decades. Finally, in 2006, General Electric (GE) announced the first use of TiAl alloys for rotating part in civil turbojet engine GEnx [7].The Japan has also important activities of research

on these alloys, especially through the Science Innovative Promotion Program (SIP). **Figure 1-5** shows a schematic illustration of the GEnx engine where the two last stages of low pressure turbine (LPT) blade were replaced by Ti-48Al-2Nb-2Cr (at.%) alloy with a fully lamellar microstructure and an operating temperature around 650°C [8].

Table 1-1. Physical, mechanical and metallurgical properties of TiAl alloy, titanium alloys and superalloys [9].

Property	Ti-based alloys	Ti_3Al-based alloys	TiAl-based alloys	Superalloy
Density – $g.cm^3$	4.5	4.1-4.7	3.7-3.9	8.3
RT Modulus – GPa	96-115	120-145	160-176	206
Yield Strength – MPa	390-1150	700-990	400-630	–
Tensile Strength – MPa	480-1200	800-1140	450-700	–
Creep Limit – °C	600	750	1000	1090
Oxidation – °C	600	650	900-1000	1090
RT Ductility – %	10-20	2-7	1-3	3-5
HT Ductility – %	High	10-20	10-90	10-20

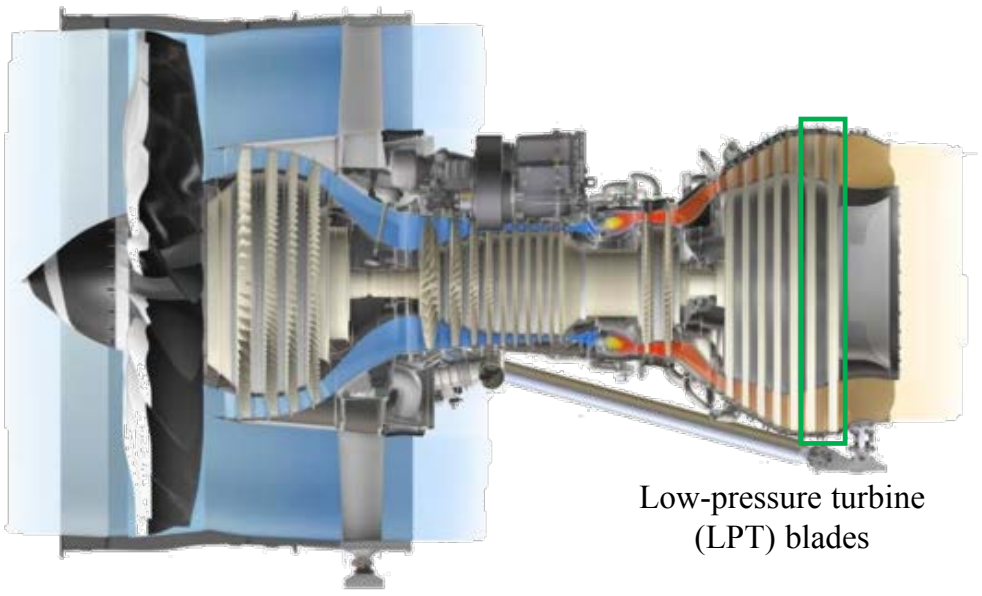

Fig. 1-5. Schematic illustration of GEnx engine with the two last stages of LPT in TiAl alloy [8].

Furthermore, the current target is to increase temperature capability of the TiAl alloys to replace not only the two lasts stage of LPT blades but also other stages and also to increase **toughness** in order to replace also the high-pressure compressor (HPC) blades.

1.2 Titanium Aluminides Alloys

As explained previously, titanium aluminides alloys show low density (4~4.5) depending on the additional elements, good mechanical properties and good oxidation resistance at intermediate temperature up to 800°C [9-13] as illustrated in **Figure 1-6** with the comparison for different class of alloys of (a) the specific modulus and (b) the specific strength [14]. Up to 700~800°C, the characteristics of TiAl alloys are higher than nickel-based alloys and explain why TiAl alloys have been introduced in replacement of these materials.

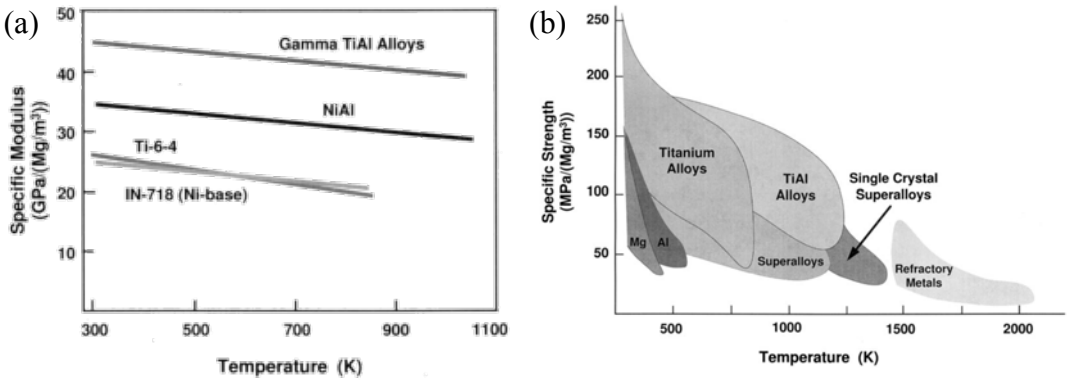

Fig. 1-6. Mechanical properties of TiAl alloys with (a) specific modulus and (b) specific strength of different class of alloy with temperature [14].

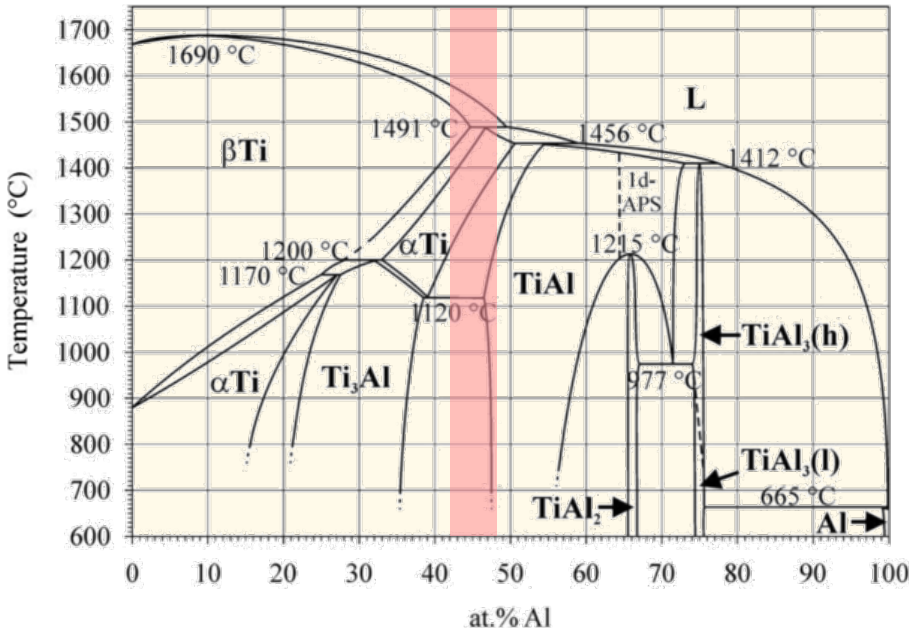

Fig. 1-7. TiAl binary phase diagram [15]. Red rectangle (42~48Al at.%) represent the γ-based TiAl alloys.

Figure 1-7 shows the most recent assessment of the binary phase diagram of titanium aluminides established by Schuster and Palm in 2006 [15] with a band that shows the delimited range of gamma titanium aluminides based alloys. The standard aluminum of γ-TiAl based alloy content is usually between 42 and 50 (at.%Al). Although, this TiAl phase diagram is reliable, our research group continues to refer to the phase diagram published by Petzow and Effenberg [16] for composition with an aluminum content lower than 35 at.%. Indeed, we demonstrated that the existence of peritectoid α_2 phase depends of the oxygen content and therefore, the phase diagram showed a congruent α_2 phase [17].

Based on the phase diagram, the constituent phases of TiAl can be identified. There are shown in **Figure 1-8** and the crystallographic data are presented in **Table 1-2** [18].

Table 1-2. Crystallographic data of phases occurring in the TiAl alloys [18].

Phases	Pearson symbol	Space group	Strukturberickt designation	Prototype	Lattice parameters
β-Ti	cI2	Im-3m	A2	W	a = 3.31 Å
β_0, B2	cP2	Pm-3m	B2	CsCl	-
α-Ti	hP2	$P6_3/mmc$	A3	Mg	a = 2.95 Å c = 4.68 Å
α_2-Ti_3Al	hP8	$P6_3/mmc$	$D0_{19}$	Ni_3Sn	a = 5.77 Å c = 4.46 Å
γ-TiAl	tP4	P4/mmm	$L1_0$	AuCu	a = 4.00 Å c = 4.08 Å

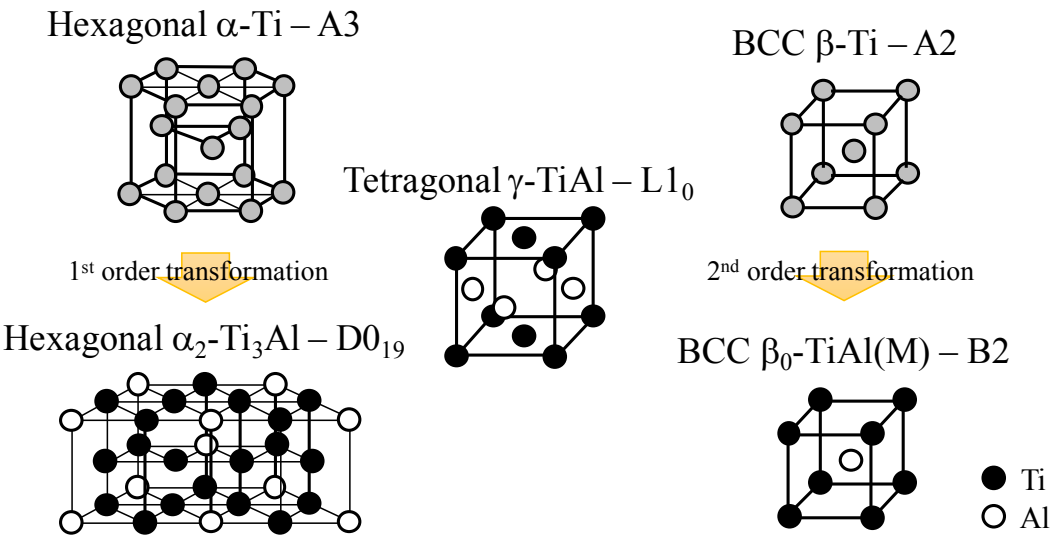

Fig. 1-8. Crystal structure of TiAl in the range of 30-50Al at.%. B2 structure may not exist in the binary TiAl alloy [18].

The main phases found in the range of TiAl alloys are β-Ti, β_0-TiAl(M), α-Ti, α_2-Ti_3Al and γ-TiAl. It should be noted that the existence of β_0 phase in binary alloy is still subject to controversy [19, 20]. The α_2 and β_0 phase are the first and second order ordering transformation of α and β phases, respectively. The following phase transformation imply these phases: peritectic L + β → α, L + α → γ, first order ordering transformation α → α_2, and second order ordering transformation β → β_0.

Based on the phase diagram, it is possible to achieve various microstructure in γ-TiAl alloys as shown in **Figure 1-9** [21]. Using same alloy composition, it is possible to control γ phase precipitation by changing heat treatments. By holding the specimen in α-single phase followed by air cooling the fully lamellar (FL) microstructure can be obtained from the decomposition of α grain α → α + γ. By holding the specimen in α + γ two phases region with eventually some subsequent heat treatments it is possible to change the ratio between α_2/γ lamellar structure and γ-grains from nearly lamellar (NL) to duplex (DP) microstructures. Finally, by holding the specimen near or in the γ-single phase, around 1473 K, it is possible to obtain near-gamma or γ equiaxed microstructures.

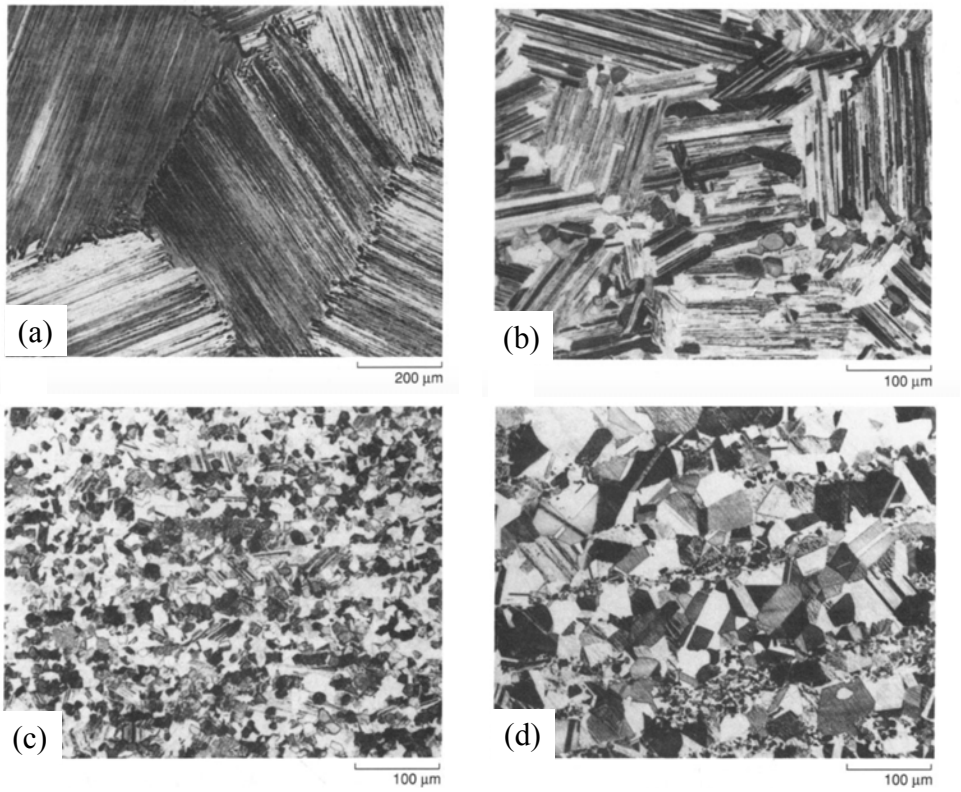

Fig. 1-9. OM images of typical microstructures of γ-based alloys: (a) fully lamellar, (b) near lamellar, (c) duplex and (d) near-gamma [21].

The formation of α_2/γ lamellar structure has been explained by Denquin *et al.* as the motion of Shockley partial dislocations in α or α_2 every two planes which lead to the crystal structure change into $L1_0$ structure (γ phase) [22]. The γ precipitation process leads to the following orientation relationship, called Blackburn orientation relationship, between the two phases [23]:

$$\{111\}_\gamma // (0001)_\alpha \text{ and } \langle 1\bar{1}0]_\gamma // \langle 11\bar{2}0\rangle_\alpha \quad (1\text{-}2)$$

These γ lamellae precipitate according two different sequences of the fcc structure (ABCABC or ACBACB). Moreover, the $\langle 1\bar{1}0\rangle$ orientation are not equivalent due to the tetragonal primitive cell of γ phase and lead to six different orientation variants called OR1 to OR6 and shown in **Figure 1-10** [24].

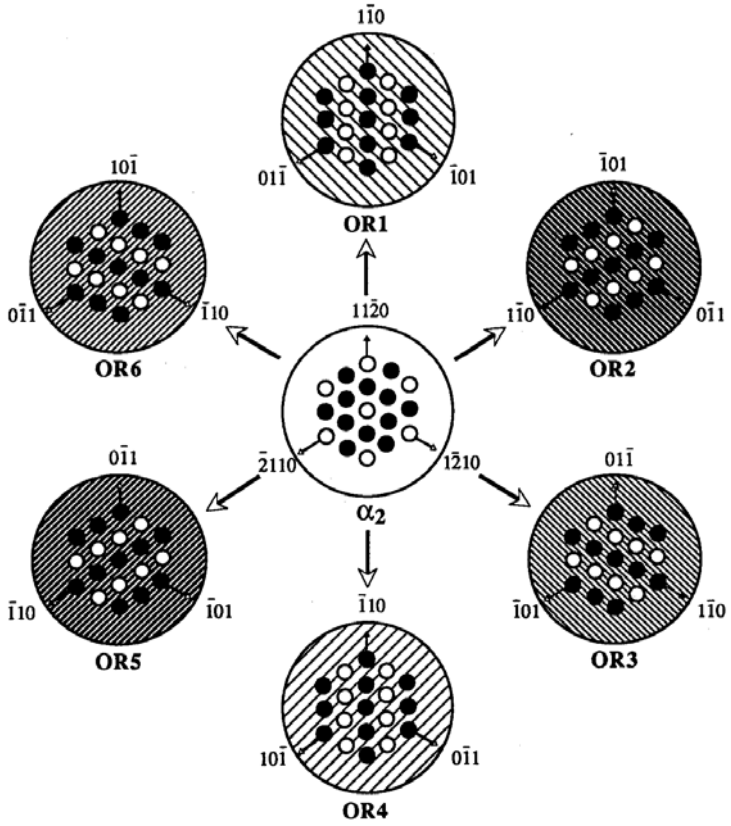

Fig. 1-10. Schematic representation of the six orientation variants of the γ phase [24].

1.3 Microstructure design principle of wrought TiAl alloys

Conventional alloy design concept of titanium aluminides is to find a good balance of mechanical properties for the desired applications. Indeed, the duplex microstructure improves the ductility and the low fatigue cycle properties whereas the fully lamellar microstructure improves the creep resistance and the fracture toughness.

Table 1-3 represents a list of common investigated TiAl based alloys. When the aluminum content decreases and the β-stabilizer content increases, the processes change from cast/SPS to forging. However, only two different compositions are commercialized nowadays for applications (4822 and TNM) [7, 10, 25-30].

Table 1-3. Composition and process of conventional TiAl alloys.

Alloys	Composition (at.%)				Process	Application	References
	Ti	Al	β-stabilizer	others elements			
4822 (GE)	**bal.**	**48**	**4**		**casting, AM***	**GEnx, LEAP, GE9x***	**7**
IRIS	bal.	48	2	B	SPS		25
CTI-8	bal.	47	4	B	casting		26
G4	bal.	47	2	Si	SPS		27
ABB-2	bal.	46	2	Si	casting		28
K5	bal.	46	5.2		forging		29
45XD	bal.	45	4	B	casting		30
TNB	bal.	45	5 - 10	C	forging		27
TNM	**bal.**	**43.5**	**5**	**B**	**forging**	**PW1100G**	**10**

* in service in 2020

The first generation of TiAl alloys consisted of binary Ti-(42-48)Al at.%. Nevertheless, in order to increase the mechanical properties, the second generation of TiAl alloys were developed using alloying elements as follows [7]:

$$\text{Ti-(45-48)Al-(1-3)X-(2-5)Y-(<1)Z} \qquad (1\text{-}3)$$

Where X and Y are small contents of β-stabilizer elements, respectively Cr, Mn, V and Nb, Ta, W, Mo. Z consists of interstitials elements such as B, C or Si. Boron is used as a grain refiner. Carbon and silicon addition contribute to improve mechanical properties, especially creep resistance [31]. The 4822 alloy from General Electric (Ti-48Al-2Nb-2Cr at.%) is one of the most known alloys from this generation. With an aluminum content higher than 45 at.%, α phase is the major primary solidifying phase as shown in **Figure 1-11** [32]. Therefore, these alloys are also called α-solidified γ-TiAl alloys.

In order to use the wrought process of γ-based TiAl, the third generation of TiAl alloys was developed. The alloys of this generation contains usually a lower aluminum content and higher fraction of β-stabilizer as follows [10]:

$$\text{Ti-(42-48)Al-(0-10)X-(0-3)Y-(0-1)Z-(0-0.5)RE} \qquad (1\text{-}4)$$

Where X and Y are higher contents of β-stabilizer elements, respectively Cr, Mn, Nb, Ta and W, Mo, Hf, Wr. Z consists of interstitials elements such as B, C or Si added for

mechanical properties and RE are small amount of rare earths. TNM (Ti-43.5Al-4Nb-1Mo-0.1B at.%) and TNB Ti-45Nb-(5-10)Nb-(0-0.5)B,C at.%) alloys are examples of this TiAl generation. Due to the lower aluminum content and the higher fraction of β-stabilizer elements, the primary phase to solidify is β phase and present fine-grained lamellar structure. These alloys are so called β-solidified γ-TiAl alloys. Although effects of carbon and silicon are similar in case of α-solidified γ-TiAl alloys, in these alloys, the effect of silicon is not beneficial for mechanical properties compared to the carbon addition [33]. The presence of β phase with a bcc structure at high temperature permit hot-working process, especially forging at high temperature unlike of 2nde generation of TiAl alloys.

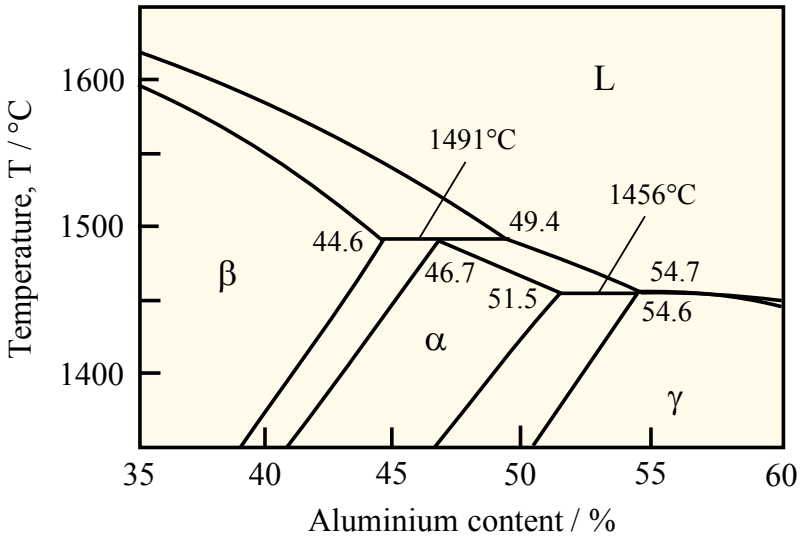

Fig. 1-11. Partial section of Ti-Al binary phase diagram according the thermodynamic calculation of Witusiewicz [32].

Takeyama and his co-workers were the first who investigated the wrought TiAl alloy approach with high toughness potential and successfully manufactured a blade in 2002 [34, 35]. Nakashima *et al.* [36] recently demonstrated that combine two β-stabilizer elements is more efficient that their individual β-stabilizer effect. **Figure 1-12** show an illustration of the microstructure design conducted on wrought TiAl based alloy with Ti-43Al-4Nb-5V system as an example. The vertical section determined by both calculations and experiments at 43Al and 4Nb (at.%) are shown in (a) [37]. This alloy system shows a unique phase transformation pathway as follow:

$$\beta+\alpha \rightarrow \alpha \rightarrow \alpha+\gamma \rightarrow \beta+\alpha+\gamma \rightarrow \beta+\gamma \qquad (1\text{-}4)$$

Therefore, the alloy could be forged in β+α two phases region, around 1300°C (b). Then post forging heat treatment are usually used to reduce the volume fraction of β phase at low temperature (c). Finally, in service, phase transformations will occur, especially cellular reaction α+γ → β+γ (d). Thus, understanding the relationship between β phase and the mechanical properties are the key to predict the behavior of wrought TiAl alloy in service.

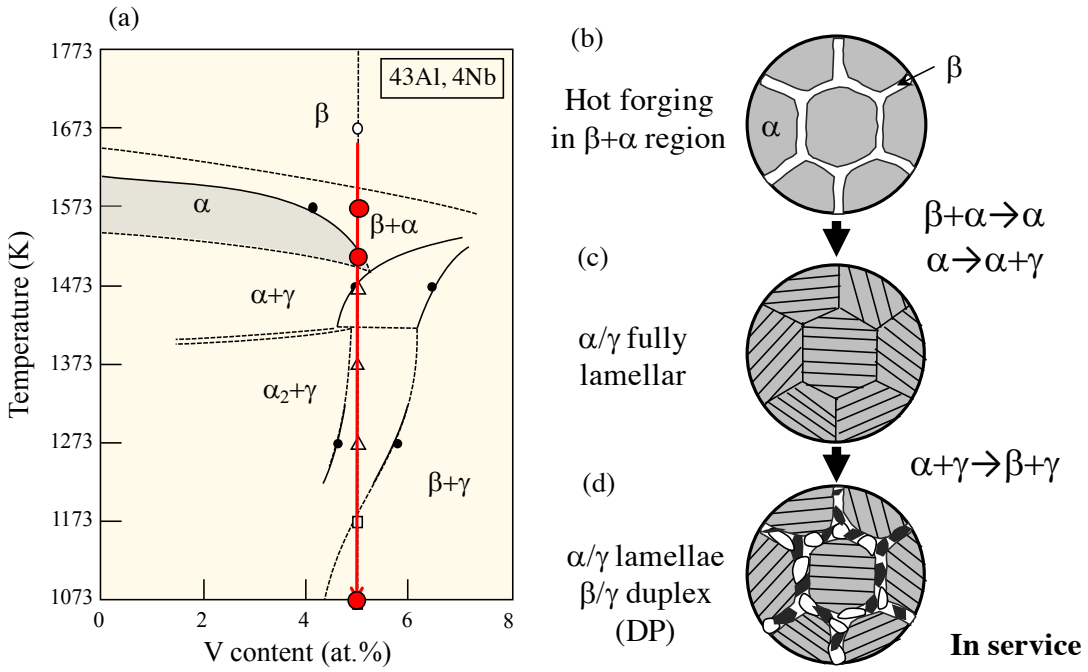

Fig. 1-12. Microstructure design of wrought TiAl alloy (a) vertical section of Ti-43Al-4Nb-xV, (b) hot forging, (c) heat treated and (d) in service microstructure [37].

1.4 Effect of β phase on mechanical properties

It is generally considered that β phase is detrimental for both mechanical properties (creep and toughness) and fully lamellar microstructure shows better properties [12]. Thus, microstructure design in β-solidified TiAl alloys aims to minimize the β phase at service temperature using optimized heat treatment. However, the role of the β phase on the mechanicals properties was not systematically investigated.

Recently, Clemens's group studied the effect of microstructure, that contain β phase, on mechanical properties but not on the properties of β phase itself. Schwaighofer *et al*. focused on how the heat treatments affect the microstructures and hence the mechanicals properties of Ti-43.5Al-4Nb-1Mo-0.1B (TNM) alloys [38]. Leitner *et al*. demonstrated

how large differences of the grain boundaries could modify the R-curve behavior [39]. Despite the difference relatively was quite small, they noticed that a large β/γ duplex structure (DP) obtained by cellular reaction α+γ → β+γ enhanced slightly fracture toughness whereas a continuous β phase surrounded the lamellar colonies seems to be detrimental for the fracture toughness as shown in **Figure 1-13**. Therefore, β phase could be an efficient phase based on the morphology.

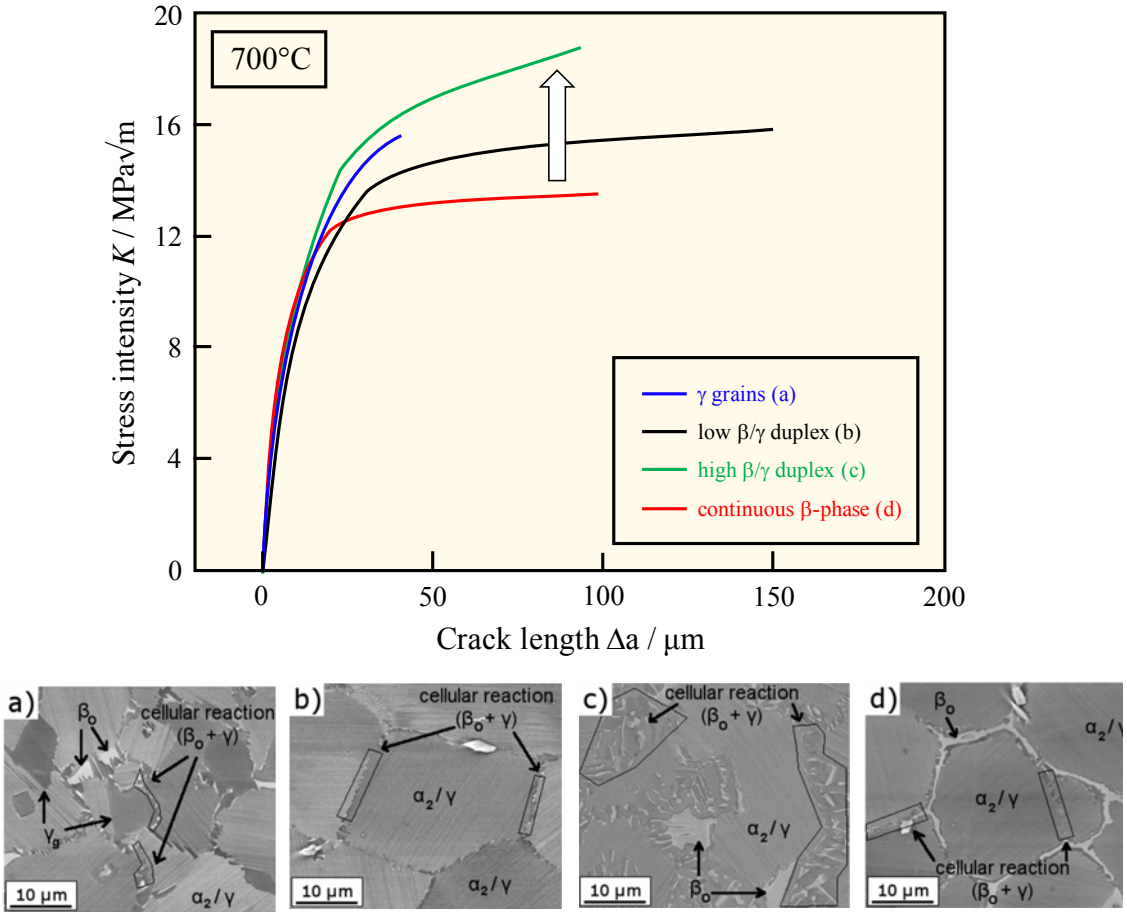

Fig. 1-13. Average crack resistance curves of four microstructures with different grain boundary structures at 700°C along with the corresponding microstructures [39]

Based on TTP diagram, Oinuma *et al*. introduced β phase at lamellar interface in α_2/γ colonies of TiAl alloys and investigated the effect on toughness. **Figure 1-14** shows the impact test results between the fully lamellar microstructure and this microstructure [40]. It can be shown that the presence of β phase increases drastically the total energy needed for rupture and so enhanced the toughness of the alloy.

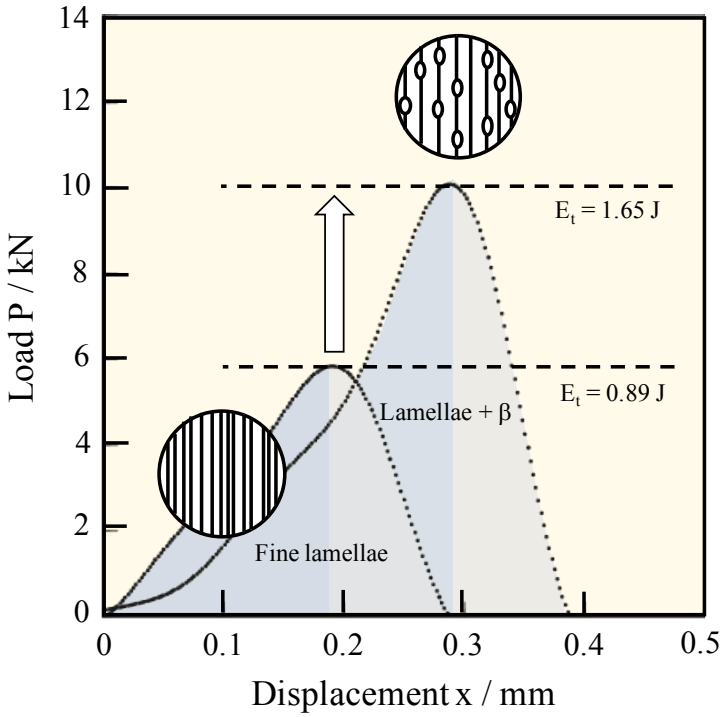

Fig. 1-14. Effect of microstructure on Charpy impact tests with fine lamellar microstructure and colonies with β particles at lamellar interface [40].

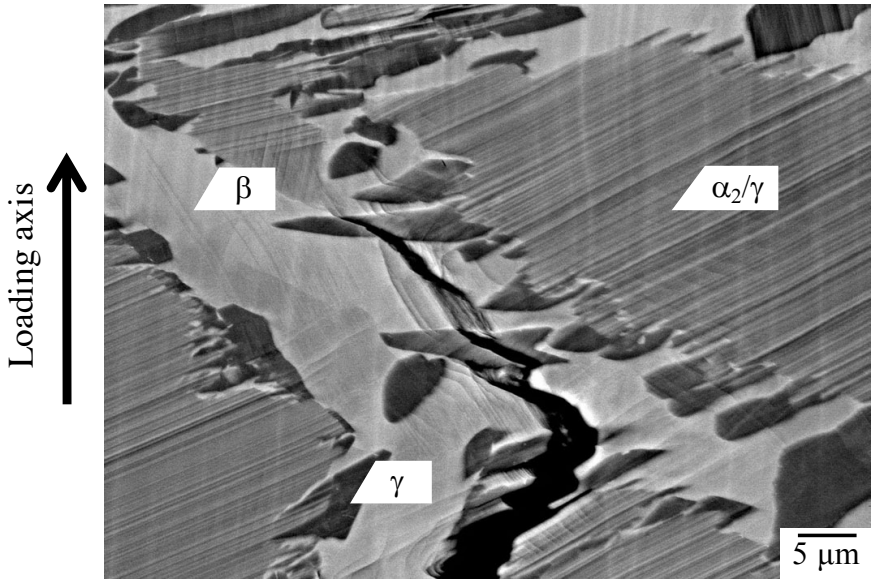

Fig. 1-15. Crack appeared during three points bend test at room temperature in Ti-42Al-8V alloy [41].

Nakashima *et al*. conducted preliminary in-situ bending studies at room temperature on microstructure containing β phase using the microstructure design for wrought alloy introduced previously. They clarified that β phase located at the front of the crack tip reveals plastic deformations as shown in **Figure 1-15** [41]. Thus, the crack propagation is suppressed and the toughness is enhanced.

Based on this study, Usui *et al*. focused on the tensile properties at high temperature, both *ex-situ* and *in-situ* [42]. **Figure 1-16** shows the quantification of the crack-type appearing during tests. They identified three kinds of cracks, at lamellar interface, at grain boundaries with β/γ DP and at grain boundaries without DP. During tests, the cracks appeared preferentially at grain boundaries which not present β/γ duplex. Nakamura *et al*. continued these researches and evaluated the effect of the volume fraction of β/γ duplex on tensile properties as shown in **Figure 1-17** [43]. They demonstrated that increase volume fraction V_{DP} of β/γ duplex not only increases the young modulus but also increases the deformability.

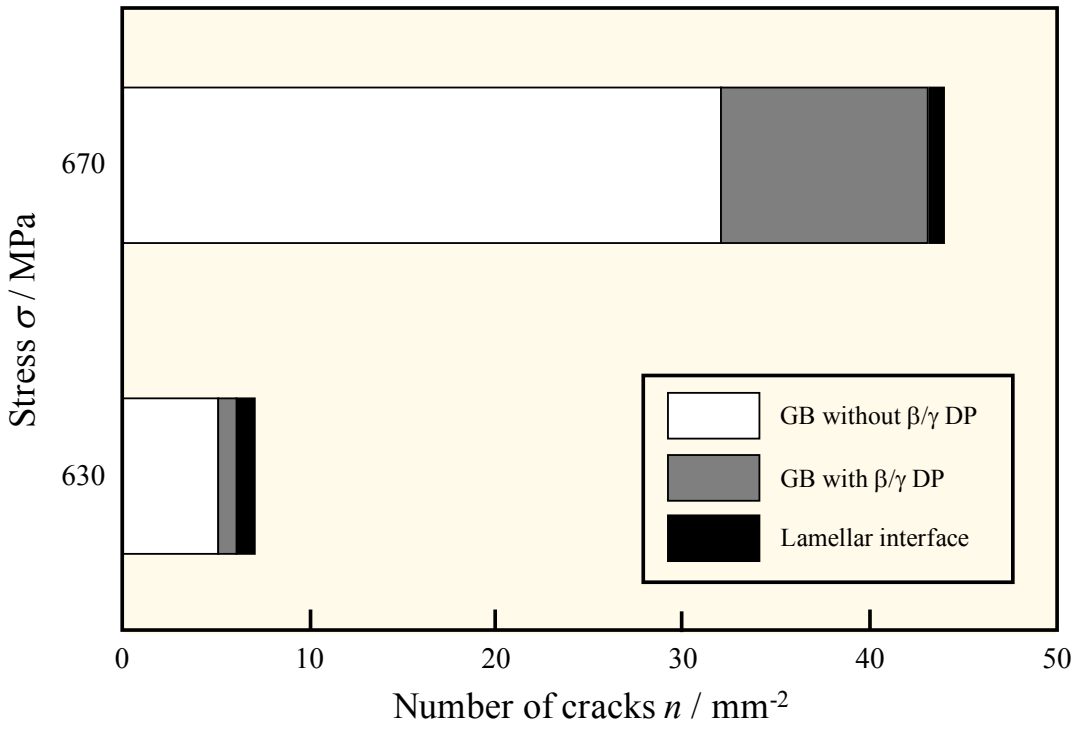

Fig. 1-16. Quantification of cracks observed at different stresses [42].

Therefore, the β phase seems to have interesting effect on mechanical properties. Wakabayashi *et al*. evaluated the effect of morphology of β phase on creep behavior [44]. The **Figure 1-18** shows the Larson-Miller parameter for Ti-43Al-4Nb-5V alloys with

different microstructures. The presence of elongated grains of β/γ phases, called LTL, slightly improve the creep properties compared to globular grains, called GTL.

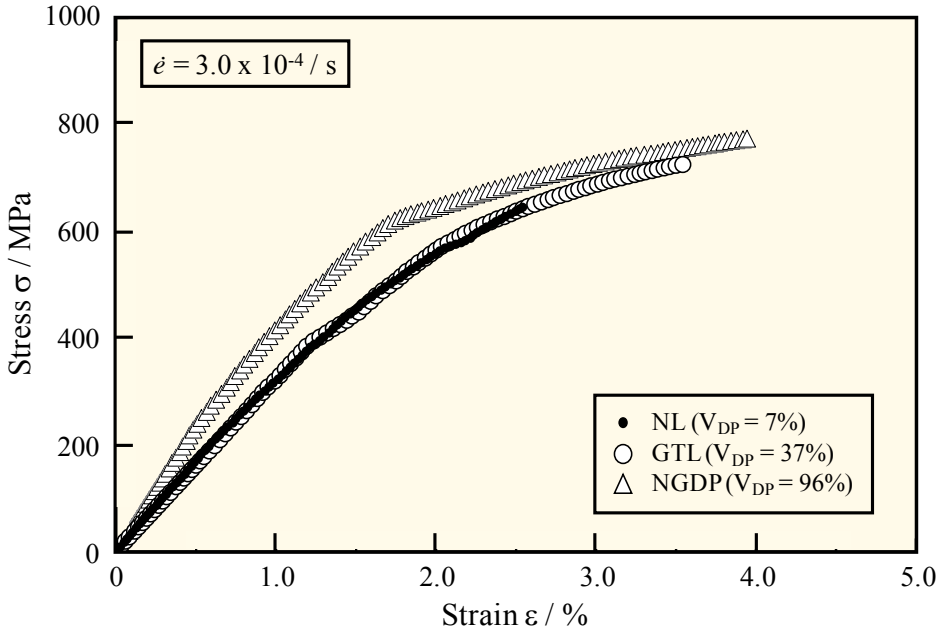

Fig. 1-17. *In-situ* stress-strain curve of Ti-43Al-4Nb-5V with different volume fractions of β/γ duplex structure at room temperature [43].

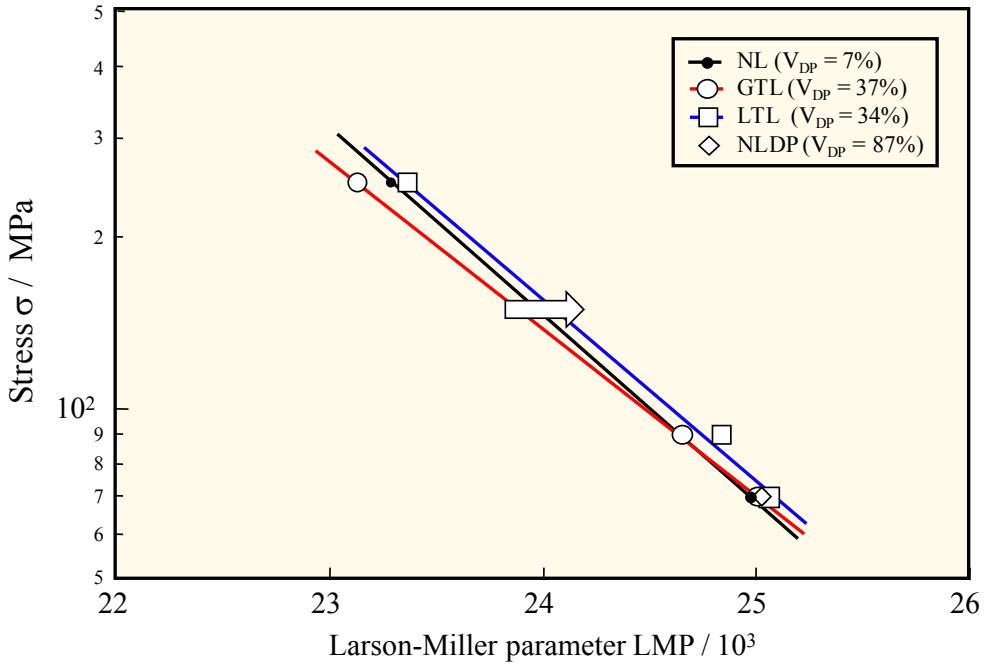

Fig. 1-18. Larson-Miller parameter of Ti-43Al-4Nb-5V with different volume fractions and/or morphology of β/γ duplex structure [44].

Many studies investigated the effects of microstructure, lamellar spacing, process, temperature and/or atmosphere on fatigue crack growth (FCG) behavior in γ-based titanium aluminides alloys. However, mainly investigated alloys do not have β phase. Lately, Dahar *et al*. investigated the FCG of 4822 (as-cast) 4822 and TNM (as-cast and forged) alloys at room temperature [45, 46]. Fully lamellar microstructure shows higher stress intensity threshold than TNM alloy. But this study does not focus on the effect of β phase on fatigue crack growth behavior and it is still not clear how β phase affects these properties in wrought TiAl alloy at ambient and elevated temperatures.

1.5 Objective

The objective of this thesis is to identify the relationship between the microstructure with a particular attention to β phase and the fatigue crack growth properties, especially the stress intensity threshold, the crack growth rate and the maximum stress at the rupture in wrought titanium aluminides alloy at ambient and high temperatures.

1.6 Outline

The flowchart of this thesis is shown in **Figure 1-19**.

Chapter 1 is "General Introduction". This chapter presents the research background, some results, problems and the main objectives of this thesis. Microstructure proposal design of wrought titanium aluminides alloy using β phase is presented. Our previous study show presence of β phase improve toughness and if the morphology is control can also improve creeps. However, no one study this effect of β phase on fatigue crack propagation, especially at high temperature. Finally, the objective and outline of this thesis are detailed.

Chapter 2 is "Phase Equilibria Among β-Ti/α_2-Ti_3Al/γ-TiAl in Ti-Al-M Systems". In this chapter, phases equilibria of simple ternary alloys Ti-Al-M, where M is vanadium or manganese element, is investigated at "relatively lower" temperature, namely between 1073 and 1273 K. Moreover, phases equilibria reassessment at higher temperature will be conducted. The evolution of the β/α(α_2)/γ co-existing region with temperature and the role of α/α_2 ordering transformation will be discussed.

Chapter 3 is "Phase Transformation Involving β-Ti Phase and Microstructure Control of Wrought Alloys". This chapter explores the effect of the different phase transformations on the microstructure of model alloys, based on phase equilibria

determined previously. Some representative microstructures have been designed for the mechanical tests.

Chapter 4 is “Effect of Microstructure on Fatigue Crack Growth Behavior at Ambient Temperature”. In this chapter, the effect of β/γ duplex structure will be investigated at room temperature, both volume fraction V_{DP} and morphology of grain boundaries using microstructures designed in chapter 3 and also microstructures from another alloy system for comparison.

Chapter 5 is “Effect of Microstructure on Fatigue Crack Growth Behavior at Elevated Temperatures”. In this chapter, the effect of volume fraction V_{DP} of β/γ duplex structure at high temperature in air will be discussed.

The Chapter 6, “General Conclusions” summarizes the outcome of all chapters and the future work is also explained.

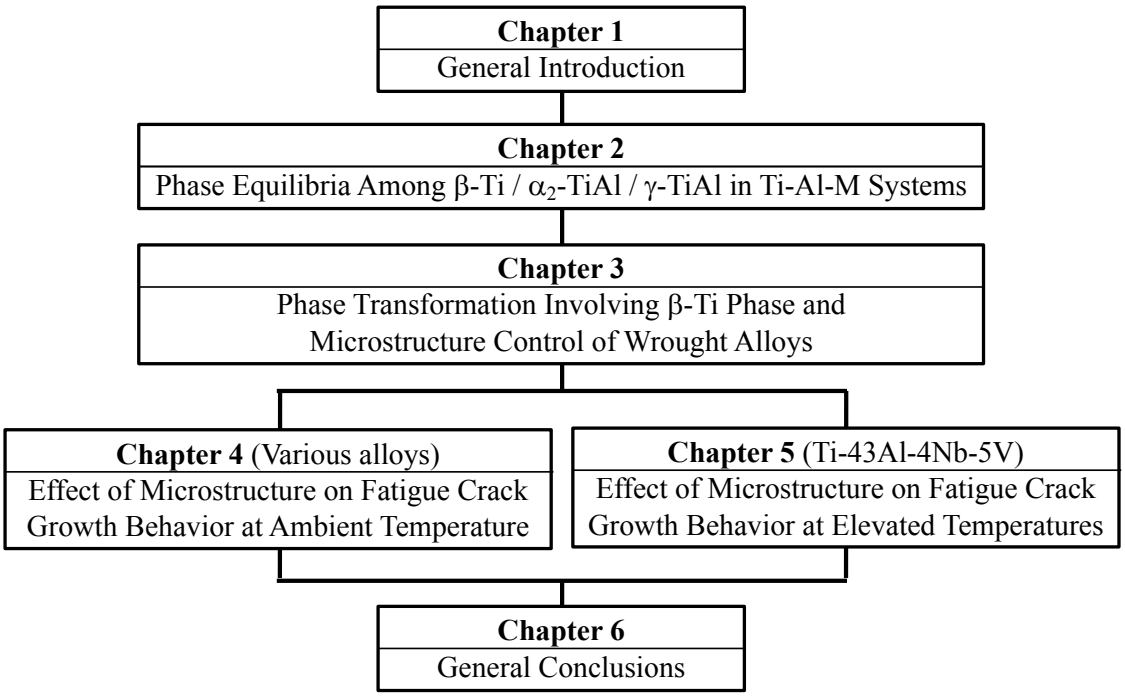

Fig. 1-19. Flowchart of the thesis.

References

[1] International Civil Aviation Organization (ICAO).
https://www.icao.int/sustainability/Pages/Facts-Figures_WorldEconomyData.aspx

[2] Airbus Global Market Forecast 2017-2036 Growing Horizons, pp 8.

[3] IATA Roadmap Technology, 4th edition, June 2013, pp 8.

[4] ICAO assembly – 39th session, report of the executive committee, 2016/10/06.

[5] Energy Information Administration (EIA).
https://www.eia.gov/dnav/pet/hist/LeafHandler.ashx?n=pet&s=ema_eppk_pwg_nus_dpg&f=m

[6] J. D. Anderson, Aircraft Performance and Design, 1st Ed., McGraw-Hill Education (1998)

[7] B. P. Bewlay, S. Nag, A. Suzuki and M. J. Weimer, TiAl alloys in commercial aircraft engines, Materials at High Temperatures 33, n°4-5 (2016) 549-559.

[8] Boeing – Aero QTR_03 2012.

[9] Y. W. Kim, Intermetallic alloys based on gamma titanium aluminides, Journal of Metallurgy 41 (1989) 24-30.

[10] H. Clemens, S. Mayer, Design, processing, microstructure, properties, and ap- plications of advanced intermetallic TiAl alloys, Advanced Engineering Material 15 (2013) 191-215.

[11] M. P. Brady, W. J. Brindley, J. L. Smialek, and I. E. Locci, The Oxidation and Protection of Gamma Titanium Aluminides, Journal of Metallurgy 48 (1996) 46-50.

[12] Y. W. Kim, Ordered intermetallic alloys, part III: Gamma titanium aluminides, Journal of Metallurgy 46 (1994) 30-39.

[13] S. Mayer, P. Erdely, F. D. Fischer, D. Holec, M. Kastenhuber, T. Klein and H. Clemens, Intermetallic β-Solidifying γ-TiAl Based Alloys From Fundamental Research to Application, Advanced Engineering Materials 19 (2007) 1600735.

[14] D. M. Dimiduk, Gamma titanium aluminide alloys – an assessment within the competition of aerospace structural materials, Materials Science and Engineering A263 (1999) 281-288.

[15] J. C. Schuster, M. Palm, Reassessment of the Binary Aluminum-Titanium Phase Diagram, Journal of Phase Equilibria and Diffusion 27 (2006) 255-277.

[16] G. Petzow, G. Effenberg, Aluminium-Titanium-Vanadium, Ternary Alloys 8, VCH, Weinheim, Germany (1993) 426-445.

[17] A. Suzuki, M. Takeyama, T. Matsuo, Transmission electron microscopy on the phase equilibria among β, α and α_2 phases in Ti-Al binary system, Intermetallics 10 (2002) 915-924.

[18] F. Appel, J. D. H. Paul, M. Oehring, Gamma titanium aluminide alloys: science and technology, first ed., Wiley-VCH, 2011.

[19] R. Kainuma, M. Palm, G. Inden, Solid Phase Equilibria in the Ti-rich Part of the Ti-Al System, Intermetallics 2 (1994) 321-332.

[20] T.B. Massalski, K. Muraleedharan, The Current Status of Ti-Al and Al-Li Binary Phase Diagrams, Advanced Light Alloys and Composites, R. Ciach, Ed., Kluwer Academic Publishers, Dordrecht, The Netherlands, NATO ASI Series 3, High Technology 59 (1998) 1-10.

[21] Y. W. Kim, D. M. Dimiduk, Progress of the understanding of gamma titanium aluminides, Journal of Metallurgy 43 (1991) 40-47.

[22] A. Denquin, S. Naka, Phase transformation mechanisms involved in two phase TiAl-based alloy – I. Lamellar structure formation, Acta Mater. 44 (1996) 343-352.

[23] J.M. Blackburn, The science technology and application of titanium, Pergamon Press, New York (1970).

[24] S. Zghal, S. Naka, A. Couret, A Quantitative TEM Analysis of the Lamellar Microstructure in TiAl Based Alloys, Acta Materialia 45 (1997) 3005-3015.

[25] T. Voisin, J. P. Monchoux, M. Thomas, C. Deshayes, A. Couret, Mechanicals properties of the TiAl IRIS Alloy, Metal. and Mater. Trans. 47A (2016) 6097-6108.

[26] W. J. Zhang, B. V. Reddyn S. C. Deevi, Physical properties of TiAl-base alloys, Scripta Mater. 45 (2001) 645-651.

[27] H. Jabbar, J. P. Monchoux, M. Thomas, F. Pyczak, A. Couret, Improvement of the creep properties of TiAl alloys densified by Spark Plasma Sintering, Intermetallics 46 (2014) 1-3.

[28] G. Hénaff, A. L. Gloanec, Fatigue properties of TiAl alloys, Intermetallics 13 (2005) 543-558.

[29] Y. W. Kim, Effects of microstructure on the deformation and fracture of γ-TiAl alloys, Mater. Sci. and Eng. A192/193 (1995) 519-533.

[30] H. Zhu, D. Seo, K. Maruyama, Microstructural Characteristics and Creep Behavior of 45XD TiAl Alloys, Mater. Trans. 45 (2004) 2618-2621.

[31] Y. W. Kim, S. L. Kim, Effects of microstructure and C and Si additions on elevated temperature creep and fatigue of gamma TiAl alloys, Intermetallics 53 (2014) 92-101.

[32] V. T. Witusiewicz, A. A. Bondar, U. Hecht, S. Rex, T. Y. Velikanova, The Al–B–Nb–Ti system III. Thermodynamic re-evaluation of the constituent binary system Al–Ti, Journal of Alloys and Compounds 465 (2008) 64–77.

[33] A. Denquin, Z. Huvelin, L. Signori, A. Bachelier-Locq, M. Perrut, S. Naka, Influence of Si and C additions on microstructure and mechanical properties of the Ti-43.5Al-1Mo-4Nb-0.1B alloy, Materials at High Temperatures 33 (2016) 542-548.

[34] T. Tetsui, K. Shindo, S. Kobayashi, M. Takeyama, A newly developed hot worked TiAl alloy for blades and structural components, Scripta Materialia 47 (2002) 399-403.

[35] M. Takeyama and S. Kobayashi, Physical metallurgy for wrought gamma titanium aluminides microstructure control through phase transformations, Intermetallics 13 (2005) 993–999.

[36] H. Nakashima, M. Takeyama, Phase Stability of β phase in the TiAl alloys with the Combined Addition of M Elements, Materials Research Society Symposia Proceedings 1760 (2015).

[37] H. Nakashima, Phase equilibria in the quaternary TiAl alloys with the combined Addition of substitutional Elements – phase stability of high and low-temperature β-Ti phase, Doctor Thesis, Tokyo Institute of Technology, 2015.

[38] E. Schwaighofer, H. Clemens, S. Mayer, J. Lindemann, J. Klose, W. Smarsly, V. Güther, Microstructural design and mechanical properties of a cast and heat-treated intermetallic multi phase-TiAl based alloy, Intermetallics 44 (2014) 128-140.

[39] T. Leitner, M. Schloffer, S. Mayer, J. Eßlinger, H. Clemens, R. Pippan, Fracture and R-curve behavior of an intermetallic β-stabilized TiAl alloy with different nearly lamellar microstructures, Intermetallics 53 (2014) 1-9.

[40] S. Oinuma, 鍛造 TiAl 基合金のβ-Ti 相を利用した組織制御による高靭性化, Master Thesis, Tokyo Institute of Technology, 2010.

[41] H. Nakashima, 鍛造 TiAl 基合金のβ相を利用した組織制御とき裂伝播特性, Master Thesis, Tokyo Institute of Technology, 2011.

[42] S. Usui, Microstructure Control and In-situ observation of high temperature tensile deformation behavior of quaternary TiAl alloy, Master Thesis, Tokyo Institute of Technology, 2014.

[43] T. Nakamura, 鍛造 TiAl 基合金の疲労き裂進展特性に及ぼす組織の影響, Master Thesis, Tokyo Institute of Technology, 2017.

[44] H. Wakabayashi, TiAl 基合金のクリープ変形に及ぼす組織安定性の影響, Master Thesis, Tokyo Institute of Technology, 2016.

[45] M. S. Dahar, S. A. Tamirisakandala, J. J. Lewandowski, Fatigue crack growth and fracture behavior of as-cast Ti-43.5Al-4Nb-1Mo-0.1B (TNM) compared to Ti-48Al-2Nb-2Cr (4822), Intermetallics 91 (2017) 158-168.

[46] M. S. Dahar, S. A. Tamirisakandala, J. J. Lewandowski, Evolution of fatigue crack and fracture behavior in gamma titanium aluminide Ti-43.5Al-4Nb-1Mo-0.1B (TNM) forgings, Inter. J. of Fatigue 111 (2018) 54-69.

Chapter 2

Phase Equilibria Among β-Ti/α_2-Ti_3Al/γ-TiAl in Ti-Al-M Systems

2.1 Introduction

In **Chapter 1**, it has been clarified that bcc β phase is used for processing at high temperature due to its high ductility. Thus, it has been showed that LPT blades have been manufactured using wrought process and implemented in the PW1100G engines. It has been also reported that during cooling the β phase could be partially decomposed into the ordered ω phase and leads to the embrittlement of the materials [1]. Clemens' group also reported on the effect of the ω phase [2]. Therefore, many researchers consider the β phase as a detrimental phase for mechanical properties in γ-TiAl alloy and try to reduce its volume fraction at service temperature. However, recently few studies focused on the relationship between microstructures containing the β phase and mechanical properties, and it is found that controlling the morphology of β phase could be effective on some mechanicals properties.

In this aim, understanding the phase equilibria of Ti-Al-M ternary alloys where M is a β-stabilizer, such as V^{th} (V, Nb, Ta), VI^{th} (Cr, Mo, W) and VII^{th} (Mn, Re) elements is critical to control the microstructure. Almost twenty years ago, these phase equilibria have been intensively investigated at high temperatures (T > 1473 K) to improve the wrought process [3-6]. However, the data at lower temperatures, closer to the target

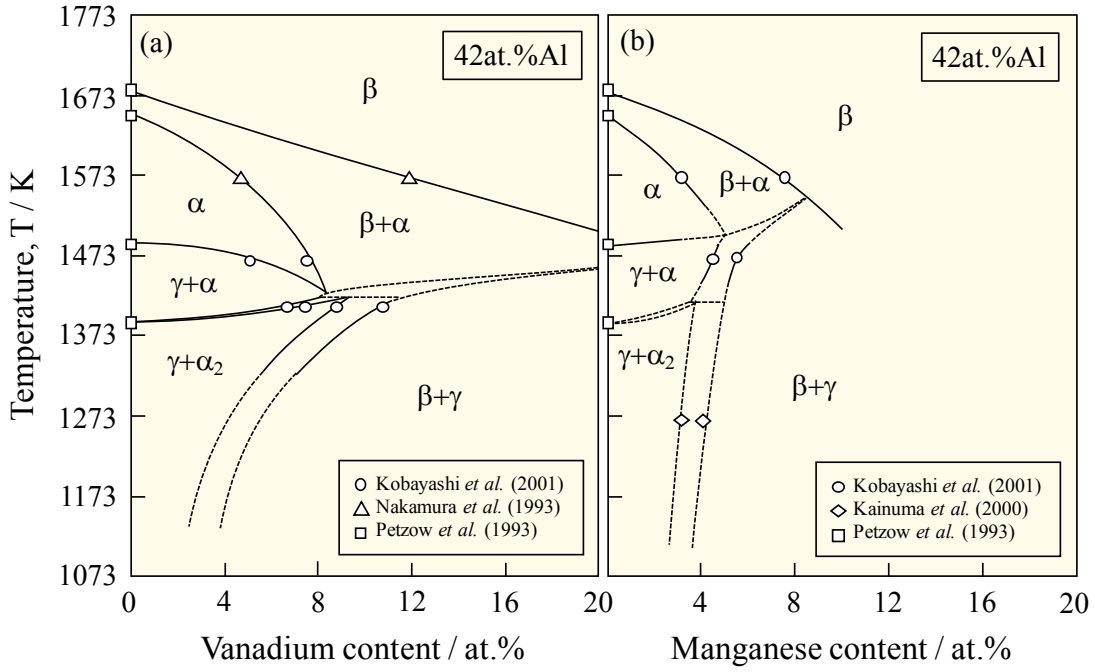

Fig. 2-1. Reported vertical section of (a) Ti-Al-V and (b) Ti-Al-Mn system at 42Al at.% [8].

service temperature are limited (T < 1373 [7]. **Figure 2-1** shows the reported vertical section of Ti-Al-V and Ti-Al-Mn ternary system at 42Al (at.%) [8]. It can be seen that large range of temperatures has not been experimentally investigated yet.

At high temperature, a three-phase coexisting region of β+α+γ exists in all TiAl ternary systems. However, at lower temperature the tie triangle becomes β+α_2+γ with ordered α_2 phase (1st order). This phenomenon has been described by Takeyama and Kikuchi [9]. According to the effect of M element on the relative stability between α/α_2, it could be either a transition peritectoid transformation when α_2 is stabilized against α or a ternary eutectoid reaction in opposite case as illustrated in **Figure 2-2**. Takeyama *et al.* were the first to demonstrate that in case of Ti-Al-Nb system, niobium stabilizes the α_2 phase against the α phase and confirmed the existence of an α_2 island above the $\alpha \leftrightarrow \alpha_2$ congruent temperature in binary system as shown in **Figure 2-3** [10]. Kobayashi *et al.* studied the phase equilibria in ternary system and paid attention to the $\alpha \rightarrow \beta + \gamma$ decomposition at intermediate temperatures and found that in case of vanadium, a transition peritectoid transformation also takes place [8]. However, the effect of chromium or manganese elements on the α/α_2 relative stability has not been clarified yet. Therefore, it is important to understand how the phase stability between α/α_2 affects the microstructure control based on what kind of phase transformation takes place.

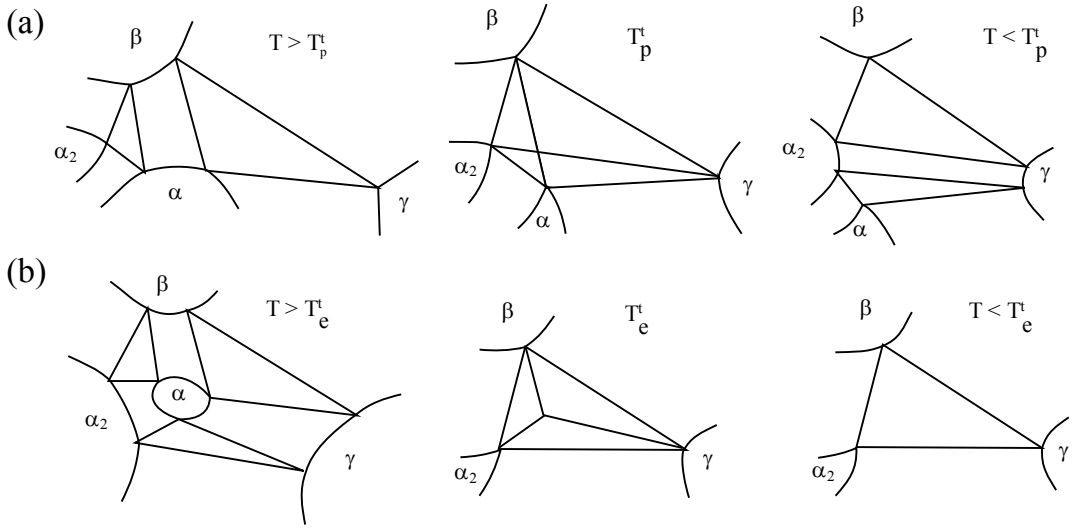

Fig. 2-2. Effect of M element on the relative stability between α/α_2 in case of (a) α_2 is stabilize against a with a transition peritectoid reaction: $\alpha + \beta \rightarrow \alpha_2 + \gamma$ and (b) α is stabilized against α_2 with a ternary euctectoid reaction: $\alpha \rightarrow \beta + \alpha_2 + \gamma$ [9].

Recently, Nakashima *et al.* demonstrated the strong effect of the combination of two β-stabilizer elements [11]. As a part of the Japanese SIP (Strategic Innovation Promotion Program) project, in order to refine our calculation database for quaternary Ti-Al-M1-M2 alloy and taking into account the effect of interstitial elements as oxygen and carbon, our research group is conducting basic experimental investigations on simple binary and ternary systems [12-14].

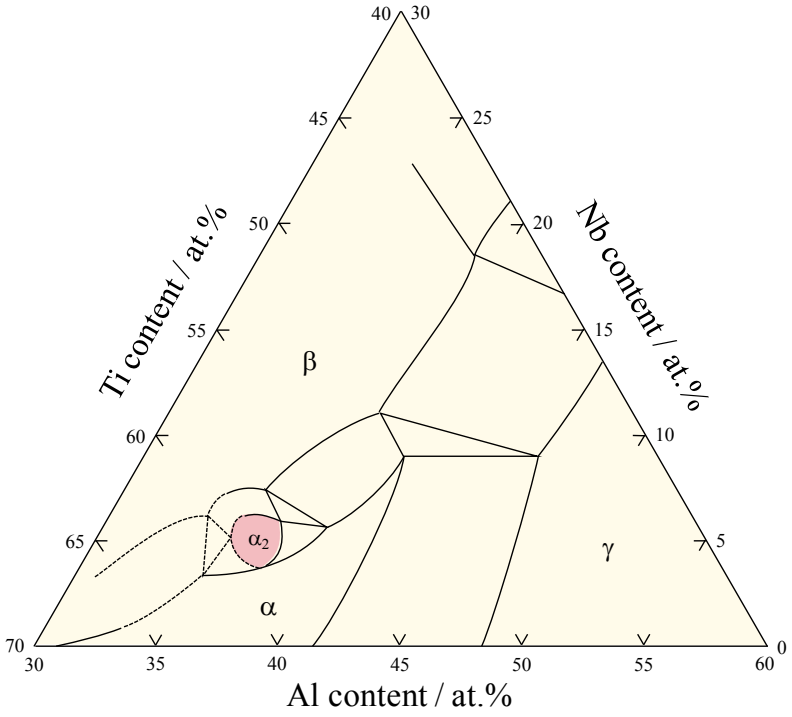

Fig. 2-3. Reported isothermal section of Ti-Al-Nb system at 1473 K with an existence of α_2 island above the α congruent temperature [9].

Thus, the objective of the chapter is to identify the phase equilibria at low temperature in Ti-Al-Mn and Ti-Al-V ternary system, below 1473 K and to investigate the α_2/α relative stability effect on microstructure of manganese system comparing to vanadium system. Moreover, a reassessment at intermediate and higher temperatures is carried out.

2.2 Experimental procedures

The experimental procedures are shown in **Figure 2-4**. Two different Ti-Al-M ternary systems have been investigated: Ti-Al-V and Ti-Al-Mn within a composition range of Ti-(36-42)Al-(3-9)V and Ti-(36-42)Al-(3-5)Mn in at.%, respectively. Each alloy is denoted by Al and M contents, i.e. 42-3V correspond to Ti-42Al-3V (at.%).

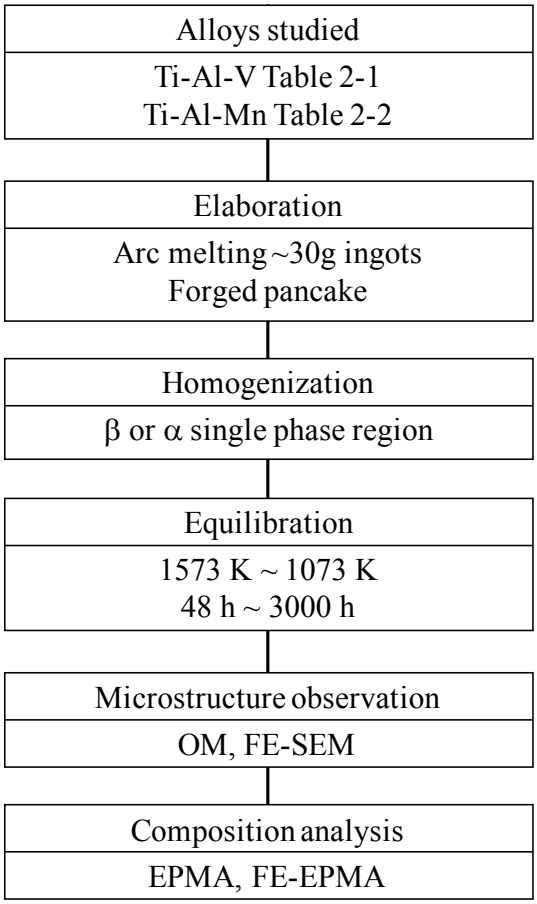

Fig. 2-4. Flowchart of experimental procedures for determination of phase equilibria in Ti-Al-V and Ti-Al-Mn systems at intermediate temperatures.

Button ingots, of around 30 g weight, were prepared from pure elements (Al, Ti, V or Mn) using an arc melting with a non-consumable tungsten electrode in argon atmosphere. The starting materials were of the following purity: rod-shaped titanium (99.99%), aluminum grains (99.99%), vanadium grains (99.9%) and manganese grains (99.9%). Each alloy was melted at least four times in order to homogenize the composition. Some pieces were taken from forged pancake and were used in the next chapters (for microstructures control and mechanicals tests).

The homogenization heat treatment was conducted either in the α or the β single phase in order to erase microstructure variations and possible segregation. Each as-cast or as-forged specimen was wrapped with Ta-foil and then heat treated. Homogenization heat treatments were done between 1723 K and 1473 K for 30 min to 1 h under argon atmosphere using superkanthal furnace for high temperatures ($T \geq 1573$ K) or using

siliconate furnace for lower temperature (T < 1573 K), followed by water quench.

Subsequently, the homogenized specimens were wrapped again with Ta-foil, and then sealed in an evacuated quartz capsule (P < $4x10^{-2}$ Pa), backfilled with argon and with small Ta foils as oxygen getter. Different sets of these quartz tubes were equilibrated between 1573 K and 1073 K up to 2200 h as shown in **Table 2-2** in either kantal (T < 1373 K) or siliconate (T ≥ 1373 K) furnaces. After annealing, the specimens were water quenched.

Table 2-2. Nominal compositions and heat treatment conditions of the Ti-Al-V and Ti-Al-Mn alloys.

Composition (at.%)	Heat treatment condition							
	Homogenization	Equilibration						
	Various	1573 K	1473 K	1423 K	1373 K	1273 K	1173 K	1073 K
Ti-36Al-9V	1523 K / 1 h	–	–	4 weeks	–	6 weeks	6 weeks	13 weeks
Ti-39Al-9V	1603 K / 1 h	72 h	–	–	–	6 weeks	6 weeks	13 weeks
Ti-40Al-6.5V*	1723 K / 1 h	48 h	2 weeks	–	–	–	–	–
Ti-42Al-3V	1523 K / 1 h	–	–	4 weeks	–	6 weeks	0.6 ~ 6 weeks	13 weeks
Ti-42Al-5V	1523 K / 1 h	–	–	–	–	6 weeks	0.6 ~ 6 weeks	13 weeks
Ti-42Al-7V	1673 K / 30 min	48 h	2 weeks	–	–	6 weeks	6 weeks	13 weeks
Ti-42Al-8V*	1523 K / 2 h / FC	–	–	–	–	6 weeks	6 weeks	9 weeks
Ti-36Al-5Mn	1673 K / 30 min	48 h	–	4 weeks	4 weeks	4 ~ 8 weeks	4 ~ 8 weeks	–
Ti-37Al-3.5Mn	1673 K / 30 min	–	2 weeks	4 weeks	4 weeks	–	–	–
Ti-39Al-3Mn	1673 K / 30 min	48 h	–	4 weeks	–	4 ~ 8 weeks	4 ~ 8 weeks	–
Ti-39Al-5Mn	1673 K / 30 min	48 h	–	4 weeks	4 weeks	4 ~ 8 weeks	4 ~ 8 weeks	9 weeks
Ti-42Al-5Mn*	1673 K / 30 min	–	2 weeks	2 weeks	–	–	–	11 weeks

* as-forged alloy

In order to observe the microstructure, as-cast, as-forged, homogenized and equilibrated specimens were mounted using Bakelite tablets. Then, the samples were mechanically polished using emery papers (#400, #800 and #1200). Finally, the specimens were electro-polished in a solution of perchloric acid (90 vol.% Ethanol, 6 vol.% $HClO_4$, 4 vol.% H_2O). Electro-polishing conditions were 3 mA/mm^2, 243 K and 60 seconds. The specimens were examined using a Leica OM (Optical Microscope), and then using a JEOL JSM-7000F FE-SEM (Field Emission Scanning Electron Microscope) with an acceleration voltage of 15 kV and a working distance of 10 mm.

In order to analyze the composition of the phases, previous equilibrated specimens were re-mechanically polishing using emery papers (#400, #800, #1200 and #2000), polished by diamond paste with size of 3 and then 1 μm followed by colloidal silica with a size of 0.05 μm. The different phases were analyzed by using either a JEOL EPMA (Electron Probe MicroAnalyser) under the condition of 20 kV and 20 nA with a probe

diameter of 0 μm or JEOL FE-EPMA (Field Emission Electron Probe MicroAnalyser) under the condition of 20 kV and 20 nA with a probe diameter of 0 μm. The phase compositions were determined by averaging the EPMA data from 10 points for each phase without included aberrant data, e. g. total weight percent 100 ± 2 %. The conditions used for EPMA and FE-EPMA are shown in **Table 2-2**. Homogenized 42-3V alloy and homogenized 39-5Mn alloy were used as standard samples for all analyzes.

Table 2-2. Analyzed conditions for each element in EPMA and FE-EPMA.

Equipment	Element	Channel	Analyzing crystal	Characteristic X-ray	Analysis condition			Back /mm	
					Acceleration voltage / kV	Beam current / nA	Dwell time / ms	(-)	(+)
EPMA	Ti	4	PETJ	Kα	20	20	200	5	5
	Al	2	TAP	Kα				7	3
	V	3	LIFH	Kα				5	5
	Mn	3	LIFH	Kα				4	4
FE-EPMA	Ti	3	PETJ	Kα	20	20	200	5	5
	Al	2	TAP	Kα				7	3
	V	1	LIFH	Kα				5	5
	Mn	1	LIFH	Kα				4	4

Due to the martensitic microstructure of 39-5Mn, different beam diameters were used in order to eliminate laths effect and the results for are shown in **Figure 2-5**. Despite a small change between 0 and 2 μm (1500 to 1520 cps), there was no significant difference observed by increasing the diameter from 0 to 10 μm, thus, diameter 0 μm were used for all experiments. An example of quantitative analysis performed on these systems is shown in **Figure 2-6** along with the analysis range.

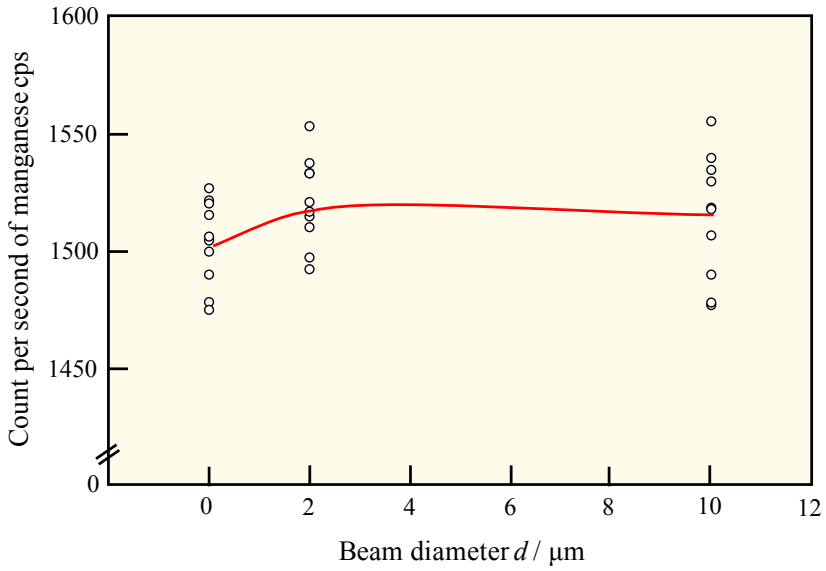

Fig. 2-5. Change of count per second of manganese in homogenized β phase of 38.1-3.7Mn alloy with beam diameter.

A JEOL JEM 2010 Transmission Electron Microscope (TEM), operated at an acceleration voltage of 200 kV, was used to distinguish α and α_2 phases based the presence of anti phase boundaries (APB). TEM foil with less than 150 nm in thickness and 3 mm in diameter were machined and then mechanically polished followed by twin-jet polishing in a solution of ethanol with 6 vol.% perchloric acid at 20 V at 253 K.

The error bars used in this chapter for the results are determined using standard deviation; the method is described in **Appendix A1**.

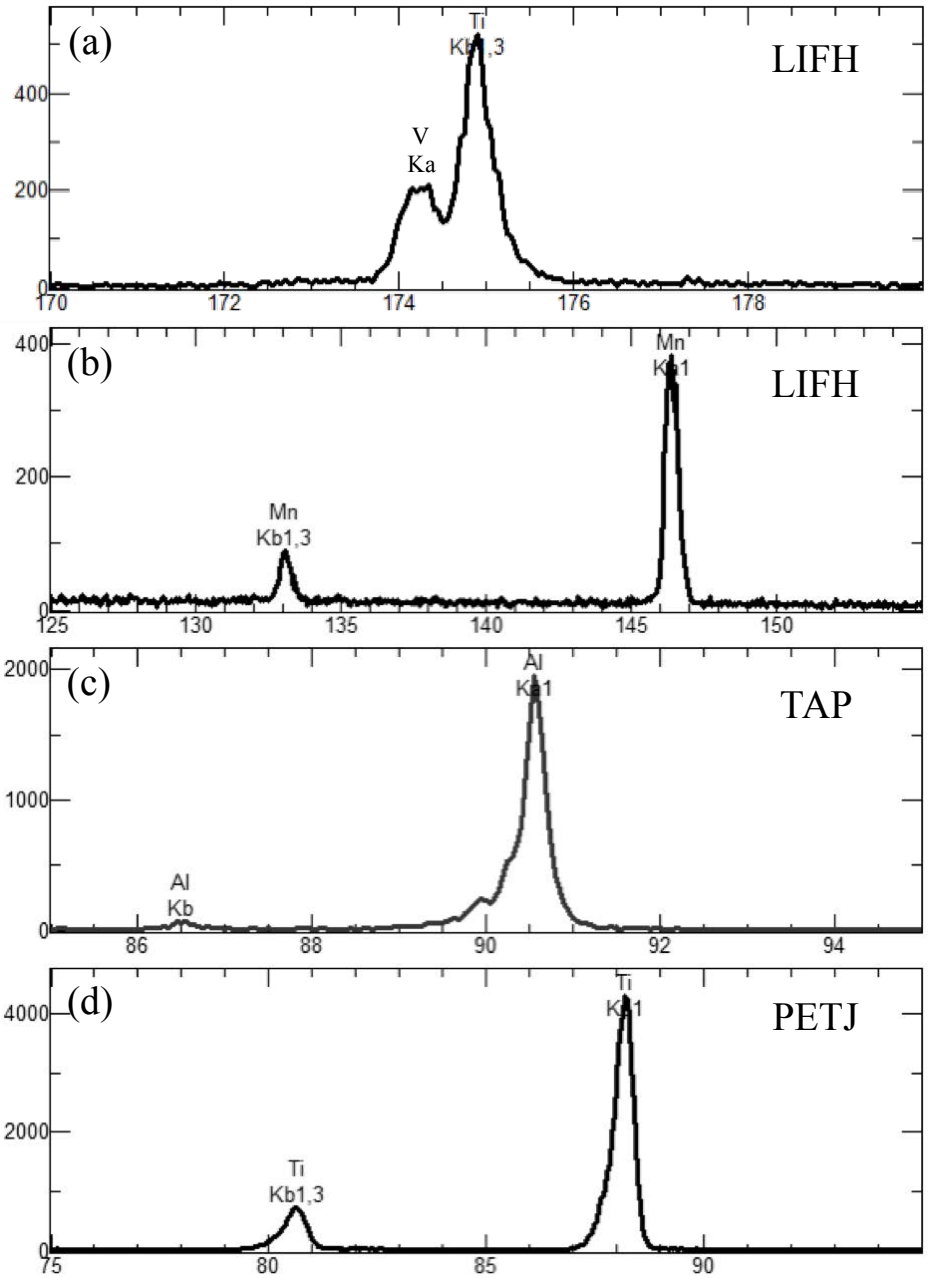

Fig. 2-6. Qualitative analysis of ternary system elements with (a) vanadium, (b) manganese, (c) aluminum and (d) titanium. (a) and (b-d) analysis were conducted on two different samples.

2.3 Ti-Al-V ternary system

2.3.1 Change in microstructure with vanadium addition

(A) As-cast and as-forged microstructures

The BSE (backscattered electron) images of the as-cast microstructures (36-9V, 39-9V, 42-3V, 42-5V and 42-7V) and as-forged (40-6.5V and 42-8V) are shown respectively in **Figure 2-7 and 2-8**.

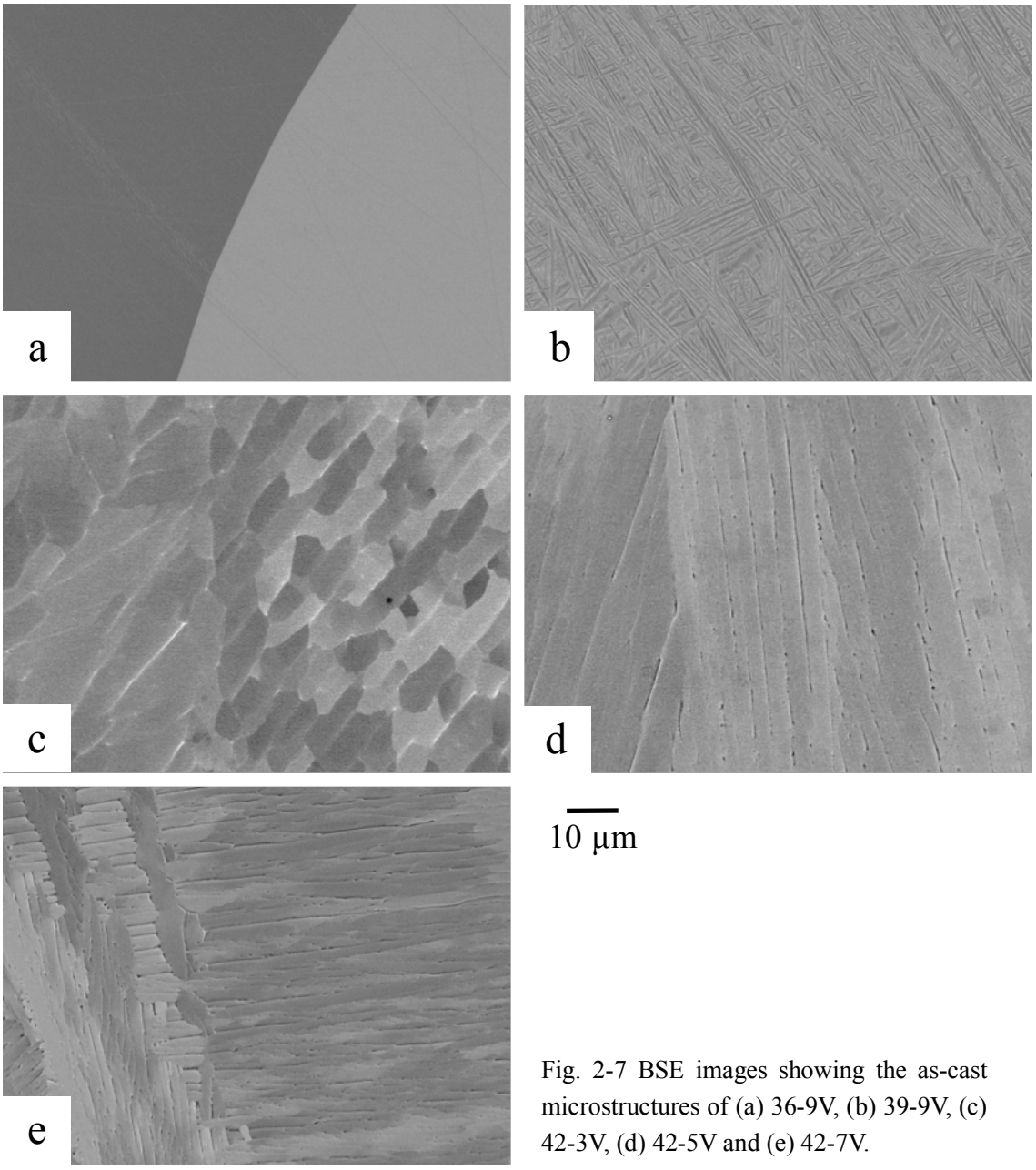

Fig. 2-7 BSE images showing the as-cast microstructures of (a) 36-9V, (b) 39-9V, (c) 42-3V, (d) 42-5V and (e) 42-7V.

The as-cast microstructure of 36Al-9V showed massive α phase at the center and at the top of the ingot (**Fig. 2-7 (a)**) and martensitic transformed on the bottom of the ingot in contact with copper crucible where the cooling rate was higher whereas 39Al-9V showed Widmanstädten microstructure from the top to the bottom of the ingot (**Fig. 2-7 (b)**). The other compositions showed plate-like and equiaxed α_2 grains that had grown in the direction of heat flow for high aluminum content (**Fig. 2-7 (c-e)**).

The as-forged microstructures showed elongated α_2/γ colony grains perpendicular to the forged direction surrounded by γ and β phases. In case of 40-6.5V alloy, γ grains were globular (**Fig. 2-8 (a)**) but in 42Al-8V, higher magnification image showed plate γ grains (**Fig. 2-8 (b)**).

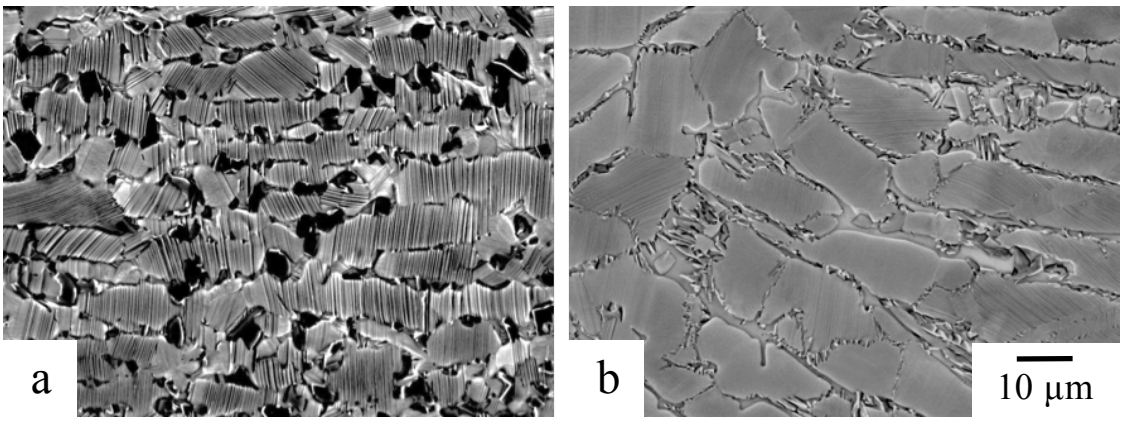

Fig. 2-8 BSE images showing the as-forged microstructures of (a) 40-6.5V and (b) 42-8V.

(B) Homogenized microstructures

The homogenization heat treatments were conducted either in α or β single region phase. BSE images of the microstructures are shown on **Figure 2-9 and 2-10**, respectively.

The heat treatments were conducted in or near α single region for alloys that contains a high aluminum content (42-3V, 42-5V and 42-8V). 42-3V and 42-5V alloys showed α grains with a grains size larger than 1 mm (**Fig 2-9 (a, b)**). In case of 42-8V alloy, homogenization did not reach the α-single phase and explained the presence of β phase and few γ grains along the colony boundaries (**Fig 2-9 (c)**). The residual volume fraction of β phase was less than 5 %. However, the α grains showed a globular morphology, indicating that the initial as-forged microstructure has been erased during the heat treatment.

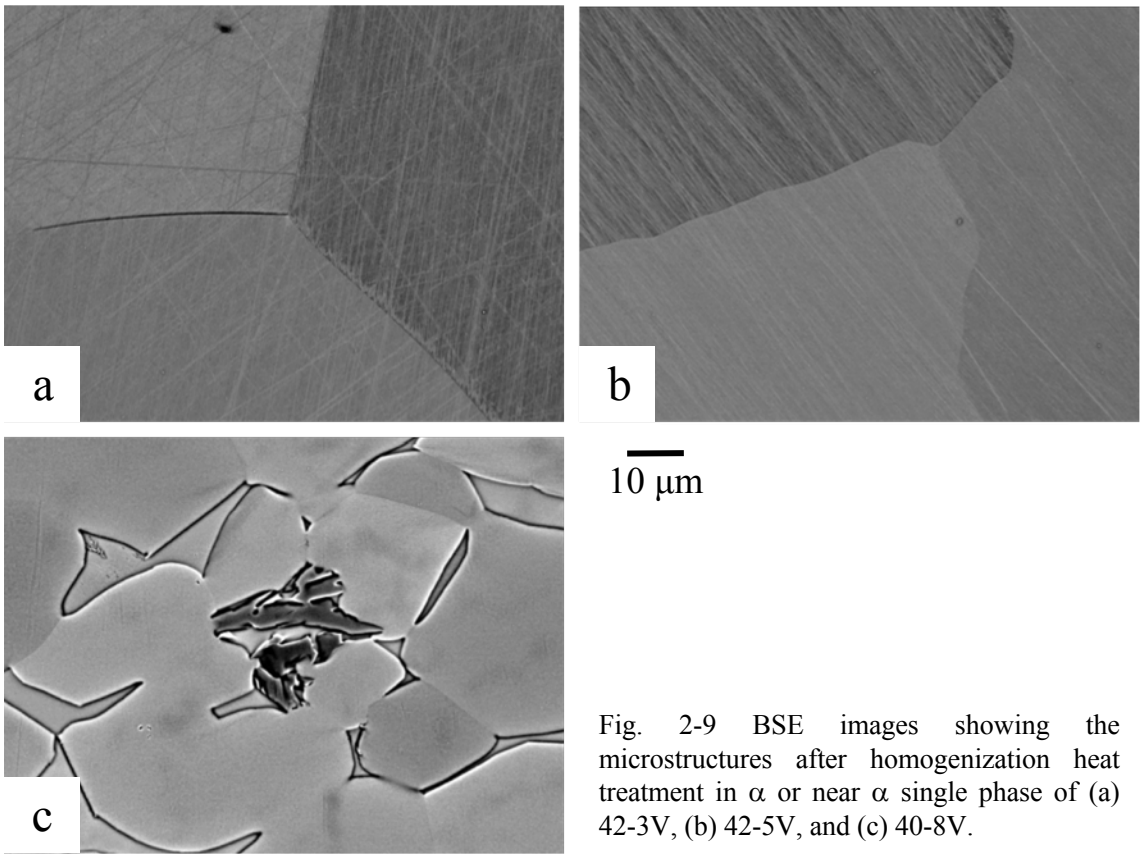

Fig. 2-9 BSE images showing the microstructures after homogenization heat treatment in α or near α single phase of (a) 42-3V, (b) 42-5V, and (c) 40-8V.

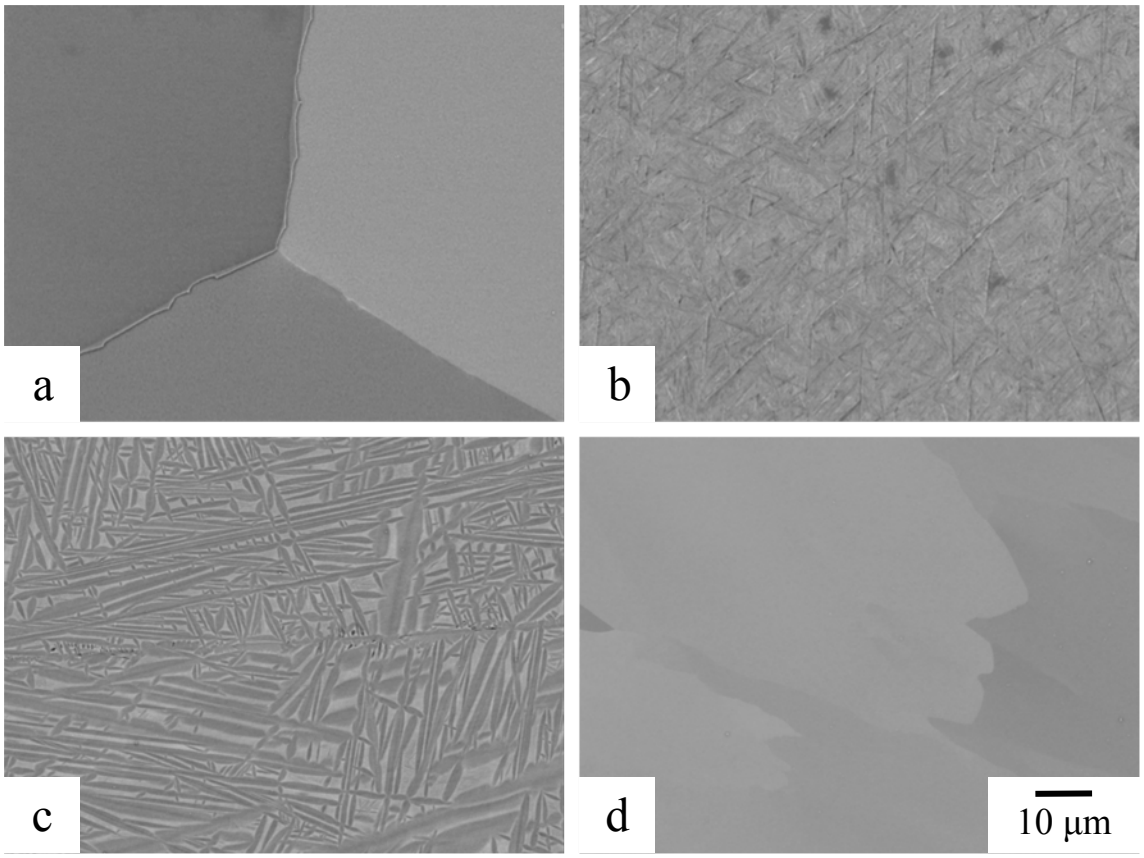

Fig. 2-10 BSE images showing the microstructures after homogenization heat treatment in β single phase of (a) 36-9V, (b) 39-9V, (c) 40-6.5Al (d) 42-7V.

The others compositions were heat treated in β region. 36-9V presented large α grains due to β → α_m massive transformation (**Fig. 2-10 (a)**) whereas in 42-7V alloy, grains size after homogenization were around 100 μm (**Fig. 2-10 (d)**). 39-9V and 40-6.5V alloys showed a Widmanstädten microstructure (**Fig. 2-10 (b, c)**). This indicates that β → α' martensitic transformation occurred during water quenching and confirmed that the β single phase was formed during homogenization heat treatment.

(C) Equilibrated microstructures

The **Figure 2-11** shows the equilibrated microstructure at 1573 K for 48 to 72 h. 39-9V alloy showed β single phase microstructure with large grains size of about few millimeters **(Fig. 2-11 (a, b)**). 40-6.5V and 42-7V alloys showed α_m grain surrounded by α' Widmanstädten type microstructure after water quenching that indicated β + α two-phase region at high temperature **(Fig. 2-11 (c-f)**). In case of 40-6.5V alloy, α_m grains size was of around 100 μm whereas in 42-7V alloy, α_m phase was spread across the microstructure (thickness around 30 μm).

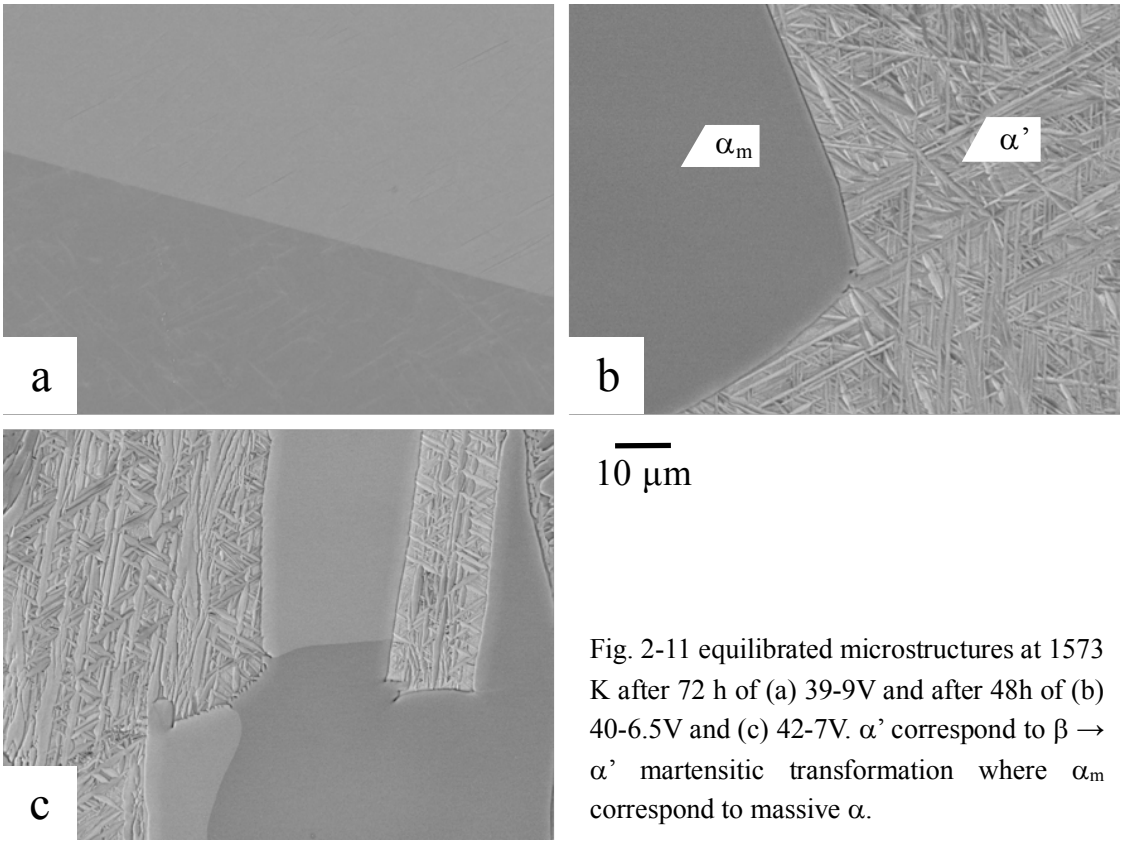

Fig. 2-11 equilibrated microstructures at 1573 K after 72 h of (a) 39-9V and after 48h of (b) 40-6.5V and (c) 42-7V. α' correspond to β → α' martensitic transformation where α_m correspond to massive α.

The equilibrated microstructure at 1473 K for 2 weeks are shown in **Figure 2-12**. 40-6.5V showed large elongated α grains dispersed in β matrix. The difference of contrast of α grains came from the grains' orientation and not from difference in composition (**Fig. 2-12 (a, b)**). 42-7V alloy showed α single phase microstructure.

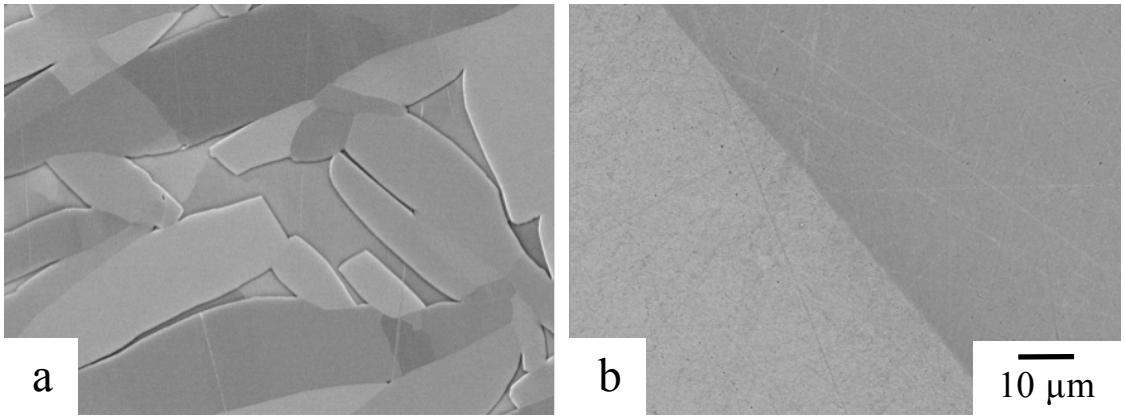

Fig. 2-12 BSE images showing the equilibrated microstructures at 1473 K after 336 h of (a) 40-6.5V and (b) 42-7V.

Figure 2-13 shows the equilibrated microstructure of 36-9V and 42-3V alloys at 1413 K for 4 weeks. 36-9V microstructure consisted of α_2 grains within β matrix. However, the microstructure was not homogenous after heat treatment with some large α_2 grains whereas other regions showed a dispersion of fine α_2 grains. Nevertheless, the difference of microstructure did not affect the phase analysis composition which are presented in the following part. 42-3V alloy showed γ grains within α matrix (**Fig. 2-13 (c, d)**). Coarse γ grains were formed at the grain boundaries while thick γ lamellae in the α grains of the initial microstructure.

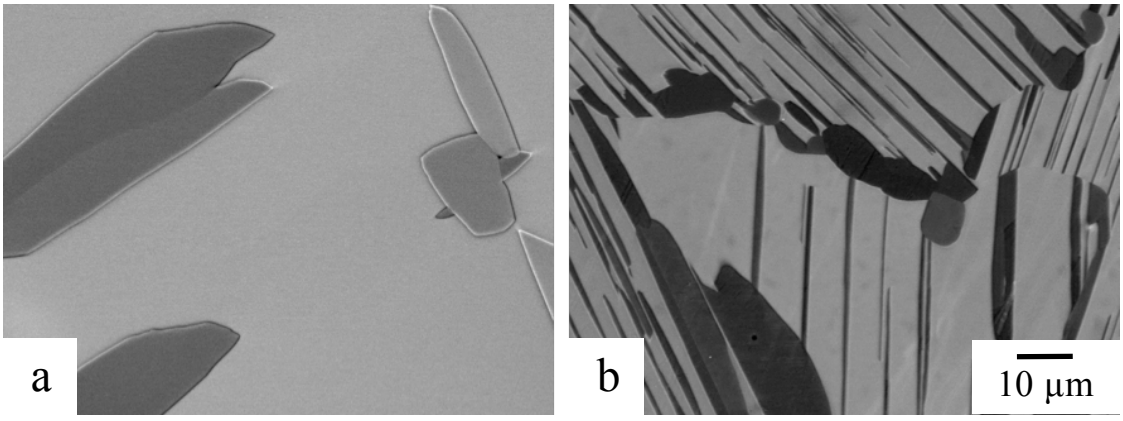

Fig. 2-13 BSE images showing the equilibrated microstructures at 1413 K after 336 h of (a) 36-9V and (b) 42-3V.

Equilibrated microstructure at 1273 K for 6 weeks are shown in **Figure 2-14**. 36-9V alloy showed β+α_2 two phases in a β-based microstructure. On the grain boundaries, continuous α_2 phase precipitated with a thickness of around 20 μm. In the grain interior, fine needle-shaped α_2 grains with a size around 10 μm in length was observed (**Fig. 2-14 (a)**). The difference in contrast that was observed in the BSE images came from the difference in grains orientation. By increasing the aluminum content, the β/α_2/γ three-phase region was reached in 39-9V and also in 42-7V. 39-9V alloy showed α_2 and γ precipitated at the grain boundaries with a thickness of around 5 μm. In the grain interior, fine needle-shaped α_2 grains and globular γ grains were observed (**Fig 2-14 (b)**). High aluminum and low vanadium content alloys showed α_2 + γ two phases region. Both 42-3V and 42-5V alloys showed primary α_2/γ lamellar colony grains. At the grain boundaries, secondary α_2/γ lamellae were produced by cellular reaction (**Fig 2-14 (c, d)**). 42-7V microstructure consisted mainly of γ and β grains with a small fraction of α_2 grains (**Fig. 2-14 (e)**). Coarse γ and α_2 grains were formed at the grain boundaries. Initial α grains transformed into β and γ phases according the sequential decomposition that will be introduced in **Chapter 3**, and therefore the microstructure showed β particles precipitated at the lamellae interface. Finally, 42-8V showed β+γ two phases region with β phase as matrix and globular γ grains with a size of around 15 μm. Microstructure was inhomogeneous with some large β phase areas (**Fig. 2-14 (f)**).

Figure 2-15 shows the different equilibrated microstructure at 1773 K after 6 weeks. Low aluminum and high vanadium content alloys (36-9V and 39-9V) showed β+ α_2 + γ three phases region. The matrix was composed of β phase with distribution of fine needle-shaped α_2 grains and globular γ grains. The grains size of both phases was around 4 μm. By increasing the Al content, the volume fraction of γ phase increased (**Fig. 2-15 (a, b**). The microstructures of 42-3V and 42-5V were similar to that at 1273 K. Both alloys showed primary α_2/γ lamellar colony grains with secondary α_2/γ lamellae at the grain boundaries. However, the cell sizes were smaller than that for higher temperature ones. The kinetics of the cellular reaction at 1173 K will be briefly introduced later in this chapter. 42-7V and 42-8V showed similar microstructure with mainly β and γ phases, however small α_2 grains were found in case of 42-7V composition. In the colony grains, $\alpha+\gamma \rightarrow \beta+\gamma$ transformation took place and within the grain the equilibrated composition is reached. The difference of microstructures between 42-7V and 42-8V alloys can be

explained by the initial microstructure. Indeed 42-7V showed large α/γ colony grains decorated by β/γ cells whereas 42-8V showed initial α grains transformed into β/γ surrounded by initial β phases.

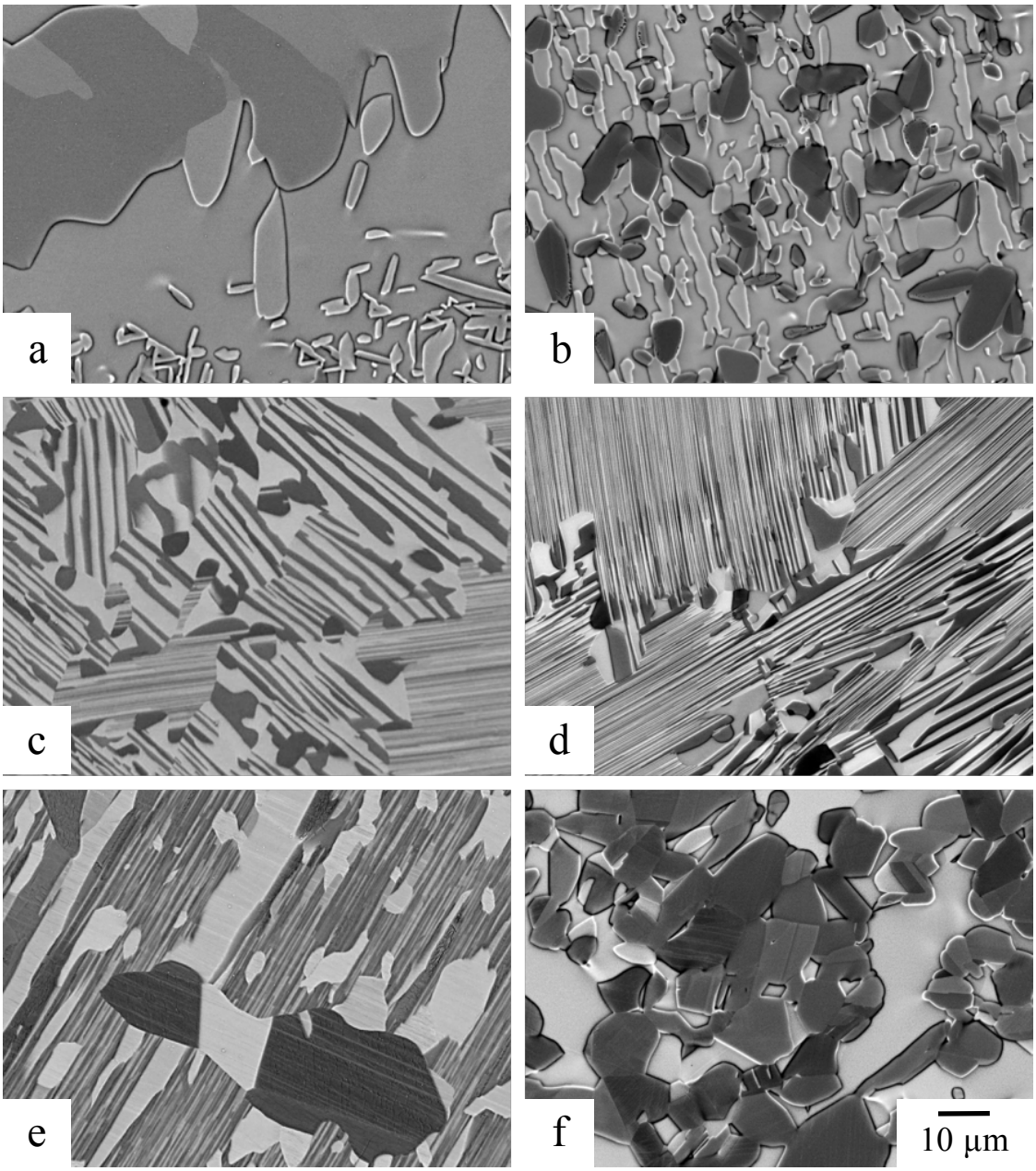

Fig. 2-14 BSE images showing the equilibrated microstructures at 1273 K after 1000 h of (a) 36-9V, (b) 39-9V, (c) 42-3V, (d) 42-5V, (e) 42-7V and (f) 42-8V.

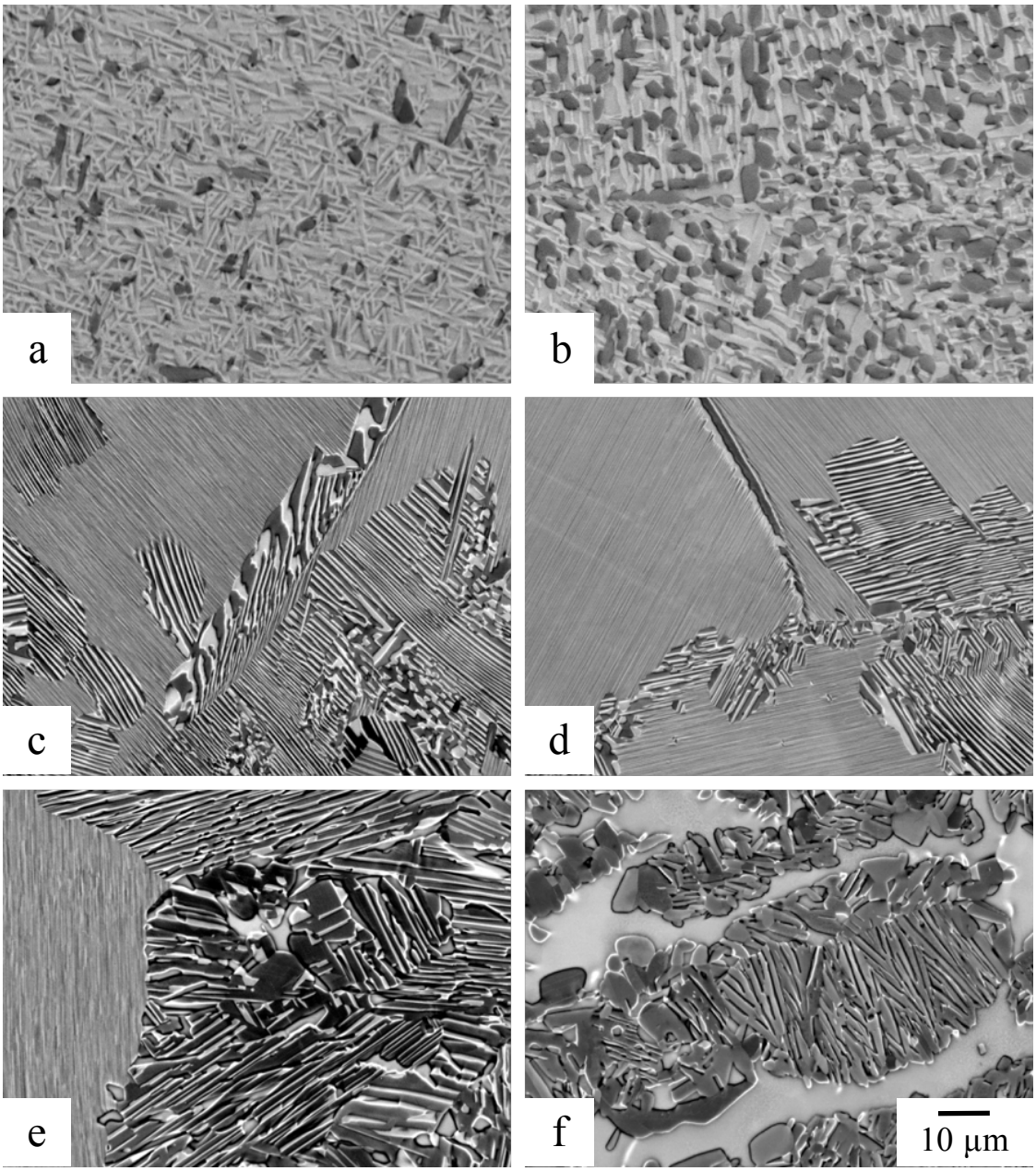

Fig. 2-15 BSE images showing the equilibrated microstructures at 1173 K after 1000 h of (a) 36-9V, (b) 39-9V, (c) 42-3V, (d) 42-5V, (e) 42-7V and (f) 42-8V.

Finally, alloys were heat treated at 1073 K for 1500~2200 h and the microstructures are shown in **Figure 2-16**. The phases in equilibria were as same as that at 1173 K. The major difference was the grains size that was much smaller due to the lower diffusion rate at this temperature. However, it should be noted that in 42-8V alloy, the fraction of β phase decreasing with decreasing temperature. Moreover, some remained colonies were

still observed in this microstructure. The size of some microstructural features was not large enough to be analyzed by EPMA but the phase equilibria have been identified.

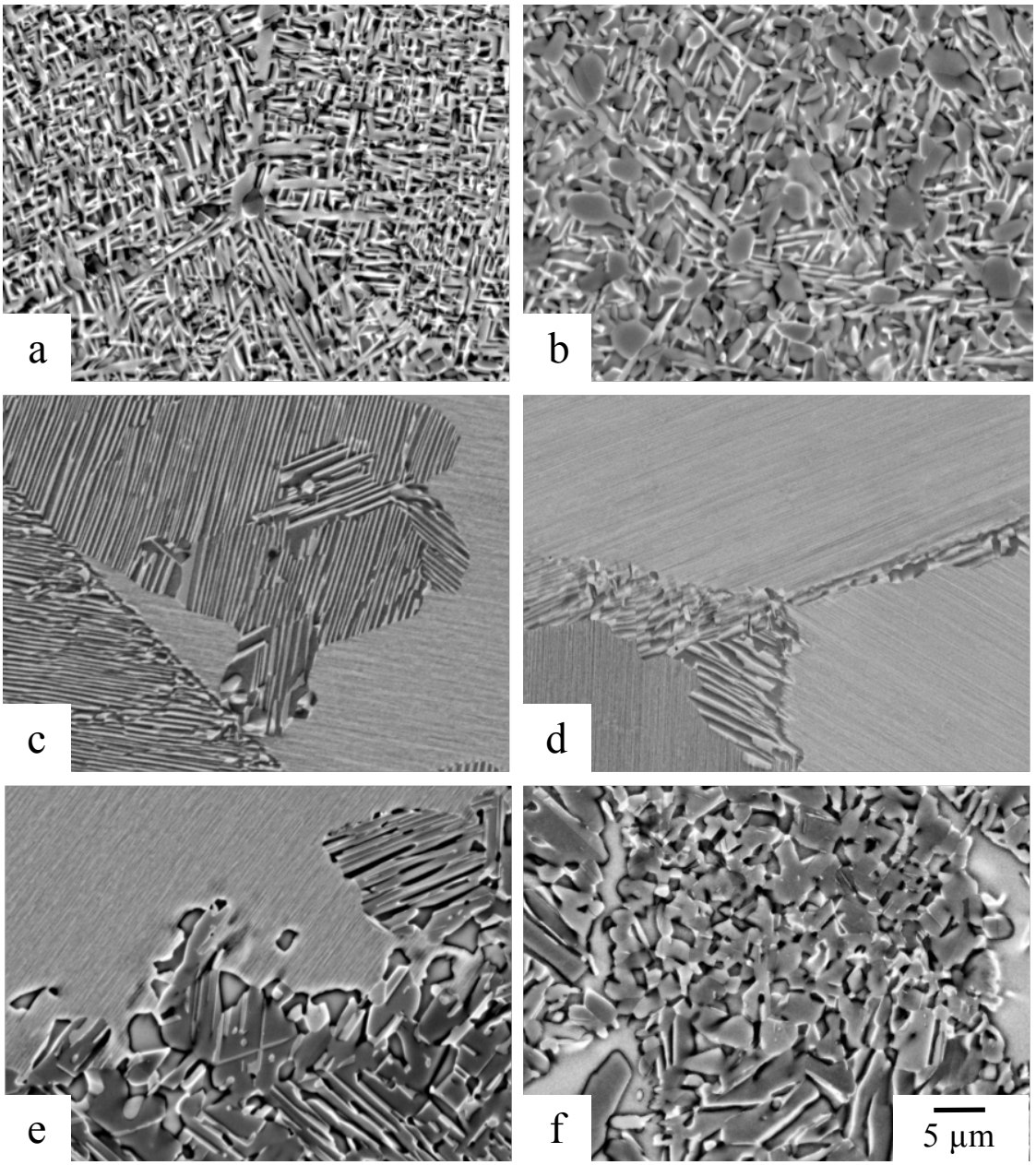

Fig. 2-16 BSE images showing the equilibrated microstructures at 1173 K after 2200 h of (a) 36-9V, (b) 39-9V, (c) 42-3V, (d) 42-5V, (e) 42-7V and (f) 42-8V.

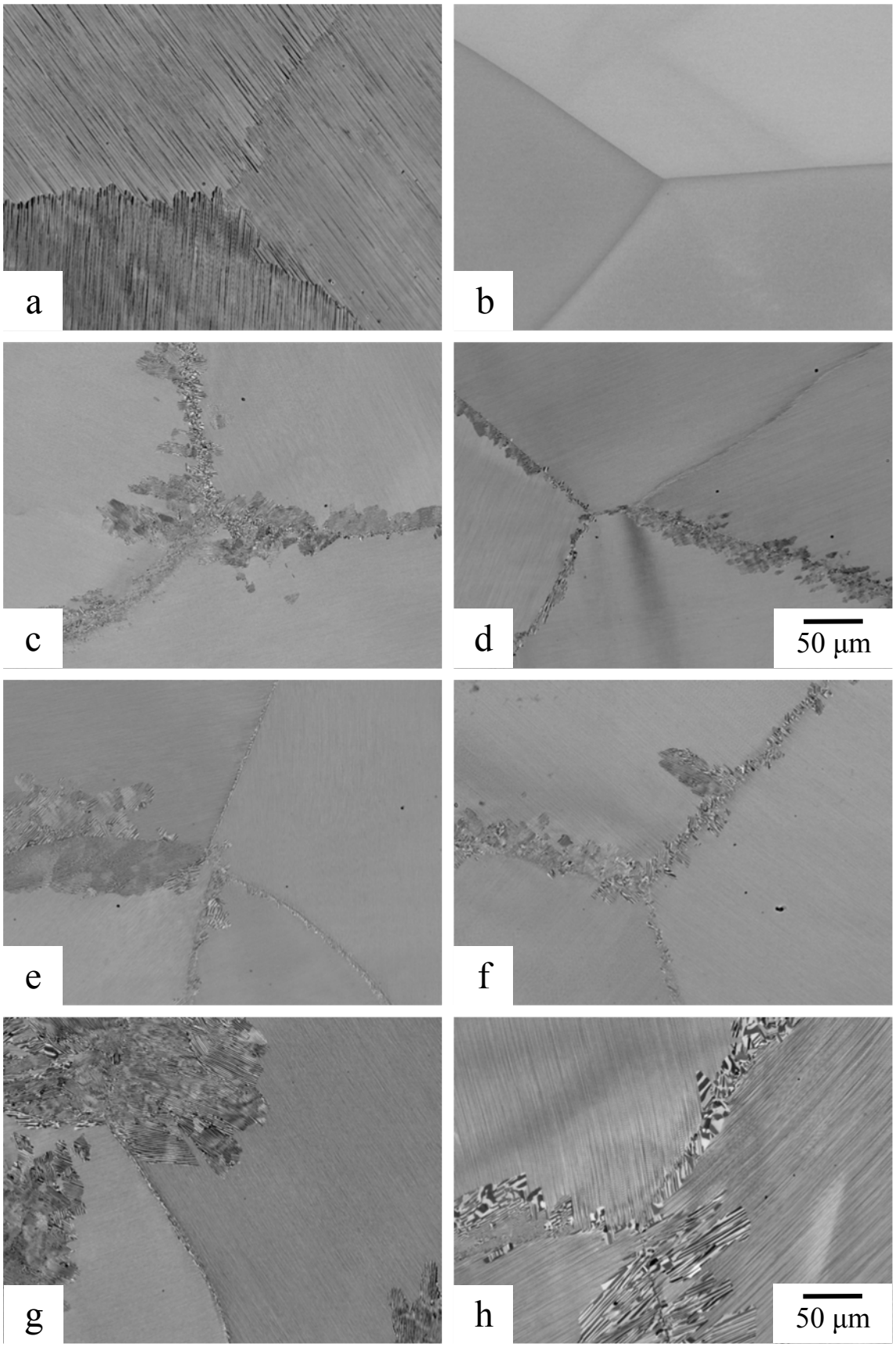

Fig. 2-17 BSE images showing the cellular reaction occurred at 1173 K in (a, c, e, g) 42-3V and (b, d, f, h) 42-5V alloys heat treated at 1173 K after (a, b) furnace cooling, (c, d) 100 h, (e, f) 500h and (g, h) 1000h.

2.3.2 Change of cellular reaction kinetics with vanadium addition

It is possible to design a fully lamellar microstructure by conducted heat treatment in the α single phase. Therefore, 42-3V and 42-5V were heat treated at 1523 K for 1 h followed by furnace cooling (1 K/min) up to 1423 K and then air cooled. The samples were subsequently aged at 1173 K for 100 to 1000 h as shown in **Figure 2-17**. 42-3V presented fully lamellar microstructure with thick lamellae. However, in 42-5V alloy, γ lamellae did not precipitate due to the lower driving force for lamellar precipitation with vanadium addition, as will be discussed in **Chapter 3**. Then, during ageing heat treatment in α_2+γ two phases region, secondary lamellar growth through cellular reaction**.**

Figure 2-18 shows the change of volume fraction of secondary lamellae (V_{SL}) with the time. The increase of 2 % of Al (at.%) decreased the cellular reaction growth rate by almost 3 times. After 1000 h, V_{SL} increased to 37 % in 42-3V but only 13 % in 42-5V alloy.

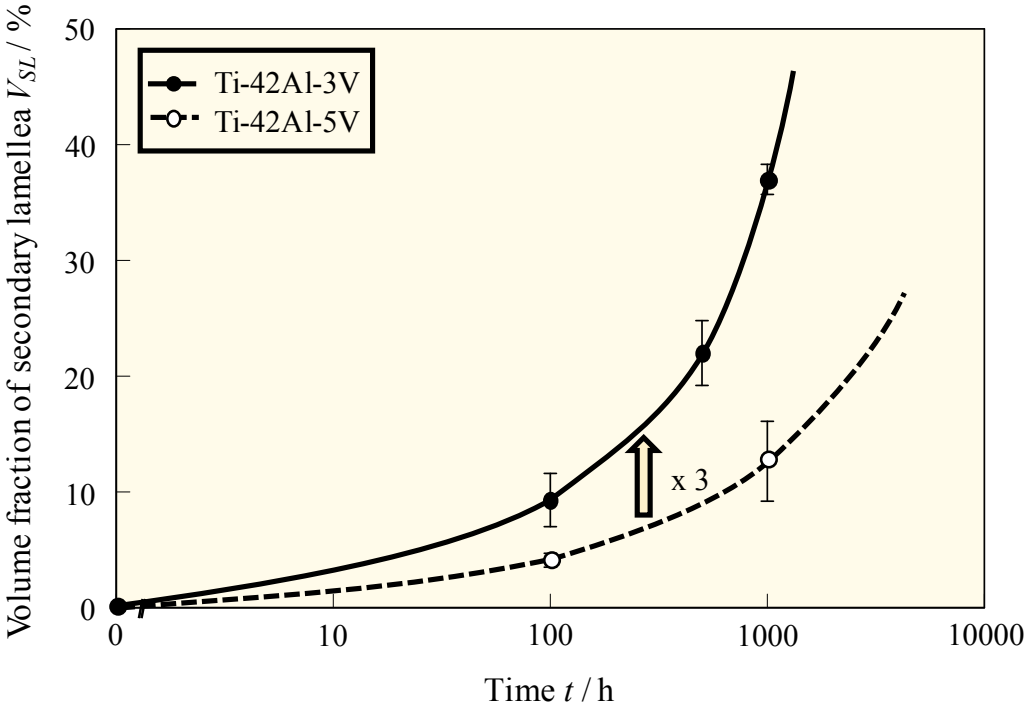

Fig. 2-18. Change in volume fraction of secondary lamellae with time in 42-3V and 42-5V alloys.

2.3.3 Phase equilibria among β-Ti / α-Ti / α_2-Ti_3Al / γ-TiAl phases

Table 2-3 shows the analyzed composition of different phases β, α, α_2 and γ that were found in Ti-Al-V alloys. Different isothermal sections of the investigated temperatures of

Ti-Al-V ternary system are shown in **Figure 2-19** along with the reported data from literature [3, 4, 7, 10, 11, 15, 16]. Red lines indicate the updated regions. Due to the low melting point of aluminum, evaporation of aluminum may took place during elaboration and the alloy compositions might slightly change. This explain why sometimes the nominal compositions do not fit completely with the tie-line between the analyzed data in the isothermal sections.

Table 2-3. Composition of the phases after equilibration heat treatment at different temperatures in Ti-Al-V ternary system determined by EPMA.

Temperature	Alloy	Phases	Composition / at.%		
			Ti	Al	V
1573 K	39-9V	β	–	–	–
	40-6.5V	β	53.8 ± 0.1	39.7 ± 0.2	6.5 ± 0.1
		α	53.7 ± 0.1	41.4 ± 0.1	41.4 ± >0.1
	42-7V	β	51.8 ± 0.5	41.0 ± 0.4	7.3 ± 0.1
		α	51.2 ± 0.2	43.1 ± 0.2	5.7 ± 0.2
1473 K	40-6.5V	β	54.3 ± 0.1	37.6 ± 0.1	8.1 ± 0.1
		α	54.2 ± 0.1	40.0 ± 0.1	5.8 ± 0.1
	42-7V	α	–	–	–
1413 K	36-9V	β	55.8 ± 0.2	35.0 ± 0.2	9.2 ± 0.1
		α_2	58.6 ± 0.2	35.5 ± 0.2	5.8 ± 0.1
	42-3V	α	56.2 ± 0.1	40.5 ± 0.1	3.3 ± >0.1
		γ	50.1 ± 0.1	47.9 ± 0.1	2.0 ± >0.1
1273 K	36-9V	β	54.7 ± 0.1	34.5 ± 0.1	10.8 ± >0.1
		α_2	57.2 ± 0.1	36.1 ± >0.1	6.8 ± >0.1
	39-9V	β	52.5 ± 0.1	35.6 ± 0.1	12.0 ± 0.1
		α_2	55.3 ± 0.2	37.1 ± 0.1	7.6 ± 0.1
		γ	49.1 ± 0.1	46.6 ± 0.1	4.2 ± >0.1
	42-3V	α_2	60.4 ± 0.1	35.8 ± 0.2	3.8 ± >0.1
		γ	52.7 ± 0.2	45.0 ± 0.2	2.2 ± 0.1
	42-5V	α_2	57.7 ± 0.1	36.0 ± 0.1	6.3 ± >0.1
		γ	51.0 ± 0.2	45.4 ± 0.2	3.6 ± 0.1
	42-7V	β	52.6 ± 0.2	35.7 ± 0.2	11.7 ± 0.1
		α_2	55.3 ± 0.4	37.4 ± 0.4	7.3 ± 0.1
		γ	49.0 ± 0.2	46.9 ± 0.2	4.1 ± >0.1
	42-8V	β	51.6 ± 0.1	34.6 ± 0.1	13.8 ± 0.2
		γ	49.1 ± 0.1	46.1 ± 0.1	4.8 ± >0.1

Table. 2-3. (continued) Composition of the phases after equilibration heat treatment at different temperatures in Ti-Al-V ternary determined by EPMA.

Temperature	Alloy	Phases	Composition / at.%		
			Ti	Al	V
1173 K	36-9V	β	–	–	–
		α_2	56.8 ± 0.2	36.1 ± 0.4	7.1 ± 0.2
		γ	49.8 ± 0.1	46.2 ± 0.2	4.0 ± 0.1
	39-9V	β	51.6 ± 0.3	35.3 ± 0.3	13.1 ± 0.2
		α_2	56.1 ± 0.1	36.4 ± 0.1	7.6 ± 0.1
		γ	48.6 ± 0.1	47.3 ± 0.2	4.1 ± 0.1
	42-3V	α_2	60.4 ± 0.5	35.8 ± 0.5	3.8 ± 0.1
		γ	52.5 ± 0.7	45.1 ± 0.8	2.4 ± 0.1
	42-5V	α_2	57.3 ± 0.6	36.4 ± 0.9	6.3 ± 0.4
		γ	50.9 ± 0.4	45.2 ± 0.5	3.8 ± 0.2
	42-7V	β	52.4 ± 0.1	34.1 ± 0.1	13.5 ± 0.2
		α_2	–	–	–
		γ	49.7 ± 0.1	46.2 ± 0.1	4.1 ± >0.1
	42-8V	β	50.6 ± 0.2	34.0 ± 0.2	15.3 ± 0.2
		γ	48.9 ± 0.1	46.4 ± 0.1	4.7 ± 0.1
1073 K	36-9V	β	–	–	–
		α_2	57.8 ± 0.3	34.4 ± 0.2	7.8 ± 0.4
		γ	50.5 ± 1.4	45.3 ± 0.3	4.2 ± 1.1
	39-9V	β	51.6	34.3	14.1
		α_2	–	–	–
		γ	49.5 ± 0.2	46.7 ± 0.3	3.9 ± 0.2
	42-3V	α_2	60.8 ± 0.7	35.2 ± 0.5	3.9 ± 0.2
		γ	52.2 ± 0.7	45.5 ± 0.9	2.3 ± 0.2
	42-5V	α_2	–	–	–
		γ	50.6	45.7	3.8
	42-7V	β	51.4 ± 1.1	33.9 ± 0.3	14.8 ± 1.1
		α_2	–	–	–
		γ	49.9 ± 0.3	45.8 ± 0.7	4.3 ± 0.5
	42-8V	β	50.2 ± 0.3	33.7 ± 0.1	16.0 ± 0.2
		γ	49.1 ± 0.4	46.7 ± 0.7	4.2 ± 0.4

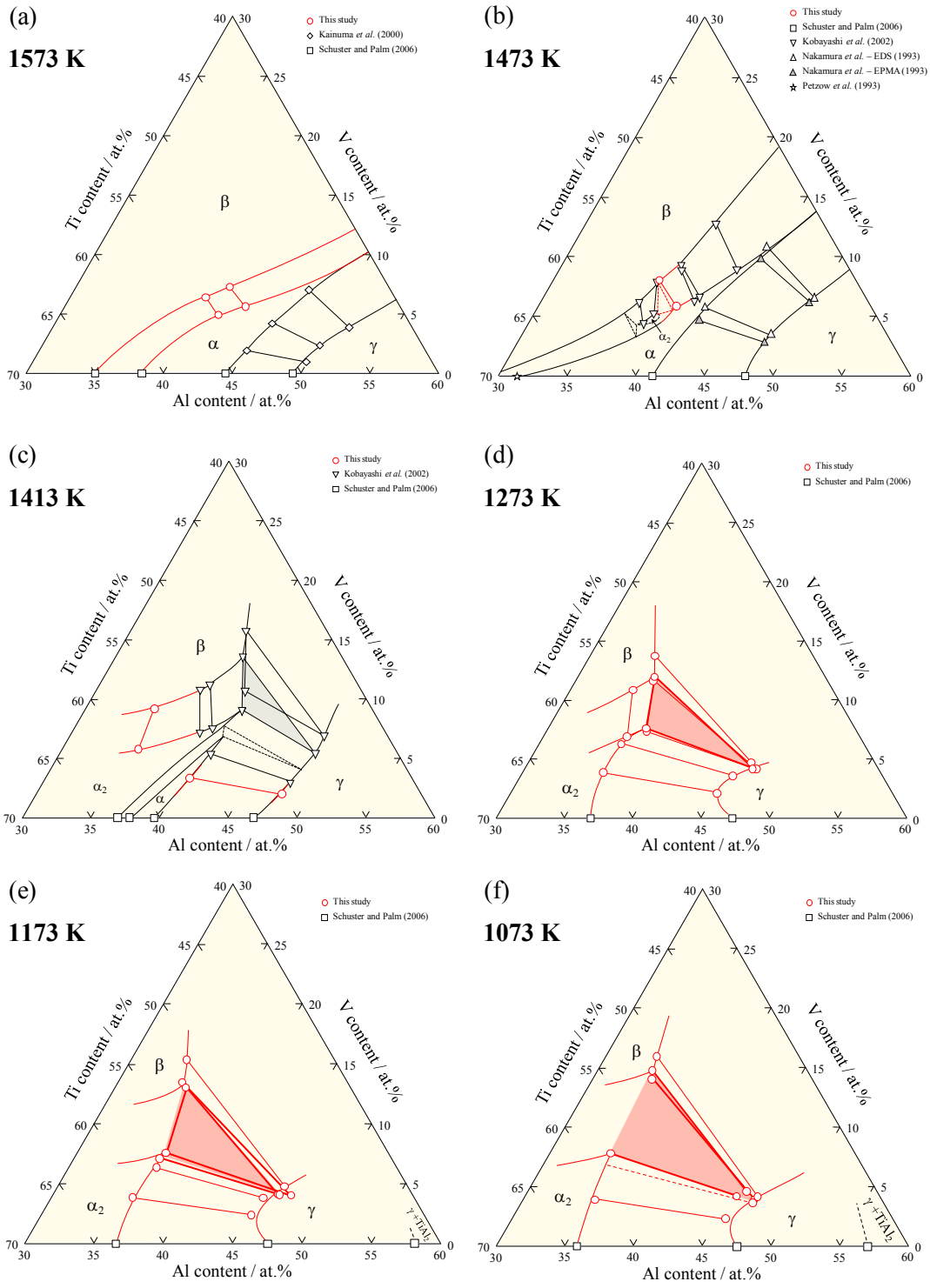

Fig. 2-19. Isothermal sections of Ti-Al-V that were determined experimentally at (a) 1573 K, (b) 1473 K, (c) 1413 K, (d) 1273 K, (e) 1173 K and (f) 1073 K with the reported data [3, 6, 7, 10, 13, 15, 16].

Despite vanadium have been identified as an α_2 stabilizer against α, only α and β phase equilibria have been found at 1573 K (**Fig. 2-19 (a)**). Moreover, the solubility of β and α phases has been found lower than reported data of Nakamura *et al.* [3]. Kobayashi [8] identified α_2 island at 1473 K and expected two different β+α+α_2 tie triangles. Based on his results, 40-6.5V bulk composition could be in these tie triangles, however the analysis of 40-6.5V did not shows significant difference in the α grains that could support this hypothesis. Moreover, the tie-line fitted well with the β+α phase boundaries at high aluminium content. It resulted that the α_2 island should be smaller as shown in (**Fig. 2-19 (b)**). The phase equilibria determined at 1413 K confirmed the reported data. It should be noted that the tie-line between β and α_2 phase shifted toward α_2 direction (**Fig. 2-19 (c)**). The phase equilibria at 1273 K was similar to the one at 1173K, except for the solubility of vanadium in β phase at 1173 K that was higher than at 1273 K. At 1073 K, the three-phase region continued to expand toward the β phase with a solubility of vanadium in β phase up to 15 at.%.

Based on the different isothermal sections, vertical sections at 36, 39, 42 and 45 at.% of vanadium were drawn and are shown in **Appendix A2**.

2.4 Ti-Al-Mn ternary system

2.4.1 Change in microstructure with manganese addition

(A) As-cast and as-forged microstructures

The BSE images of the as-cast microstructures (36-5Mn, 37-3.5Mn, 39-3Mn, 39-5Mn) and as-forged (42-5Mn) are shown in **Figure 2-20 and 2-21,** respectively.

The as-cast microstructure of 36Al-5Mn showed massive α_m phase whereas 37-3.5Mn and 39-5Mn alloys showed a Widmanstädten pattern. In case of 37-3.5Mn, the laths were thicker than in 39-5Mn. As for as-cast 39-3Mn, it showed columnar α_2 grains that had grown in the direction of heat flow for high aluminum content (**Fig. 2-20 (c)**).

The as-forged microstructure showed elongated α_2/γ colony grain perpendicular to the forged direction with a size around 50 μm surrounded by γ grains (5 μm) and β phase. The fraction of lamellar colonies was around 50%.

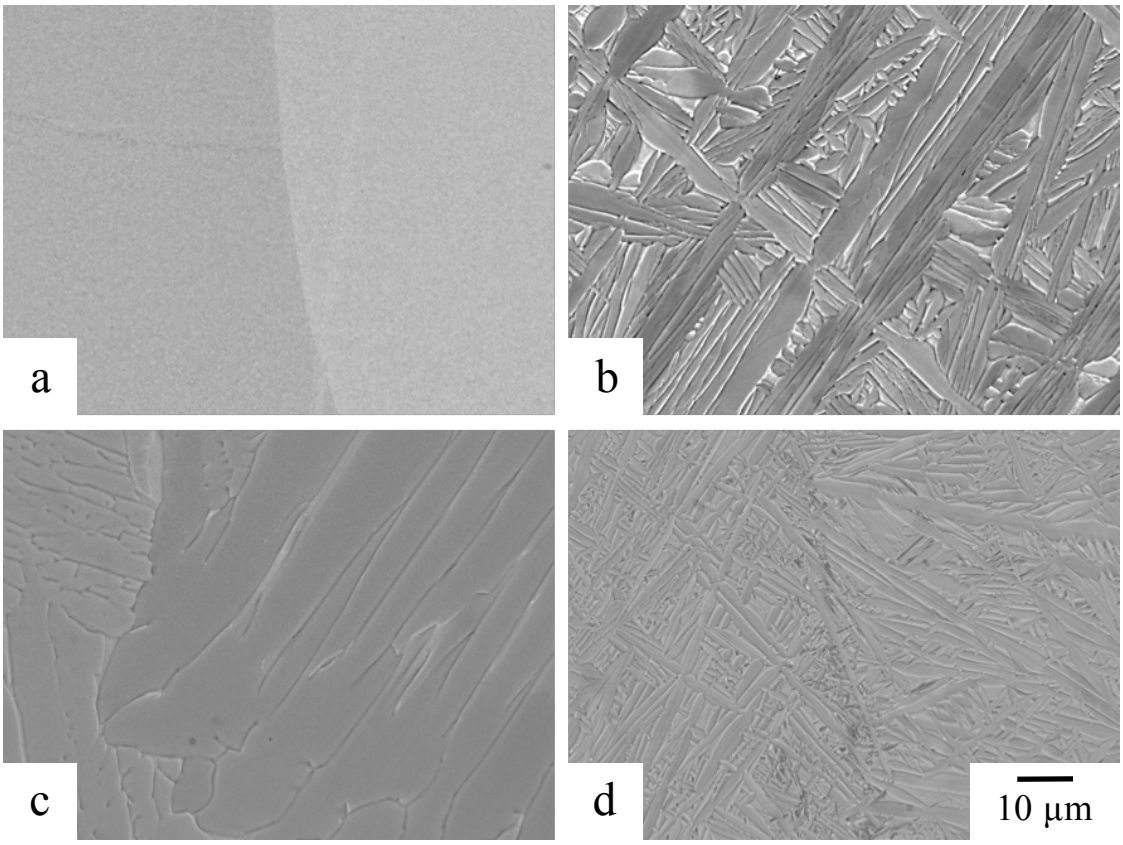

Fig. 2-20. BSE images showing the as-cast microstructures of (a) 36-5Mn, (b) 37-3.5Mn and (c) 39-3Mn and (d) 39-5Mn.

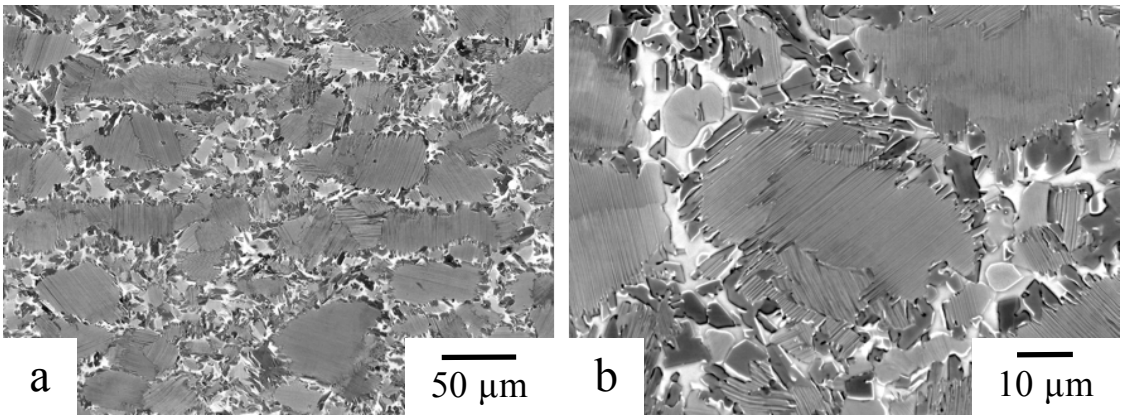

Fig. 2-21. BSE images showing the as-forged microstructures of 42-5Mn.

(B) Homogenized microstructures

All different cast alloys showed a Widmanstädten-type microstructure after homogenization heat treatments as shown in **Figure 2-22**. This indicated that β → α' martensitic transformation occurred during water quenching and confirmed that the β single phase was formed during homogenization heat treatment.

However, the forged 42-5Mn alloy showed massive α grains with dispersion of fine small γ-grains with a size of around 1 μm.

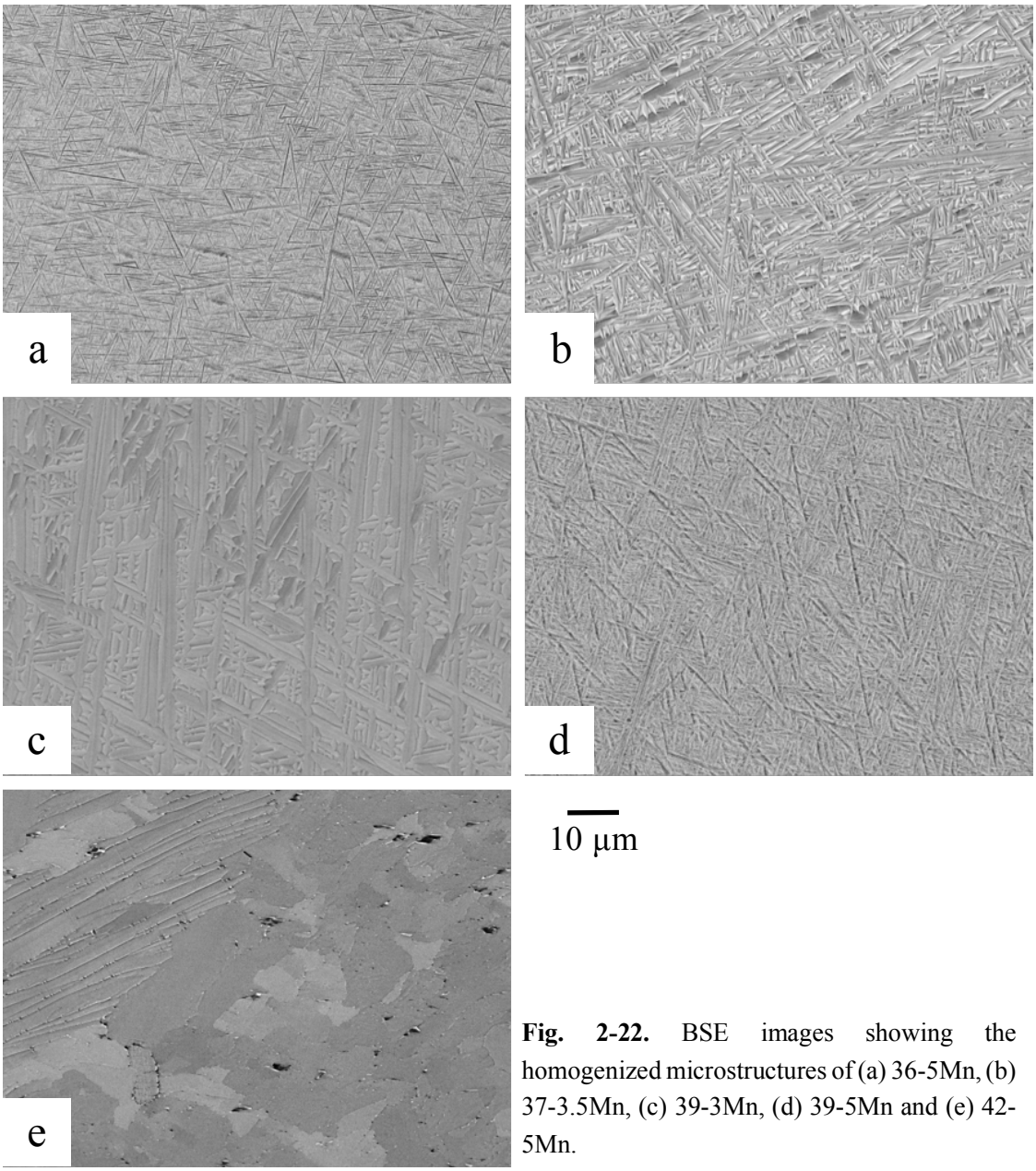

Fig. 2-22. BSE images showing the homogenized microstructures of (a) 36-5Mn, (b) 37-3.5Mn, (c) 39-3Mn, (d) 39-5Mn and (e) 42-5Mn.

(C) Equilibrated microstructures

In order to investigate the β phase boundaries, heat treatments were done at 1573 K for 48 h. The microstructures after equilibration are shown in **Figure 2-23**. 36-5Mn showed massive transformation β → α_m phase whereas 39-3Mn and 39-5Mn showed a Widmanstädten-type microstructure. At 1573 K, only β phase existed in these range of composition.

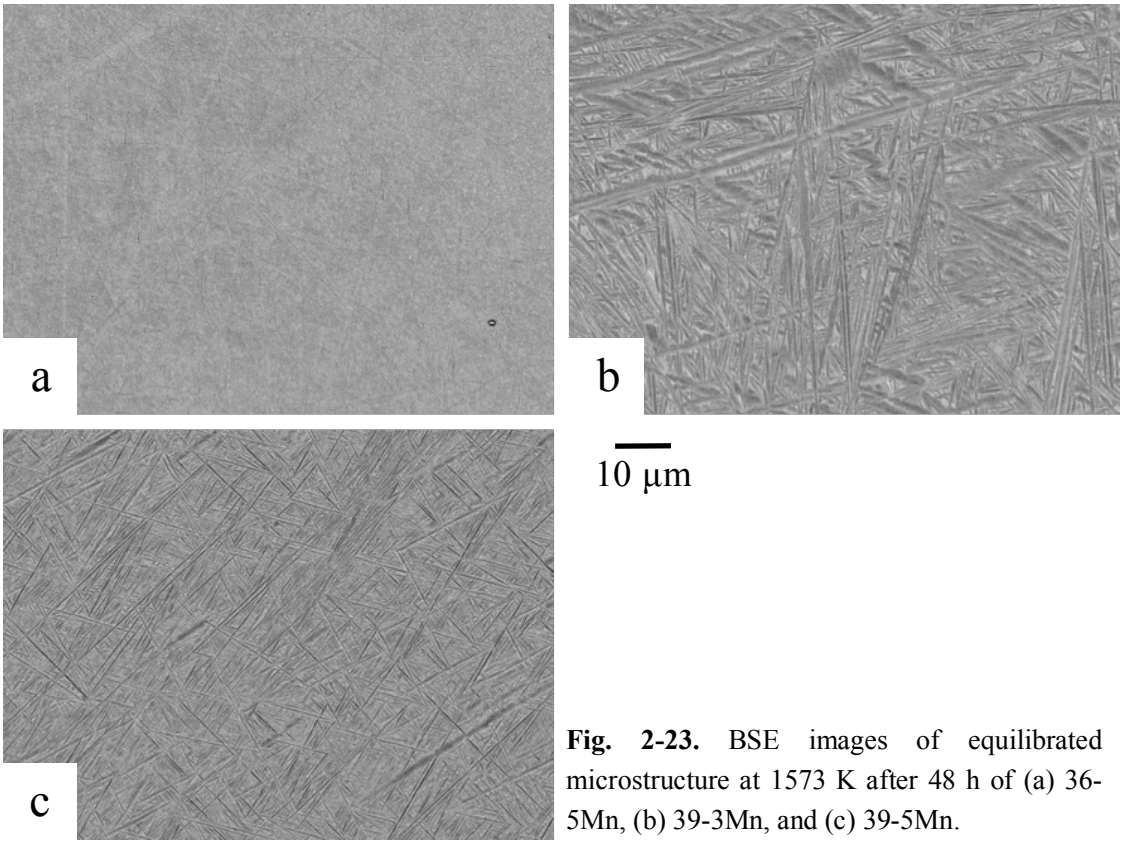

Fig. 2-23. BSE images of equilibrated microstructure at 1573 K after 48 h of (a) 36-5Mn, (b) 39-3Mn, and (c) 39-5Mn.

Then, heat treatments were conducted between 1473 and 1373 K in order to identify whether manganese is α-stabilizer against α_2 or α_2-stabilizer against α.

Figure 2-24 shows the equilibrated microstructures at 1473 K for 2 weeks. The microstructure of 42-5Mn showed three phases with large α and γ grains (around 50 μm) surrounded by β phase with a martensitic pattern as expected from reported data. As for lower aluminum content, β+α two-phase region exists as shown in 37-4.5Mn alloy.

After 4 weeks of equilibration heat treatement at 1413 K, microstructures showed only β+α(α_2) two-phase region (a-d) as shown in **Figure 2-25**. The bright phase corresponds to β and the dark phase corresponds to either α or α_2. The difference in contrast in Fig. 2-25 (a) in the α(α_2) phase was not due to composition differences but came from the

grains orientation. 39-3Mn showed the highest volume fraction of $\alpha(\alpha_2)$ whereas 39-5Mn shows the lowest one. 42-5Mn showed mainly β and γ phases with small amount of $\alpha(\alpha_2)$ grains.

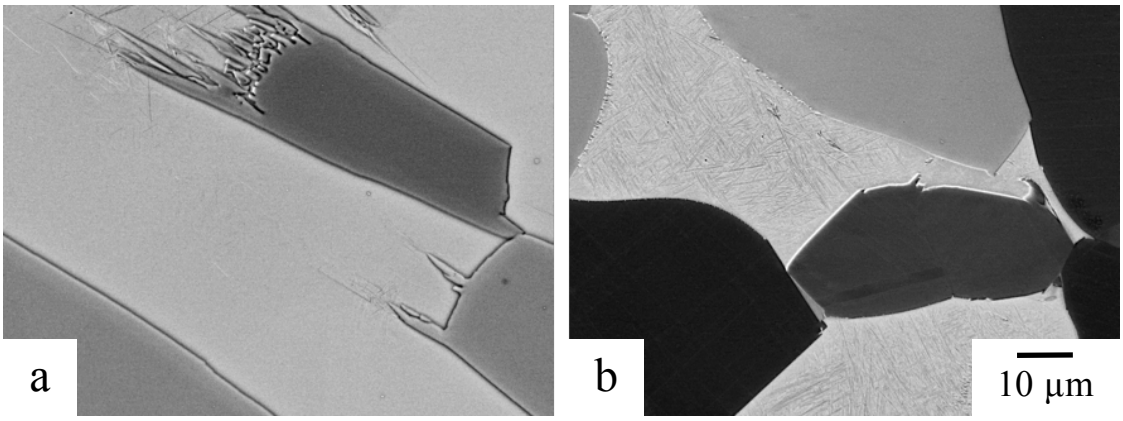

Fig. 2-24. BSE images of equilibrated microstructure at 1473 K after 2 weeks of (a) 37-3.5Mn and (b) 42-5Mn.

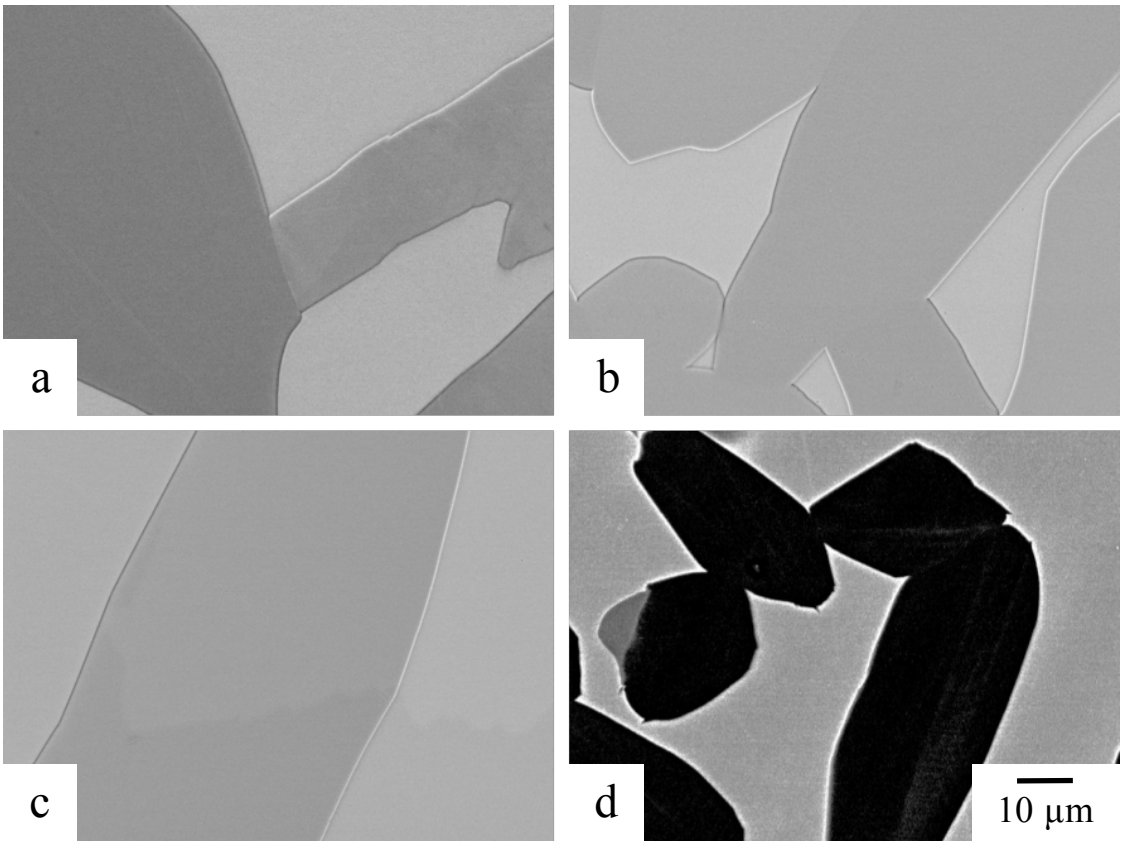

Fig. 2-25. BSE images of equilibrated microstructure at 1423 K after 4 weeks of (a) 37-3.5Mn, (b) 39-3Mn, (c) 39-5Mn and (d) 42-5Mn.

In order to verify which phase between α_2 and α exists at 1413 K, TEM observations were conducted on 37-3.5Mn alloy as shown in **Figure 2-26**. The absence of anti-phase boundaries (APB) in α_2 grains (**Fig. 2-26 (a)**) indicated that at equilibration temperature, α_2 was stable. Moreover, the analysis of β region revealed the presence of fine precipitates with a size of about 10 nm (**Fig. 2-26 (b)**). These precipitates have been identified as ω_0 phase based on the diffraction pattern. Moreover, the small size of these grains indicated the precipitation probably occurred during the water quenching.

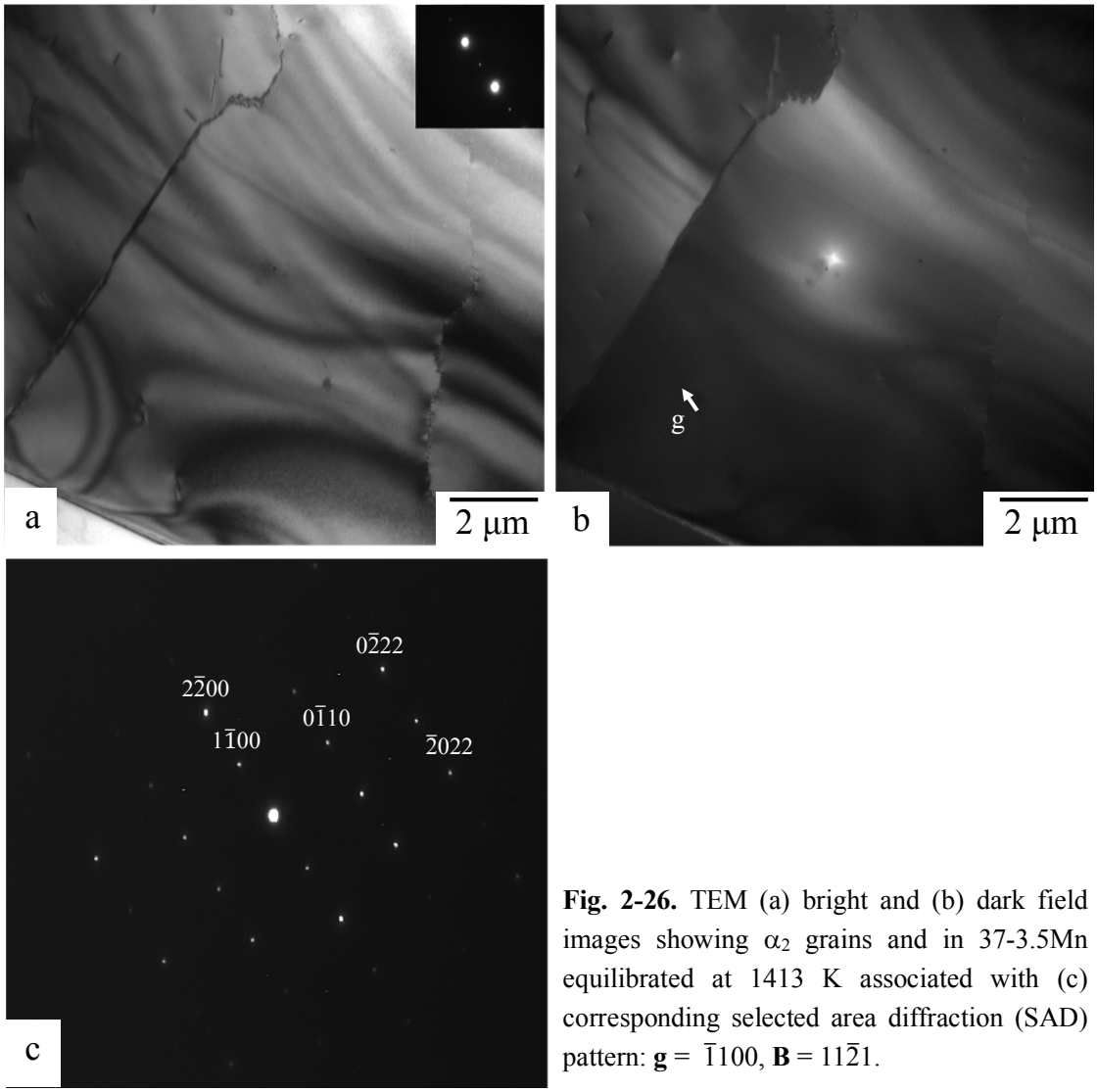

Fig. 2-26. TEM (a) bright and (b) dark field images showing α_2 grains and in 37-3.5Mn equilibrated at 1413 K associated with (c) corresponding selected area diffraction (SAD) pattern: **g** = $\bar{1}100$, **B** = $11\bar{2}1$.

The equilibrated microstructures at 1373 K for 4 weeks are shown in **Figure 2-27**. 36Al-5Mn alloy showed $\beta + \alpha_2$ two phases with large α_2 phase precipitated at grain boundaries with a thickness of around 50 μm whereas smaller α_2 grains precipitated in grains interior with size around 25 μm (**Fig. 2-27 (a)**). 39-5Mn alloy showed $\beta + \alpha_2 + \gamma$ three-phase microstructure. At grain boundaries and grains interior, α_2 and γ grains with a size of around 15 μm precipitated (**Fig. 2-27 (b)**).

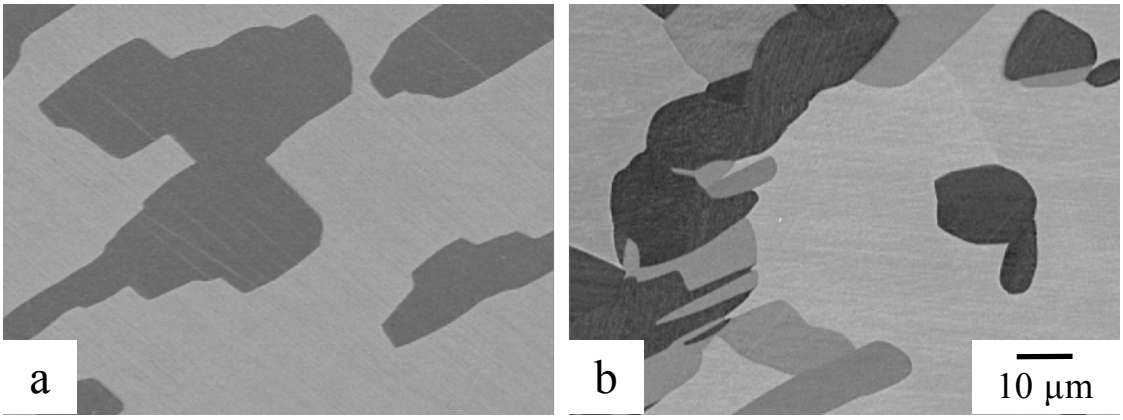

Fig. 2-27. BSE images of equilibrated microstructure at 1373 K after 4 weeks of (a) 36-5Mn and (b) 39-5Mn.

The annealed microstructures at 1273 K for 8 weeks are shown in **Figure 2-28**. 36Al-5Mn alloy showed $\beta + \alpha_2 + \gamma$ three-phase microstructure with a small fraction of γ grains. γ grains were globular with a size of 5 μm whereas α_2 grains were elongated with a size of around 3 μm in width and 15 μm in length. At grain boundaries only α_2 phase precipitated. 39-3Mn alloy showed $\alpha_2 + \gamma$ two-phase microstructure. The matrix consisted of α_2 grains with dispersion of fine globular precipitates of γ phase. The difference in contrast of α_2 phase in (**Fig. 2-28 (d)**) comes from the grains orientation and not the change in composition. 39-5Mn showed a β matrix with elongated α_2 grains and globular γ grains. The grains size for all phases was larger than the other compositions at the same temperature with a size of around 15 μm.

Figure 2-29 shows the equilibrated microstructure at 1173 K for 8 weeks. Phase equilibria at this temperature was similar at 1273 K. 36-3Mn and 39-5Mn showed $\beta + \alpha_2 + \gamma$ three phases whereas 39-3Mn showed $\alpha_2 + \gamma$ two phases. However, the grains size was much smaller than 1273 K due to slow diffusion rate at lower temperature and became difficult to be analyzed by EPMA. In 36-5Mn and 39-5Mn alloys, the relative volume fraction of β at 1173 K decreased compared to 1273 K.

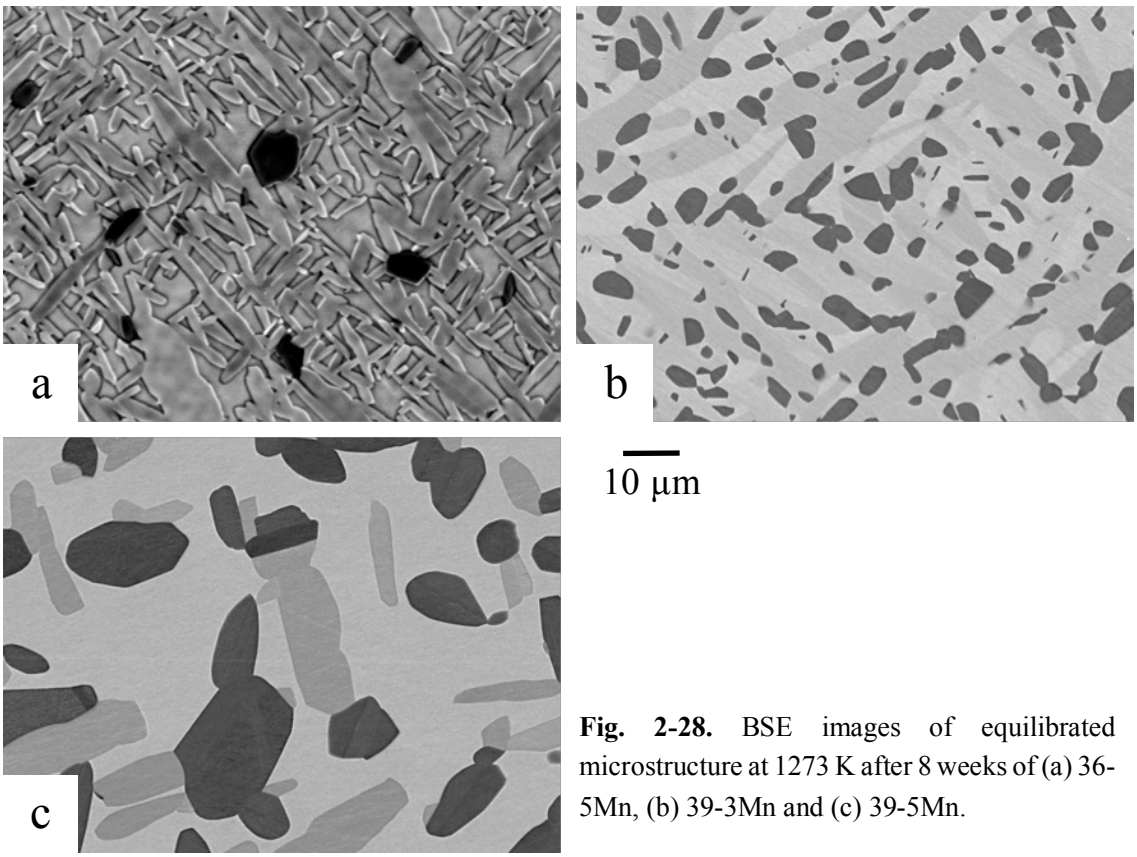

Fig. 2-28. BSE images of equilibrated microstructure at 1273 K after 8 weeks of (a) 36-5Mn, (b) 39-3Mn and (c) 39-5Mn.

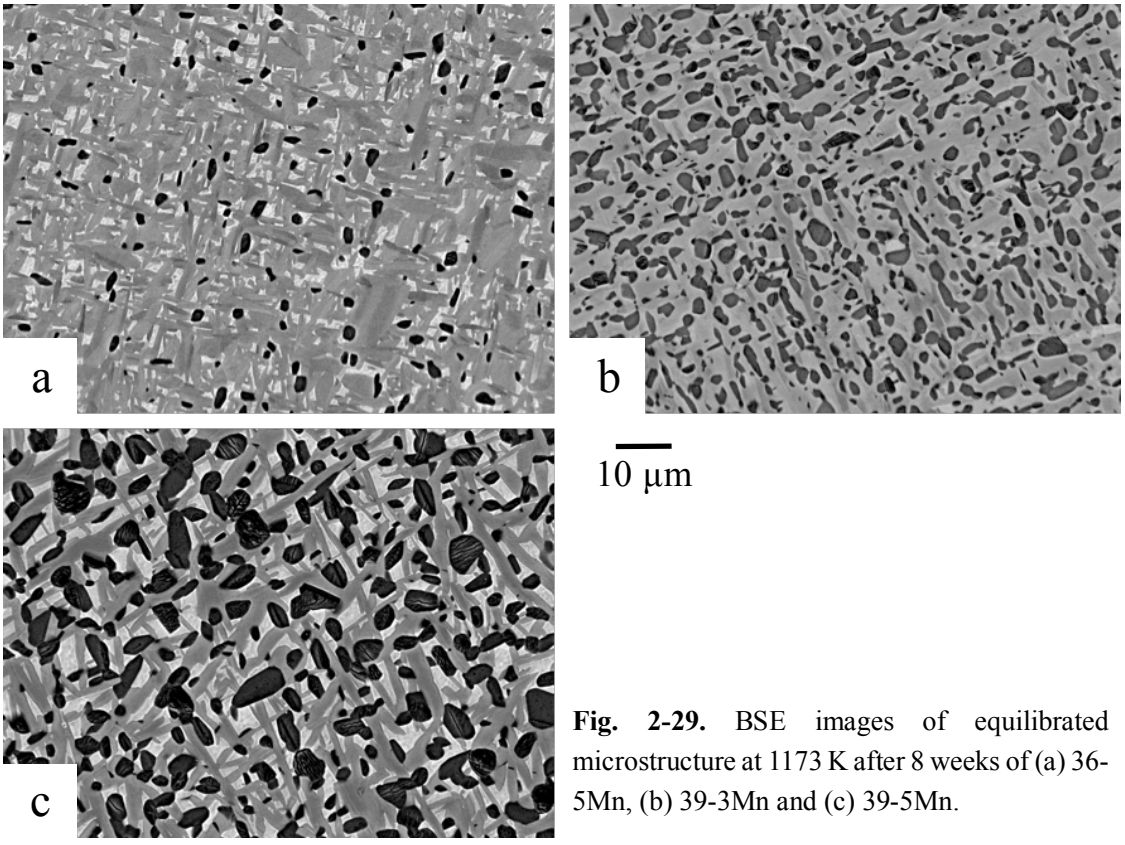

Fig. 2-29. BSE images of equilibrated microstructure at 1173 K after 8 weeks of (a) 36-5Mn, (b) 39-3Mn and (c) 39-5Mn.

Finally, at 1073K, 39-5Mn and 42-5Mn alloys have been equilibrated for 9 and 11 weeks, respectively, and the equilibrated microstructures are shown in **Figure 2-30**. It showed a three phases microstructure with α_2 and γ phases as main phases and a distribution of fine and bright globular phase that shows clearly different contrast expected from β phase. It should be not that the difference of the phases morphology, especially in 42-5Mn alloy, is explained by the differences in the initial microstructure.

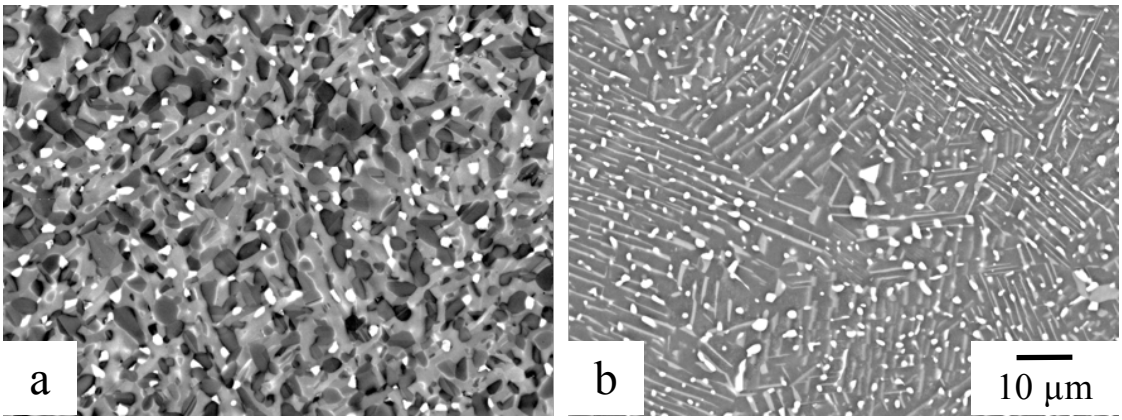

Fig. 2-30. BSE images of equilibrated microstructure at 1073 K (a) after 9 weeks of 39-5Mn alloy and (b) after 11 weeks of 42-5Mn alloy.

2.4.2 Phase equilibria among β-Ti / α-Ti / α_2-Ti_3Al / γ-TiAl phases

(A) Composition analysis of β / α / α_2 / γ phases

Table 2-4 shows the composition of the different phases (β, α, α_2, γ and C14). The phases compositions were used for draw the isothermal sections of the manganese system at the different investigated temperatures as shown in **Figure 2-31** along with the reported results from the literature [5, 9, 13, 15-17]. As explained previously, due to the low melting point of aluminum and low vapor pressure of manganese, evaporation of aluminum and manganese took place during elaboration and the alloy compositions might slightly change.

At 1473 K, 37-4.5Mn alloy showed a tie-line with a slope equivalent to the β/α phase boundary of the reported β+α+γ three-phase triangle (**Fig. 2-30 (a)**). Hence, it can be conclude that 37-4.5Mn alloy shows only β and α phases at this temperature. No evidence of the existence of α_2 phase island has been found in contrary of V or Nb elements. Nevertheless, the maximum solubility of manganese in β and α seems to be higher than previous studies. The slope of the tie-line between β and α phase of the three-phase

Table 2-4. Composition of the phases after equilibration heat treatment at different temperatures in Ti-Al-Mn ternary determined by EPMA.

Temperature	Alloy	Phases	Composition / at.%		
			Ti	Al	Mn
1573 K (48 h)	36-5Mn	β	–	–	–
	39-3Mn	β	–	–	–
	39-5Mn	β	–	–	–
1473 K (2 weeks)	37-3.5Mn	β	60.1 ± 0.1	36.0 ± 0.2	3.8 ± 0.2
		α	60.7 ± 0.2	37.3 ± 0.2	2.0 ± 0.1
	42-5Mn	β	54.1 ± 0.2	38.2 ± 0.1	7.8 ± 0.1
		α	54.3 ± 0.1	40.6 ± 0.1	5.2 ± 0.1
		γ	50.4 ± 0.1	46.4 ± 0.1	3.2 ± 0.1
1413 K (4 weeks)	37-3.5Mn	β	59.5 ± 0.1	36.2 ± 0.2	4.4 ± 0.1
		α(α_2)	60.6 ± 0.1	37.1 ± 0.1	2.3 ± 0.1
	39-3Mn	β	57.5 ± 0.1	37.7 ± 0.1	4.8 ± 0.1
		α(α_2)	57.5 ± 0.1	39.7 ± 0.1	2.8 ± 0.1
	39-5Mn	β	56.8 ± 0.2	37.3 ± 0.2	5.8 ± 0.1
		α(α_2)	57.6 ± 0.1	39.1 ± 0.1	3.2 ± 0.1
	42-5Mn (only 2 weeks)	β	53.6 ± 0.1	37.9 ± 0.3	8.5 ± 0.1
		α(α_2)	55.2 ± 0.1	40.0 ± 0.1	4.8 ± 0.1
		γ	49.1 ± 0.1	47.5 ± 0.1	3.4 ± 0.1
1373 K (4 weeks)	36-5Mn	β	57.4 ± 0.1	35.9 ± 0.1	6.7 ± 0.1
		α_2	59.8 ± 0.1	36.9 ± 0.1	3.3 ± 0.1
	39-5Mn	β	56.1 ± 0.1	37.0 ± 0.1	6.9 ± 0.1
		α_2	57.6 ± 0.1	38.7 ± 0.1	3.7 ± 0.1
		γ	50.1 ± 0.1	47.1 ± 0.1	2.8 ± 0.1
1273 K (8 weeks)	36-5Mn	β	58.2 ± 0.1	34.5 ± 0.1	7.3 ± 0.1
		α_2	59.9 ± 0.1	36.6 ± 0.1	3.5 ± 0.1
		γ	50.8 ± 0.3	46.3 ± 0.2	2.9 ± 0.1
	39-3Mn	α_2	59.6 ± 0.1	37.3 ± 0.1	3.2 ± 0.1
		γ	51.3 ± 0.1	46.2 ± 0.1	2.5 ± 0.1
	39-5Mn	β	57.6 ± 0.1	34.9 ± 0.1	7.5 ± 0.1
		α_2	59.5 ± 0.1	37.0 ± 0.1	3.6 ± 0.1
		γ	51.1 ± 0.1	46.1 ± 0.1	2.8 ± 0.1
1173 K (8 weeks)	36-5Mn	β	56.8 ± 0.2	33.4 ± 0.1	9.8 ± 0.2
		α_2	60.6 ± 0.1	35.5 ± 0.1	3.9 ± 0.1
		γ	51.3 ± 0.1	45.2 ± 0.1	3.5 ± 0.1
	39-3Mn	α_2	61.3 ± 0.1	35.3 ± 0.1	3.4 ± 0.1
		γ	51.4 ± 0.2	45.6 ± 0.2	3.0 ± 0.1
	39-5Mn	β	56.4 ± 0.2	33.1 ± 0.1	10.5 ± 0.2
		α_2	60.8 ± 0.1	35.0 ± 0.1	4.1 ± 0.1
		γ	50.8 ± 0.1	45.7 ± 0.1	3.6 ± 0.1
1073 K (11 weeks)	42-5Mn	C14	–	–	–
		α_2	65.4 ± 1.4	32.3 ± 0.7	2.3 ± 0.7
		γ	49.8 ± 0.2	46.7 ± 0.5	3.5 ± 0.7

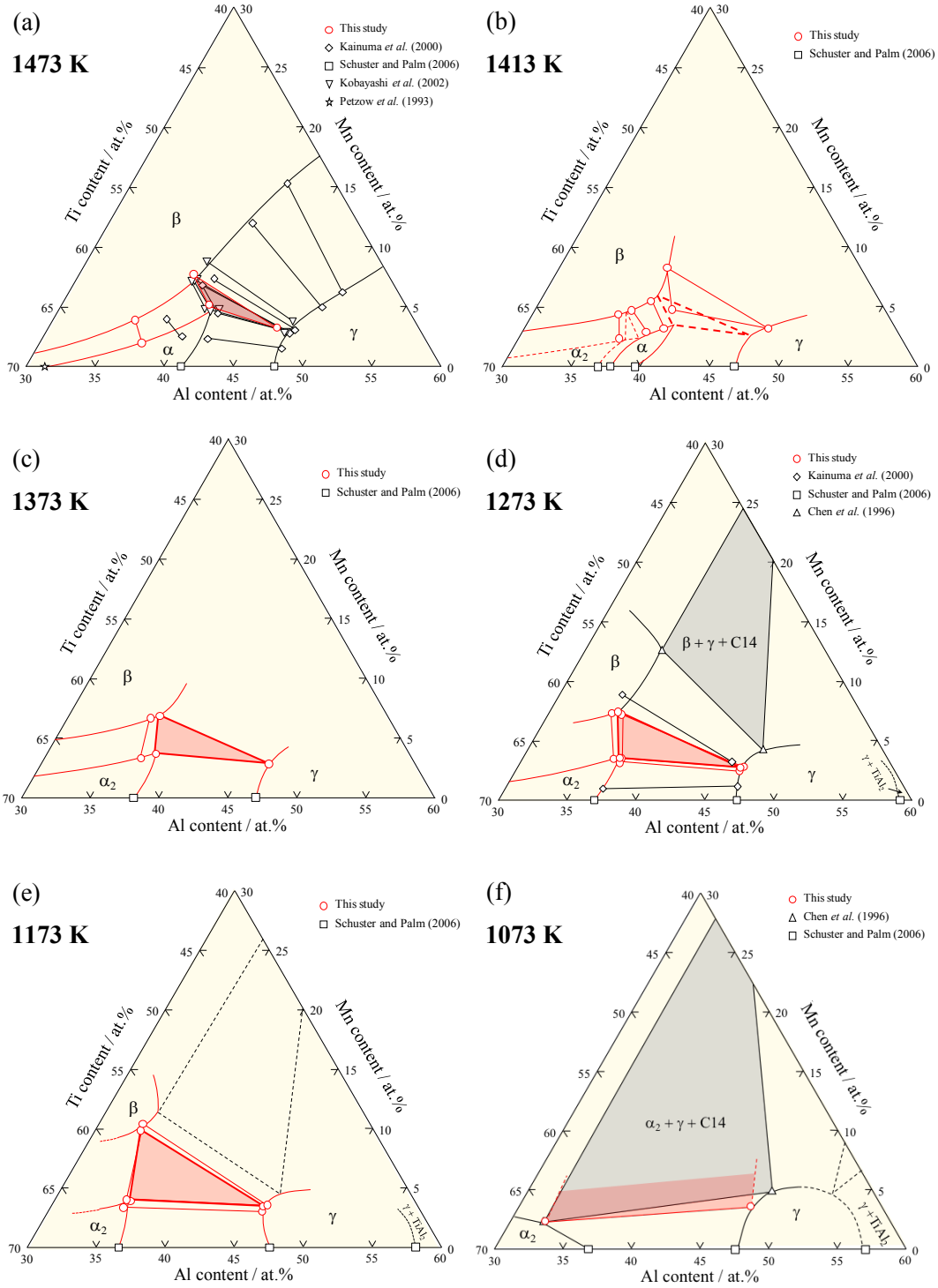

Fig. 2-31. Isothermal sections of Ti-Al-Mn that were determined experimentally at (a) 1473 K, (b) 1413 K, (c) 1373 K, (d) 1273 K, (e) 1173 K and (f) 1073 K with the reported data [5, 9, 12, 15-17].

triangle at 1473 K is similar with those of 39-3Mn and 39-5Mn alloys at 1413 K. It indicated that for the both alloys, the phase observed was α phase instead of α_2. Moreover, the slope changes clockwisely between 1413 and 1373 K. It results that the $\alpha \leftrightarrow \alpha_2$ ordering transformation probably occurs between these two temperatures, as will be detailed in the discussion part. It should be noted that 42-5Mn was aged for shorter time at 1413 K and could explain why α phase is observed in small fraction. Therefore, the β/γ tie-line gave an indication about the phase boundaries direction.

The phases equilibria at 1273 K (**Fig. 2-31 (d)**) was similar to the one at 1373 K (**Fig. 2-31 (c)**). The solubility limit of Al in β and α phases decreased with decreasing temperature while the solubility limit of Mn was almost the same between 1373 and 1273 K. Therefore, the three-phase triangle moved toward only a lower aluminum content with decreasing temperature. At 1273 K, the solubility limit of manganese in γ phase was in good agreement with calculated data by Chen *et al*. [18].

The isothermal section determined at 1173 K (**Fig. 2-31 (e)**) showed a significant difference compared to higher temperature equilibria. Despite the solubility limit of aluminum in β and α phases continued to decrease, the solubility limit of manganese in β drastically increased. Therefore, the three-phase triangle moved toward a lower aluminum but also to a higher manganese content. By carrying out different equilibration times of the heat treatment, it was confirmed that the movement of the $\beta+\alpha_2+\gamma$ tie triangle come from the phase equilibria that was already reached as will be explain just after.

Between 1473 K and 1273 K, the γ and the α_2 phase boundaries go toward high Mn and high Al contents whereas at 1173 K, γ phase boundaries direction change slightly go toward high Mn and low Al content.

Finally, at 1073 K, the analyzed composition of α and γ phases are in good agreement with reported data established by Chen *et al*. Despite the composition of bright phase previously reported could not be fully analyzed due to the small size of the grains, rough analysis showed a Mn content drastically higher than β phase (more than 30 at.%). Short heat treatment time at 1273 and 1073 K revealed the existence of C14 Mn_2Ti Laves phase in this ternary system for higher manganese content as reported by Chen *et al.* [17]. In this study, four times longer heat treatment times were applied and TEM observations confirm the existence of this C14 phase but the results will be publish later. Mn_2Ti Laves phase is probably stable at 1073 K even at low Mn content, and therefore, a different phase transformation occurs between 1173 and 1073 K. With decreasing temperature, the

$\beta + \alpha_2 + \gamma$ and $\beta + \gamma$ + C14 tie triangles moved closer each other's until reach a four phases equilibrium temperature with an invariant reaction, and then transformed into a $\alpha_2 + \gamma$ + C14 tie triangle. In other words, at low temperature a ternary eutectoid reaction involving Laves phases $\beta \rightarrow \alpha_2 + \gamma$ + C14 take place.

Based on the different isothermal sections, the vertical sections at 36, 39, 42 and 45 Mn at.% were plotted and are shown in **Appendix A2**.

(B) Influence of time on equilibrium

Despite Nakamura *et al.* [19] studied the diffusivity of manganese in α-Ti, the diffusion data for Ti-Al-Mn system is very limited and did not allow to estimate the required heat treatment time to reach the equilibrium state. Therefore, the heat treatments at lower temperature (1273 and 1173 K) were conducted for 4 and 8 weeks in order to compare the change in elements' concentrations. **Figure 2-32** shows the evolution of Mn and Al concentration with time in 36-5Mn alloy.

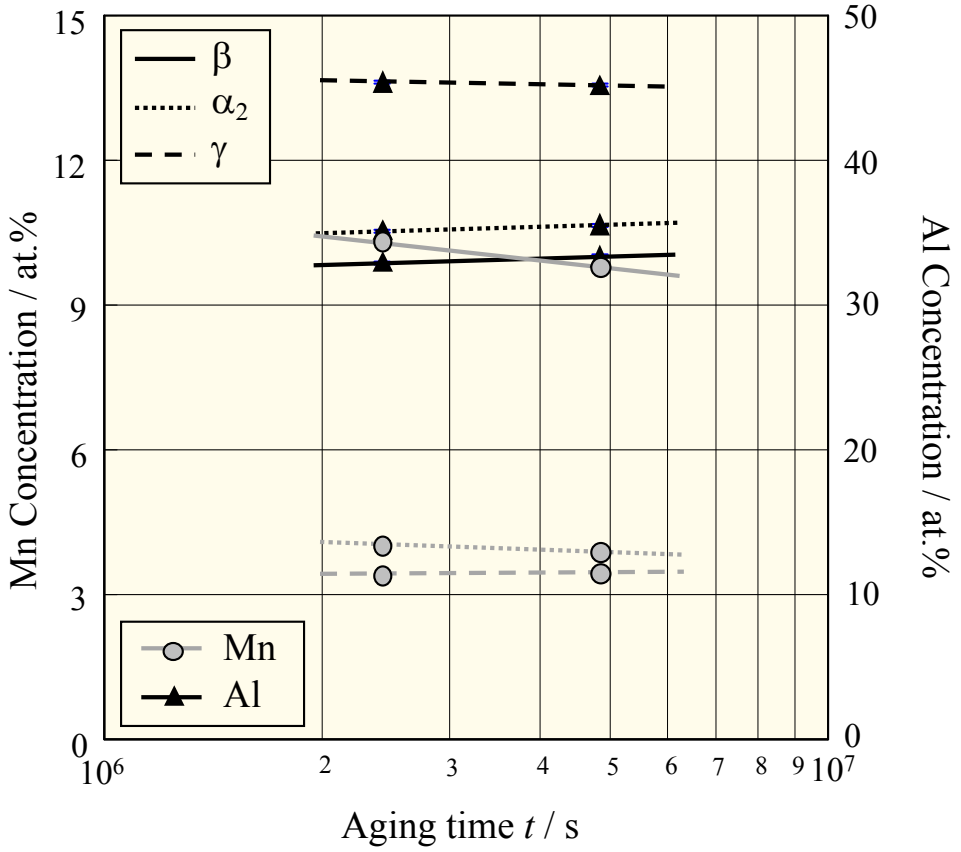

Fig. 2-32. Evolution of the concentration of Mn and Al after 4 and 8 weeks equilibration at 1173 K in 36-5Mn alloy.

Increased time from 4 to 8 weeks slightly affect the content of the different phases in the three phases triangle. The largest difference was observed in β phase where the average manganese concentration decreased by 0.5 at.% between 4 and 8 week's heat treatments. Same results were observed in 39-5Mn alloy. Hence, despite that twice longer heat treatments were applied at 1173 and 1273 K, the composition difference were not significant and confirms that the phase equilibrium was reached.

2.5 Discussion

2.5.1 Effect of M addition on the three-phase triangle below 1473 K

The temperature dependence of the three-phase triangle β/α(α_2)/γ of the two studied systems was plotted in **Figure 2-33** along with literature data [5, 7, 12, 20]. The phase equilibria among β-Ti, α-Ti and γ-TiAl revealed that in any Ti-Al-M ternary system the three-phase coexisting region exists at temperatures above 1473 K. Moreover, it has been reported that the three phases triangle moves toward lower aluminum and lower M contents with decreasing the temperature [9]. However, these studies focused on high temperature dependence, higher than 1473 K. Though, it is the first time that evolution of the tie triangle is deeply investigated at lower temperatures, between 1473 and 1073 K in such ternary systems. Although the composition range at which the three-phase region seems depended on the third element, in both systems, the tie triangle continued to move toward low M and low aluminum contents with decreasing temperature up to 1273 K. Below 1273 K, the tie triangle direction changed and moved toward high M content but continued to move toward low aluminum concentration as shown in **Fig. 2-33**. It can also be noticed that in case of vanadium system, the β/α tie-line of the tie-triangle shifted toward β region at lower temperature.

Furthermore, it can be noticed that the shape of the three-phase triangle in Ti-Al-Mn ternary system change between 1473 and 1373 K. As briefly presented in the introduction, this phenomenon has been described in Ti-Al-M system by Takeyama and Kikuchi [9] as the transformation which take place during the α → α_2 ordering. It have been found that in case of vanadium system, α_2 is stabilized against α with the existence of an α_2 island above the α ↔ α_2 congruent temperature T_C^b in binary system, and therefore, β+α → α_2+γ transition peritectoid reaction occurred between 1413 and 1473 K [8], but the effect of manganese element was still unclear. Either of both transition peritectoid or ternary eutectoid reactions could take place between 1393 and 1473 K. In both cases, the shape

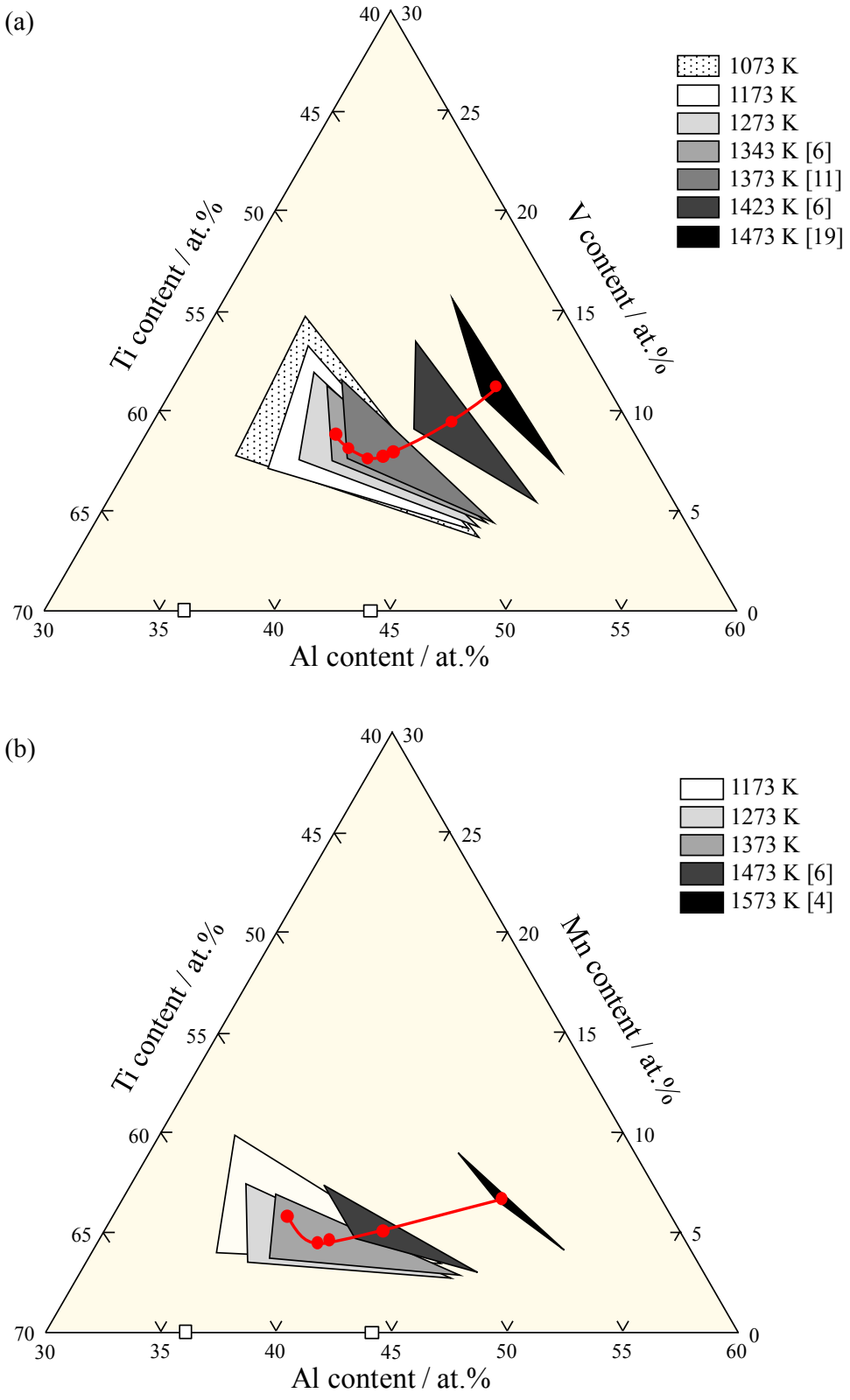

Fig. 2-33. Temperature dependence of the three-phase triangle β/α(α_2)/γ in (a) Ti-Al-V and (b) Ti-Al-Mn systems.

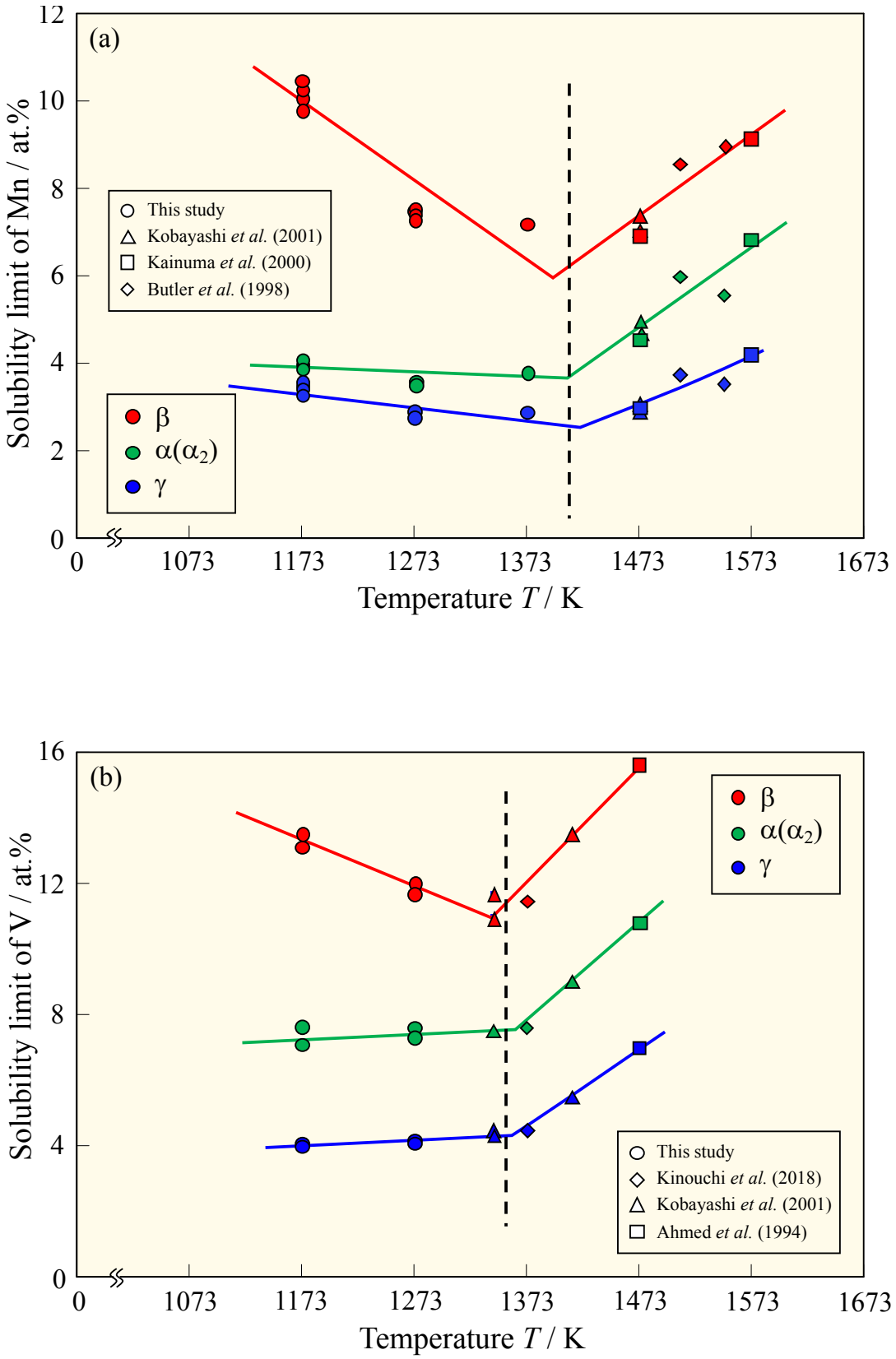

Fig. 2-34. Solubility limits of M-elements (a) Mn and (b) V at three-phase equilibrium in Ti-Al-M system with temperature change.

of the tie-triangle before and after the phase transformation will be the same. The change of tie-triangle shape in the manganese system indicated that the reaction occurred between 1373 and 1473 K. However, further investigations are needed to clarify which transformation takes place, as will be described below in more details.

With decreasing temperature, the equilibrium content of M element in the different phases at the β/α(α_2)/γ three-phase equilibrium decreased and reached at minimum as shown on **Figure 2-34**. Based on extrapolation lines, the minimum is estimated around 1353 K with 11 at.% of V in vanadium system and 1398 K with 6 at.% of Mn in manganese system. Then, when the temperature continued to decrease, the M content in β phase increased, i.e. at 1173 K, 13 at.%V and 10 at.%Mn. However, after reached the minimum, the equilibrium content (solubility) of M element in α(α_2) and γ phases with decreasing temperature appeared to reach a plateau. It decreased slightly in case of vanadium or increased slightly in case of manganese system but in both cases, the trend was the same. Thus, an expansion of the three-phase triangle toward β phase was observed.

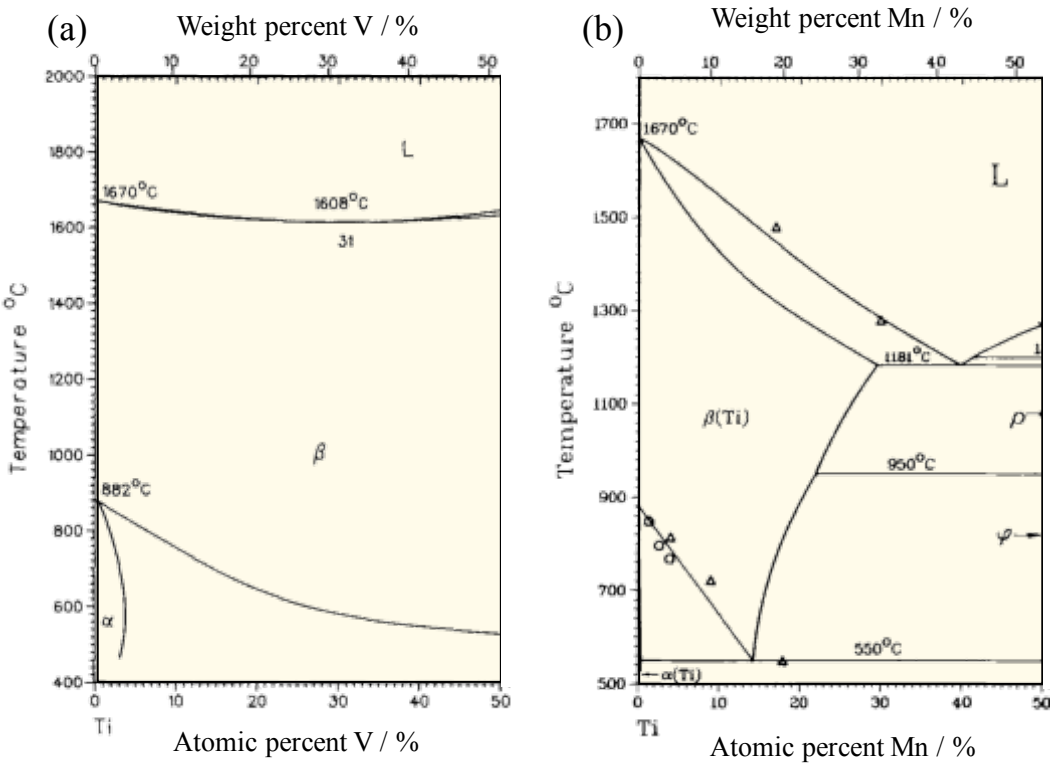

Fig. 2-35. Binary phase diagram in the titanium rich side of (a) vanadium and (b) manganese systems [22, 23].

The shift of the triangle toward low Al and low M contents up to 1273 K implied an expansion of the β phase with decreasing temperature. Moreover, the composition range at which the three-phase region existed, was enriched in titanium and depleted in M and Al. So far, it approaches the binary Ti-M phase equilibria side. The open structure of bcc phase with a packing ratio of around 0.68 is not stable against close packed structures such as fcc and hcp structures at lower temperature. Indeed, in case of Ti side, it approaches the allotropic transformation β → α that occurs at 1153 K. Thus, despite M is a β-stabilizer, as it can be seen on the binary phase diagram Ti-M in **Figure 2-35**, the solubility of α increased with decreasing temperature, even if it is very limited in case of manganese due to its stronger β-stabilizer nature. Therefore, the composition range where the β+α two phases are in equilibrium increased. **Figure 2-36** shows the relative domains of β/α(α_2) stability in the ternary Ti-Al-M system, with the normalized results at 1473 K as a reference in the β/α(α_2)/γ three-phase equilibrium. Above 1343 K, the composition range of β/α(α_2) decreased in vanadium system but it is relatively stable in case of manganese system. Then, below 1343 K, the composition range increased in both systems.

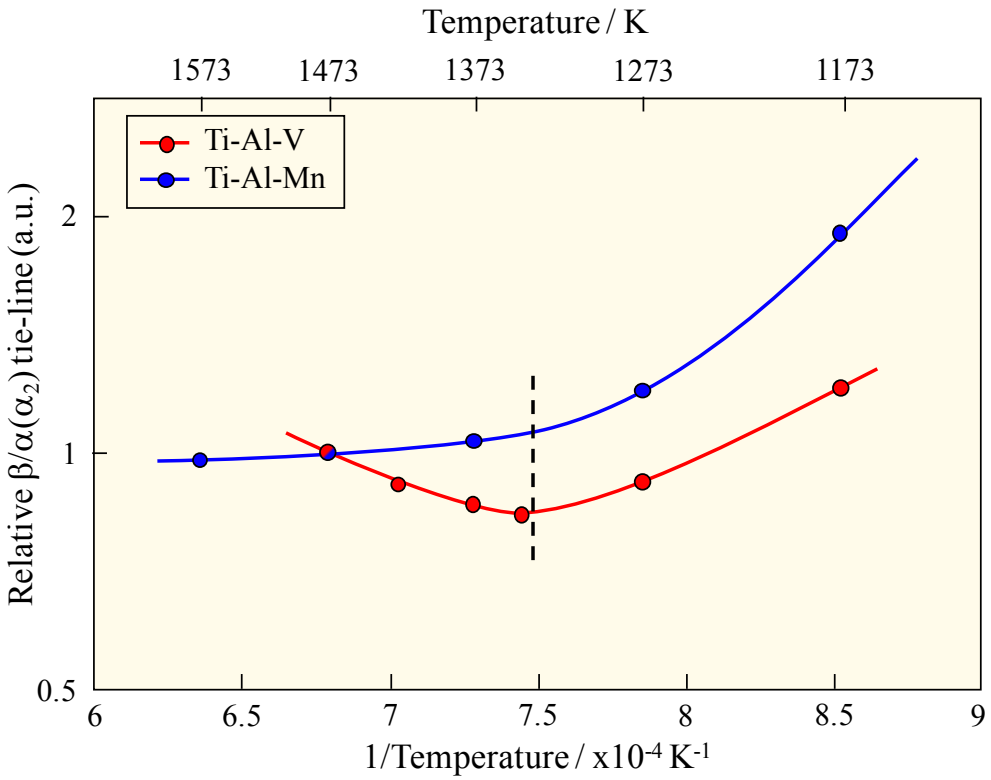

Fig. 2-36. Change in the β+α(α_2) two-phase region with temperature in Ti-Al-V and Ti-Al-Mn systems.

Given that the terminal solubility of M into α(α_2) and γ phases reached a minimum, it confirmed the change of direction of the three-phase triangle toward high M content through the expansion of β+α two-phase region as seen in **Fig. 2-33**. Thus, at low temperature, precipitation of α_2 phase may occur for composition ranges of high M contents.

2.5.2 Effect of manganese on α/α_2 relative stability effect

The direct method to determine which phase is stabilized between α and α_2 phases by the addition of third element is to find the α/α_2 coexisting region. But these two phases exist only in a small range of temperature and composition. Hence, an indirect method based on partition coefficients is used in this study.

At equilibrium, the partition coefficient $k^{i/j} = x_i/x_j$ is used to discuss the partitioning behavior of an alloying element between two phases *i* and *j*, here β, α, α_2 or γ where x_i and x_j represent the equilibrium mole fraction of the alloying element in the phases *i* and *j*. The partition coefficients of vanadium and manganese between β/(α)α_2, β/γ and (α)α_2/γ were obtained by averaging the $k^{i/j}$ of the different tie-lines and are listed in in **Table 2-5**. The temperature dependence of the partition coefficients was plotted in accordance with Arrhenius' relationship and summarized in **Figure 2-37** along with the temperature range where the α → α_2 invariant reaction takes place. Moreover, reported results obtained at higher temperature were added for comparison [5, 7, 12, 24].

Table. 2-5. Partition coefficient in the V and Mn system between the β, α, α_2 and γ phases.

System	Temperature	Partition coefficient				
		$k_{\beta/\alpha}$	$k_{\beta/\alpha 2}$	$k_{\alpha/\gamma}$	$k_{\alpha 2/\gamma}$	$k_{\beta/\gamma}$
Ti-Al-V	1573 K	1.30	–	–	–	–
	1473 K	1.40	–	–	–	–
	1413 K	–	1.57	1.64	–	–
	1273 K	–	1.59	–	1.74	2.86
	1173 K	–	1.73	–	1.70	3.24
	1073 K	–	1.90	–	1.67	3.63
Ti-Al-Mn	1473 K	1.75	–	–	–	–
	1413 K	1.80	–	–	–	–
	1373 K	–	1.97	–	1.30	2.48
	1273 K	–	2.08	–	1.27	2.64
	1173 K	–	2.52	–	1.14	2.92
	1073 K	–	–	–	0.66	–

The values of the partition coefficient $k^{\beta/\gamma}$ for vanadium and manganese systems obtained between 1073 and 1373 K shows that the values increased with decreasing

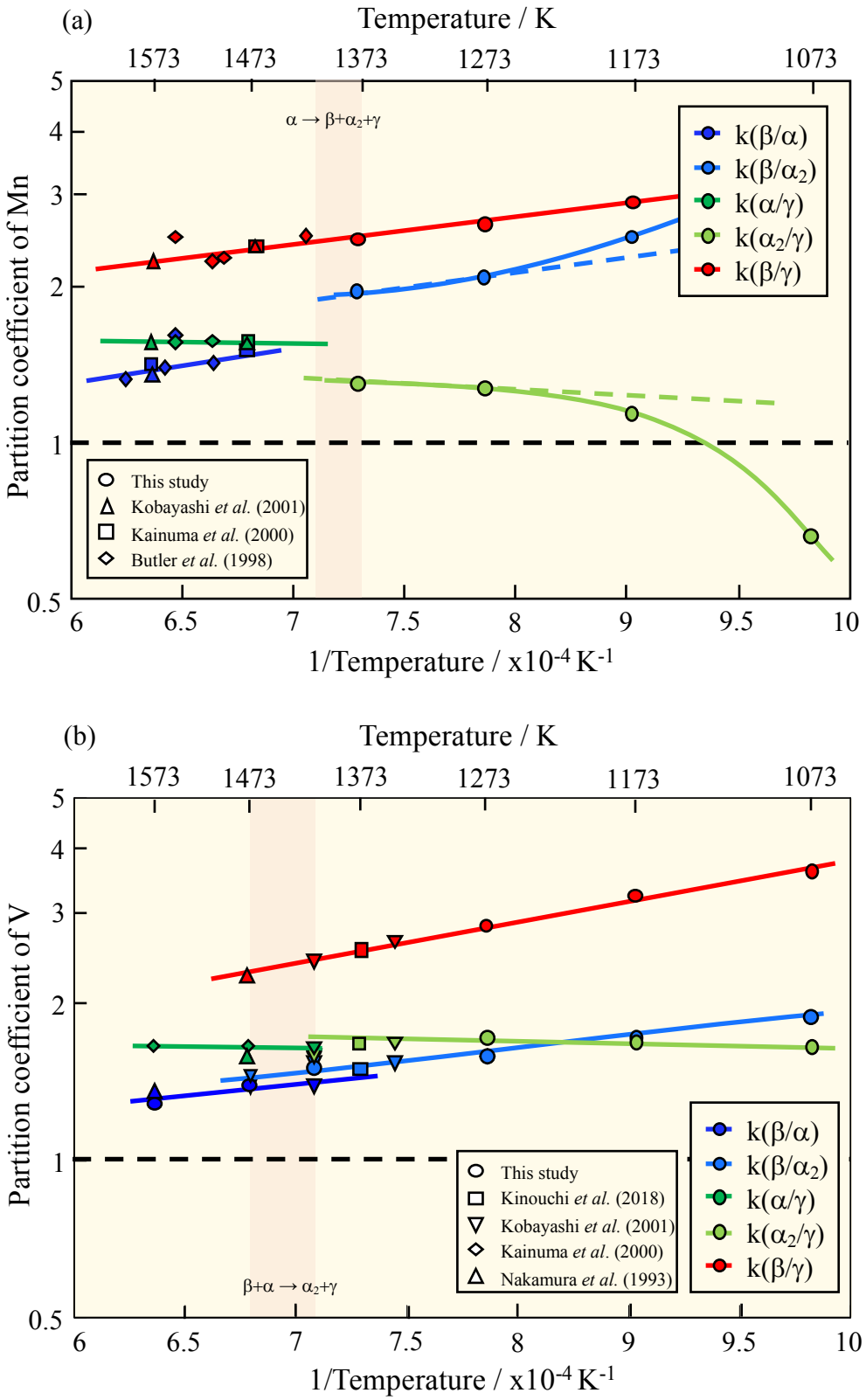

Fig. 2-37. Temperature dependence of the partition coefficients in (a) manganese and (b) vanadium

systems.

temperature and this is in good agreement with the literature observations [5]. At 1573 K, $k^{\beta/\gamma}$ was about 2 and increased up to around 3 at 1173 K. Whereas slightly differences at elevated temperature was observed, at low temperatures the Mn became more β-former than V against γ phase.

In the case of the others coefficients $k^{\beta/\alpha(\alpha2)}$ and $k^{\alpha(\alpha2)/\gamma}$, the $\alpha \rightarrow \alpha_2$ ordering transformation takes place. Because these two phases are slightly different, a change between the partitioning behavior of the α and the α_2 phases should be expected. Indeed, a gap was observed between in the temperature dependency between $k^{\beta/\alpha}$ and $k^{\beta/\alpha2}$ just as $k^{\alpha/\gamma}$ and $k^{\alpha2/\gamma}$. The value of the partition coefficients $k^{\alpha/\gamma}$ and $k^{\alpha2/\gamma}$ lied between 1.1 and 1.3 for Mn and decreased with decreasing temperature whereas there was almost no difference observed between these two coefficients in case of V with a value around 1.7. as shown in **Fig. 2-37 (b)**. In both cases, the values were higher than 1 at all temperatures, this implied that Mn and V trended to stabilize the α phase rather the γ phase. Though, the partitioning behavior of Mn get closer to 1 at 1173 K and may change at lower temperatures. Finally, the $k^{\beta/\alpha}$ and $k^{\beta/\alpha2}$ coefficient showed a similar tendency to $k^{\beta/\gamma}$: the values increased with decreasing temperature. In both systems, the values of $k^{\beta/\alpha(\alpha2)}$ and $k^{\alpha(\alpha2)/\gamma}$ intersected at 1473 K for Mn and at 1173 K for V element. The evolution of partitioning behavior of vanadium and manganese between the different phases with temperatures is shown in **Figure 2-38**. The results of Nb (α_2 stabilized against α) [10] and Cr (α stabilizes against α_2) [25] were added for comparison. The arrows indicated the evolution of the partition coefficient with decreasing temperatures. The change of direction in case of Ti-Al-V system corresponded to the shift of the β/α_2 tie-line at lower temperature. The partitioning behaviors of V and Mn were similar: $\beta > \alpha > \gamma$ at elevated temperatures and then $\beta > \alpha_2 > \gamma$ at lower one. Moreover, they became more β-former at low temperatures, however, it can be observed a difference between the evolution of $k^{\alpha/\gamma}$ and $k^{\alpha2/\gamma}$ values corresponding to the difference of partitioning behavior of α and α_2, as mentioned above.

In case of Nb and V, both elements showed $k^{\alpha2/\gamma}$ closer to α_2 region than $k^{\alpha/\gamma}$ to the α region, that means M elements stabilized rather α_2 than α, which is confirmed by the reported experimental results. In case of Cr, which is α stabilizer, and Mn, the opposite trend was observed and could indicated that Mn is a stronger α-stabilizer compared to α_2.

In order to confirm this hypothesis, the $k^{\alpha/\alpha2}$ partition behavior, between the α and the

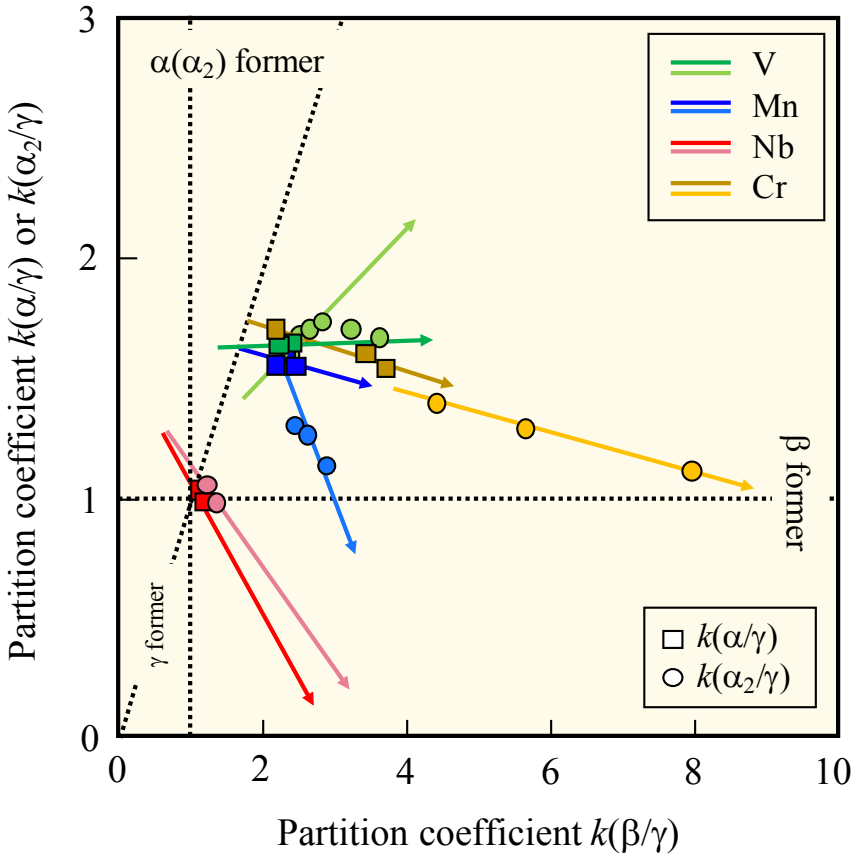

Fig. 2-38. Change of partitioning behavior between β, α or α_2 and γ phases with temperature change of different elements. The arrows direction shows the evolution with decreasing temperatures.

α_2 phases has been estimated based on the reported gap between the $k^{\beta/\alpha}$ and $k^{\beta/\alpha 2}$ coefficients and the $k^{\alpha/\gamma}$ and $k^{\alpha 2/\gamma}$ coefficients, respectively. As explained before, it exists a gap of the partition coefficient between 1473 and 1373 K due to the ordering transformation $\alpha \leftrightarrow \alpha_2$. Hence, it became possible to determine the partition behavior k^{α/α_2} between α and α_2 phases. The change with temperature of $k^{\beta/\alpha}$ and k^{β/α_2} coefficients were determined by linear regression as shown in example in **Eq. 2-1**:

$$k_{Mn}^{\beta/\alpha} = 3140{,}9*(1/T)-0{,}6128$$
$$k_{Mn}^{\beta/\alpha_2} = 4491{,}7*(1/T)-1{,}3502 \quad (2\text{-}1)$$

In the same way, $k^{\alpha_2/\gamma}$ and $k^{\alpha/\gamma}$partition coefficients could be used for calculations. Then, the ratio of the partition coefficients were calculated at different temperatures and are represented along the reported data of vanadium and niobium system in **Fig. 10** [22, 27].

The evolution of the $k^{\alpha/\alpha 2}$ partition coefficient of different elements with temperature was plotted in **Figure 2-39**. Because the number of experimental data was limited, some differences between the $k^{\alpha/\alpha 2}$ determined from the $k^{\beta/\alpha(\alpha 2)}$ and the $k^{\alpha(\alpha 2)/\gamma}$ coefficients were observed but the trends of both calculations were similar.

Because the α and α_2 phases were relatively close, the $k^{\alpha/\alpha 2}$ partition behavior was around 1 for all elements.

In the range of α ordering transformation, the averaged partition coefficient is smaller than 1 for Nb and V elements which are both known as α_2-stabilizer elements against α. Moreover, the $k^{\alpha/\alpha 2}$ values of Nb and V did not change significantly with temperature whereas it increased for Mn. In case of Mn, the value of the partitioning behavior lie between 1.09 at 1573 K to 1.30 at 1173 K and suggested that manganese element is α-former against α_2 compared to Nb and V.

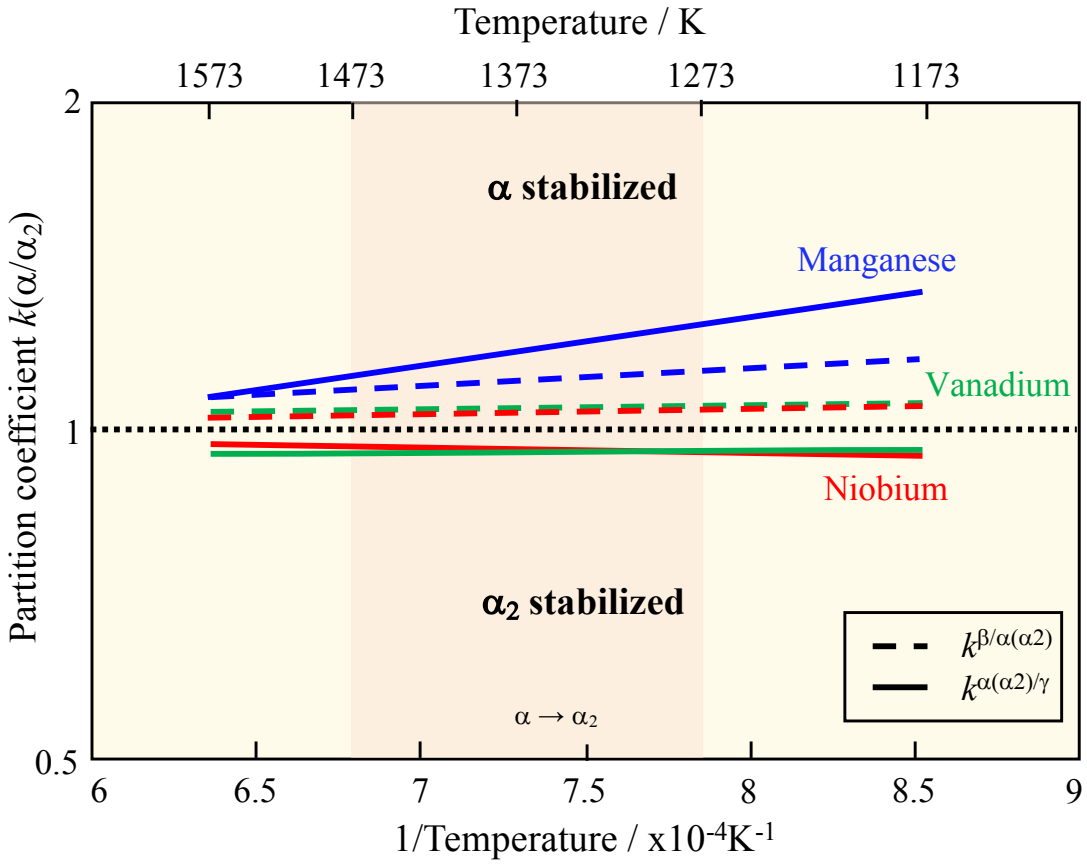

Fig. 2-39. Change of $k^{\alpha/\alpha 2}$ partition coefficient of different elements with temperature change.

Therefore, the manganese element is probably α-stabilizer against α_2 and lead to the

$\alpha \rightarrow \beta + \alpha_2 + \gamma$ ternary eutectoid reaction which takes place between 1393 (binary eutectoid temperature) and 1373 K. In this chapter, the different isothermal sections or figures were based on this hypothesis. However, no coexisting region between α_2 and α phases have been found to support this idea.

2.5.3 Eutectoid transformation involving Mn_2Ti C14 Laves phase

Short heat treatment time at 1273 and 1073 K revealed the existence of C14 Mn_2Ti Laves phase in this ternary system for higher manganese content as reported by Chen *et al.* [17]. In this study, four times longer heat treatment times were applied and TEM observations confirmed the existence of this C14 phase. Moreover, shorter times heat treatment showed that C14 Laves phase also precipitated at 1123 K in 42-5Mn as shown in **Figure 2-40**.

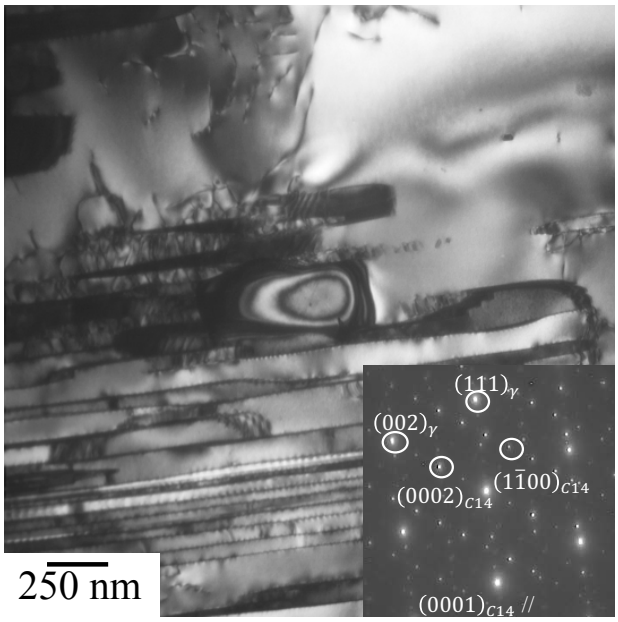

Fig. 2-40. TEM bright field images of C14 Laves phase particles in 42-5Mn alloys aged at 1488 K for 1 h follow by 1123 K for 100 h along with corresponding SAD patterns.

Hence, Mn_2Ti Laves phase is probably stable below 1123 K even at low Mn content, and a different phase transformation occurs between 1173 and 1123 K. With decreasing temperature, the $\beta + \alpha_2 + \gamma$ and $\beta + \gamma$ + C14 tie triangles moved closer each other's until reach a four phases equilibrium temperature with an invariant reaction, and then

transformed into a $\alpha_2 + \gamma$ + C14 tie triangle. In other words, at low temperature a ternary eutectoid reaction involving Laves phases $\beta \rightarrow \alpha_2 + \gamma$ + C14 take place.

2.5.4 Vertical section used for microstructure control

Finally, based on the results obtained in this chapter, the vertical sections of the two systems have been updated. As example the vertical sections at 42 at.%Al in the both systems are shown in **Figure 2-41**.

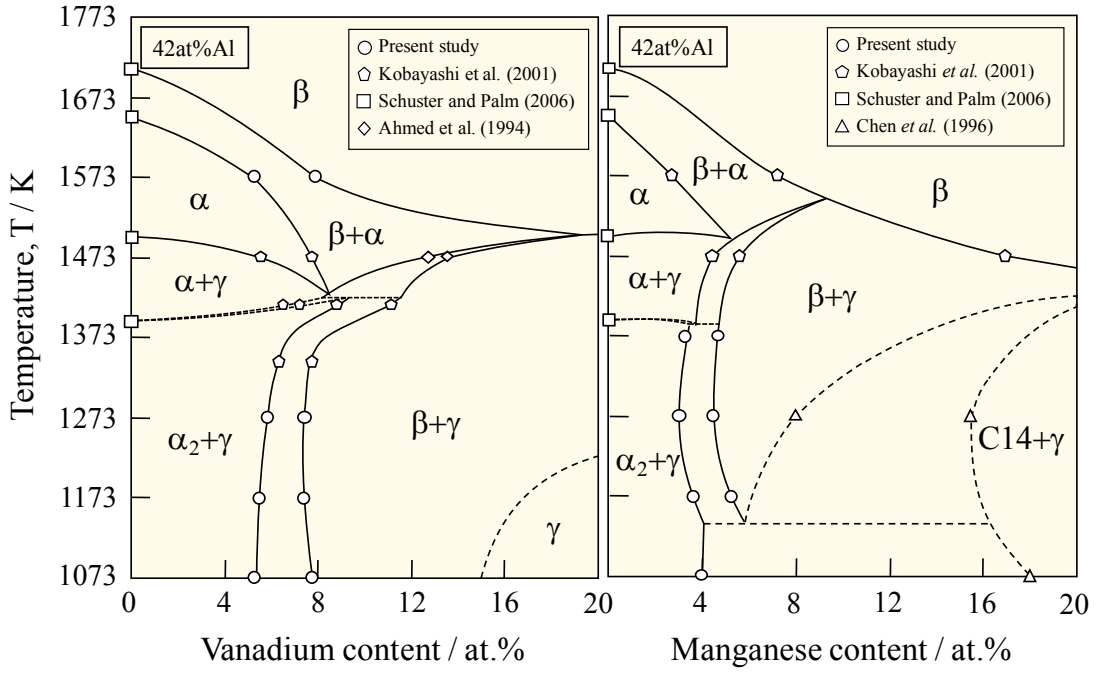

Fig. 2-41. Updated vertical sections of Ti-Al-V and Ti-Al-Mn ternary system at 42 at.%Al.

Thus, possible phase transformations can be observed easily:

(1) The existence of two type of β, above and below the α single phase region for a certain composition range as reported by Kobayashi *et al.* [7]

(2) The transition peritectoid reaction $\alpha+\beta \rightarrow \alpha_2+\gamma$ between 1393 and 1473 K in vanadium system.

(3) The ternary eutectoid reaction $\alpha \rightarrow \beta+\alpha_2+\gamma$ between 1373 and 1493 K in Mn system.

(4) The existence of two type of $\alpha(\alpha_2)$, above and below the $\beta+\gamma$ two-phase region for a certain composition range. The transformation pathway consists of $\beta+\alpha_2+\gamma \rightarrow \beta+\gamma \rightarrow \beta+\alpha_2+\gamma$ in case of vanadium system, and $\beta+\alpha+\gamma \rightarrow \beta+\gamma \rightarrow \beta+\alpha_2+\gamma$ in case of manganese system.

(5) The second ternary eutectoid reaction β → C14+α_2+γ between 1073 and 1173 K in manganese system.

The phase equilibria will be combined along with the phase transformations for the microstructure control of the β phase in wrought alloys in **Chapter 3**.

2.6 Summary

In this chapter, the phase equilibria among β-Ti / α-Ti / α_2-Ti_3Al / γ-TiAl in Ti-Al-M ternary system where M is a β-stabilizer has been investigated by SEM and EPMA between 1573 K and 1073 K. Vanadium (V^{th}) and manganese (VII^{th}) elements have been chosen based on their current state of researches. Moreover, V^{th} elements are known as α_2-stabilizer against α, e.g. Nb and V. However, in the case of VI^{th} and VII^{th} elements, the calculation results show that they had an opposite behavior with α stabilizer against α_2, but there is no experimental evidences to confirm that. Thus, the following conclusion can be drawn on this study.

1. Microstructures and phase equilibria have been determined for various compositions in both systems between 1573 and 1073 K. However, it is the first time that a study focused deeply on the temperature range below 1473 K (down to 1073 K).
2. With decreasing the temperature, the β + α(α_2) + γ three-phase triangle move toward low M and low aluminum content direction until reached a minimum in M concentration around 1173 K. Then, the tie triangle shift toward the high M and low aluminum content direction. Therefore, in the certain range of composition, the change of tie triangle direction revealed new reaction pathway β+α+γ → β+γ → β+α_2+γ.
3. The equilibrium content of M element in the different phases at the three-phase triangle show a minimum around 1353 K and 1398 K for V and Mn, respectively. Thus, the three-phase triangle expands, especially toward β phase region.
4. The partition coefficients show a gap between due to the ordering transformation between α_2 and α phase. Thus, the partition coefficient $k^{\alpha/\alpha 2}$ has been estimated and shows that the Mn trends to be more α-stabilizer than α_2-stabilizer compared to V. Thus, the α → β+α_2+γ ternary eutectoid reaction probably takes place between 1373 K and 1393 K.
5. In case of Ti-Al-Mn ternary system, a second ternary eutectoid transformations involving Laves phases β → α_2 + γ + C14 has been identified between 1073 and 1173 K.

References

[1] D. Hu, R. R. Botten, Phase transformations in some TiAl-based alloys, Intermetallics 10 (2002) 701-715.

[2] M. Schloffer, B. Rashkova, T. Schöberl, E. Schwaighofer, Z. Zhang, H. Clemens, S. Mayer, Evolution of the ω_o phase in a β-stabilized multi phase TiAl alloy and its effect on hardness, Acta Materiallia 64 (2014) 241-252.

[3] H. Nakamura, M. Takeyama, Y. Yamabe, M. Kikuchi, Phase equilibria in TiAl alloys containing 10 and 20 at% Nb at 1473 K, Scripta Metallurgica et Materialia 28 (1993) 997-1002.

[4] T. J. Jewett, B. Ahrens, M dahms, Stability of TiAl in the Ti-Al-Cr system, Materials Science and Engineering A225 (1997) 29-37.

[5] K. Hashimoto, M. Kimura, Y. Mizuhara, Alloy design of gamma titanium aluminides based on phase diagrams, Intermetallics 6 (1998) 667-672.

[6] R. Kainuma, Y. Fujita, H. Mitsui, I. Ohnuma, K. Ishida, Phase equilibria among α (hcp), β (bcc) and γ (L10) phases in Ti-Al base ternary alloys, Intermetallics 8 (2000) 855-867.

[7] T. Ahmed, H. M. Flower, The phase transformations in alloys based on titanium aluminides Ti_3Al-V and Ti-Al-V, Mater. Sci. and Eng. A152 (1992) 31-36

[8] S. Kobayashi, Phase Equilibrium and structure formation in TiAl based ternary alloys – Decomposition of α phase and generation of β phase in $\alpha \rightarrow \beta+\gamma$ reaction pathway, Doctor Thesis, Tokyo Institute of Technology, 2002.

[9] M. Takeyama, M. Kikuchi, Phase Equilibria and Microstructure Evolution of Gamma Titanium Aluminides – Effect of Third Alloying Element on Binary Ti-Al Alloys, Materia Japan 35 (1996) 1058-1064.

[10] M. Takeyama, Y. Ohmura, M. Kikuchi, T. Matsuo, Intermetallics 6 (1998) 643-646.

[11] H. Nakashima, M. Takeyama, Phase Stability of β phase in the TiAl alloys with the Combined Addition of M Elements, Materials Research Society Symposia Proceedings 1760 (2015).

[12] R. Yoshida, Master Thesis, Tokyo Institute of Technology, 2017.

[13] A. Kinouchi, Master Thesis, Tokyo Institute of Technology, 2018.

[14] A. Shaaban, H. Nakashima, M. Takeyama, Change in Phase Equilibria Among β/α/γ and β/α_2/γ Phases with Decreasing Temperature in Ti-Al-Cr System, Report of the 123rd Committee on Heat-Resisting Materials and Alloys 58 (2017) 411-412.

[15] J. C. Schuster, M. Palm, Reassessment of the Binary Aluminum-Titanium Phase Diagram, Journal of Phase Equilibria and Diffusion 27 (2006) 255-277.

[16] G. Petzow, G. Effenberg, Aluminium-Titanium-Vanadium, Ternary Alloys 8, VCH, Weinheim, Germany (1993) 426-445.

[17] Z. Chen, I. P. Jones, C. J. Small, Laves phase in Ti-42Al-10Mn alloy, Scripta Materialia 35 (1996) 23-27.

[18] L. Y. Chen, C. H. Li, A. T. Qiu, X. G. Lu, W. Z. Ding, Q. D. Zhong, Calculation of phase equilibria in Ti-Al-Mn ternary system involving a new ternary intermetallic compound, Intermetallics 18 (2010) 2229-

2237.

[19] Y. Nakamura, H. Nakajima, S. Ishioka, M. Koiwa, Effect of oxygen on diffusion of manganese in α-titanium, Acta Metall. 36 (1988) 2787-2795.

[20] T. Ahmed, H. M. Flower, Partial isothermal sections of Ti-Al-V ternary diagram, Mater. Sci. and Eng. 10 (1988) 272-288.

[21] C. J. Butler, D. G. McCarthey, An experimental study of phase transformations and a comparison with calculated phase equilibria in Ti-Al-Mn alloys, Acta mater 46 (1998) 1875-1886.

[22] J. L. Murray, The Ti-V (Titanium-Vanadium) system, Bulletin of Alloy Phase Diagram 2 (1981) 48-55

[23] J. L. Murray, The Mn-Ti (Manganese-Titanium) system, Bulletin of Alloy Phase Diagram 2 (1981) 334-343

[24] H. Nakamura, Master Thesis, Tokyo Institute of Technology, 1993.

[25] A. Shaaban, H. Nakashima, M. Takeyama, Change in Phase Equilibria among β/α(α_2)/γ Phases and Microstructure Evolution with Temperature in Ti-Al-Cr System, Japan Institute of Metals and Materials Spring Meeting, Chiba, Japan, March 2017

Chapter 3

Phase Transformation Involving β-Ti Phase and Microstructure Control of Wrought Alloys

3.1 Introduction

In order to control the β phase and design microstructures of wrought γ-based TiAl alloys, the effect of Vth group (V) and VIIth group (Mn) elements on phase equilibria of simple Ti-Al-M ternary systems have been firstly investigated in **Chapter 2**. The vertical sections of both systems has been updated as shown in **Figure 3-1**. It can be seen that in small range of composition, indicted by color bands, the same transformation pathway exists, and therefore it become possible to design similar microstructures in these two alloy systems. It should be noted that the presence of Laves phase at low temperature in manganese system may affect the microstructure but their kinetics is relatively slow. Understand the different phase transformations that occurs in these systems is also important to design model microstructures. Furthermore, these results has been not only used determine model microstructures for mechanical tests but also for the optimization of our database and the improvement of quaternary Ti-Al-M1-M2 phase equilibria calculations.

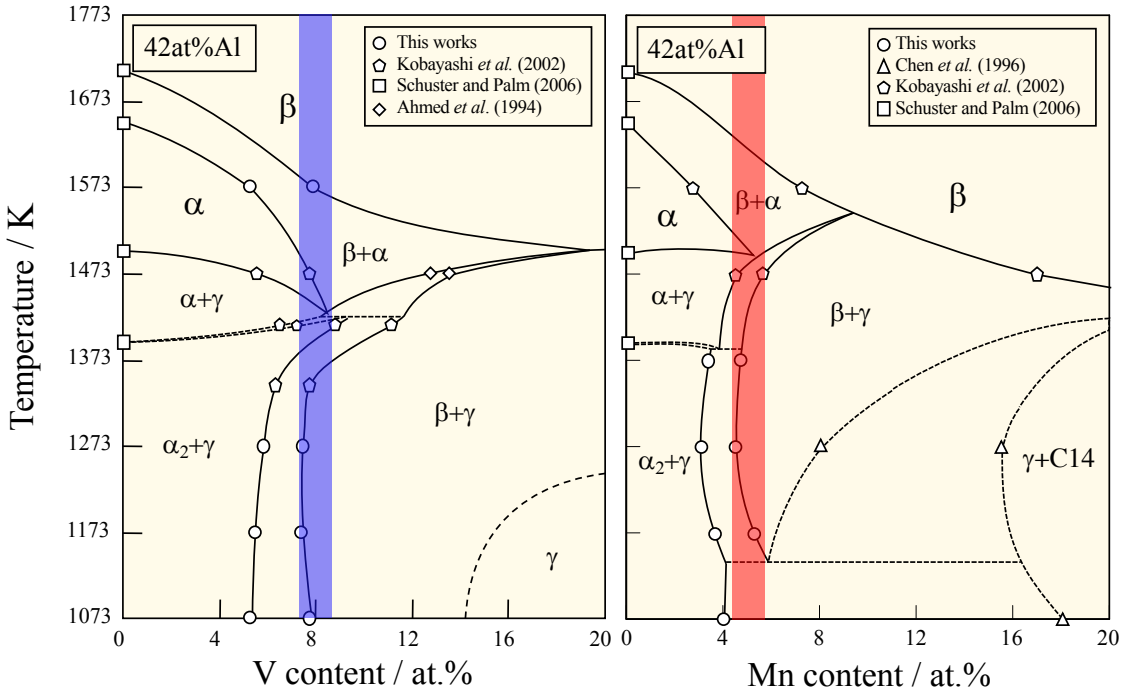

Fig. 3-1. Modified vertical sections of Ti-Al-V and Ti-Al-Mn ternary systems at 42Al at.%. based on **Chapter 2**.

Kobayashi [1] demonstrated the existence of two types of decomposition to form β phase according the composition of TiAl alloys. Indeed, there is a composition range for

some multicomponent alloys where the alloys exhibit a transformation pathway of β+α → α → β+γ under cooling as shown in **Figure 3-2**. One, β phase decomposes to α phase and another, β phase precipitates from α phase. The decomposition can be either massive or martensitic depending on the M and Al contents. The precipitation can be either through pearlitic mode or sequential mode and modified the β phase morphology. Kobayashi proposed a microstructure control method using a combination of these decompositions and precipitations pathway and thus achieved hot workability and good toughness in service for TiAl alloys.

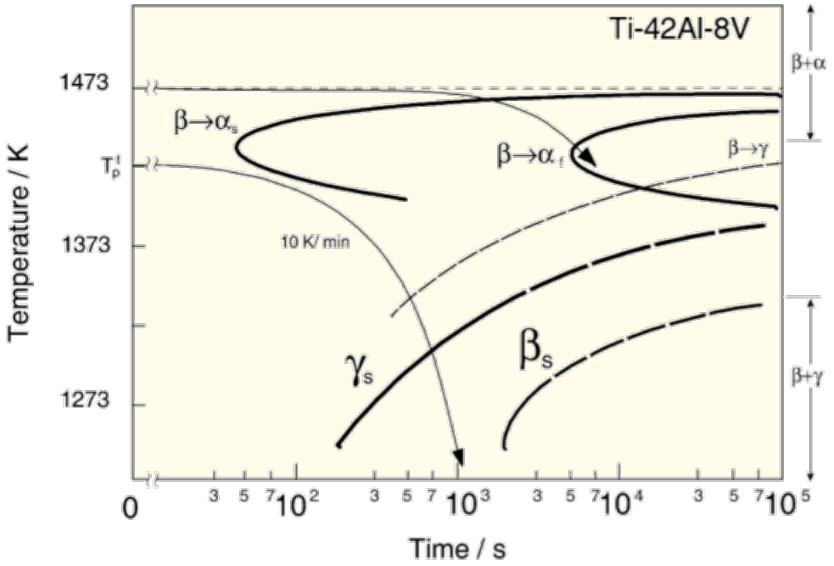

Fig. 3-2. Reported TTT diagram for Ti-42Al-8V alloys [1].

More recently, Clemens' group [2, 3] showed possibility to design different grain boundaries by changing the heat treatment conditions and using the effect of cellular reaction as shown in **Figure 3-3** in TNM alloy. Thus, it is necessary to understand not only the equilibrium state of the different alloys but also the kinetics process in order to design the microstructures, especially in the case of wrought alloys where the residual strain and the forging conditions drastically modify the microstructure.

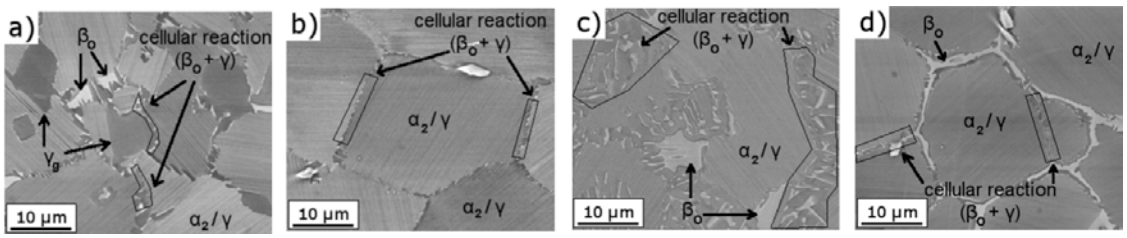

Fig. 3-3. Example of different grains boundaries obtained in TNM alloy system [2].

The objectives of this **Chapter 3** are to investigate the different phase transformations that occurs in vanadium and manganese system and which are the parameters that affect the microstructure control of wrought γ-based TiAl alloys. Then, by combine the phase equilibria and the phase transformation study, to design some representative microstructures that will be tested by fatigue crack growth tests in **Chapter 4** and **Chapter 5**.

3.2 Experimental procedures

The experimental procedures are shown in **Figure 3-4**. The nominal composition of the studied alloys is Ti-42Al-5Mn and Ti-42Al-8V (at.%). The analyzed compositions are shown in **Table 3-1**. Hereafter the alloys are referred as 42-5Mn and 42-8V, respectively. These compositions have been selected with the same aluminum content and the closest to α-single phase edge. Moreover, the β+γ two phase region exist at lower temperature.

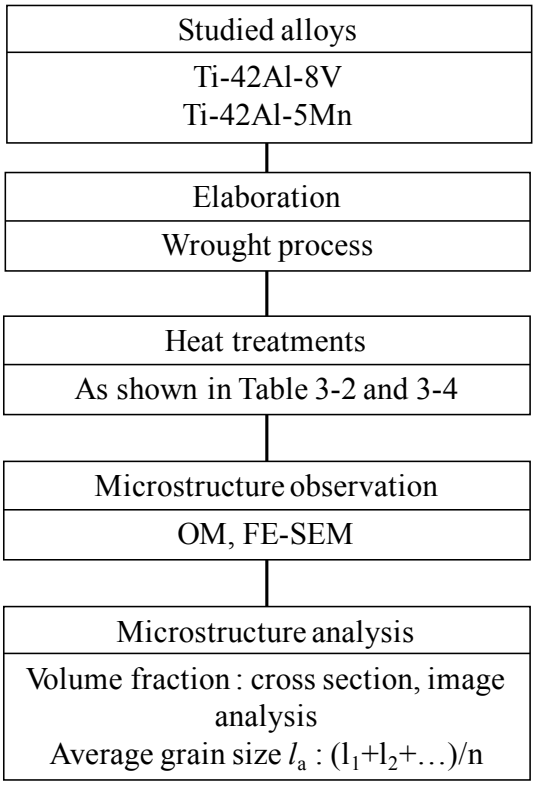

Fig. 3-4. Flowchart of the experimental procedures that were used for the microstructure control of wrought alloys.

Alloys were elaborated using cold crucible induction melting (CCIM) with a size of 50 mm in diameter and 500 mm in height. Then, the columnar ingot was cut into pieces with 120 mm in height, hold at 1573 K for 30 min in β+α two phase region and then forged with height reduction to 20 mm by four or less strokes followed by air cooling.

Table. 3-1. Analyzed composition of the forged alloys.

Name	Nominal composition (at.%)	Analysed composition (at.%)							
		Ti	Al	V	Mn	C	O	N	H
42Al-8V	Ti-42Al-8V	Bal.	42.4	8.0	–	0.03	0.20	0.01	0.06
42Al-5Mn	Ti-42Al-5Mn	Bal.	41.9	–	5.0	0.03	0.16	0.01	0.05

Afterward, the different pieces were cut by EDM (Electric Discharge Machine) and the ingot pieces were heat treated. Heat treatments were divided in two steps. First step consisted of as-forged condition or high temperature heat treatment from 1473 to 1523 K for 30 min to 2 h with different cooling rates. Subsequently, TiAl alloys were aged at lower temperature between 1123 K and 1473 K up to 100 h. All of these heat treatments were conducted either in siliconate or kanthal furnaces depending on the desired temperature and these conditions are summarized in **Table 3-2 and 3-3**.

Specimens preparation and microstructures observation were done by the same method that was described earlier in **Chapter 2**.

In order to evaluate the microstructural features, the volume fractions of the α_2/γ colonies (V_{lam}), β phase (V_β) and γ grains (V_γ) were measured by using both cross-section method and image analysis, assuming that the surface fraction was representative of the bulk microstructure. Cross-section method consisted to superimpose a square grid on the SEM images of the microstructures and count for each grid intersections the corresponding phase. Image analysis was performed by selecting manually different phase regions using ImageJ software, and then calculate the total pixels. Because, these two methods gave similar results, the image analysis method was mainly used. At least three SEM-BSE images were used for measuring the V_f with a magnification between x250 and x1000 depending the microstructural features size.

Table. 3-2. Heat treatment condition of Ti-42Al-5Mn alloy.

1st step			2nd step			Purpose
T / K	t / h	cooling	T / K	t / h	cooling	
as-forged						Initial microstructure
as-forged			1508	1	W.Q.	Investigation of γ-solvus
			1498	1	W.Q.	
			1488	1	W.Q.	
as-forged			1523	1	A.C.	lamellar microstructure design
			1503	1	A.C.	
			1488	1	A.C.	
as-forged			1523	1	W.Q.	Effect of cooling rate
					A.C.	
					1 K/min up to 1488 K	
					10 K/min up to 1488 K	
as-forged			1523	1	A.C.	Determination of phase fraction and size
			1498	1	A.C	
				100	A.C.	
			1488	1	A.C	
			1473	1	A.C.	Effect of temperature and time on microstructural features
				10	A.C.	
				100	A.C.	
			1373	1	A.C.	
				10	A.C.	
				100	A.C.	
			1273	1	A.C.	
				10	A.C.	
				100	A.C.	
			1123	1	A.C.	
				10	A.C.	
				100	A.C.	
1523	2	A.C.	1123	10	A.C.	Effect of initial condition
1498	1	A.C.		20	A.C.	
1488	1	A.C.		10	A.C.	
1488	1	A.C.	1473	1	A.C.	Determination of phase fraction and size
			1373	1	A.C.	
			1173	1	A.C.	
1523	2	A.C.	1473	1	A.C.	Determination of phase fraction and size
			1373	1	A.C.	
			1173	1	A.C.	

Table. 3-3. Heat treatment condition of Ti-42Al-8V alloy.

1st step			2nd step			Purpose
T / K	t / h	cooling	T / K	t / h	cooling	
as-forged						Initial microstructure
as-forged			1523	2	A.C.	Investigation of γ-solvus Design lamellar microstructure
			1498	2	A.C.	
			1473	2	A.C.	
			1453	2	A.C.	
			1423	2	A.C.	
			1403	1	A.C.	
as-forged			1523	2	W.Q.	Effect of cooling rate
					A.C.	
					1 K/min up to 1403 K	
					10 K/min up to 1403 K	
as-forged			1498	1	A.C.	Determination of phase fraction and size
			1473	1	A.C.	
			1403	1	A.C.	
			1373	1	A.C.	Effect of temperature and time on microstructural features
				10	A.C.	
			1273	1	A.C.	
				10	A.C.	
			1173	1	A.C.	
				10	A.C.	
1598	2	A.C.	1123	3	A.C.	Effect of initial condition
		A.C.		20	A.C.	
1473	2	A.C.		3	A.C.	
		A.C.		20	A.C.	
1453	2	A.C.		3	A.C.	
		A.C.		20	A.C.	
1423	2	A.C.		3	A.C.	
		A.C.		20	A.C.	

The V_f of each parameter (colonies, β and γ) was calculated by the **Equation 3-1**.

$$V_f = \frac{n}{N} \times 100\% \quad (3\text{-}1)$$

Where N is the total number of either the grid points or the pixels, n is the number of the grid points/pixel of each phase. The average of the selected images was taken as the

final result. The grain size of the microstructural constituents was evaluated by measuring at least 25 representative grains for each microstructure. As same as in **Chapter 2**, the error bars used for the results were determined using standard deviation (**Appendix A1**).

3.3 Results

3.3.1 As-forged microstructures

The backscattered electron (BSE) images of the as-forged microstructures are shown in **Figure 3-5**. The arrow indicates the forging direction. The 42-8V microstructure showed elongated α_2/γ lamellar colony grains surrounded by globular γ grains and β phase, also called β/γ duplex. The size of γ grains was relatively small, less than 3 μm. The structure of as-forged 42-5Mn was similar to 42-8V with β/γ duplex surrounding colonies. However, the colonies showed more globular-like lamellar grains shape and the γ grains were bigger with a size of about 5 μm. Moreover, some inhomogeneity was found in the 42-5Mn microstructure. In both microstructures, the colonies were composed of smaller sub-colony grains, originated from the forging process.

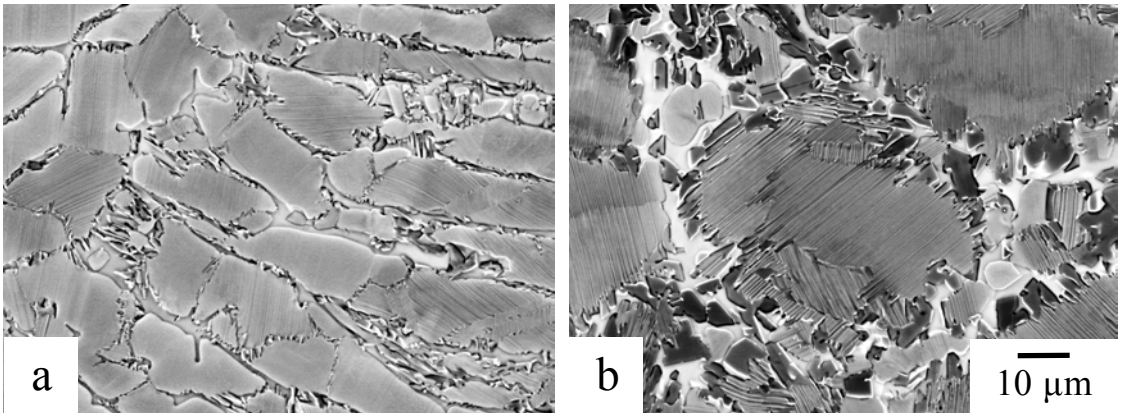

Fig. 3-5. BSE images of the as-forged microstructures (a) Ti-42Al-8V and (b) Ti-42Al-5Mn. The forging direction is vertical in the micrograph.

3.3.2 Lamellar formation

(A) Investigation of the γ-solvus

The composition of both systems have been selected at the nose of the α-single phase region and thus, in a small range of temperature $\beta+\alpha \rightarrow \alpha \rightarrow \alpha+\gamma$ transformation exists. Therefore, it became complicated to design a fully lamellar microstructure. However, by deeply investigating the "γ-solvus" temperature, or in other words the temperature where

the γ phase starts to dissolve/precipitate, it is possible to control the lamellar structure. Indeed, near the nose, the fraction of α phase will drastically increase. And then, during cooling or a second step heat treatment, the lamellar structure will form by γ precipitation according the Blackburn orientation relationship [4].

Because of the high temperature of the α-single phase in case of manganese system compared to vanadium, heat treatments were performed between 1488 and 1508 K for 1h followed by water quench as shown in **Figure 3-6**. At 1488 K, microstructure was composed of large α grains (around 50 μm) surrounded by martensitic transformed β phase. However, microstructures obtained at lower temperature present globular coarsened γ grains, α grains and martensitic transformed β phase. Furthermore, "faceted" γ grains have been observed in the β phase and indicated by arrow in **Fig. 3-6 (d)**. In the α grains, remaining coarse γ lamellae from the forged microstructure exists. Therefore, the γ-solvus has been identified between 1498 and 1508 K which is in good agreement with the phase equilibria determined in **Chapter 2**.

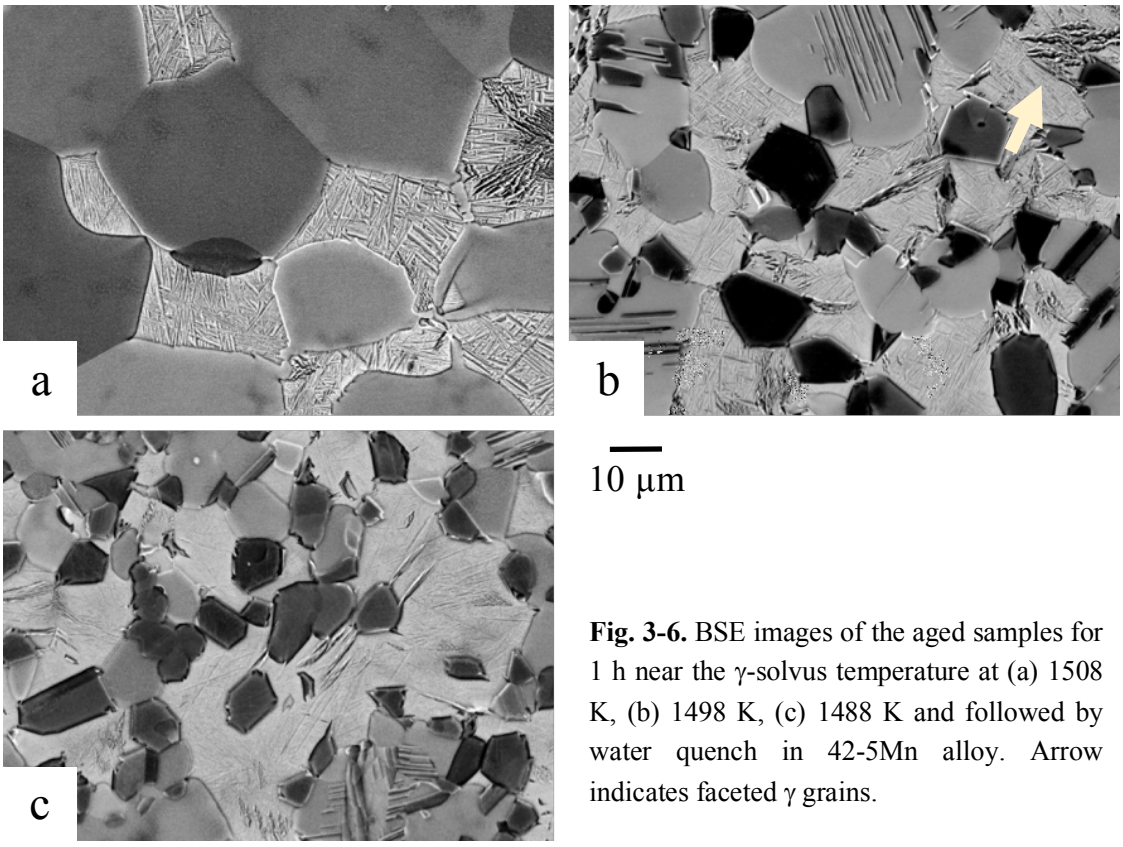

Fig. 3-6. BSE images of the aged samples for 1 h near the γ-solvus temperature at (a) 1508 K, (b) 1498 K, (c) 1488 K and followed by water quench in 42-5Mn alloy. Arrow indicates faceted γ grains.

Then, three heat treatments were conducted above, close and below the γ-solvus temperature, estimated at 1503 K, to determine the effect of this transformation on lamellar colonies formations. The selected temperatures were 1523, 1503 and 1488 K and the microstructure are shown in **Figure 3-7**. The heat-treated microstructure in β+α two phases region showed homogeneous large globular colonies (**Fig. 3-7 (a)**). The globular γ grains were dissolved during heat treatment but two different populations of γ grains were observed after cooling. A small fraction of β/γ with a pearlitic morphology, which is formed by α+γ → β+γ cellular reaction took place and are indicated by a circle in the figure. However, the kinetics is relatively slow compared to the cooling rates. Then, the second population of γ phase consisted of what is called "faceted" γ grains which have precipitated within the β phase, and were indicated by arrow.

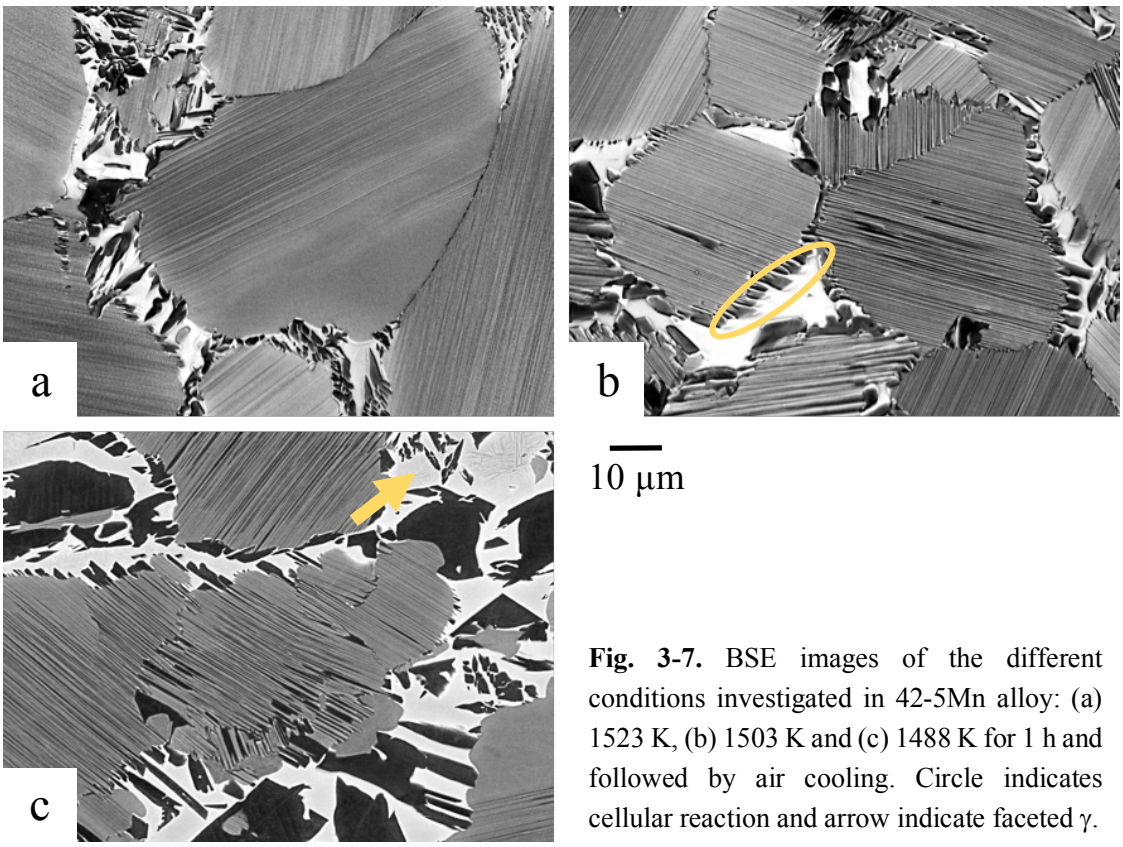

Fig. 3-7. BSE images of the different conditions investigated in 42-5Mn alloy: (a) 1523 K, (b) 1503 K and (c) 1488 K for 1 h and followed by air cooling. Circle indicates cellular reaction and arrow indicate faceted γ.

The alloy heat treated close to the γ-solvus, showed homogeneous globular colony grains with a size smaller than that at higher temperature but with thicker lamellae. These colonies are surrounded by β/γ duplex (**Fig. 3-7 (b)**). Furthermore, three different populations of γ grains have been identified. The first one corresponded to the initial

globular γ grains which existed either in grain boundaries or in the interior of some α_2/γ colonies. Their sizes were similar to that in the as-forged microstructure but their number drastically decreased. The second population consisted of $\alpha+\gamma \rightarrow \beta+\gamma$ cellular reaction. However, the ratio of β/γ was relatively small and almost γ grains precipitated. The last population was a smaller fraction of faceted γ grains precipitated within the β phase.

The last microstructure that was heat treated at 1488 K below the γ-solvus, showed colony grains with a inhomogeneous distribution of thick lamellae surrounded by higher β/γ duplex fraction compared to others microstructures (**Fig. 3-7 (c)**). The γ phase consisted of large globular γ grains, cellular reaction and small fraction of faceted γ. The major difference with microstructure heat treated at 1503 K came from the higher coarsening of the pre-existing γ grains of the initial microstructure with a size of bout 20 μm.

In case of vanadium system, six different temperatures were investigated between 1523 and 1403 K for 2 h directly followed by air cooling and the microstructures are shown in **Figure 3-8**.

For temperature above 1473 K, the initial γ grains of presented were dissolved (**Fig. 3-8 (a-c)**). Microstructures is consisted of globular α grains with a small fraction of martensitic transformed β phase at the grain boundaries. The fraction of β phase increased with temperature increasing. Lamellar structure was not observed, in contrary of manganese system. However, faceted γ grains were observed in the β region.

For temperature below 1453 K, microstructures consisted of α grains and globular γ grains in a β matrix (**Fig. 3-8 (d-f)**). With decreasing the temperature, the volume fraction of γ phase and the α_2/γ lamellar grains fraction increased. At 1453 K, lamellae were coarse (**Fig. 3-8 (d)**) whereas at 1403 K, lamellae were thin (**Fig. 3-8 (f)**). Faceted γ grains or β martensitic were not observe at these temperatures.

Because the γ grains of the initial as-forged microstructure were completely erased after aging for 2 h above 1473 K, and the γ grains size increased for heat treatments below 1453 K, the γ-solvus was identified between 1453 and 1473 K in case of vanadium system. Moreover, above 1473 K the volume fraction of β phase increased with increasing temperature. Thus, for optimized the volume fraction of α_2/γ lamellar colonies, heat treatments should be conducted near 1473 K. Nevertheless, at 1473 K the lamellar structure was not observed and so, the role of subsequent heat treatments on lamellar formation have to be investigated.

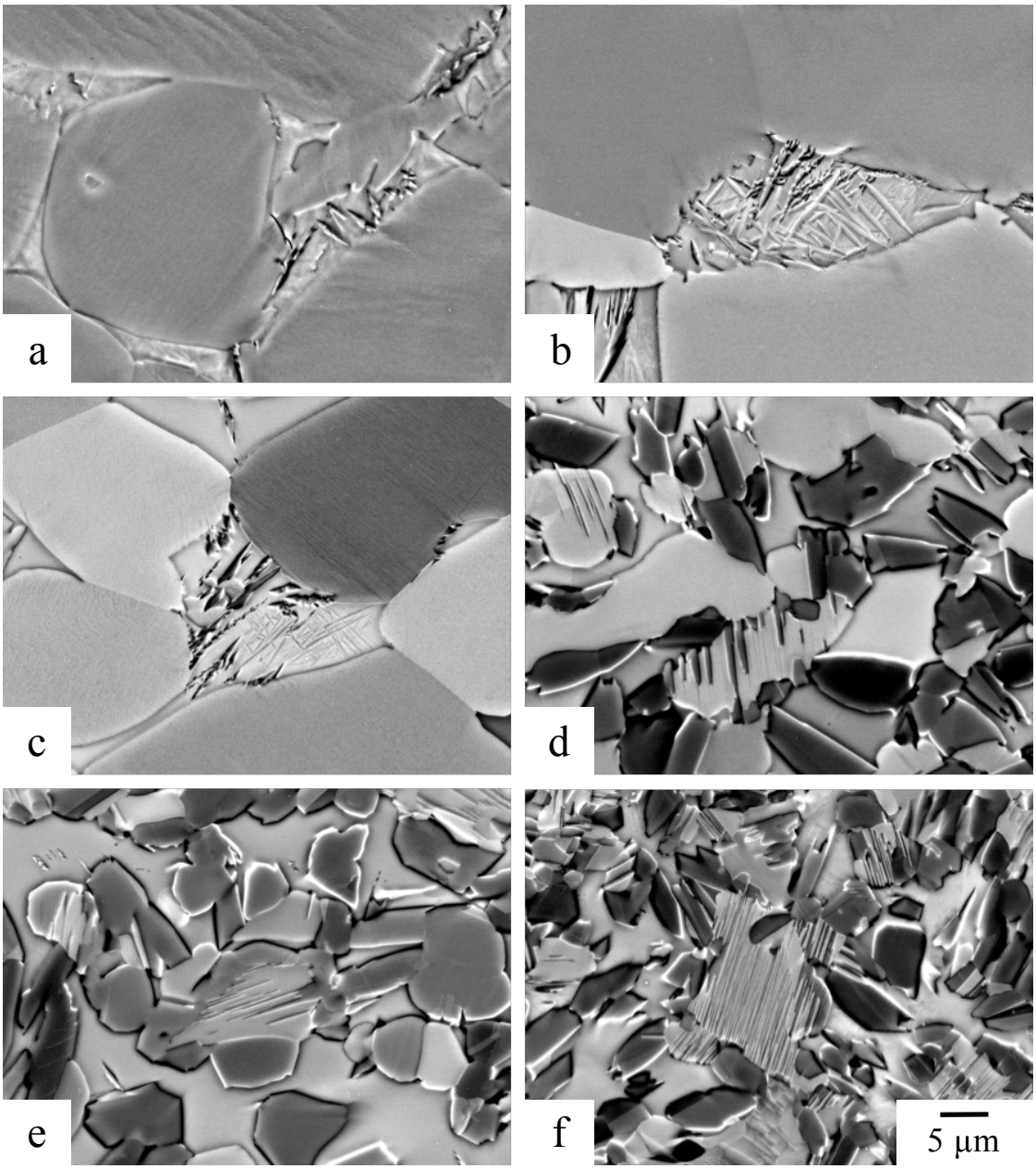

Fig. 3-8. BSE images of the aged samples at (a) 1523 K, (b) 1498 K, (c) 1473 K, (d) 1453 K, (e) 1423 K for 2 h and (f) 1403 K for 1 h followed by air cooling in 42-8V alloy.

(B) Effect of cooling rate

Another parameter to control the α_2/γ lamellar structure is the cooling rate. Thus, the effect of cooling rate on the formation of grains size and lamellar thickness have been investigated in both systems using different cooling rates: water quench, air cool, 1 K/min and 10 K/min, from the β+α two phase region just above the α-single phase to the β+α+γ three phase region. The cooling rate controlling was conducted between 1523 and 1488

K for 42-5Mn and between 1523 and 1403 K in case of 42-8V. The different microstructures are shown in **Figure 3-9 and 3-10**, respectively.

In 42-5Mn alloy, the microstructure aged with a fast cooling rate presented α grains surrounded by martensitic β and some faceted γ grains (**Fig. 3-9 (a)**). However, microstructure with slow cooling rates showed nearly lamellar microstructure with larger colonies grains surrounded the colonies by faceted γ and also a small fraction of cellular reaction. Lamellar structure was observed with all the others cooling rates. Though, the lamellae were thinner in case of 1K/min cooling rate (**Fig. 3-9 (d)**).

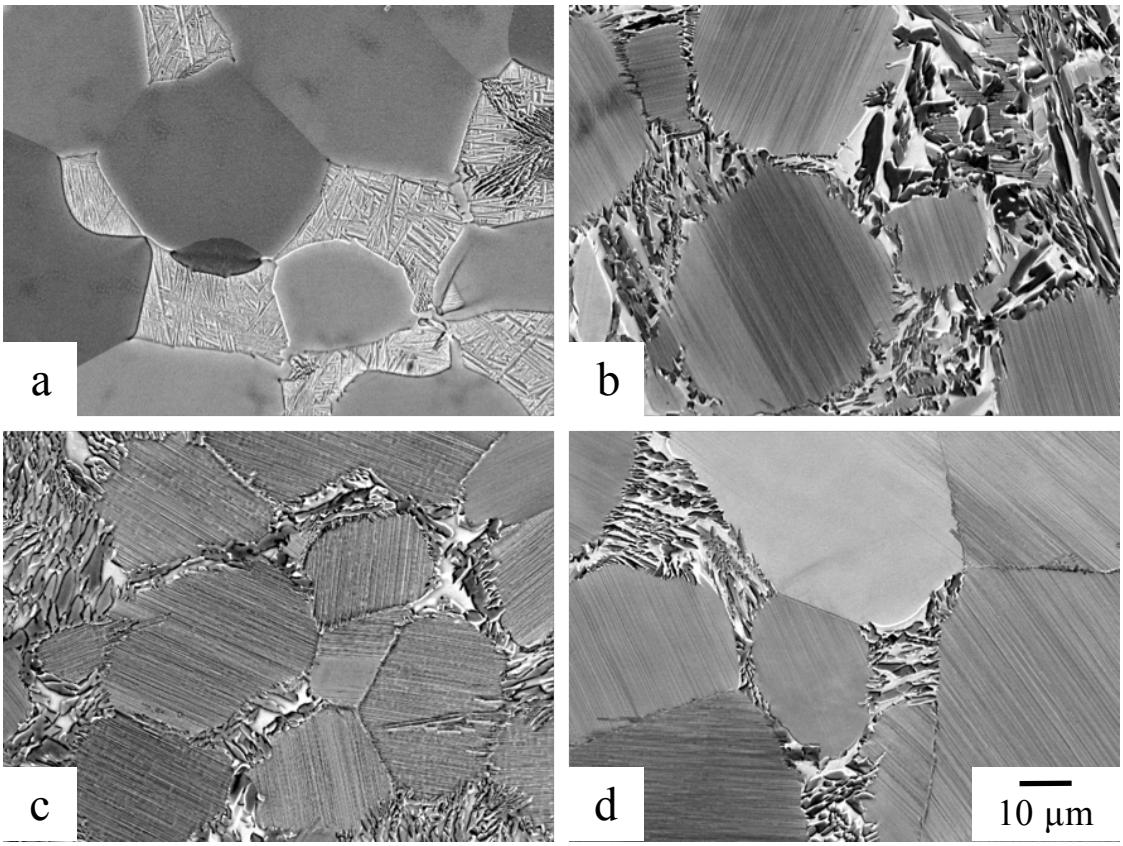

Fig. 3-9. Influence of the cooling rate on the microstructure in Ti-42Al-5Mn after aging at 1523 K for 1 h: (a) water quench, (b) air cooling, (c) 10 K/min and (d) 1 K/min up to 1488 K followed by air cooling.

After heat treatment at 1523 K, 42-8V alloy showed β+α two phase microstructure. However, even by decreasing the cooling rate, lamellar formation did not occur whether at 1K/min or 10K/min (**Fig. 3-10 (a-d)**). After air cool, few faceted γ grains precipitated. For slower cooling rates, large γ grains with an irregular shape were observed, up to 25 µm. More the cooling rate was slow, more the density and the size of these γ grains

increased. Nevertheless, it should be noted that these γ grains did not show a globular morphology as observed in heat treated microstructures below the γ-solvus but a morphology similar to the small faceted γ. Indeed, faceted γ grains started to precipitate and acted as germs for coarsening during slower cooling rates.

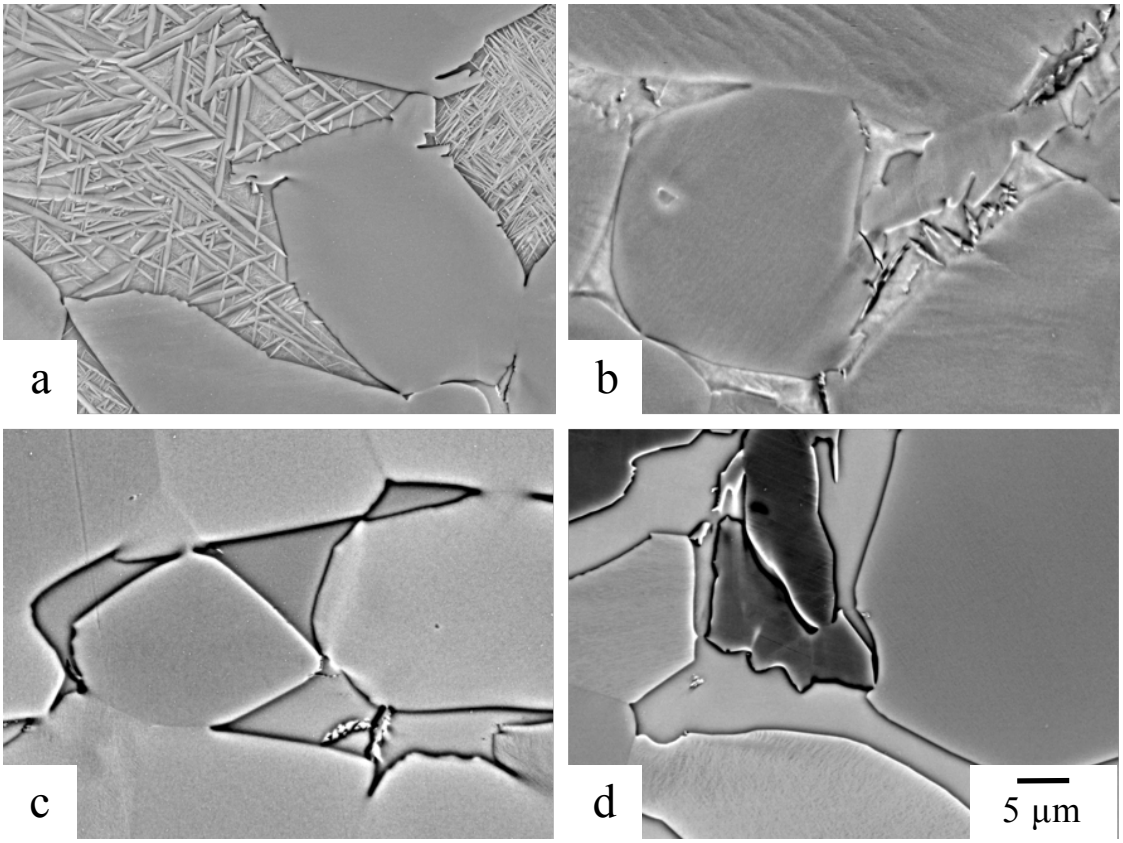

Fig. 3-10. Influence of the cooling rate on the microstructure in Ti-42Al-8V aged for 2 h at 1523 K: (a) water quench, (b) air cooled, (c) 10 K/min and (d) 1 K/min up to 1403 K followed by air cooling.

In both systems, by decreasing the cooling rates, the colonies size increased. It could be explained by the time to go through the single phase ($\beta+\alpha \rightarrow \alpha \rightarrow \alpha+\gamma$) was longer and, thus, allowed the α grains to grow.

3.3.3 β/γ duplex formation

(A) Effect of temperature

In order to determine how the transformations may affect the microstructure, the effect of temperature has been investigated. In both systems, the temperatures have been chosen in $\beta+\alpha+\gamma$ three phase region at high temperature, and then in $\beta+\gamma$ two phase region at two different temperatures to investigate the effect of the change in driving force for the

transformation. Moreover, in case of manganese system, heat treatment was also conducted below the ternary eutectoid reaction involving Laves phases. Based on the vertical section determined in **Chapter 2**, a second three phase region ($\beta+\alpha_2+\gamma$) should exists in both systems but the range of temperature was too narrow to conduct investigations.

Figure 3-11 shows the microstructure change for the different temperature after 1 h followed by air cooling in 42-8V. At 1373 K, the α_2/γ colonies have been almost completely erased. The microstructure consisted mainly of β and γ phases with small fraction of α grains. At 1273 K, the initial microstructures still can be distinguished, however the lamellar colonies were transformed into β and γ phases by the $\alpha+\gamma \rightarrow \beta+\gamma$ cellular reaction, resulting elongated γ grains. At 1173 K, transformations were limited and do not affected significantly the initial microstructure with aging time.

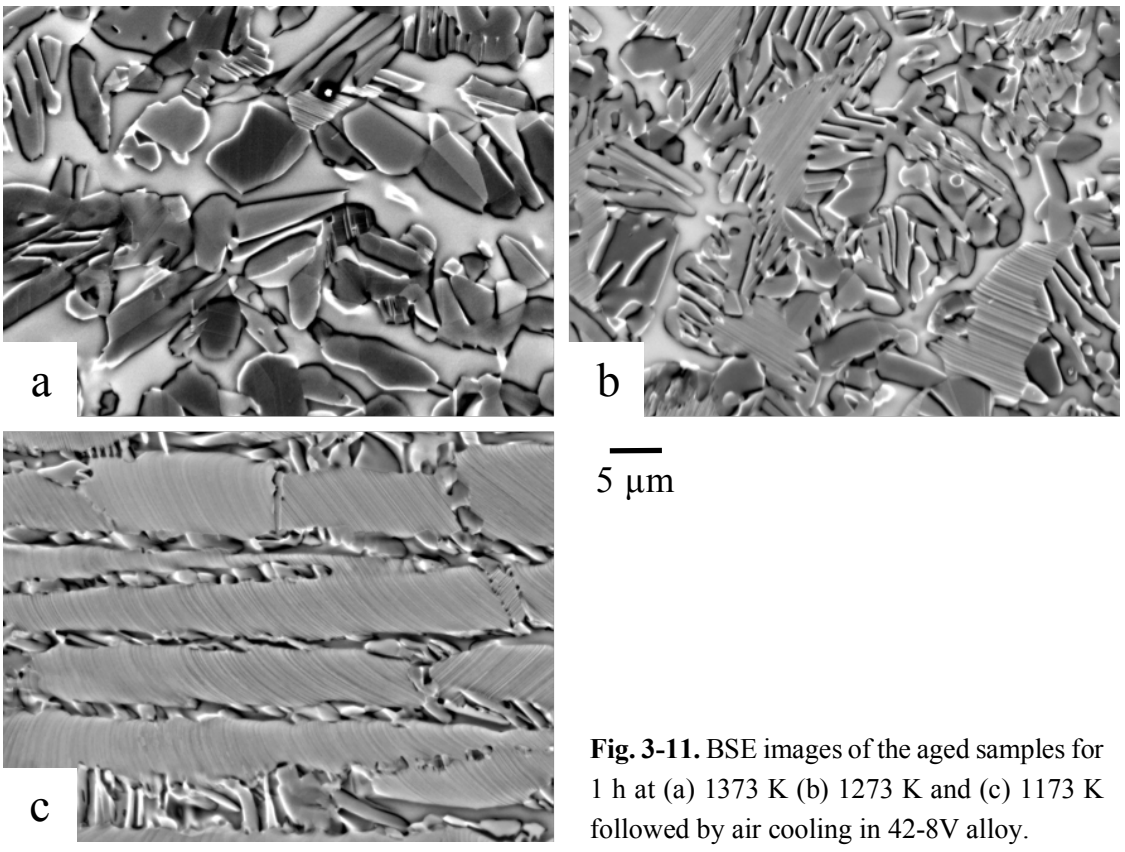

Fig. 3-11. BSE images of the aged samples for 1 h at (a) 1373 K (b) 1273 K and (c) 1173 K followed by air cooling in 42-8V alloy.

Figure 3-12 shows the microstructure change of as-forged microstructure for the different temperature after 1 h in 42-5Mn alloy. The aged microstructure at 1473 K in three phases region showed a coarsening of the γ grains and a decreasing of α_2/γ colony grains size. The microstructure was characterized by an increasing in β/γ duplex at

colonies boundaries. At 1373 K, the lamellar microstructure almost disappeared, only few colony grains remained. It resulted in an important fraction of β and γ phases. However, the growth effect of γ grains was smaller than that at 1473 K. The aged microstructure at 1273 K was similar to the initial as-forged but a limited increase of duplex region was observed. At both 1373 and 1273 K, small precipitates of β phase were observed within the lamellar structure. Finally, the aged microstructure at 1123 K does not present significant difference at lower magnification but at higher magnification, small grains with a bright contrast was precipitated at the sub-colony grains boundaries and was identified as C14 Laves phase as detailed in **Chapter 2** (**Fig. 3-12 (d)**).

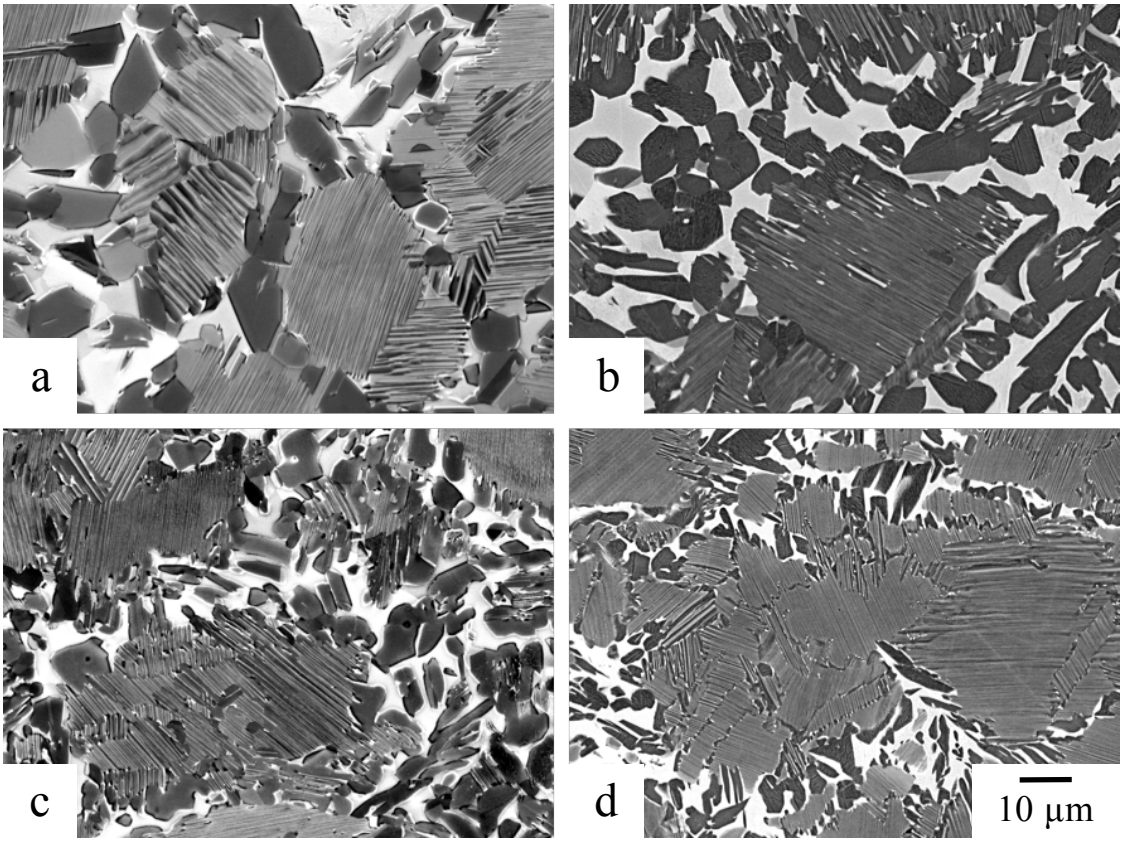

Fig. 3-12. BSE images of the samples aged for 1 h at (a) 1473 K, (b) 1373 K, (c) 1273 K and (d) 1123 K followed by air cooling in 42-5Mn alloy.

(B) Effect of time

The change of microstructure with time have been investigated in order to evaluate the stability and evolution of different phases.

The microstructures of 42-8V alloy aged for 10 h are shown in **Figure 3-13**. At 1373 K, the microstructure consisted of β and γ grains coarser compared to that of shorter heat treatment and that of a small fraction of α grains (**Fig. 3-13 (a)**). The lamellar colonies disappeared at 1273 K (**Fig. 3-13 (b)**). At lower temperature, the initial microstructure still existed with elongated α_2/γ colonies but a higher fraction of β/γ duplex region was formed. The ratio of β phase precipitated in β/γ DP was very low. It found that the remained colonies appeared decorated by a necklace of γ grains.

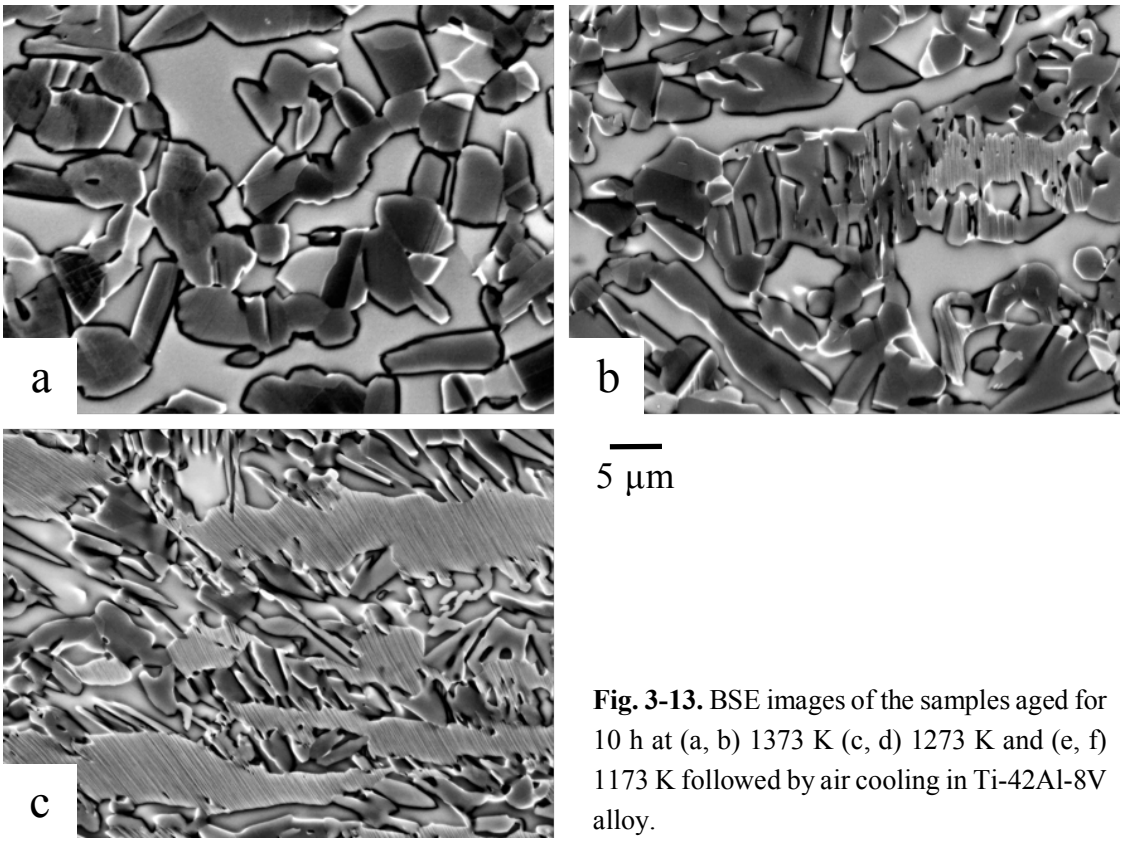

Fig. 3-13. BSE images of the samples aged for 10 h at (a, b) 1373 K (c, d) 1273 K and (e, f) 1173 K followed by air cooling in Ti-42Al-8V alloy.

In the manganese system, the forged alloy was heat treated up to 100 h and the change in microstructure with temperature are shown in **Figure 3-14 and 3-15**, respectively.

After 10h, the coarsening become important at 1473 and 1373 K as shown in **Figure 3-14**. At 1473 K, the number of γ grains decreased but their size increased. Within the colony grains, the coarsening of γ phase also occurred and thus, large α grains appeared. Moreover, faceted γ started to precipitate within the β phase (**Fig. 3-14 (a, b)**). In the microstructure at 1373 K, the lamellar colonies almost disappeared. The remained colonies showed coarse and thick γ lamellae. Moreover, the volume fraction of β phase was relatively high compared to the other temperatures. The same evolution of the

microstructural features was observed at 1273 K, but the effect was less important. The microstructure aged at 1173 K did not change significant change by increasing time. However, it should be noticed that at the colonies boundaries, the size and the fraction of Laves precipitates increased.

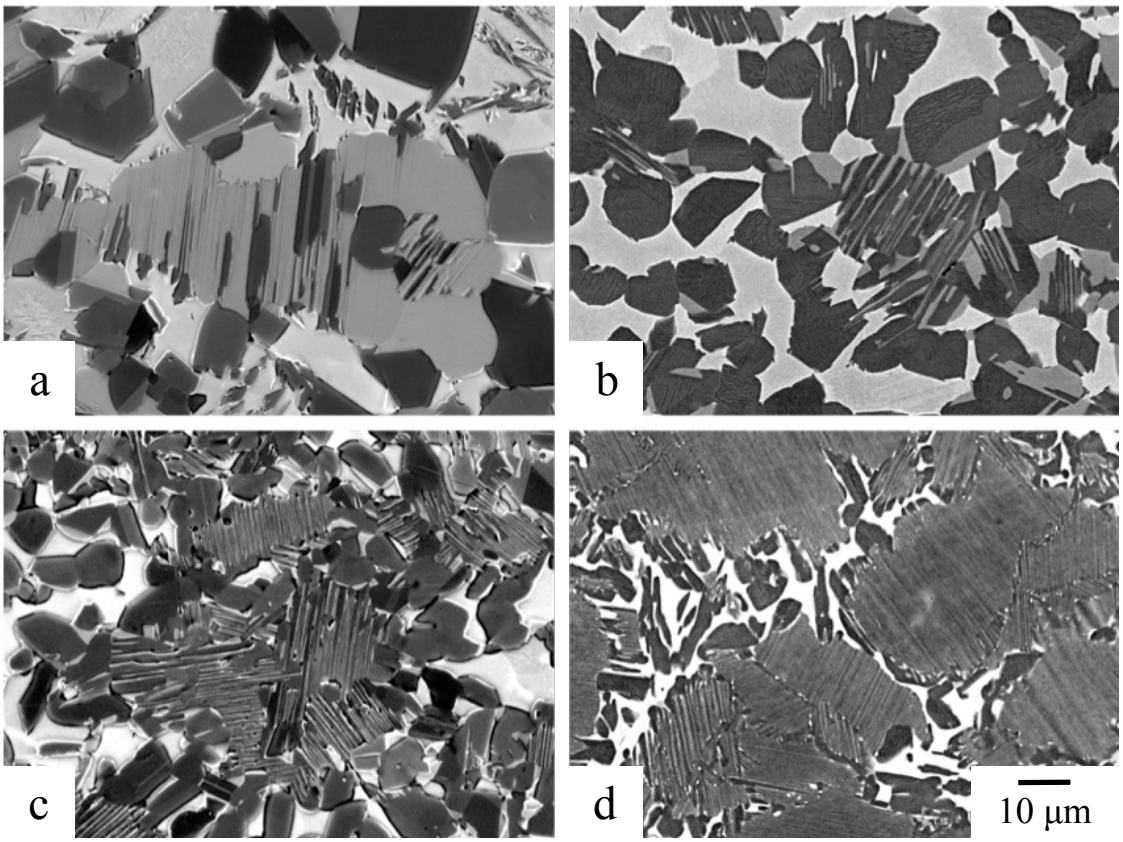

Fig. 3-14. BSE images of the samples aged at (a) 1473 K, (b) 1373 K, (c) 1273 K and (d) 1123 K for 10 h followed by air cooling in Ti-42Al-5Mn alloy.

Figure 3-15 shows the evolution of microstructure with temperature after 100 h heat treatment. At 1473 K, the microstructure was composed of large α and γ grains, with a size of about 50 μm, dispersed in β matrix. Few α grains still contain some coarse γ lamellae vestiges. The faceted γ precipitates were found in all β matrix (**Fig. 3-15 (a)**). The microstructures aged at 1373 K and 1273 K were mainly composed of γ grains with a β phase matrix. By decreasing the temperature, the volume fraction of γ increase. Furthermore, a small fraction of α grains was observed only at 1373 K. This could be explained by the competition between coarsening, which is faster at higher temperature, and α+γ → β+γ cellular reaction kinetics. Finally, after 100 h, microstructure aged at

1023 K did not show a significant difference compare to shorter heat treatments, excepted the increase of Laves phase size up to 2 μm.

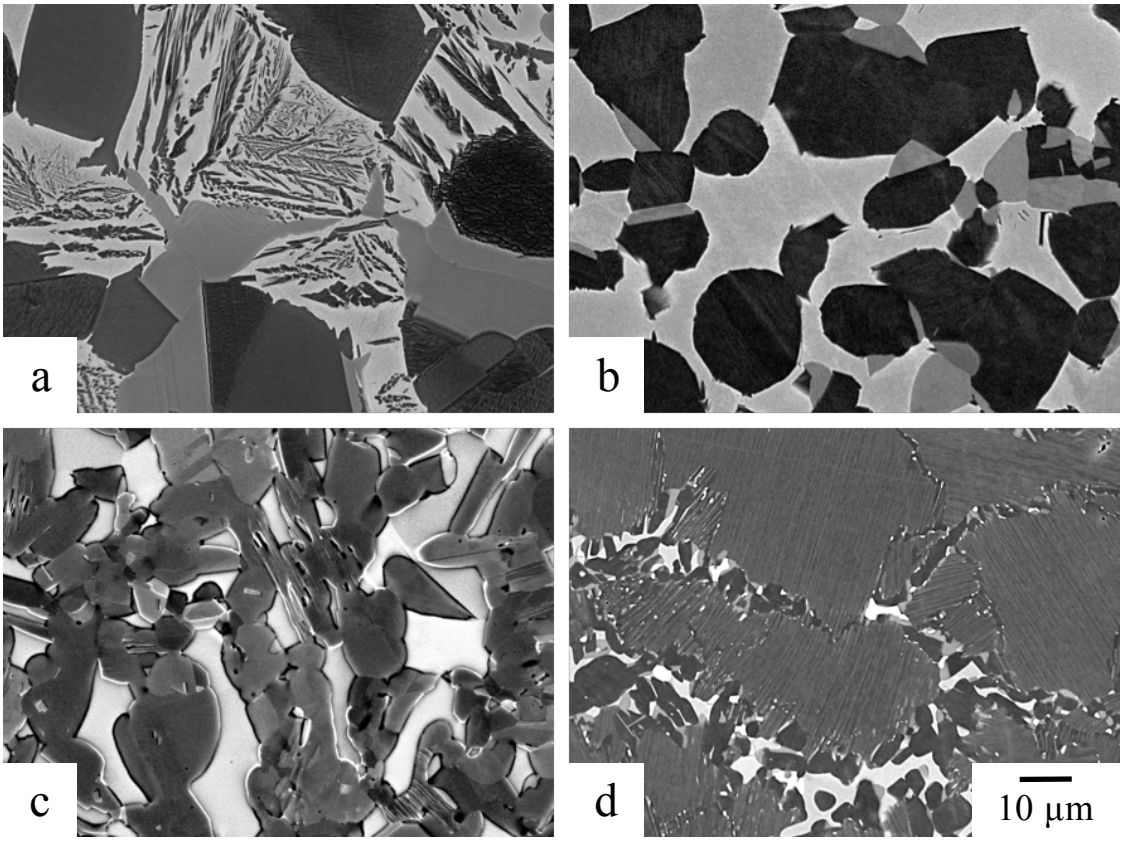

Fig. 3-15. BSE images of the samples aged at (a) 1473 K, (b) 1373 K, (c) 1273 K and (d) 1123 K for 100 h followed by air cooling in Ti-42Al-5Mn alloy.

(C) Effect of the initial conditions

In the previous sections, it has been demonstrated how the different parameters such as the temperature, the time and the cooling rates may affect the lamellar formation and how it was possible to control the morphology and the fraction of the γ and β phases. This part will describe the change in microstructure during subsequent heat treatment, especially β/γ duplex, after a first step heat treatment.

In both systems, microstructures were stabilized at 1123 K for two different times, 3 and 20 h. The microstructures can be divided into three groups depending on the first step heat treatment, whether it was conducted below, close, or above the γ-solvus.

In Ti-42Al-8V alloy, after aged at 1123 K, the microstructures where the initial state was in β+α two phases region showed lamellar γ precipitation within the former colonies

grains as shown in **Figure 3-16 (a-d)**. Moreover, $\alpha_2+\gamma \rightarrow \beta+\gamma$ cellular reaction occurred at the colony grain boundaries. As introduced earlier, it is possible to control the ratio between γ and β phases, however, at low temperature, this transformation generated mainly γ phase. Furthermore, precipitation of fine γ grains occurred in β region (indicated by arrow in **Fig. 3-16 (a)**). Thus, the volume fraction of β after the second heat treatment drastically dropped. More the temperature of the first heat treatment was higher more the cellular reaction was important.

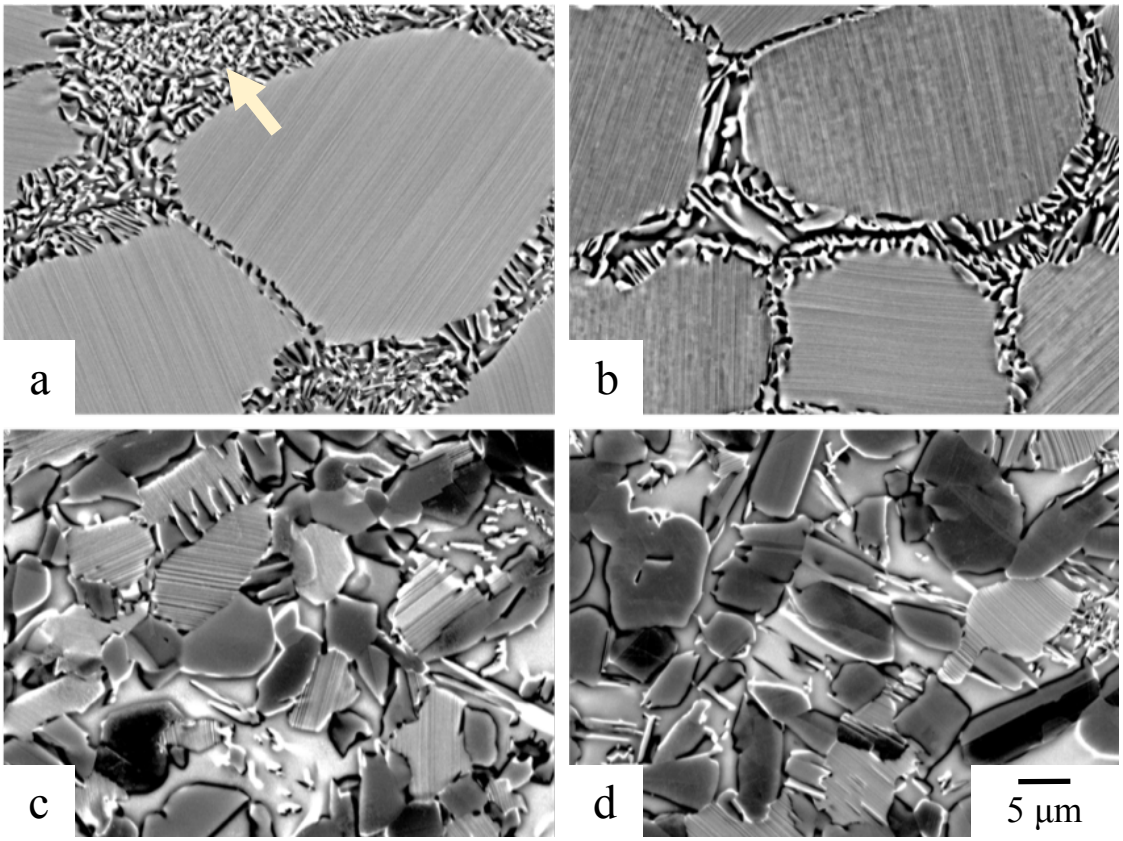

Fig. 3-16. Microstructure of samples aged for 2 h at (a) 1498 K, (b) 1473 K (c) 1423 K and (d) 1423 K followed by 2nd step heat treatment at 1123 K for 3 h with air cooling.

By increasing time to 20 h, the cellular reaction continues and β/γ duplex fraction increased from 30 to 60 % of the microstructure (**Figure 3-17 (a-d)**). In the microstructures where the initial state was below the γ-solvus, few differences were observed after 3 h annealing as shown in **Fig. 3-16 (e-h)**. The γ phase precipitated and formed α_2/γ lamellar grains in the former α grains. Moreover, the initial γ grains became coarser. At 1403 K, the fraction of globular γ was higher than the microstructure that was aged at 1433 K. By increasing time to 20 h (**Fig. 3-17 (e-h)**), the coarsening of grains

continued. The microstructures, where the initial state was in β+α two phases region, show cellular reaction which occurred on the grains boundaries. As introduced earlier, this transformation generates mainly γ phase. Moreover, fine γ precipitation occurred in β region. Thus, the volume fraction of β after the second heat treatment drastically dropped. More the temperature of the first heat treatment was higher more the cellular reaction was important. Furthermore, after 20 h, the cellular reaction continues and β/γ duplex represents more than 50 % of the microstructure.

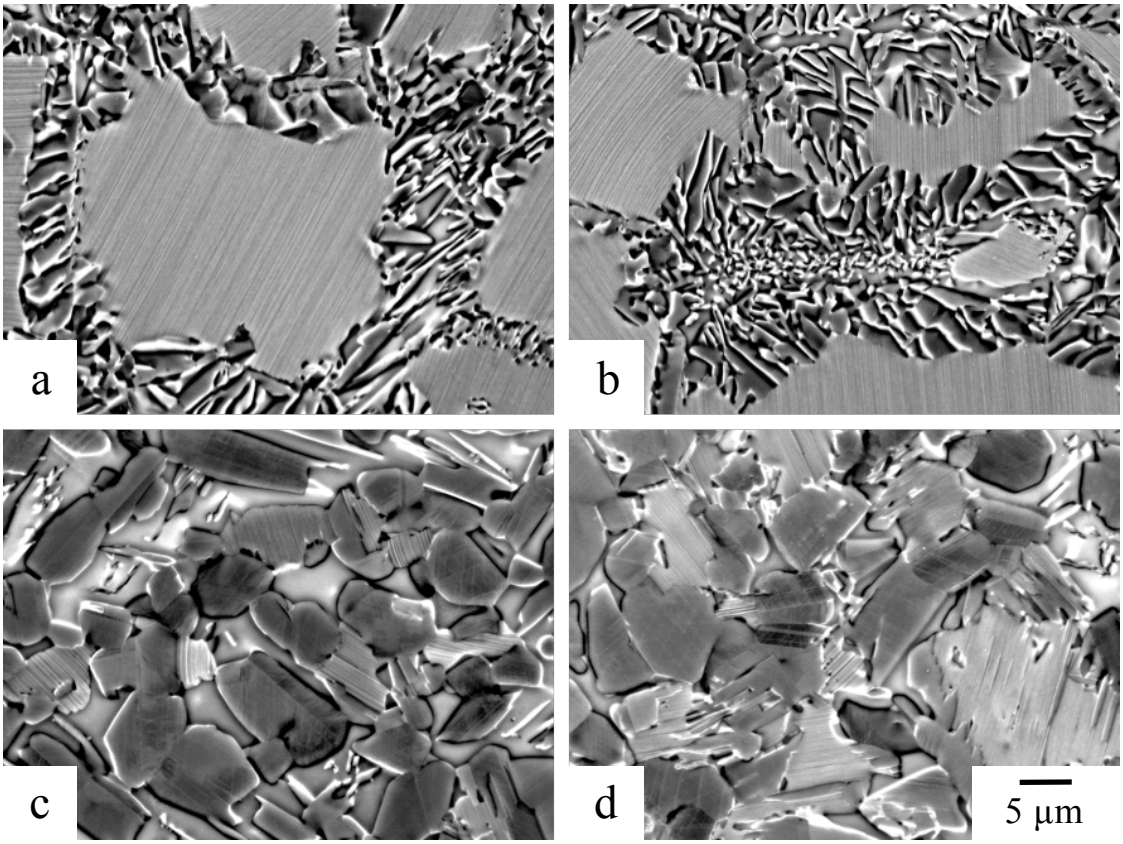

Fig. 3-17. Microstructure of samples aged for 2 h at (a) 1498 K, (b) 1473 K (c) 1423 K and (d) 1423 K followed by 2nd step heat treatment at 1123 K for 20 h with air cooling.

The manganese system showed very stable microstructures even after 20 h aged at 1123 K as shown in **Figure 3-18**. Indeed, after annealing heat treatment, the three microstructures did not show significant different compared to the initial state, either grains size or volume fraction. However, it should be noted that the initial faceted γ grains of the microstructure aged at 1523 K became smoother due to coarsening mechanism.

Whereas in case of Ti-42Al-5Mn, the microstructure design is mainly determined by the initial condition, the annealing heat treatments of Ti-42Al-8V drastically affected the

microstructures. Precipitation of the lamellar structure occurred in all initial α grains independently of the initial conditions. But the morphology of the γ phase is determined by the temperature of the initial step. Morphology could be either globular (T < γ-solvus) by coarsening or plate/elongated (T > γ-solvus) by cellular reaction.

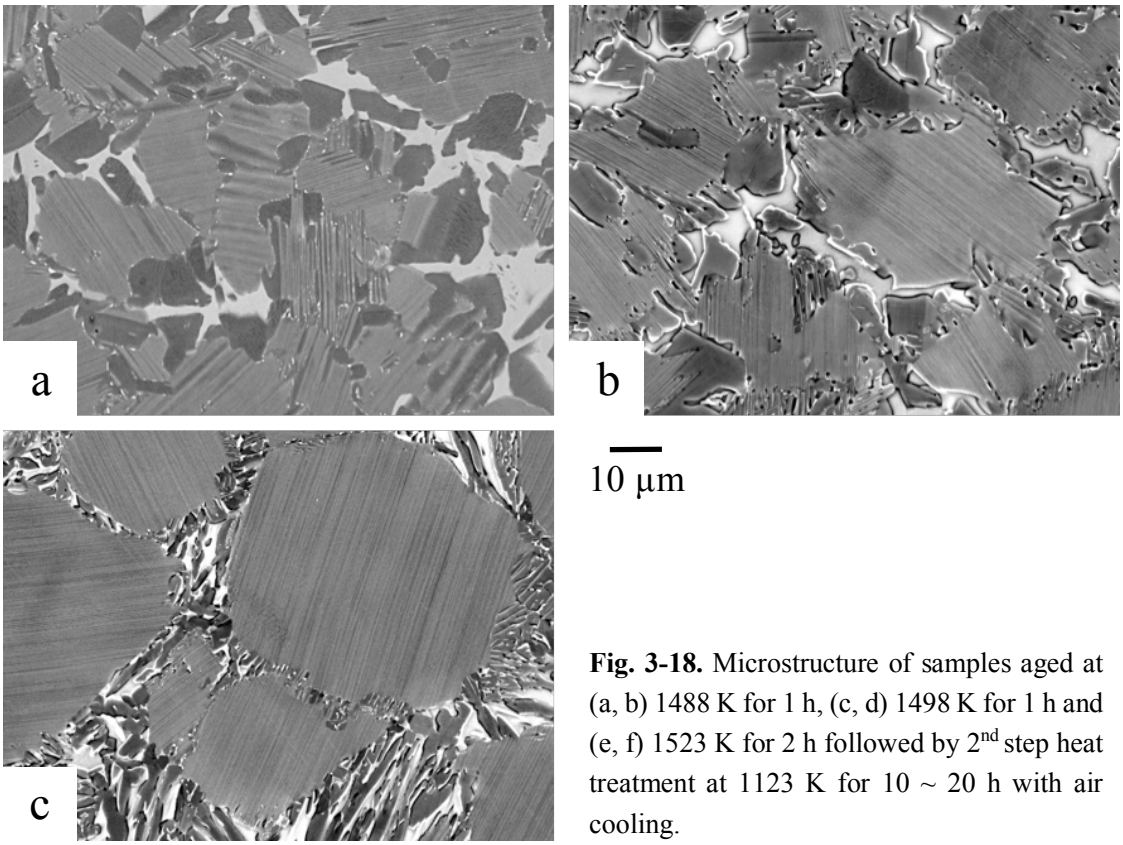

Fig. 3-18. Microstructure of samples aged at (a, b) 1488 K for 1 h, (c, d) 1498 K for 1 h and (e, f) 1523 K for 2 h followed by 2nd step heat treatment at 1123 K for 10 ~ 20 h with air cooling.

3.3.4 Quantitative measurements and their change with heat treatment conditions

In order to investigate the effect of heat treatment conditions on the microstructural features, and thus, design the desired microstructure, some quantitative measurements were done. The volume fraction of the different phases and the grains size were measured in both systems.

(A) Volume fraction *V* of the different microstructural features

The volume fraction of the lamellar colonies, γ grains, both globular/elongated and sharp-like shapes, β and α/α_2 grains of 42-5Mn and 42-8V alloys are summarized in **Table 3-4 and 3-5**, respectively.

Table. 3-4. Volume fraction of the microstructural features in Ti-42Al-5Mn alloy.

Heat treatment condition		Phase fraction / %				
1st step	2nd step	Lamellar Colonies V_L	β/γ duplex V_{DP}			α/α_2 grains V_α
			γ-phase V_γ		β-phase V_β	
			Globular V_{glob}	Sharp V_{dec}		
as-forged	–	47.9 ± 8.5	38.5 ± 6.4	–	13.6 ± 2.3	1 <
	1123 K / 1 h	53.0 ± 1.4	32.0 ± 1.4	–	14.9 ± 0.8	1 <
	1123 K / 10 h	52.5 ± 5.6	30.6 ± 3.6	–	13.5 ± 1.6	3.4 ± 0.6
	1123 K / 100 h	49.6 ± 10.1	34.8 ± 7.0	–	10.8 ± 2.5	4.9 ± 0.6
	1273 K / 1 h	28.7 ± 7.6	48.9 ± 4.2	–	22.4 ± 3.4	–
	1273 K / 10 h	15.0 ± 1.8	63.5 ± 2.4	–	21.5 ± 1.1	–
	1273 K / 100 h	1.2 ± 0.7	79.2 ± 3.4	–	18.9 ± 2.7	–
	1373 K / 1 h	18.3 ± 1.5	51.6 ± 0.8	–	25.0 ± 0.8	5.0 ± 0.5
	1373 K / 10 h	5.5 ± 0.4	58.9 ± 0.1	–	29.4 ± 1.3	6.2 ± 0.8
	1373 K / 100 h	–	59.0 ± 0.8	–	30.5 ± 3.2	10.6 ± 2.7
	1473 K / 1 h	31.1 ± 8.0	41.1 ± 4.1	1 <	17.9 ± 3.6	9.9 ± 1.2
	1473 K / 10 h	10.9 ± 4.4	39.3 ± 1.6	3.8 ± 0.4	20.6 ± 1.1	25.4 ± 3.2
	1473 K / 100 h	–	36.6 ± 3.1	7.6 ± 0.9	22.2 ± 2.2	33.5 ± 2.2
	1488 K / 1 h	61.5 ± 1.0	10.9 ± 0.3	7.0 ± 0.4	16.2 ± 0.4	4.5 ± 0.5
	1503 K / 1 h	72.5 ± 3.8	19.2 ± 2.4	1 <	8.3 ± 1.4	–
	1503 K / 100 h	67.8 ± 7.1	6.6 ± 1.6	19.6 ± 4.2	6.1 ± 1.8	–
	1523 K / 1h	75.4 ± 7.5	–	15.9 ± 4.2	8.7 ± 3.6	–
1488 K / 1 h	1123 K / 1 h	50.1 ± 6.8	32.2 ± 4.4	1.2 ± 0.2	16.5 ± 7.2	1 <
	1373 K / 1 h	20.7 ± 1.6	47.0 ± 1.3	–	28.7 ± 1.2	3.5 ± 0.3
	1473 K / 1 h	26.3 ± 5.0	39.7 ± 3.4	0.9 ± 0.1	26.3 ± 2.7	6.8 ± 1.4
1523 K / 2 h	1123 K / 1 h	68.6 ± 2.4	19.0 ± 1.2	–	12.4 ± 1.3	1 <
	1373 K / 1 h	10.0 ± 4.7	57.1 ± 2.7	–	24.3 ± 1.6	8.6 ± 0.6
	1473 K / 1 h	15.4 ± 1.7	44.7 ± 0.5	3.1 ± 0.9	23.4 ± 2.2	13.4 ± 2.6

Table. 3-5. Volume fraction of the microstructural features in Ti-42Al-8V alloy.

Heat treatment condition		Phase fraction / %				
1st step	2nd step	Lamellar Colonies V_L	β/γ duplex V_{DP}		β-phase V_β	α/α_2 grains V_α
			γ-phase V_γ			
			Globular V_{glob}	Sharp V_{dec}		
as-forged	–	72.2 ± 2.1	19.2 ± 0.7	–	8.6 ± 0.2	–
	1173 K / 1 h	64.7 ± 4.3	29.2 ± 4.0	–	6.1 ± 1.4	1 <
	1173 K / 10 h	24.8 ± 6.1	43.6 ± 8.0	–	31.6 ± 1.9	1 <
	1273 K / 1 h	10.1 ± 4.3	77.2 ± 1.8	–	12.7 ± 1.6	1 <
	1273 K / 10 h	1.0 ± 0.3	67.5 ± 5.1	–	31.5 ± 5.1	1 <
	1373 K / 1 h	1.4 ± 1.0	63.8 ± 3.8	–	32.6 ± 2.0	2.2 ± 0.8
	1373 K / 10 h	–	60.1 ± 1.9	–	39.9 ± 1.9	1 <
	1403 K / 1 h	9.1 ± 2.2	39.3 ± 4.0	–	41.1 ± 2.2	10.7 ± 0.7
	1473 K / 1 h	–	–	1 <	10.7 ± 2.2	89.3 ± 2.2
	1498 K / 1 h	–	–	1 <	15.9 ± 2.7	84.1 ± 2.7
1473 K / 2 h	–	–	–	1 <	11.5 ± 3.3	88.5 ± 3.3
	1123 K / 3 h	66.8 ± 1.8	27.9 ± 0.5	–	5.3 ± 1.3	–
	1123 K / 20 h	39.7 ± 5.5	48.8 ± 4.5	–	11.5 ± 1.0	–
1498 K / 2 h	–	–	–	1 <	21.9 ± 2.6	78.1 ± 2.6
	1123 K / 3 h	65.5 ± 6.7	28.0 ± 5.5	–	6.6 ± 1.3	–
	1123 K / 20 h	34.5 ± 1.7	53.0 ± 1.3	–	12.4 ± 0.3	–

The change in the lamellar volume fraction V_L with temperature for different ageing time, i. e. for 1 to 100 h, in as-forged 42-5Mn and 42-8V alloys is illustrated in **Figure 3-19**. In both system, four regions have been identified. With increasing the temperature, the lamellar volume fraction did not change up to a certain temperature, then the lamellar fraction decreased with a low slope up to a minimum and increased with high slope up to a maximum; finally, the volume fraction decreased again.

In 42-8V alloy, the initial colonies fraction was of about 72 % and did not change up to 1073 K. Then in the β+γ two phase region, the fraction decreased up to a minimum at 1373 K with less 1 % of lamellar grains after 1 h of ageing time. It should be noted that in vanadium alloy, for ageing time higher than 1453 K, no lamellar precipitation was

observed after air cool, however, the fraction of α grains provided an estimation of the possible "lamellar grains". Therefore, once the ageing temperature was higher than the γ-solvus, the fraction of colonies (α grains) increased up to 88% at 1473 K and then decreased in the β+α region.

Despite the trend was similar for 42-5Mn alloy, some differences were noticed. The initial colonies fraction was of about 48 % and did not change up to 1173 K. The minimum fraction was measured at 1373 K with 20 % and the maximum was around 75% at 1523 K. Therefore, the transformations and coarsening kinetics in the β+γ two phase region were faster in the vanadium system. Moreover, the peak position was directly correlated with the γ-solvus (or α region) position that was at higher temperature for 42-5Mn.

In both alloys, by increasing time the effect was enhanced. After 100 h, the fraction of lamellar was almost null between 1173 and 1373 K in 42-8V and between 1273 and 1473 K in 42-5Mn.

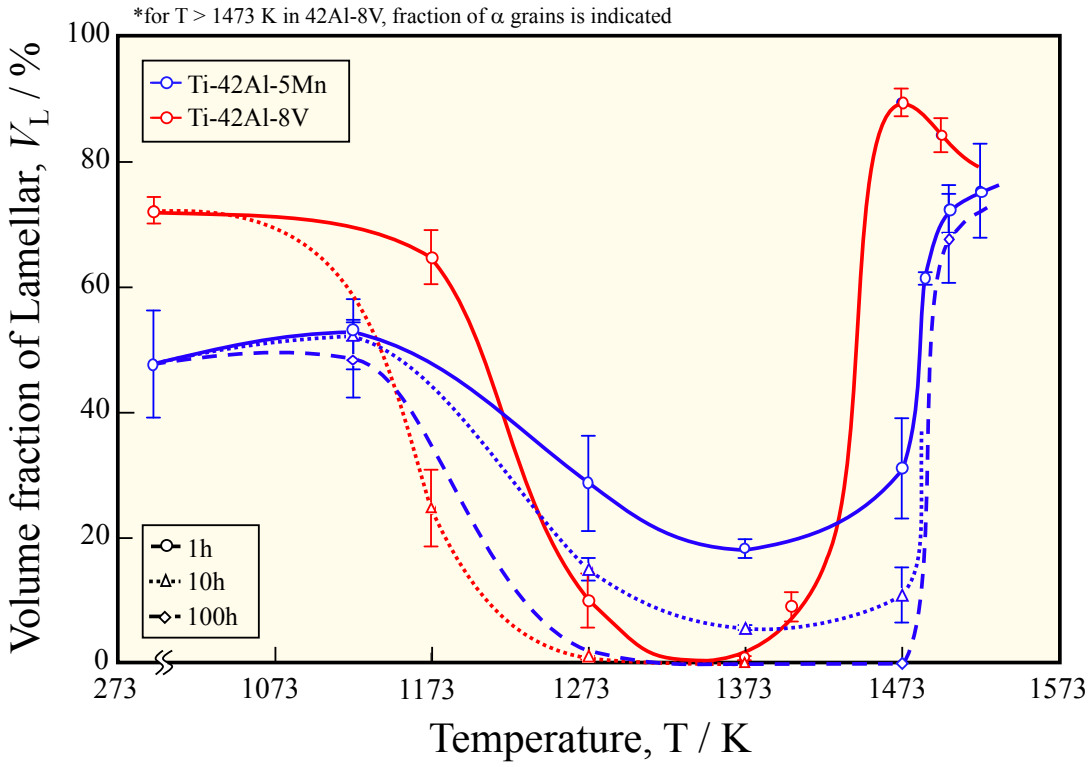

Fig. 3-19. Change in volume fraction of α_2/γ lamellar colonies with temperature for different time. In case of Ti-42Al-8V, for temperatures higher than 1473 K, no γ precipitation were observed and the α grains size is given for indication.

Figure 3-20 shows the change of lamellar fraction with temperature after 1 h of ageing time for different initial conditions in 42-5Mn. By changing the initial conditions, the shape of the curve and the peaks position did not change. Nevertheless, more the initial lamellar fraction was higher, more the decrease of colony grains was faster. It can be easily explained by the higher driving force of the cellular reaction. In the as-forged microstructure, the colonies fraction decreased from 48 % to 20 % while in the 1523 K / 2 h microstructure, the colonies fraction decreased from 69 % to 15 % between 298 and 1373 K.

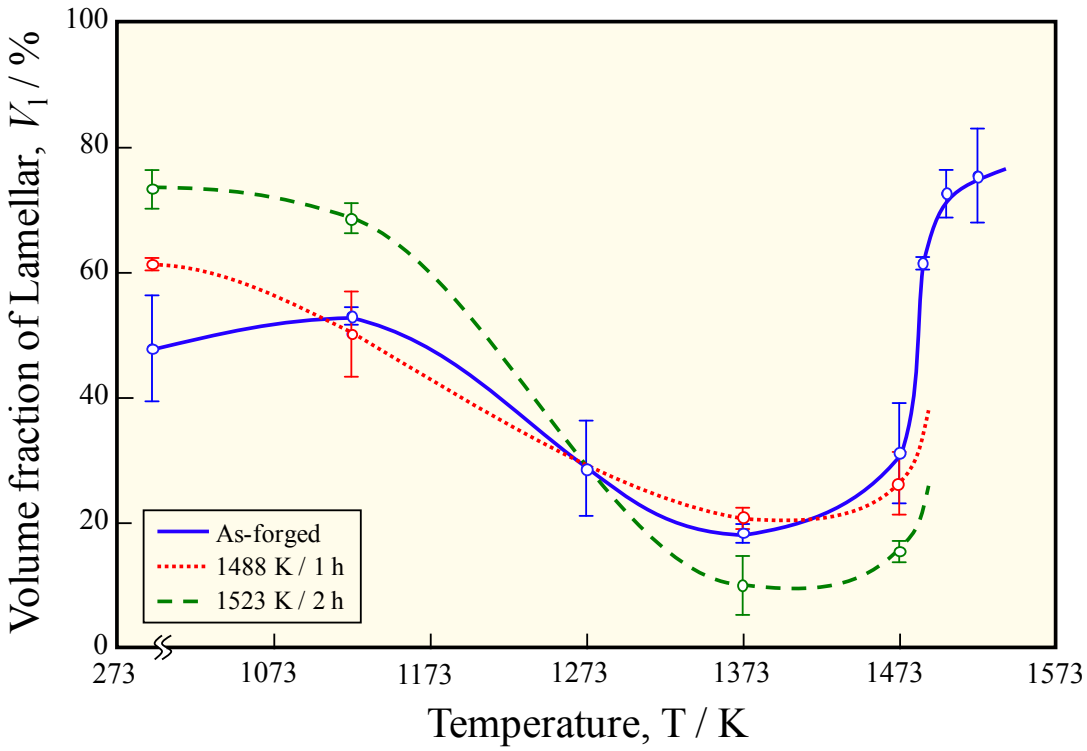

Fig. 3-20. Change in volume fraction of α_2/γ lamellar colonies with temperature after 1 h with different initial heat treatment conditions in Ti-42Al-5Mn alloy.

The effect of heat treatments on the lamellar colonies has been described but other constituents are present in the microstructures. The change of γ phase and β phase with temperature for different ageing time in the 42-5Mn alloy is illustrated in **Figure 3-21 and 3-22**, respectively.

The γ phase has been divided in two categories: the globular or elongated grains observed in β+γ two phase and β+α+γ three phase regions, and the faceted grains observed in β+α+γ three phase and β+α two phase regions. The fraction of

globular/elongated grains did not change significantly up to 1123 K with a value of about 35 %. Then, the fraction increased up to a maximum between 52 % after 1 h to 79 % after 100 h. The peak position decreased from 1373 K to 1273 K by increasing time. Afterward the fraction drastically decreased up to 0 % once the temperature became higher than the γ-solvus. Though from 1473 K, faceted γ started to precipitated within the β phase. With increasing both time and temperature the fraction become more important. The fraction of the faceted γ is directly correlated to the fraction of β phase.

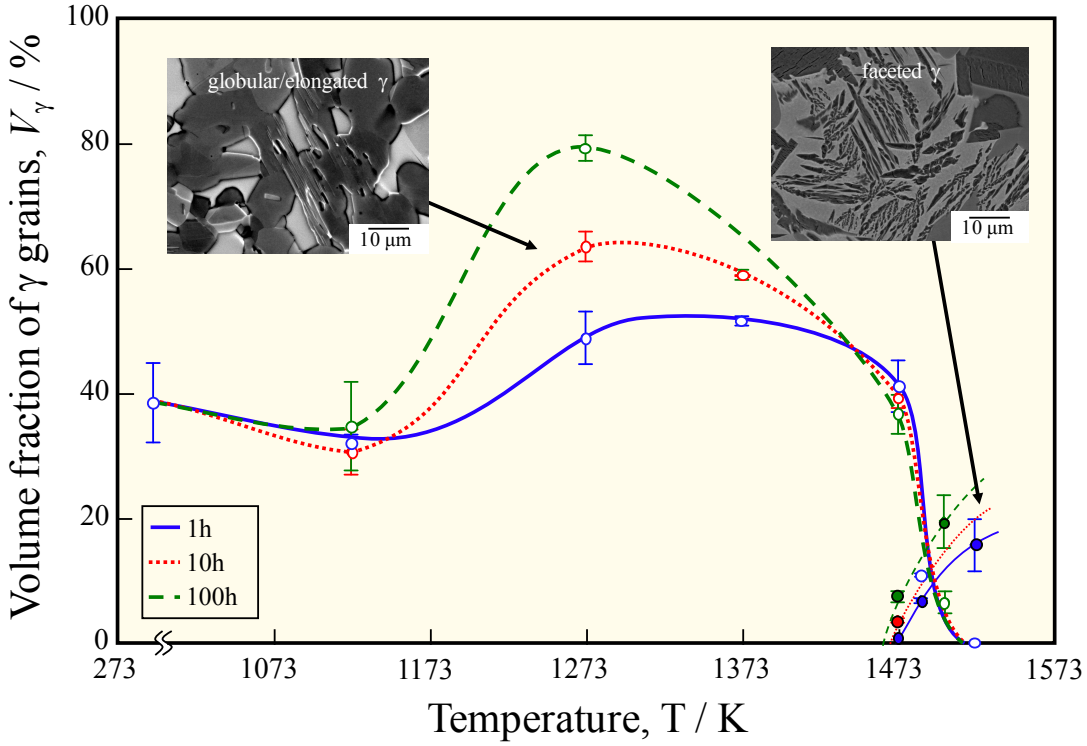

Fig. 3-21. Change in volume fraction of γ phase with temperature for different times in Ti-42Al-5Mn alloy.

The change of volume fraction of β phase Vβ showed three different regions (**Fig. 3-22**). The fraction of β showed a minimum at 1123 K, a maximum at 1373 K and then decreased and approached 0 % at high temperature. The peak position was not affected by increasing the ageing time but the fractions were enhanced. After 100 h, the minimum volume fraction was of around 10 % and the maximum of around 30% in the β+γ two phase region. Based on the vertical section, by increasing temperature above the α region, γ phase should not exist and β fraction should increase which is in contrary of the observation and measurement. In fact, as will be detailed in the discussion part, after heat

treatments at high temperature, β phase decomposed into β' and faceted γ grains. Therefore, by combined the fraction of β phase and the faceted γ grains, it became possible to estimate the original fraction of β phase at high temperature. After reached the peak at 1373 K (β+γ two phase region), the fraction of β slightly decreased up to 1473 K (β+α+γ three phase region) and then increased again in the β+α region as predicted by the phase diagram.

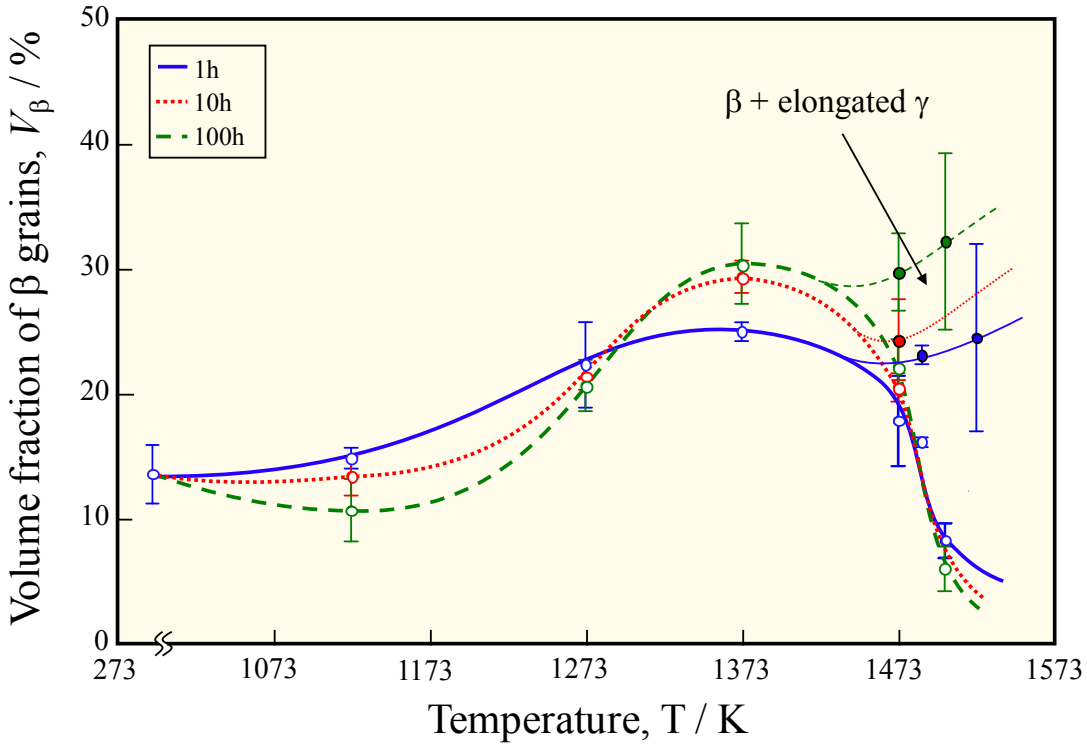

Fig. 3-22. Change in volume fraction of β phase with temperature for different times in Ti-42Al-5Mn alloy.

Finally, it should be noticed that, between 1373 and 1488 K in the β+α+γ three phase region, large fractions of α grains were measured up to 34 % after 100 h of ageing time. Moreover below 1173 K, due to the ternary eutectoid reaction, α_2 grains started to growth and their fraction increased up to 5% after 100 h. These both grains should be taking into account during microstructure design.

(B) Grain size *d* of the different constituents

The lamellar colonies lengths, widths and aspect ratio, as the γ grains size of Ti-42Al-5Mn and Ti-42Al-8V are summarized in **Table 3-6**.

Table. 3-6. Size of lamellar colonies and γ grains in 42-5Mn and 42-8V alloys.

Alloy	Heat treatment	Grains size / μm			
		α_2/γ lamellar colonies			γ grains *d*
		Length *L*	Width *W*	Aspect ratio	
Ti-42Al-5Mn	as-forged	41.1 ± 6.4	26.5 ± 4.2	1.6 ± 0.2	5.8 ± 1.0
	1123 K / 1 h	44.5 ± 4.1	26.2 ± 3.7	1.8 ± 0.2	6.7 ± 1.3
	1123 K / 10 h	39.2 ± 4.9	22.9 ± 2.9	1.8 ± 0.2	6.7 ± 1.1
	1123 K / 100 h	44.8 ± 6.8	28.7 ± 4.2	1.6 ± 0.2	6.8 ± 1.3
	1273 K / 1 h	34.9 ± 3.1	22.1 ± 2.8	1.7 ± 0.2	7.5 ± 1.3
	1273 K / 10 h	33.2 ± 4.6	17.8 ± 1.8	1.9 ± 0.3	10.2 ± 1.4
	1273 K / 100 h	14.5 ± 3.7	8.4 ± 1.9	1.9 ± 0.3	12.9 ± 2.3
	1373 K / 1 h	36.3 ± 4.1	26.8 ± 3.8	1.4 ± 0.2	9.5 ± 1.6
	1373 K / 10 h	16.6 ± 4.3	9.7 ± 2.6	1.8 ± 0.2	11.7 ± 1.4
	1373 K / 100 h	–	–	–	16.4 ± 2.9
	1473 K / 1 h	40.2 ± 5.5	29.1 ± 3.6	1.4 ± 0.2	14.7 ± 2.3
	1473 K / 10 h	21.0 ± 3.7	11.2 ± 1.5	1.9 ± 0.2	23.9 ± 3.8
	1473 K / 100 h	–	–	–	48.6 ± 10.7
	1488 K / 1 h	53.2 ± 8.0	37.9 ± 7.6	1.5 ± 0.2	21.7 ± 3.1
	1503 K / 1 h	46.4 ± 6.7	33.1 ± 4.5	1.4 ± 0.2	8.8 ± 0.2
	1503 K / 100 h	100.1 ± 14.0	77.9 ± 9.5	1.3 ± 0.1	64.2 ± 13.2
	1523 K / 1h	66.2 ± 8.1	50.2 ± 5.6	1.3 ± 0.1	–
Ti-42Al-8V	as-forged	44.3 ± 8.5	11.8 ± 1.2	3.8 ± 0.6	2.1 ± 0.5
	1173 K / 1 h	55.6 ± 17.5	16.5 ± 2.4	3.9 ± 1.3	2.6 ± 0.4
	1173 K / 10 h	35.5 ± 9.9	7.3 ± 0.7	3.4 ± 0.8	4.4 ± 0.6
	1273 K / 1 h	12.7 ± 2.8	5.7 ± 0.9	2.3 ± 0.4	4.9 ± 0.6
	1273 K / 10 h	8.5 ± 2.1	4.6 ± 1.0	1.9 ± 0.3	5.7 ± 0.8
	1373 K / 1 h	6.2 ± 1.5	3.9 ± 1.3	1.9 ± 0.3	6.5 ± 0.7
	1373 K / 10 h	–	–	–	8.1 ± 1.1
	1403 K / 1 h	8.7 ± 2.5	4.2 ± 0.7	2.0 ± 0.3	7.4 ± 0.8
	1453 K / 1 h	22.3 ± 2.9	11.4 ± 1.9	2.0 ± 0.2	9.6 ± 1.3
	1473 K / 1 h	43.8 ± 7.0	25.6 ± 4.0	1.7 ± 0.2	–
	1498 K / 1 h	39.1 ± 7.6	24.9 ± 2.0	1.6 ± 0.2	–

Figure 3-23 shows the change in α_2/γ lamellar colonies size length L of both compositions with time for different ageing time (1 to 100 h).

In 42-5Mn, up to 1173 K, the lamellar colonies size did not change with time. Between 1173 K and 1423 K, corresponding to the β+γ two phase region, the colonies size slightly decreased after 1 h and did not change near 1473 K in the three phase region. Indeed, at this temperature the lamellae of the colonies showed a strong coarsening that led to the formation of large α and γ grains together at long time. Higher than the γ-solvus, the lamellar colonies size increased. Moreover, the grains size aspect ratio that was around 1.8 in the initial microstructure decreased up to 1.3 with the growth of α grains in the β+α two phase region. By increasing time, the effect was stronger and finally the colonies disappeared between 1373 and 1473 K whereas the size increased from 41 to 100 µm after 100 h at 1503 K.

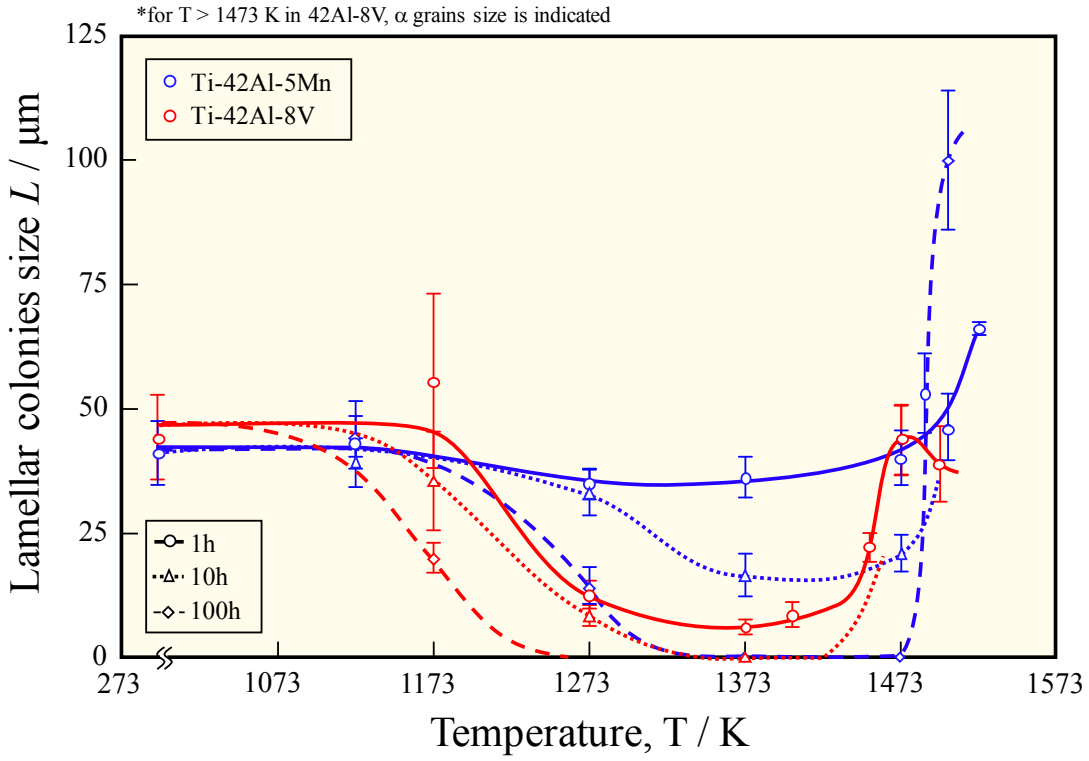

Fig. 3-23. Change in colonies size with temperature for different times.

In 42-8V, the general trend was similar to manganese alloy but faster and within larger range. Indeed, after only 1 h the colonies size decreased from 44 to 6 µm at 1373 K. Furthermore, between 1173 and 1403 K the colonies lost them integrity and showed irregular shapes. Thus, the grains size aspect ratio dropped from 3.8 to 2.0, though, at

higher temperature, the grains size aspect ratio decreased at around 1.7 due to the growth of α grains in the β+α two phase region. It should be reminded that after air cool from temperature higher than 1473 K, no γ precipitation was observed with the grains and the grains size indicated on the figure correspond to the α grains, in other words, to the possible colonies size.

The change of the globular γ grains (faceted grains were not considered) with time is shown in **Figure 3-24**. Ti-42Al-5Mn alloy showed larger initial γ grains. Between ambient temperature and 1423 K, the γ grains size increased slightly with the temperature and increasing time, increased the grains size. However, the grains size drastically increased in the β+α+γ three phase region from 6 to 64 μm after 100 h in the 42-5Mn alloy, whereas such behavior was not noticed in 42-8V alloy. In both case, above the γ-solvus, the grains size dropped and became null. An acceleration of the growth rate of the grains was observed in vanadium system between 10 and 100 h where the grains size increased from 4 to 19 μm.

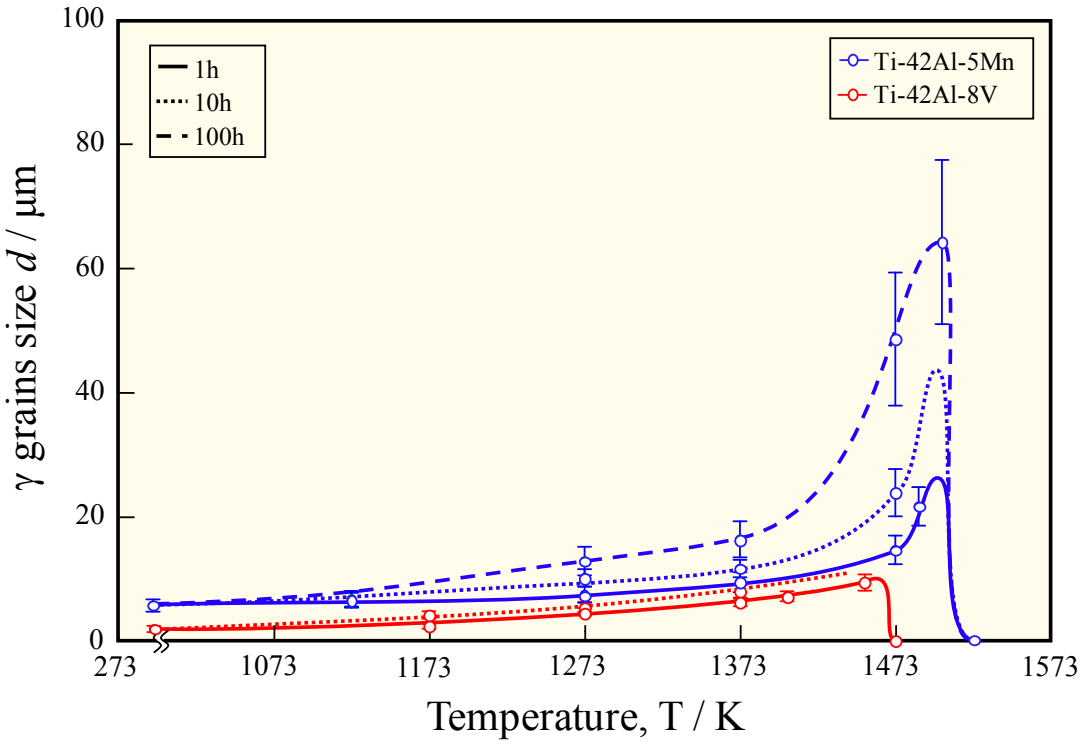

Fig. 3-24. Change in globular/elongated γ grains size with temperature for different times.

Therefore, it became possible not only control both the volume fraction and morphology but also the grains size to design model microstructures.

3.4 Discussion

A variety of different phase transformations may occur either during cooling from the high temperature regions or during subsequent heat treatment and thus modify the microstructure. In this section, different phase transformations that were observed in the studied systems will be compared and discussed.

3.4.1 Formation of (α_2+γ) lamellae colonies

Lamellar colonies consist of stacks of lamellae of the α_2 and γ phases that form during the phase formation sequence $\alpha \rightarrow \alpha+\gamma \rightarrow \alpha_2+\gamma$ at medium cooling rates [5]. The formation of α_2/γ lamellar structure has been explained by Denquin and Naka as the motion of Shockley partial dislocations in α or α_2 every two planes which leads to the crystal structure change into γ phase [6]. The γ lamellae precipitated in α according the Blackburn orientation relationship [4]:

$$\{111\}_\gamma // (0001)_\alpha \text{ and } \langle 1\bar{1}0]_\gamma // \langle 11\bar{2}0\rangle_\alpha \quad (3\text{-}1)$$

These γ lamellae may precipitate according two different sequences on the fcc structure (ABCABC or ACBACB). Moreover, the $\langle 1\bar{1}0\rangle$ directions are not equivalent due to the tetragonality of γ phase and lead to six different orientation variants called OR1 to OR6 [7].

The lamellae precipitation kinetics strongly depend on the studied system. Based on the microstructural observations of specimens cooled at different rates (water quench, air cooling, 10 K/min and 1 K/min), a schematic CCT diagram was constructed to illustrate the difference in lamellae precipitation between 42-5Mn and 42-8V alloys. Controlled cooling rates were applied between 1523 K and 1488 K for 42-5Mn and between 1523 and 1403 K for 42-8V and then were followed by air cooling. The CCT diagram is shown in **Figure 3-25**. The BSE images of the microstructures after different cooling rates were shown previously in **Fig. 3-9 and 3-10**. The lamellar precipitation occurred at higher cooling rate in 42-5Mn while in 42-8V, even after slow cooling rate (1 K/min), lamellar colonies were not observed. Xu *et al*. estimated to start temperature of lamellar precipitation between 1216 and 1410 K with the cooling range in the range of 50 to 0.1 K/s, respectively [8]. The driving force for lamellar precipitation under cooling were much lower in case of 42-8V alloy, and required a slower cooling rate or a subsequent heat treatment to precipitate.

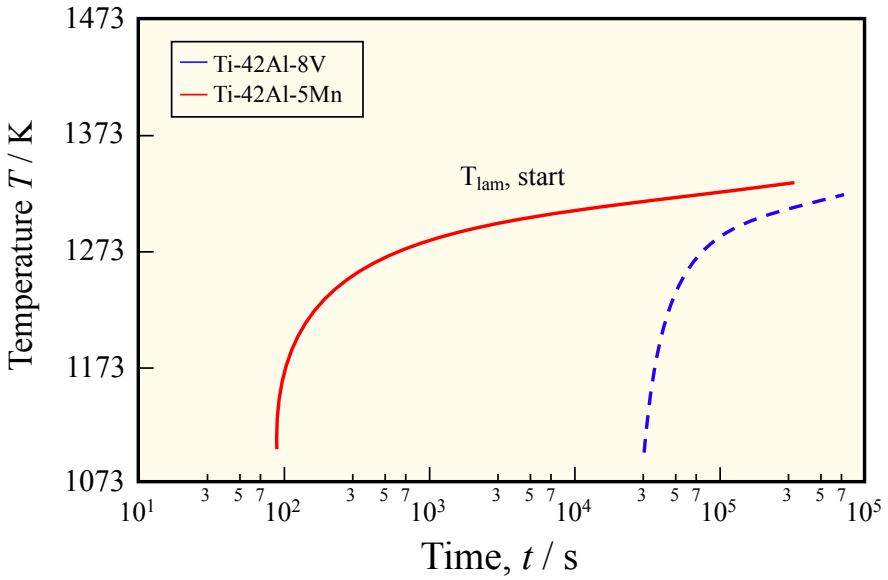

Fig. 3-25. Schematic CCT diagram for 42-5Mn and 42-8V alloys showing the $\alpha_2 \rightarrow \alpha_2+\gamma$ lamellar precipitation.

3.4.2 Phase transformation evolving β-Ti phase

With the development of the wrought process using β-solidified γ-TiAl alloy, the microstructure control using the β phase became a key to achieve high toughness alloys, and it is important to understand the phase transformation involving γ phase. Moreover, the β phase is often associated with the γ phase in the microstructure of ternary systems, and therefore, the phase transformation involving β phase will also modify the γ phase.

(A) Phase transformation from β to α

The β phase at high temperature can transforms to α phase by martensitic or massive modes. The composition invariant massive transformation through short range diffusion shows large curved grains as reported by Suzuki *et al.* [9] and Takeyama and Kobayashi [10]. The diffusionless martensitic transformation lead to a Widmanstädten-type morphology. Moreover, the transformation mode change from massive to martensitic by increasing M or decreasing Al content. Note that all α phase ordered into α_2-Ti_3Al after cooling.

The studied systems did not show massive transformation, however martensitic transformations were observed after quenching and air cooling in both systems dependin of the heat treatment conditions as shown in **Figure 3-26**. After air cooling, 42-5Mn alloy

showed only a small fraction of martensitic transformed β phase and will small laths size, the transformation led to thicker α' laths in 42-8V.

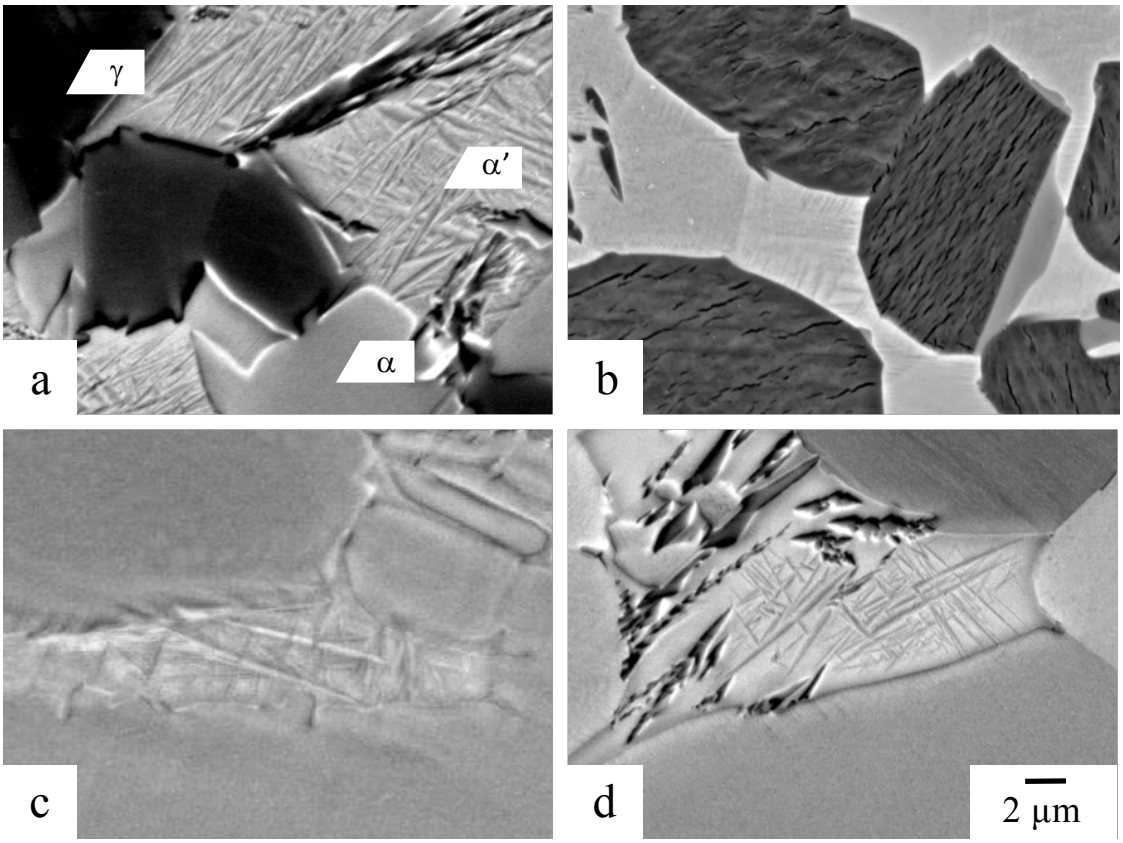

Fig. 3-26. Effect of heat treatment condition on β → α' martensitic transformation in (a, b) Ti-42Al-5Mn and (c, d) Ti-42Al-8V. (a) 1498 K / 1 h / WQ, (b) 1373 K / 1 h / AC, (c) 1523 K / 2 h / AC and (d) 1473 K / 2 h / AC.

(B) Phase transformation from β to γ

During cooling from high temperature, typically from the β+α two phase or the β+α+γ three phase regions, decomposition of β phase into γ grains may occur. Chang and Loretto deeply investigated the phase transformation involving β phase and identified two distinguished morphology of γ grains originated from the β phase decomposition as shown in **Figure 3-27** [11]. The first γ grains formed under furnace cooling from 1625 K with a globular morphology whereas the second type formed after quenching from 1583 K with a faceted morphology. They identified the orientation relationship between the γ precipitates and the near β phase by TEM and found the same orientation as follows:

$$\{\bar{1}1\bar{1}\}_\gamma // \{110\}_\beta \text{ and } \langle 011\rangle_\gamma // \langle 1\bar{1}1\rangle_\beta \quad (3\text{-}2)$$

The authors could not confirm if these two morphologies were resulted from the same mechanism. However, they proposed a direct nucleation mechanism of γ grains within β phase in both cases.

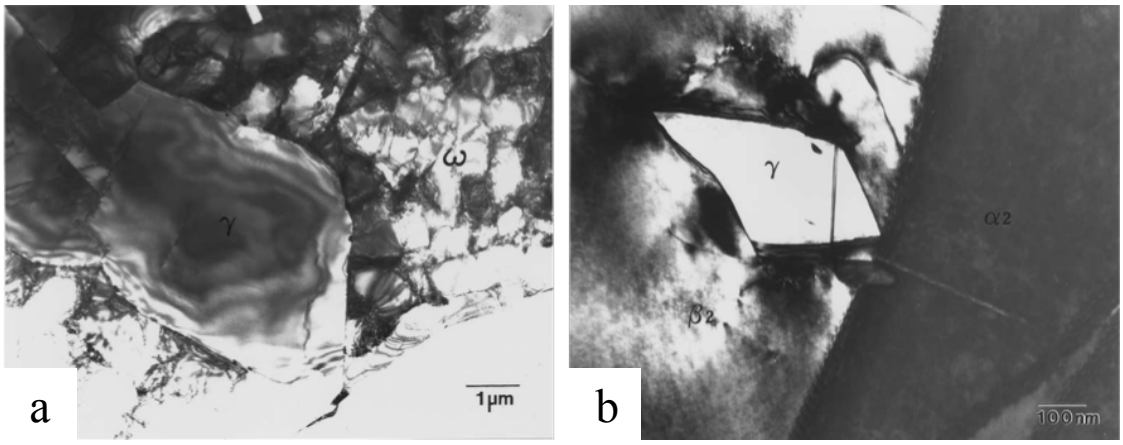

Fig. 3-27. Example of decomposition mode occurred in β phase obtained by TEM [11]: (a) after furnace cooling from 1623 K and (b) after water quenching from 1583 K.

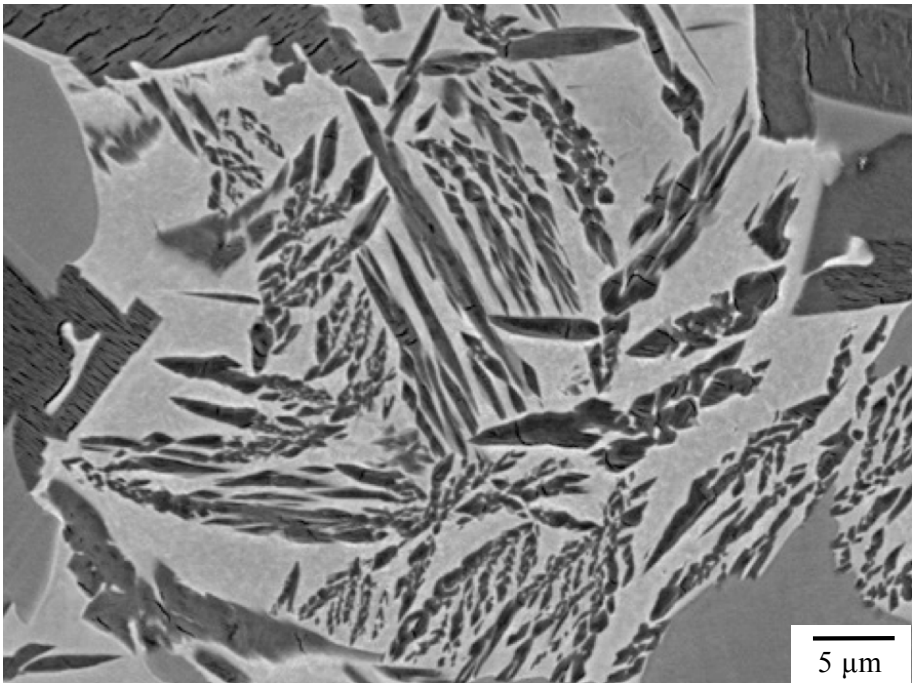

Fig. 3-28. Direct nucleation of faceted γ grains within β in 42-5Mn aged at 1473 K for 100 h.

The study conducted on 42-5Mn and 42-8V revealed the existence of the same faceted γ grains as shown in **Figure 3-28**. The faceted γ grains were found either in water quenched samples or in air cooled samples after heat treatment conducted between 1373

and 1473 K. The decomposition may occur for different cooling rates but appears at higher rates in case 42-5Mn system. Moreover, during slow cooling or during subsequent heat treatment at lower temperature, the faceted γ grains grew by coarsening and became smoother and larger. This explains why Chang and Loretto found the same orientation for the two morphologies after different cooling rates, i.e. the origin of the grains was the same.

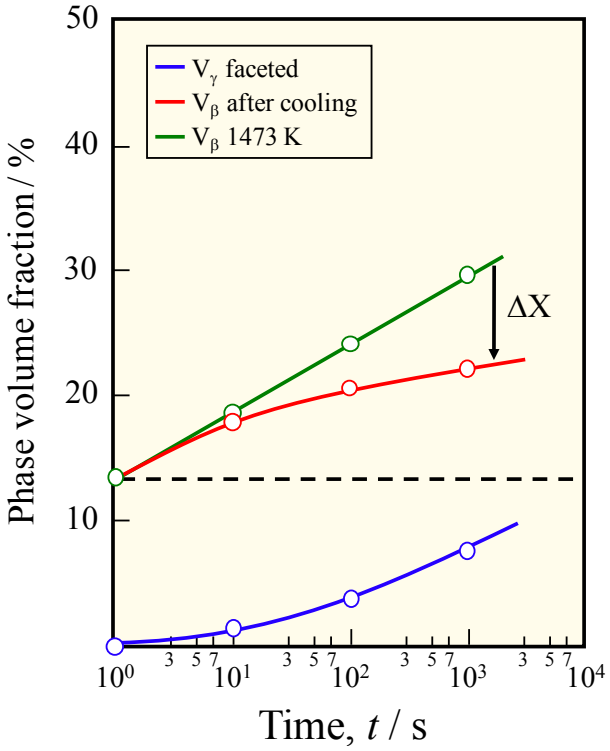

Fig. 3-29. Change in volume fraction in 42-5Mn between of the β phase and the faceted γ grains.

The precipitation mechanism consists of nucleation of γ precipitates within β phase according the orientation relationship described earlier. However, the driving force of the precipitation is still unclear but it is related to the supersaturation of solutes in β phase at high temperature. Therefore, more the fraction of β phase increased at high temperature, higher the driving force, and the precipitation of facetted γ grains, was important as illustrated in **Figure 3-29**. Higher the fraction of β phase at 1473 K was important, e. g. by longer holding time, more the precipitation of the faceted γ grains increased. However, the β phase at room temperature trend to reach a plateau. Therefore, the driving force could be the supersaturation of solute (probably Al) in β phase.

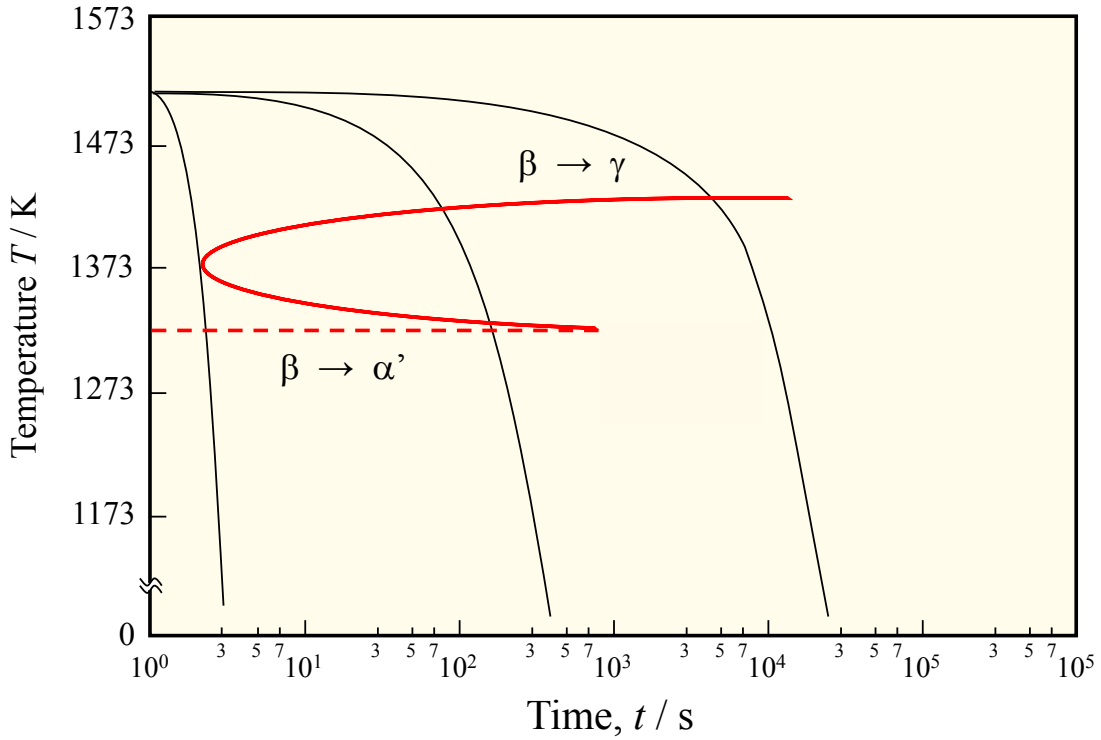

Fig. 3-30. Schematic CCT diagram showing the competition between β → γ decomposition and β → α' martensitic precipitation.

Competition occurred between the martensitic transformation and the γ precipitation should be taken into account. Schematic CCT diagram of the decomposition is shown in **Figure 3-30**. Despite it is also depending on the composition and the temperature, it resulted in different possible cases:

(a) At very high cooling rate, only the martensitic transformation occurred and transformed all β phase into Widmanstädten type microstructure.

(b) The sample reaches the nose of C-curve under cooling. The faceted γ grains start to precipitate but the martensitic transformation take place right after. The faceted γ nucleates are small and limited as observed in the case of water quenched samples, especially in 42-8V alloy.

(c) The sample cross completely the C-curve at intermediate cooling rate, e. g. air cooling. Because the shape of the curve is relatively elongated, faceted γ grains nucleate for a longer time. It results in a higher fraction with a larger size of faceted γ, that seems corresponding to the observation of the 42-8V alloy.

(d) The cooling rates is very slow. No martensitic transformation is observed at ambient temperature. Eventually coarsening of γ grains occurred and the faceted γ become large with irregular shapes.

(C) Phase transformation from α to β

They exist two modes of transformation from α phase to β phase: the pearlitic/cellular reaction mode where both β and γ precipitates simultaneously (α+γ→ β+γ) and the sequential mode where the γ plate precipitates first followed by β phase (α+γ→ β_s). This two transformations were intensely investigated by Kobayashi [1]. The cellular reaction lead to the formation of coarse β/γ elongated grains whereas the sequential mode shows β particles precipitated within the lamellae. The precipitation of β phase in lamellar structure has been explained as the supersaturation of M in the prior γ lamellae; the supersaturation depending of the M element and the temperature.

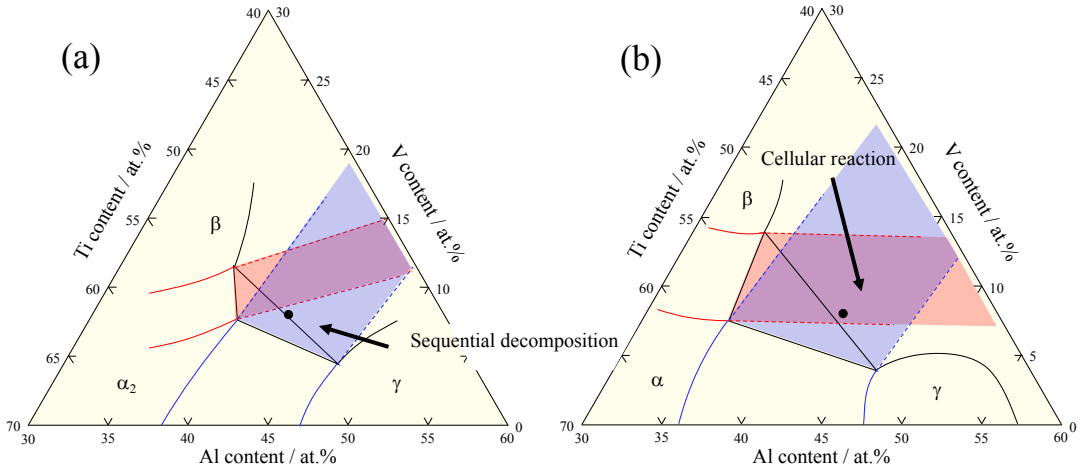

Fig. 3-31. Isothermal sections showing where the pearlitic/cellular reaction and the sequential decomposition modes in Ti-Al-V ternary system at (a) 1373 K and (b) 1123 K.

The transformation mode can be predicted based on the phase equilibria of the studied system as illustrated in **Figure 3-31**. Sequential mode occurs in the α+γ metastable region, excluding the overlapped part (blue region) while pearlitic mode occurs when the β+α and α+γ metastable regions are overlapped (purple region). Moreover, the results obtained in the **Chapter 2** showed that the three phase triangle change direction toward high M and low Al content from a certain temperature. It can be concluded that, depending on the alloy composition, the transformation mode can change between high

temperature to low temperature and, usually sequential mode is observed at higher temperature (**Fig. 3-31 (a)**) rather than cellular reaction (**Fig. 3-31 (b)**).

The two modes of decomposition have been observed in 42-8V alloy as shown in **Figure 3-32**. After aging for 10 h at 1173 K, β_s particles precipitated through the sequential mode despite that the coarsening was fast and almost erased the lamellar structure **(Fig. 3-32 (a))**, while at 1123 K, cellular reaction at the colonies boundaries occurred structure (**Fig. 3-32 (b)**). In case of 42-5Mn alloy, only the sequential mode of β precipitation has been observed as shown after ageing at 1373 K for 1 h in **Fig. 3-32 (c)**. Based on the phases equilibria, cellular reaction may occur at 1123 K, however due to the second eutectoid that take place at around 1148 K, the phase transformations changed as will be discussed in the following part.

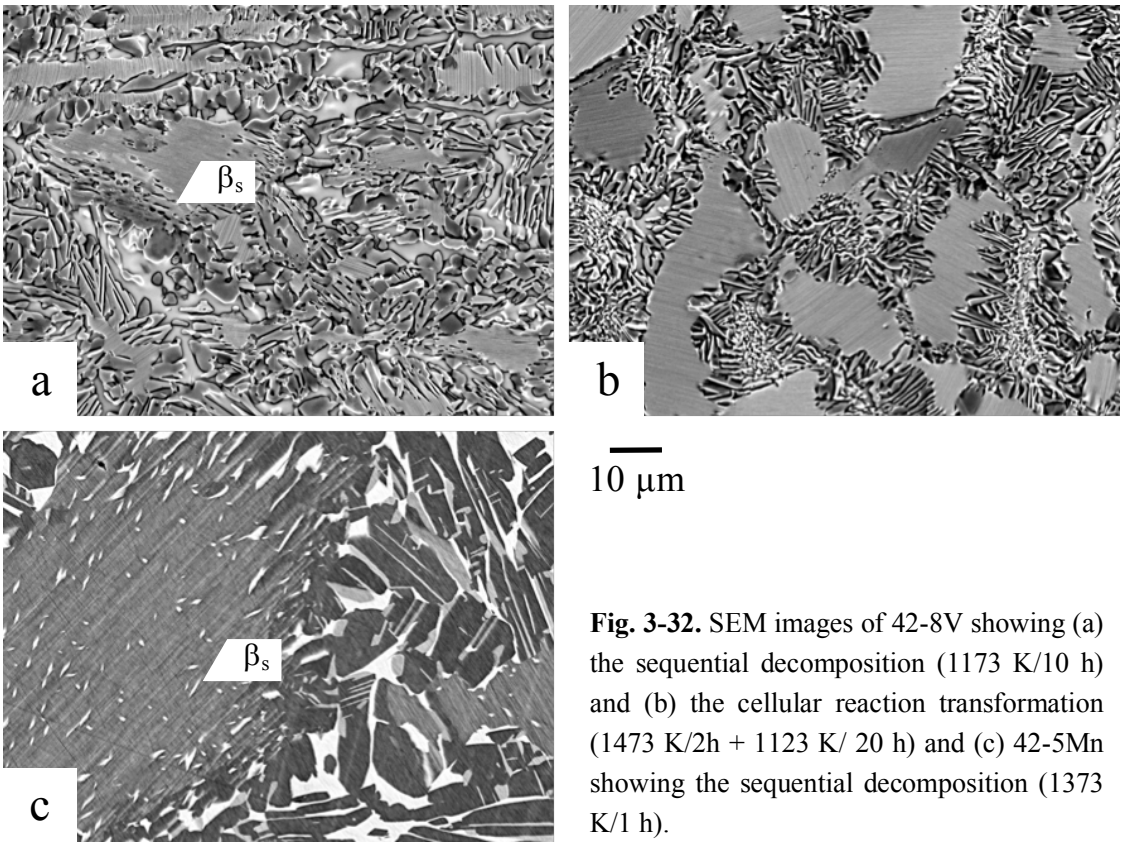

Fig. 3-32. SEM images of 42-8V showing (a) the sequential decomposition (1173 K/10 h) and (b) the cellular reaction transformation (1473 K/2h + 1123 K/ 20 h) and (c) 42-5Mn showing the sequential decomposition (1373 K/1 h).

Finally, in case of 42-8V, both faceted γ grains and Widmanstädten type microstructure were observed simultaneously in the former β phase due to the competition between martensitic transformation and γ nucleation as described above. After aging for 3 h at 1123 K, the faceted γ grains are still observed but the martensitic α' (α_2 at ambient temperature) transformed into fine γ and β precipitates as observed in **Figure 3-33**.

Although the mechanism was not deeply investigated, the cellular reaction that take place in the neighborhood lamellar grains may also occur in the martensitic α' though α'→ α_2+γ→ β+γ phase transformation. The small size of γ grains resulted from the originated thin α' laths. However a complementary study is needed to fully understand the mechanism.

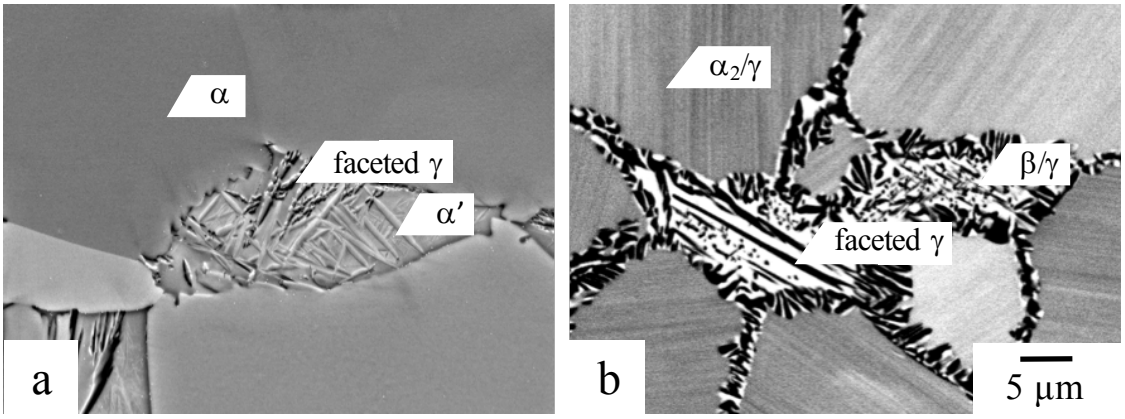

Fig. 3-33. SEM images of 42-8V aged at 1473 K for 2 h and (a) air cooled and (b) subsequently heat treated at 1123 K for 3 h.

3.4.3 Other phase transformations

There are two types of α phase along the pathway β+α(α_2)+γ → β+γ → β+α_2+γ observed in introduction on vertical section (**Fig. 3-1**). One at high temperature and the other one at low temperature, above and below the β+γ two phase region, respectively. The former one decomposes through pearlitic or sequential modes as described above, whereas the latter one precipitates (β → α_2). Moreover, in case of 42-5Mn alloy, around 1148 K, a second ternary eutectoid reaction take place β+γ → C14+α_2+γ. Thus, in this section the phase transformation involving low temperature α_2 phase and C14 Laves phase will be introduced.

(A) Precipitation of α_2 phase at low temperature

The region of the lower β+α_2+γ tie triangle has been estimated below 1073 K for 42-8V alloy. In case of 42-5Mn, due to the second ternary eutectoid reaction, the tie-triangle exists only on a small range between 1148 and 1173 K. The microstructural observations after ageing time at 1123 K revealed that the α_2 grains nucleate on γ grains, probably with a particular orientation relationship, and then growth into β phase with increasing time

along $\beta \rightarrow \alpha_2$ transformation reaction as shown in **Figure 3-34**. The nucleation and growth processes increased with undercooling below $\beta+\gamma \rightarrow \beta+\alpha_2+\gamma$ phase boundaries temperature. Though, temperature difference of about 50 K was small and therefore, the kinetics was relatively slow.

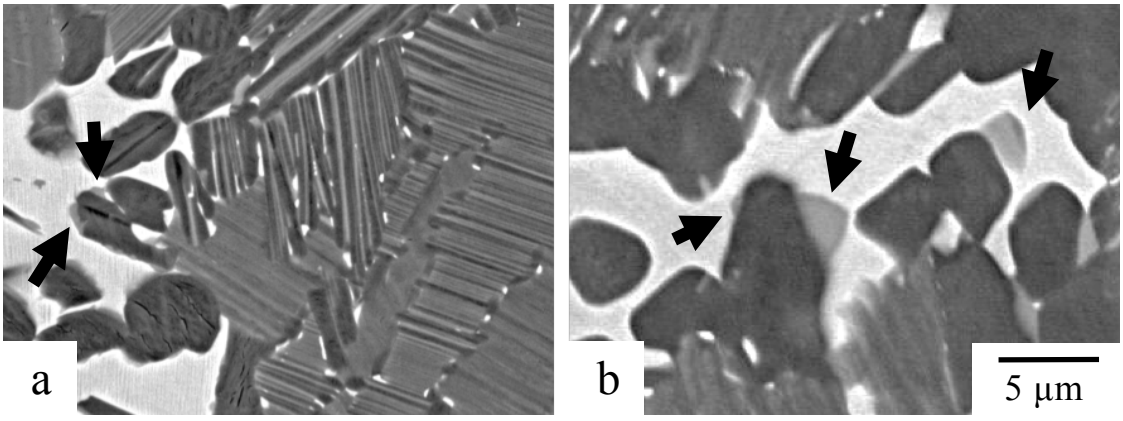

Fig. 3-34. Microstructure of 42-5Mn aged at 1123 K for (a) 1 h and (b) 100 h showing the nucleation and growth of α_2 grains. Arrows indicate initiation sites of α_2 grains.

(B) C14 Laves phase

Heat treatments conducted below the eutectoid temperature revealed the existence of different types of morphologies relates to the Laves phase depending on their locations as shown in **Figure 3-35 (a)**.

- large globular C14 at the colonies/duplex boundaries (arrow number 1)
- small globular C14 at the colonies/colonies boundaries (arrow number 2)
- lamellar C14 at the α_2/γ lamellae boundaries (arrow number 3)

The microstructural observations revealed that Mn_2Ti nucleates at α_2/γ interfaces and grew in the α_2 phase. This is in good agreement with the results of Babu *et al.* that observe the formation of a C14 phases in Ti-47Al-2Cr-2Nb always at the γ interfaces [12]. Below the eutectoid reaction, the change of slope of α_2/γ phase boundaries with the decrease of solubility of Mn in α_2 led to a supersaturation for both Al and Mn elements (See phase equilibria of Ti-Al-Mn system between 1173 and 1073 K in **Chapter 2**). Thus, Mn element precipitated into Laves phase whereas the Mn-depleted and Al-rich region transform in γ phase along the $\alpha_2 \rightarrow$ C14+γ phase transformation pathway.

Moreover, different morphologies can be easily explained by the surrounded environment of the Laves phase. At the α_2/γ lamellae interfaces, the C14 phase replaced

the α_2 to form γ/C14 lamellar microstructure as shown in **Fig 3-35 (b)** aged for 1500 h at 1023 K. At the colonies/colonies boundaries, coarser regions exist and thus, the Laves phase could grew as small globular shape whereas at colonies/duplex boundaries, the growth of C14 is not constraint by the surrounding lamellae and the Mn_2Ti showed large size. Hence, the mechanism of precipitation of Laves phase is similar to the sequential mode mentioned earlier: $\alpha_2 \rightarrow \alpha_2+\gamma \rightarrow C14+\gamma$ and shows the same microstructure than those reported by Takeyama and Kobayashi [10] where the β phase is replaced by C14 phase.

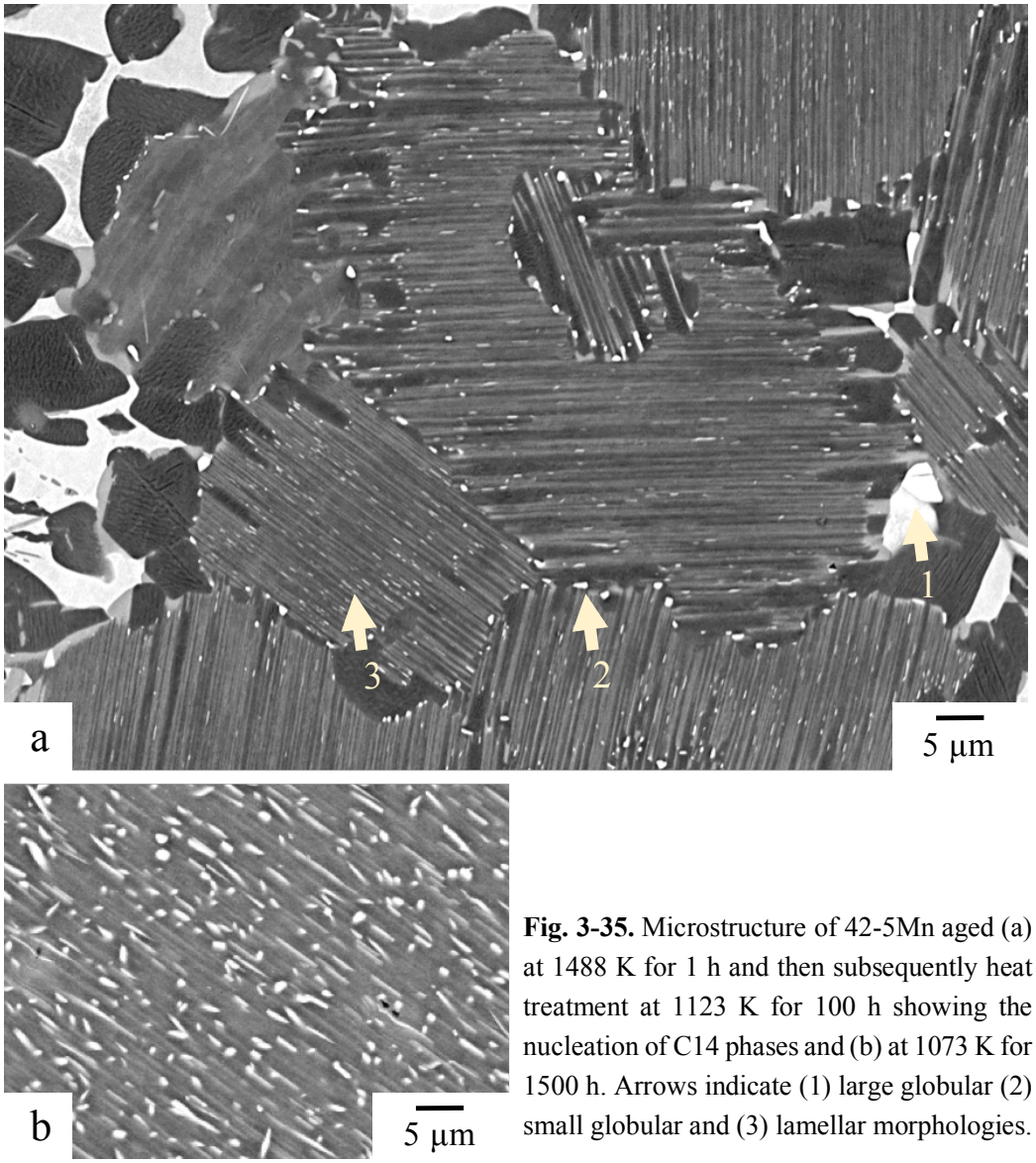

Fig. 3-35. Microstructure of 42-5Mn aged (a) at 1488 K for 1 h and then subsequently heat treatment at 1123 K for 100 h showing the nucleation of C14 phases and (b) at 1073 K for 1500 h. Arrows indicate (1) large globular (2) small globular and (3) lamellar morphologies.

Probably a competition between growth of α_2 phase in the β phase against the growth of C14 in the α_2 phase occurred. Despite both β and C14 phases are rich in manganese element, the Laves phase seems to not transform directly from the β phase. C14 phase also precipitated after an intermediate transformation along $\beta \rightarrow \alpha_2 \rightarrow C14+\alpha_2+\gamma$ transformation pathway. The reason that C14 precipitated in lamellae is not clear, but it could be related to the crystallography structures of the phases. Indeed, both α_2 ($D0_{19}$) and Mn_2Ti (C14) present a hexagonal system as shown in **Figure 3-36**.

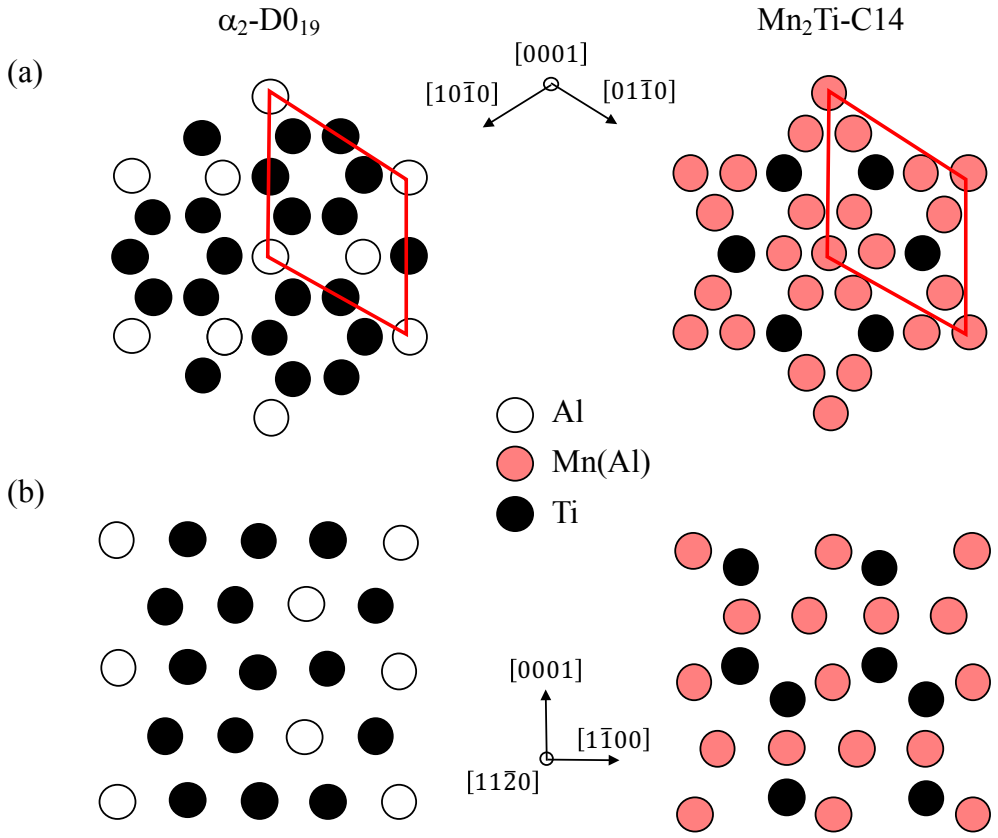

Fig. 3-36. Comparison of α_2 (D019) and Mn_2Ti (C14) crystal structure along (a) (0001) and (b) (11$\bar{2}$0).

(C) Ternary eutectoid reaction $\alpha \rightarrow \beta + \alpha_2 + \gamma$

It have been shown in **Chapter 2** that manganese element stabilized α phase rather α_2 phase and thus, a ternary eutectoid reaction $\alpha \rightarrow \beta + \alpha_2 + \gamma$ occurs. Despite that Ti-42Al-5Mn alloy's composition could not show this transformation, it is important to determine how it could affect the microstructure.

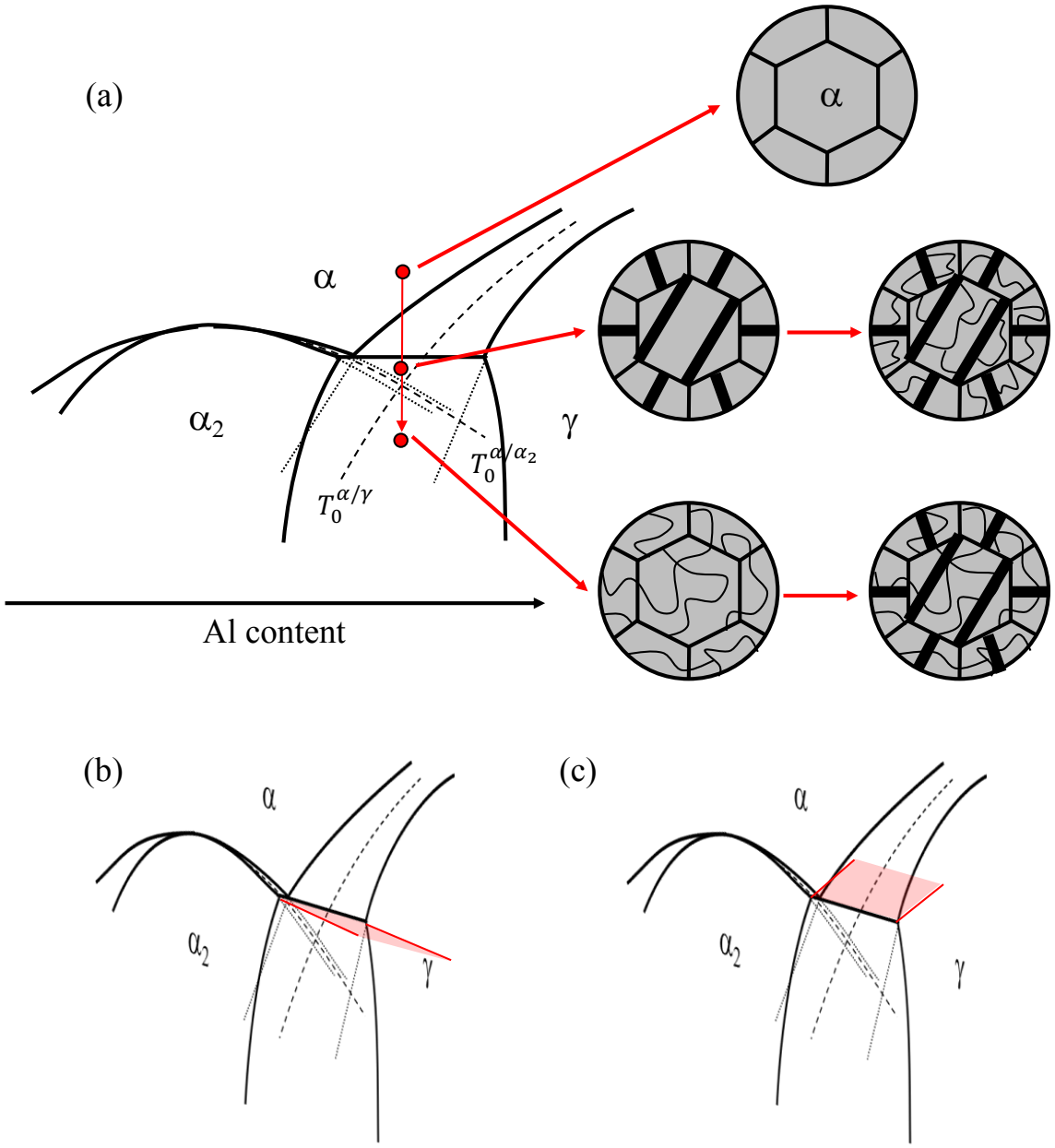

Fig. 3.37. Effect of relative stability between α and α_2 phases in case of (a) binary system, (c) ternary system where M is an α-stabilizer (c) ternary system where M is an α_2-stabilizer.

It might be related to the metastable region of α phase below the eutectoid temperature (1393 K) defined by the T_0 curve. The T_0 curve correspond to the points of the compositions and temperatures where the free energies of two phases are equal. Yamabe deeply investigated the effect of the T_0^{α/α_2} curve on the microstructure formation in binary γ-TiAl alloys [13]. Yamabe revealed that by quenching a sample from α-single phase to $\alpha_2 + \gamma$ two phase region above the T_0^{α/α_2} curve, lamellar formation occurred

first and then the ordering transformation, whereas below the T_0^{α/α_2} curve, the ordering transformation occurred first and then the lamellar precipitation as illustrated in **Figure 3-37 (a)**. By adding M elements, i.e. β-stabilizers, the relative stability between α and α_2 is changed. In case of Mn, which is α-stabilizer against α_2, the eutectoid temperature decrease in ternary system and thus, the T_0^{α/α_2} curve also decrease (**Fig. 3-37 (b)**). Therefore the metastable α may exist at lower temperature compared to binary case. If α_2 is stabilized against α, the opposite reasoning applies (**Fig. 3-37 (c)**).

Concerning the transformation that involve β phase, it is probably similar to α_2-stabilizer effect such as V or Nb and therefore same microstructure could be design but the β precipitation may occur faster in case of Mn. However deeply investigation should be conducted.

3.4.4 Microstructure control of β/γ duplex region

Previous studies on the effect of microstructure on the mechanicals properties of γ-TiAl alloys focused on the α_2/γ fully lamellar microstructure on one hand and α_2/γ lamellar / γ grains duplex microstructure in the other hand. The β phase was not considered as potential phase to improve the mechanical properties due to it brittleness at ambient temperature. However, recently the wrought process of γ-TiAl alloys using the β phase was developed. The alloys developed for this process show a certain fraction of β phase in the final microstructures.

In the previous sections, different phase transformations that occurred either in 42-5Mn, 42-8V or both alloys have been investigated. Hence, as it has been investigated in this chapter, by optimizing the heat treatment conditions, it becomes possible to achieve various morphologies and phase fraction of the β phase associated with γ phase and decorates the lamellar colonies boundaries as illustrated schematically in **Figure 3-38**. This figure did not take into account the precipitation of α_2 and Laves phases in 42-5Mn alloy. Moreover, **Figure 3-39** shows the equivalent morphology observed in microstructures.

By conducted heat treatments of forged alloys below the γ-solvus, coarsening of grains occurs. Initial γ grains grow and lamellae become thicker as shown in **Fig. 3-39 (a)**. The coarsening rate is directly correlated to the temperature of heat treatment. However, by aging above the γ-solvus, the initial microstructure is erased and the α grains grow by boundaries migration.

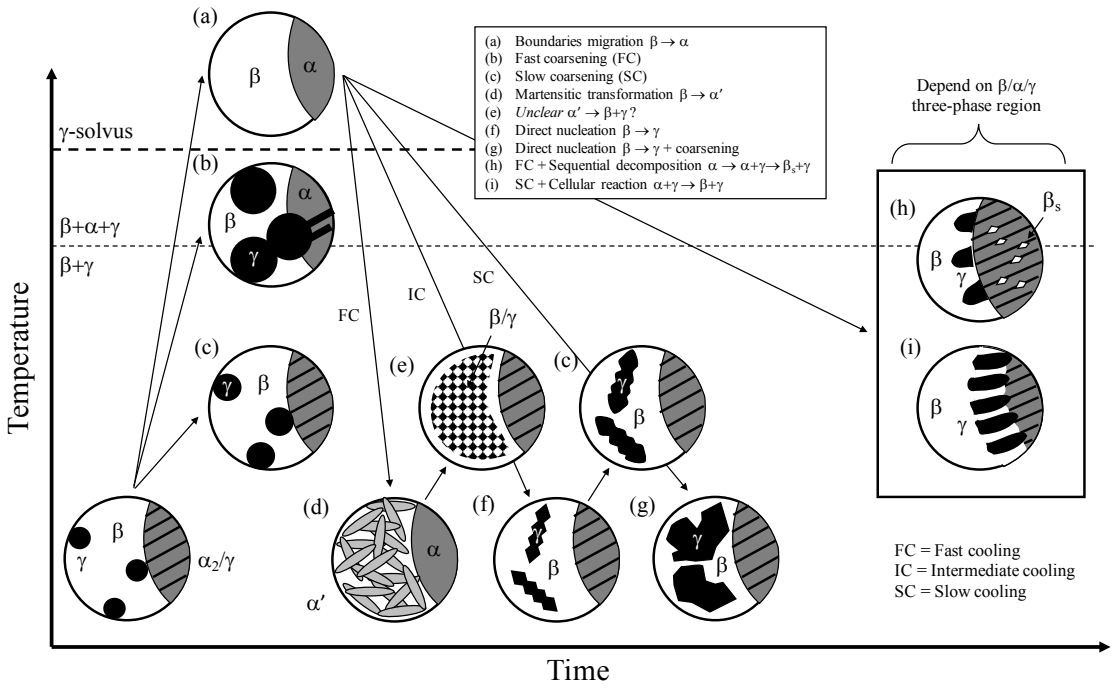

Fig. 3-38. Schematic illustration of the different morphology of β/γ duplex region observed in the studied alloys.

By conducted heat treatments of forged alloys below the γ-solvus, coarsening of grains occurs. Initial γ grains grow and lamellae become thicker as shown in **Fig. 3-39 (a)**. The coarsening rate is directly correlated to the temperature of heat treatment. However, by aging above the γ-solvus, the initial microstructure is erased and the α grains grow by boundaries migration.

Depending of the cooling rate different transformations may occurred. After a fast cooling rate, Widmanstädten type microstructures is observed (**Fig. 3-39 (b)**). Despite the unclear mechanism, a subsequent heat treatment at low temperature in β+γ two phase region transforms the martensitic α into fine dispersion of γ and β grains as observed in **Fig. 3-39 (c)**. For intermediate cooling, β phase decomposed into faceted γ grains (**Fig. 3-39 (d)**). The faceted γ grains ecome smoother by coarsening after a subsequent heat treatment at low temperature in β+γ two phase region (**Fig. 3-39 (e)**). The β decomposition into faceted γ grains occurred at high temperature, therefore using a slow cooling in the high temperature region just after the precipitation, fast coarsening of faceted γ grains takes place. It resulted in large γ grains with an irregular shape as shown in **Fig. 3-39 (f)**.

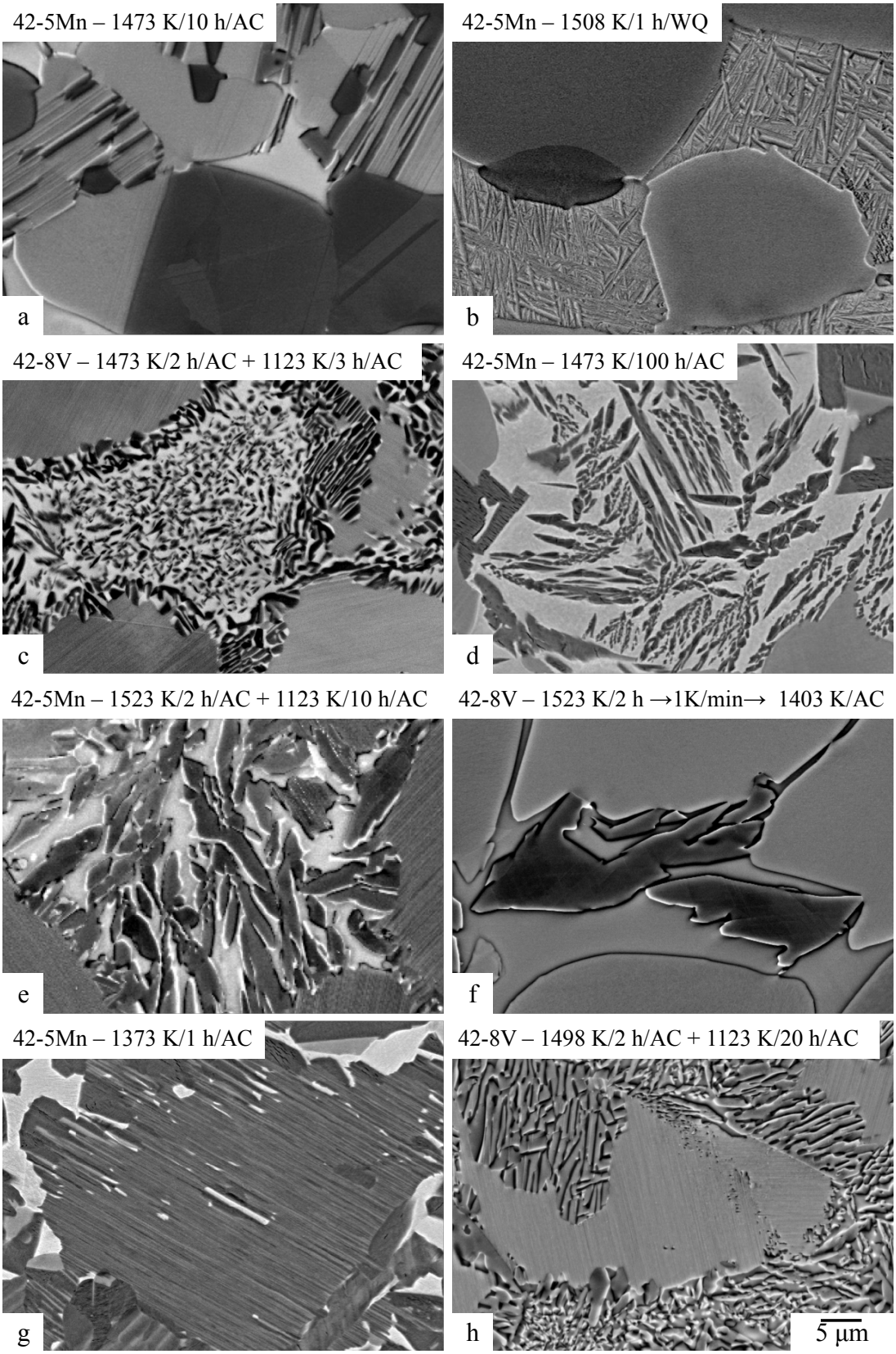

Fig. 3-39. Examples of different morphologies obtained for β/γ duplex along with the corresponding heat treatment.

Finally, in the β+γ two phase region, the precipitation of β phase may occur either by sequential mode (**Fig. 3-39 (g)**), with the β precipitation within the lamellar structure, or cellular reaction (**Fig. 3-39 (h)**) at the colony boundaries.

However, in most cases, different phase transformations occur simultaneously.

Based on the phase equilibria analysis conducted in **Chapter 2** along with the phase transformations study of the **Chapter 3**, different model microstructures with various β/γ duplex (DP) have been selected for FCG tests, **independently of the alloy composition** as shown in **Figure 3-40**. Two parameters have been investigated as follow:

(1) Different volume fractions of β/γ duplex. Small (DP < 10%), intermediate (DP ≈ 35%) and almost β and γ duplex (DP > 90 %).

(2) Different morphologies of γ grains in DP with same volume fraction. Globular (by coarsening) and Lamellar (by cellular reaction). Moreover, by changing the temperature it is possible to change the ratio between β and γ phases in the cells.

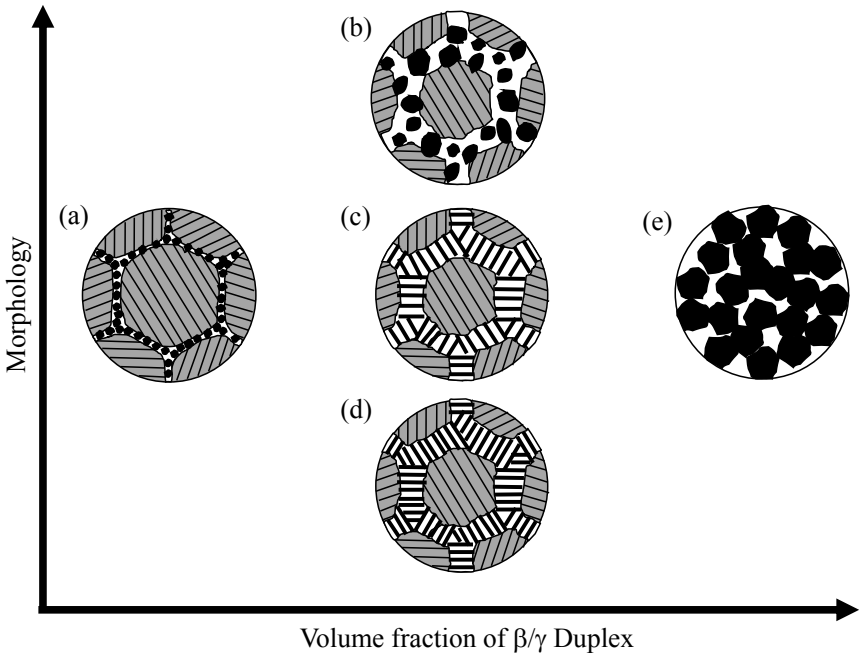

Fig. 3-40. Model microstructure designed for fatigue crack growth test (a) Nearly Lamellar NL, (b) Globular Triplex GTL, (c) Lamellar Triplex LTL, (d) Near γ Cellular Triplex NCT and (e) Nearly Globular β/γ Duplex.

3.5 Summary

In order to develop wrought γ-TiAl alloys a certain amount of β phase is needed for processing. Therefore, in this chapter, the microstructure control of β phase using phase transformation has been investigated in 42-5Mn and 42-8V wrought alloys. Conclusion can be stated as follows

1. Eight different phase transformations have been identified in these systems: $\beta \rightarrow \alpha'$ martensitic, $\alpha_2 \rightarrow \alpha_2+\gamma$ lamellar precipitation, $\alpha_2+\gamma \rightarrow \beta_s+\gamma$ sequential decomposition, $\alpha_2+\gamma \rightarrow \beta+\gamma$ cellular reaction, $\beta \rightarrow \gamma$ decomposition, $\alpha' \rightarrow \beta+\gamma$, $\beta \rightarrow \alpha_2$ and $\alpha_2 \rightarrow$ C14 (only in 42-5Mn alloy). Moreover, the ordering $\alpha \rightarrow \alpha_2$ and $\beta \rightarrow \beta_0$ also took place.
2. Competition occurs between martensitic transformation β and decomposition that take place between 1373 and 1473 K in both alloys. However, these phase transformations occurred under faster cooling rate in 42-5Mn compared to 42-8V.
3. In β+γ two phase region a competition occurs between coarsening of γ grains and the others mechanisms (sequential decomposition, cellular reaction…). At elevated temperatures, the coarsening is faster due to the higher diffusivity, and thus microstructure appears mainly with large γ globular. At lower temperature, both mechanisms coexisting and therefore, various morphologies of γ grains can be designed: elongated, globular, irregular or faceted.
4. In case of 42-5Mn alloys, below the second eutectoid reaction, another competition between α_2 grains and Mn_2Ti Laves phase growth takes place. However, in lamellar grains, the decomposition of α_2 grains led to the formation of γ/C14 lamellar structure. The transformation of α_2 grains into Mn_2Ti Laves phase is facilitated by their similar hexagonal system.
5. Finally, five model microstructures have been selected for fatigue crack growth tests with different volume fractions and morphologies of β/γ duplex region.

References

[1] S. Kobayashi, Phase Equilibrium and structure formation in TiAl based ternary alloys – Decomposition of α phase and generation of β phase in α → β+γ reaction pathway, Doctor Thesis, Tokyo Institute of Technology, 2002

[2] T. Leitner, M. Schloffer, S. Mayer, J. Eßlinger, H. Clemens, R. Pippan, Fracture and R-curve behavior of an intermetallic β-stabilized TiAl alloy with different nearly lamellar microstructures, Intermetallics 53 (2014) 1-9.

[3] E. Schwaighofer, H. Clemens, S. Mayer, J. Lindemann, J. Klose, W. Smarsly, V. Güther, Microstructural design and mechanical properties of a cast and heat-treated intermetallic multi phase γ-TiAl based alloy, Intermetallics 44 (2014) 128-140.

[6] J.M. Blackburn, The science technology and application of titanium, Pergamon Press, New York (1970).

[5] C. McCullough, J. J. Valencia, C. G. Levi, R. Mehrabian, Phase equilibria and solidification in Ti-Al alloys, Acta Metall. 37 (1989) 1321-1336.

[6] A. Denquin, S. Naka, Phase transformation mechanisms involved in two phase TiAl-based alloy – I. Lamellar structure formation, Acta Mater. 44 (1996) 343-352.

[7] S. Zghal, S. Naka, A. Couret, A Quantitative TEM Analysis of the Lamellar Microstructure in TiAl Based Alloys, Acta Materialia 45 (1997) 3005-3015.

[8] H. Xu, X. Li, W. Xing, L. Shu, Y. Ma, K. Liu, Phase transformation behavior of a Mn containing β-solidifying γ-TiAl alloy during continuous cooling, Intermetallics 99 (2018) 51-58.

[9] A. Suzuki, M. Takeyama, T. Matsuo, Transmission electron microscopy on the phase equilibria among β, α and α_2 phases in Ti–Al binary system, Intermetallics 10 (2002) 915-924.

[10] M. Takeyama, S. Kobayashi, Physical metallurgy for wrought gamma titanium aluminides Microstructure control through phase transformations, Intermetallics 13 (2005) 993–999.

[11] T. T. Cheng, H. Loretto, The decomposition of the beta phase in Ti-44Al-8Nb and Ti-44Al-4Nb-4Zr-0.2Si alloys, Acta mater. 46 (1998) 4801-4819.

[12] R. P. Babu, K. V. Vamsi, S. Karthikeyan, On the formation and stability of precipitate phases in a near lamellar γ-TiAl based alloy during creep, Intermetallics 98 (2018) 115-125.

[13] Y. Yamabe, γ-TiAl 金属間化合物基合金における組織形成, Doctor thesis, Tokyo Institute of Technology (1993).

Chapter 4

Effect of Microstructure on Fatigue Crack Growth Behavior at Ambient Temperature

4.1 Introduction

Based on phase equilibria, it is possible to achieve various kind of microstructure in TiAl binary alloy from a α_2/γ fully lamellar (FL) to $\alpha_2+\gamma$ duplex microstructure [1]. In the previous chapters, it has been introduced the phase equilibria (**Chapter 2**) and the phase transformations (**Chapter 3**) for microstructures design of wrought TiAl alloys. Some representative microstructures with different volume fractions and morphologies of β/γ duplex (DP) have been selected for fatigue crack growth (FCG) tests.

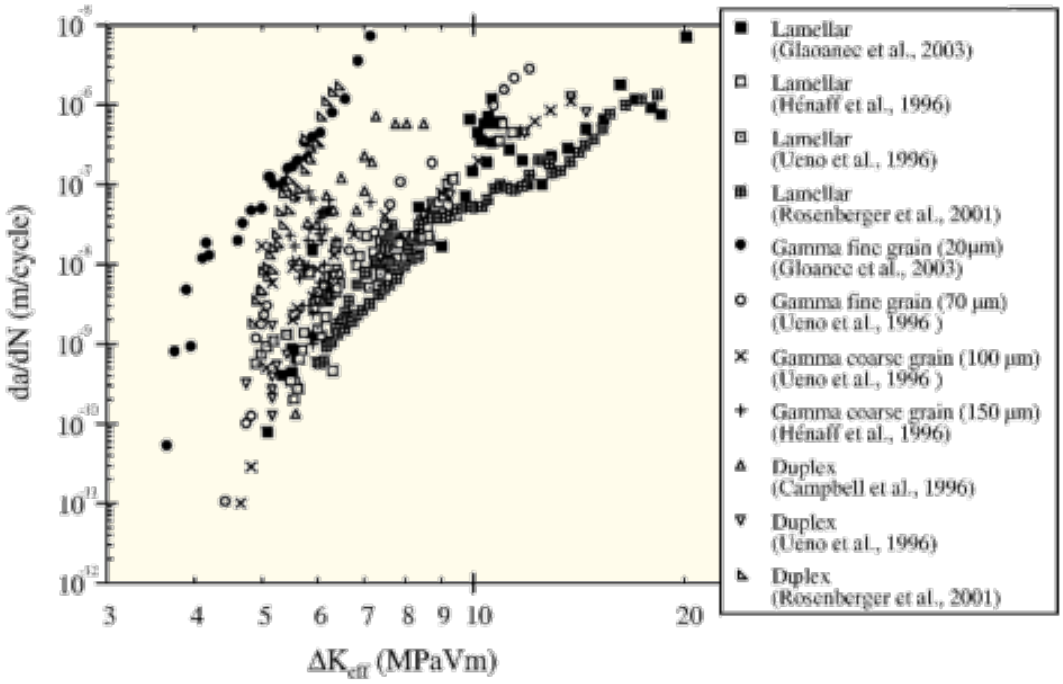

Fig. 4-1. Influence of microstructure on fatigue crack growth behavior at room temperature [4].

The presence of defects occurring during elaboration, machining or in service could lead to critical damages and cause the failure of a jet engine blade. Understanding the crack propagation behavior of these materials becomes crucial for the development of new class of wrought TiAl alloys with high toughness. Many studies investigated the effects of microstructure, lamellar spacing, process, temperature or atmosphere on fatigue crack growth behavior in γ-based titanium aluminides alloys with microstructures which mainly combine α_2/γ colonies and equiaxed γ grains [2-5]. Therefore, it has been clarified that the FL microstructure present the higher fatigue crack propagation resistance than duplex (lamellar and γ grains) microstructure as shown in **Figure 4-1**. Nevertheless, these microstructures do not contain β phase (or a small fraction). Indeed, it is considered that

β phase is detrimental for mechanicals properties. The fatigue crack growth behavior at ambient temperature of TiAl alloys such as γ-single phase TiAl (Ti-55Al at.%) [6], Fully lamellar 48-2-2 [7] or forged TNM [8] along with other metals such as Ti-6Al-4V [9] and Inconel 718 [10] are summarized in **Table 4-1**.

Table 4-1. Fatigue crack growth behavior of TiAl alloys compared with others materials [6-10].

Sample	ΔK_{th} / MPa$\sqrt{m}$	m	C	K_{max} / Mpa$\sqrt{m}$
γ-single phase (Ti-55Al)	6	29.4	1E-30	NA
FL 48-2-2	9.2	6.5 – 10.4	1E-11	20.4
TNM (forged + HT)	5.4 – 10.1	14	NA	12.8 – 18
Ti-6Al-4V	4.2	NA	NA	NA
Inconel 718	8 – 10	3.6 – 10.7	2E-9	> 100

Recently, Dahar *et al.* investigated the effect of processing, sample orientation and load ratio of the TNM alloys [8]. Though, it is still not clear how β phase could affect the fatigue crack growth behavior in TiAl alloy. Recently, Nakamura *et al.* established that β phase could be effective for improving toughness, and investigated if the same trend could be observed during fatigue crack growth tests (FCG) [11].

In the present chapter, the fatigue crack growth behavior of wrought γ-TiAl alloys with different microstructures containing various volume fractions and morphologies of β phase associated with γ phase at the colony grain boundaries have been examined at room temperature using *in-situ* and *ex-situ* observations, and the role of β phase on crack propagation behaviors will be discussed.

4.2 Experiment procedure

The flowchart of the experimental procedure is shown in **Figure 4-2**. Three different alloys with the following composition: Ti-42Al-8V, Ti-42Al-5Mn and Ti-43Al-4Nb-5V (at.%) were used in this chapter. These alloys will be called hereafter 42-8V, 42-5Mn, and 43-4-5. The nominal and analyzed composition are shown in **Table 4-2.**

Analyzed composition of 43-4-5 alloy was determined to be Ti-43.7Al-4.1Nb-5.2V (at.%), and matches well with the nominal composition despite a small aluminum excess. The phase transformation pathway of this system allows to design various microstructures, equivalent to those find in 42-5Mn and 42-8V [12].

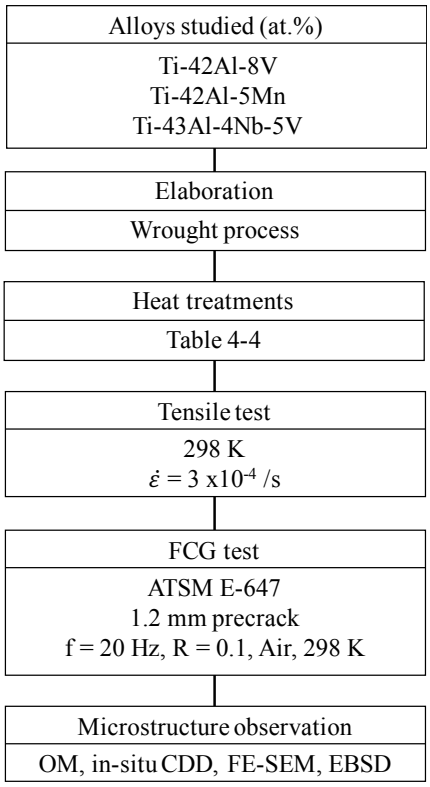

Fig. 4-2. Flowchart of the experimental procedures for determination of the fatigue crack growth behavior at room temperature.

Table 4-2. Nominal and analyzed compositions of the studied wrought TiAl. Two different pancakes were used for 42-5Mn alloy.

Alloys	Composition / at.%	
	Nominal	Analyzed
42-5Mn	Ti-42Al-5Mn	Ti-41.7Al-5.4Mn Ti-41.9Al-5.0Mn
42-8V	Ti-42Al-8V	Ti-42.4Al-8.0V
43-4-5	Ti-43Al-4Nb-5V	Ti-43.7Al-4.1Nb-5.2V

4.2.1 Microstructure design

As explained in **Chapter 3,** in order to investigated the effect of microstructure on fatigue crack growth behavior, two parameters have been investigated: the **volume fraction** V_{DP} and the **morphology** of β/γ duplex. It is important to consider further the microstructure than the alloy composition despite elements influence may also the FCG

behavior. The as-forged 42-5Mn (AF) microstructure will be also tested for comparison.

Elaboration of vanadium and manganese alloys was detailed in **Chapter 3**. 43-4-5 alloy was elaborated using cold crucible induction melting (CCIM) with a size of 70 mm in diameter and 900 mm in height. Then, the columnar ingot was cut into pieces with 100 mm in height, and hot forged for 30 min in β+α two phases region around 1573 K with height reduction to 45 mm by one stroke and the oxide layer was removed.

The different pieces were cut by EDM (Electron Dispersive Machine) and covered using Deltaglaze™ in order to prevent oxidation during heat treatment. The ingot pieces were heat treated using muffle furnace. The heat treatment conditions are summarized in **Table 4-3**. Tensile and compact tension specimens were machined in L-T direction (perpendicular to the forging direction) outside the laboratory.

Table 4-3. Heat treatment conditions.

Alloys	Microstructure	Name	Heat treatments	
			1st step	2nd step
42-5Mn	As-forged	AF	–	–
	Globular Triplex	GTL	1503 K / 1 h / AC	1123 K / 20 h / AC
	Nearly Globular β/γ Duplex	NGDP	1273 K / 100 h /AC	
42-8V	Near γ Cellular Triplex	NCT	1473 K / 2 h / AC	1123 K / 3 h / AC
43-4-5	Nearly Lamellar	NL	1573 K / 1 h / AC	1173 K / 1 h / AC
	Near γ Cellular Triplex	NCT	1573 K / 1 h / AC	1173 K / 100 h / AC
	Nearly Globular β/γ Duplex	NGDP	1373 K / 42 h / AC	

The microstructure with small volume fraction of β/γ duplex (DP < 10%) as-called **Nearly Lamellar (NL)** microstructure was design using the 43-4-5 alloy. The microstructure shows equiaxed α_2/γ lamellar grains with an average size of 100 μm surrounded by β and γ grains, called β/γ duplex (DP) structure (**Fig. 4-3 (a)**). The volume fraction of β/γ duplex V_{DP} in NL microstructure is around 7 %. This microstructure was obtained by heating up the as-forged sample at 1573 K in $\beta + \alpha$ two phase region, followed by air cooling and then, subsequently heat treated at 1173 K for 1 h (air cooling).

Three different microstructures with an intermediate volume fraction of β/γ duplex (DP ≈ 35%) were designed. Each microstructures show a different β/γ morphology,

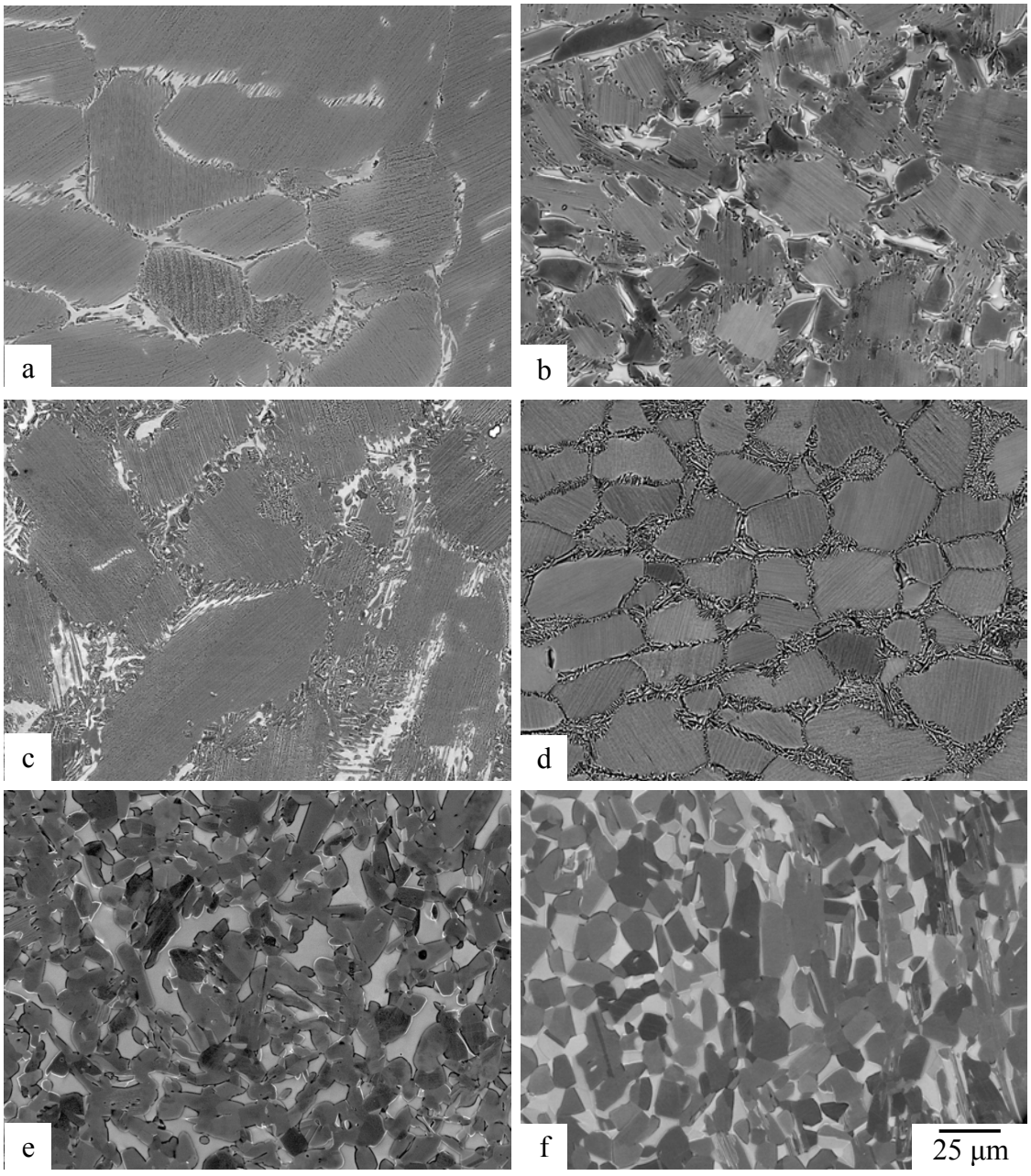

Fig. 4-3. Backscattered electron (BSE) images after heat treatment of the different microstructures (a) 43-4-5 NL, (b) 42-5Mn GTL, (c) 43-4-5 LTL, (d) 42-8V NCT, (e) 42-5Mn NGDP and (f) 43-4-5 NGDP.

globular as-called **Globular Triplex (GTL)**, Lamellar as-called **Lamellar Triplex (LTL)** and a second Lamellar morphology but small β/γ ratio as-called **Near γ Cellular Triplex (NCT)**. The GTL microstructure was obtained by heating up as the as-forged 42-5Mn alloy at 1503 K in $\beta + \alpha + \gamma$ three phase region just below the γ solvus for 1 h followed by air cooling. It resulted in lamellar microstructure surrounded by β and small γ grains

that will act as seed for coarsening and will growth during the subsequently heat treatment at 1123 K for 20 h with air cooling (**Fig. 4-3 (b)**). The LTL microstructure was obtained by heating the 43-4-5 alloy specimen at 1573 K for 1 h, the subsequent heat treatment was conducted for 100 h in order to increase the volume faction of β/γ duplex V_{DP} up to 33% using cellular reaction. Therefore, the lamellar colonies size decreased to around 80 μm **(Fig. 4-3 (c))**. Lastly, the NCT microstructure consisted of lamellar colonies where cellular reaction took place and led to the formation of small and elongated γ grains. Due to the very small β/γ ratio, of around 0.19, the lamellar colonies seem to be decorated by almost γ phase. This microstructure was obtained using 42-8V alloy by heating up the as-forged sample at 1273 K in β + α two phase region for 1 h, followed by air cooling and then, subsequently heat treated at 1123 K for 3 h with air cooling (**Fig. 4-3 (d)**).

Finally the microstructure which consisted of almost β and γ duplex (DP > 90 %) as-called **Nearly Globular β/γ Duplex (NGDP)** were design using both 42Al-5Mn and 43-4-5 alloys. This microstructure consists of β and γ grains (V_{DP} > 95 %) of around 20 μm in size and with a small fraction of α_2 grains and remaining α_2/γ lamellar colonies grains **(Fig. 4-3 (e, f))**. In 42-5Mn, the microstructure was obtained by heating up the as-forged sample at 1273 K in β + γ two phase region for 100 h followed by air cooling whereas in 43-4-5 alloy, the as-forged sample was held at 1373 K for 42h in β + α + γ three phase coexisting region, followed by air cooling.

The microstructural features such as grains size or phase fraction of these three microstructures are summarized in **Table 4-4**.

Table 4-4. Microstructural features of the Ti-43Al-4Nb-5V (at.%) microstructures.

Alloy	Microstructure	α_2/γ lamellar colonies		Duplex			
				γ grains		β grains	Ratio β/γ
		Fraction / %	size / μm	Fraction / %	size / μm	Fraction / %	
42-5Mn	As-forged (AF)	47.9 ± 8.5	41.1 ± 6.4	38.5 ± 6.4	5.8 ± 1.0	13.6 ± 2.3	0.35
	Globular Triplex (GTL)	66.4 ± 3.7	45.9 ± 6.0	23.5 ± 1.7	10.4 ± 2.0	10.1 ± 1.9	0.43
	Nearly Globular β/γ Duplex (NGDP)	1.2 ± 0.7	14.5 ± 3.7	79.9 ± 3.4	12.9 ± 2.3	18.9 ± 2.7	0.24
42-8V	Near γ Cellular Triplex (NCT)	66.8 ± 1.8	34.9 ± 5.8	27.9 ± 0.5	2.4 ± 0.7	5.3 ± 1.3	0.19
43-4-5	Nearly Lamellar (NL)	89.6 ± 0.4	101.8 ± 34.9	6.4 ± 0.4	4.8 ± 1.4	4.0 ± 0.4	0.63
	Lamellar Triplex (LTL)	68.2 ± 3.0	70.9 ± 20.9	13.8 ± 3.0	7.1 ± 1.9	18.0 ± 3.0	1.30
	Nearly Globular β/γ Duplex (NGDP)	5.8 ± 1.2	13.9 ± 2.6	73.7 ± 2.4	16.4 ± 5.1	20.5 ± 3.5	0.28

4.2.3 Mechanicals tests and characterization

Tensile tests were carried out using tensile specimen in accordance with JIS G0567 standard as shown in **Figure 4-4 (a)**. Tests were conducted in air at room temperature with a strain rate $\dot{\varepsilon}$ = 3 x 10^{-4} /s using a Shimadzu Autograph AG-1 machine. FCG tests were carried out using half size compact tension specimen (W = 25 mm) in accordance with ASTM E-647 standard with a V-notch of 7 mm (a_0) [13] as shown in **Fig. 4-4 (b)**.

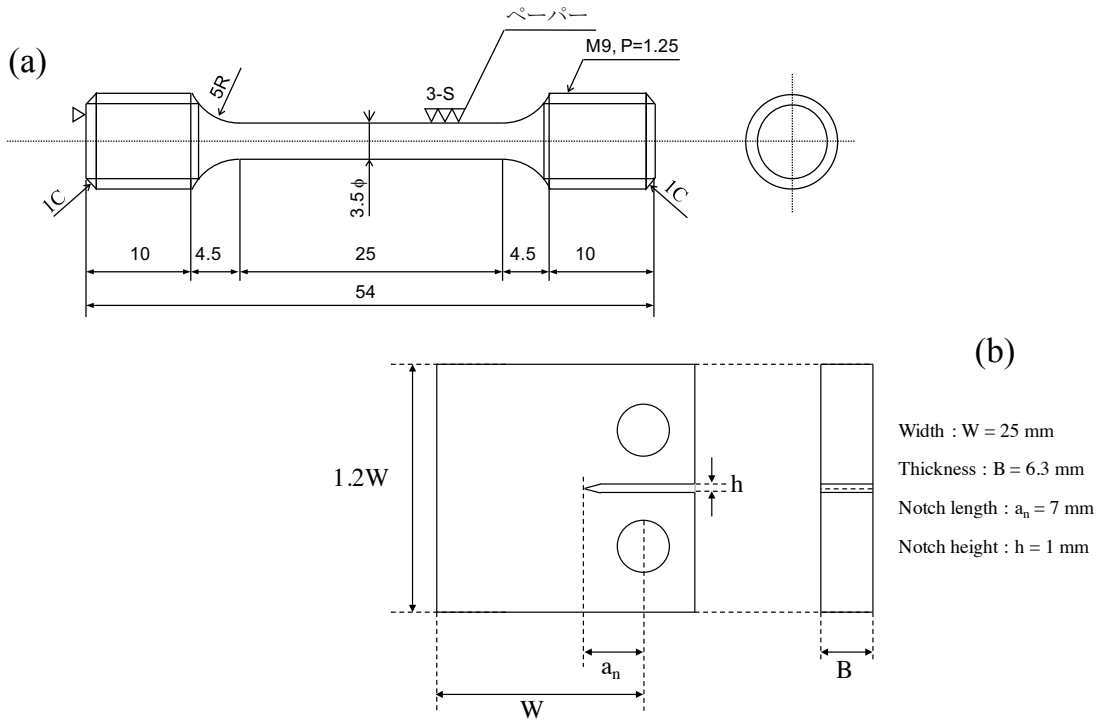

Fig. 4-4. Schematic illustration of (a) tensile test specimen and (b) half-size compact tension (CT) specimen for room temperature tests.

Tensile parameters e.g., σ_{YS} and σ_{UTS} that were used in this study for fatigue crack growth are presented in **Table 4-5**. Moreover, detailed strain-stress curves are shown in **Appendix A4**.

Specimens were mechanically polished using emery papers (#400, #800 and #1200). Then, the specimens were electro-polished in a solution of perchloric acid (90 vol.% Ethanol, 6 vol.% $HClO_4$, 4 vol.% H_2O). Electro-polishing conditions were 3 mA/mm^2 at 243 K for 60 seconds. Due to the large size of specimens, current was often higher than 5 A during polishing. Some of the specimens were immerged in 0.75 vol.% HF - 1.75 vol.% HCl solution for few seconds in order to reveal clearly the microstructure during in-situ observation. Moreover, post-mortem bulk cracks were also observed. **Figure 4-5**

shows experimental procedure of inside and slice cracks preparation.

Table 4-5. Tensile properties of Ti-43Al-4Nb-5V (at.%) at ambient and elevated temperature. Figures in bracket correspond to *in-situ* results [11].

Microstructures	Young's Modulus E / GPa	Yield stress σ_y / MPa	Ultimate Tensile Strength σ_{UTS} / MPa	Elongation ε / %
AF	150	440	888	0.5
GTL	157	315	680	0.3
NGDP-Mn	148	375	812	0.9
NCT	159	470	951	0.3
NL	137 (34)	480	900 (664)	0.1 (0.7)
LTL	168	430	632	0.1
NGDP-4345	(47)	(495)	(775)	(2.3)

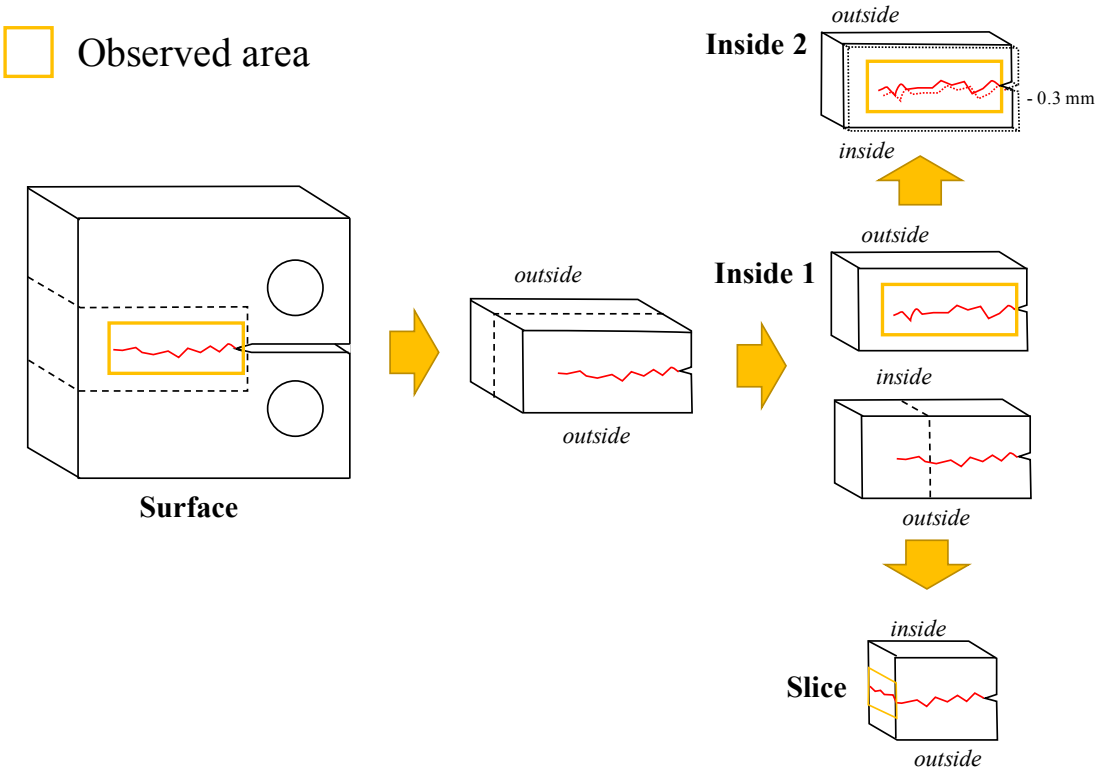

Fig. 4-5. Experimental procedure of inside and slice cracks preparation for observations.

The suitable introduction of precrack was a critical point in these experiments. Nakamura *et al.* demonstrated the importance of the correct precrack introduction on the reliability of fatigue crack growth curves [11]. To determine the effect of precrack

introduction on the fatigue crack behavior, two different tests were conducted using Nearly Lamellar microstructure. The first test was carried out by load shedding without introducing a precrack. On the other hand, the second test was performed after 1.2 mm precrack introducing. The results are shown in **Figure 4-6**. The effect of precrack introduction is clearly observed. The specimen without precrack shows very scattered data points and the stress intensity threshold is difficult to be defined. However, in the precracked specimen, the fatigue threshold is clearly identified.

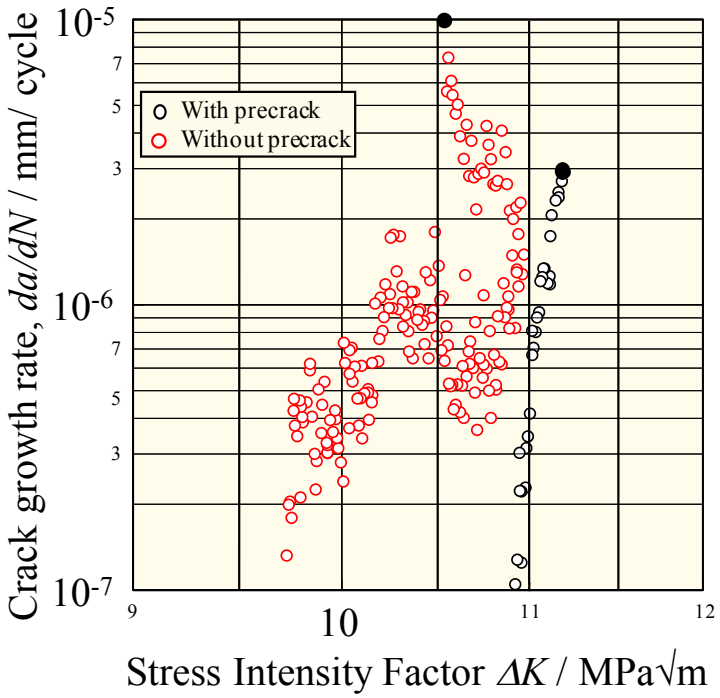

Fig. 4-6. Effect of pre-crack introduction effect during *K*-decreasing test in Nearly Lamellar microstructure. Black spots indicate the initial positions [11].

The initial fatigue precracks were introduced with a maximum crack growth rate lower than $1x10^{-5}$ mm/cycle at the tip of the CT specimen notch and with a current flow of 1 A by cyclic tension-tension load in elastic region. Alumel wires were attached by spot welding to provide the electrical current and measure the voltage drop at the notch, necessary for determining the crack length by the use of the potential drop technique DCPD as shown in **Figure 4-7**. Because Alumel weld was weak, Ø0.5 mm wires were used between specimen and Alumel with welding conditions as follow: **pressure 10, power 70, time 5 Hz**. However, this diameter was difficult to bend and to avoid weld failure, Ø0.3 mm wires were weld with the larger Alumel diameter and used for

connections with the following welding conditions: **pressure 10, power 50, time 5 Hz**.

To control the crack growth rates, low initial value of K_{max} was chosen below the stress intensity threshold ΔK_{th} of reported TiAl alloys [14]. This value was increased gradually until the crack start to propagate. This method was inspired by the works of Gnanamoorthy *et al.* [15] that was conducted on bending test. The precrack length measured by direct current potential drop (DCPD) method was set to 8.2 mm (including 7.0 mm of a_0 notch) as shown in **Figure 4-8**.

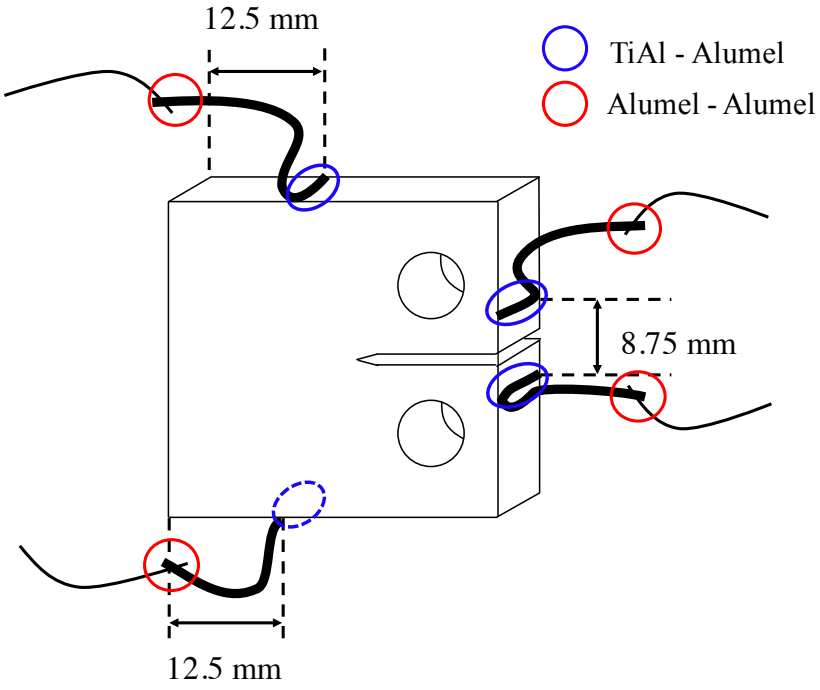

Fig. 4-7. Schematic illustration of the welding spots location.

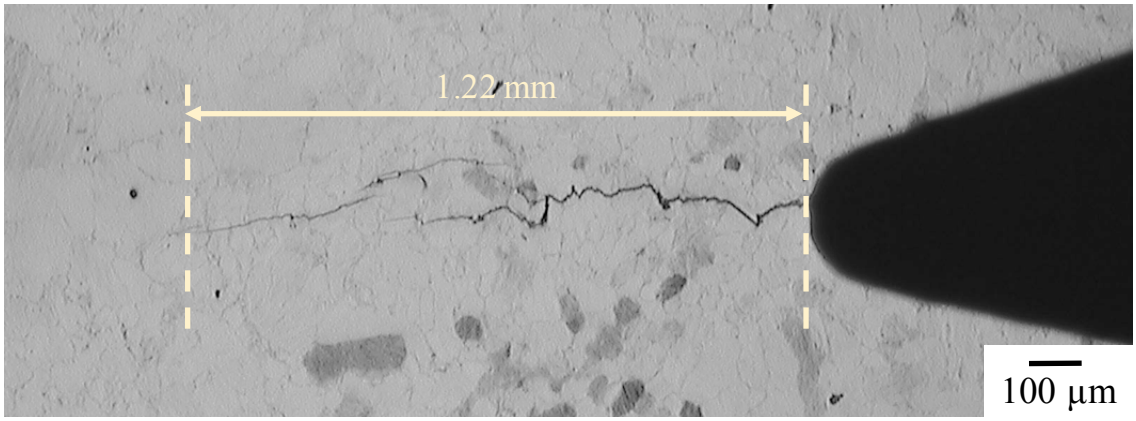

Fig. 4-8. OM image of NL microstructure after introducing 1.2 mm pre-crack controlled by DCDP with the comparison of OM measurement.

The fatigue crack growth tests were conducted using MTS Landmark™ Servo-hydraulic Test Systems. During tests, specimens were subjected to sinusoidal stress-time pattern at constant amplitude and fixed frequency as shown in **Figure 4-9**. The FCG tests can be described by the given term [16]:

Maximum stress in the cycle: σ_{max}

Minimum stress in the cycle: σ_{min}

$$R = \frac{\sigma_{min}}{\sigma_{max}} \tag{4-1}$$

$$\Delta\sigma_a = \sigma_{max} - \sigma_{min}$$

The hypothesis that the crack is long compared to microstructural features (α_2/γ colonies or γ grains for example) have been considered. Therefore, the Linear Elastic Fracture Mechanisms (LEFM) applies and the stress intensity ΔK which is the difference between the maximum and minimum value is given by:

$$\Delta K = Y(\sigma_{max} - \sigma_{min})\sqrt{\pi a} = K_{max} - K_{min} \tag{4-2}$$

Where σ_{max} is the maximum stress and σ_{min} is the minimum stress in the cycle, Y is a dimensionless factor of value around one which depend of the geometry of the sample and a is the actual crack length.

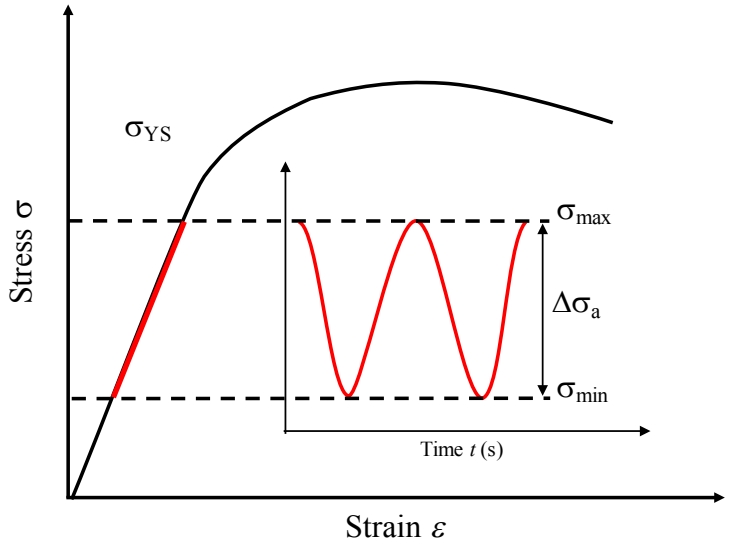

Fig. 4-9. Sinusoidal stress-time pattern with constant amplitude and fixed frequency occurring during tests.

A schematic crack growth curve is shown in **Figure 4-10**. The horizontal axis present the stress intensity factor ΔK and the vertical axis present the crack growth rate da/dN. K-

decreasing tests and *K*-increasing tests are required to acquire a complete curve. The curve can be divided in three part:

Region I: The crack growth rate becomes very small. It is considered that, when the crack growth rate become lower than 10^{-10} m/cycle, the crack does not propagate. This value is called the fatigue threshold ΔK_{th}.

Region II: It is characterized by a linear slope between the stress intensity and the crack growth rate in log scale and described by the Paris law [17]:

$$\frac{da}{dN} = C(\Delta K)^m \tag{4-3}$$

Where *C* and *m* are the Paris coefficient and the Paris exponent, respectively.

Region III: The crack growth rate accelerates in this region. Two reason could explain this phenomenon. K_{max} approaches fracture toughness K_{IC} of the materials or the sectional area carrying the load become too small for the load.

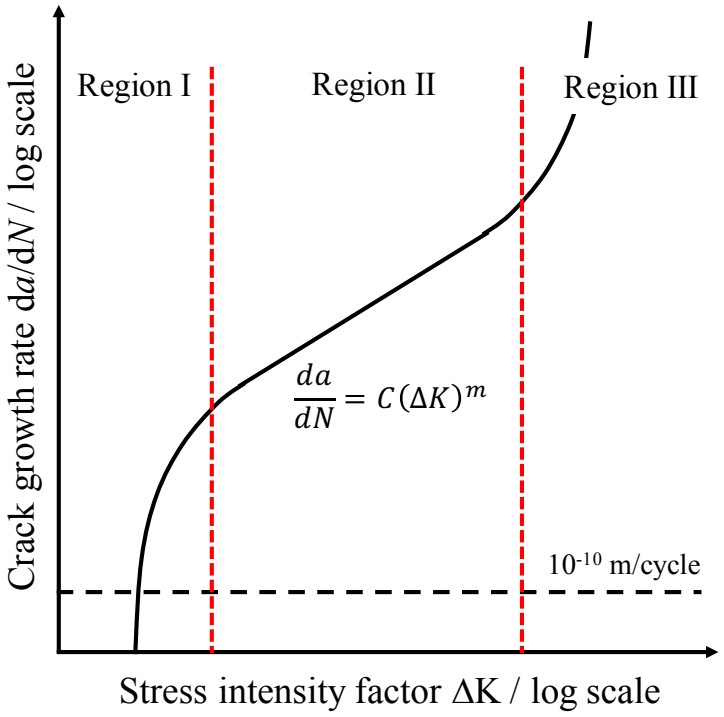

Fig. 4-10. Schematic illustration of a fatigue crack growth curve.

Tests were carried out at room temperature in air under cyclic stress intensity (ΔK) controlled with load ratio *R* of 0.1 and a frequency of 20 Hz. *K*-decreasing tests and *K*-increasing tests were conducted, respectively, by load shedding and by constant load amplitude independently, where *K* is the stress intensity factor at the tip of the crack with

a current flow of 3 A. Initial stress intensity K value of K-increasing and K-decreasing tests was chosen higher than the K value of the precrack test in order to eliminate the stress field occurred during precrack introduction.

K-decreasing test is performed using normalized K gradient (C) as the following equation:

$$\Delta K = \Delta K_0 \exp[C(a - a_0)] \quad (4\text{-}4)$$

Where C is the normalized K gradient C = -0.08/mm used during load shedding. It represents how much the K value decrease when the crack propagates by 1 mm. ΔK_0 is the initial stress intensity, a_0 and a are the initial and the actual crack length, respectively. Crack size was measured in-situ with alumel wire with the direct current potential drop technique.

The specimens were examined using a Nikon LV150 OM (Optical Microscope), and then using a JEOL JSM-7000F FE-SEM (Field Emission Scanning Electron Microscope) with an acceleration voltage of 15 kV and a working distance of 14 mm after the different stages of the experiments: initial microstructure, precrack tests, K-decreasing tests and K-increasing tests. In-situ observation of crack growth behavior was performed using Hirox KH 1300 CCD camera. Finally, the fracture surface observations were studied using SEM model JEOL JSM 6610 at 15-20 kV.

4.3 Results

4.3.1 Fatigue crack growth behavior

(A) Comparison between as-forged and heat treated samples

The influence of microstructure between as-forged and heat treated sampled has been investigated on wrought 42-5Mn alloy. Fatigue crack growth curve (da/dN as a function of ΔK) for samples with as-forged (AF), globular triplex (GTL) and nearly globular β/γ duplex microstructures (NGDP) of 42-5Mn alloy are shown in **Figure 4-11**. Although the FCG curve represents only one test, all the fatigue thresholds ΔK_{th} values where the cracks stop to propagate, the Paris regime exponents m and coefficients C, and the maximum stress intensities at overload K_{max} are summarized in **Table 4-6**. Detailed FCG curves are shown in **Appendix A5**.

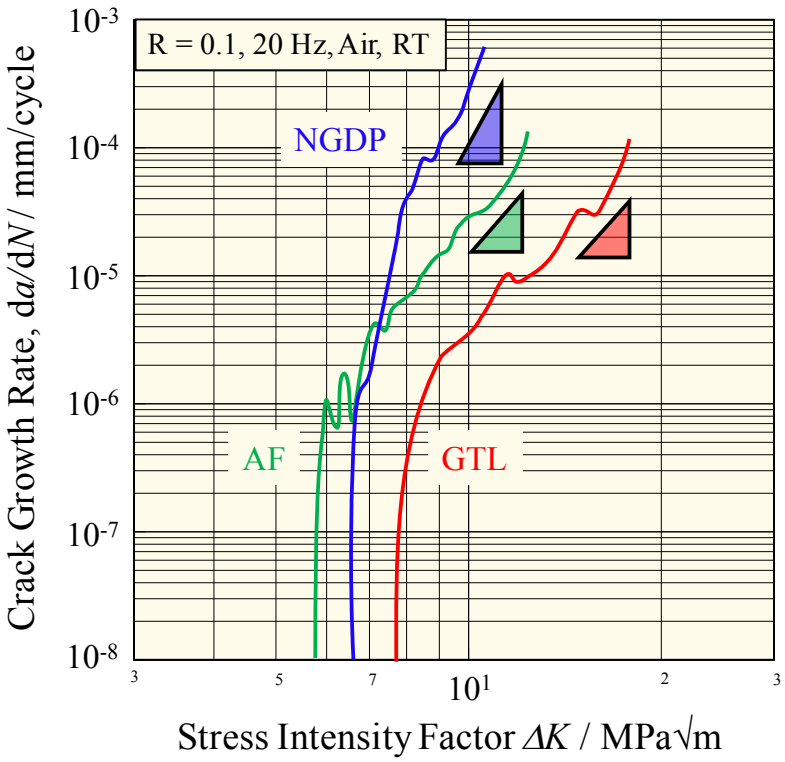

Fig. 4-11. Effect of heat treatment on the fatigue crack growth behavior of wrought 42Al-5M alloy.

The heat treatment conditions drastically affected the fatigue resistance properties by modifying the microstructure. GTL microstructure shows the highest fatigue threshold (ΔK_{th} ~8.6 MPa$\sqrt{m}$) and the smallest Paris slope whereas the as-forged microstructure shows the smallest fatigue threshold equivalent to NDGP microstructure. The difference of fatigue threshold, around 3 MPa$\sqrt{m}$ is relatively important and not negligible. In opposite, the Paris slope of AF is similar to GTL results and is around 6.5. NGDP microstructure shows the highest Paris slope (about 10.5). Moreover, the fatigue crack growth of as-forged and globular triplex microstructures propagates stepwise, which could be related to the presence of α_2/γ colony grains microstructure, whereas the FCG curve of NGDP microstructure grows smoothly. The maximum stress intensity K_{max} at the overload region can provide a correct idea of the toughness of the materials. Heat treatment conditions affected also the stress intensity K_{max} which varies by a factor of 2 with 12.0 MPa$\sqrt{m}$ in NGDP microstructure to 20.3 MPa$\sqrt{m}$ in GTL. Thus, controlling microstructure through heat treatments can completely modify the fatigue resistance either improve or worsen it.

Table 4-6. Fatigue crack growth results in 42-5Mn.

Microstructure	Sample	ΔK_{th} / Mpa$\sqrt{m}$	m	C	K_{max} / Mpa$\sqrt{m}$
As-forged	42-5Mn-A	5.3	8.0	1E-12	–
	42-5Mn-B	5.9	6.1	2E-11	14.1
	42-5Mn-C	–	7.4	9E-11	–
	Average	**5.6 ± 0.4**	**6.8 ± 1.0**	**–**	**14.1**
GTL	42-5Mn-D	8.6	4.6	8E-11	–
	42-5Mn-E	7.7	8.0	2E-14	20.3
	42-5Mn-F	9.5	–	–	–
	42-5Mn-G	8.5	–	–	–
	Average	**8.6 ± 0.7**	**6.3 ± 2.3**	**–**	**20.3**
NGDP	42-5Mn-H	–	10.5	9E-15	12.0
	42-5Mn-I	6.8			
	Average	**6.8**	**10.5**	**–**	**12.0**

(B) Effect of alloys composition

Before to investigate in detail the effect of the microstructure and especially the β phase, the alloys composition has been briefly studied in order to determine if the elements composition affects more the FCG properties than the microstructural features. Therefore, the same microstructure Nearly Globular β/γ Duplex has been designed for the 42-5Mn and 43-4-5 alloys and the fatigue crack growth curve are shown in **Figure 4-11** and the results are summarized in **Table 4-7**. Detailed FCG curves are shown in **Appendix A5**.

The alloys composition does not affect significantly the fatigue crack behavior. The stress intensity threshold in all microstructures is nearby 7.0 MPa$\sqrt{m}$ and the Paris slope is also similar with a value of about 10.5. Finally, rupture occurred at a comparable stress intensity, indicating an equivalent fracture toughness. Therefore, the effect of composition revealed to be negligible against the effect of microstructure and it became possible to compare different alloys with different microstructures.

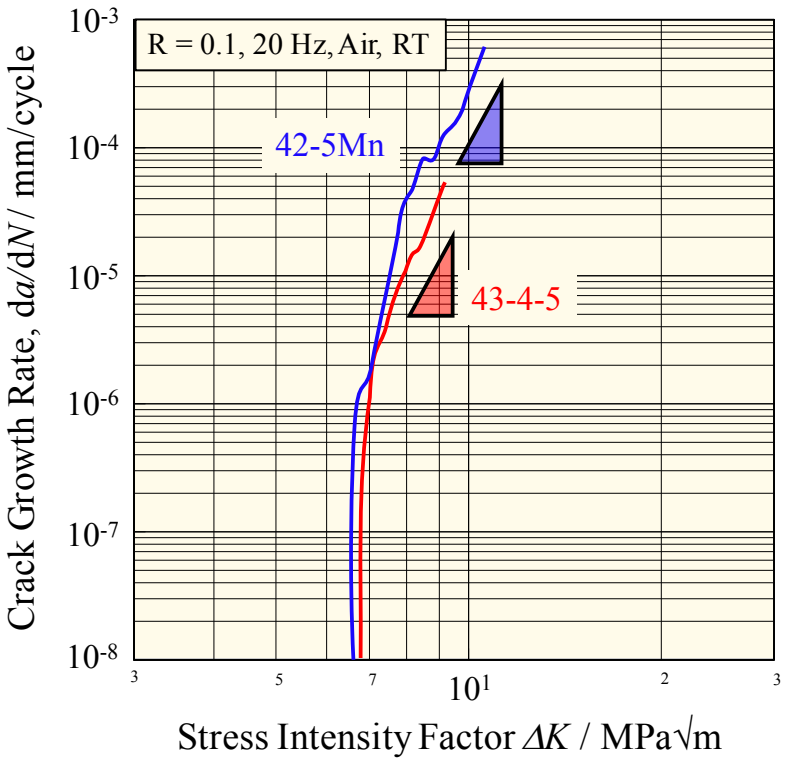

Fig. 4-11. Effect of alloying element on the fatigue crack growth behavior of wrought alloys with a nearly globular β/γ duplex (NGDP) microstructure.

Table 4-7. Fatigue crack growth results of NGDP microstructure in different alloys.

Microstructure	Sample	ΔK_{th} / Mpa$\sqrt{m}$	m	C	K_{max} / Mpa$\sqrt{m}$
42-5Mn NGDP	**Average (Table 4-6)**		**10.5**	**–**	**12.0**
43-4-5 NGDP	43-4-5-J	7.5	–	–	–
	43-4-5-K	6.8	12.7	8E-17	–
	43-4-5-L	–	8.1	5E-13	11.8
	43-4-5-M	7.0	–	–	–
	Average	**7.1 ± 0.4**	**10.4 ± 3.2**	**–**	**11.8**

(C) Effect of β/γ duplex volume fraction V_{DP}

The first parameter to be studied was the volume fraction of β/γ duplex V_{DP}. Indeed, in service, the $\alpha_2 + \gamma \rightarrow \beta + \gamma$ cellular reaction takes place at the grain boundaries and thus, it becomes necessary to understand how it is affected the fatigue crack growth

behavior. **Figure 4-12** and the **Table 4-8** show the fatigue crack growth curves and the detailed results, respectively, of three microstructures which have an increasing volume fraction β/γ duplex. Detailed FCG curves are shown in **Appendix A5**.

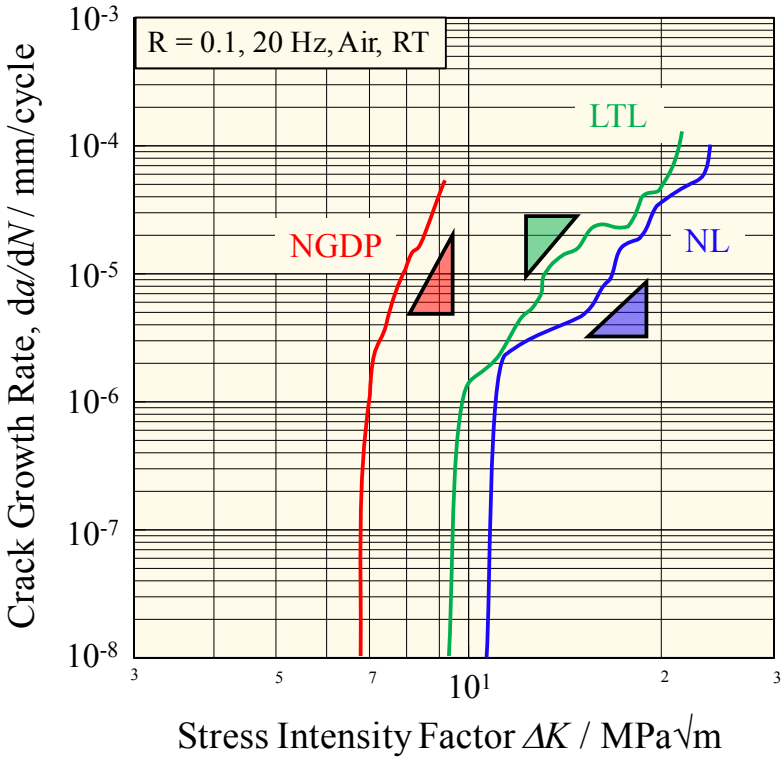

Fig. 4-12. Effect of β/γ duplex volume fraction V_{DP} on the fatigue crack growth behavior in 43-4-5 alloy.

As shown in **Fig. 4-12**, it is obvious that the fatigue properties strongly depend on the β/γ duplex structure volume fraction V_{DP} and by increasing it, the stress intensity threshold ΔK_{th} decreases and the Paris slope increases. The Nearly Lamellar microstructure exhibits the highest fatigue threshold (ΔK_{th} ~10.4 MPa$\sqrt{m}$) and the lowest Paris slope. Lamellar Triplex microstructure shows an intermediate behavior with a fatigue threshold around 10.1 MPa$\sqrt{m}$ close to the NL microstructure, and a higher Paris slope whereas, at the opposite, the Nearly Globular β/γ Duplex microstructure exhibits the lowest threshold and the highest Paris slope. Moreover, it should be noticed that the fatigue crack growth of NL and LTL microstructures propagates stepwise with different "local" slopes whereas the FCG curve of NGDP microstructure grows smoothly same as previously reported with the 42-5Mn alloy. The effect of the difference in local Paris slope will be discussed later.

Table 4-8. Fatigue crack growth results of microstructures with different β/γ duplex volume fraction V_{DP} in 43-4-5 alloy.

Microstructure	Sample	ΔK_{th} / Mpa$\sqrt{m}$	m	C	K_{max} / Mpa$\sqrt{m}$
NL (V_{DP} = 7%)	43-4-5-A	–	6.5	5E-13	–
	43-4-5-B	10.9	–	–	–
	43-4-5-C	10.2	4.7	4E-11	27.1
	43-4-5-D	–	6.6	5E-13	–
	43-4-5-E	10.0	8.0	3E-15	–
	Average	**10.4 ± 0.5**	**6.4 ± 1.4**	**–**	**27.1**
LTL (V_{DP} = 32%)	43-4-5-F	9.4	13.0	8E-21	22.6
	43-4-5-G	10.6	5.3	9E-12	23.8
	43-4-5-H	–	7.2	1E-13	20.0
	43-4-5-I	10.4	–	–	–
	Average	**10.1 ± 0.6**	**8.5 ± 4.0**	**–**	**22.1 ± 1.9**
NGDP (V_{DP} = 96%)	**Average (Table 4-7)**	**7.1 ± 0.4**	**10.4 ± 3.2**	**–**	**11.8**

(D) Effect of β/γ morphology

A second parameter was investigated: the morphology of β/γ duplex at the grain boundaries. Since, the composition was not affect drastically the FCG behavior, different alloys were studied due to their different phase transformation pathway and three unique morphologies were designed with the same volume fraction of β/γ duplex. **Figure 4-13** shows the fatigue crack growth curves of the tested samples, GTL, LTL and NCT. Fatigue threshold, Paris exponent and coefficient, and K_{max} are summarized in **Table 4-9**. Detailed FCG curves are shown in **Appendix A5**.

Specimens with a Globular Triplex microstructure exhibited a lower fatigue threshold (ΔK_{th} ~8.6 MPa$\sqrt{m}$) than specimens with another microstructure, but a similar Paris slope to Near γ Cellular Triplex microstructure. Lamellar Triplex specimens showed higher fatigue threshold (ΔK_{th} ~10.1 MPa$\sqrt{m}$) and faster crack growth rates with a Paris slope of around 8.5. These differences appeared to be small, taking into account that the three tested microstructures show significant variations concerning their grain boundary morphologies. However, the difference of K_{max} at failure increased between these three

microstructures. Moreover, the variation of "local" slope in NCT specimens was more pronounced and occurred often than in GTL and LTL microstructures.

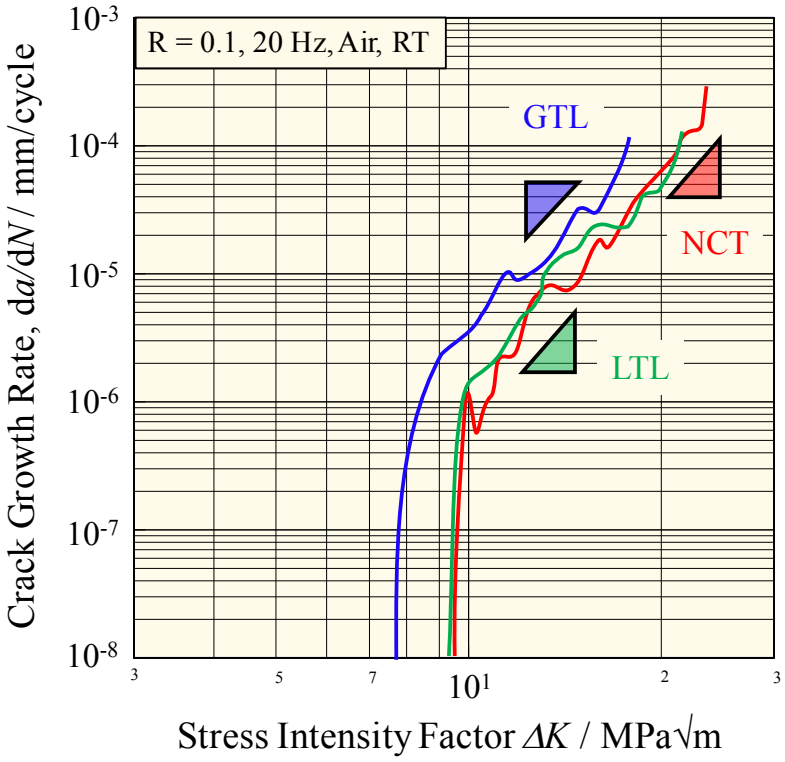

Fig. 4-13. Effect of β/γ duplex morphology on the fatigue crack growth behavior of wrought alloy.

Table 4-9. Fatigue crack growth results of microstructures with different β/γ duplex morphologies.

Microstructure	Sample	ΔK_{th} / Mpa$\sqrt{m}$	m	C	K_{max} / Mpa$\sqrt{m}$
43-4-5 LTL (V_{DP} = 32%)	**Average (Table 4-8)**	**10.1 ± 0.6**	**8.5 ± 4.0**	–	**22.1 ± 1.9**
42-8V NCT (V_{DP} = 33%)	42-8V-A	9.6	6.1	8E-13	26.8
	42-8V-B	9.7	–	–	–
	Average	**9.7 ± 0.1**	**6.1**	–	**26.8**
42-5Mn GTL (V_{DP} = 34%)	**Average (Table 4-6)**	**8.6 ± 0.7**	**6.3 ± 2.3**	–	**20.3**

4.3.2 Fatigue crack propagation of wrought alloys

The crack pathways were reconstituted using OM images. The crack pathways after *K*-decreasing tests of the different microstructures (NL, NGDP and LTL for the effect of V_{DP} and LTL, GTL and NCT for the effect of DP morphology) are shown in **Figure 4-14 to 4-18**. Higher magnification SEM or OM images focused on:

- Initial position, after the precrack test where the stress intensity was the highest.
- During the test in Paris law regime
- At the crack tip, corresponding to the stress intensity threshold where the crack stop to propagate.

The crack pathway after K-increasing was also reconstituted and shown in **Figure 4-19 and 4-20** but only for NL and NGDP microstructures. Indeed, in most cases after the *K*-increasing tests specimens reached the fracture toughness and it was no longer possible to observed their crack pathways.

Clear differences crack propagation pathways were observed. Morphology of the cracks could be either tortuous with many secondary branches and ligament bridges or relatively flat. The zigzagged shape depends on α_2/γ lamellar orientation of each grain with respect to the stress axis, the grains size and the DP morphology. Thus, NL (**Fig. 4-14 and 4-19**) and LTL (**Fig. 4-16**) microstructure presented the most zigzagged crack pathways with a larger number of crack deviations. Then, GLT (**Fig. 4-17**) and NCT (**Fig. 4-18**) microstructures shown an intermediate behavior with few secondary crack and limited deviations. Finally, the crack went through straight in the NGDP (**Fig. 4-15 and 4-20**) specimens.

In this section, a particular attention will be paid on the crack tip, at the stress intensity threshold, and on the crack during Paris regime. Some *in-situ* results will be described to support the observations. Finally, a comparison between crack propagation at the surface and in the bulk will be introduced.

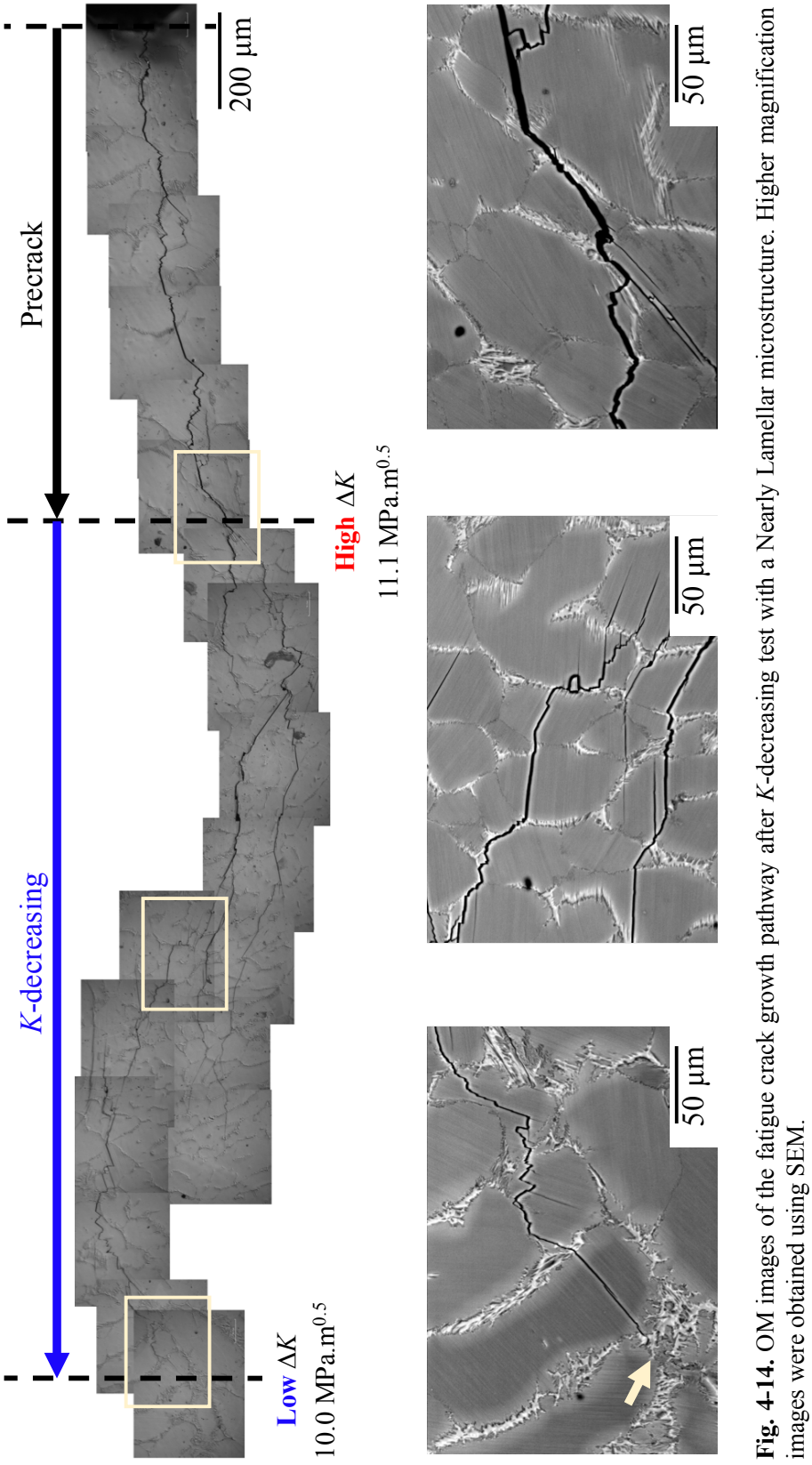

Fig. 4-14. OM images of the fatigue crack growth pathway after *K*-decreasing test with a Nearly Lamellar microstructure. Higher magnification images were obtained using SEM.

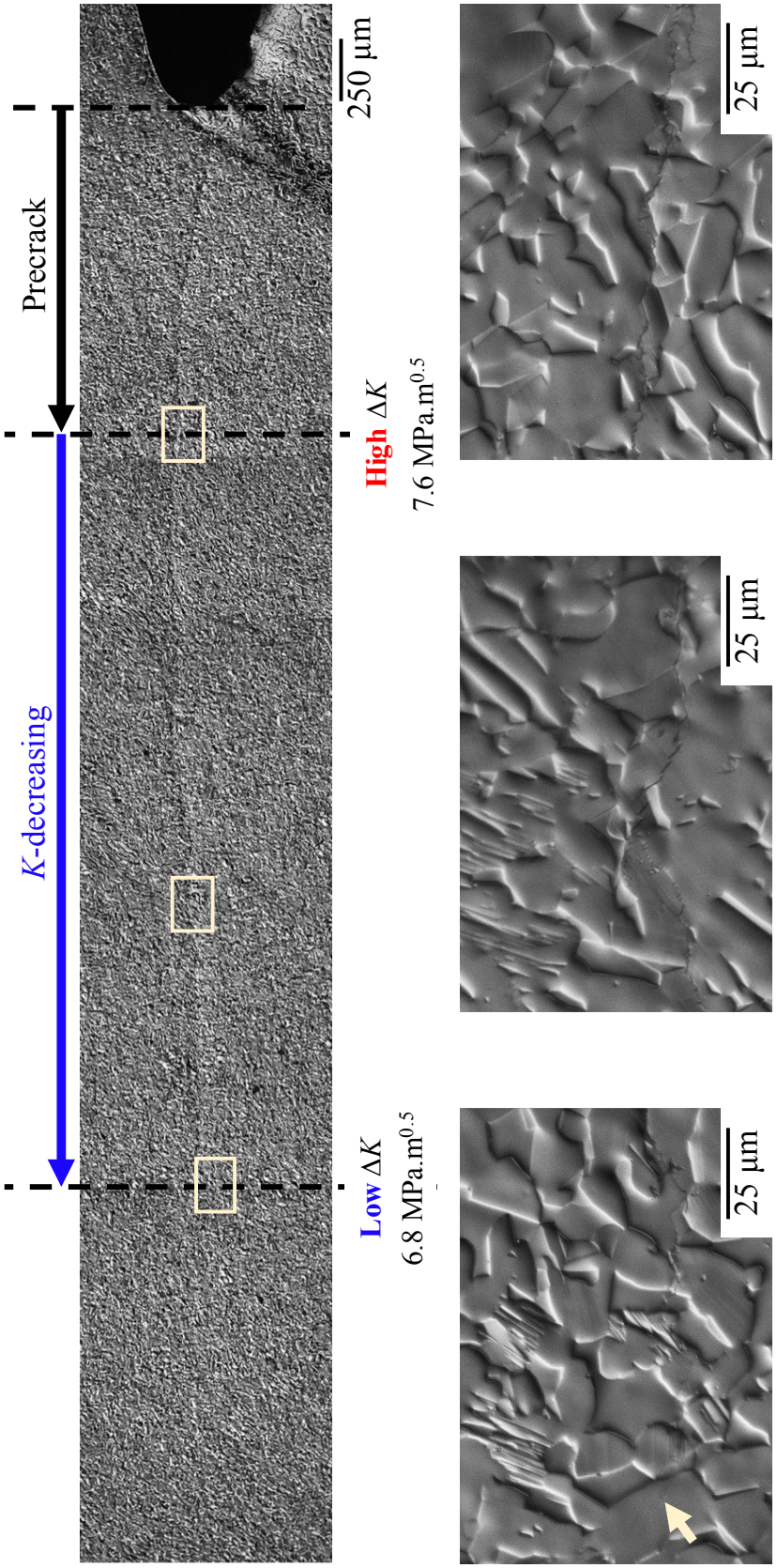

Fig. 4-15. OM images of the fatigue crack growth pathway after *K*-decreasing test with a Nearly Globular β/γ Duplex microstructure.

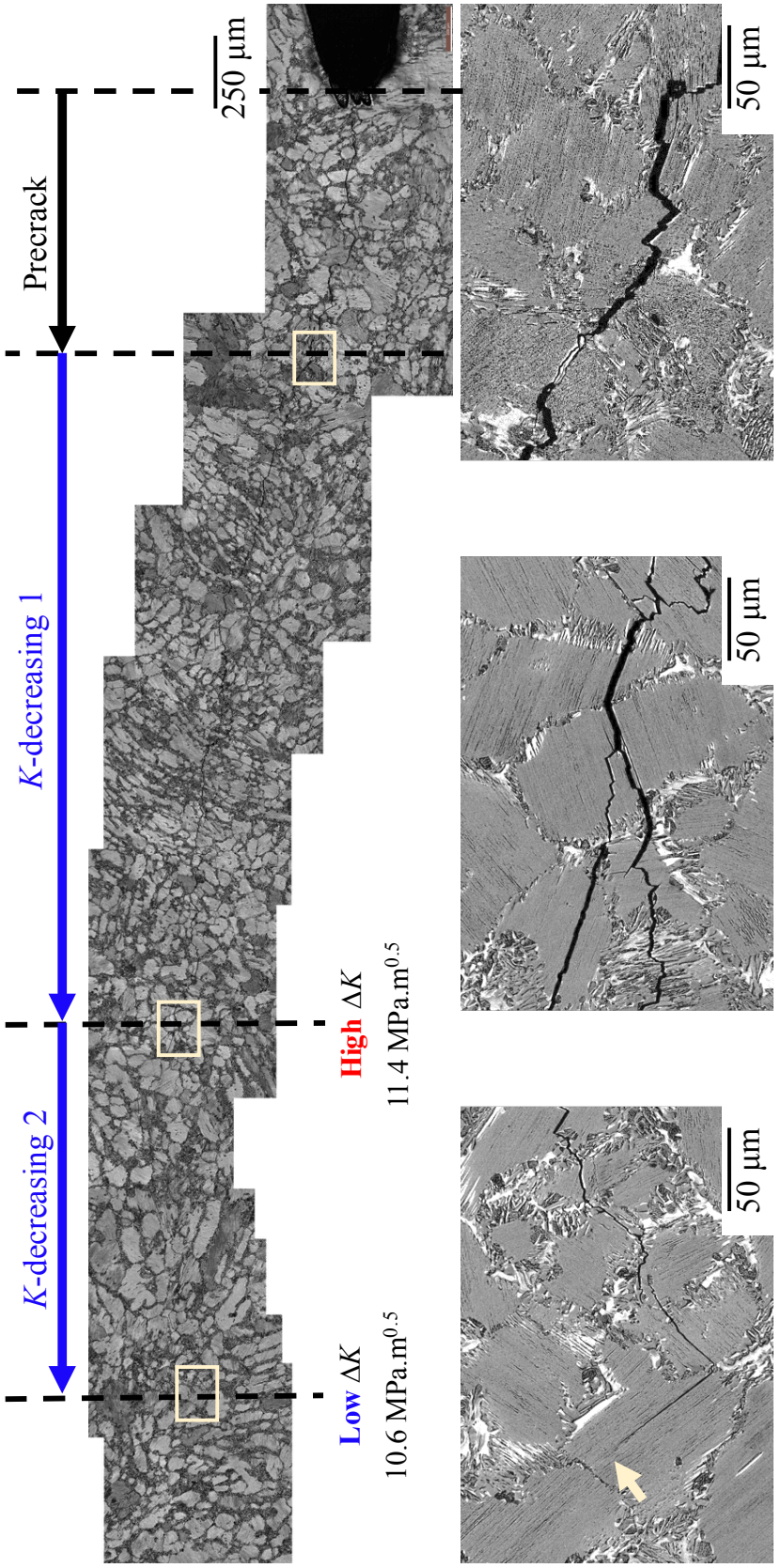

Fig. 4-16. OM images of the fatigue crack growth pathway after *K*-decreasing test with a Lamellar Triplex microstructure. Higher magnification images were obtained using SEM.

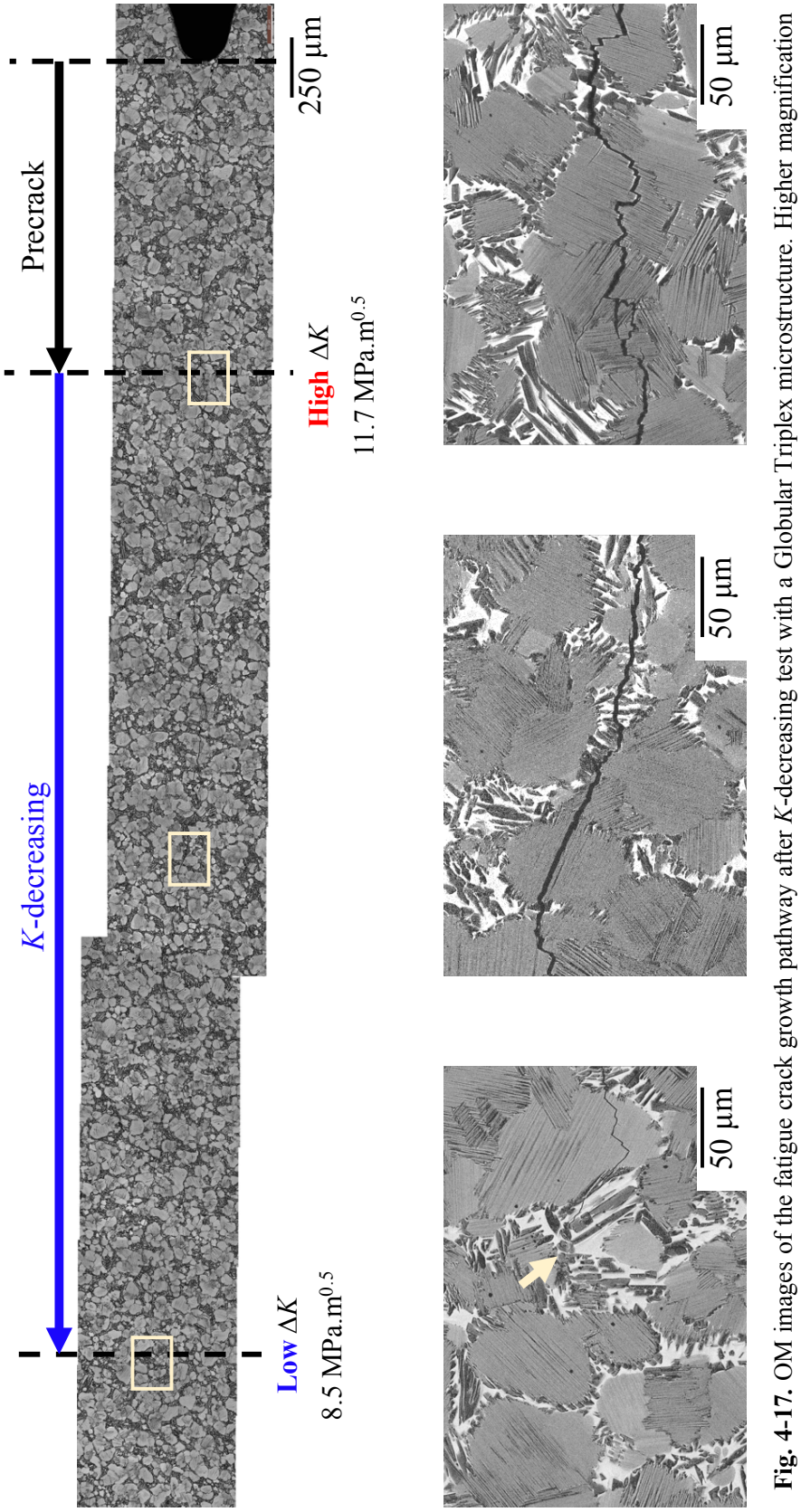

Fig. 4-17. OM images of the fatigue crack growth pathway after *K*-decreasing test with a Globular Triplex microstructure. Higher magnification images were obtained using SEM.

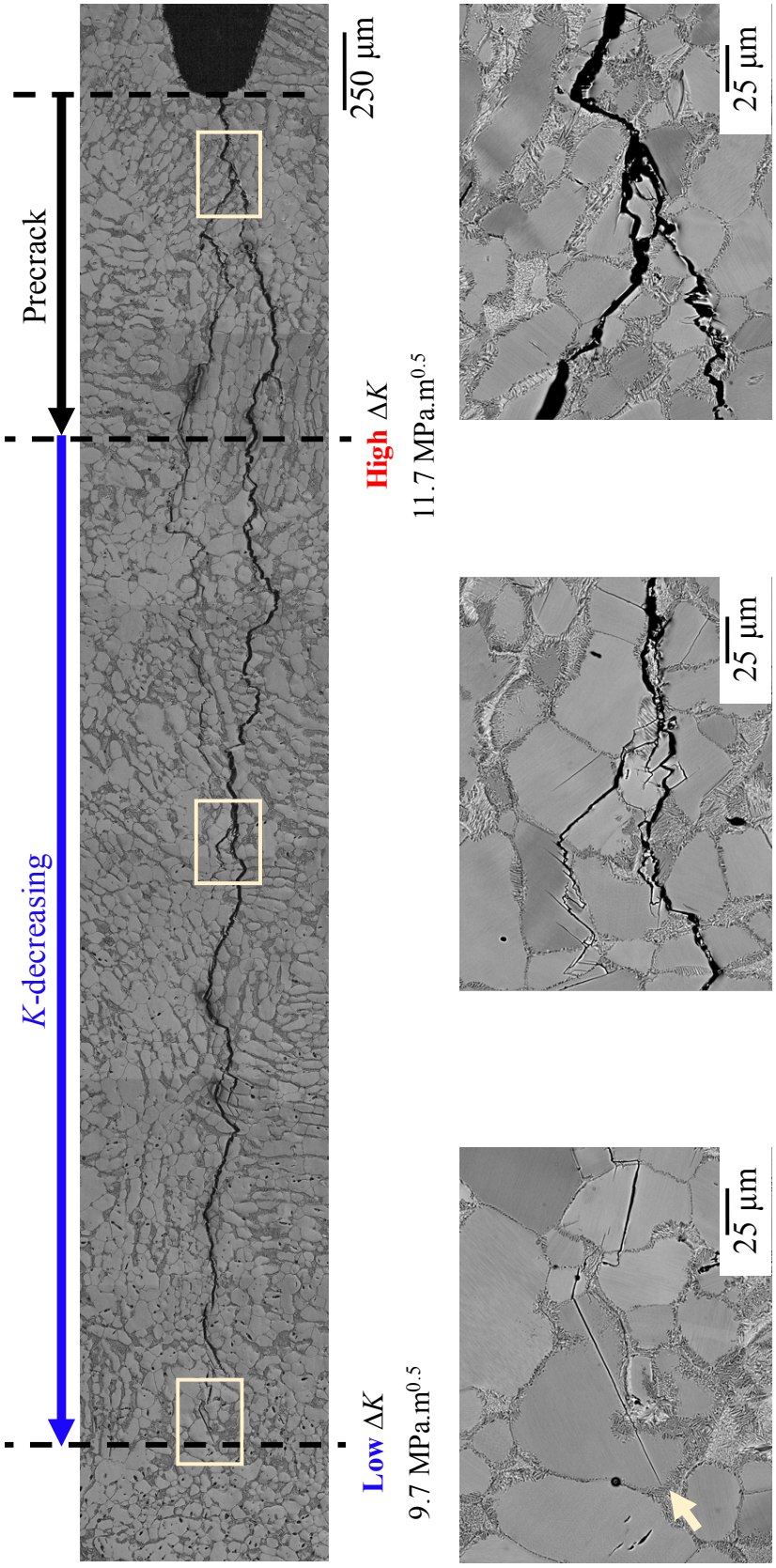

Fig. 4-18. OM images of the fatigue crack growth pathway after *K*-decreasing test with a Near γ Cellular Triplex microstructure. Higher magnification images were obtained using SEM.

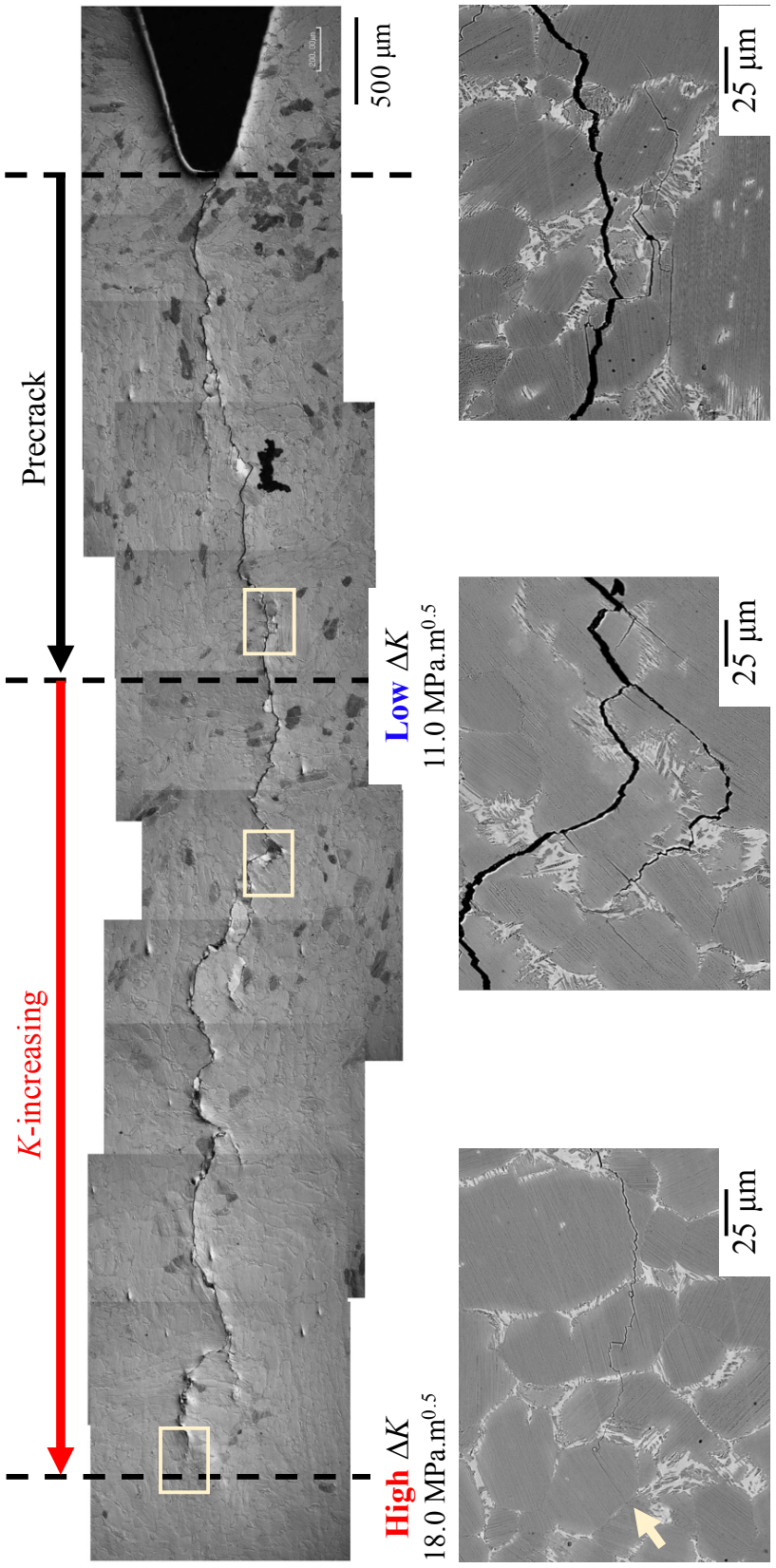

Fig. 4-19. OM images of the fatigue crack growth pathway after *K*-decreasing test with a Nearly Lamellar microstructure. Higher magnification images were obtained using SEM.

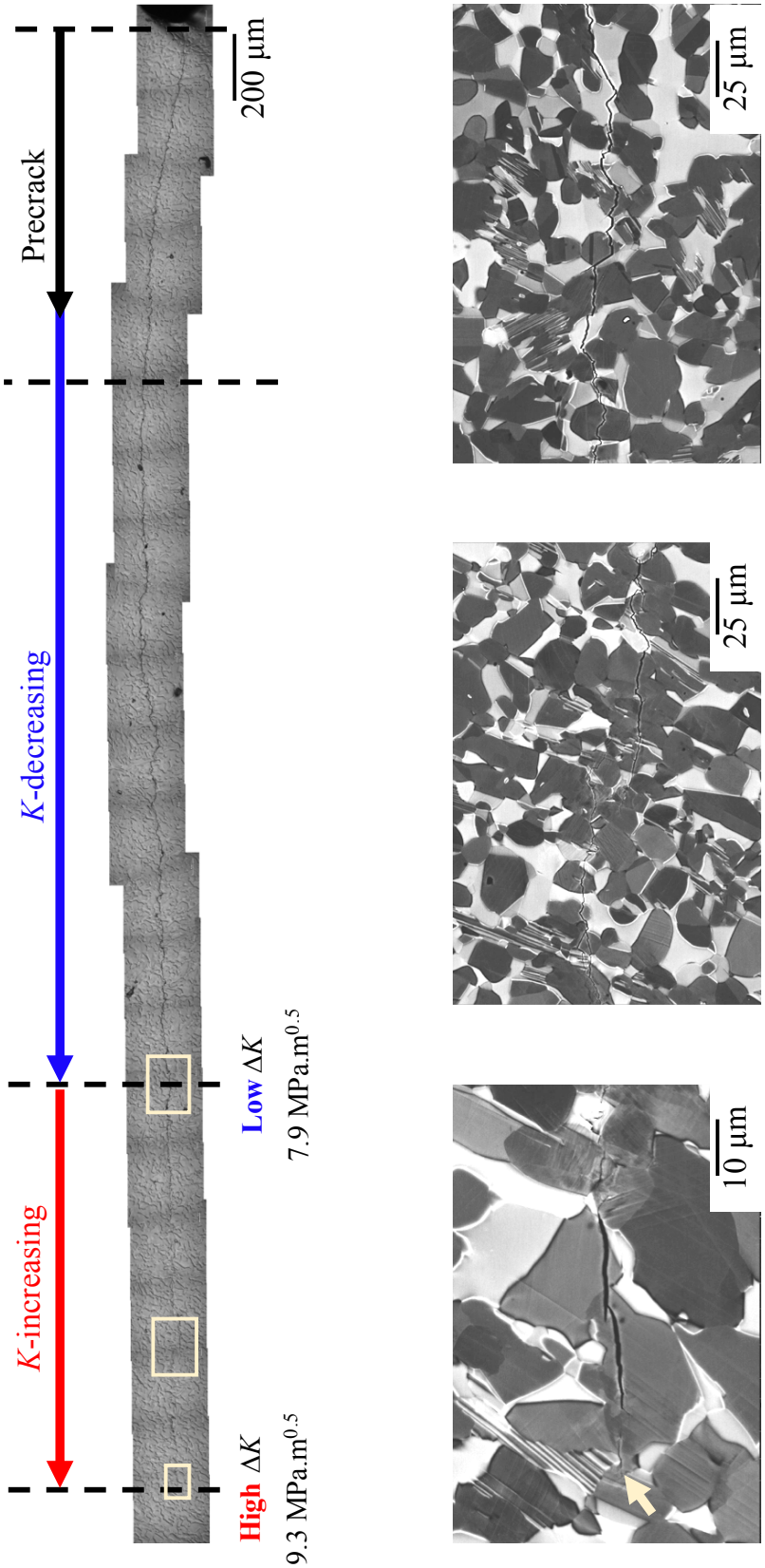

Fig. 4-20. OM images of the fatigue crack growth pathway after *K*-decreasing test with a Nearly Globular β/γ Duplex microstructure. Higher magnification images were obtained using SEM.

(A) Crack propagation near the stress intensity threshold

The crack tip at the stress intensity threshold of the different microstructures are shown in **Figure 4-21**. The crack stopped mainly in β/γ duplex region either in γ grains (**Fig. 4-21 (d), (f) and (g)**) or at β/γ grain boundaries (**Fig. 4-21 (b) and (h)**) indicate that β phase acts as strong features against the crack propagation. It should be noted that cracks stop sometimes in colonies as presented in **Fig. 4-16**.

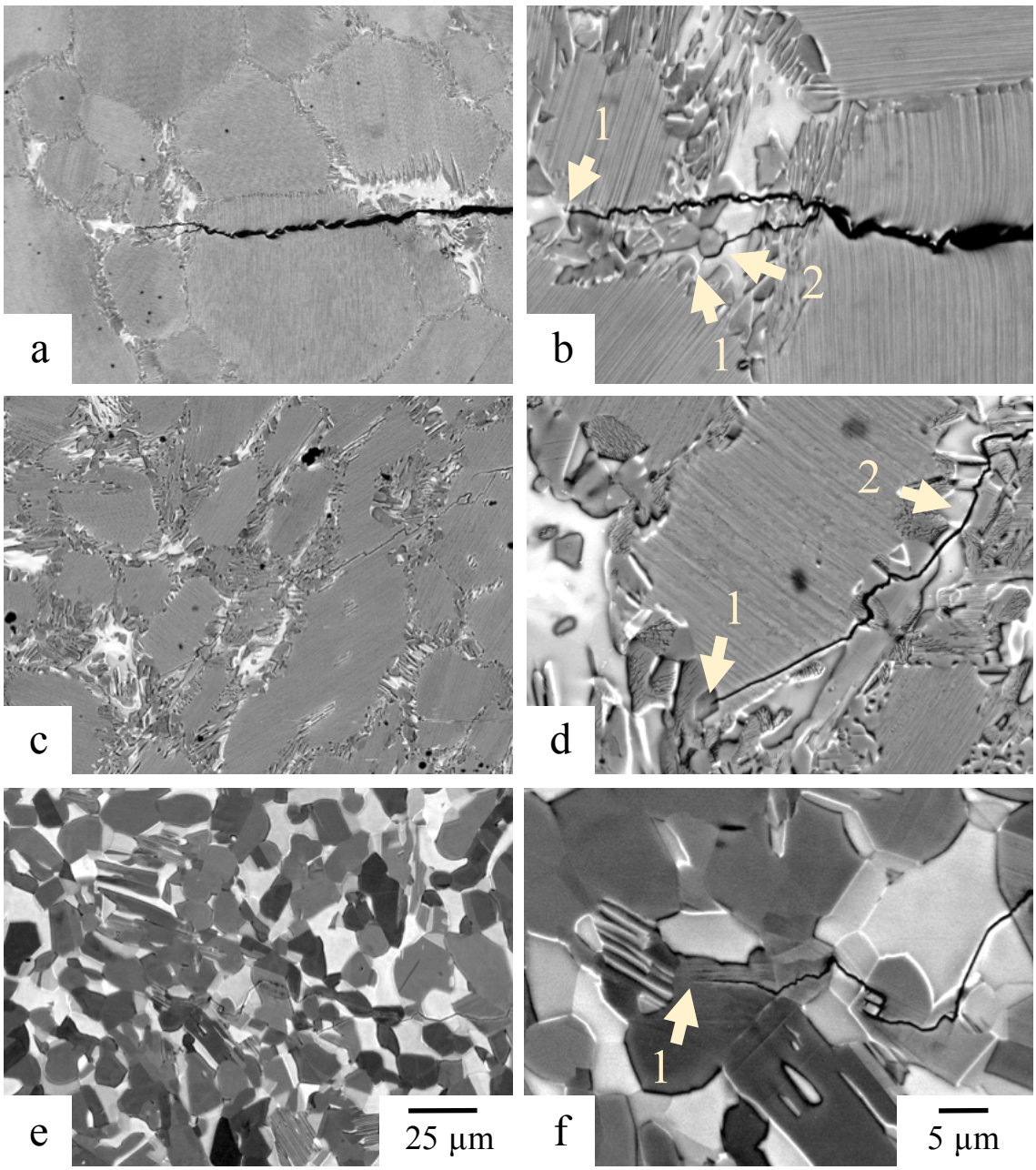

Fig. 4-21. BSE images of (a, b) Nearly Lamellar, (c, d) Lamellar Triplex and (e, f) Nearly Globular β/γ Duplex microstructures near the stress intensity threshold ΔK_{th}. Arrows indicate (1) crack stop position and (2) β/γ interface crack propagation.

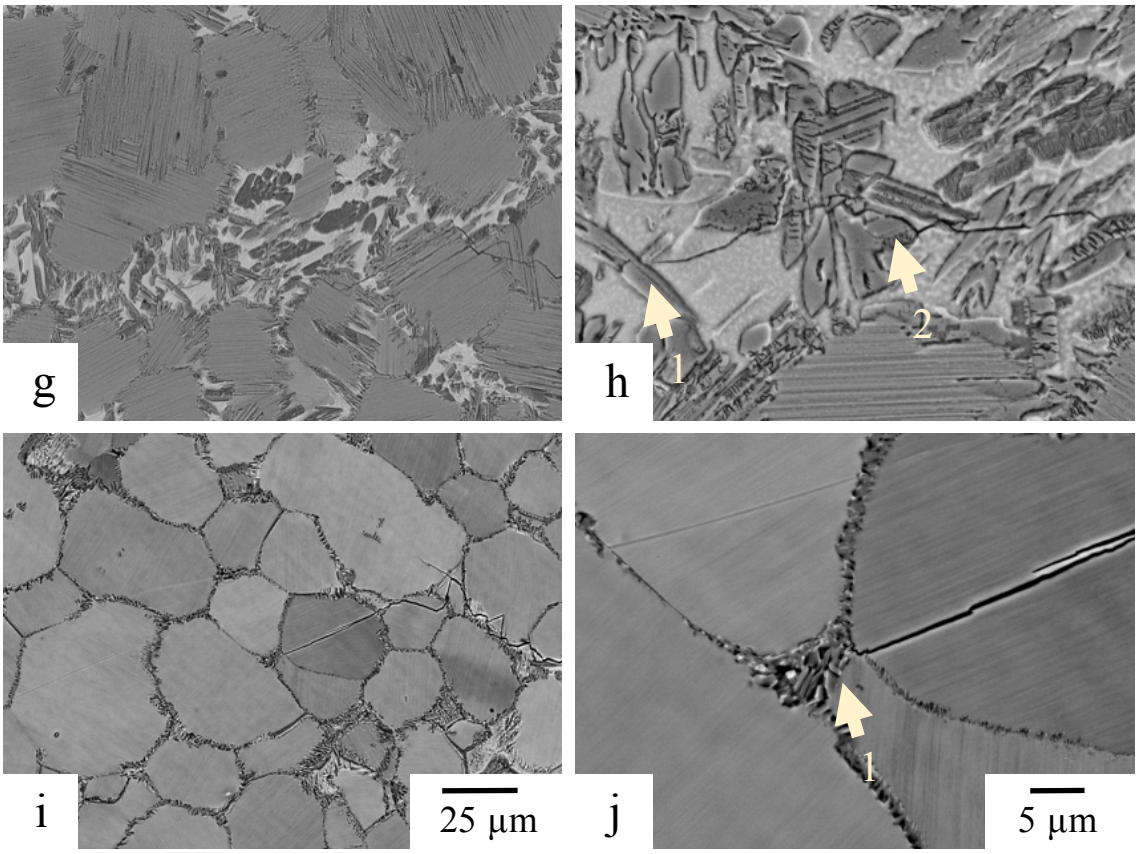

Fig. 4-21. (continued) BSE images of (g, h) Globular Triplex and (i, j) Near γ Cellular Triplex microstructures near the stress intensity threshold ΔK_{th}. Arrows indicate (1) crack stop position and (2) β/γ interface crack propagation.

During *K*-decreasing test, approaching the fatigue stress intensity threshold, the crack propagation diverted from the Paris law. The crack propagates less than 200 µm before reach the fatigue threshold. During this stage, the crack pathways indicate a step by step crack propagation with many small deviations in γ grain or in colonies which are perpendicular to the crack propagation. In NGDP microstructure, it can be clearly observed that crack prefer to go through γ phase and avoid β region. Cracks also grow at the β and γ interfaces, indicated a weak fatigue resistance of these regions against crack propagation as shown in NL, LTL and GTL microstructures with arrows.

(B) Crack propagation during Paris law regime

The crack pathways in Paris regime of the different microstructure at higher magnification are shown in **Figure 4-22 to 4-26**.

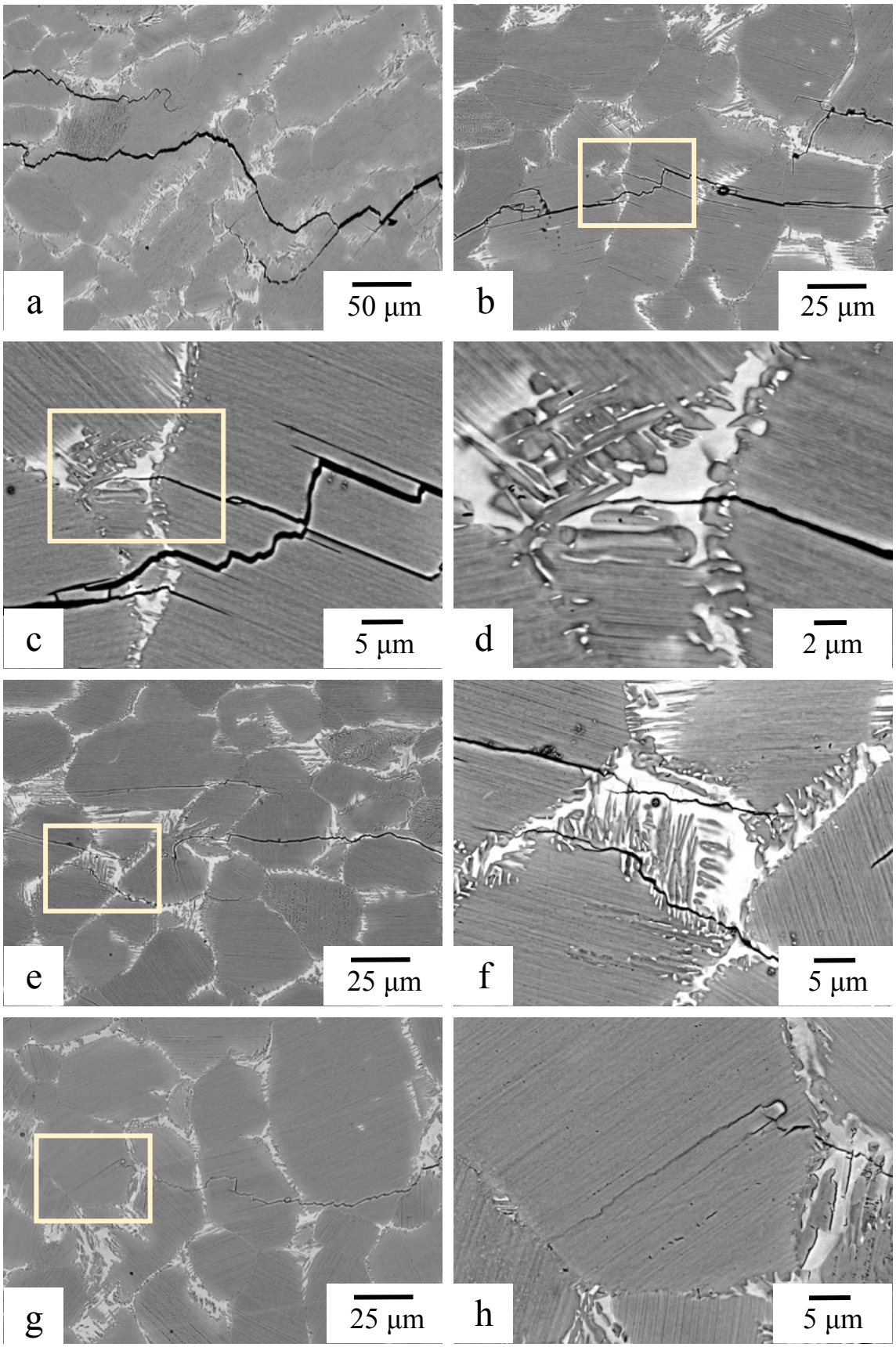

Fig. 4-22. SEM images of crack propagation pathway in NL microstructure (43-4-5 alloy).

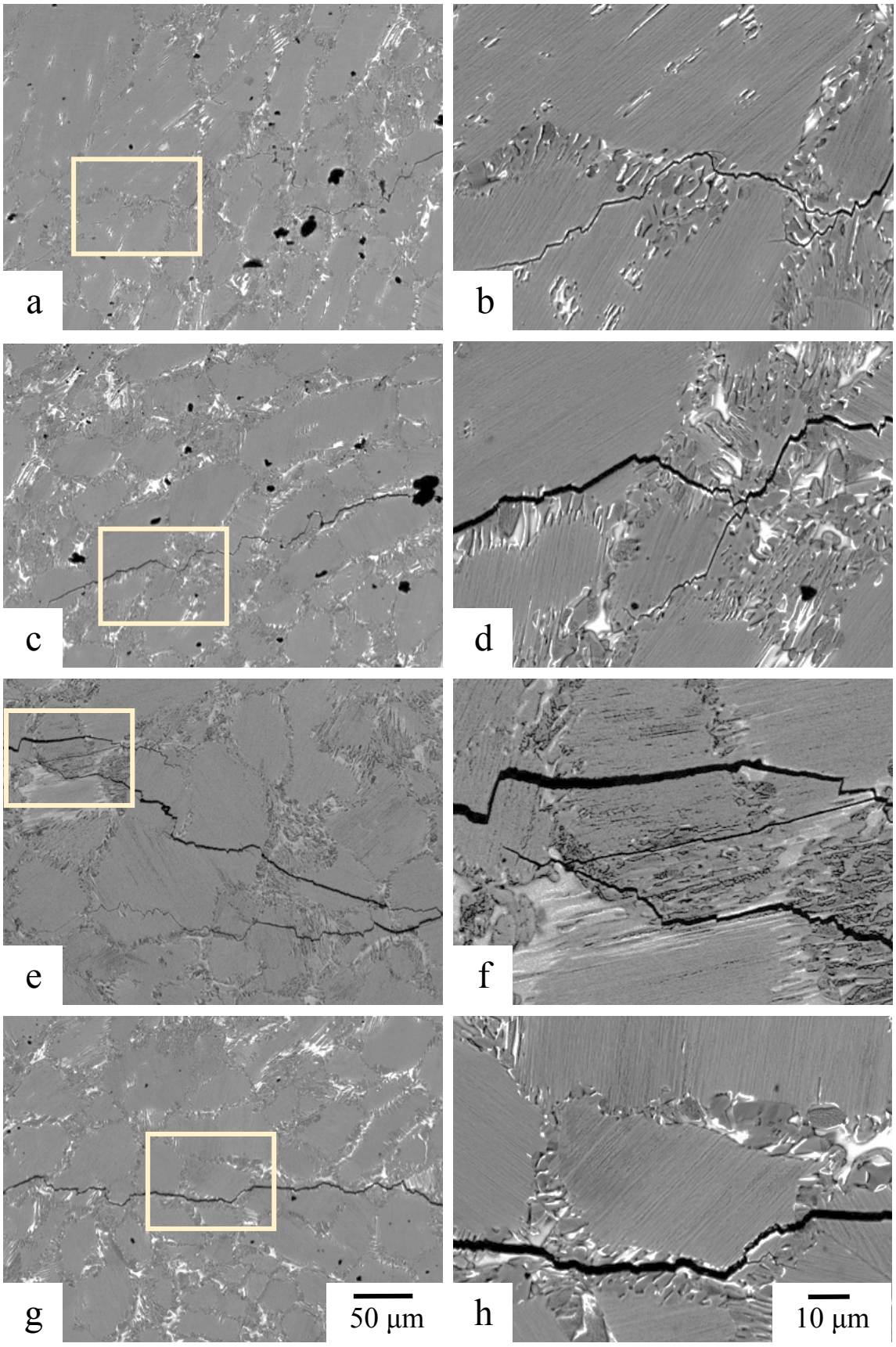

Fig. 4-23. SEM images of crack propagation pathway in LTL microstructure (43-4-5 alloy).

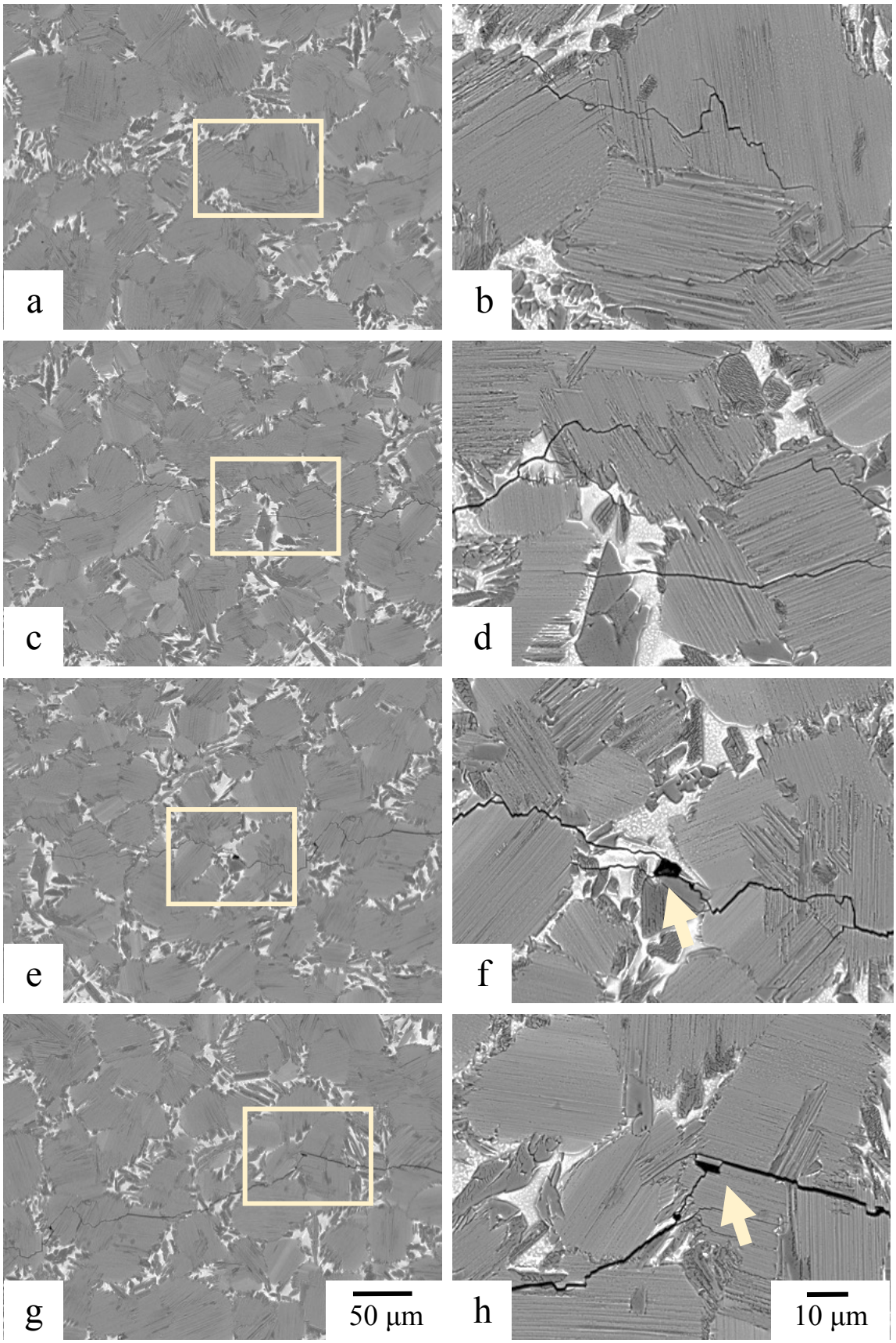

Fig. 4-24. SEM images of crack propagation pathway in GTL microstructure (42-5Mn alloy). Arrows indicates particles ejection.

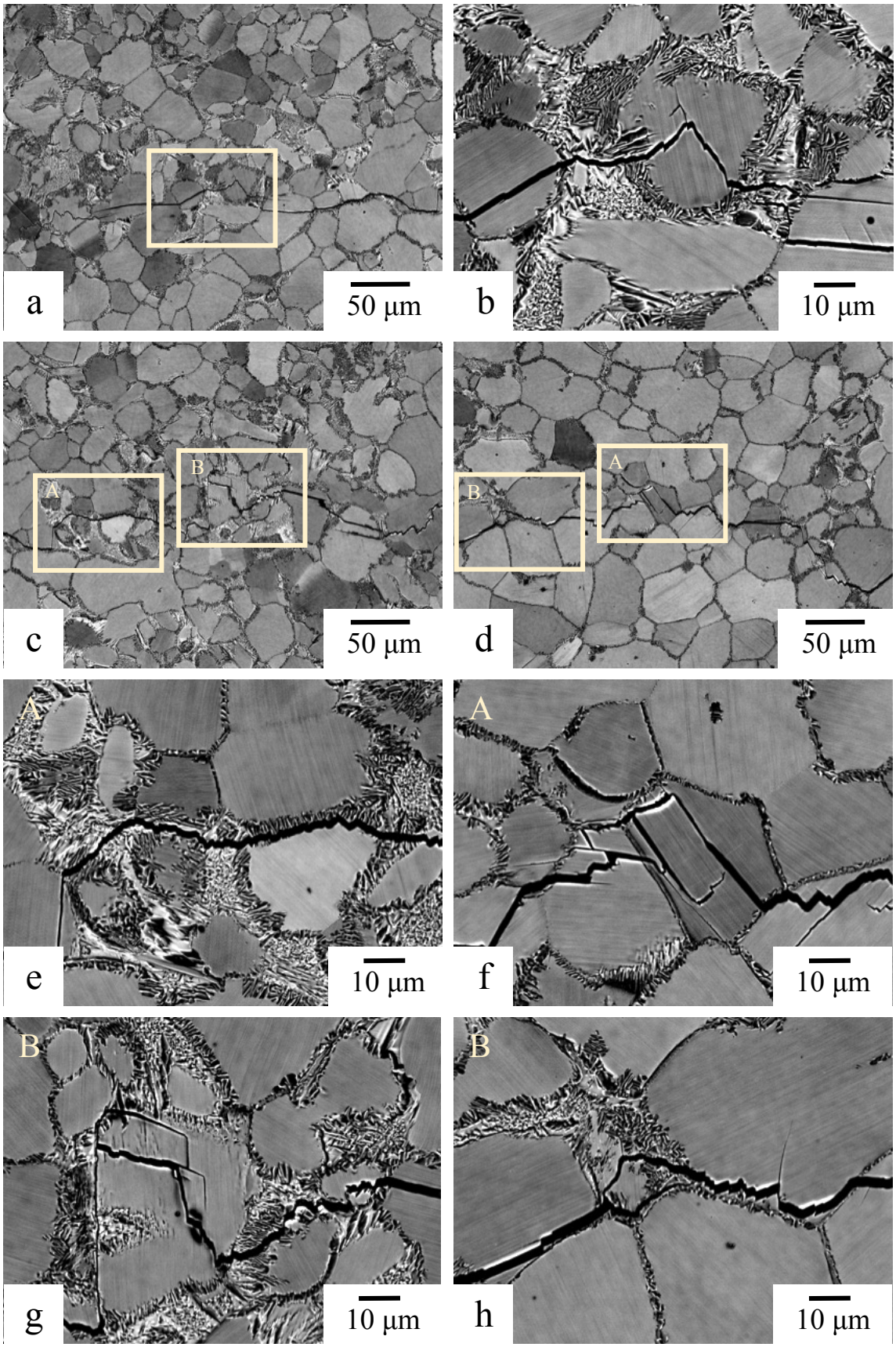

Fig. 4-25. SEM images of crack propagation pathway in NCT microstructure (42-8V alloy).

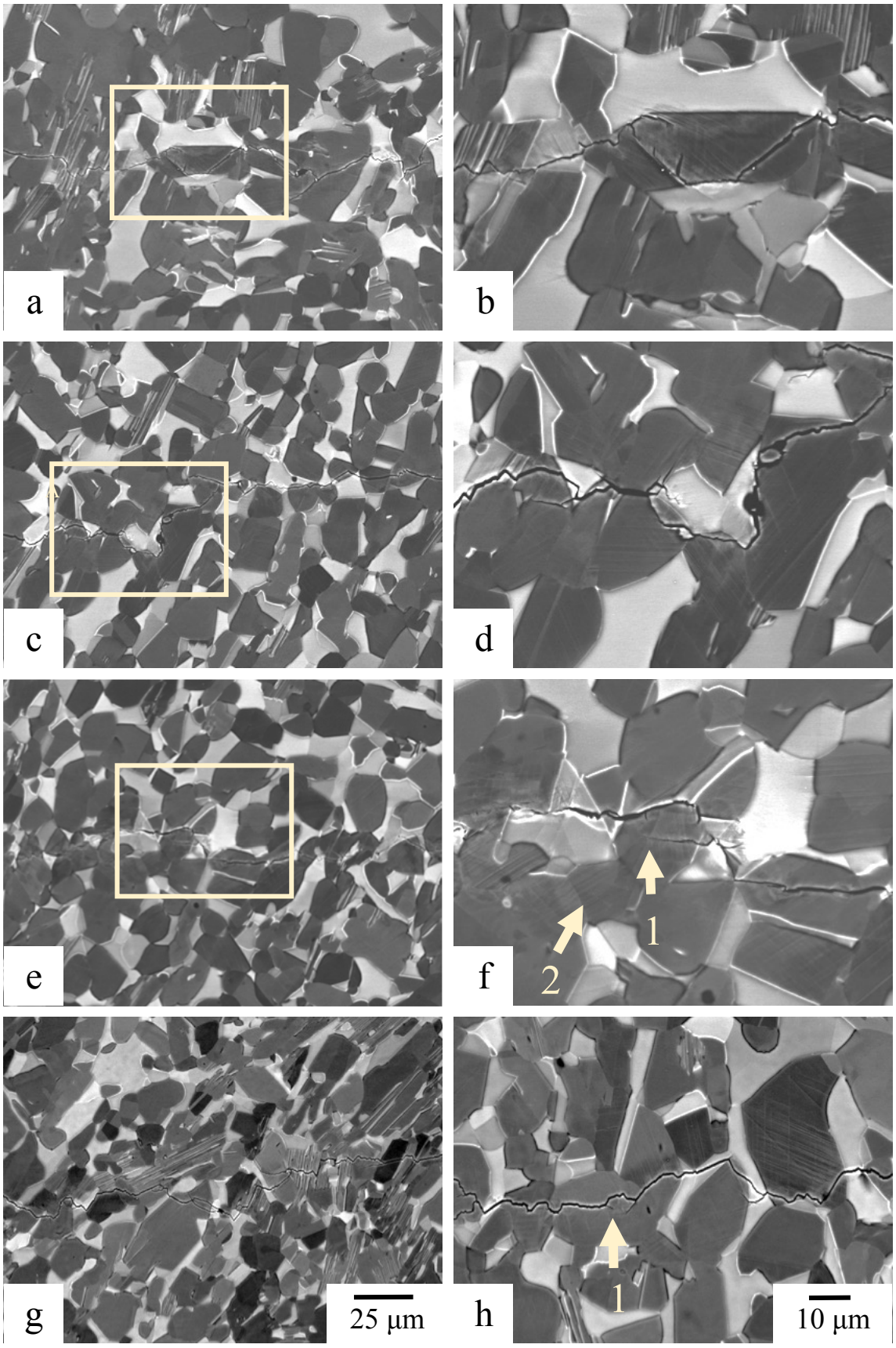

Fig. 4-26. SEM images of crack propagation pathway in NGDP microstructure (43-4-5 alloy). Arrows indicate (1) secondary cracks and (2) deformation of γ grains.

Due to the low fraction of β/γ duplex at the grains boundary, crack mainly propagated through α_2/γ lamellar grains in NL microstructure. **Figure 4-22** shows many secondary cracks and crack deviations. Crack deviation occur when the crack arrests at a strong point and cannot propagates forward anymore. Then, the crack growth in a different direction. If the crack cannot find an easy direction, a secondary crack appears in the crack wake causing sometimes bridging ligament effects. Bridging ligaments could have either short range, usually within one grains (**Fig. 4-22 (e)**) or long range, more a colonies grain of distance (**Fig. 4-22 (a)**). The observation of the tip of the different cracks (secondary, bridges…) shows that the crack stopped preferentially at the β/γ duplex region (**Fig. 4-22 (g, h)**).

In the Lamellar Triplex microstructure and Globular Triplex, the crack growth mechanisms are similar to NL specimens. Nevertheless, the β/γ regions at the grain boundaries are thicker and so, allow the crack to deviate slightly between two colonies grains (**Fig. 4-23 (b, h)**). In the bridging regions, some particles removed from the specimen as indicated by arrows on **Fig. 4-24 (f, h)**.

Due to smaller α_2/γ colonies size, many small range ligament are observed in lamellar grains of NCT microstructures (**Fig. 4-25 (d, f)**). Moreover, if the β/γ duplex region is aligned parallel to the crack direction, crack propagates straightly though the γ grains.

Finally, in the NGDP microstructure, the high fraction of β/γ duplex lead to an almost continuous γ-grains region. The crack mainly propagates straight through the γ phase as reported on NCT β/γ region. At higher magnification, small secondary cracks deviation is clearly observed from the main crack as indicated by arrow (1) on **Fig. 4-26**. However, these small cracks never propagate more than 10 μm and stopped in γ-grains or at β/γ grains interface. Furthermore, many line are observed on γ grains as evidences of γ deformation (arrow (2) on **Fig. 4-26**), that will be detailed in discussion part.

(C) In-situ observations

During FCG tests, the crack propagation was monitoring using *in-situ* CCD camera. An example of *in-situ* observation that was performed on Nearly Lamellar microstructure during *K*-decreasing test is shown in **Figure 4-27**. Therefore, it is possible to determine the region where the crack stopped (**Fig. 4-27 (a)**), not only the crack tip or the secondary cracks but also the intermediate stop points. And then, investigate the microstructural features of these regions in detail using electron microscopy (**Fig. 4-27 (b-d)**).

In this part, different examples of *in-situ* observation will be described in order to improve the crack propagation understanding and especially compare the observations with the previous *ex-situ* results. In case of Nearly Globular β/γ Duplex microstructures, due to small grains size, it was not possible to identified the *in-situ* intermediates crack stop points.

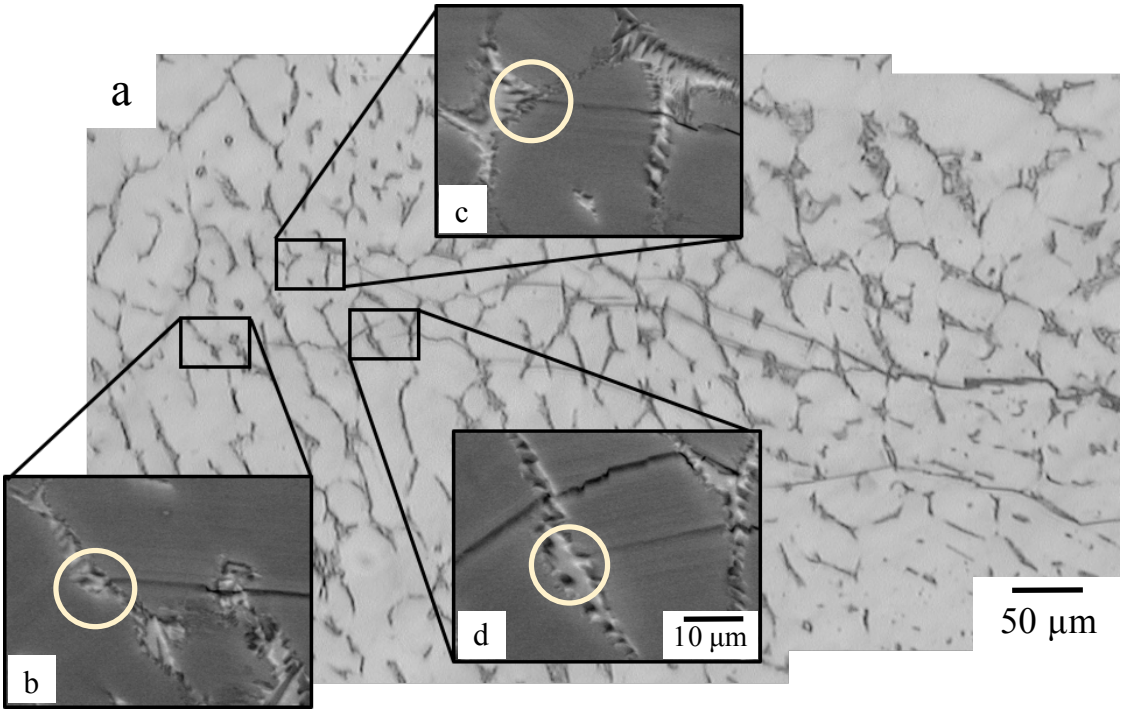

Fig. 4-27. *In-situ* CCD image obtained in (a) NL microstructure, (c, d, d) BSE images corresponding to the region where the cracks stopped during the test.

The *in-situ* observation can also provide information concerning the crack propagation mechanisms. An example of the formation of a long-range crack ligament bridging in Lamellar Triplex microstructure are shown in **Figure 4-28**. Crack ligament bridging causes a crack tip shielding and therefore, enhances the crack propagation resistance. This mechanism could be observed in microstructures which show a large volume fraction of α_2/γ colony grains. Indeed, bridges appear when the crack could not easily find a way to propagate through colony grains and preferentially moves around them. In **Fig. 4-28 (a)**, crack stopped at β/γ duplex region. Despite that is hard to observe, a plastic deformation occurred and is located at least more than one colonies grain in distance far from the crack tip. Then, a microcrack appeared in this region as shown in **Fig. 4-28 (b)**. This new crack is delimited by β/γ duplex structure at both ends and then it continues to growth independently of the main crack. At the both tips of the microcrack, new plastic

deformations take place. Moreover, small particles, originated from DP region, probably γ grains are ejected from the specimen (**Fig. 4-28 (c)**). As long as the crack propagates, the bridging ligament takes part of the load away from the crack tip. Finally, the bridge ruptures and the new crack connects the main crack (**Fig. 4-28 (d)**). The microcrack became the main crack and continued to propagate (**Fig. 4-28 (e)**).

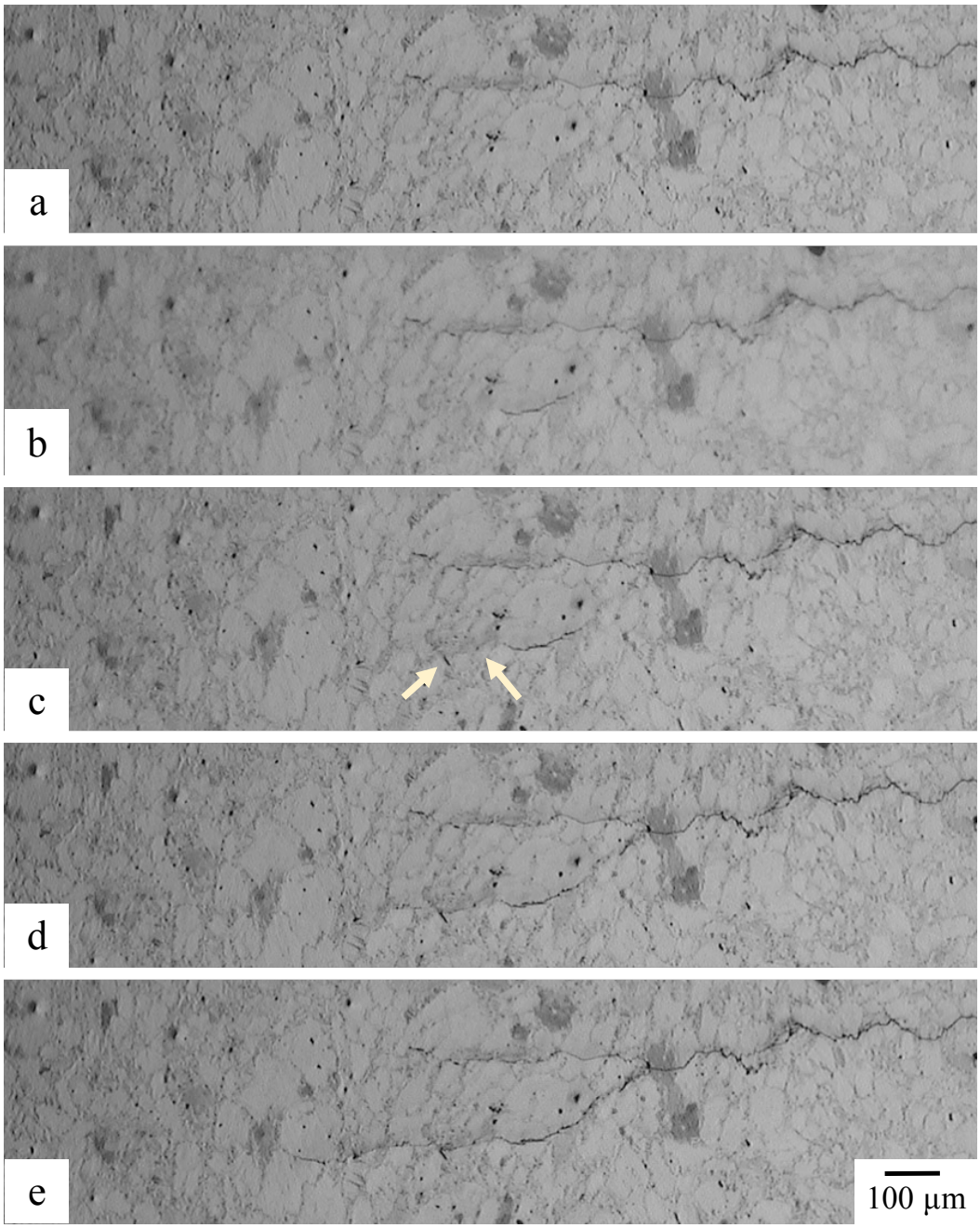

Fig. 4-28. *In-situ* observation of the formation of bridging ligament in Lamellar Triplex microstructure after (a) 6.000, (b) 13.000, (c) 14.000, (d) 15.000 and (e) 28.000 cycles. Arrows represent the TiAl particles expulsion due to alloy deformation.

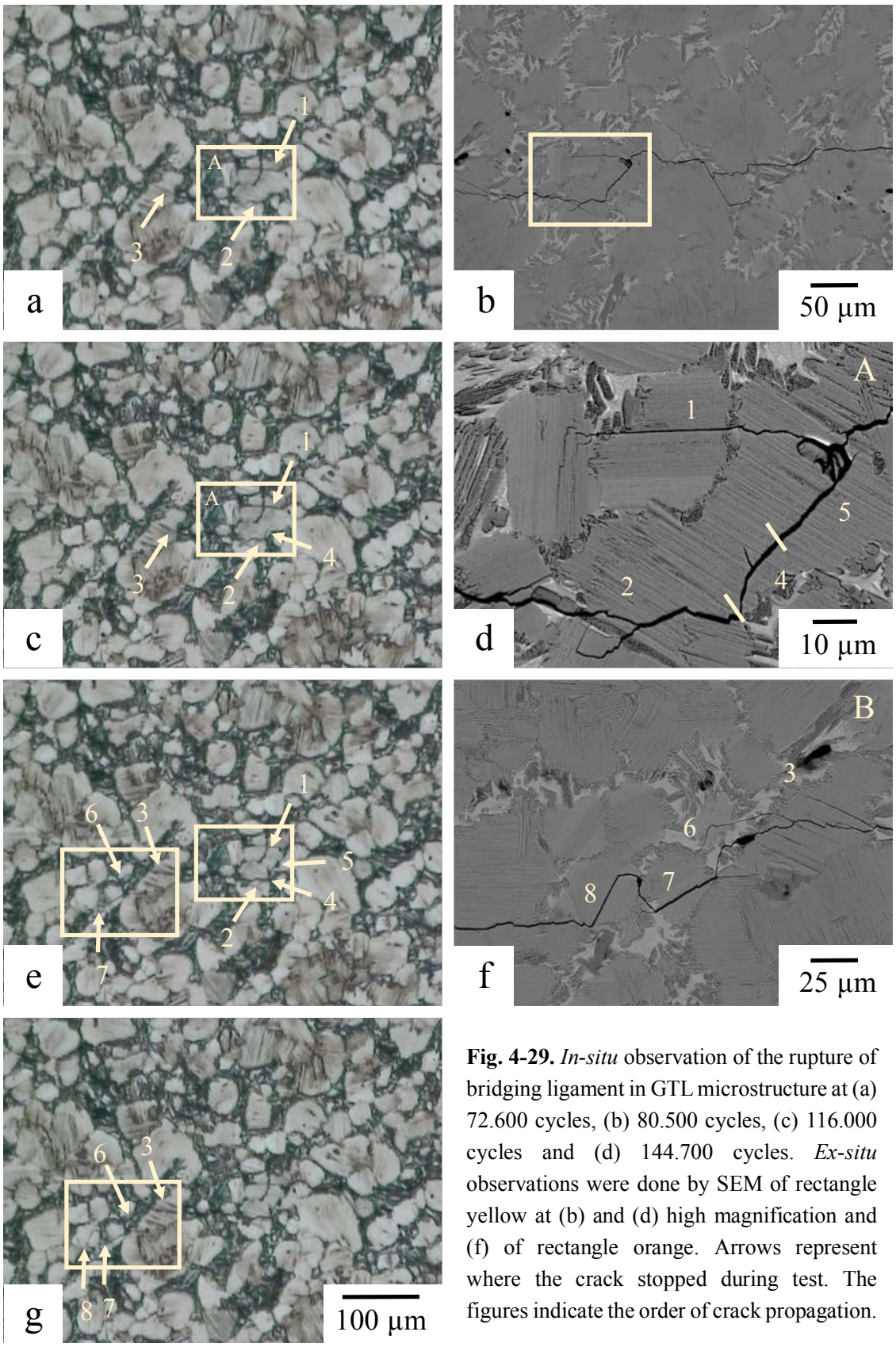

Fig. 4-29. *In-situ* observation of the rupture of bridging ligament in GTL microstructure at (a) 72.600 cycles, (b) 80.500 cycles, (c) 116.000 cycles and (d) 144.700 cycles. *Ex-situ* observations were done by SEM of rectangle yellow at (b) and (d) high magnification and (f) of rectangle orange. Arrows represent where the crack stopped during test. The figures indicate the order of crack propagation.

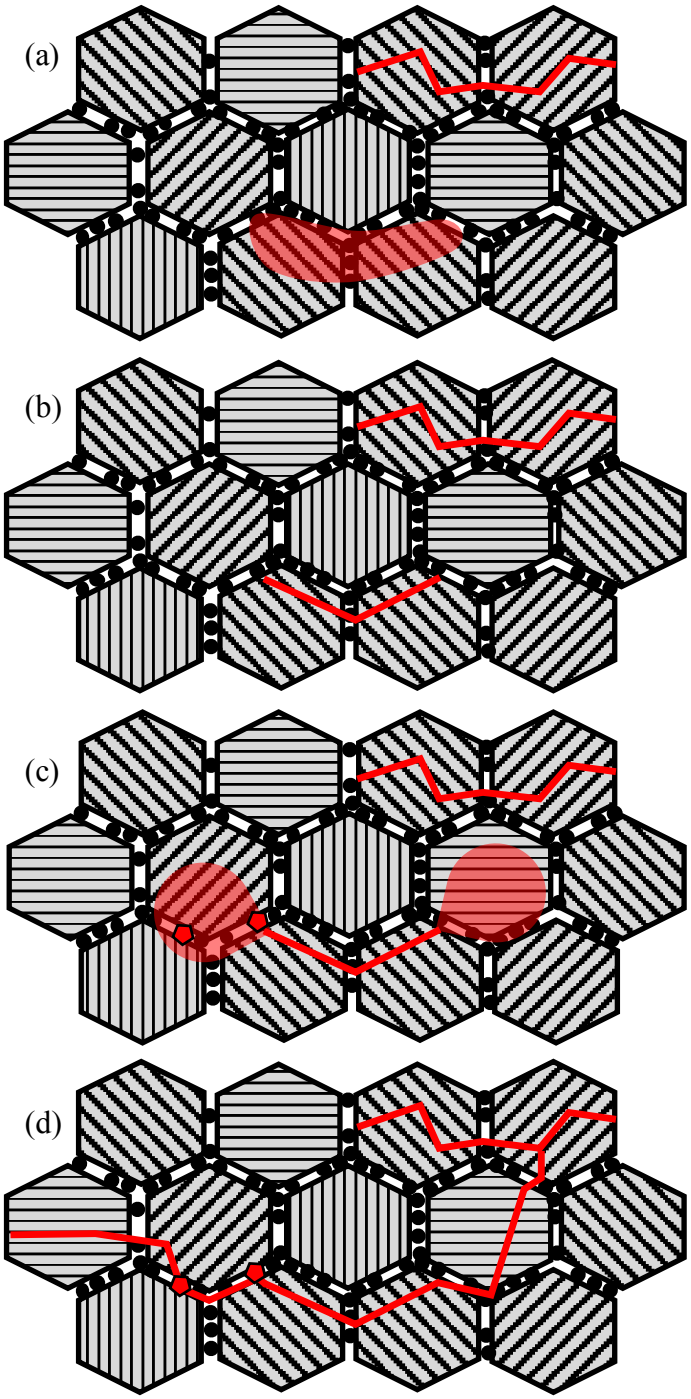

Fig. 4-30. Schematic illustration of the long-range bridging mechanism observed in microstructure containing β/γ duplex at grain boundaries with (a) crack stop at DP region and deformation occurred far from the tip, (b) formation of new crack, (c) plastic deformation at the ends of the new crack and expulsion of particles and (d) rupture of the bridging ligament.

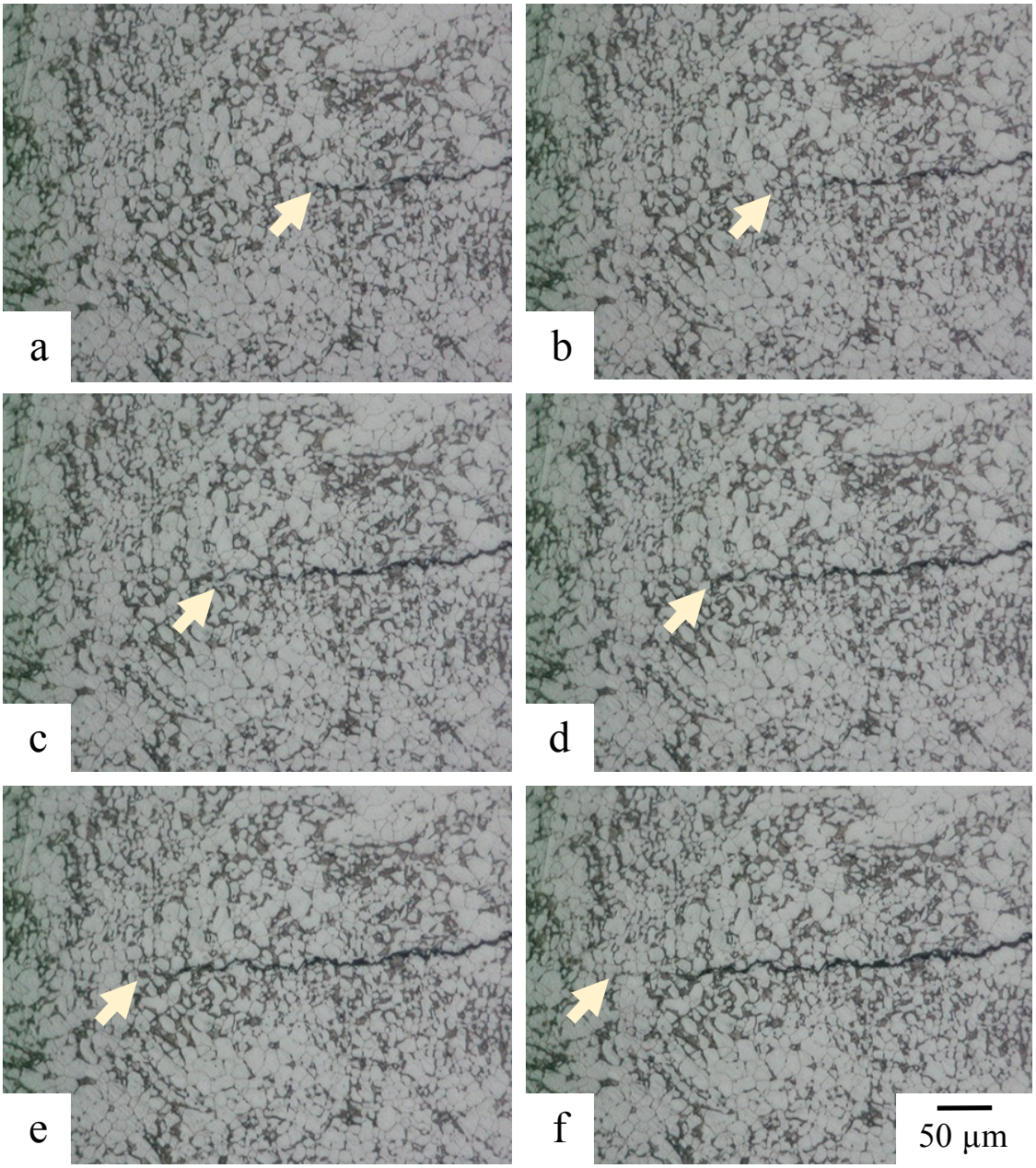

Fig. 4-31. *In-situ* observation of crack propagation in NCT specimen during Paris regime at (a) 1.066.000 cycles, (b) 1.081.000 cycles, (c) 1.100.000 cycles, (d) 1.105.000 cycles, (e) 1.116.000 cycles and (f) 1.123.000 cycles.

A second example of bridging ligament on globular triplex microstructure is given in **Figure 4-29**. The *in-situ* observations were coupled with *ex-situ* SEM in order to rebuilt the crack propagation process given by figures. As observed in **Fig. 4-29 (a)**, the microcrack already appeared. However, the bridge rupture in two times thought translamellar propagation between **Fig. 4-29 (a) and (c)** and not in one step as could be supposed. Furthermore, the particle expulsed came from a lamellar grain. Following the

bridge, the intermediate stop points of the crack, indicated by arrows 6, 7 and 8, have been identify as β/γ duplex. Based on the two previous examples, a schematic illustration of the long-range bridging mechanism is shown in **Figure 4-30**.

Last example of *in-situ* crack propagation of Near γ Cellular Triplex is shown in **Figure 4-31**. NCT microstructures is characterize by smaller colony grains than NL or LTL microstructures and so, the crack deviation is less important. The observations show that crack propagates thought the colonies and always arrest in DP region which reinforced the previous observations.

Therefore, the microstructures consisting of colonies surrounded by β/γ duplex (NL, LTL, GTL and NCT) show similar crack pathway. Regardless the α_2/γ colonies orientation, the *in-situ* as the *ex-situ* observations corroborate that the crack mainly trapped at β/γ duplex areas and thus, confirms that β/γ duplex microstructure could be effective in crack propagation resistance when it decorates the colony boundaries.

(D) Difference between surface and bulk propagation

The CT notched specimens are subjected to tensile load, however, due to the large CT specimen thickness, the contraction due to the Poisson coefficient in the thickness direction is not free around the crack tip. Thus, the deformation of the bulk is restricted by the surface of the specimen, resulting a crack propagation under plane strain condition. Therefore, some difference could exist between the surface and the bulk crack propagation. This section will be briefly clarified this point.

Figure 4-32 shows the difference between surface and bulk propagation of NL and NCT microstructures. The crack length was measured by OM and does not shown significant different between the bulk and the surface which indicate that the crack propagates linearly between the two side of the specimens. The crack pathway under Paris regime is comparable between bulk and surface with many secondary crack of cracks deviation in both microstructures. Moreover, the crack at the fatigue threshold in bulk stopped also mainly in DP region as reported for surface observation. Thus, the observations, results and discussion based on surface analysis apply also to the bulk behavior.

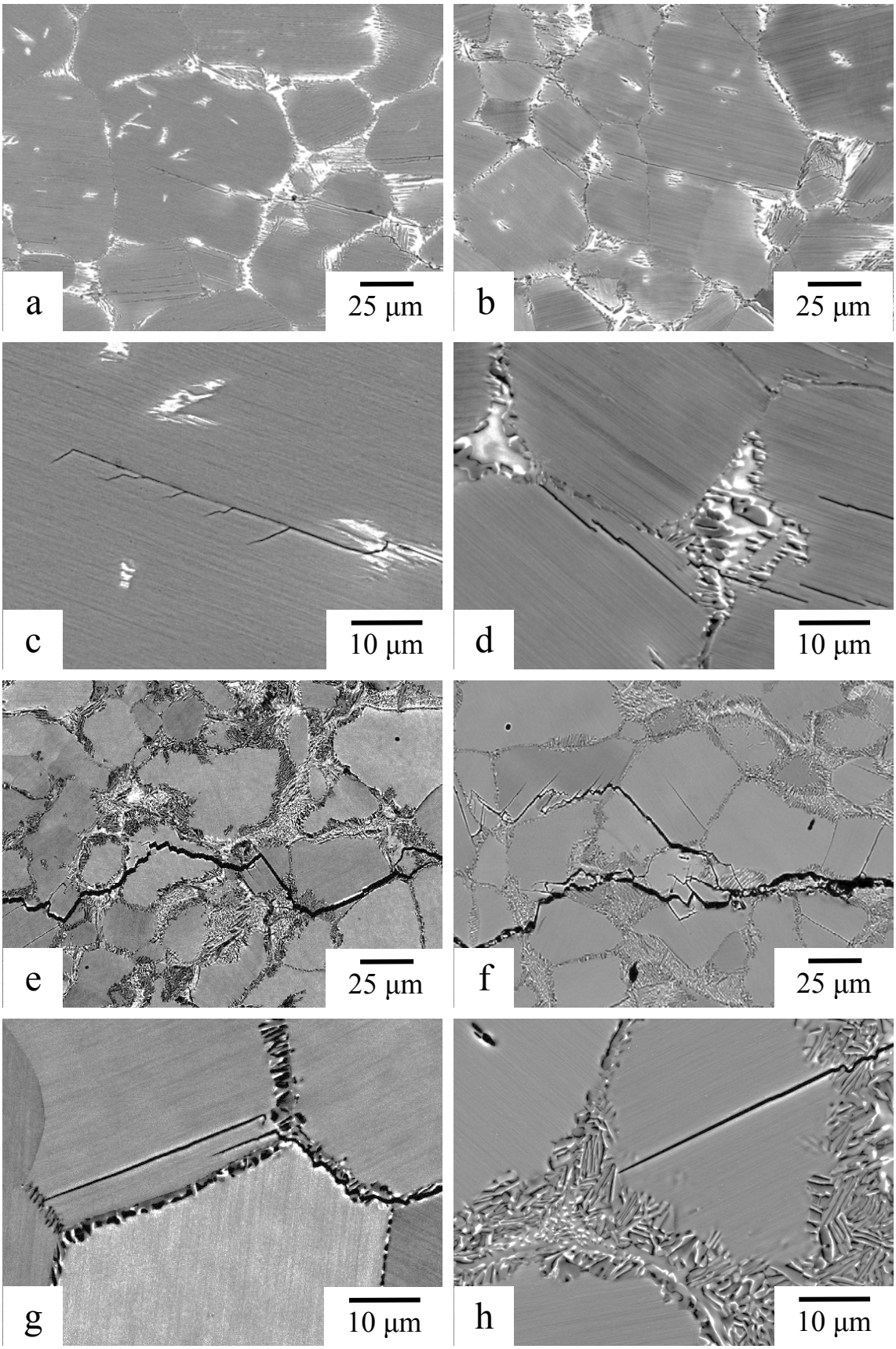

Fig. 4-32. Difference between surface (left side) and bulk (right side) crack propagation in (a-d) NL microstructure and (e-h) NCT microstructures.

4.4.3 Fracture surface

The differences between the microstructure fracture surfaces are shown in **Figure 4-33**. The notch is located on the right side and the crack propagated from the right to the left of the CT specimen. During the introduction of the precrack, especially before to find the optimal parameter conditions, the initial K_{max} of some samples was set too high. It resulted a high crack growth rate and difference between OM and DCDP measurement as explained in experiment procedure section but it did not affect the FCG tests. This explains why in **Fig. 4-33**, the precrack of Nearly Lamellar and Lamellar Triplex microstructures is larger than expected.

The examined fracture surfaces at low magnification in **Fig. 4-33** revealed that NL show the roughest surface. The Nearly Globular β/γ Duplex fracture surface is almost flat whereas LTL and NCT microstructure present an intermediate roughness which are in concordance with crack propagation pathway observation. The roughness is directly correlated with the grains size; more the grains size is smaller, more the fracture surface becomes smooth. The crack occurred during *K*-decreasing test propagated less than 2 mm before reaches the stress intensity threshold. The influence of ΔK on the fractographic features is small. However, it should be noticed that in low ΔK region the roughness is lower than in high ΔK or overload region in all microstructures.

Before fracture, the crack propagation occurred during *K*-increasing in NL is more longer than in LTL microstructure which confirms the higher K_{max} of NL microstructure compared to LTL. Fracture crack size, from the beginning of the notch until the overload region, is almost same in both specimens due to either the remained section could no longer carry on the load or the K_{max} become close to the fracture toughness. It should be noted that some LTL specimen present some pores at the fracture surface but it did not seem to affect the FCG behavior after repeating tests. On the other hand, the NGDP and NCT specimens fracture occurs only after few millimeter. The maximum stress intensity K_{max} at overload probably approaches the fracture toughness values. However, its value was twice higher in case of NCT compared to NGDP.

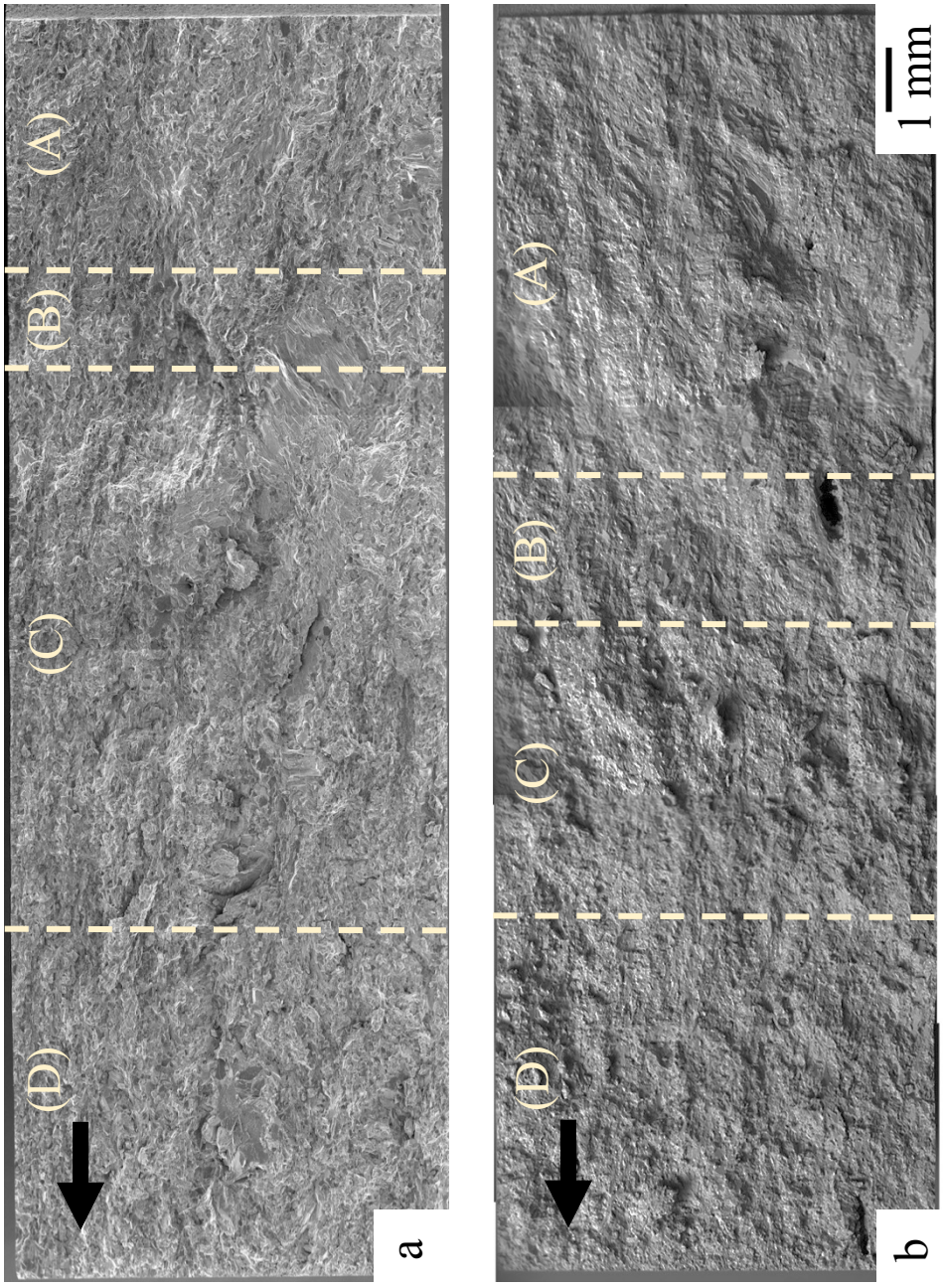

Fig. 4-33. SE images of fracture surface of CT specimen for (a) NL and (b) LTL microstructures. From right to left (A) precrack, (B) *K*-decreasing test, (C) *K*-increasing test and (D) overload region. The vertical line at the right side of the image correspond to the end of the notch and the crack propagated from the right to the left side as indicated by the arrows.

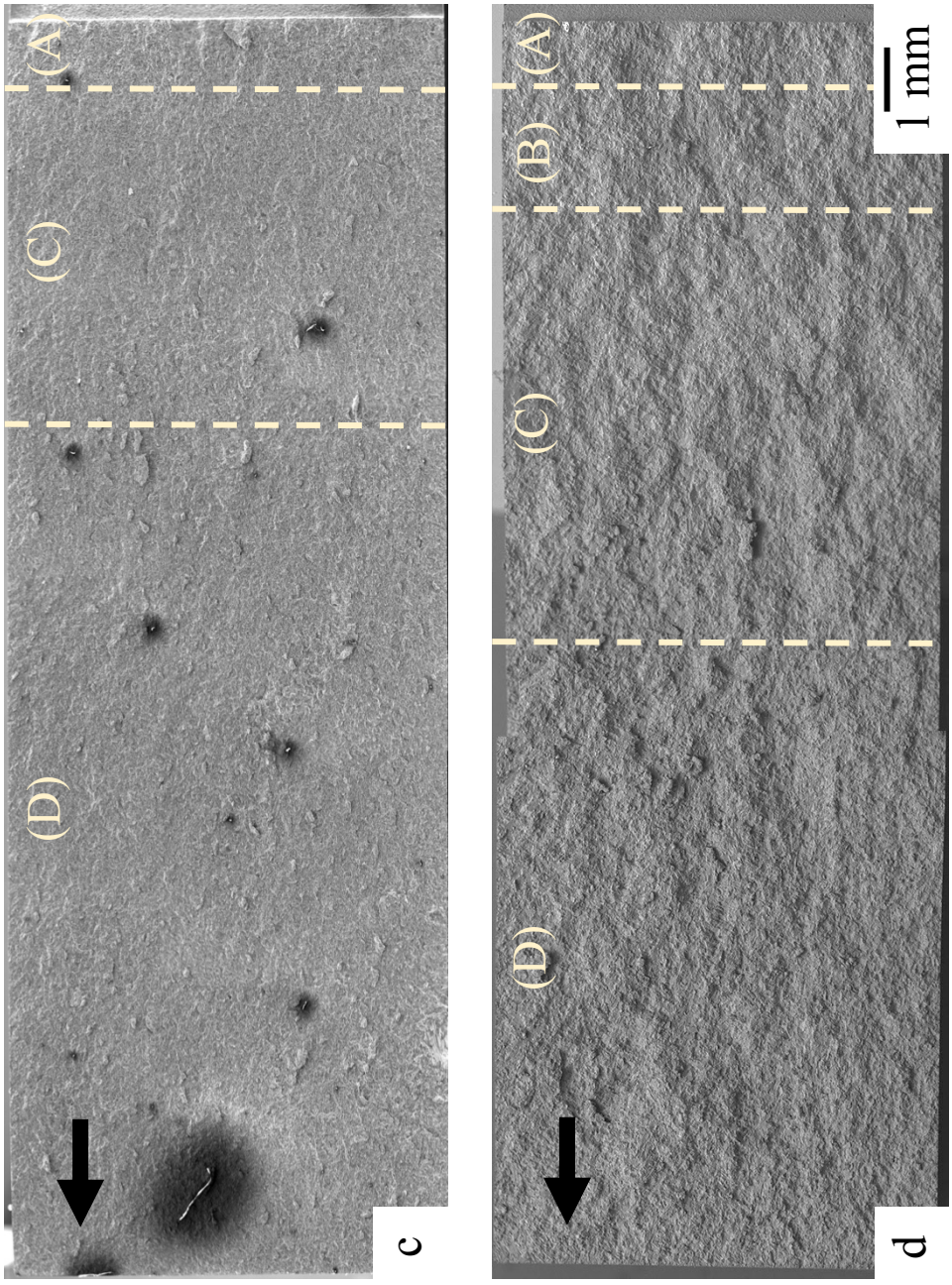

Fig. 4-33. (continued) SE images of fracture surface of CT specimen of (c) NGDP and (d) NCT microstructures. From right to left (A) precrack, (B) *K*-decreasing test, (C) *K*-increasing test and (D) overload region. The vertical line at the right side of the image correspond to the end of the notch and the crack propagated from the right to the left side as indicated by the arrows.

Typical fatigue fractographs of the different microstructures at higher magnification in the *K*-decreasing region, the *K*-increasing region and the overload region are shown in **Figure 4-34 to 4-36**, respectively. Crack propagated from the right to the left. All microstructures show mainly brittle faceted fracture with small amount of plastic deformation. The examination of the flat facets in the Paris law regime fail to reveal fatigue striations in all microstructures. The different fracture mechanisms such as intergranular (along the boundaries) and transgranular modes are observed. Transgranular mode can be sub-divided into interlamellar when the fracture is parallel to the lamellae, translamellar when the crack go through to the lamellae, and simple transgranular when it splitting γ or β grains. The fracture mode are indicated by arrows in the different microstructures. The intergranular fracture (arrows 1) and the simple transgranular type (arrows 2) are observed in the four microstructures. Translamellar (arrows 3) and interlamellar (arrows 4) fracture modes are mainly observed in the microstructures with a high α_2/γ colonies volume fraction as NL, LTL and NCT microstructures. In the Paris life region, when the stress intensity ΔK is higher than the fatigue stress intensity threshold ΔK_{th}, it is possible to observe secondary cracks occurred in the specimens (arrow 5). However, these secondary cracks are multiple and larger (few hundred of micrometers) in the case of NL and LTL microstructures, intermediate for NCT and infrequent and relatively small for NGDP, only few micrometers. Microstructures containing colonies show similar fracture surface; with decreasing the stress intensity, fracture surface shows either interlamellar or translamellar fracture depending on the grain orientation. The main difference comes from the higher fraction of intergranular fracture mode occurred in LTL microstructure. It can be easily explained by the thicker β/γ DP region at the colony boundaries compared to NL and NCT microstructures. More the stress intensity increases, more the transgranular cleavage become dominant. In the overload region, intergranular and transgranular modes govern the fracture behavior. Finally, in case of NGDP microstructure, the fracture surface is relatively homogeneous, as observed at lower magnification, and show plastic deformation of γ grains with transgranular fracture and intergranular cleavage along all the different regions.

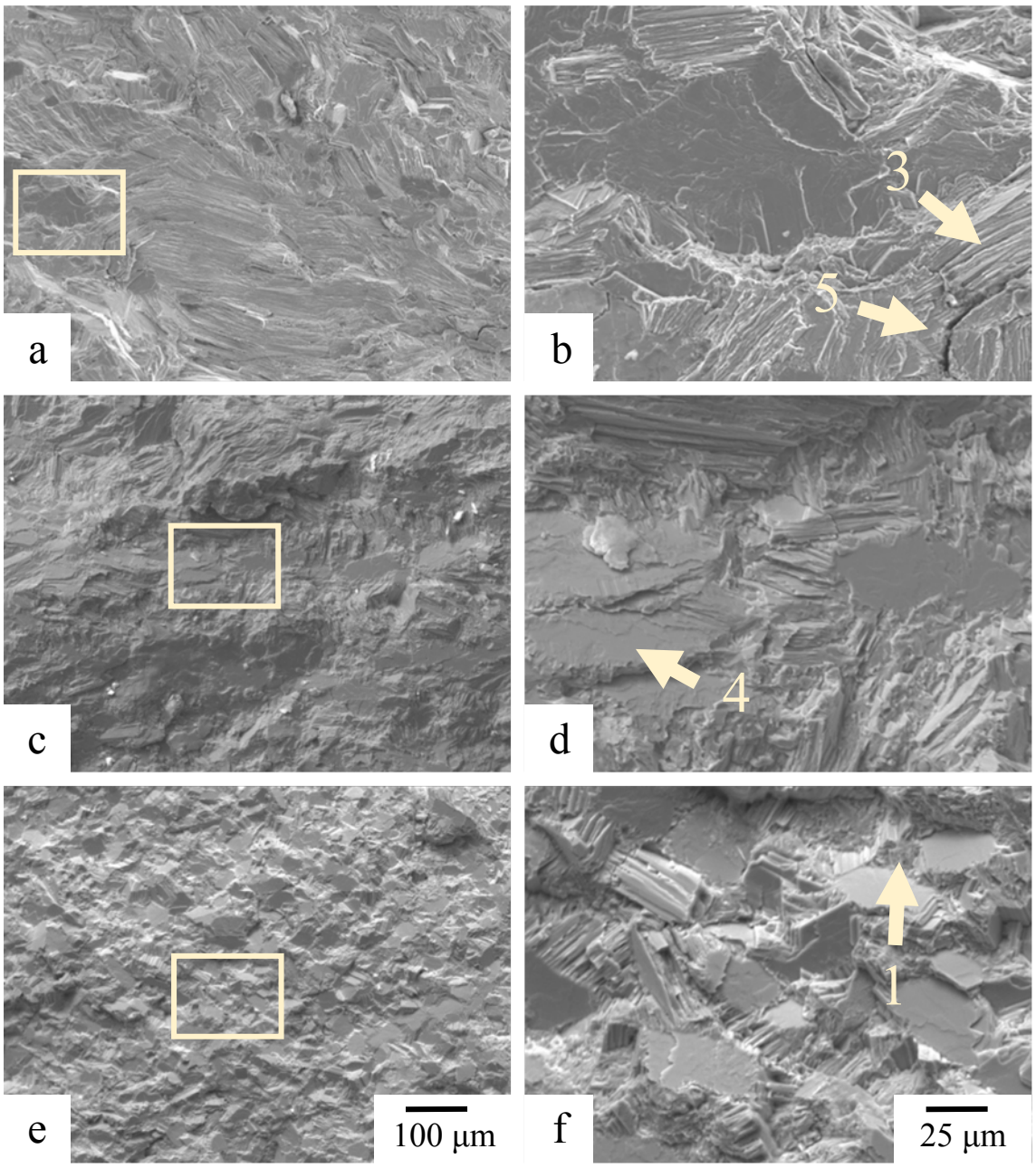

Fig. 4-34. SE images of fracture surface at low stress intensity during *K*-decreasing tests for (a, b) NL, (c, d) LTL and (e, f) NCT microstructures. The crack propagated from the right to the left side. Different fracture modes are marked by arrows (1) interglobular, (2) transglobular, (3) translamellar, (4) interlamellar. (5) correspond to secondary cracks.

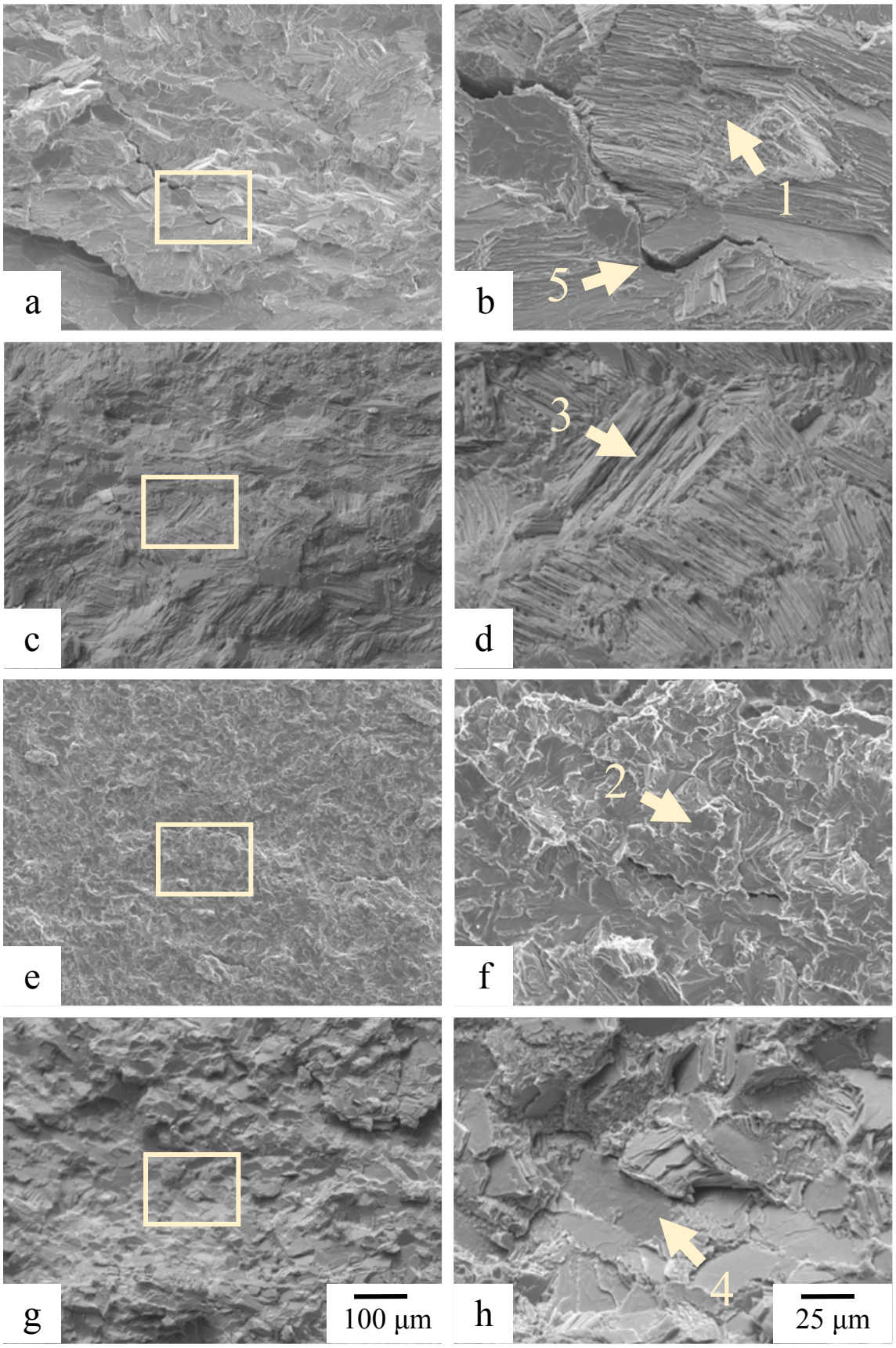

Fig. 4-35. SE images of fracture surface at intermediate stress intensity during *K*-increasing tests for (a, b) NL, (c, d) LTL, (e, f) NGDP and (g, h) NCT microstructures. The crack propagated from the right to the left side. Different fracture modes are marked by arrows (1) interglobular, (2) transglobular, (3) translamellar, (4) interlamellar. (5) correspond to secondary cracks.

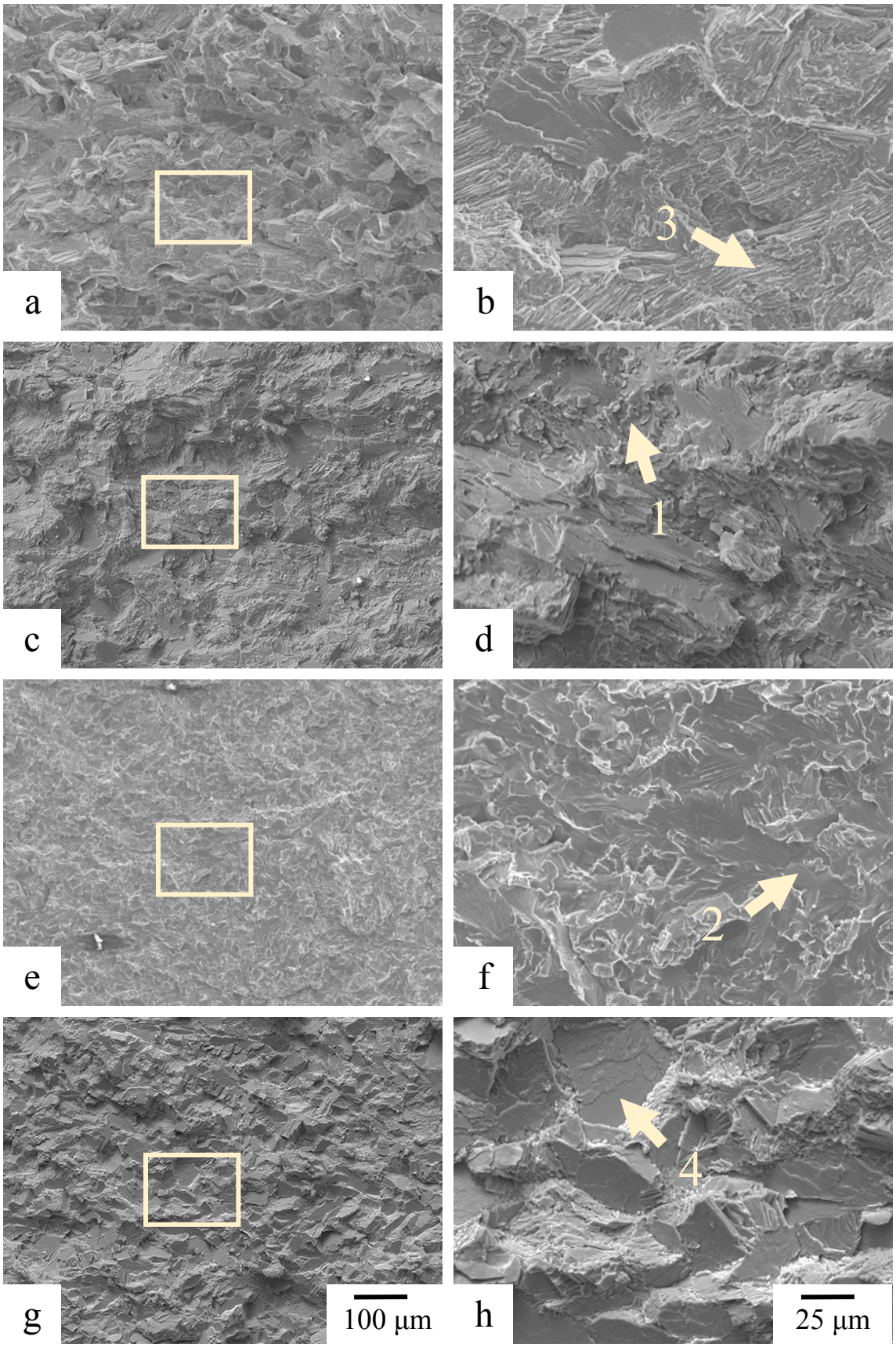

Fig. 4-36. SE images of fracture surface in overload region for (a, b) NL, (c, d) LTL, (e, f) NGDP and (g, h) NCT microstructures. The crack propagated from the right to the left side. Different fracture modes are marked by arrows (1) interglobular, (2) transglobular, (3) translamellar, (4) interlamellar. (5) correspond to secondary cracks.

4.4 Discussion

4.4.1 Comparison of the FCG curves

The fatigue crack growth curves of the investigated microstructures present completely different behaviors. Increase the volume fraction of β/γ duplex at the grain boundaries leads to decrease the threshold intensity, increase Paris slope and decrease the maximum stress intensity at the rupture as shown in **Figure 4-37 to 4-39**, respectively.

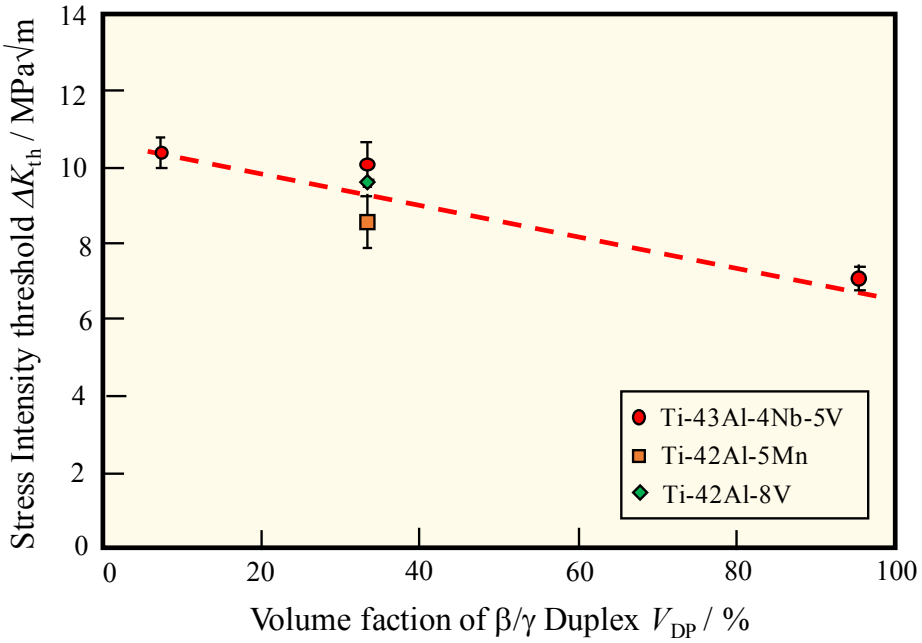

Fig. 4-37. Effect of β and γ phases on the stress intensity threshold.

Because as-forged microstructure was not homogeneous and so, affects the FCG behavior, the data of this microstructure was not added. Stress intensity threshold ΔK_{th} values between 10.4 MPa$\sqrt{m}$ in NL (V_{DP} = 7%) and 7.1 MPa$\sqrt{m}$ in NGDP-4345 (V_{DP} = 96%) were observed. Paris slopes m vary from 6.1 in NCT to 10.5 in NGDP-Mn and K_{max} change from 27.1 MPa$\sqrt{m}$ in NL to 11.9 MPa$\sqrt{m}$ NGDP-4345. The fatigue crack growth behavior can be divided in three categories. First, the Nearly Globular β/γ Duplex microstructures which show a low stress intensity threshold and a steep Paris slope. Second, the Nearly Lamellar, the Lamellar Triplex and the Near γ Cellular Triplex microstructures which present higher stress intensity threshold and gentler Paris slope. Finally, the Globular triplex microstructure shows an intermediate ΔK_{th} but a low Paris slope. Moreover, the slope of the two last categories appeared as stepwise. The major difference between these two categories and NGDP microstructures is the volume fraction

of α_2/γ lamellar colonies. Volume fraction of colonies in NL, LTL, GTL and NCT microstructures is almost equal but it drops drastically in NGDP. Furthermore, the local microstructural inhomogeneity is more important in microstructures containing colony grains and explains the presence of steps in the Paris slope in NL and LTL microstructures.

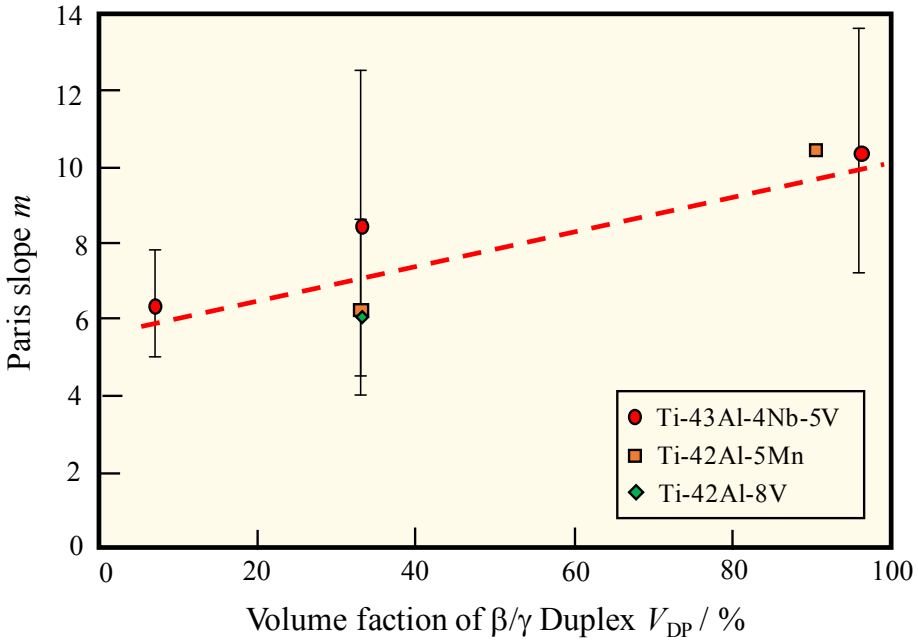

Fig. 4-38. Effect of β and γ phases on the Paris slope

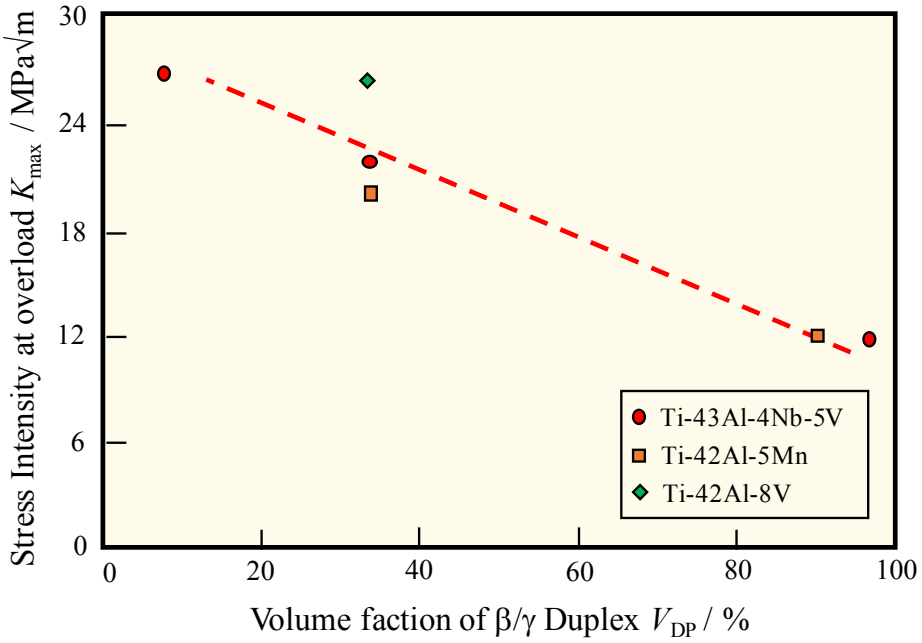

Fig. 4-39. Effect of β and γ phases on the maximum stress intensity at overload.

Therefore, the local Paris slope have deeply investigated in NL and LTL microstructures. Their values have been measured and summarized along with NGDP results in **Table 4-9**. There can be represented as high Paris slope m^+, low Paris slope m^-, and average Paris slope m. While the average Paris slope m increased with the increase of the volume fraction of β/γ duplex, the local Paris slope change depending on the microstructure from Nearly Lamellar to Lamellar Triplex. The low Paris slopes m^- decreased from 2.0 to 0.8 but in opposite the high Paris slope m^+ increased from 13.6 to 20.2.

Table 4-9. Difference in local Paris slope in NL and LTL microstructure.

Microstructure	V_{DP} / %	m^-	m	m^+
Nearly Lamellar	7	2.0	6.5	13.6
Lamellar Triplex	32	0.8	8.5	20.2
Nearly Globular β/γ Duplex	96	–	10.4	–

The observation of the fracture surfaces before and after a low Paris slope can provided some complementary information as shown in **Figure 4-40** during *K*-increasing test in Lamellar Triplex microstructure. Large region of cleavage fracture of γ-grains or intergranular fracture at the grain boundaries were observed in the m^+ region and were indicated by arrows **Fig. 4-40 (a, c)**. These fracture mechanisms are preferentially found in NGDP microstructure that shows the highest Paris slope. In the other hand, the fraction of these mechanisms is lower in low Paris slope region (**Fig. 4-40 (b)**) that shows mainly translamellar and transgranular fracture depending of the α_2/γ colonies orientation.

Thus, the low Paris slopes m^- correspond to a region where the crack propagates preferentially through α_2/γ colony grains whereas the high Paris slopes m^+ correspond to a region where the crack propagates in colony grains and through the grains boundaries. The rise of the high Paris slope m^+ between NL and LTL microstructure could be explained by the increase of β/γ duplex fraction at the grains boundaries, especially by the larger γ grains that promote crack growth through cleavages. The reason for the reduction of the low Paris slope m^- with increasing the volume fraction of β/γ duplex V_{DP} could be explained by the reduction of α_2/γ colony grains size as will be detailed later.

Changing the morphology of DP region from large globular γ grains (GTL) to plate (LTL) or small γ grains (NCT) increase the fatigue threshold and the K_{max} at the rupture. However, whereas LTL microstructure shows higher, but similar, stress intensity threshold than NCT, Near γ Cellular Triplex present significantly higher maximum stress

intensity at the rupture. This could be explained by the ratio β/γ which is more important in LTL microstructure.

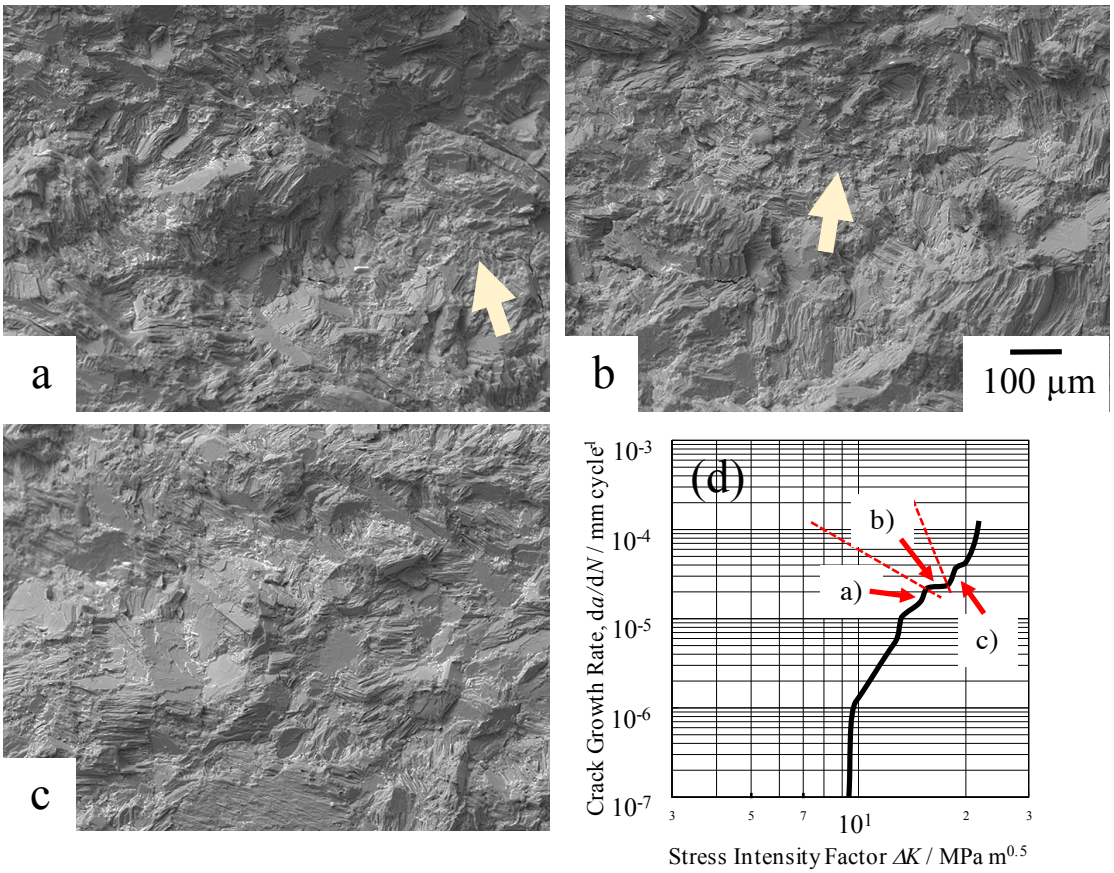

Fig. 4-40. Fracture surface of LTL microstructure in the region (a) before a low Paris slope, (b) at a low Paris slope and (c) after a low Paris slope, associated with (d) the corresponding fatigue crack growth curve. Arrows indicate fracture at β/γ DP region.

It is interesting that despite the significant difference in β/γ volume fraction (more than 20 %), the difference between stress intensity threshold can be very small, e. g. only 0.3 MPa√m between NL and LTL microstructure whereas NGDP microstructure, which consist almost of β and γ grain, present large difference of around 3.0 MPa$\sqrt{m}$. Moreover, it should be noticed that microstructures with the same in β/γ duplex volume fraction but different morphologies present also large differences of around 2.5 MPa$\sqrt{m}$. The reason probably comes from how much β and γ phases interact together and affect the fatigue crack growth propagation as it will be discussed in the following sections.

4.4.2 Fatigue crack growth mechanisms

During FCG tests, the crack propagation is determined by presence of a crack driving force which is defined by the stress intensity factor range ΔK. The resistance of the microstructure opposes to this driving fatigue crack growth force. Therefore, it is possible to restrain the crack advance by toughening the materials though solution strengthening (change the alloy composition) or microstructural modification. The toughening mechanism are divided into intrinsic and extrinsic mechanisms. Intrinsic mechanisms depend of the inherent microstructural resistance (atoms bonding strength, ductility) whereas extrinsic mechanisms reduce locally the fatigue crack propagation force by mechanical, microstructural or environmental factors [18].

It has been shown that in TiAl alloys, crack closure mechanisms can significantly affect the stress intensity ΔK such as plasticity-induced crack closure, roughness-induced crack close, transformation-induced crack closure or oxide-induced crack closure. By closely studying the crack propagation pathways both *in-situ* and *ex-situ* and the fracture surfaces, the fatigue crack growth resistance mechanisms and the fatigue reducing mechanisms were identified.

For all microstructures, the cleavage fracture of grains at the crack tip promote the crack growth. It is strongly dependent of the nature of each phase. β-Ti phase shows the highest fracture toughness with a value of about 1300 MPa but is also very brittle phase at room temperature [19] whereas γ-TiAl phase shows a low fracture toughness, about 450 MPa but a better deformability than α_2 or β phases [20].

The ability of γ phase to deform lead to the appearance during the crack propagation of small lines on the γ grains surface near the crack pathway. **Figure 4-41** shows an example of the deformation occurred in γ grains. These step line have been observed mainly in NDGP and GTL microstructures due to the large size of γ grains in these microstructures but are also present in the others microstructures These steps have been identified as small twins [21]. It has been reported that these mechanical twinning reduces the stresses at the crack tip and consequently delay the cleavage fracture [22].

It should be noted that, deformations were also observed in colony grains as reported in **Fig. 4-26**. The deformation field is strongly related to the plastic affected area and it will be discussed in the following part. The deformation of the colonies and the γ grains by mechanical twinning lead to the formation of microcracks. When a microcrack is formed in front of the crack tip (see **Fig. 4-29 (a)**) it causes an increase of the stresses of

the crack tip and, therefore, negatively affects fatigue resistance. However, the microcracks take a part of the load when they appeared in the crack wake.

All microstructures show crack ligament bridging and crack deflection. However, these mechanisms were more pronounced in microstructures containing colonies compare to NGDP. A bridge appears when the crack could not find an easy way to propagate through a grain, mainly colonies grains, and therefore, moves around them to find a more favorably orientated one. Two family of bridging were observed: short-range and long-range bridges. In case of short-range bridge, the dimension of ligament is limited within the grain size whereas long-range bridging ligament measured few grains dimension. Short-range bridges have been observed in all microstructures, including NGDP whereas long-range bridging appeared for microstructures containing colonies and, thus, explained why NGDP crack pathway is relatively straight in these samples. Indeed long-crack bridges can explain the higher roughness of the fracture surface as seen previously. Finally, these bridges rupture by shear or cleavage. As long as the crack flanks are connected by the crack ligament, a part of the load is take away from the crack tip.

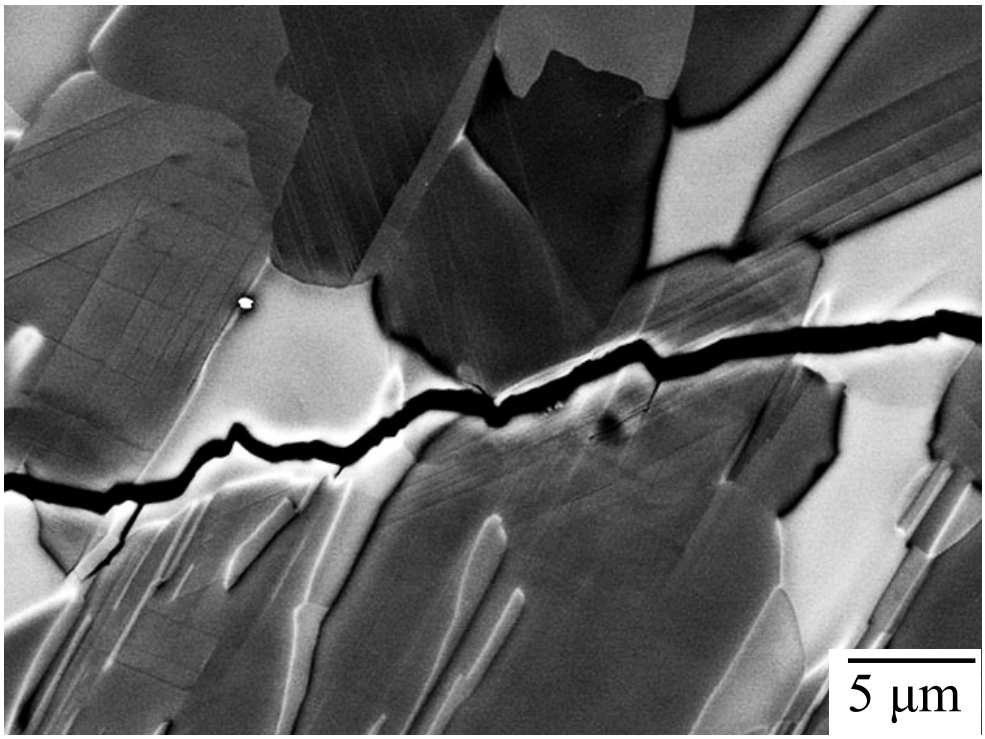

Fig. 4-41. Twinning occurred in Nearly Globular β/γ Duplex microstructure near the crack pathway.

4.4.3 Effect of β/γ duplex on fatigue crack growth behavior

(A) On stress intensity threshold ΔK_{th}

The investigated microstructures in this study consist of a certain volume fraction (V_{DP}) and morphology of β grains and γ grains decorating the α_2/γ colony grains boundaries. It has been seen, both *in-situ* during FCG tests and *ex-situ* by SEM, that the crack preferentially arrest in β/γ DP region, showing the high fatigue resistance of this region. DP region consist of β and γ grains along the grains boundaries decorated the colony grains.

It has been seen previously that the γ phase shows a low fracture stress, about 450 MPa but a high deformability. Despite the deformation of γ grains, resulting with a blunting of the crack tip, reduce the stresses at the crack tip, the titanium aluminides alloys with a duplex microstructure (equiaxed γ and α_2/γ colonies) that have a high-volume fraction of equiaxed γ grains usually show lower fatigue properties [14]. Indeed, γ grains can easily fractured by cleavage due to their low toughness. This crack propagation mechanism is mainly observed in NGDP, as observed on fractographs, and somehow in the others microstructures. This could be attributed the high fraction of γ grains in NGDP microstructure (more than 75%) which lead to the formation of an almost continuous γ phase. In fact, by observing the crack pathway of this microstructure, the crack propagates mainly through transgranular γ grains or at β/γ grain boundaries but rarely in β phase. It is probably the reason why the fatigue crack growth behavior of NGDP microstructure e.g., the stress intensity threshold, is close to the results find for γ-single phase alloys. The small difference of the fatigue crack behavior comes principally from the presence of β phase (V_β = 20%) and somewhat of the remain colonies grains. The important point is when the total γ volume fraction becomes high, the crack propagation behavior is mainly controlled by the continuous γ phase.

On the other hand, the β phase shows the opposite behavior compared to the γ phase with a very high fracture toughness. Although in the investigated microstructures β phase is always associates with γ phase, it is possible to estimate the effect of this phase. Indeed, the work conducted by Leitner et al. [23] on fracture and *R*-curve behavior in TNM alloy shown that the existence of continuous β phase seems to reduce, even lightly, the fracture toughness of the specimens. Due to the brittleness of β phase, when the crack propagation initiates, the crack grows fast until collide the nearest obstacle. In case of continuous β phase at the grain boundaries, the crack propagates and avoid the α_2/γ colonies. The

evidence which can support this observation have been found during crack propagation tests. Indeed, in all microstructures and especially in NGDP, when the crack starts to propagate through β phase, it continues until reach the next γ grains or colonies and thus, never trapped within this phase.

The plastically affected region could give an estimation of the effect of ΔK on the crack pathway change regardless the microstructural features and help to understand how β/γ duplex affected the stress intensity threshold. The **monotonic plastic zone** size at the maximum peak stress for plane strain is given by **Equation 4-5** in Ref. [25].

$$r_O = \frac{1}{6\pi}\left[\frac{K_{max}}{\sigma_y}\right]^2 \tag{4-5}$$

Where r_0, σ_y and K are the radius of the plastically affect zone, the maximum stress intensity and the yield stress of the material, respectively. As the minimum load in a cycle is approached, the change in plastic zone leaves a wake plasticity behind the crack tip and therefore, induces residual stresses in the vicinity of the crack. At the minimum load the remained **cyclic plastic zone** is given by the **Equation 4-6** [25]:

$$r_O{}' = \frac{1}{6\pi}\left[\frac{\Delta K}{2\sigma_y}\right]^2 \tag{4-6}$$

Where r_0', σ_y and ΔK are the radius of the plastically affect zone, the stress intensity and the yield stress of the material, respectively. The monotonic and cyclic plastic zone size are illustrated in **Figure 4-42**.

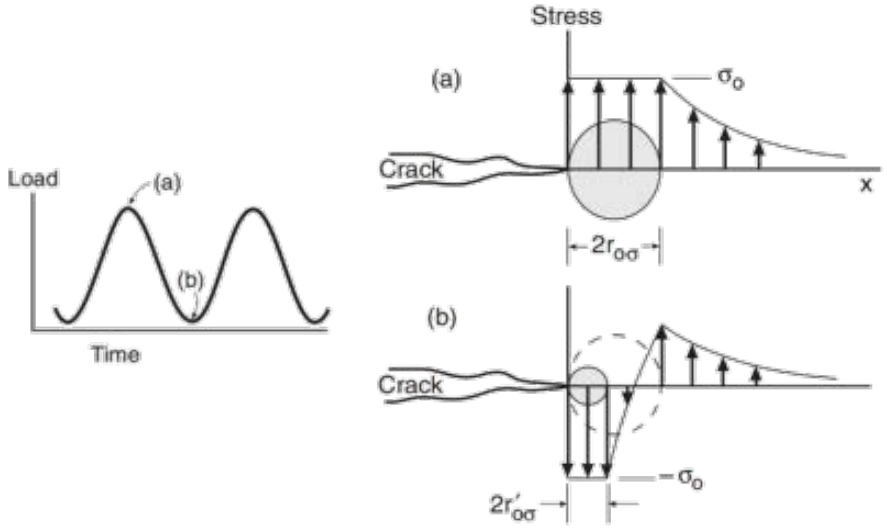

Fig. 4-42. Schematic illustration of (a) monotonic and (b) cyclic plastic zone size [25].

The calculated sizes of the monotonic and cyclic plastic zone area of the different studied microstructures along with the FL results obtained by Dahar *et al.* [7] at the stress intensity threshold assuming the plane strain conditions are given in **Table 4-10** and illustrated in **Figure 4-43**. It can been see the plastic zone size of Fully Lamellar microstructure is considerably smaller than the grain size. The plastic zone size at the fatigue threshold of NL, LTL and NCT microstructures is smaller than the grain size whereas GTL and NGDPs microstructures show a plastic zone at ΔK_{th} equivalent or smaller than the grain size, and, therefore, fracture cleavages occur easily between the grain even at low stress intensity and explain the lower threshold of these microstructures.

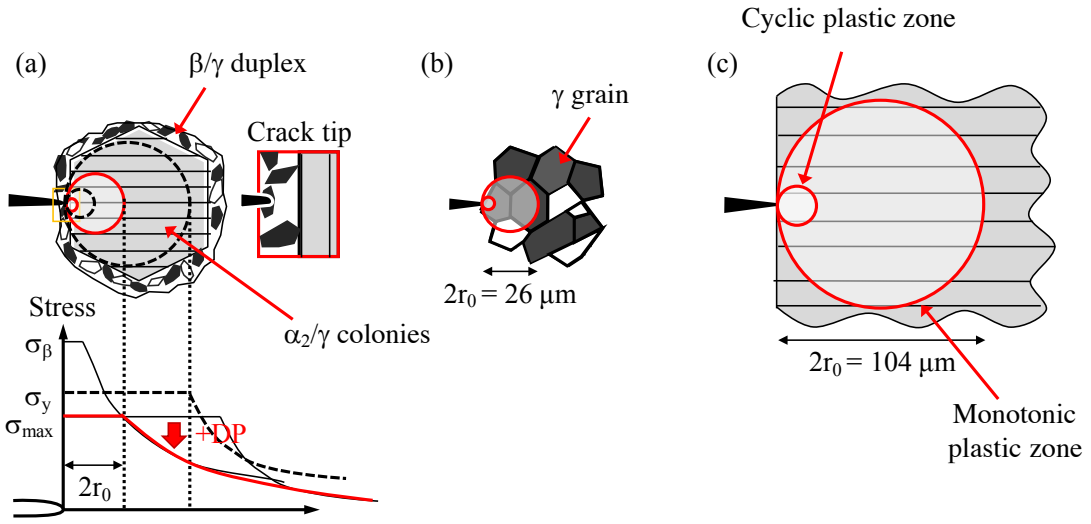

Fig. 4-43. Schematic illustration (a) of the effect of β/γ duplex region on the plastic affected area in NL compared to the (b) NGDP and (c) FL microstructures at the stress intensity threshold.

Table 4-10. Plastic zone size determined at fatigue threshold DK_{th} along with Fully Lamellar results obtained by Dahar *et al.* [7]

Microstructure	V_{DP} / %	Grain size / µm	ΔK_{th} / MPa$\sqrt{m}$	K_{th} / MPa$\sqrt{m}$	Monotonic plastic zone r_0 / µm	Cyclic plastic zone r_0' / µm
Fully Lamellar [7]	0	1000	9.2	10.2	52	9.7
Nearly Lamellar	7	100	10.4	11.6	31	6.2
Globular Triplex	31	46	8.6	9.6	49	9.9
Lamellar Triplex	32	80	10.1	11.2	36	7.3
Near γ Cellular Triplex	33	35	9.7	10.8	28	5.6
Nearly Globular β/γ Duplex – 42-5Mn	90	13	6.8	7.6	22	4.4
Nearly Globular β/γ Duplex – 43-4-5	96	15	7.1	7.9	13	2.7

The fatigue crack growth stress intensity threshold has been plotted as a function of colonies volume fraction in **Figure 4-44** and compared to β-free TiAl duplex alloy [14]. The microstructures containing β phase show always higher threshold than the corresponding TiAl duplex, except the as-forged 42-5Mn (inhomogeneous microstructure). While a small reduction of volume fraction of colonies lead to a significant decrease of the stress intensity threshold in conventional TiAl alloy. This difference in fatigue threshold ΔK_{th} is unexpectedly small between NL and LTL or NCT microstructures. Independently, the β and γ phases seem to have a detrimental effect due to brittleness of β phase and low toughness of γ phase. The increase of γ phase lead to a loss of FCG properties whereas a continuous β phase could act as a brittle cage around the colonies and could explain why GTL microstructure, which has large β regions, shows slightly lower ΔK_{th} compared to LTL and NCT microstructures. However, the independent effects of β and γ are diminished when the two phases coexist together. Indeed, in NL and LTL or NCT microstructures, the β phase always associates with the γ phase through the cellular reaction that occurred during subsequent heat treatment. Thus, it is possible to achieve fatigue crack growth comparable to a fully lamellar microstructure even with high fraction of β phase. Nevertheless, when the volume fraction of γ phase become dominant in the microstructure, the beneficial effect of combined phase is lost and only the γ phase control the fatigue crack growth behavior as observed in the different NGDP microstructures.

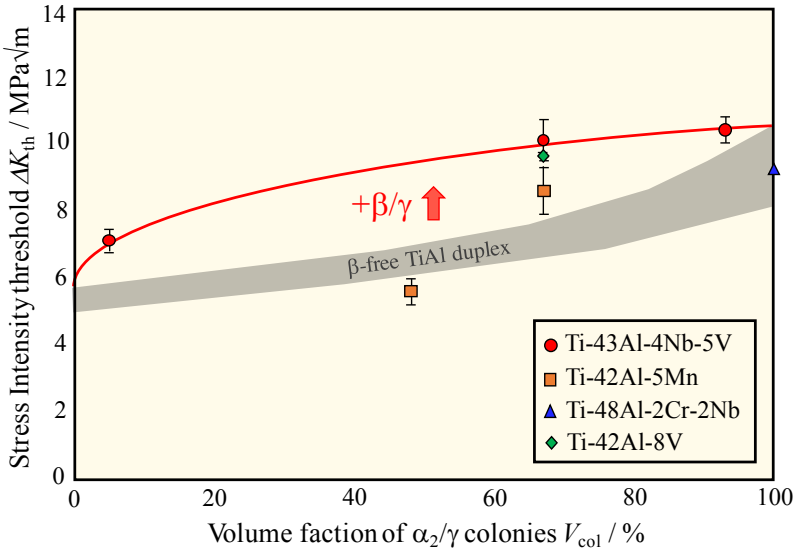

Fig. 4-44. Combined effect of β and γ phases on the stress intensity threshold compared to the duplex TiAl microstructure [14].

(B) On the Paris slope

The same reasoning can be applied in Paris regime. The calculated sizes of the monotonic and cyclic plastic zone area at the overload assuming the plane strain conditions are given in **Table 4-11**. In the work of Dahar *et al.* [7], the colonies grains size is always larger than the plastic zone size even at overload. In that case, the fatigue crack growth properties appeared to be controlled by the lamellar orientation.

Table 4-11. Plastic zone size determined at the overload along with Fully Lamellar results obtained by Dahar *et al.* [7]

Microstructure	V_{DP} / %	Grain size / μm	ΔK_{max} / MPa$\sqrt{m}$	K_{max} / MPa$\sqrt{m}$	Monotonic plastic zone r_0 / μm	Cyclic plastic zone r_0' / μm
Fully Lamellar [7]	0	1000	17.5	19.4	190	38.6
Nearly Lamellar	7	100	24.4	27.1	169	34.2
Globular Triplex	31	46	18.3	20.3	220	44.6
Lamellar Triplex	32	80	19.9	22.1	140	28.4
Near γ Cellular Triplex	33	35	24.1	26.8	172	34.9
Nearly Globular β/γ Duplex – 42-5Mn	90	13	10.8	12.0	54	11.0
Nearly Globular β/γ Duplex – 43-4-5	96	15	10.6	11.8	30	6.1

However, in the studied wrought alloys, the presence of β phase at high temperature refined the grains size during microstructure design to and explain why α_2/γ lamellar grains are relatively small, ten to twenty times smaller than FL microstructure. This explain why the plastic zone becomes larger than colonies grains when the stress intensity increases in all studied microstructures. In that case, when the crack arrests in DP region and does not find an easy way to propagate, secondary cracks can initiate far from the crack tip, in region where the crack propagation is easier. **Figure 4-45** shows a schematic illustration of the formation of secondary crack in the plastically affected region that located in front of the crack tip compare to the FL microstructure. In that case, the fatigue crack growth properties appeared to be controlled by the lamellar orientation and the existence of β/γ duplex at low stress intensity, as explained previously, whereas at high stress intensity, the grains size effect become more important.

Due to the cellular reaction $\alpha_2+\gamma \rightarrow \beta+\gamma$ which take place in LTL during subsequent heat treatment at 1173 K, the grain size is smaller comparing to NL. GTL and NCT

microstructures show also small grain size. Therefore, secondary cracks could appear at lower stress intensity in these microstructures

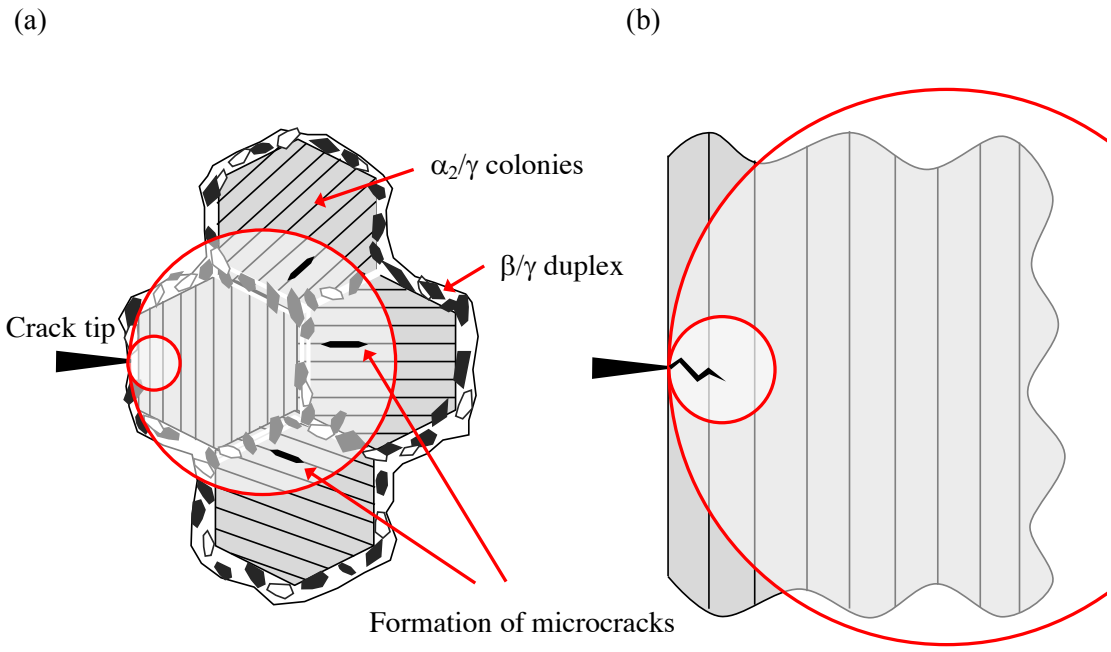

Fig. 4-45. Schematic illustration of (a) the effect of β/γ duplex region on the plastic affected area in NL compared to (b) FL microstructures during Paris regime.

In case of NGDP microstructure, plastic zone is always within the grain size, even at high stress intensity and explain why long-range bridge are not observed in this microstructure. The fatigue crack growth properties appeared to be controlled by the γ and β grains fracture toughness.

4.5 Summary

In this chapter, the fatigue crack growth behavior of wrought alloys containing β phase was determined for microstructures with different β/γ duplex volume fractions and morphologies at the α_2/γ colonies grain boundaries. Based on this study, the following conclusion can be drawn.

1. The fatigue crack growth behavior depends of several parameters. However, the effect of element solution strengthening is limited compared to the effect of microstructures Thus, different compositions with different microstructures can be compared together. The effect of β/γ duplex volume fraction and morphology has been investigated. The

stress intensity threshold ΔK_{th} and the Paris slope m varies from 10.4 MPa√m and 6.5 for NL microstructure to 7.1 MPa√m and in 10.4 for NGDP, respectively.

2. The fatigue crack pathways and the fracture surfaces are similar between microstructures containing α_2/γ colonies with many secondary cracks and crack deviations and a high roughness, respectively. The fractographs showed translamellar, interlamellar and cleavage fracture at the grain boundaries. NGDP microstructures present straight crack propagation as a flat surface with mainly cleavage fracture.
3. Local Paris slopes have been investigated in NL and LTL microstructures and show two different kind of Paris slope. Low Paris slopes m^- represent the crack propagates preferentially through α_2/γ colonies and high Paris slopes m^+ represent a high crack propagation at the grains boundaries. The reason of decrease of m^- with increasing V_{DP} is not clear but could it be related to the decrease of colonies size which led to the appearance of secondary crack earlier. The increase of m^+ is explained by the increase of the volume fraction and size of the γ grains in the β/γ duplex region.
4. Finally, it should be noticed than the introduction of β phase in γ-based TiAl alloys does not worsted the FCG behavior. In the contrary, this chapter demonstrates that the introduction of a certain fraction and morphology of β/γ along colonies is effective in toughening of TiAl alloy. The presence of β phase associated with γ grains in wrought TiAl alloy increase the stress intensity threshold and decrease the Paris slope compared to corresponding duplex TiAl alloy. The reason come from the combined effect of deformable γ phase and high toughness of discontinuous β phase on the plastically affected area. By using the β/γ structure, it is possible to achieve high fatigue crack growth behavior, comparable to a fully lamellar microstructure, even with a fraction not negligible of β phase V_β in the microstructure. Nevertheless, when the volume fraction of β/γ duplex become too high, the fatigue crack growth properties is mainly controlled by the continuous γ phase. Furthermore, the studied microstructures were just models and it is probably possible to continue to improve the FCG properties by optimizing the microstructural features.

References

[1] Y. W. Kim, Intermetallic alloys based on gamma titanium aluminides, JOM 41 (1989) 24-30.

[2] K.T. Venkateswara Rao, Y.W. Kim, C.L. Muhlstein, R.O. Ritchie, Fatigue-crack growth and fracture resistance of a two phase (γ+α_2) TiAl alloy in duplex and lamellar microstructures, Mater. Sc. Eng. A, 192/193 (1995) 474-482.

[3] C. Mabru, D. Bertheau, S. Pautrot, J. Petit, G. Hénaff, Influence of temperature and environment on fatigue crack propagation in a TiAl-based alloy, Engineering Fracture Mechanics 64 (1999) 23-47.

[4] G. Hénaff, A. Gloanec, Fatigue properties of TiAl alloy, Intermetallics 13 (2005) 543–558.

[5] Y. Mutoh, S.J. Zhu, T. Hansson, S. Kurai, Y. Mizuhara, Effect of microstructure on fatigue crack growth in TiAl intermetallics at elevated temperature, Mater. Sc. Eng. A 323 (2002) 62–69.

[6] K. T. Venkateswara Rao, G.R Odette, R. O Ritchie, Ductile-reinforcement toughening in g-TiAl intermetallic-matrix composites: effects on fracture toughness and fatigue-crack propagation resistance, Acta metal. mater. 42 (1994) 893-911.

[7] M. S. Dahar, S. M. Seifi, B.P. Bewlay, J. J. Lewandowski, Effects of test orientation on fracture and fatigue crack growth behavior of third generation as-cast Ti-48Al-2Nb-2Cr, Intermetallics 57 (2015) 73-82.

[8] M. S. Dahar, S. A. Tamirisakandala, J. J. Lewandowski, Evolution of fatigue crack growth and fracture bahavior in gamma titanium aluminide Ti-43.5Al-4Nb-1Mo-0.1B (TNM) forgings, Inter. J. of Fatigue 111 (2018) 54-69.

[9] B.L. Boyce and R.O. Ritchie, Effect of load ratio and maximum stress intensity on the fatigue threshold in Ti-6Al-4V, Eng. Fract. Mech. 68 (2001) 129-147.

[10] Y. Yamada, J.C. Newman Jr., Crack closure under high load-ratio conditions for Inconel-718 near threshold behavior, Eng. Fract. Mech. 76 (2009) 209–220.

[11] T. Nakamura, 鍛造 TiAl 基合金の疲労き裂進展特性に及ぼす組織の影響, Master Thesis, Tokyo Institute of Technology, 2017.

[12] H. Nakashima, Phase equilibria in the quaternary TiAl alloys with the combined Addition of substitutional Elements – phase stability of high and low-temperature β-Ti phase, Doctor Thesis, Tokyo Institute of Technology, 2015.

[13] ASTM Standard E647-15, Standard Test Method for Measurement of Fatigue Crack Growth Rates, In: ASTM book of standards, West Conshohocken, PA, ASTM International, 2015.

[14] J. P. Campbell, R. O. Ritchie, K. T. Venkateswara Rao, The effect of microstructure on fracture toughness and fatigue crack growth behavior in γ-titanium aluminide based intermetallics, Mater. Sc. Eng. A, 30 (1999) 563-577.

[15] R. Gnanamoorthy, Y. Mutoh, N. Masahashi and Y. Mizuhara, Fracture properties of γ-base TiAl alloys with lamellar microstructure at room temperature, Mater. Sc. Eng. A 184 (1994) 37-44.

[16] F. Appel, J. D. H. Paul, M. Oehring, Gamma titanium aluminide alloys: science and technology, first ed., Wiley-VCH, 2011.

[17] P. C. Paris, M. P. Gomez, W. E. Anderson, A rational analytic theory of fatigue, Trend Eng. 13 (1961) 9-14.

[18] R. O. Ritchie, Mechanisms of Fatigue Crack Propagation in Metals, Ceramics and Composites: Role of Crack Tip Shielding, Mater. Sc. Eng. A103 (1988) 15-28.

[19] S. V. Kamat, A. K. Gogia, D. Banerjee, Effect of alloying elements and heat treatment on the fracture toughness of Ti-Al-Nb alloys, Acta Mater. 46 (1998) 239-251.

[20] T. Tetsui, Effects of high niobium addition on the mechanical properties and high-temperature deformability of gamma TiAl alloy, Intermetallics 10 (2002) 239-245.

[21] B.A. Simkin, B.C. Ng, M.A. Crimp, T.R. Bieler, Crack opening due to deformation twin shear at grain boundaries in near-γ TiAl, Intermetallics 15 (2007) 55-60.

[22] F. Appel, R. Wagner, Microstructure and deformation of two phase γ-titanium aluminides", Mater. Sc. Eng. R 22 (1998) 187-268.

[23] T. Leitner, M. Schloffer, S. Mayer, J. Eßlinger, H. Clemens, R. Pippan, Fracture and R-curve behavior of an intermetallic β-stabilized TiAl alloy with different nearly lamellar microstructures, Intermetallics 53 (2014) 1-9.

[24] M. S. Dahar, S. A. Tamirisakandala, J. J. Lewandowski, Evolution of fatigue crack and fracture behavior in gamma titanium aluminide Ti-43.5Al-4Nb-1Mo-0.1B (TNM) forgings, Inter. J. of Fatigue 111 (2018) 54-69.

[25] N. E. Dowling, Mechanical behavior of materials, 4th ed., Pearson, 2012

Chapter 5

Effect of Microstructure on Fatigue Crack Growth Behavior at Elevated Temperatures

5.1 Introduction

In the **Chapter 4**, the relationship between β/γ duplex structure (DP), both volume fraction and morphology, and the fatigue crack growth behavior at room temperature has been introduced. It suggests that independently both β and γ phases are detrimental for FCG resistance, but their combined effects lead to achieve high fatigue stress intensity threshold and low Paris slope compared to β-free equivalent duplex microstructure.

Most on the previous study at elevated temperature focused on lamellar and duplex (lamellar colonies and γ grains) microstructures. It has been shown that in these systems, the fatigue crack growth (FCG) properties in air decrease up to 873 K, and then increase with a maximum around 1073 K [1-3] as shown in **Figure 5-1**. The oxidation-induced crack closure effect that retard the near-threshold crack growth rate at 1073 K, has been proposed by McKelvey *et al.* [4] to explain this dependence to the temperature.

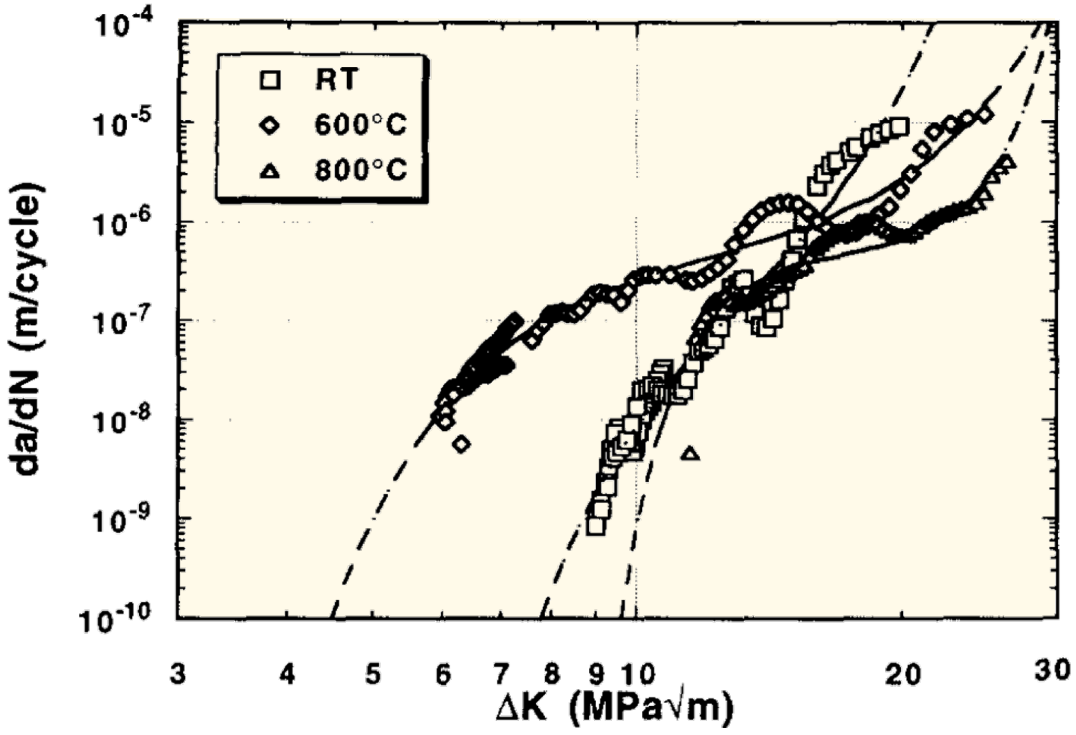

Fig. 5-1. Effect of temperature on Fully microstructure (Lamellar (Ti-46.5A1-3Nb-2Cr-0.2W) in air with a frequency of 1 Hz and load ratio R = 0.1 [3].

Furthermore, it has been established that, even at elevated temperature, lamellar microstructure shows better fatigue resistance than duplex one. However, there are no study about the relationship between microstructure containing β phase and FCG

behavior at high temperature and it is still unclear how this phase will affect the fatigue resistance.

Thus, the objective of this chapter is to identify the influence of β phase on fatigue crack growth resistance of wrought alloy at elevated temperature.

5.2 Experiment procedure

The flowchart of the experimental procedure is shown in **Figure 5-2**. Ti-43Al-4Nb-5V alloy was used in this chapter with two different microstructures, Nearly Lamellar (NL) and Nearly Globular β/γ Duplex (NGDP), as introduced in previous chapters. Elaboration of the ingot, heat treatments and sample processing are the same as described in **Chapter 4**.

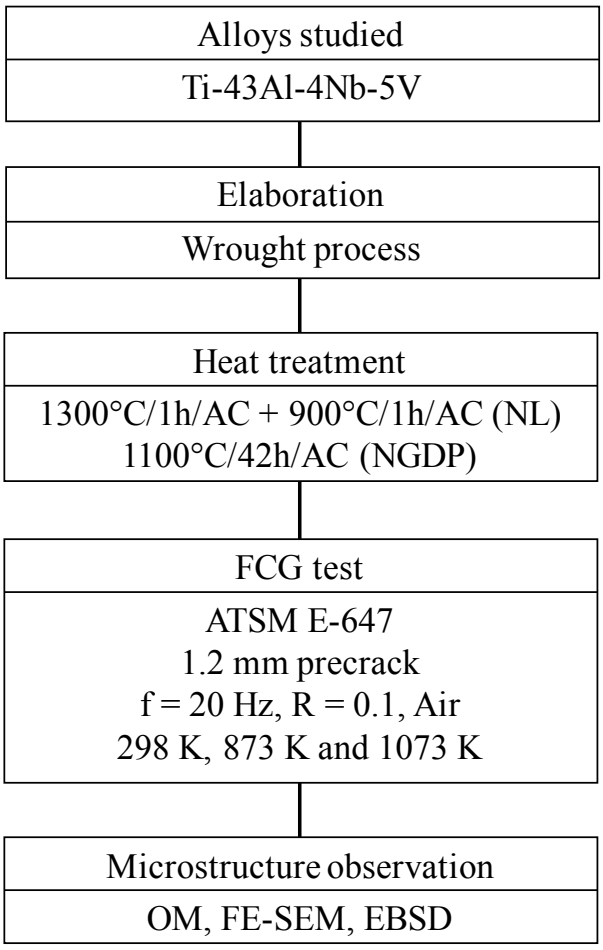

Fig. 5-2. Flowchart of the experimental procedures for determination of the fatigue crack growth behaviour of Ti-43Al-4Nb-5V at elevated temperature.

Tensile parameters e.g., σ_{YS} and σ_{UTS} that were used in this study for fatigue crack growth tests come from the *ex-situ* and *in-situ* studies performed by Nakamura *et al*. [5] on the same TiAl alloy system and are presented in **Table 5-1**.

Table 5-1. Tensile properties of Ti-43Al-4Nb-5V (at.%) at ambient and elevated temperature [5]. Figures in bracket correspond to *ex-situ* results.

Microstructures	Temperature	Young's Modulus E / GPa	Yield stress σ_y / MPa	Ultimate Tensile Strength σ_{UTS} / MPa	Elongation ε / %
Nearly Lamellar (NL)	298	34 (137)	– (480)	664 (900)	0.7 (0.1)
	1073	45 (133)	450 (445)	680 (725)	1.3 (1.6)
Nearly Globular β/γ Duplex (NGDP)	298	47	495	775	2.3
	1073	45	440	526	11.8

Precrack introduction tests were done at room temperature and are defined in **Chapter 4**. The fatigue crack growth tests were conducted using MTS Landmark™ Servo-hydraulic Test Systems. Tests were carried out at 873 and 1073 K in air under cyclic stress intensity (ΔK) controlled with load ratio R of 0.1 and a frequency of 20 Hz. **Figure 5-3** shows an illustration of the high temperature process. After the precrack test, samples were heated for around 2 h depending of the test temperature and then, the temperature was maintained for 1 h before to start the FCG tests. Depending of the test (K_{dec} or K_{inc}), the time change from 0.5 to 4 h at 1073 K. After test, furnace was cooled for one day.

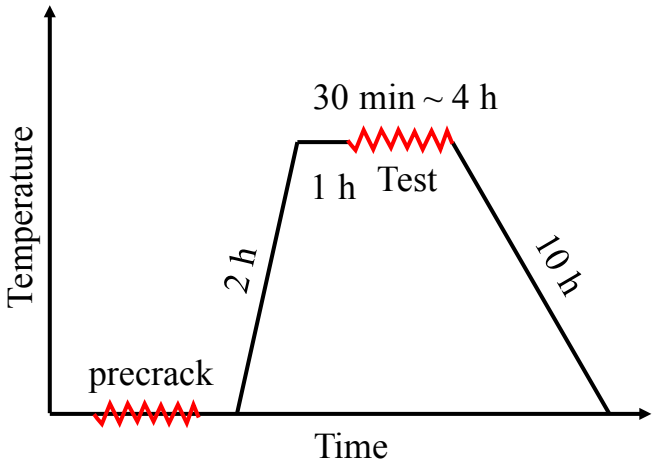

Fig. 5-3. Schematic illustration of the thermal history of CT sample during high temperature test.

K-decreasing tests and *K*-increasing tests were conducted, respectively, by load shedding and by constant load amplitude independently, where *K* is the stress intensity factor at the tip of the crack with a current flow of 3 A. Initial stress intensity *K* value of *K*-increasing and *K*-decreasing tests was chosen higher than the *K* value of the precrack test in order to eliminate the stress field occurred during precrack introduction. Normalized *K* gradient C = - 0.08 /mm were used during load shedding (*K*-decreasing tests). Crack size was measured *in-situ* with platinum wire with the direct current potential drop technique. R-type thermocouple (TC) was used for measuring CT specimens' temperature (± 2 K). The welding positions are shown in **Figure 5-4** Welding conditions for platinum wires and thermocouple were as follow: pressure 2, power 50, time 7 Hz.

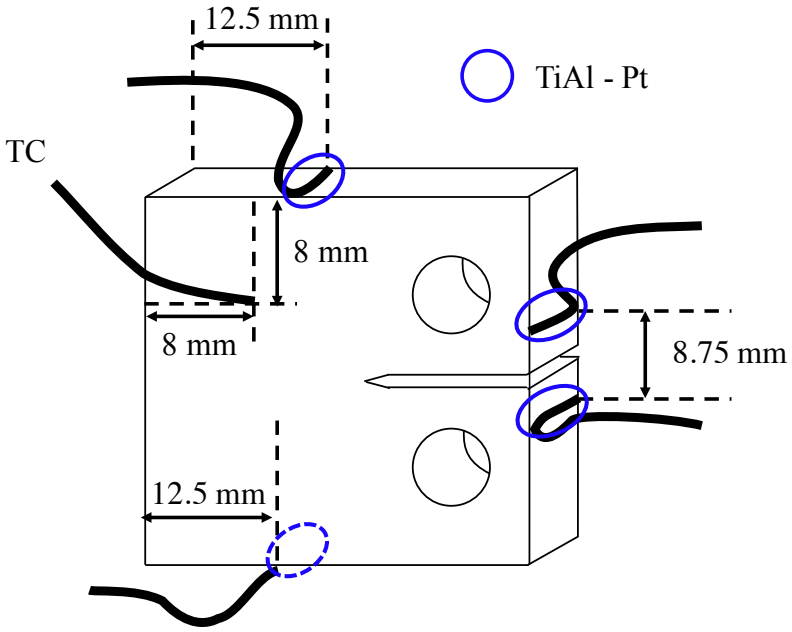

Fig. 5-4. Schematic illustration of the platinum and thermocouple (TC) welding spots location.

Samples preparation is described in **Chapter 4**. EBSD analysis also was conducted after high temperature tests. However, because the oxide layer was not eliminated by electrical polishing, the sample were prepared by vibration polishing instead. The specimens were examined using a Nikon LV150 OM (Optical Microscope), and then using a JEOL JSM-7000F FE-SEM (Field Emission Scanning Electron Microscope) with an acceleration voltage of 15 kV and a working distance of 14 mm after the different stages of the experiments: initial microstructure, precrack tests, *K*-decreasing tests and K-increasing tests. EBSD were carry out on a FIB-SEM model JIB-4601F with an

acceleration voltage of 25 kV. Finally, the fracture surface observations were studied using SEM model JEOL JSM 6610 at 15-20 kV.

5.3 Results

5.3.1 Fatigue crack growth behavior

(A) Effect of temperature

The influence of temperature on the cyclic fatigue crack growth curves of the 43-4-5 alloy is shown for the Nearly Lamellar microstructure in **Figure 5-5**. Although the FCG curves represent only one test, the fatigue threshold ΔK_{th} values, Paris exponents m, Paris coefficients C, and maximum stress intensity at overload K_{max} for the three investigated temperatures are given in **Table 5-1**. Detailed FCG curves are shown in **Appendix A5**.

It was found that the lowest fatigue threshold ΔK_{th} values was measured for 873 K (ΔK_{th} = 7.0 MPa$\sqrt{m}$), below the ductile-brittle transition temperature (DBTT) reported for γ-TiAl alloys [6], whereas the highest values of around 11.5 MPa$\sqrt{m}$ were observed above the DBTT at 1073 K. The FCG behavior at room temperature showed intermediate FCG behavior with a stress intensity threshold of around 10.4 MPa$\sqrt{m}$.

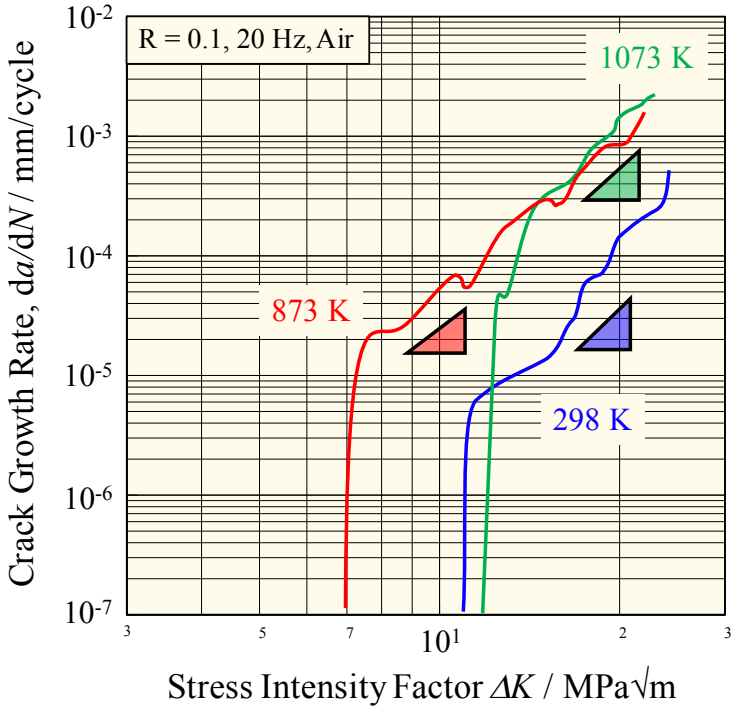

Fig. 5-5. Fatigue crack growth curves at different temperatures of wrought 43-4-5 alloy with a Nearly Lamellar microstructure.

Table 5-2. Fatigue crack growth results of NL microstructure at different temperatures.

Temperature	Sample	ΔK_{th} / Mpa$\sqrt{m}$	m	C	K_{max} / Mpa$\sqrt{m}$
298 K	**Average (Chapter 4 Table 4-8)**	**10.4 ± 0.5**	**6.4 ± 1.4**	–	**27.1**
873 K	43-4-5-N	–	4.6	7E-10	–
	43-4-5-O	–	4.2	3E-9	–
	43-4-5-P	–	4.1	4E-9	25.2
	43-4-5-Q	7.0	4.1	6E-9	–
	Average	**7.0**	**4.2 ± 0.2**	–	**25.2**
1073 K	43-4-5-R	–	3.8	1E-1	–
	43-4-5-S	10.7	–	–	–
	43-4-5-T	12.1	–	–	–
	43-4-5-U	11.8	–	–	–
	43-4-5-V	–	4.8	6E-10	30.3
	Average	**11.5 ± 0.7**	**4.3 ± 0.8**	–	**30.3**

In the near-threshold region, the cracks started to propagate in the Paris regime at different crack growth rates increasing with temperature. Thus, even is the fatigue crack growth curve at room temperature was the steepest with a Paris slope of around 6.4, the crack growth rates showed the lower values. Therefore, the crack propagation curves at 298 and 1073 K crossed each other. The Paris slopes determined at 873 and 1073 K were slower and similar with a value of around 4.3 and explain why the curves joined at ~12 MPa$\sqrt{m}$. However, the FCG curve at 1073 K was smoother compared to the two other temperatures suggestive of an increasing of the ductility in the material.

The K_{max} at the catastrophic failure in fatigue showed a similar trend to the fatigue threshold with a minimum of 25.2 MPa$\sqrt{m}$ at 873 K and a maximum of 30.3 MPa$\sqrt{m}$ at 1073 K as shown in **Table 5-2**. The K_{max} at RT was intermediate (27.1 MPa$\sqrt{m}$).

(B) Effect of β/γ duplex volume fraction V_{DP}

The fatigue crack growth curves of NL (V_{DP} = 7%) and NGDP (V_{DP} = 96%) microstructures are compared at 1073 K, along with the results determined in **Chapter 4** at ambient temperature and represented by dotted line, in **Figure 5-6**. The FCG results are given in **Table 5-3**. Detailed FCG curves are shown in **Appendix A5**.

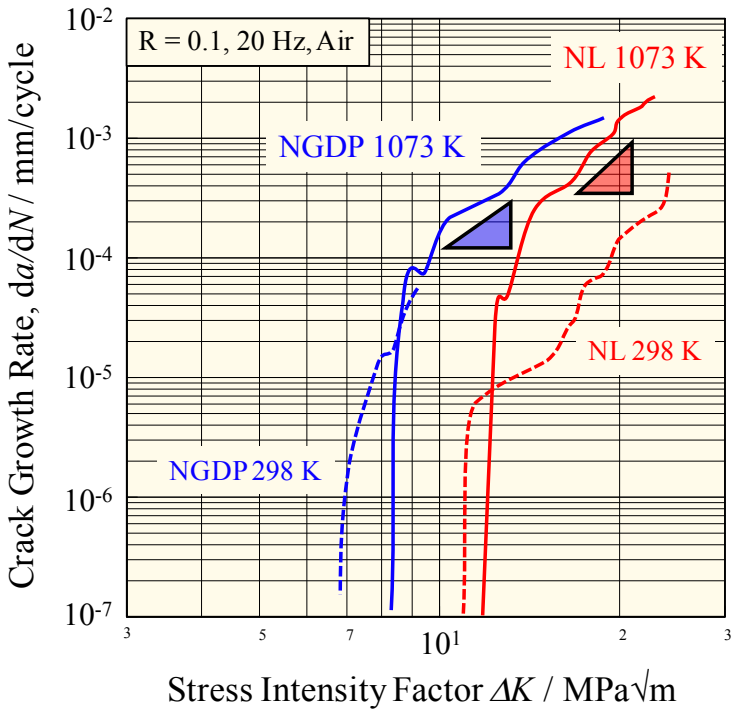

Fig. 5-6. Effect of β/γ duplex volume fraction V_{DP} on the fatigue crack growth behavior of wrought 43-4-5 alloy at 1073 K.

A comparison of the results, both room and elevated temperature, showed that NL microstructure exhibited higher fatigue crack growth resistance in the near-threshold than NGDP microstructure. In both microstructures, high temperature stress intensity threshold is higher compared to room temperature. The fatigue threshold of NL and NGDP microstructures increased from 10.4 MPa$\sqrt{m}$ and 7.1 MPa$\sqrt{m}$ at ambient temperature to 11.5 MPa$\sqrt{m}$ and 7.9 MPa$\sqrt{m}$ at 1073 K, respectively.

The crack growth curves at room temperature were steeper than those at high temperature which showed a lower Paris exponent. Although the crack growth rate of Nearly Lamellar was slower at room temperature, the opposite behavior was observed at high temperature for the NGDP Microstructure with a Paris slope of about 3.2.

In both microstructures, K_{max} at overload increasing with increasing temperature. However, whereas the K_{max} increased slightly from 27.1 MPa$\sqrt{m}$ to 30.3 MPa$\sqrt{m}$ in NL microstructure, K_{max} in NGDP microstructure almost doubled from 11.8 MPa$\sqrt{m}$ to 22.0 MPa$\sqrt{m}$ as shown in **Table 5-3**.

Table 5-3. Comparison between 298 and 1073 K fatigue crack growth results of NL and NGDP microstructures.

Microstructure	Temperature	Sample	ΔK_{th} / Mpa$\sqrt{m}$	m	C	K_{max} / Mpa$\sqrt{m}$
NL	298 K	**Average (Chapter 4 Table 4-8)**	**10.4 ± 0.5**	**6.4 ± 1.4**	**–**	**27.1**
	1073 K	**Average (Table 5-2)**	**11.5 ± 0.7**	**4.3 ± 0.8**	**–**	**30.3**
NGDP	298 K	**Average (Chapter 4 Table 4-7)**	**7.1 ± 0.4**	**10.4 ± 3.2**	**–**	**11.8**
	1073 K	43-4-5-W	–	3.1	2E-7	–
		43-4-5-X	7.6 / 8.3	–	–	–
		43-4-5-Y	–	3.3	9E-8	22.0
		43-4-5-Z	7.8	–	–	–
		Average	**7.9 ± 0.4**	**3.2 ± 0.1**	**–**	**22.0**

5.3.2 Crack growth pathway

The crack pathways were reconstituted using SEM images. The crack pathways after *K*-decreasing tests of the Nearly Lamellar at 873 and 1073 K, and Nearly Globular β/γ Duplex are shown in **Figure 5-7 and 5-8**, respectively.

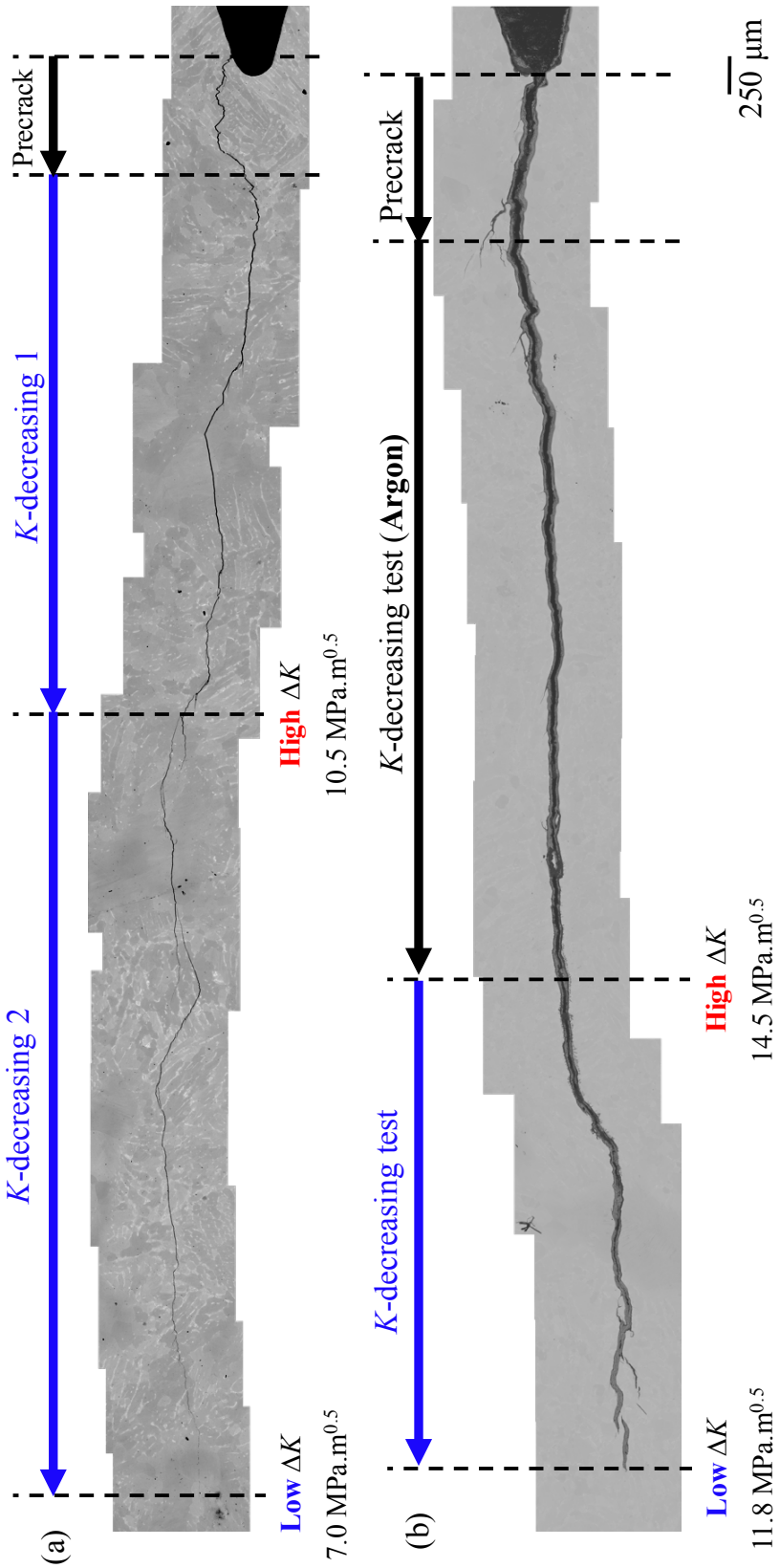

Fig. 5-7. SEM images of the fatigue crack growth pathway after *K*-decreasing test in air with a Nearly Lamellar microstructure at (a) 873 K and (b) 1073 K.

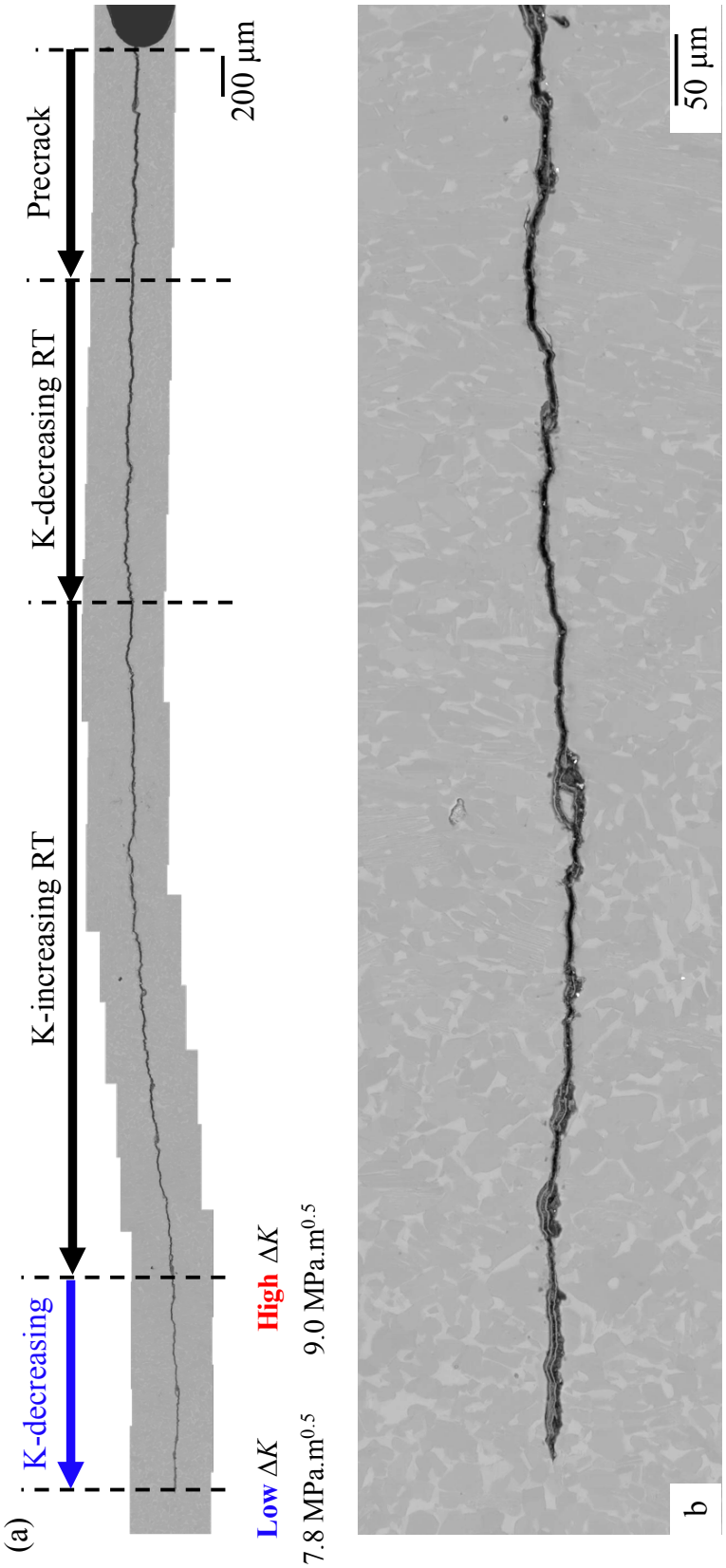

Fig. 5-8. SEM images of (a) the total fatigue crack growth pathways and (b) the fatigue crack growth pathway after *K*-decreasing test at 1073 K in air at higher magnification with a Nearly Globular β/γ Duplex microstructure.

Two different *K*-decreasing tests were conducted in NL microstructure at 873 K on the CT specimen shown in **Figure 5-7 (a)**. Clear crack propagation differences were observed compared to room temperature. Whereas at ambient temperature the cracks were tortuous with many secondary branches and ligament bridges on a small range, the crack at 873 K become smoother but still present secondary branches and ligament bridges with a lower appearance frequency. At 1073 K a thick oxide layer is observed all along the crack (**Fig. 5-7 (b)**). The crack became completely fill by the oxide near the crack tip and it also results a large crack opening compared to lower temperature.

The crack pathway of the NGDP microstructure at 1073 K is relatively flat and similar to room temperature crack propagation as shown in **Figure 5-8**. As observed in NL microstructure, an oxide layer is also observed in NGDP but thinner compared to NL one.

In this section, a particular attention will be paid on the crack pathway, both on surface and in the bulk, at the stress intensity threshold and during the Paris regime.

(A) Crack propagation near the stress intensity threshold

The crack tips near the stress intensity threshold of the Nearly Lamellar microstructures between 298 and 1073 K are shown in **Figure 5-9**. At 298 K, it can be shown that the both cracks, main and secondary, stopped in β/γ duplex region either in γ grains or at β/γ grain boundaries (**Fig. 5-9 (b)**). At 873 K, the main crack tip arrested in lamellar region. However, it can be observed a crack deviation on the crack wake. It indicates that probably a microcrack was generated in front of the main crack and as the main crack propagated, they connected together. Though, the microcrack stopping point was also in β/γ duplex region as indicated by the arrow in **Fig. 5-9 (d)**. Finally, at 1073 K the crack is thick and blunted at the tip. Actually, the dark region corresponds to the oxide layer formed during test, that completely filled and deformed the crack. Nevertheless, it can be observed that the crack also stopped in β/γ duplex region. Moreover, a secondary crack is formed in the crack wake. The secondary crack seems to propagates by the formation of microcracks in α_2/γ colonies in front of the tip which coalesced when the crack grew (**Fig. 5-9 (f)**). This indicates that, even at high temperature, DP region acts as strong features against the crack propagation.

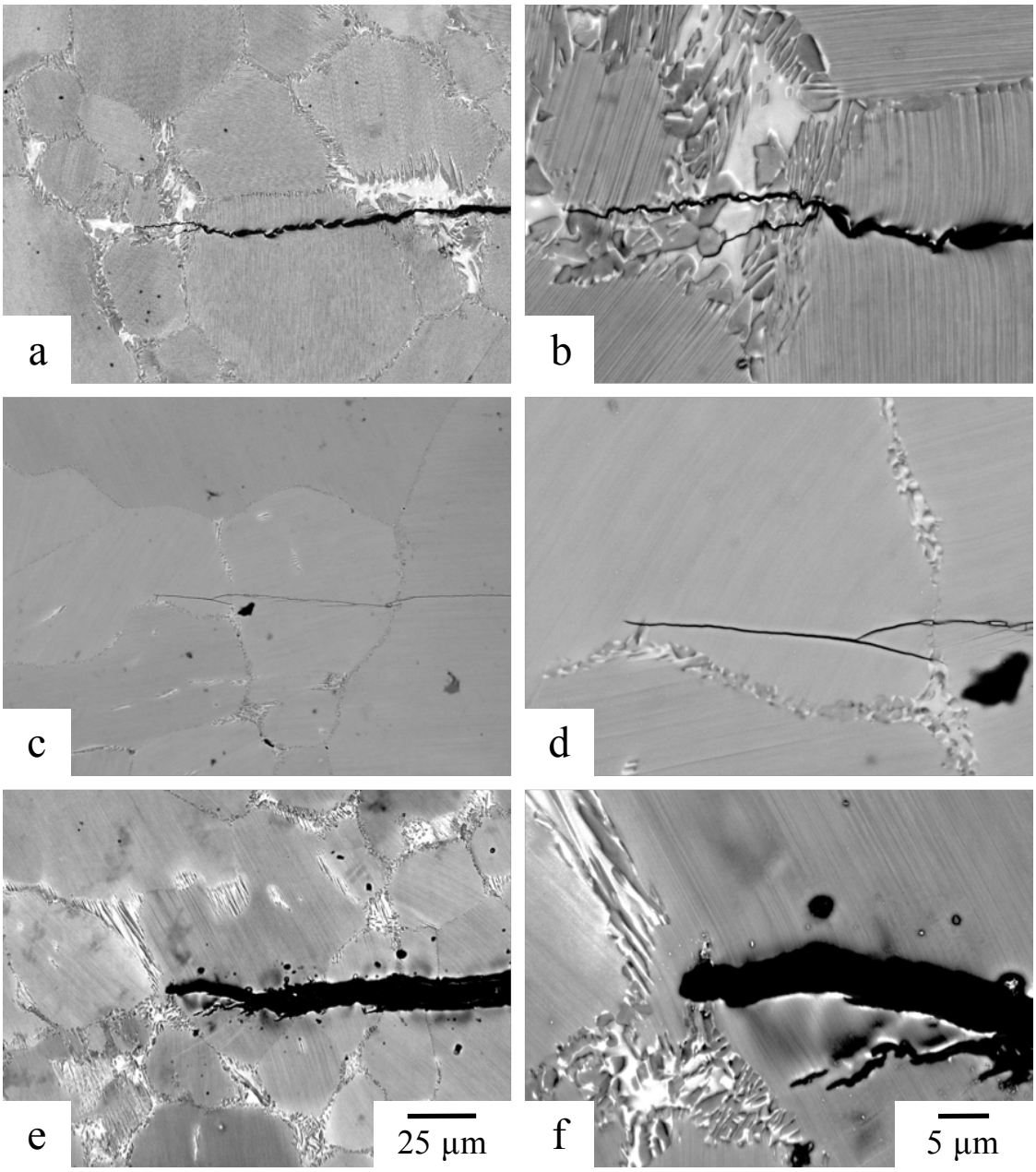

Fig. 5-9. Effect of the β/γ duplex on the crack growth pathway near the stress intensity threshold ΔK_{th}. BSE images of Nearly Lamellar microstructure at (a, b) 298 K, (c, d) 873 K and (e, f) 1073 K. The arrows indicate the β/γ duplex region.

Figure 5-10 shows the comparison of crack propagation near surface and within the bulk in NL microstructure. The final crack size in surface and bulk is equivalent and the propagation trend is similar with a crack relatively smooth, few secondary cracks and the presence of a thick oxide layer. This result indicates that the crack propagated linearly between the two sample sides as the cycles occurred as will be confirmed by the oxidation

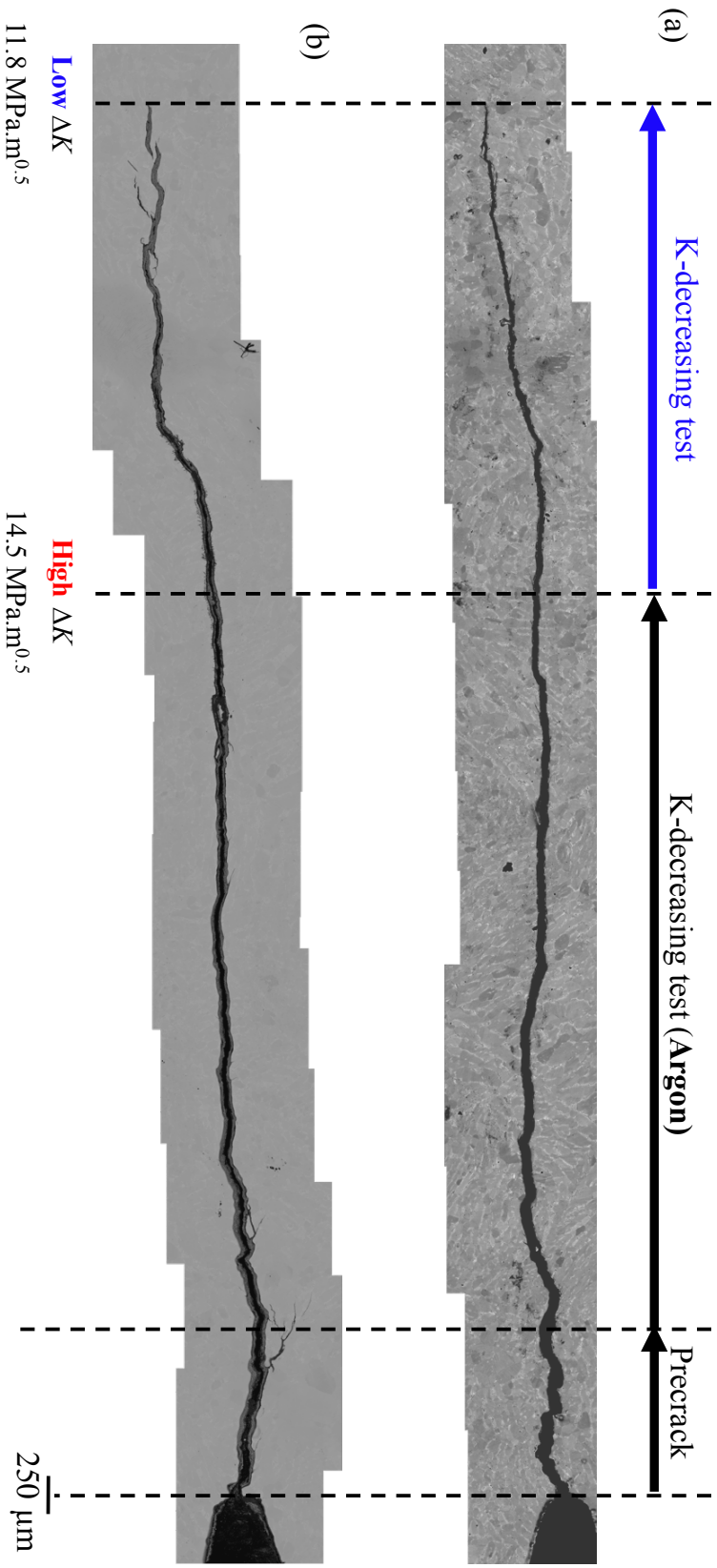

Fig. 5-10. SEM images of (a) near surface and (b) bulk crack growth pathway after *K*-decreasing test at 1073 K in air.

layer later. Moreover, the analysis of the surface pathway may also describe the bulk propagation behavior. Then, the crack tip has been investigated at two different depths as shown in **Figure 5-11**. About 50 µm has been erased between the two crack tips. Both pathways are very similar: the main crack arrested and then, in front of this crack, small crack was generated and grew, resulting bridge ligaments in the microstructure indicated by arrows. Only one ligament is observed at 3.48 mm depth (**Fig. 5-11 (a)**) but at 3.53 mm depth, a second ligament appeared. Finally, the crack stopped either in lamellar colonies (**Fig. 5-11 (b)**) or DP region (**Fig. 5-11 (d)**).

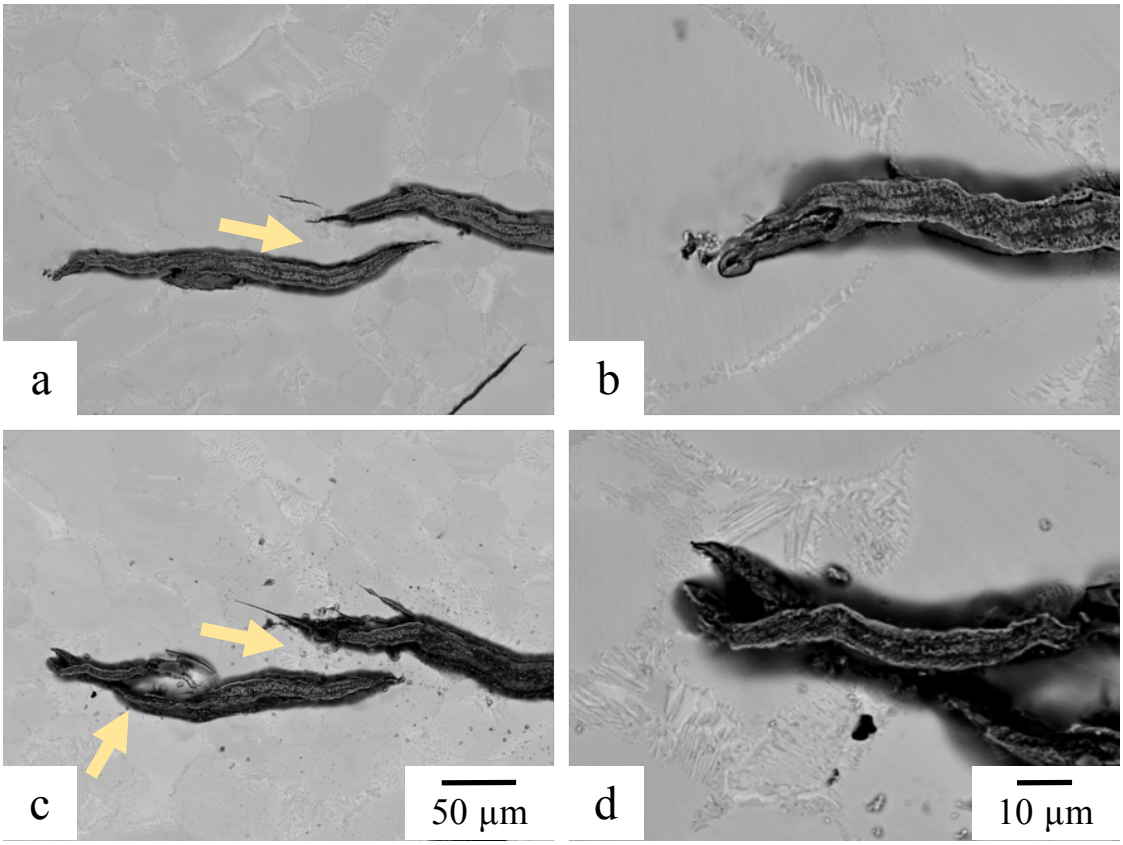

Fig. 5-11. Change in the crack pathway near the stress intensity threshold ΔK_{th} within the bulk of Nearly Lamellar sample with a thickness of 6.2 mm at (a, b) 3.48 mm and (c, d) 3.53 mm depth after *K*-decreasing test.

The comparison between crack tips near the stress intensity threshold of the Nearly Globular β/γ Duplex microstructure at 298 and 1073 K is shown in **Figure 5-12**. The crack at high temperature grew more straightly compared to ambient temperature propagation which shows more crack deviations. Whereas secondary cracks, with a size of about 10 to 20 µm are observed at room temperature near the fatigue threshold, the

cracks pathway at 1073 K did not shown such features. It should be noted that in both temperatures, the crack arrests in γ grains and these grains present many lines on the surface, despite it did not can be clearly observed in **Fig. 5-12 (d)** due to the low contrast. Moreover, all the β grains in contact of the crack, and by extension in contact with air, shown phase transformation change, nevertheless this will be discussed later. Finally, by carefully pay attention to the crack tip, it can be observed that the oxide layer was not formed yet in the last micrometer, giving indications about the crack propagation at low stresses. Moreover, it indicates that the oxide layer formation mainly occurred during fatigue test but not during cooling time.

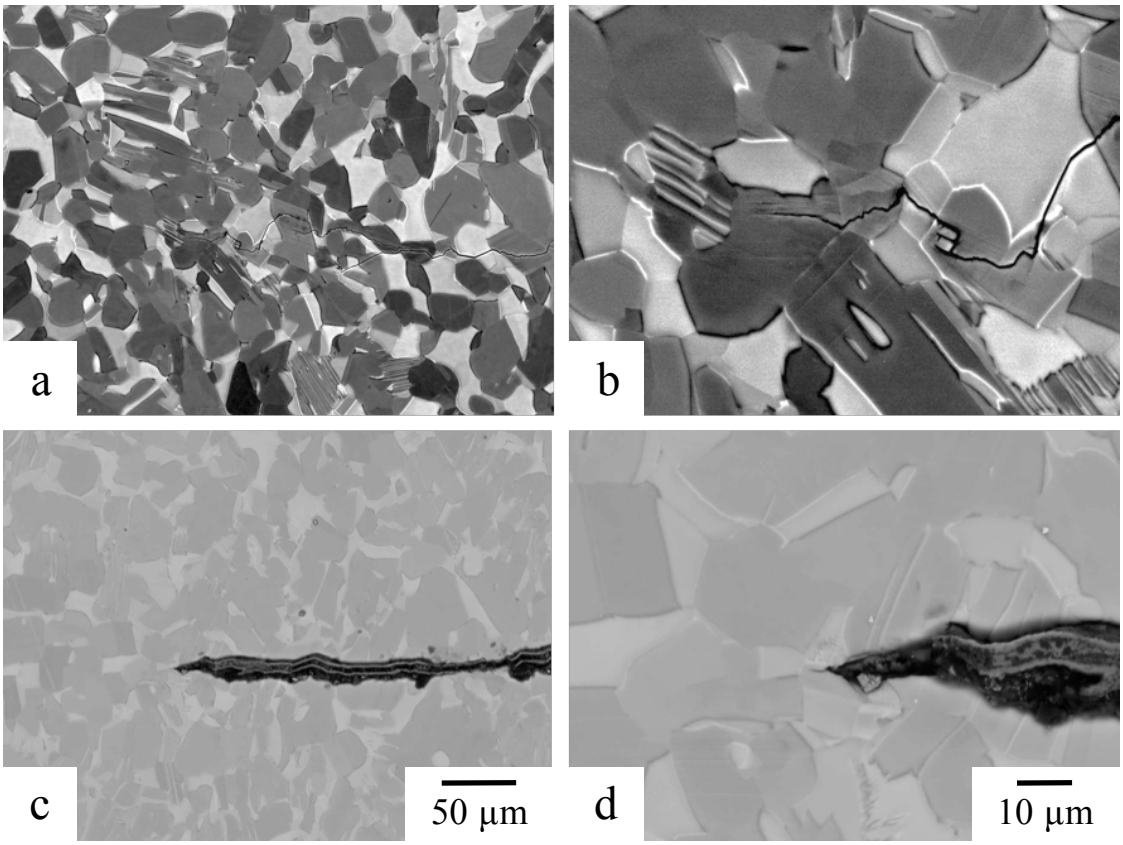

Fig. 5-12. Effect of the β/γ duplex on the crack growth pathway near the stress intensity threshold ΔK_{th}. BSE images of Nearly Globular b/g Duplex microstructure at (a, b) 298 K and (c, d) 1073 K.

(B) Crack propagation during Paris life

The crack pathway has been investigated during Paris regime, corresponding to the crack wake far from the crack tip. The following section will introduce the crack pathways of NL at 873 and 1073 K and of NGDP at 1073 K.

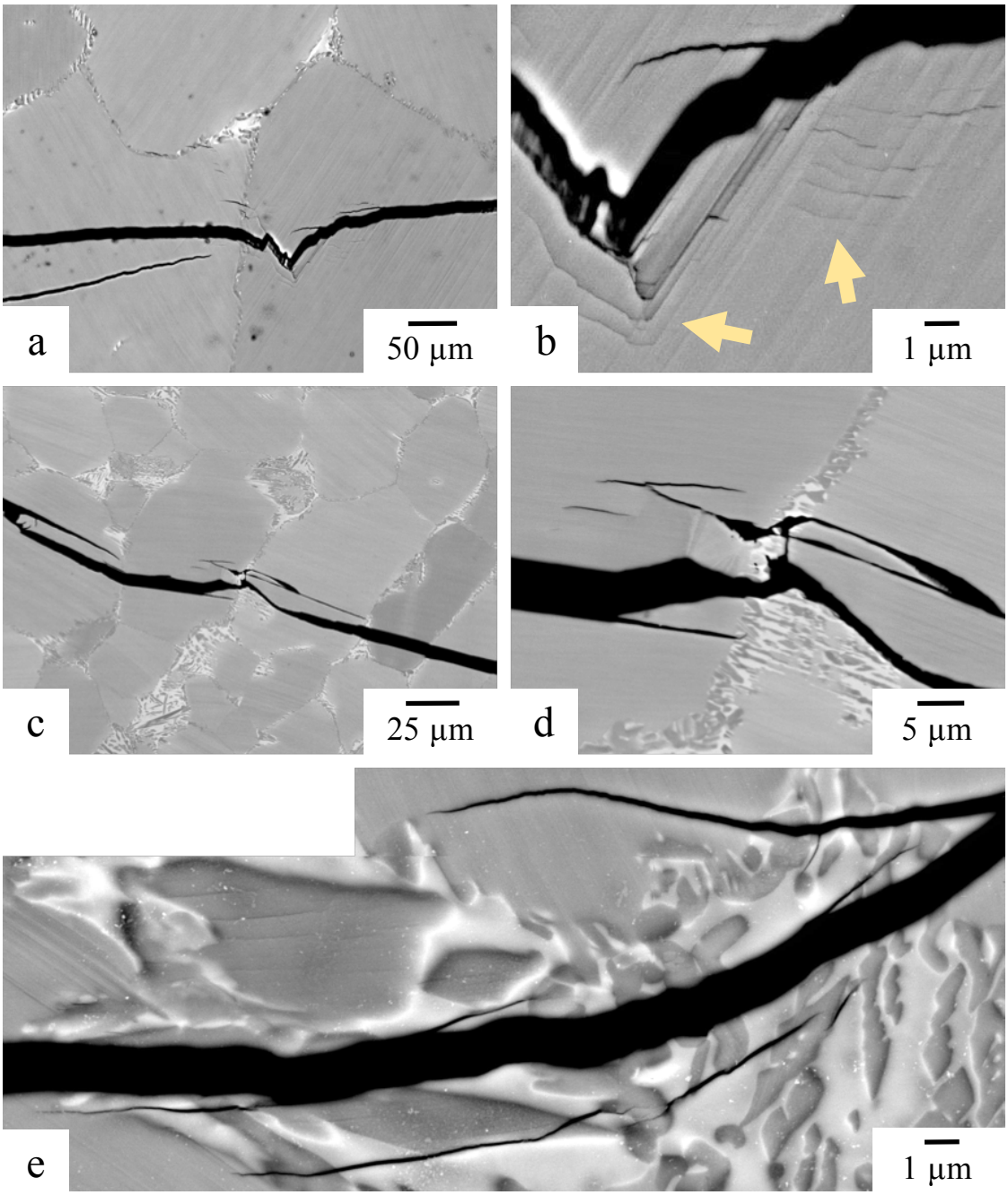

Fig. 5-13. SEM images of crack propagation pathway in Paris region in Nearly Lamellar microstructure at 873 K. (a, b) surface colonies, (c, d) bulk colonies and (e) β/γ DP region. Arrows indicate microcracks formation.

The crack pathway of NL microstructure through colonies and duplex regions at 873 K is shown in **Figure 5-13**. The oxide layer was not enough thick to be quantified by SEM. As observed in room temperature tested samples, due to the low fraction of β/γ duplex at the grains boundary, crack mainly propagated through α_2/γ lamellar grains and lead to the formation of crack bridging elements and crack deviations during test. Some

differences were observed between the crack pathway at the surface and within the bulk. At the surface, many fine microcracks parallel to each other were observed along the main and the secondary cracks in colony grains and indicated by arrow in **Fig. 5-13 (b)**. In comparison, within the bulk the microcracks were few and large as shown in **Fig 5-13 (d)**, and therefore, led to the formation of many bridging ligaments. These differences could be explained by the deformation at the surface that is free (plane stress condition) whereas inside it is contained by the surrounding materials (plain strain condition). Additionally, microcracks formed also in β/γ duplex region as shown in **Fig. 5-13 (e)**. These microcracks mainly connected two γ grains together and propagates preferentially at β/γ interfaces.

Figure 5-14 shows the crack propagation pathway of NL microstructure at 1073 K. The crack in the Paris regime show mainly long-range crack bridging elements (as described in Chapter 4) and smoother crack deviations compared to the tests conducted at lower temperatures. As mentioned above, the oxide layer filled the crack and it became difficult to analyze the pathway of the main crack. Nevertheless, the pathways can be observed from the secondary cracks or the isolated cracks due to their thinner oxide layer. The stop points at the right side of the cracks are mainly located in lamellar colonies and indicated by arrows 1 in **Fig. 5-14 (a, e, g)** whereas the left side of the cracks arrest in β/γ duplex region at the colony grain boundaries (arrows 2 in **Fig. 5-14 (b, c)**) but also in colonies. It could indicate that crack occurred in lamellar grains and then propagated until reach a strong obstacle.

Whereas the cracks mainly arrested at DP region at ambient temperature, the observation of the tip of the different cracks (secondary, bridges…) at elevated temperatures shows that the crack could stop either in DP or in lamellar region.

The transverse crack between the surface and the bulk is shown in **Figure 5-15**. Even inside the sample, the crack shows microcracks (**Fig. 5-15 (c)**), cracks deviations (**Fig. 5-15 (e)**) and crack bridging ligaments (**Fig. 5-15 (g)**). The difference in level between surface and bulk was about 200 μm. Moreover, it can be observed two different oxide layers. The thickness was small when the crack propagated through interlamellar mode, less than 2 μm, but was very thick when the crack propagated within the β/γ duplex region (around 25 μm) or through translamellar mode. The reason comes from the β phase in the β/γ duplex region and the α_2 phase in translamellar that were Ti-rich phases and thus, enhances the oxidation behavior against Al-rich γ phase.

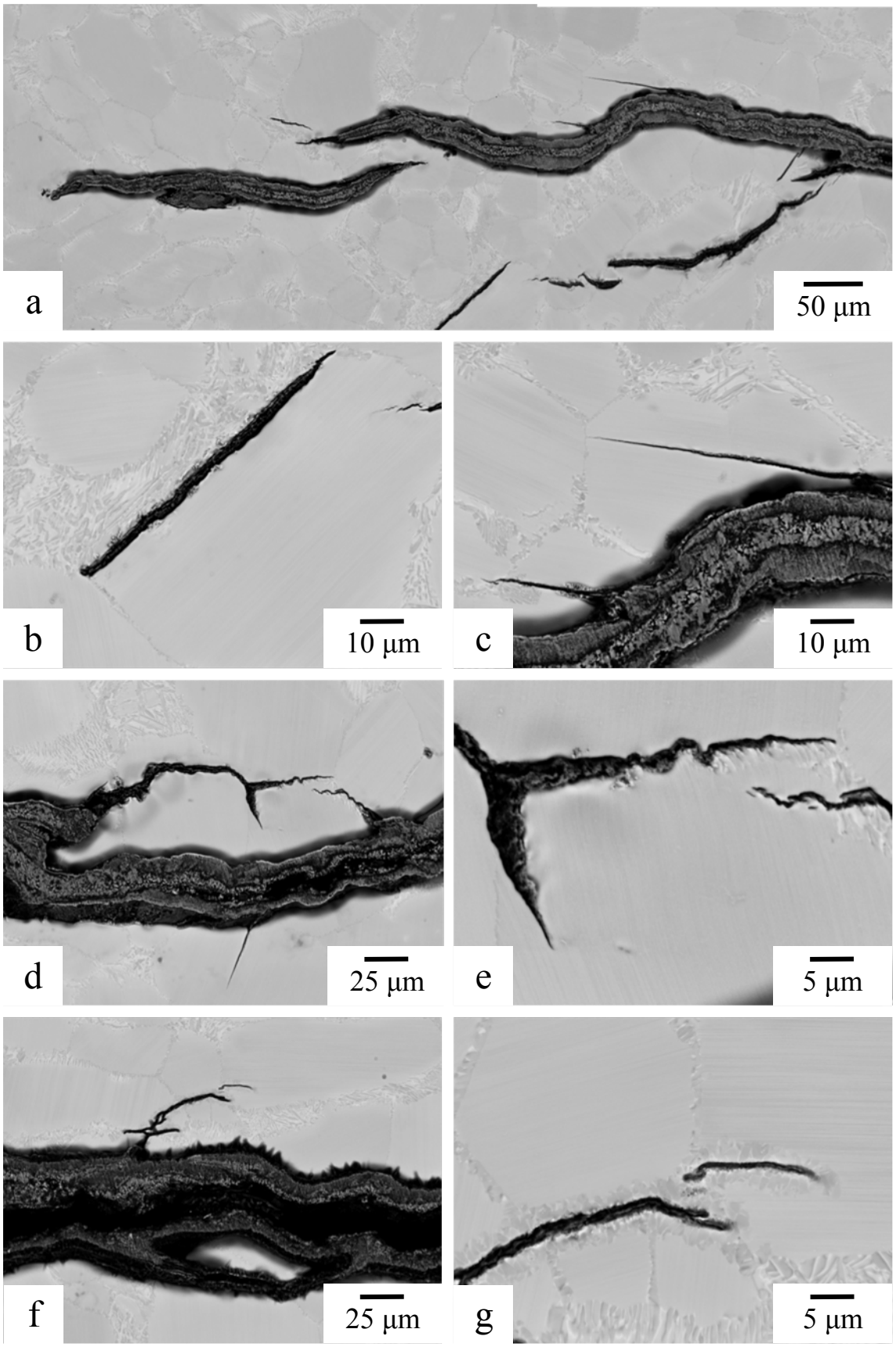

Fig. 5-14. SEM images of crack propagation pathway in Paris region of Nearly Lamellar microstructure at 1073 K.

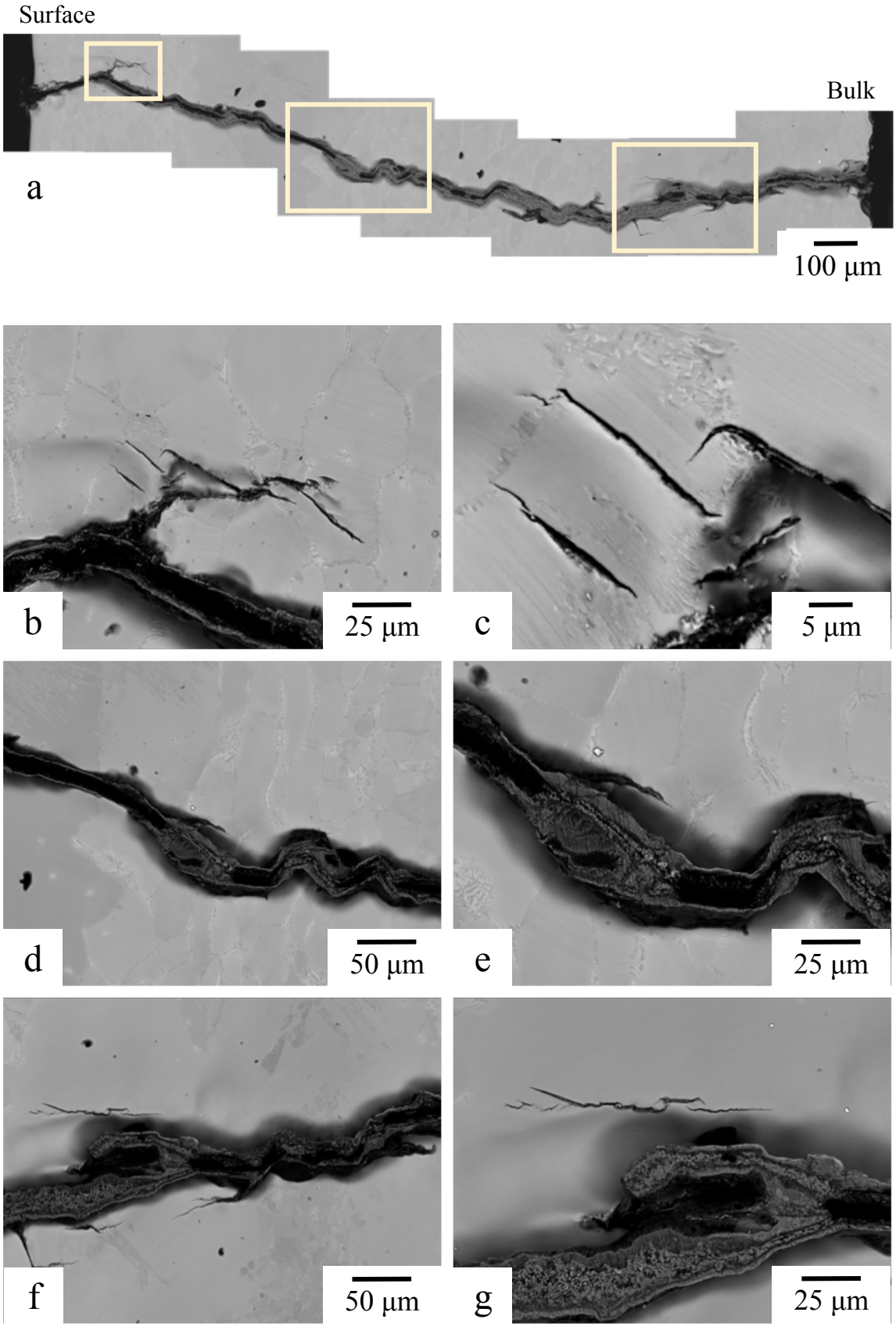

Fig. 5-15. SEM images of (a) general view of the slice between surface and bulk in Nearly Lamellar microstructure at 1073 K and (b-g) higher magnification views.

Finally, in the NGDP microstructure, the crack propagation was similar to ambient temperature one. With the high fraction of β/γ duplex, an almost continuous γ-grains region formed and the crack mainly propagated through it as shown in **Figure 5-16**. However, this crack propagation was straighter at high temperature and the crack surface was covered by an oxide layer of about 2 to 5 μm in thickness. In others words crack deviations were limited. In the same way, only rare bridging ligaments were observed as shown on **Fig. 5-16 (c)**. Furthermore, as reported near the crack tip, many line are observed on γ grains as evidences of γ deformation, that will be detailed in discussion part. The transverse crack of the NGDP microstructure was also observed by SEM as shown in **Figure 5-17** and revealed that the crack propagated more straightly in the transverse direction compared to NL with no difference in level measured between the bulk and the surface (**Fig. 5-17 (a)**). However, some differences between the surface and the transverse propagation have been reported. Despite the crack was flat in both situations, the crack deviations were more significant in the transverse direction (**Fig. 5-17 (b)**). Moreover, despite it was still rarely, the fraction of microcracks (**Fig. 5-17 (c)**) and secondary cracks (**Fig. 5-17 (e, g)**) was also more important. The microcracks were mainly reported at the β and γ phases interface which was also the initiation point of the secondary cracks. The presence in every β grains in contact of the crack, and by extension in contact with air, of a phase transformation change have been observed all along the transverse direction. Thus, this phenomenon was not limited to the surface.

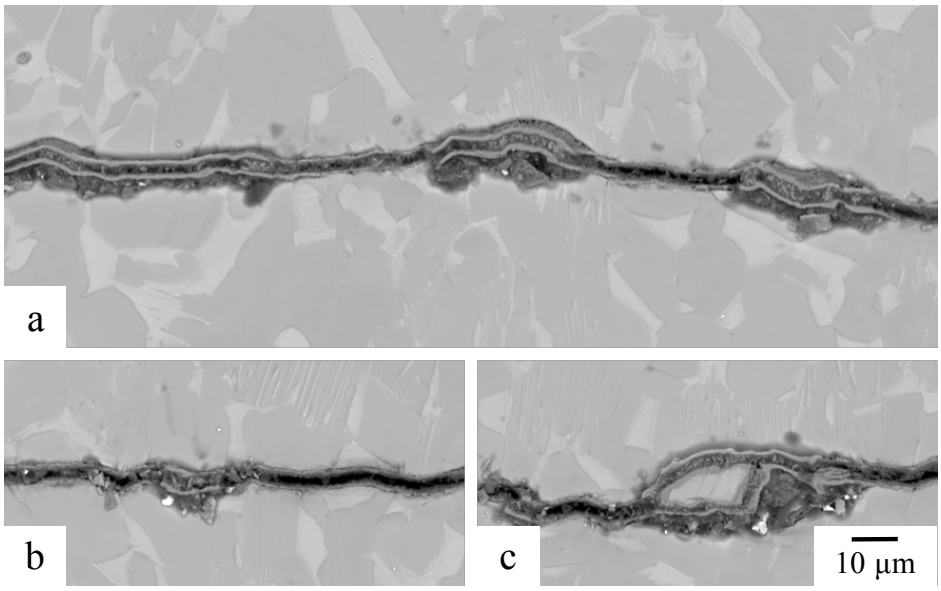

Fig. 5-16. SEM images of crack propagation pathway in Nearly Globular b/g Duplex at 1073 K.

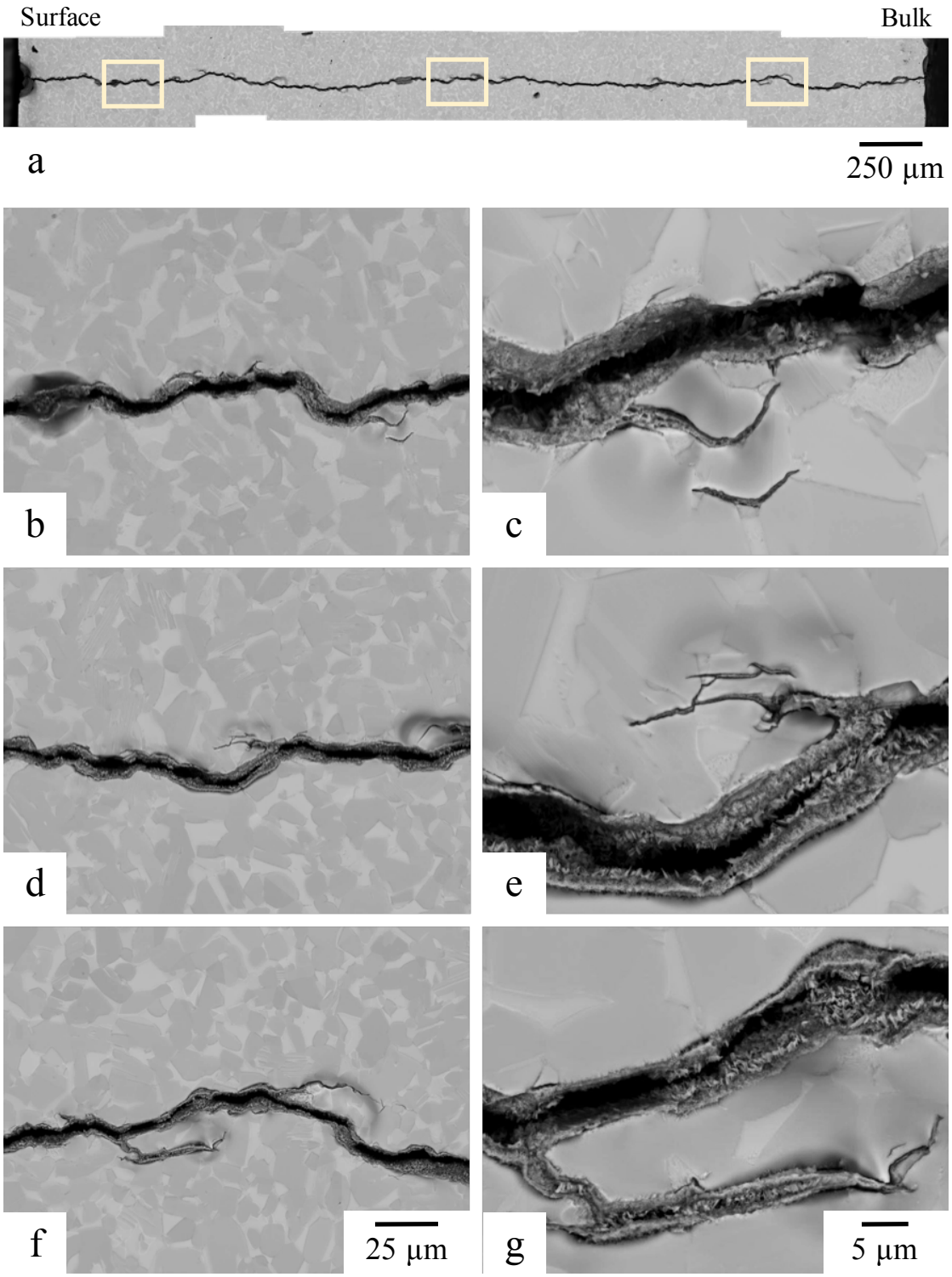

Fig. 5-17. SEM images of (a) general view of the slice between surface and bulk in Nearly Globular β/γ Duplex microstructure at 1073 K and (b-g) higher magnification views.

5.3.3 Fracture surface

Typical fractographs of the NL microstructure at 873 and 1073 K and NGDP microstructure at 1073 K are shown in **Figure 5-18**. The notch is located on the right side and the crack propagated from the right to the left of the CT specimen. The samples presented precrack, *K*-decreasing (only in case of NL at 1073 K), *K*-increasing and overload regions from right to left, respectively. Overload region corresponded to the fracture surface when the specimen ruptured.

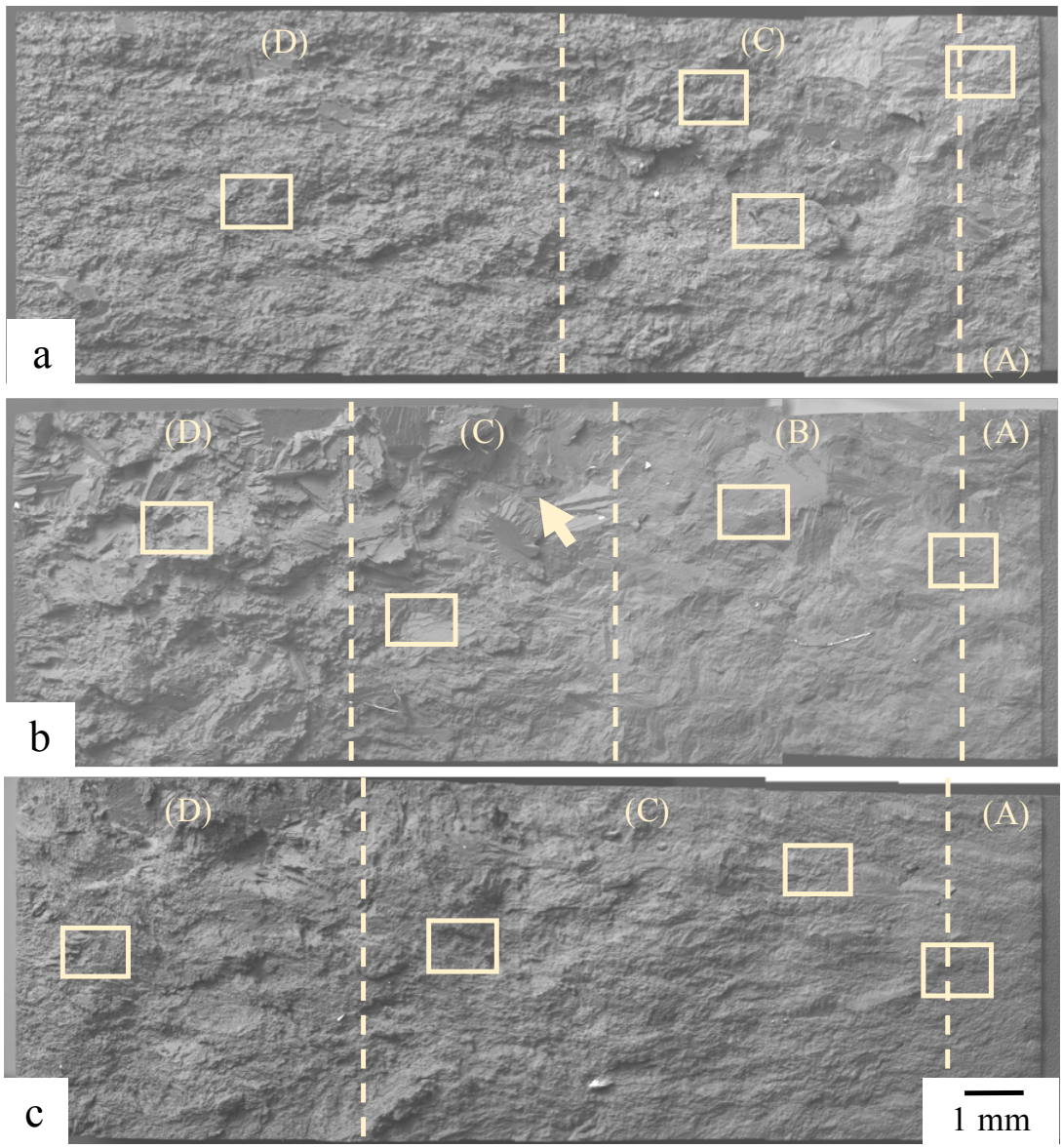

Fig. 5-18. SE images of fracture surface of CT specimen for NL microstructure at (a) 873 K and (b) 1073 K, and (c) NGDP microstructure at 1073 K. The vertical line at the right side of the image correspond to the end of the notch and the crack propagated from the right to the left side. A-D correspond to the precrack, *K*-decreasing, *K*-increasing, overload regions, respectively.

The examined fractographs at low magnification revealed that the surface at 873 K is similar to the room temperature one (**Chapter 4, Fig 4-34 (a)**) with all different regions presented an equivalent roughness. However, at 1073 K, the fracture surfaces in both microstructure showed the similar trend. As the crack propagates, the roughness drastically increased. Especially precrack and *K*-decreasing regions that were almost flat while the overload regions showed higher roughness compared to 873 K fractography. Temperature seems to enhance this phenom non. Indeed, it was also reported at room temperature and also exist at 873 K but in a lesser degree. As at ambient temperature, the roughness of NL is higher than NGDP and could be related to the grains size. Indeed, a fully lamellar inhomogeneity in microstructure have been observed on NL microstructure in the *K*-increasing region (indicated by arrow in **Fig. 5-18 (b)**) and presented the highest roughness.

Fatigue fractographs of the both microstructures at higher magnification in the precrack, *K*-decreasing, the *K*-increasing and the overload regions are shown in **Figure 5-19 to 5-21**. Cracks propagated from the right to the left. The different fracture modes have already been introduced in **Chapter 4** and have showed than it depends strongly of the microstructure. There are indicated by arrows in the figures. NL microstructure at 873 K show mainly brittle faceted fracture with small amount of plastic deformation (**Fig. 5-19**). At 1073 K and low ΔK, crack advance in the lamellar structure occurred mainly by translamellar fracture, resulting in the smoother fracture surface as reported earlier (**Fig. 5-20 (d)**). Moreover, due to the low crack growth rate near the ΔK_{th}, small globular particles of oxide were formed at the surface (long time needed to propagate). At higher ΔK, high propagation rates led to an increase of the interlamellar incidence and the formation of the rough surface. The frequency of secondary crack was limited compared to lower temperatures. Finally, in case of NGDP microstructure, the fracture surface is relatively flat, as observed at lower magnification, and show higher plasticity compared to RT with transgranular fracture and intergranular cleavage along all the different regions. However, in opposite to ambient temperature fracture, more the stress intensity increases, more the intergranular cleavage become dominant (**Fig. 5-21 (f)**), indicating a ductile fracture. Thus, at 1073 K, the crack propagation take place above the DBT temperature of NGDP microstructures. In the overload region, intergranular and transgranular modes govern the fracture behavior.

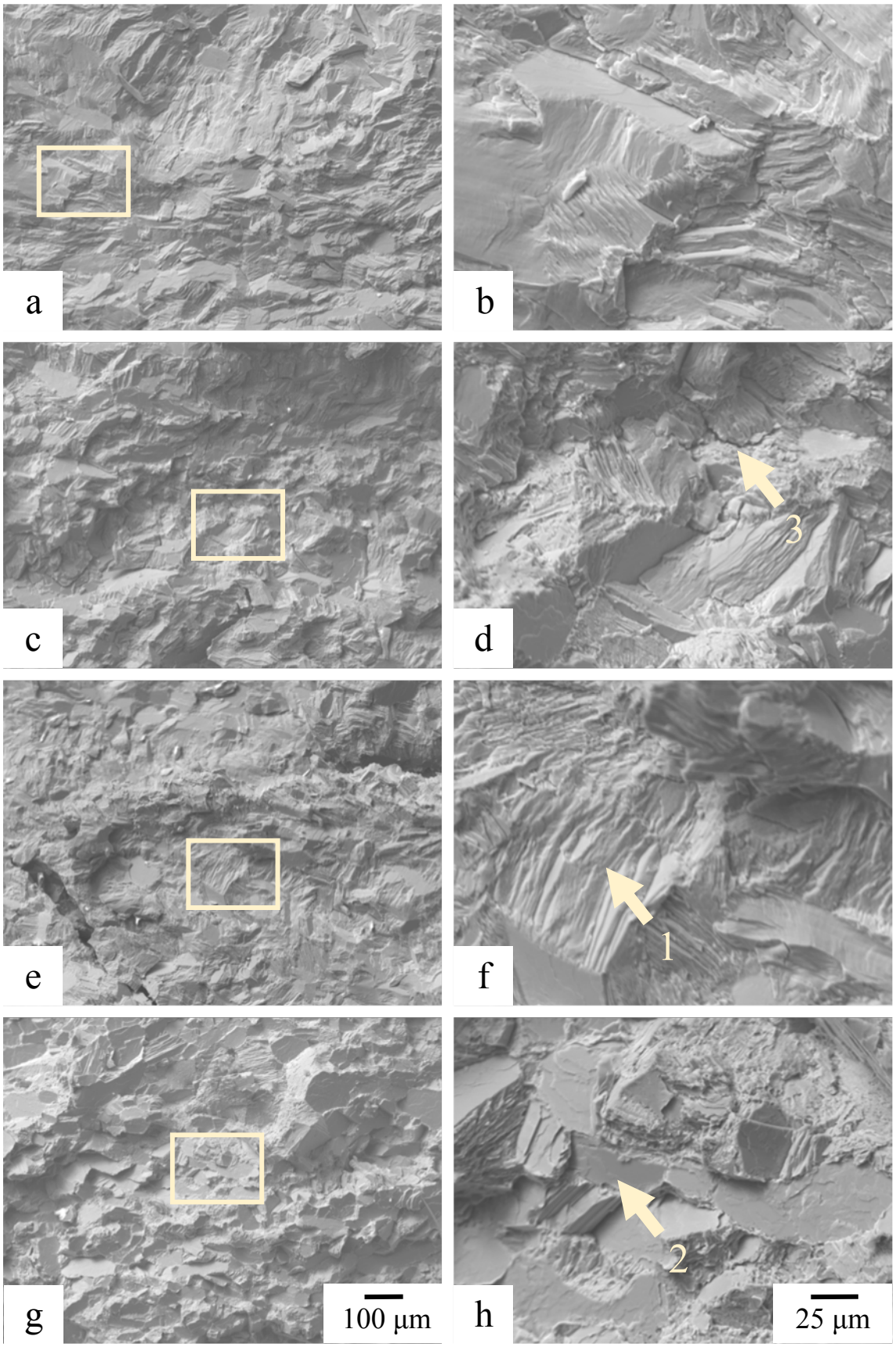

Fig. 5-19. Higher magnification SE images of fracture surface of NL sample tested at 873 K in (a, b) precrack region, (c-f) *K*-increasing region and (g, h) overload region. Different fracture modes are marked by white arrows (1) translamellar, (2) interlamellar. (3) correspond to secondary cracks.

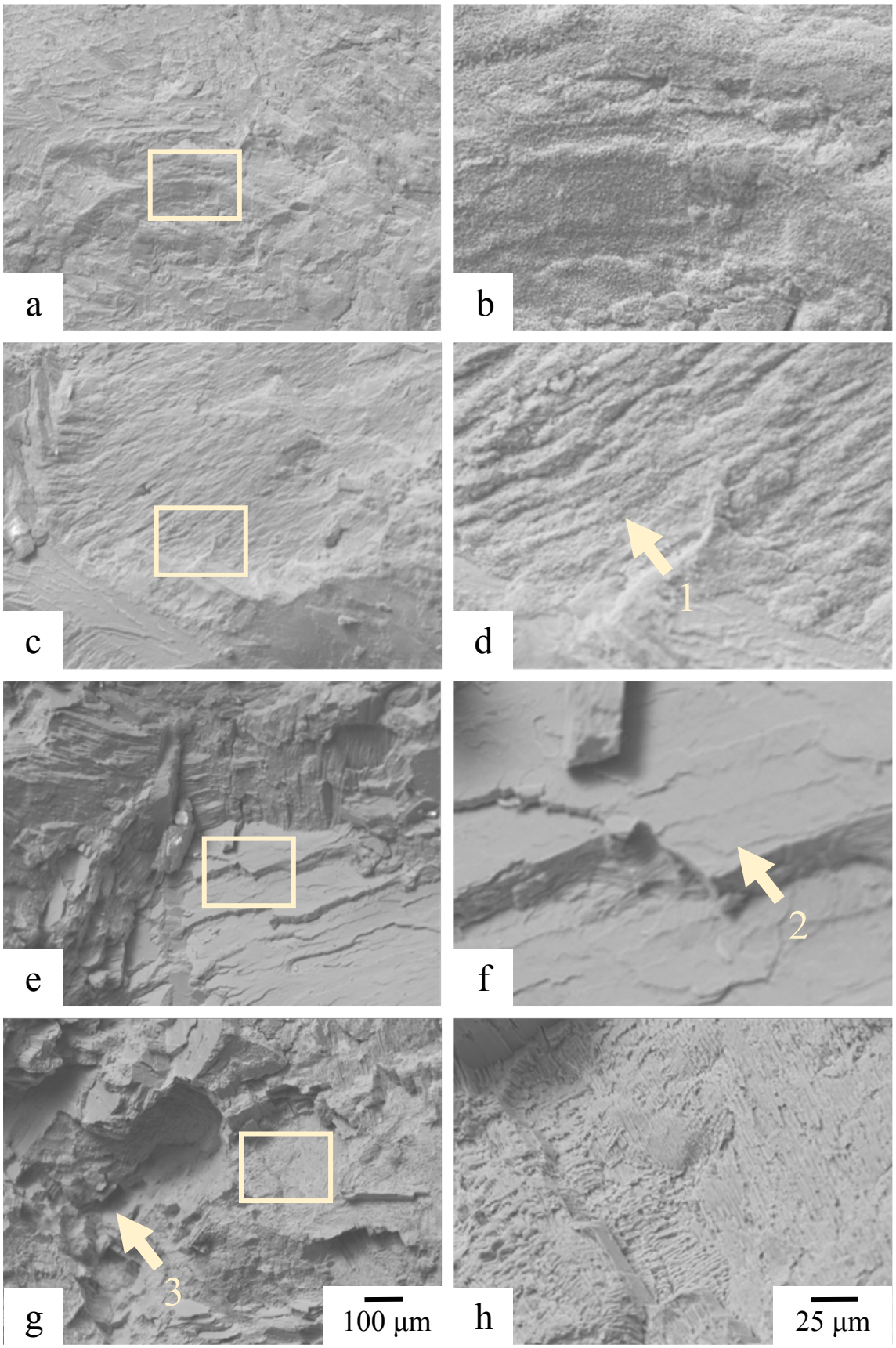

Fig. 5-20. Higher magnification SE images of fracture surface of NL sample tested at 873 K in (a, b) precrack region, (c-f) *K*-increasing region and (g, h) overload region. Different fracture modes are marked by white arrows (1) translamellar, (2) interlamellar. (3) correspond to secondary cracks.

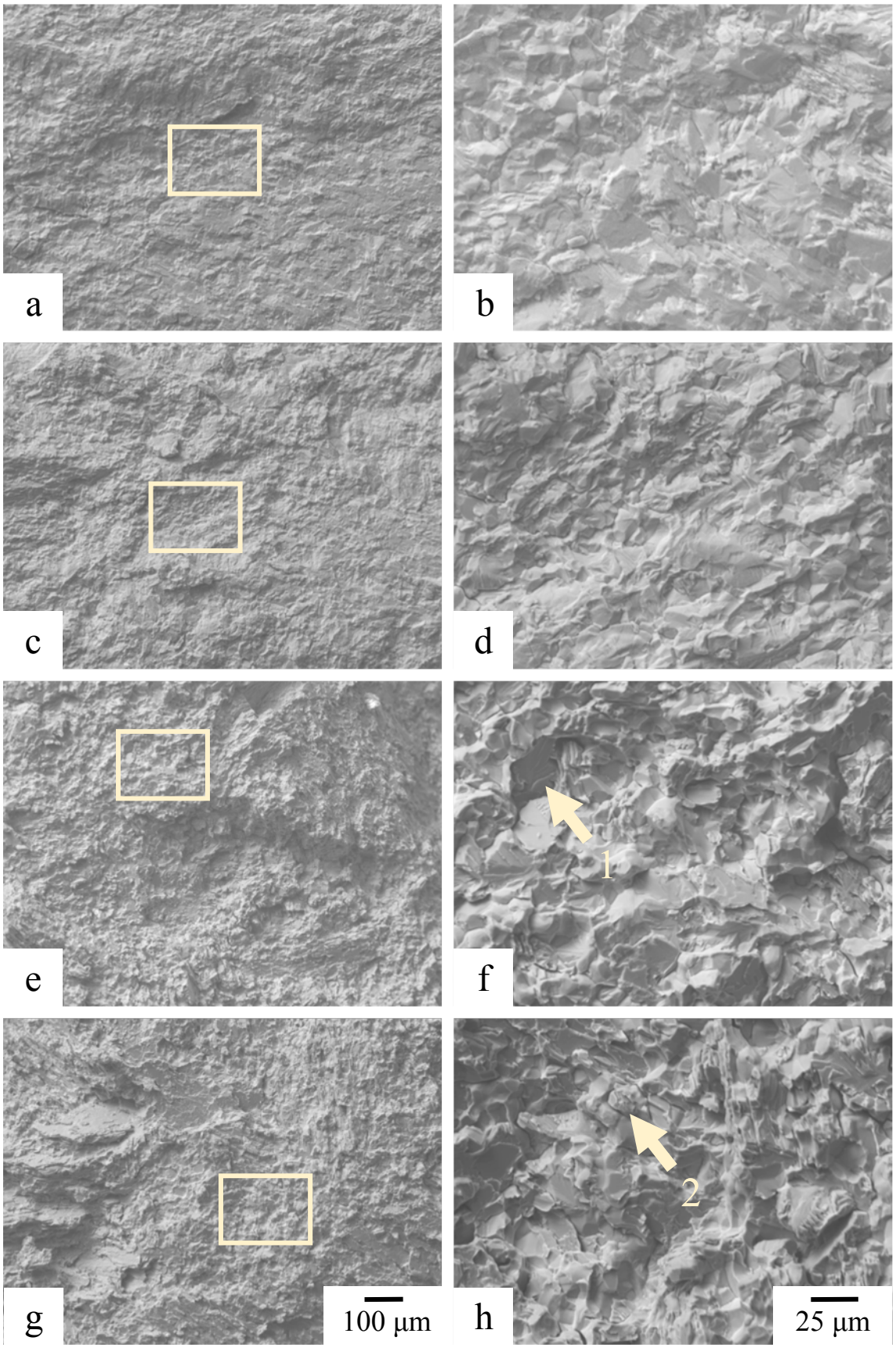

Fig. 5-21. Higher magnification SE images of fracture surface of NL sample tested at 873 *K* in (a, b) precrack region, (c-f) K-increasing region and (g, h) overload region. Different fracture modes are marked by white arrows (1) transglobular, (2) interglobular.

5.4 Discussion

5.4.1 Comparison of the FCG curve

The influence of temperature on the FCG behavior of the Nearly Lamellar microstructure of 43-4-5 alloy is shown and compared with others fully lamellar microstructures and the forged TNM alloy in **Figure. 5-22** [7, 8]. It should be noted that the FCG behavior at elevated temperature depends on frequency. The fatigue threshold gradually decrease between 298 and 873 K, went through a minimum and then steeply increase up to 1073 K. The difference between ambient and 1073 K fatigue threshold is about 1.1 MPa$\sqrt{m}$. The same phenomenon has already been reported for Fully Lamellar and Duplex microstructure [1, 3] with an increase of ΔK_{th} in the same order between 0.9 and 2.2 MPa$\sqrt{m}$ as shown in **Fig. 5-22 (b)**. The same tendency was observed in case of the maximum stress at the rupture. For remind, the maximum stress at the rupture can provide an estimation of the fracture toughness of the material. However, the Paris slope showed an opposite behavior: it decreased rapidly up to 873 K, indicating an improvement of crack propagation resistance, and then stabilized at higher temperature with a value of around 4.3. Between 873 K and 1073 K: both ductile-brittle transition temperature (DBTT) and oxidation occurred. The DBTT modified the nature of the present phases and strongly depend of microstructure with duplex microstructures causing lower DBTTs (around 873 K) and FL microstructures causing higher DBTTs (close to 1073 K). No evidence of thick oxide has been found at 873 K compared to 1073 K tested specimens. The specimen fracture occurred at high stress intensity, corresponding to high crack growth rates, and therefore the oxidation is relatively limited as observed on the fractography **(Fig. 5-20)**. In contrary, oxides can be formed at low stress, near fatigue threshold. However, the relative contribution of these both effects on the FCG behavior will be discussed in the following section.

At first glance, the fatigue crack growth resistance of Nearly Lamellar is also higher compared to β/γ duplex structure at elevated temperature. The effect of β/γ duplex volume fraction V_{DP} on fatigue threshold, Paris slope and maximum stress at overload at 298 and at 1073 K is illustrated on **Figure 5-23**. Whereas increased the volume fraction of β/γ duplex at the grain boundaries did not significantly affect the fatigue threshold – ΔK_{th} increased by 1.1 MPa$\sqrt{m}$ for NL and 0.8 MPa$\sqrt{m}$ for NGDP between 298 K and 1073 K – it showed major different for the maximum stress K_{max} at the rupture. For high β/γ duplex volume fraction, the stress K_{max} of NGDP increase by 10.2 and thus, reduced the

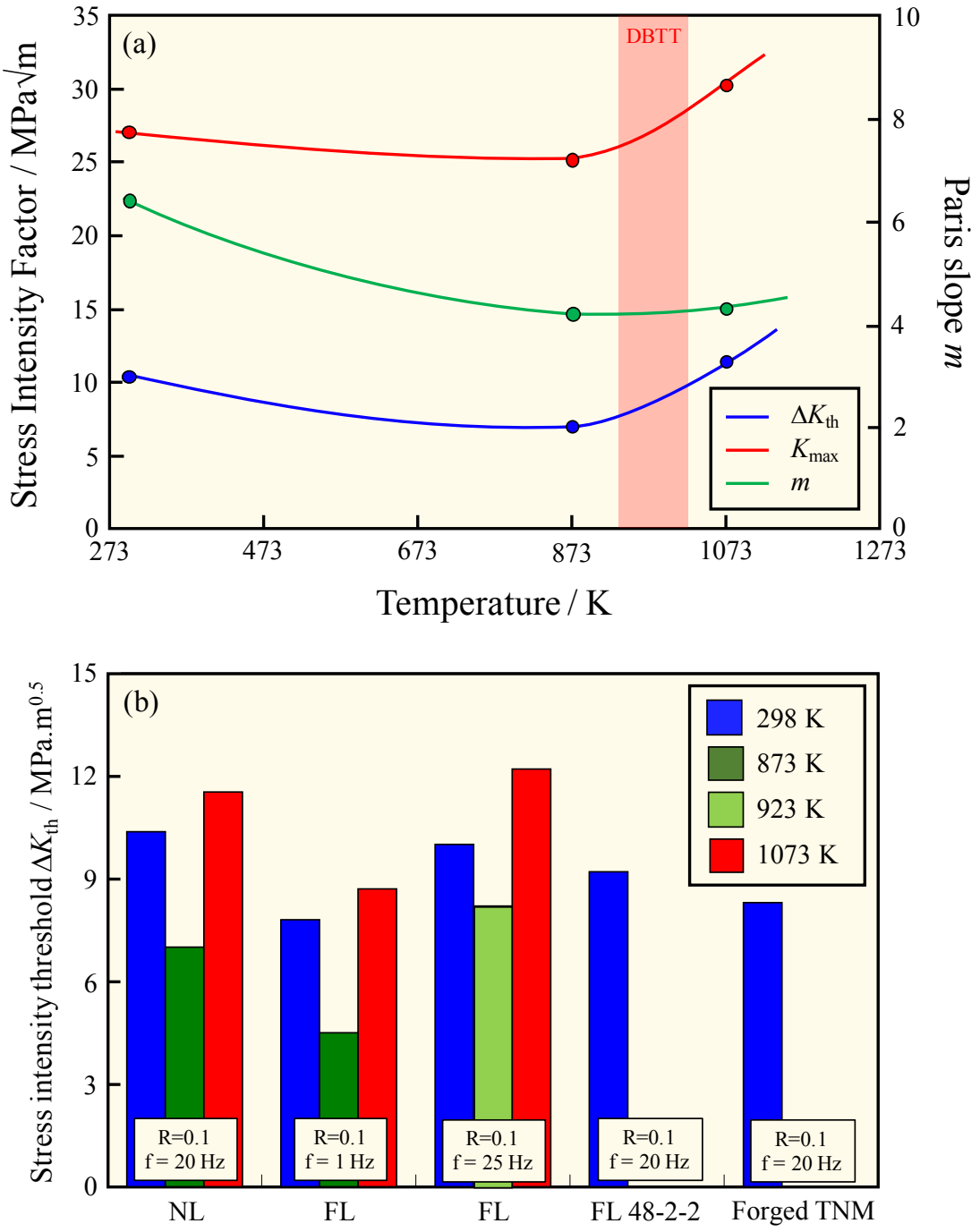

Fig. 5-22. Effect of temperature on (a) the fatigue crack growth behavior of wrought 43-4-5 alloy with the Nearly Lamellar microstructures and (b) comparison of ΔK_{th} with others γ-based TiAl [1, 3, 7, 8].

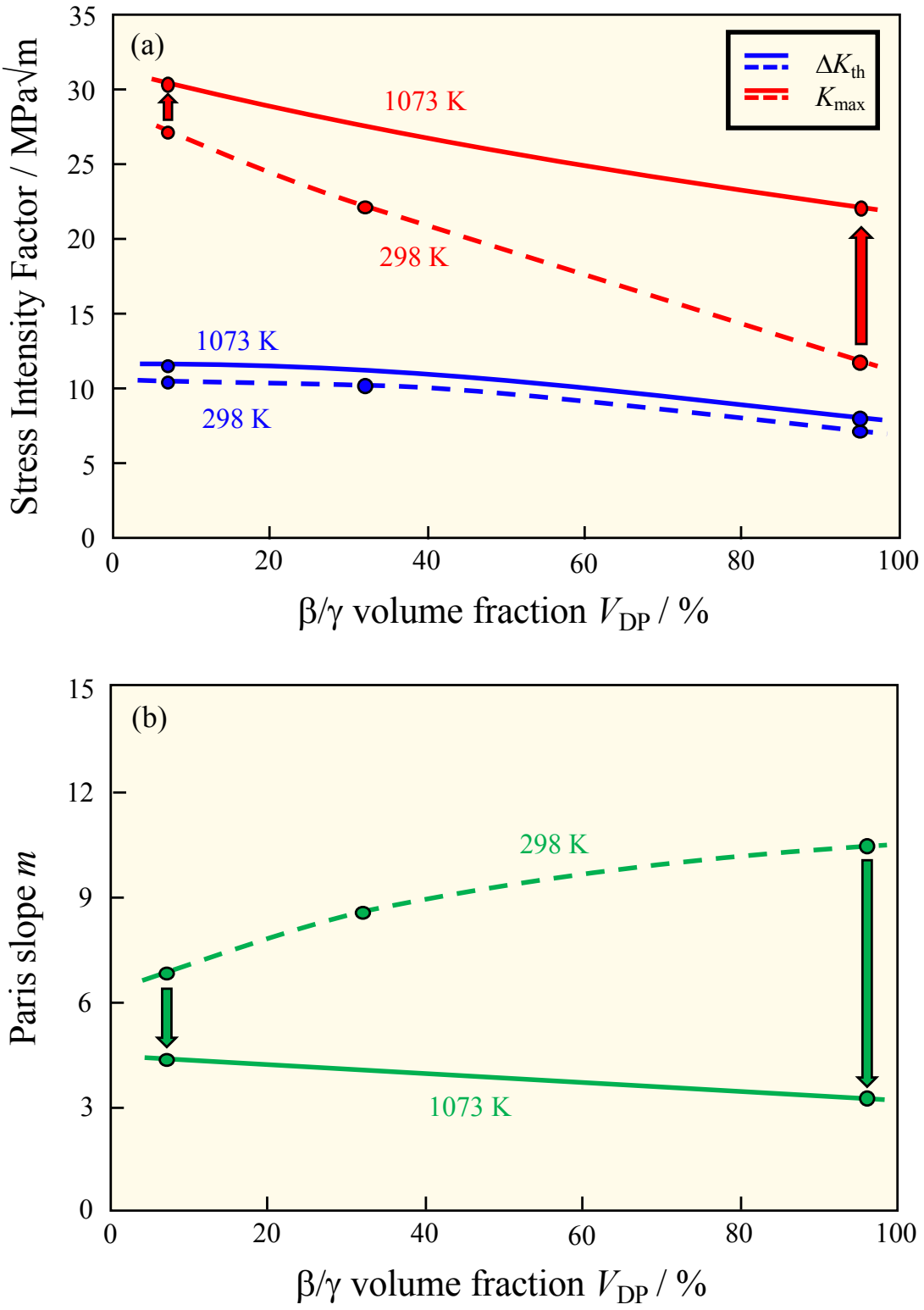

Fig. 5-23. Comparison of the effect of β/γ duplex volume fraction V_{DP} on (a) the fatigue threshold and the maximum stress at the rupture and (b) Paris slope of 43-4-5 alloy between 298 and 1073 K.

difference with the NL microstructures, regarding the room temperature results. Moreover, it has been reported that even at high temperature the presence of γ grains degraded the fatigue resistance in duplex alloy compared to lamellar microstructure. Therefore, despite the Paris slope decrease at high temperature, the duplex microstructure showed higher Paris exponents than lamellar [3, 9]. However, in case of β/γ duplex alloy (NGDP), the Paris slope at high temperature become lower compared to NL microstructure. So, β phase is effective to enhance the FCG behavior in Paris regime which became better than Nearly Lamellar microstructure.

5.4.2 Fatigue crack growth mechanisms

By closely studying the crack pathways and the fracture surfaces at elevated temperature, the fatigue mechanisms, which enhance or worsen the fatigue crack growth resistance, were identified and compared with those at ambient temperature. It revealed that generally the same mechanisms took place but in different proportions. Some examples are shown in **Figure 5-24**.

At 1073 K, in the NGDP microstructures, small linear steps can be seen on the surface in the γ grains or lamellar colonies surrounding the crack flanks (**Fig. 5-24 (a)**). As described in **Chapter 4**, it has been identified as thin twins with only a few hundred nanometers in thickness. These mechanical twinning reduces the stresses at the crack tip and consequently delay the cleavage fracture. The dislocations movement shows similar effect to twinning, however, its effect become much more pronounced at high temperatures. These both mechanisms modified locally the crystal structure and form microcracks in front of the crack tip (reduce fatigue resistance) or in crack wake (enhance fatigue resistance). An example is given with microcrack formation is NL at 1073 K in **Fig. 5-24 (b)**. The formation of multiple microcracks has been identified on surface of NL at 873 K, especially along the crack flank, and could explain why the fatigue threshold shows the minimum values at this temperature by increasing the stress at the crack tip. Eventually, the microcrack will coalesced with the main crack.

Others mechanism were identified at high temperature such as crack ligament bridging (**Fig. 5-24 (c)**) and crack deflections, which cause crack tip shielding.

It has been reported that crack closure mechanisms can significantly affect the stress intensity ΔK. At 1073 K, thick oxide layer has been identified and thus, may affect the FCG behavior through oxide-induced crack closure mechanism. Furthermore, by

increasing the temperature, the nature of the present phase will change, and, phase transformations may occur and therefore, also affects the fatigue resistance.

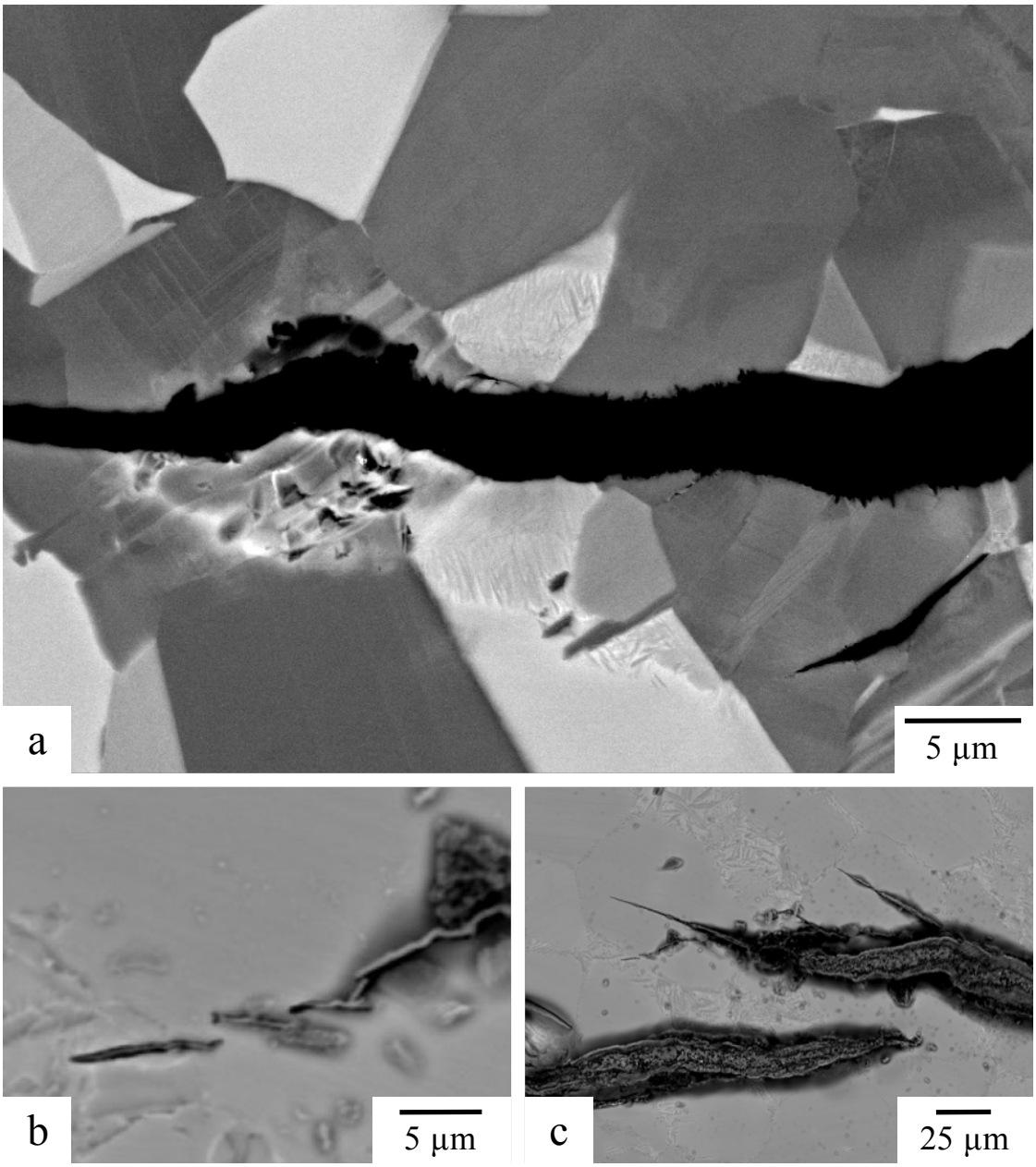

Fig. 5-24. Fatigue crack growth mechanisms at high temperature: (a) deformation of γ grain in NGDP, (b) microcrack formations and (c) Crack ligament bridging in NL.

In the following section, the effect of different mechanisms on FCG behavior such as oxide-induced crack closure or the nature of the phase will be discussed. Moreover, different phase transformations occurred during tests and their effect on FCG behavior will be also investigated.

5.4.3 Effect of temperature on fatigue threshold ΔK_{th}

In this part, the effect of temperature on the fatigue threshold will be discussed based on environmental embrittlement, oxide-induced crack closure and also oxidation phase transformation.

(A) Environmental embrittlement

Many authors reported that in case of γ-TiAl alloys, the fatigue resistance at 1073 K is similar to those at ambient temperature [3, 4, 18]. In the same time, at intermediate temperature, the fatigue resistance of γ-TiAl alloys drastically dropped and showed the worst fatigue behavior around 873 K. In this study, the same trend have been observed in both NL and NGDP microstructures. However, the reason of the loss of fatigue resistance is still not clear.

Larsen *et al.* [10] have proposed that the resistance to fatigue crack growth should normally increases with temperature, and that the "anomalous" fatigue crack growth behavior observed at intermediate temperatures was caused by an unspecified environmental embrittlement. This embrittlement is outweighed at higher temperatures by the higher plasticity of the microstructure (nature of phase). Hénaff *et al.* [11] investigated the effect of atmosphere and demonstrated that similar to steels or titanium alloys with hydrogen embrittlement at the crack tip, as-called Environmentally Assisted Fatigue Crack Propagation (EAFCP) mechanism, also occurs in γ-TiAl alloys. Therefore, this embrittlement is probably enhanced with the temperatures.

At the opposite, McKelvey *et al.* [4] suggested that the fatigue crack growth should normally decreases with temperatures based on different models for intrinsic fatigue crack growth. One of these models will be detailed later, i.e. minimum crack tip opening displacement ($CTOD_{min}$). They proposed that the fatigue crack growth are retarded at 1073 K and that the increase of the fatigue resistance was explained by the oxide-induced crack closure effect. This is consistent with the observations of NL and NGDP samples tested at 1073 K where a thick oxide layer completely filled the crack.

This apparent insensitivity of the fatigue resistance of γ-TiAl alloys between 298 and 1073 K is probably the result of several mechanisms (embrittlement, nature of phase or oxidation), which act simultaneously. Between 298 and 873 K, **environmental embrittlement** could the dominant mechanism. However, complementary investigations

should be conducted in inert atmosphere at intermediate temperature to clarify this. Preliminary results obtained at low vacuum are shown in **Appendix A.6**.

(B) Oxide-induced crack closure

Based on the model of oxide-induced crack closure proposed by McKelvey *et al.* mentioned before [4], the effect of the oxide layer formation have been evaluated.

The effect of temperature of the CT specimens surface is shown in **Figure 5-25** on NL microstructure. At 673 K, after few hours test, a thin oxide layer with a blue color formed at the surface. Moreover, the fracture surface showed different colored straight bands; each band correspond to a different level of oxidation (**Fig. 5-25 (g)**). These oxide bands were evidences that the front of the crack propagated at the same rates between the two side of the specimen and was in good agreement with the comparison of the crack on surface and in the bulk. Three bands were identified and corresponded respectively to the precrack (dark blue), *K*-increasing test (gold) and overload (chrome) regions. As

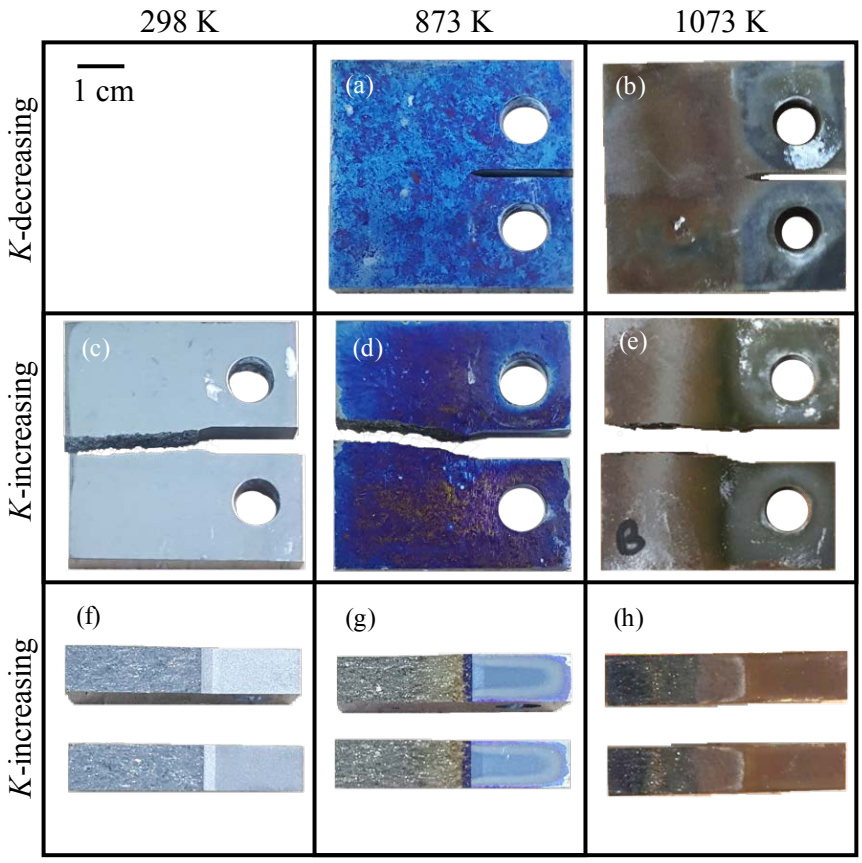

Fig. 5-25. Change of CT specimens surface and fracture of NL microstructures after tests at different temperatures.

mentioned in the experimental procedures, before starting tests, specimens were kept at the test temperature for 1 h and, therefore, explained why the precrack showed a higher oxidation level. However, the oxide layer was enough thin to conduct SEM observation without preparation directly after the fatigue test. At 1073 K, the thickness of the oxide layer drastically increased and the color change to brown. Furthermore, the initial microstructure could not be observed anymore. The fracture surface revealed five oxidation bands. From right to left, respectively: precrack (white), *K*-decrease at 298 K (brown), *K*-decrease at 1073 K in argon (gray), *K*-increase (gold) and overload (blue) regions. Only the three last bands showed metallic surfaces whereas the precrack and the *K*-decrease at 298 K regions showed oxide surface.

The rapid development of the oxide layer can be easily explained by the oxidation resistance of TiAl alloy. Indeed, γ-based TiAl alloy showed usually a good oxidation resistance up to 900°C [12]. However, addition of vanadium trend to decrease the oxidation resistance. Domingo *et al.* determined the oxidation kinetic at 1073 K of the 43-4-5 system along with the 48-2-2 and the TNM alloy as shown in **Figure 5-26** [13]. The studied alloy showed an oxidation resistance 10 times and 20 times worsted than 48-2-2 and TNM alloys, respectively.

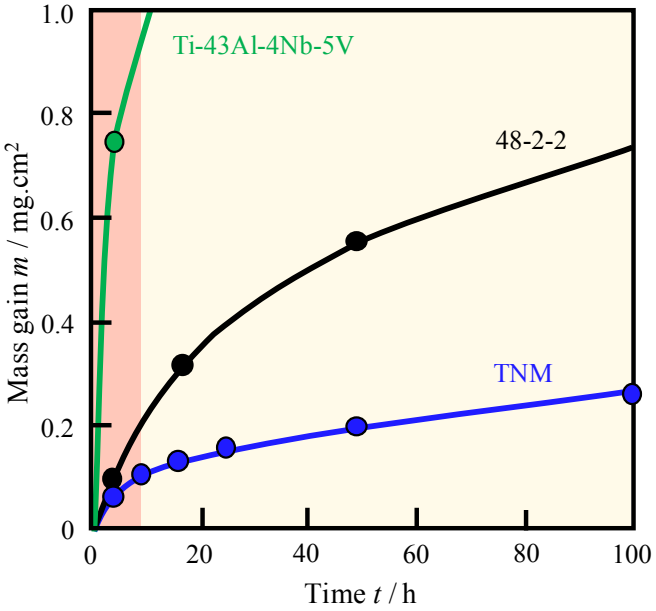

Fig. 5-26. Comparison of the oxidation kinetic at 1073 K of 43-4-5 alloy with 48-2-2 and TNM alloys [13]. Red band indicated tests time.

In order to determine what kind oxides formed during fatigue tests, SEM were conducted on NL microstructure after high temperature test as shown in **Figure 5-27**. It revealed that the oxide was composed of four different layers. The deepest one appeared white on the figure and measured only few hundred nanometers of thickness. The second layer was the thicker one. The third layer was also thin (less than 1 μm) and the last layer showed columnar morphology. A qualitative analysis of the oxide composition of a secondary crack was conducted by SEM-EDS and the element mapping is shown in **Figure 5-28**. The analysis of aluminum and titanium indicated that the different layers consisted of TiO_2, Al_2O_3, a second layer of TiO_2 and, a composed oxide TiO_xN_y. However, the oxide film mainly consisted of the two TiO_2 oxide layers.

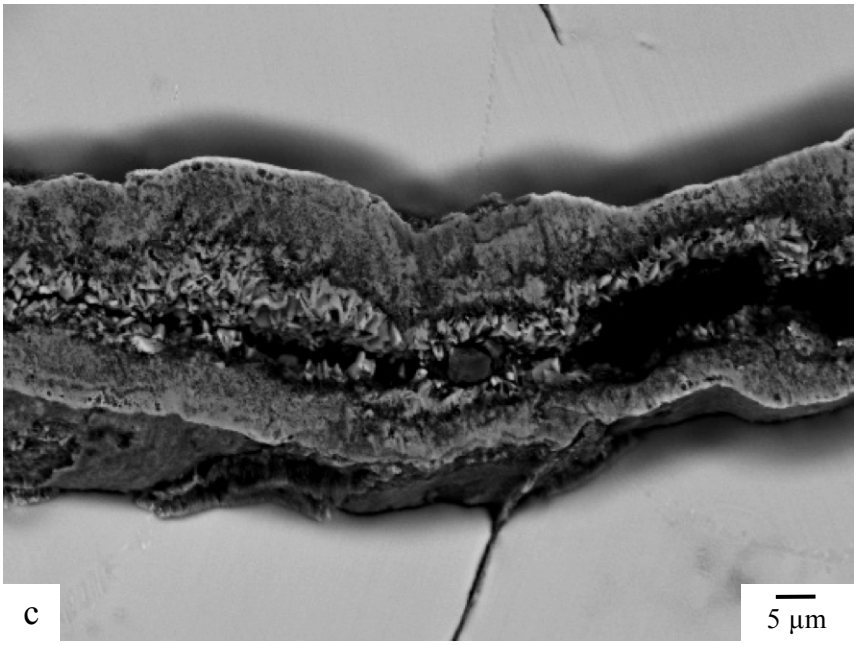

Fig. 5-27. Oxides formation composed different layer occurred at cracks surface during tests at 1073 K. Here an example is given from the NL microstructure.

The following part will describe how this oxide layer affected the FCG behavior at high temperature. Actually, more the oxide formed during test, more the crack was filled, resulting of an oxide-induced crack closure effect. The fatigue crack growth occurs only when the crack is fully open. However, under unload cycles, the stresses preload the crack faces against each other, reducing the crack driving force. This effect is called crack closure effect and therefore an effective stress intensity range, ΔK_{eff}, can be defined as shown in **Equation 5-1**:

$$\Delta K_{eff} = K_{max} - K_{cl} \text{ when } K_{cl} \geq K_{min} \quad (5\text{-}1)$$

With K_{cl} represent the closure stress intensity. The theoretical effect of the oxide-induced crack closure can be calculated based on the closure model developed by Suresh and Ritchie, assuming that the oxide layer is a rigid wedge inside the crack [14]:

$$K_{cl} = \frac{dE}{4\sqrt{(\pi l)}(1-\nu^2)} \tag{5-2}$$

Where d is the excess oxide thickness, $2l$ is the length oxide film close behind the crack, ν is the Poisson coefficient and E is the Young's modulus as illustrated in **Figure 5-29** [15]. The length $2l$ where the oxide completely filled the crack was difficult to measure and have been estimated at 930 μm based on SEM images in NL microstructure with a thickness of about 14.2 μm. In order to determine the excess oxide relative to the total oxide thickness, the Pilling-Bedworth (P-B) ratio that was used in the study of McKelvey *et al.* was applied for comparison [4]. P-B ratio give the volume ratio of oxide to metal of an oxidation reaction [16]. Despite the authors only consider the formation of TiO_2 and Al_2O_3, it could provide a good approximation of the excess materials. Therefore, the calculated excess oxide thickness d was about 10.7 μm. Results indicated than film-oxide show larger thickness compared to the minimum crack tip opening displacement ($CTOD_{min}$) calculated at 1073 K (46.1 nm). The crack tip opening displacement ν under plain strain was determined using **Equation 5-3** in Ref. [17]:

$$\upsilon = \frac{K^2}{2\sigma_Y E} \tag{5-3}$$

Where $CTOD_{min}$ is calculated using K_{min}. *Ex-situ* Young's modulus E and yield stress σ_y of NL at 1073 K, i.g. 133 GPa and 445 MPa, respectively, and a Poisson coefficient of 0.3 were used for calculations. From **Eq. 5-2**, values of K_{cl} at 1073 K of the analyzed specimen with a NL microstructure was estimated to be 10.2 MPa$\sqrt{m}$ at load ratio of 0.1 as shown in **Figure 5-30**. Since the extent of crack oxidation became important with d about 200 times larger than $CTOD_{min}$, resulting a reduction of near crack-tip driving force (K_{cl}/K_{max}) by about 84%. These results should be compared with the reduction of 77% observed in Duplex microstructure (30% of γ grains) [4]. Moreover, effective stress intensities have been determined in K5 alloy (Ti-46A1-3Nb-2Cr-0.2W) with coarse lamellar and duplex microstructures showed that the fatigue threshold at 1073 K were about 7 and 5 MPa$\sqrt{m}$, respectively [18]. These results are more important than the studied Nearly Lamellar microstructure containing β-phase. The ΔK_{eff} of NL microstructure is lower in comparison of β-free TiAl alloys (FL or Duplex), however the

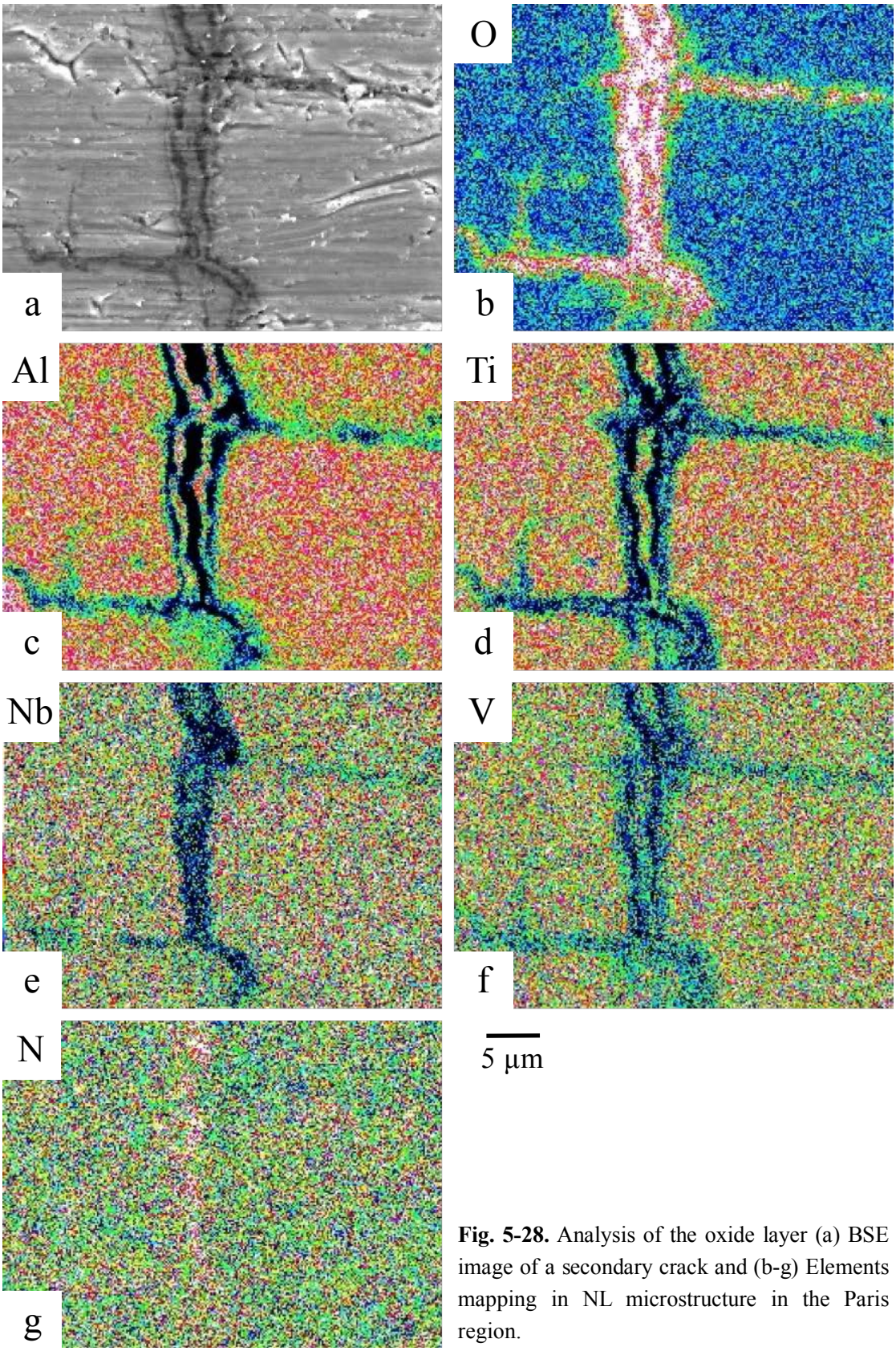

Fig. 5-28. Analysis of the oxide layer (a) BSE image of a secondary crack and (b-g) Elements mapping in NL microstructure in the Paris region.

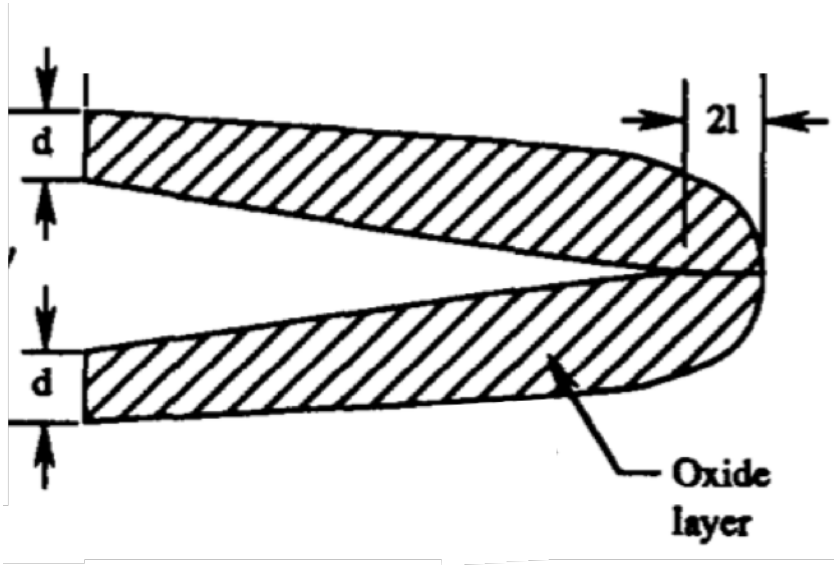

Fig. 5-29. Schematic illustration of the mechanism of oxide-induced crack closure [15].

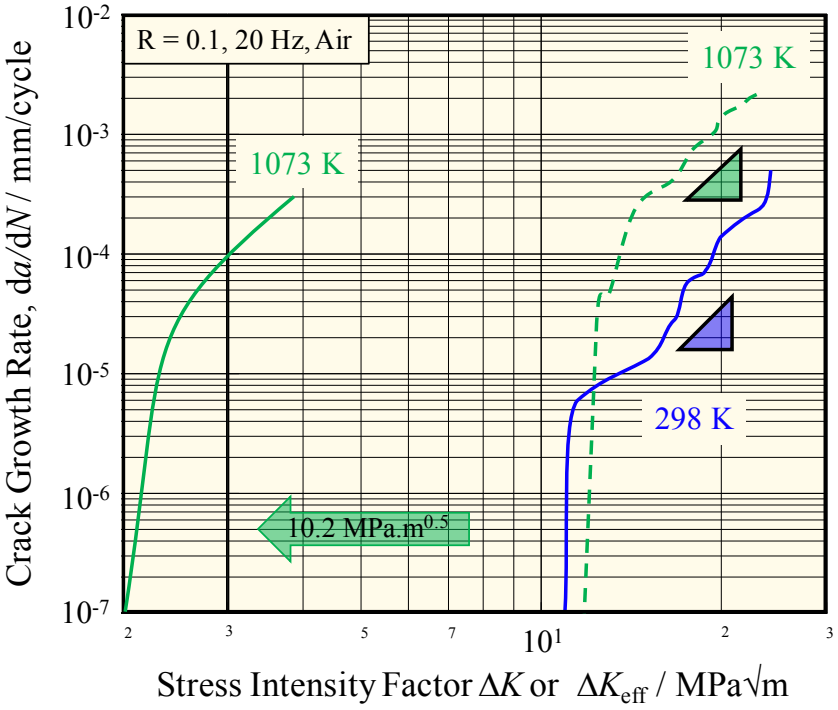

Fig. 5-30. Effect of oxide-induced closure on fatigue threshold of NL microstructures at 1073 K. Dotted line represent the measured stress intensity at 1073 K.

K_{cl} measured was relatively important. It resulted a stress intensity ΔK equivalent to Fully Lamellar at 1073 K. These results indicated than the presence of β phase decreased the ΔK_{eff} but promoted the oxide-film formation during the test, resulting a high reduction of the near-crack tip driving force. Indeed, as observed in **Fig. 5-15**, the β/γ duplex region that contained βphase shown higher oxide thickness.

- **Effect of the plastic zone at near fatigue threshold intensities**

As detailed in **Chapter 4**, the plastically affected region could give an estimation of the effect of ΔK on the crack pathway and fracture roughness change regardless the microstructural features and help to understand how β/γ duplex affected the FCG behavior in both Paris regime and fatigue threshold.

In case of low stress intensities, near-threshold value, the calculated sizes of the plastically affected zones radius of both microstructures between ambient and elevated temperature at the fatigue threshold assuming the plane strain conditions are given in **Table 5-4**. It can be seen that at the fatigue threshold the plastic zone size of NL decreased from 31 μm at 298 K to 16 μm at 873 K. Then, it increased up to 44 μm at 1073 K. The decrease of the stress yield with increasing temperature did not affected significantly the plastic zone. However, as mentioned in the previous section, at elevated temperature oxidation occurred. The plastic region has been also determined using the effective stress intensity ΔK_{eff} calculated, i.e. ΔK_{th} = 2.1 MPa$\sqrt{m}$. It can be see that the monotonic plastic zone radius dropped drastically to 1.5 μm. This size was in the same order of the oxide

Table 5-4. Plastic zone size determined at the stress intensity threshold at different temperature of NL and NGDP microstructures.

Microstructure	Temperature / K	ΔK / Mpa$\sqrt{m}$	K_{max} / Mpa$\sqrt{m}$	Monotonic plastic zone r_0 / μm	Cyclic plastic zone r_0' / μm
Nearly Lamellar	298	10.4	11.6	31	6.2
	873*	7.0	7.8	16	3.2
	1073	11.5	12.8	44	8.9
	1073**	2.1	2.3	1.5	0.3
Nearly Globular β/γ Duplex	298	7.1	7.9	13	2.7
	1073	7.9	8.8	21	4.3
	1073**	1.9	2.1	1.2	0.3

*σ_y was calculated using linear regression between 298 and 1073 K; σ_y = 454 MPa.
**ΔK_{eff} was used for calculation

thickness formed near the crack tip. Hence, at the fatigue threshold the plastic zone size became smaller than the hard but brittle oxide layer. In other words, more the crack propagated and the stress intensity decreased (approaching the ΔK_{th}), more the oxide layer thicknesses increased. Therefore, the crack closure effect was more important and the plastically affected region size decreased. Finally when the plastic zone become smaller than the oxide, the cracks stopped to propagate. A schematic illustration of the change of plastic zone size in NL is illustrated in **Figure 5-31**. At 873 K, this effect also exist but in less proportion due to the thin oxide-layer.

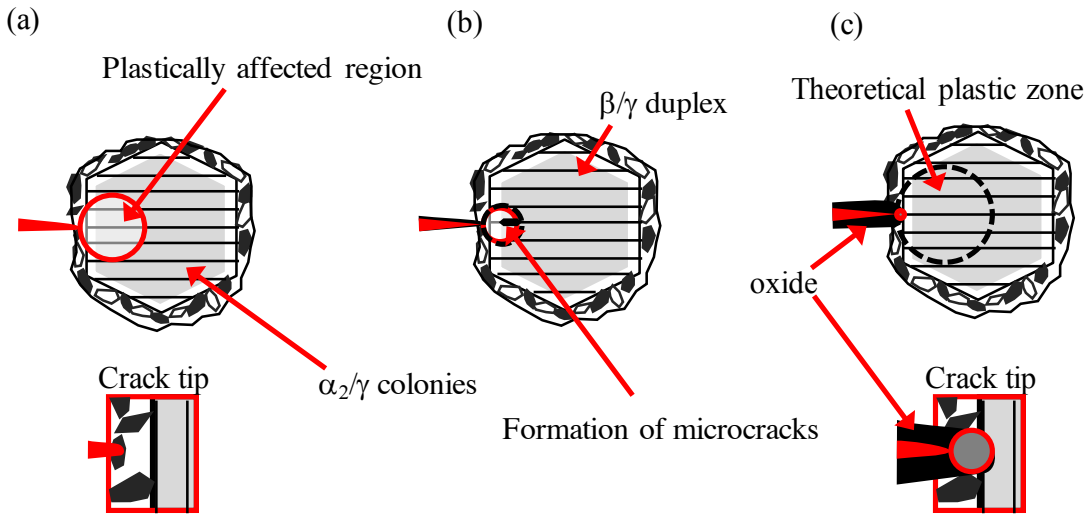

Fig. 5-31. Schematic illustration of the effect the plastic zone at the stress intensity threshold in NL compared at (a) 298 K, (b) 873 K and (c) 1073 K.

Therefore, the **Oxide-Induced Crack Closure (OICC)** effect seems to be a dominant factor of the control of fatigue threshold ΔK_{th} at high temperatures (around 1073 K). This effect is enhanced by the presence of β phase in DP region that promote TiO_2 oxide formation as Ti-rich source.

(C) Oxidation-induced phase transformations

During FCG test, it has been reported that phase transformations may induced crack closure due to volume changes. Moreover, stress-induced phase transformations have been identified in titanium aluminides alloys such as TNB-V2 where the orthorhombic B19 (equivalent to α_2 superstructure) transformed into γ phase [19]. In the studied wrought alloy, two different phase transformations have been identified and will be discussed in this section.

- **Decomposition of β phase: $\beta \rightarrow \alpha_2 + \gamma$**

The effect of β phase on the fatigue crack behavior have been investigated in NGDP microstructure due to the higher volume fraction of β phase in comparison to NL. After tests at 1073 K, precipitates have been observed only in β grains and along the crack flanks, indicated that phase transformation occurred. The observation of the crack revealed that the phase transformation was decomposed in two steps as shown in **Figure 5-32**. At the crack tip, a first phase precipitated with elongated shape and a size smaller than 2 μm orientated from the crack to the β grain (**Fig. 5-32 (a)**). Between these grains, the remained matrix β showed higher brightness. Then, near the crack tip, the precipitated coalesced to form a continuous film and the thickness increased up to 5 μm (**Fig. 5-32 (b)**). Finally, far from the tip in the crack wake, a secondary phase precipitated with globular shape grains but the total thickness of the phase transformed region was not changed (**Fig. 5-32 (c)**). The phase transformation was observed only in β grains that were in direct contact with the crack indicating a possible oxidation-induced effect.

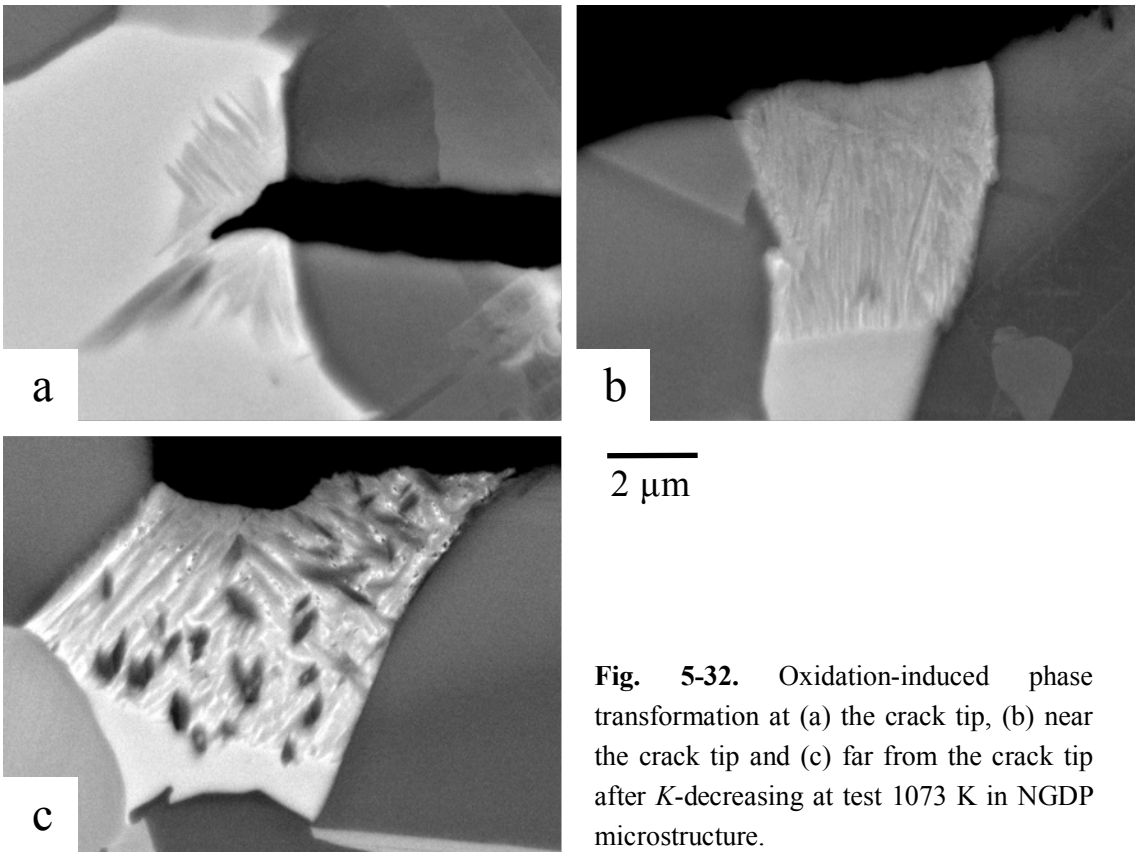

Fig. 5-32. Oxidation-induced phase transformation at (a) the crack tip, (b) near the crack tip and (c) far from the crack tip after *K*-decreasing at test 1073 K in NGDP microstructure.

In order to verify the origin of the phase transformation (stress-induced or oxidation-induced), heat treatment was conducted on NGDP microstructure, without conducting test, at 1073 K for 4 h. This time corresponded roughly to the duration of a FCG *K*-decreasing test. The SEM images observation of the microstructure revealed also that in β grains directly below the oxide layer, phase transformation also occurred as shown in **Figure 5-33**. Therefore, **Oxidation-Induced Phase Transformation (OIPT)** took place into β during test.

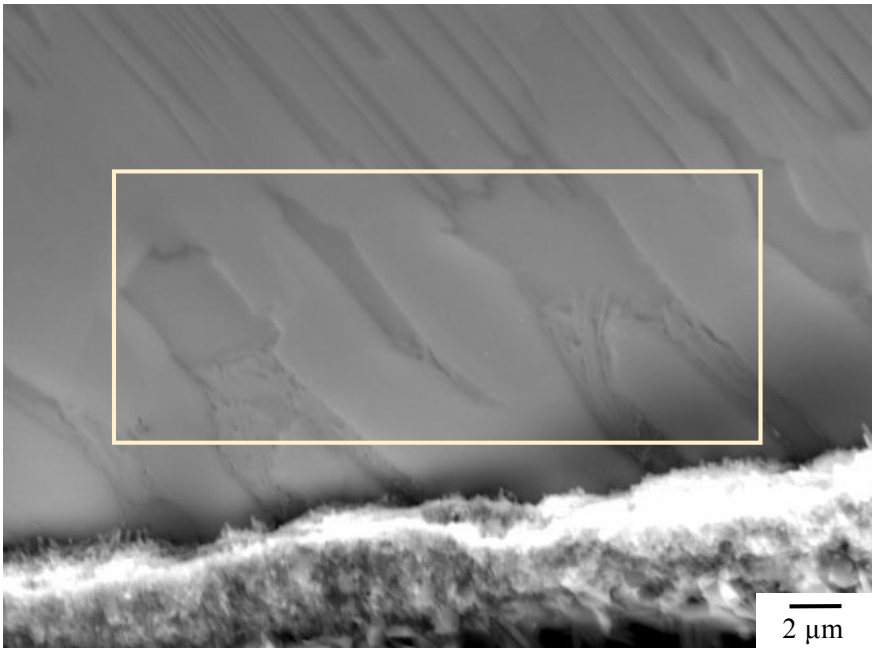

Fig. 5-33. SE image of oxidation-induced phase transformation occurred out of test in NGDP microstructure aged at 1073 K for 4 h.

In order to determine the nature of the different precipitates, EBSD analysis was conducted as shown in **Figure 5-34**. It revealed that the primary and secondary phase were α_2-Ti_3Al and γ-TiAl phases, respectively.

The oxidation-induced phase transformation has been identified as follow:

(1) When β phase was in contact with air, oxygen diffused into the grains. The increase of oxygen content modified locally the phase equilibrium (**Fig. 5-35 (a)**). Kinouchi demonstrated that oxygen trend to shift the β/α_2/γ tie-triangle toward higher aluminum and higher M content [20]. Therefore, the **decomposition $\beta \rightarrow \beta' + \alpha_2$** take place, where β and β' are the same phase but with different compositions. The precipitates α_2 grew with a columnar-like shape. Moreover, the remained β' showed a higher M concentration

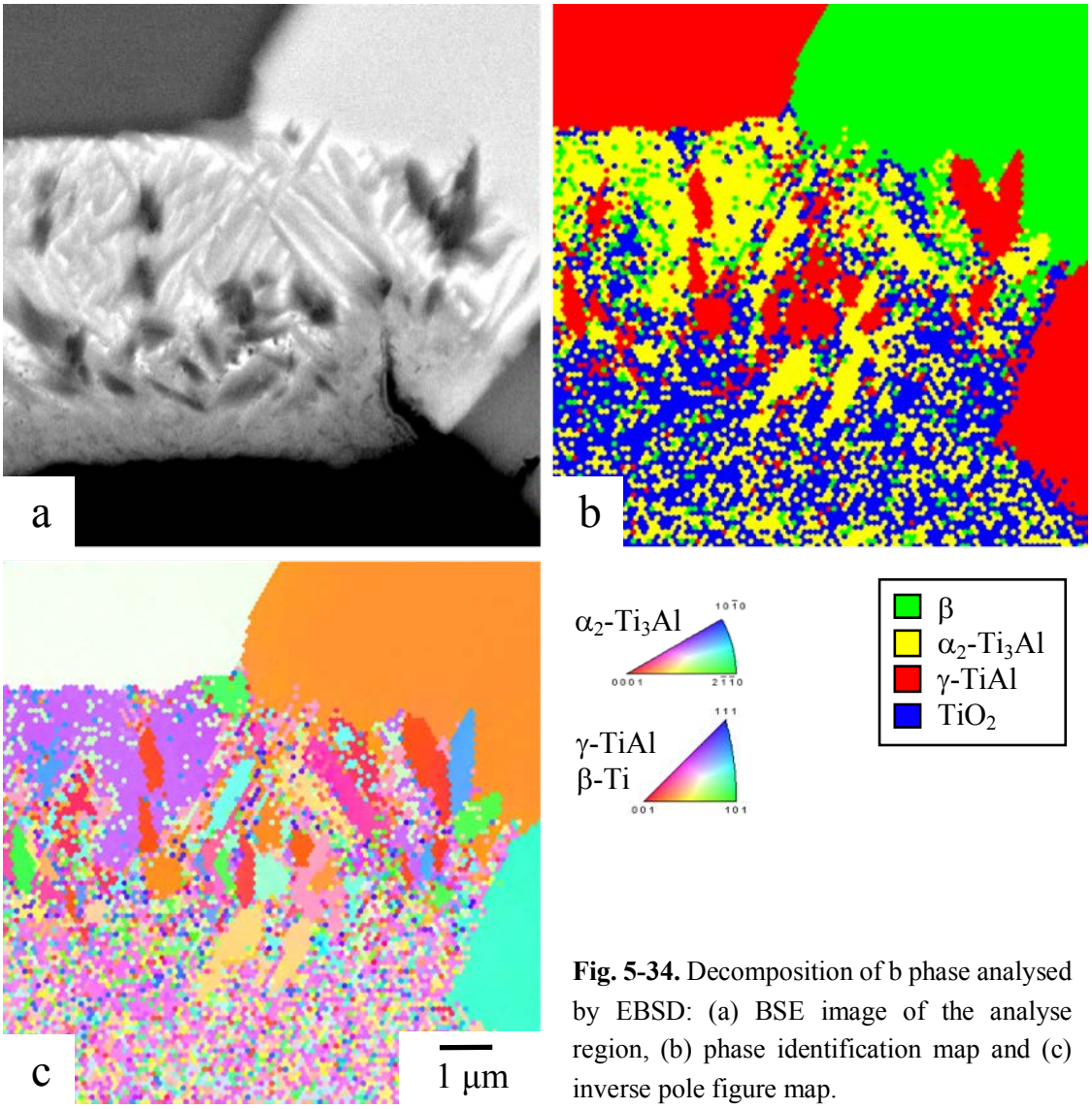

Fig. 5-34. Decomposition of b phase analysed by EBSD: (a) BSE image of the analyse region, (b) phase identification map and (c) inverse pole figure map.

and explained why the phase appeared brighter on the SEM image.

(2) As, identified in the previous section, the oxide-film consisted mainly of TiO_2 and somewhat of Al_2O_3. Thus, the formation of TiO_2 oxide conducted to a depletion of titanium content in the region close to the crack (**Fig. 5-35 (b)**). Due to the Ti depletion, the local alloy composition is changed and shift toward higher Al content. Moreover, by acting as a titanium source, the oxide layers close to the β grains were sensibly thicker in both NL and NGDP microstructures.

(3) Finally, the precipitate α_2 became no longer stable and a second **decomposition $\alpha_2 \rightarrow \alpha_2' + \gamma$** took place with globular γ grains (**Fig. 5-35 (c)**).

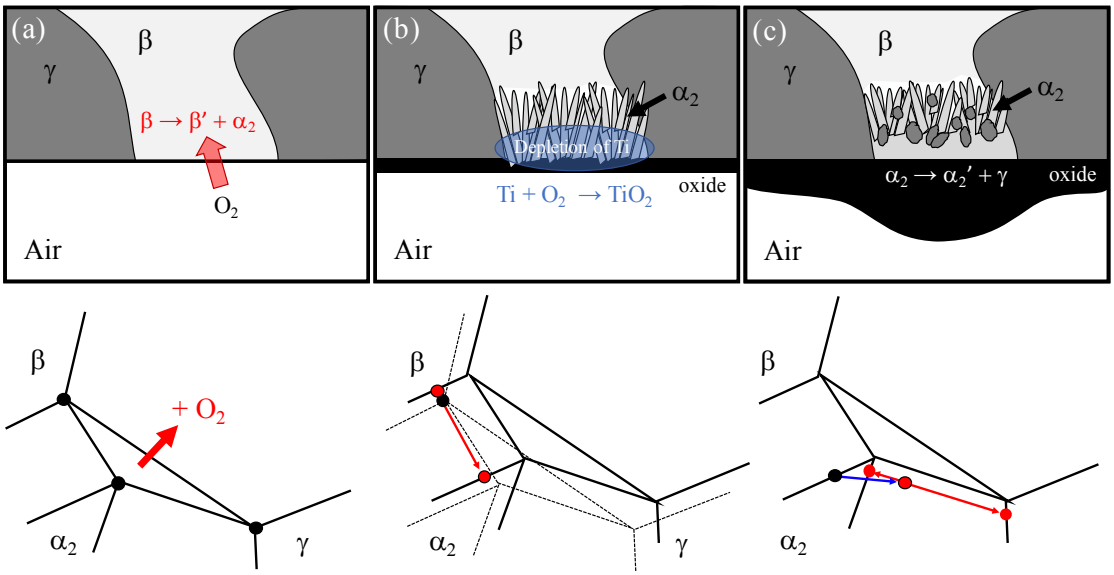

Fig. 5-35. Oxidation-induced phase transformation mechanism of β phase. (a) Diffusion of oxygen modify local phase equilibria and α_2 phase precipitated. (b) Then, during formation of the oxide layer, the depletion of titanium changed the local composition which led to (c) the precipitation of γ grains.

The decomposition process is directly correlated to the oxygen exposure time at high temperature: more the fatigue test was longer more the phase transformation occurred. However, the effect of this phase transformation on FCG properties was difficult to evaluate quantitatively.

As mentioned, phase transformation can induce crack closure of the tip due to the volume change between the two phase. Because at the crack tip, only α_2 precipitated, the volume change between α_2 and β have been calculated. Since, the elementary cell of α_2 have 6 atoms, three β cells were used for equivalent comparison. The volume ratio was estimated to be 1.18. Therefore, the β decomposition created a positive stress field at the crack tip that could induce crack closure effect. Though, with a thickness of only 2 µm and in the β grains only (V_β = 20 % in NGDP) the phase transformed region closure effect was probably negligible against the oxide-induced crack closure mechanism and did not effected the FCG behavior.

Nevertheless, a second effect have to be considered: the weakening of the crack tip. Indeed, the phase transformation occurred directly at the tip. The crack pathways analysis revealed that even at 1073 K crack stopped at DP region in γ or at β/γ interface. Hence, as same as ambient temperature, the β phase has also the higher toughness at high temperature. By precipitating the α_2 phase, the phase transformation created a weak point

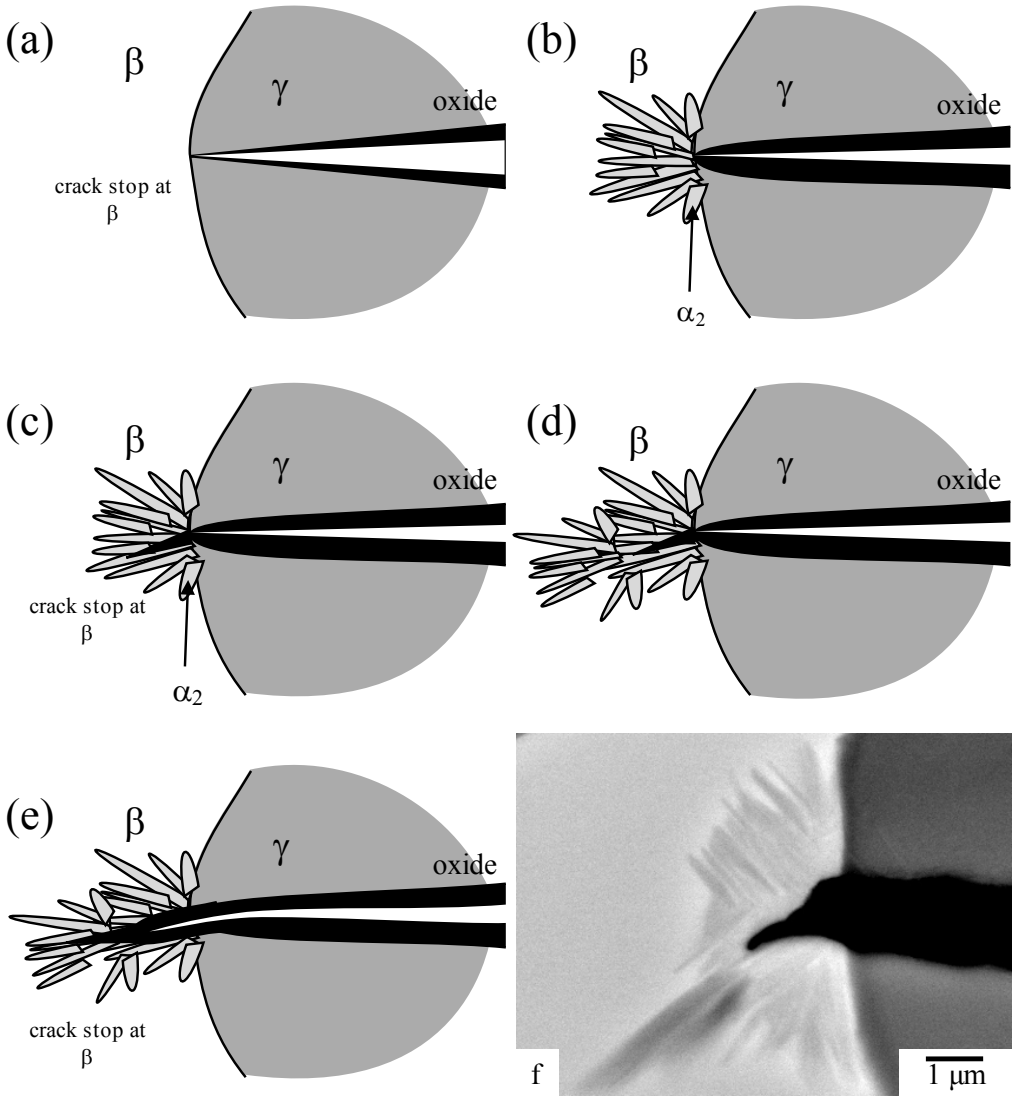

Fig. 5-36. β phase transformation-induced weakening of the crack tip mechanism: (a) crack stopped at β interface. (b) oxide formed and α_2 precipitated in β grains, (c) small crack propagation through α_2 phase and crack stopped at again β interface, (d) and (e) new precipitation followed by crack propagation occurred alternatively and (f) SEM image representative of the mechanism.

in the microstructure. Thus, the crack can propagate easier in the β grains step by step through the α_2 phase as illustrated in **Figure 5-36**. This **β phase transformation-induced weakening of the crack tip** mechanism is in good agreement with the observations conducted at the crack tip in NGDP microstructure (**Fig. 5-36 (f)**). A first crack stopped at β/γ interface, and then phase transformation and oxidation took place and explain the thickness of the crack and blunting of the tip. Then, due to the weak precipitates, crack propagated until found a new strong point, here again the β grains. The new crack was

still sharp because the FCG test was stopped and the oxidation did not continue. This mechanism could also explain why despite the strong oxidation of β region, and thus, a strong crack closure effect, the difference between 298 and 1073 K of the fatigue threshold in NGDP microstructure was relatively small in comparison of NL microstructure, where the total fraction of β phase was limited.

- **Dissolution-precipitation of the lamellar structure: $\alpha_2 + \gamma \rightarrow \gamma$**

Figure 5-37 shows example of secondary crack in lamellae located in the crack wake, i.e. in the precrack or early stage regions of the FCG test. Phase transformation occurred along the crack flanks with grains that grew with a perpendicular direction to the crack. This phase transformation occurred independently of the initial crack direction, either after translamellar (left grain) or interlamellar (right grain) propagation. The thickness of the nucleated grains is around 3 μm.

EBSD analysis was conducted in order to identified the nature of the precipitates as shown in **Figure 5-38**. The grains were identified as γ phase and grew independently each other's. Therefore, the **phase transformation $\alpha_2+\gamma \rightarrow \gamma$** took place. As same as the phase transformation that took place into β phase, this transformation only occurred near the crack. Thus, it was identified as oxidation-induced phase transformation mechanism where the diffusion of oxygen in the lamellar structure modified locally the phase

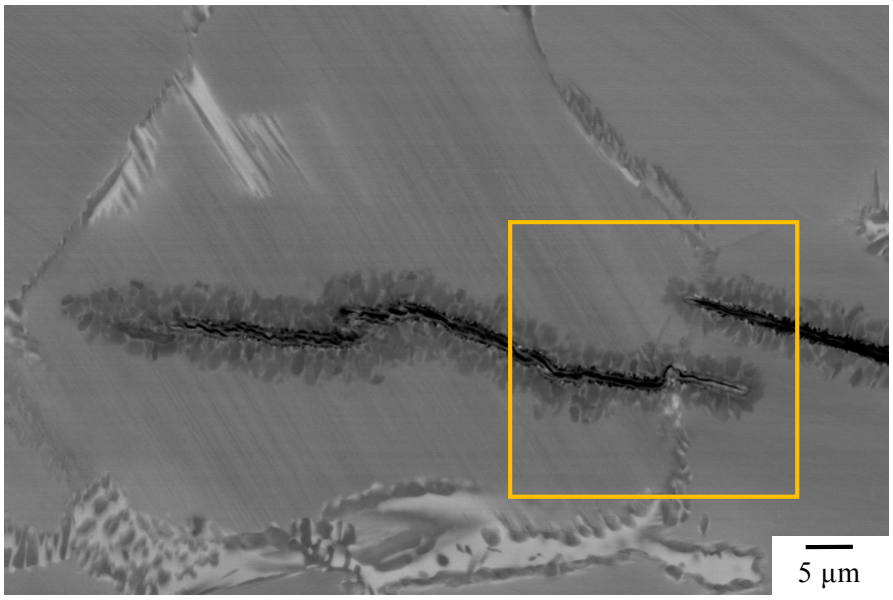

Fig. 5-37. Oxidation-induced phase transformation at a_2/g lamellar colonies in NL microstructure during tests at 1073 K. The square indicated the analyzed region carry out by EBSD.

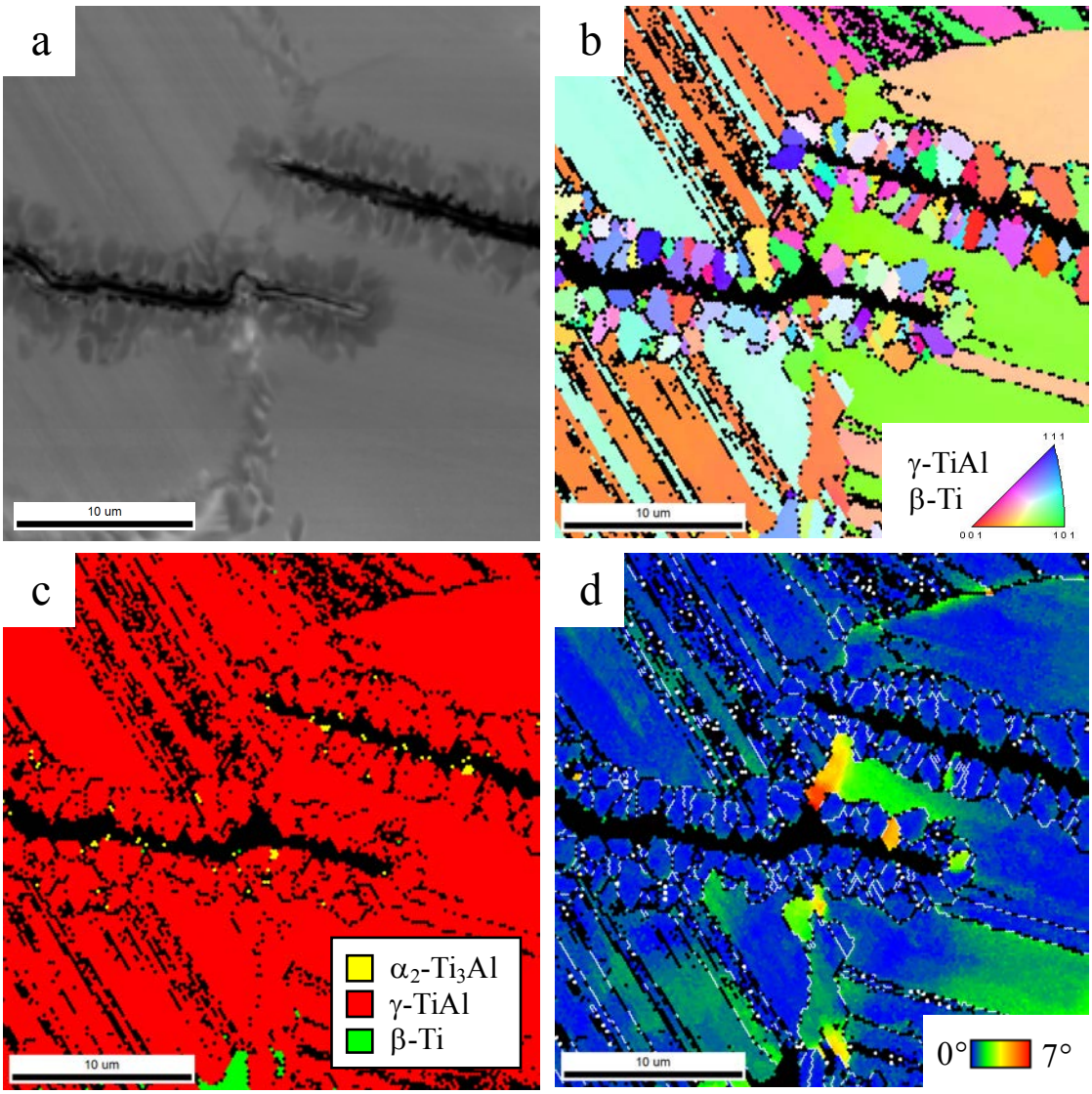

Fig. 5-38. Dissolution-precipitation of α_2/γ lamellar structure analysed by EBSD: (a) BSE image of the analyse region, (b) inverse pole figure, (c) phase identification and (d) GROD maps.

equilibria and stabilize γ phase against α_2. The diffusion of oxygen occurred at the crack interface and new α_2 grains nucleated. As far as the oxygen diffusion take place in the colonies, the nucleates grow with in columnar shape in the lamellar grain. The grains growth reduced the stress that occurred initially when this secondary crack grew (**Fig. 5-38 (d)**). However, the phase transformation occurred excessively late and far from the crack tip to affect the crack propagation behavior. Moreover, the volume transformed is very limited.

5.4.4 Effect of temperature on Paris slope *m*

With increasing temperature, at higher stress intensity, the Paris slope value decrease in both Nearly Lamellar and Nearly Globular β/γ Duplex microstructures. Preliminary results obtained at low vacuum (**Appendix A.6**) showed that the Paris slope seems to be independent of the atmosphere. Hence, the effect of the plastically affected region and nature of phases on the Paris slope *m* will be discussed in this section.

- **Effect of the plastic zone size**

The calculated sizes of the monotonic and cyclic plastic zone area of NL and NGDP microstructures between 298 and 1073 K at the overload region assuming the plane strain conditions are given in **Table 5-5**. The plastic zone size of NL microstructure at 298 and 1073 K is illustrated in **Figure 5-39**. It can be seen that the plastic zone size of Nearly Lamellar microstructure between 298 K and 873 K is equivalent despite the increase of temperature with the values of about 169 and 163 μm, respectively. Its explain well why the roughness observed in the fracture surfaces was similar. However, the plastic zone size at 1073 K were much greater. This is the reason why the roughness of the fracture surface was more important in Paris region compared to lower temperature and also explain the more wavy shape of the crack pathway at 1073 K. Similar trend was observed in NGDP microstructure with an increase of the plastic zone from 30 to 133 μm (around 8 times the grains size) between ambient temperature and 1073 K.

Though, the Paris slope of NL microstructure at 873 K showed the lowest value that could not be explained only by the plastic zone size. It could be related to the nature of the phases included in the plastically affected region.

Table 5-5. Plastic zone size determined at the overload at different temperature of NL and NGDP microstructures.

Microstructure	Temperature / K	ΔK / Mpa$\sqrt{\text{m}}$	K_{max} / Mpa$\sqrt{\text{m}}$	Monotonic plastic zone r_0 / μm	Cyclic plastic zone r_0' / μm
Nearly Lamellar	298	24.4	27.1	169	34.2
	873*	22.7	25.2	163	33.1
	1073	27.3	30.3	246	49.8
Nearly Globular β/γ Duplex	298	10.6	11.8	30	6.1
	1073	19.8	22.0	133	26.9

*σ_y was calculated using linear regression between 298 and 1073 K; σ_y = 454 MPa.

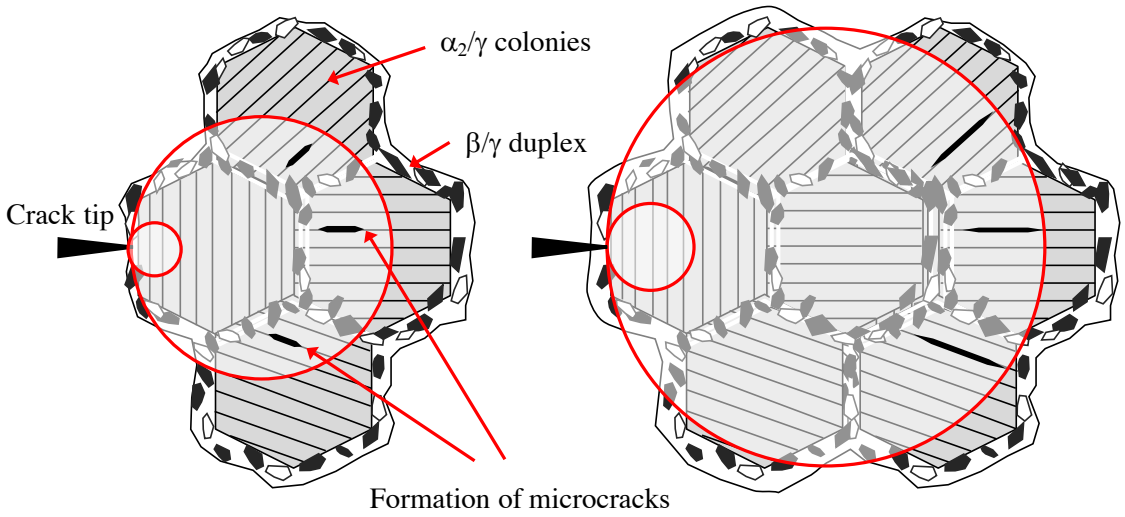

Fig. 5-39. Schematic illustration of the plastic affected area in NL (a) between 298 and 873 K and (b) at 1073 K near the overload.

- **Effect of the nature of phases**

With increasing the temperature, the nature of phases change. Fully Lamellar microstructures have a Ductile-Brittle Transition Temperature (DBTT) around 1073 K whereas γ equiaxed / Lamellar duplex microstructure have a DBTT at lower temperature between 873 and 1073 K.

The comparison of β phase deformation between ambient and elevated temperatures is shown in **Figure 5-40**. At room temperature, the deformation have been observed only along the crack flank (**Fig. 5-40 (b)**) whereas at 1073 K, the deformation occurred also far from the crack (**Fig. 5-40 (d)**). In other words, β phase is very effective at high temperature on crack propagation.

Nakamura showed that even from 873 K, the ductility of the 43-4-5 alloys increased in either NL or NGDP [5]. The EBSD analysis of the crack at 873 K in NL microstructure showed that β grains also deformed along the crack flanks, whereas at room temperature mainly the γ grains deformed as shown in **Figure 5-41**. The grain orientation deviation (GROD) mapping showed that despite the both β and γ grains are deformed, the γ phase continue to be more deformable at high temperature. However, the toughness of β phase is still higher compared to the γ phase. The deformation of these two phases led to the decrease of the Paris slope with increasing temperature. However, Nearly Lamellar microstructure showed higher Paris slope than reported results for FL microstructure [3].

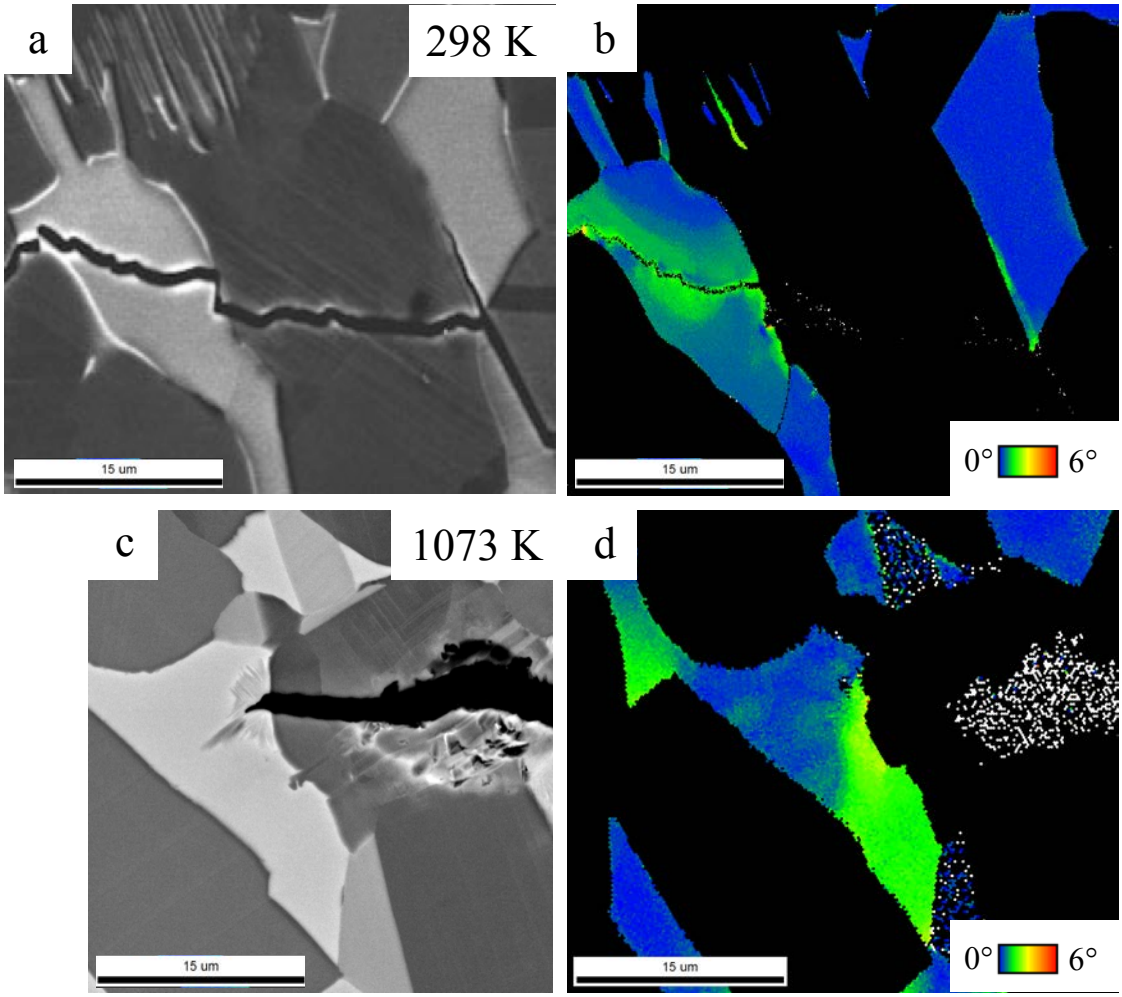

Fig. 5-40. Deformation of β phase analysed by EBSD on NGDP microstructure: (a,b) at 298 K with (a) BSE image of the crack and (b) GROD map, and (c,d) at 1073 K with (c) BSE image of the crack and (d) GROD map.

Though, in case of NGDP microstructure, the total volume fraction of β phase V_β is higher than in NL, and thus, more β grains could be deformed, resulting in a lower Paris slope compared to the Nearly Lamellar microstructure. The Paris slope *m* becomes even lower than β-free duplex microstructures [3, 9]. The deformation of β phase led also to a tremendously higher K_{max} at overload compared to ambient temperature tests.

Consequently, the addition of a certain amount of β phase in the microstructure enhanced both the crack propagation in the Paris regime and the maximum stress K_{max} of the material (indication of the toughness K_{IC}).

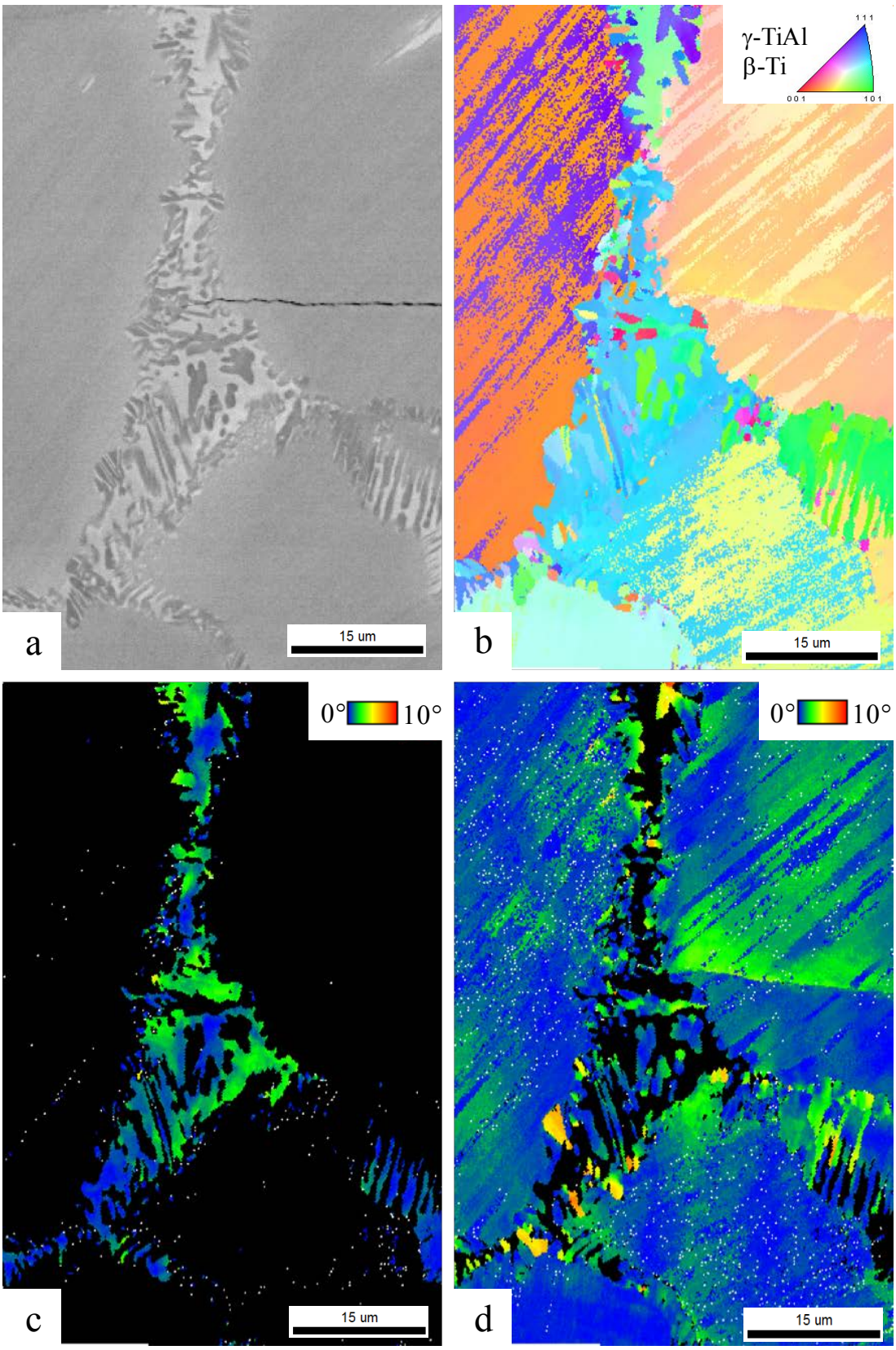

Fig. 5-41. Fatigue crack tip at 873 K in NL microstructure analysed by EBSD: (a) BSE image of the tip, (b) inverse pole figure map, (c) and (d) GROD map of β and γ phase, respectively.

5.5 Summary

In this chapter, the fatigue crack growth behavior of wrought Ti-43Al-4Nb-5V alloy was determined between 298 and 1073 K for two microstructures (NL and NGDP) containing different β/γ duplex volume fractions at the α_2/γ colonies grain boundaries. Based on this study, the following conclusion can be drawn.

1. The fatigue threshold decreased with increasing temperature up to a minimum around 873 K and then it increased and become higher than ambient temperature values. The K_{max} at overload showed a similar trend. At opposite, the Paris slope decreased up to 873 K, indicated a higher crack propagation resistance in Paris region. Between 873 K and 1073 K, the Paris slope did not change.
2. At both ambient and elevated temperature NL showed higher fatigue threshold and higher K_{max} than NGDP. However, NGDP microstructure presented the lowest Paris slope. The reason come from the higher fraction of β phase that can deformed at high temperature and thus improve the crack propagation during Paris regime.
3. The fatigue crack pathways and the fracture surfaces are similar between 298 and 873 K microstructures but showed higher roughness at 1073 K. It could be explained by the larger plastic zone size.
4. Oxide-induced crack closure effect have been identified in NL microstructure and shown that it was the main effect to control fatigue threshold.
5. Two oxidation-induced phase transformations have been identified during test: dissolution-precipitation of lamellar colonies in the crack wake and decomposition of β phase at the crack tip. However, only the precipitation of α_2 phase in β grains could influence the fatigue threshold.

Finally, it should be noticed than the introduction of β phase in γ-based TiAl alloys at high temperature showed different effects: by the phase transformation-induced, the weakening of the crack tip mechanism reduces slightly the effective fatigue threshold whereas the deformation at high temperature enhance crack propagation in Paris regime and improve toughness of the materials.

References

[1] K. T. Venkateswara Rao, Y. W. Kim, R. O. Ritchie, High-temperature fatigue-crack growth behavior in two-phase ($\gamma+\alpha_2$) TiAl intermetallic alloy, Scripta Metallurgica et Materialia 33 (1995) 459-465.

[2] C. Mabru, D. Bertheau, S. Pautrot, J. Petit, G. Hénaff, Influence of temperature and environment on fatigue crack propagation in a TiAl-based alloy, Engineering Fracture Mechanics 64 (1999) 23-47.

[3] S. J. Balsone, J. M. Larsen, D. C. Maxwell, J. W. Jones, Effects of microstructure and temperature on fatigue crack growth in the TiAl alloy Ti-46.5Al-3Nb-2Cr-0.2W, Materials Science and Engineering A192/193 (1995) 457-464.

[4] A. L. McKelvey, K. T. Venkateswara Rao, R. O. Ritchie, On the anomalous temperature dependence of fatigue-crack growth in γ-based titanium aluminides, Scripta Materialia 37 (1997) 1797-1803.

[5] T. Nakamura, 鍛造 TiAl 基合金の疲労き裂進展特性に及ぼす組織の影響, Master Thesis, Tokyo Institute of Technology, 2017.

[6] H. A. Lipsitt, D. Shechtman, R. E. Schafrik, the deformation and fracture of TiAl at elevated temperatures, Metallurgical Transactions A 6 (1975) 1991-1996.

[7] M. S. Dahar, S. M. Seifi, B.P. Bewlay, J. J. Lewandowski, Effects of test orientation on fracture and fatigue crack growth behavior of third generation as-cast Ti-48Al-2Nb-2Cr, Intermetallics 57 (2015) 73-82.

[8] M. S. Dahar, S. A. Tamirisakandala, J. J. Lewandowski, Evolution of fatigue crack and fracture behavior in gamma titanium aluminide Ti-43.5Al-4Nb-1Mo-0.1B (TNM) forgings, International Journal of Fatigue 111 (2018) 54-69.

[9] P. Bowen, R. A. Chave, A. W. James, Cyclic crack growth in titanium aluminides, Materials Science & Engineering A192/193 (1995) 443-456.

[10] J.M. Larsen, B.D. Worth, S.J. Balson, A.H. Rosenberger , J.W. Jones, Fatigue'96 (ed. G. Lütjering and H. Nowak), 1996.

[11] G. Hénaff, G. Odemer, A. Tonneau-Morel, Environmentally-assisted fatigue crack growth mechanisms in advanced materials for aerospace applications, International Journal of Fatigue 29 (2007) 1927-1940.

[12] Y. W. Kim, Intermetallic alloys based on gamma titanium aluminides, Journal of Metallurgy 41 (1989) 24-30.

[13] J. Domingo, M. Takeyama, S. Hayashi, unpublished data

[14] S. Suresh, R. O. Ritchie, Some considerations on the modelling of oxide-indited fatigue crack closure using solutions for a rigid wedge inside a linear elastic crack, Scripta Metallurgica 17 (1983) 575-580.

[15] W.O Soboyejo, J. E. Deffeyes, P. B; Aswath, Investigation of room and elevated temperature fatigue crack growth in Ti-48Al, Material Science and Engineering A138 (1991) 95-101.

[16] ASM Handbook Vol.13 Corrosion, ASM International, 1987

[17] T. L. Anderson, Fracture Mechanics: Fundamentals and Applications, 3rd ed., CRC Press, 2005.

[18] G. Hénaff, A. Gloanec, Fatigue properties of TiAl alloys, Intermetallics 13 (2005) 543-558.

[19] F. Appel, T. K. Heckel, H. Christ, Electron microscope characterization of low cycle fatigue in a high-strength multiphase titanium aluminide alloy, International Journal of Fatigue 32 (2010) 792-798.

[20] A. Kinouchi, Master Thesis, Tokyo Institute of Technology, 2018.

Chapter 6

General Conclusions

6.1 Summary

This thesis focused on the microstructure control of β-Ti phase in γ-based alloys and its effect on the fatigue crack growth (FCG) resistance. Fully Lamellar (FL) microstructures are known to show the highest FCG properties but these microstructures do not contain β phase. Therefore, after a study on the phase equilibria of Ti-Al-M (where M is a β-stabilizer element) ternary alloys and phase transformations in order to control the β phase, model microstructures have been designed with various phase fractions and morphologies of β and γ phases combined together as-called β/γ duplex (DP). Finally, the FCG behavior of the different microstructures have been investigated at ambient and high temperatures, up to 1073 K, and the role of the β phase according to the different crack resistance mechanisms have been discussed. Followings are conclusions obtained in this study.

In **Chapter 1** "**General Introduction**", context of the study with both the increase of the aircraft fleet and the limitation of CO_2 emissions have been described. The necessity to develop lighter materials to improve turbojet engines efficiency and the current activities, applications, and future trends on development of titanium aluminides based on γ phase to replace the nickel based alloys have been introduced. The state of the art on γ-TiAl alloy such as crystallography and microstructures have been reported. The microstructure design principal of wrought TiAl alloys for developing high toughness materials, and thus, replace not only low pressure turbine blades but also high pressure compressor, and the importance of using the β phase have been detailed. Previous studies on the effect of microstructure and especially how the β phase may affect the mechanical properties was pointed. Finally, the structure and the objectives of this thesis have been outlined.

Chapter 2 presents the "**Phase Equilibria Among β-Ti / α_2-Ti_3Al / γ-TiAl in Ti-Al-M Ternary Systems**". In this chapter, the phase equilibria between 1073 K and 1473 K of Ti-Al-M ternary system where M is a β-stabilizer have been introduced. Moreover, a reassessment above 1473 K have been conducted. Two different ternary systems where the M element was **vanadium** (V^{th}) and **manganese** (VII^{th}) have been studied. The effect of M element on the movement of the β/α(α_2)/γ three phase triangle with the change of temperature is investigated. By decreasing the temperature, the tie-triangle shifts toward low Al and low M contents up to a minimum and then, change direction and move toward

low Al and high M contents and reveal a new transformation pathway $\beta+\alpha(\alpha_2)+\gamma \rightarrow \beta+\gamma \rightarrow \beta+\alpha_2+\gamma$ near 1073 K with the existence of two types of α_2 phase. It has been reported that V^{th} elements stabilize α_2 against α, however it was unclear concerning the manganese effect. The results suggest that Mn is stronger α-stabilizer than α_2-stabilizer and thus, $\alpha \rightarrow \beta+\alpha_2+\gamma$ ternary eutectoid reaction may occur between 1173 and 1193 K. Finally, in manganese system, C14 Laves phase has been observed below 1173 K. Therefore, a second ternary eutectoid reaction $\beta \rightarrow C14+\alpha_2+\gamma$ takes place in this system.

Chapter 3 introduces the "**Phase Transformations Involving β-Ti Phase and Microstructure Control of Wrought Alloys**". In this chapter, the control of the β phase based on the phase transformations of wrought γ-TiAl alloys containing V or Mn have been studied using the vertical section of the phase equilibria. The competition between $\beta \rightarrow \beta+\gamma$ decomposition, coarsening and $\alpha+\gamma \rightarrow \beta+\gamma$ cellular transformation allowed to design various morphologies of β phase associated with the γ phase surrounded the lamellar colonies. Moreover, the adjustment of time and temperature control the volume fraction and the ratio between the two phases. Finally, model microstructures with different β/γ volume fractions and morphologies have been designed for mechanical tests.

Chapter 4 presents the "**Effect of β/γ duplex Microstructure on Fatigue Crack Growth Behavior at Ambient Temperature**". The fatigue crack growth behaviors of different model microstructures containing various volume fractions and morphologies of β/γ duplex structure have been tested at ambient temperature. It is revealed that the introduction of a certain fraction of β phase associated with γ grains in wrought TiAl alloy increase the stress intensity threshold and decrease the Paris slope compared to the corresponding β-free TiAl alloy. The deformable γ phase combined with strong but brittle β phase reduced the stress at the crack tip, and thus, improve the fatigue threshold, whereas the refinement of the microstructure allowed by the presence of the β phase during heat treatments lead to the formation of multiple crack deviations and crack bridging ligaments that decrease the Paris slope.

In **Chapter 5** "**Effect of β/γ Duplex Microstructure on Fatigue Crack Growth Behavior at Elevated Temperatures**", the fatigue resistance of Nearly Lamellar (NL) and Nearly Globular β/γ Duplex (NGDP) microstructures have been investigated at different temperatures. The increase of temperature reduces the fatigue threshold and decreases the Paris slope up to the minimum. Then, the fatigue threshold drastically

increases and becomes higher than that at ambient temperature whereas no change in the Paris slope is observed. The oxidation-induced crack closure effect has been proposed to explain the rise of the fatigue threshold. Furthermore, the presence of β, Ti-rich phase, increase the oxidation behavior and therefore, reinforced the crack closure mechanism. In contrary, the change in the nature of phases within the plastic zone could explain the reduction of Paris slope. Moreover, this effect is higher for NGDP that contains a larger fraction of β phase. Therefore, the deformation of β phase at elevated temperatures trends to reduce the crack propagation rate. Finally, oxidation-induced phase transformation of the β phase has been observed, even at the crack tip, and thus, may affect negatively, even slightly, the fatigue threshold.

In **Chapter 6** "**General Conclusions**", the conclusions obtained in different chapters have been summarized. In addition, possible microstructure to achieve high fatigue crack resistance have been proposed, together with future work.

As a conclusion of this thesis, the important point for the fatigue crack growth resistance is that the introduction of β phase in γ-based TiAl alloys does not worsen the fatigue crack growth behavior. In contrary, it has been clearly demonstrated in this study that, unlike the general thought, the introduction of a certain fraction and morphology of β/γ along the lamellar colony boundaries is effective in toughening of TiAl alloy. The presence of β phase associated with γ grains in wrought TiAl alloy improves both crack initiation and propagation resistance, and the latter effect is more obvious at elevated temperatures

6.2 Development of high fatigue resistance alloy based on this thesis

This thesis has identified the fundamental knowledges of fatigue crack growth behavior of wrought γ-TiAl alloys containing β-Ti phase at ambient and elevated temperatures based on the microstructure control of wrought alloy using both phases' equilibria and phases' transformations. The combination effect of β and γ phases at the colonies boundaries improves the FCG properties in comparison of β-free alloys at ambient temperature. Therefore, it becomes possible to design microstructure with high fraction of β phase and also γ grains that will enhance the tensile properties without reducing the fatigue resistance behavior. At high temperatures, a high fraction of β improves the Paris life of the alloy whereas large β grains weakening the materials near the fatigue threshold

by phase transformation. Thus, a high total fraction of fine β grains will be more efficient to obtain high fatigue crack growth resistance at high temperature, as well.

Figure 6-1 shows microstructure design proposal to achieve high fatigue resistance behavior based on the knowledge acquired in this study. In a first step, the alloy is forged in β+α two phase region. Then, it is necessary to design a nearly lamellar microstructure by conducted heat treatment, above the γ-solvus, in α-single phase region followed by air cooling. If α-single phase does not exist, the remained β phase have to be split into smaller parts, e.g. using the β decomposition that occurs during cooling. Therefore, in order to increase the decomposition, the highest temperature should be used. However, the higher temperature, the lower the fraction of lamellar colonies will be: a good balance between temperature and α grains fraction should be considered. It have been shown in **Chapter 1** that β particles dispersed within lamellar structure improve the toughness of the wrought alloys, despite this factor was not consider in this work. A second step heat

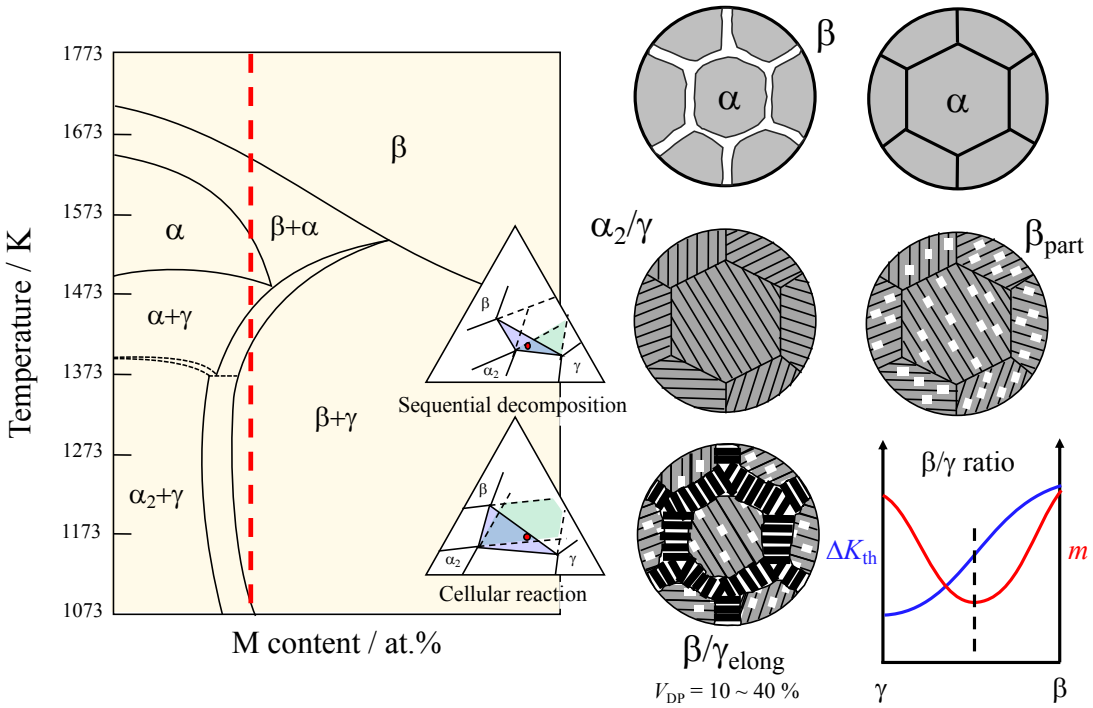

Fig. 6-1. Microstructure design proposal of high fatigue resistance γ-TiAl alloy containing β phase

treatment should be conducted in order to precipitate β particles, through the sequential decomposition. This transformation depend on the system and the temperature. It have

been shown in **Chapter 2 and 3** that due to the change of the tie triangle direction, it is possible that the transformation change from sequential decomposition at high temperature to cellular reaction a lower temperature. Hence, a third heat treatment should be conducted to promote the cellular reaction (elongated γ grains) against coarsening (globular γ grains) until the total volume fraction of β/γ duplex V_{DP} is the highest possible without lose FCG resistance, i.e. about 35 ~ 40 %. It is also possible to control the ratio β/γ by changing the temperature until to find the optimal balance between high ΔK and low m, but further experiment are required for this point. Finally, the alloy microstructure should be stable up to 1073 K for the possible applications. In that case, the three phase coexisting region may exist at these temperature for the considered alloy composition.

6.3 Future works

Although this thesis investigated many aspects of the relationship between microstructure, especially β/γ duplex, and the fatigue crack growth behavior of wrought TiAl alloys, there are several points that are still unclear. These points are shown as following.

I. The crack closure effects at room temperature were not studied and only the measured stress intensities were discussed. As future work, they should be considered to compare the effective stress intensities. Indeed, it has been reported that for load ratio higher than 0.45, it is considered that crack closure effects did not occur. Therefore, a study conducted at higher load ratio could be a way to proceed.

II. For same DP fraction, the effect of elongated (LTL), small (NCT) and large (GTL) γ grains with different β/γ ratio have been investigated. However, some microstructural parameters already observed in wrought alloys could be interesting to be studied, e. g. secondary β precipitates within the lamellae, continuous β phase, faceted γ grains and colonies size. Moreover, the presence of Laves phase has been reported in the manganese system in the range of the operating temperature and may play a role in the FCG resistance.

III. At high temperature, the air (oxygen) seems to have an important effect on fatigue threshold by oxidation-induced crack closure and by oxidation-induced phase transformation of the β grains. Preliminary investigations have been carried out in GTL microstructure as shown in **Figure 6-2** (and also in **Appendix A-6**). The results indicate that in vacuum, the crack growth rate is much's lower than that in air but shows a similar

Paris slope. Moreover, the fatigue threshold is lower compared to the tests done in air. Nevertheless, a thorough study has to be conducted to reveal in detail the role of oxygen and how it affects the FCG behavior in presence of β phase.

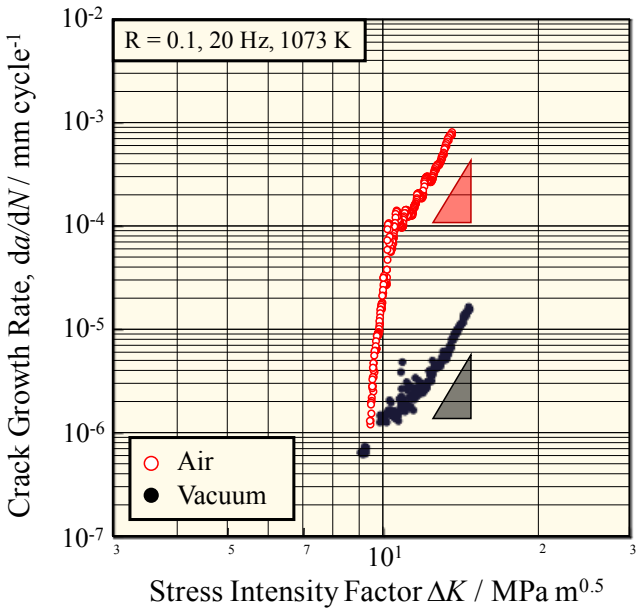

Fig. 6-2. Effect of atmosphere on stress intensity during *K*-decreasing test near fatigue threshold on GTL (Ti-42Al-5Mn) in air and in vacuum (4.1×10^{-1} Pa).

Appendix

A.1 Error bar determination using the standard deviation

Across the different chapters, data are represented using figures where each data point represents the average of measures conduct to few data points. The evaluation the significant character of these measures provides important information for results analysis. A simple way could consist to use the maximum and the minimum values as error bar. But the information about distribution of measured points are not represented. In this thesis, in order to refine the information obtained from each data point, the **sample standard deviation** have been use as error bar representation. Despite it is consider as a biased estimator, the sample standard deviation is given by the following equation [1]:

$$s_N = \sqrt{\frac{1}{N}\sum_{i=1}^{N}(x_i - \bar{x})^2} \quad \text{(A-1)}$$

Where x_i is the measure point *i*, $\bar{x}$ is the average and N the total number of data points. An unbiased estimator can be easily obtained using $N-1$ instead of N. It results the following **corrected sample standard deviation** [1]:

$$s = \sqrt{\frac{1}{N-1}\sum_{i=1}^{N}(x_i - \bar{x})^2} \quad \text{(A-2)}$$

However, it exists more accurate estimators than this one: the confidence intervals which take account the effect of sample size and measurement variations. If we suppose that the sample follow a normal distribution, the **confidence interval IC** is obtained using the following equation [1]:

$$IC_{1-\alpha} = \left[\bar{x} - t_{1-\frac{\alpha}{2}}^{N-1}\frac{s}{\sqrt{N}}, \bar{x} + t_{1-\frac{\alpha}{2}}^{N-1}\frac{s}{\sqrt{N}}\right] \quad \text{(A-3)}$$

Where $\bar{x}$ is the average (or expected values), t_γ^k is the Student distribution quantile of γ order and *k* degree of freedom, s is the corrected sample standard deviation and N the total number of data points.

In this thesis, the confidence interval with α = 95 % is used as error bar. Its means that the "real average" has 95 % of chance to be included between IC_{min} and IC_{max}.

A.2 Vertical sections of Ti-Al-M ternary systems

In the **Chapter 2**, the phases equilibria of Ti-Al-V and Ti-Al-Mn ternary system have been studied and the isothermal sections were presented. Moreover, the vertical sections

of these systems at 42%.at with changing alloying content (V and Mn) has been introduced in chapter 3 in order to illustrate the transformation pathway of the wrought studied alloys. However, in this section, some vertical sections of Ti-Al-M ternary system as a function of M element are represented between at 36, 39, 42 and 45 Al at.%. **Figure A-1** to **A-4** and **A-5** to **A-8** show the vertical sections of vanadium and manganese ternary system along with reported data [2-6], respectively.

A.3 Charpy impact tests

The resilience of Ti-42Al-5Mn and Ti-42Al-8V alloys were estimated in order to refine the microstructural features to investigate for fatigue crack growth tests. The resilience of a material corresponds to the energy the material can absorb before rupture. Two different standard tests exist to measure the resilience of a material; Charpy and Izod tests. In this thesis, only Charpy impact tests were conducted on samples with various microstructures.

Charpy impact tests were carried out using half size specimen in accordance to ASTM E-23 standard with a V-notch of 2 mm (a_0) [7]. The Charpy impact tests were conducted at 1103 K with an initial energy of 50 J. This temperature has been previously identified in our research group as the maximum for the resilience values for TiAl alloys. Specimens were initial pre-heat for 30 min using a maffle KDF 75 furnace. The transfer time between the furnace and the pendulum was lower than 5 s. If the time for setting excessed 5 s, the test was cancelled and the specimen put back in the furnace.

The effect of β/γ volume fraction V_{DP}, β volume fraction V_{β}, lamellar colonies size L_{lam} and lamellar spacing on the resilience of 42-5Mn and 42-8V are shown in **Figure A-9 to A-12**, respectively.

The resilience of the alloys is directly correlated to the fraction of β/γ fraction. Up to 50 %, the resilience was about 2 $J \cdot cm^2$, and then, increased up to a maximum of about 4 $J \cdot cm^2$ and decreased again. The peak of the resilience was about 70 % of β/γ duplex for 42-5Mn and 85% for 42-8V. Moreover, the resilience is proportional to the total fraction of β phase as shown in 42-5Mn in **Fig. A-10**. Therefore, by controlling the ratio β/γ of duplex at grains boundaries it can be possible to increasing the energy absorption of the alloys. In others hand, the lamellar colonies size did not show any relationship with lamellar colonies size as shown in **Fig. A-11**. Nonetheless, the impact values increase with increasing lamellar thickness with a higher effect in case of 42-5Mn alloy.

A.4 Tensile properties

In order to conduct fatigue crack growth (FCG) tests in **Chapter 4** and **Chapter 5**, the tensile properties of the different model microstructures have been measured and are briefly introduced in the following section. Indeed, the FCG tests was carried out under tensile-tensile stress with a load ratio of 0.1, and hence, the determination of yield stress σ_y is required.

A.4.1 Results at room temperature

For the FCG tests of the **Chapter 4**, the tensile properties were evaluated at ambient temperature (298 K). However, it should be noted that, in case of NL and NGDP of the Ti-43Al-4Nb-5V alloy, the tensile properties have been determined either ex-situ (NL) and in-situ (NGDG) by Nakamura *et al.* [8], respectively. The strain-stress curve, the SEM images at low and high magnification and a summarized table of As-forged (42-5Mn), Globular Triplex (42-5Mn), Nearly Globular β/γ Duplex (42-5Mn), Near γ Cellular Triplex (42-8V), Nearly Lamellar (43-4-5), Lamellar Triplex (43-4-5) and Nearly Globular β/γ Duplex (43-4-5) are shown in **Figure A-13 to A-19**, respectively.

The microstructure containing higher volume fraction of DP show usually higher elongation in particular of NGDP microstructures. 42-5Mn microstructures show the lowest yield stress and ultimate tensile strength, 315 MPa and 680 MPa for GTL, respectively, whereas 42-8V presents the higher values of around 650 and 951 MPa, respectively. 43-4-5 alloy have intermediate tensile properties.

A.4.2 Results at elevated temperatures

The tensile properties used in **Chapter 5** for high temperature FCG tests were determined at 1073 K by Nakamura *et al.* [8] as illustrated in **Figure A-20** and data are summarized in **Table A-1**. At 1073 K, the elongation of NGDP microstructure drastically increased up to 12 % whereas it increased slightly in NL microstructure. This indicates that the Ductile Brittle Transition Temperature (DBTT) of NGDP microstructure have been probably reached but not yet the DBTT of NL.

It should be not that the tensile properties of NL microstructure at 873 K could not been measured in this thesis. However, by increasing the temperature the yield stress did not change drastically from 480 MPa at room temperature to 445 MPa at 1073 K. Therefore, the yield stress has been estimated at around 454 MPa using linear regression at 873 K.

Table A-1 Tensile properties of Ti-43Al-4Nb-5V (at.%) at ambient and elevated temperature [8]. Figures in bracket correspond to *ex-situ* results.

Microstructures	Temperature	Young's Modulus E / GPa	Yield stress σ_y / MPa	Ultimate Tensile Strength σ_{UTS} / MPa	Elongation ε / %
Nearly Lamellar (NL)	298	34 (137)	– (480)	664 (900)	0.7 (0.1)
	1073	45 (133)	450 (445)	680 (725)	1.3 (1.6)
Nearly Globular β/γ Duplex (NGDP)	298	47	495	775	2.3
	1073	45	440	526	11.8

A.5 Fatigue crack growth behavior of the investigated microstructures

In **Chapter 4** and **Chapter 5**, fatigue crack growth rates were carried out, however, in order to illustrated the comparison between the microstructures, only one curve was shown for each case. In this section, all the different curves obtained for each microstructure are shown.

A.5.1 Results at room temperature

The FCG curves obtained at ambient temperature for the AF, GTL, NGDP-Mn, NCT, NL, LTL and NGDP-4345 microstructures are shown in **Figure A-21 to A-27**. The influence of microstructure (volume fraction, morphologies…) is discussed in **Chapter 4**. The different tests revealed that the experiments were reproducible with a limited scattering between data both the fatigue threshold ΔK_{th} and the Paris slope m, except in case of the as-forged microstructure (Ti-42Al-5Mn alloy) for the latter one. Indeed, the Paris slope shows important difference between the two K-increasing tests. The as-forged microstructure showed large inhomogeneity in the microstructure with some regions nearly lamellar and other one nearly β/γ duplex that could explain the difference.

A.5.2 Results at elevated temperatures

In the **Chapter 5**, the FCG curves were conducted at 873 and 1073 K. **Figure A-28 to A-30** shows the different tests conducted using NL and NGDP microstructures. At 873 K, the scattering is similar to room temperature tests whereas the both NL and NGDP microstructures at 1073 K showed smaller scattering than room temperature results.

A.6 Effect of atmosphere on fatigue crack growth behavior

Some preliminary FCG tests have been conducted in vacuum to investigated why the fatigue threshold ΔK_{th} decrease at intermediate temperature. Tests have been conducted on GTL microstructure (Ti-42Al-5Mn alloy) at 1073 and 873 K. The results is shown in **Figure A-31 and A-32**, respectively. It should be noted that the vacuum conditions were low, between 0.1 and 1 Pa and also the optimal protocol for conducting efficient tests is still on investigation.

The results indicate that in vacuum, the crack growth rate is much lower than that in air. At 1073 K, the Paris slope seems to be **independent of the atmosphere**., and hence, independent of the oxidation. Moreover, the fatigue threshold is lower compared to the tests done in air despite that the fatigue threshold value could not be identified. At high temperature the crack growth rates is very fast, therefore, it exist a transition state before reach the Paris slope and this explain why at 873 K the slope is steep. Despite that the crack was too long to continue the test, it can be supposed that the result will be similar to those at 1073 K with the same Paris slope.

In any case, a thorough study has to be conducted to reveal in detail the role of oxygen and how it affects the FCG behavior in presence of β-phase.

Reference

[1] Confidence estimation, Encyclopedia of Mathematics, Springer in cooperation with the European Mathematical Society.
http://www.encyclopediaofmath.org/index.php?title=Confidence_estimation&oldid=30939 (visited June 10, 2018)

[2] J. C. Schuster, M. Palm, Reassessment of the Binary Aluminum-Titanium Phase Diagram, Journal of Phase Equilibria and Diffusion 27 (2006) 255-277.

[3] S. Kobayashi, Phase Equilibrium and structure formation in TiAl based ternary alloys – Decomposition of α-phase and generation of β-phase in α → β+γ reaction pathway, Doctor Thesis, Tokyo Institute of Technology, 2002.

[4] T. Ahmed, H. M. Flower, The phase transformations in alloys based on titanium aluminides Ti_3Al-V and Ti-Al-V, Mater. Sci. and Eng. A152 (1992) 31-36

[5] Z. Chen, I. P. Jones, C. J. Small, Laves phase in Ti-42Al-10Mn alloy, Scripta Materialia 35 (1996) 23-27.

[6] R. Kainuma, Y. Fujita, H. Mitsui, I. Ohnuma, K. Ishida, Phase equilibria among α (hcp), β (bcc) and γ (L10) phases in Ti-Al base ternary alloys, Intermetallics 8 (2000) 855-867.35 (1996) 23-27.

[7] ASTM Standard E23-07, Standard Test Methods for Notched Bar Impact Testing of Metallic Materials, In: ASTM book of standards, West Conshohocken, PA, ASTM International, 2007.

[8] T. Nakamura, 鍛造 TiAl 基合金の疲労き裂進展特性に及ぼす組織の影響, Master Thesis, Tokyo Institute of Technology, 2017.

[9] G. Hénaff, G. Odemer, A. Tonneau-Morel, Environmentally-assisted fatigue crack growth mechanisms in advanced materials for aerospace applications, International Journal of Fatigue 29 (2007) 1927-1940.

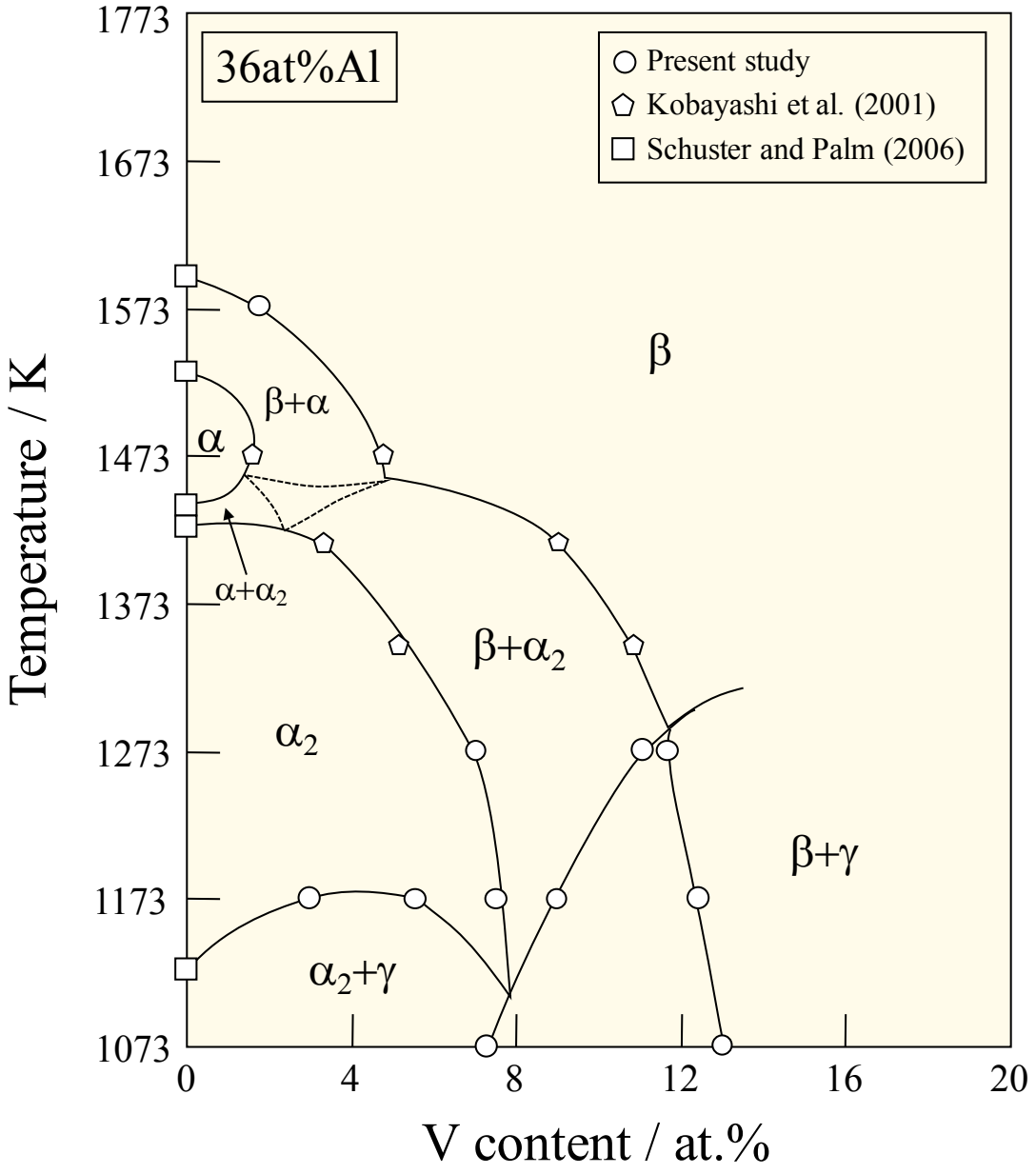

Fig. A-1. Vertical section in Ti-Al-V ternary system at 36 at%Al based on the present study along with reported data [2, 3].

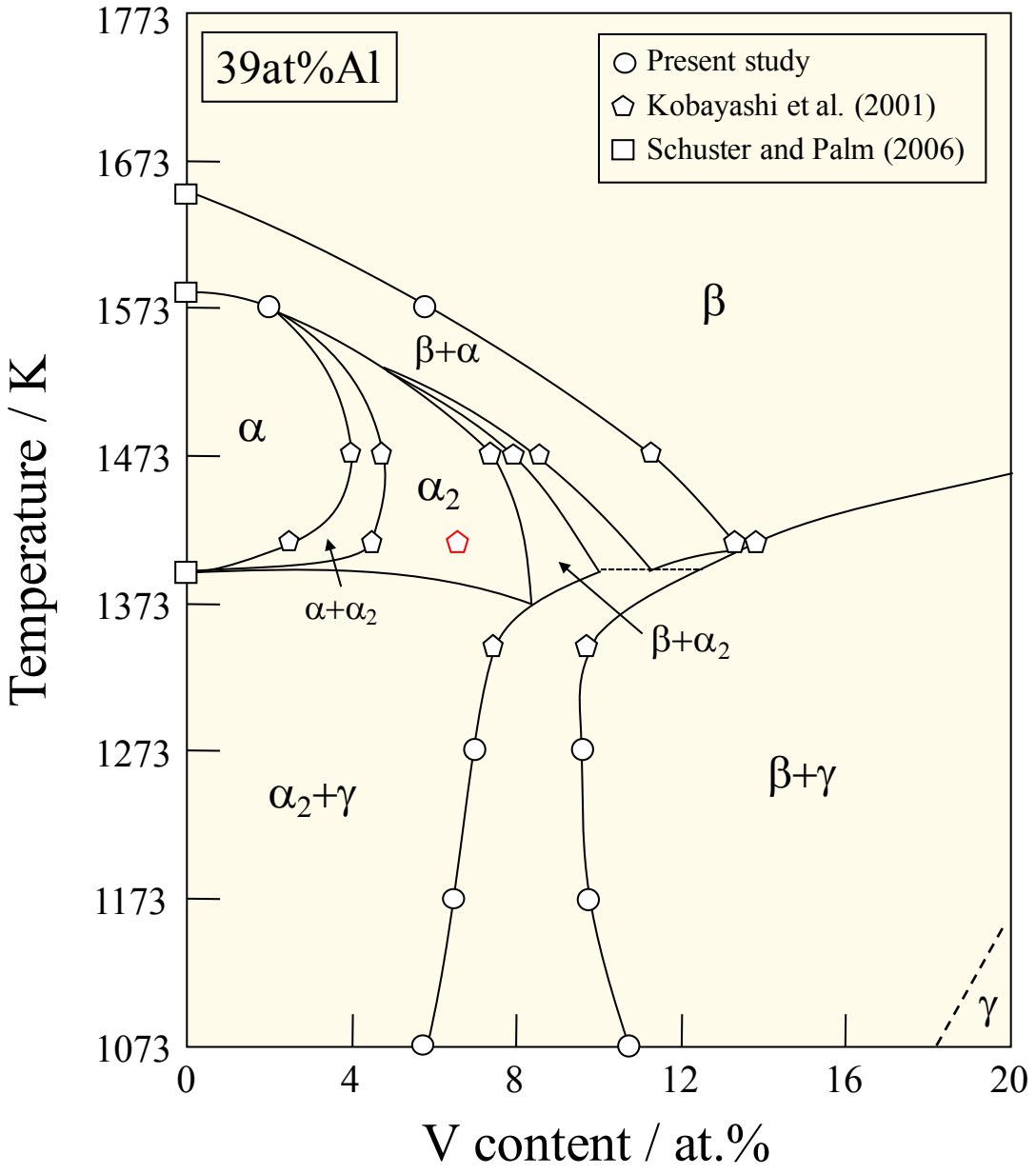

Fig. A-2. Vertical section in Ti-Al-V ternary system at 39 at%Al based on the present study along with reported data [2, 3]. The γ single phase was determined by calculation and separates the β/β_0 ordering phases.

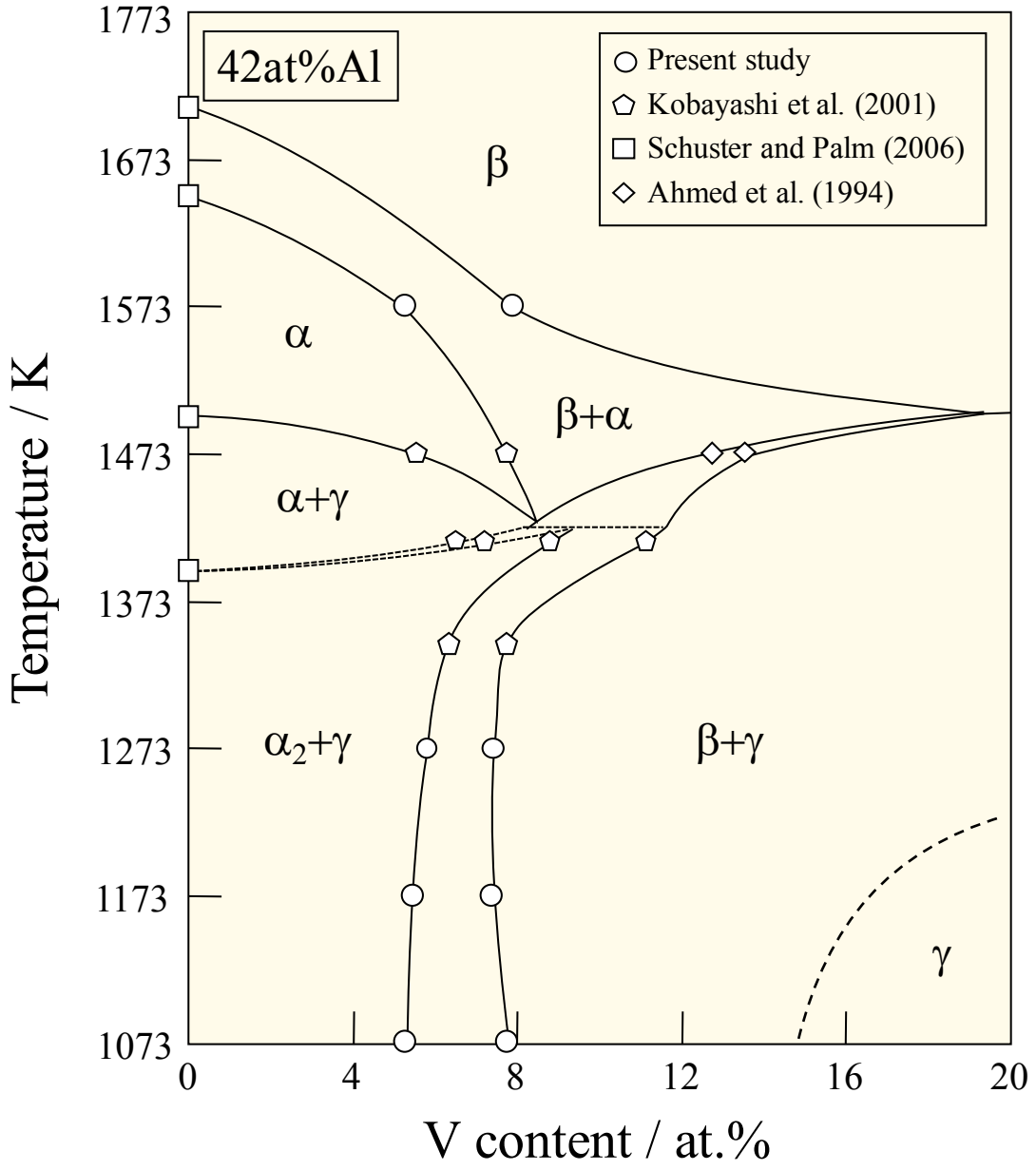

Fig. A-3. Vertical section in Ti-Al-V ternary system at 42 at%Al based on the present study along with reported data [2, 3]. The γ single phase was determined by calculation and separates the β/β_0 ordering phases.

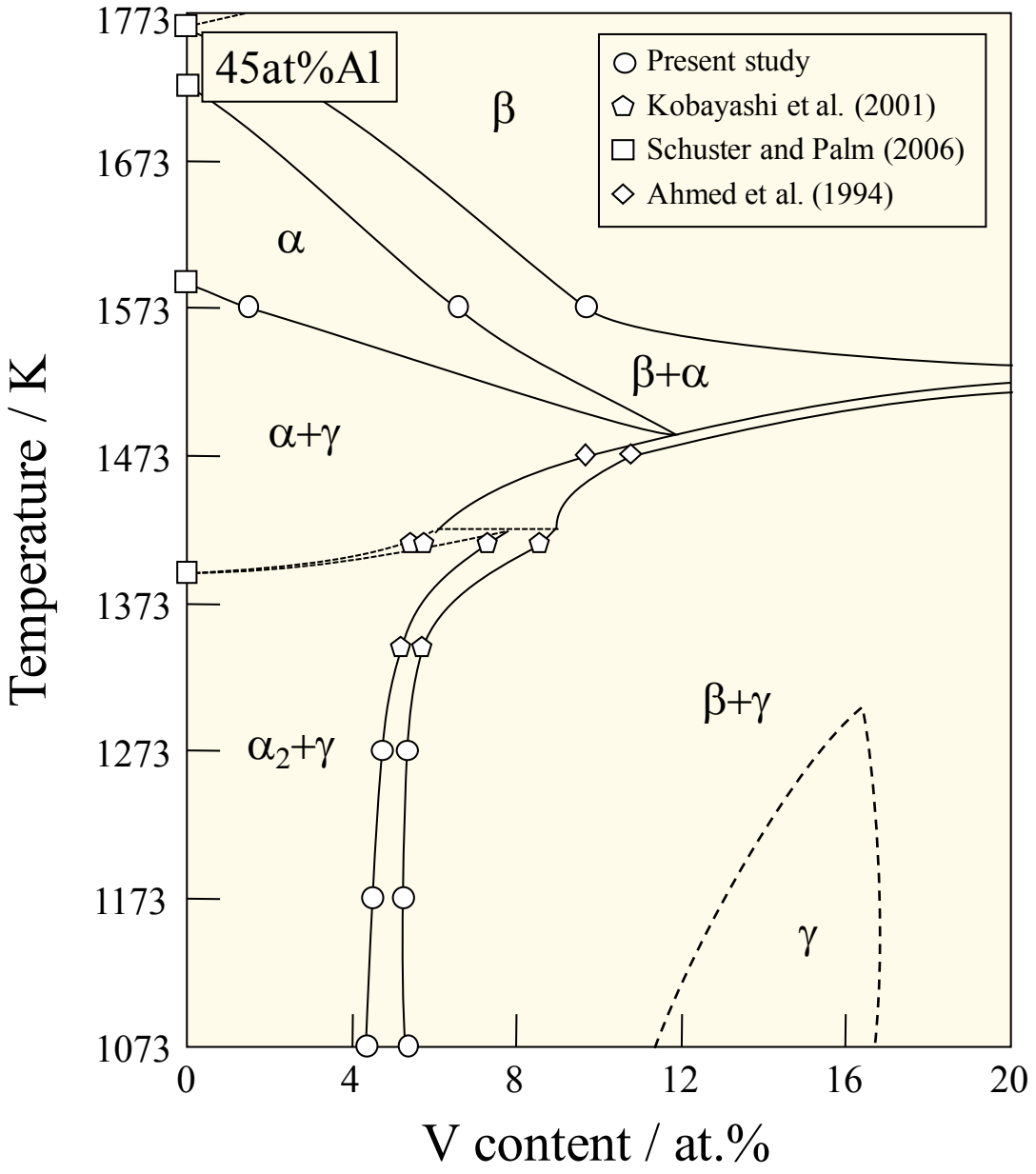

Fig. A-4. Vertical section in Ti-Al-V ternary system at 45 at%Al based on the present study along with reported data [2, 3]. The γ single phase was determined by calculation and separates the β/β_0 ordering phases.

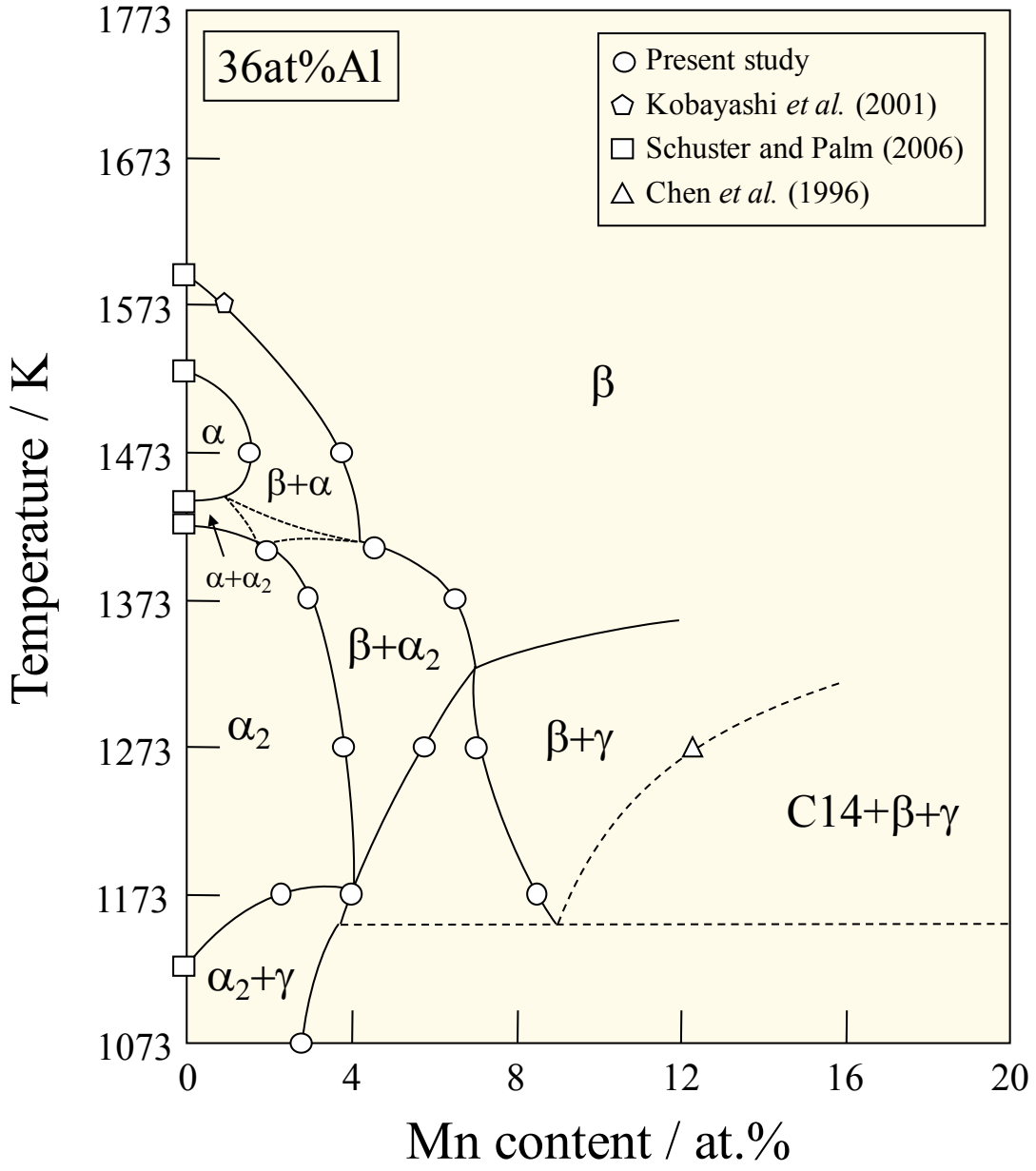

Fig. A-5. Vertical section in Ti-Al-Mn ternary system at 36 at%Al based on the present study along with reported data [2, 3, 5].

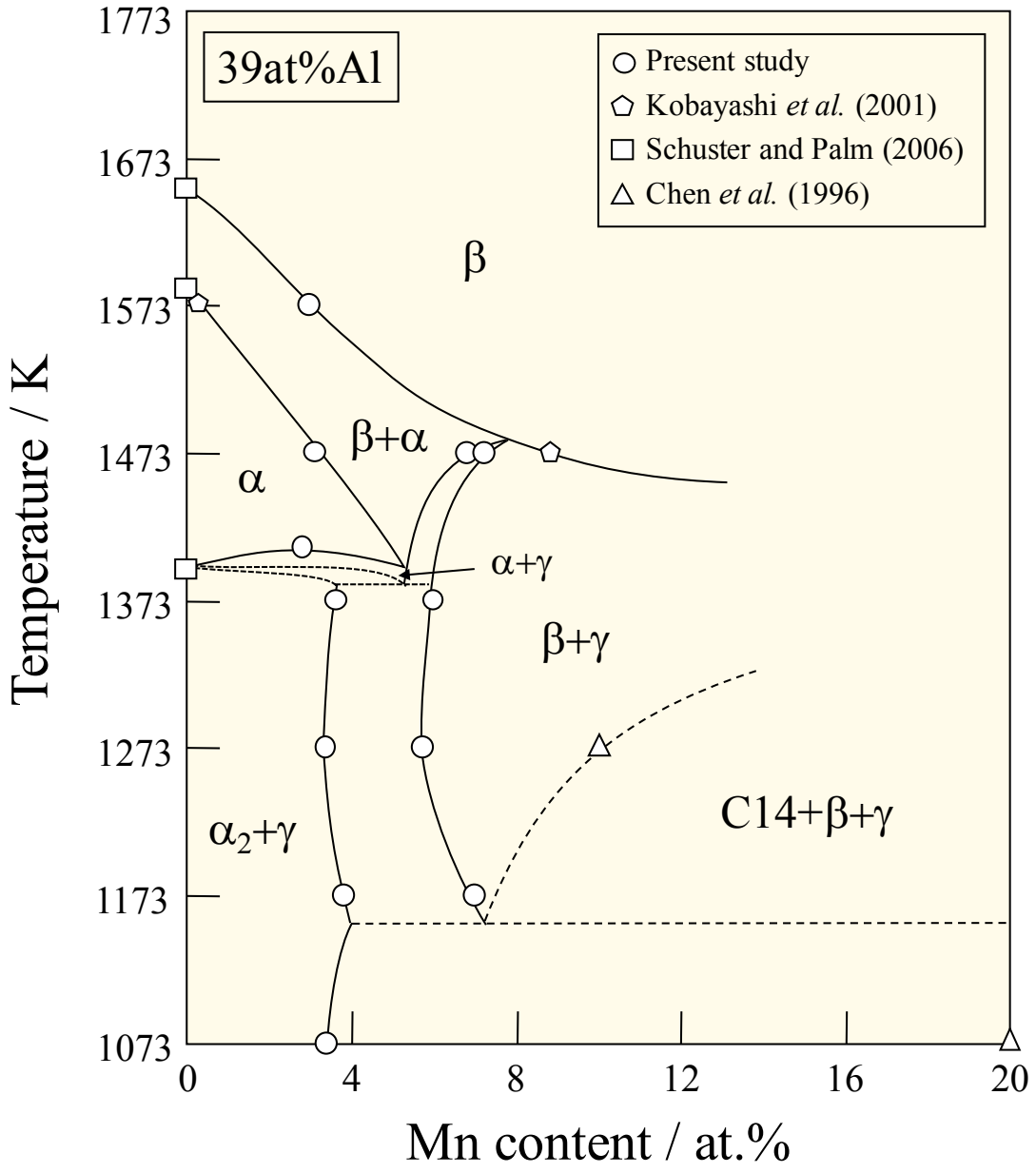

Fig. A-6. Vertical section in Ti-Al-Mn ternary system at 39 at%Al based on the present study along with reported data [2, 3, 5].

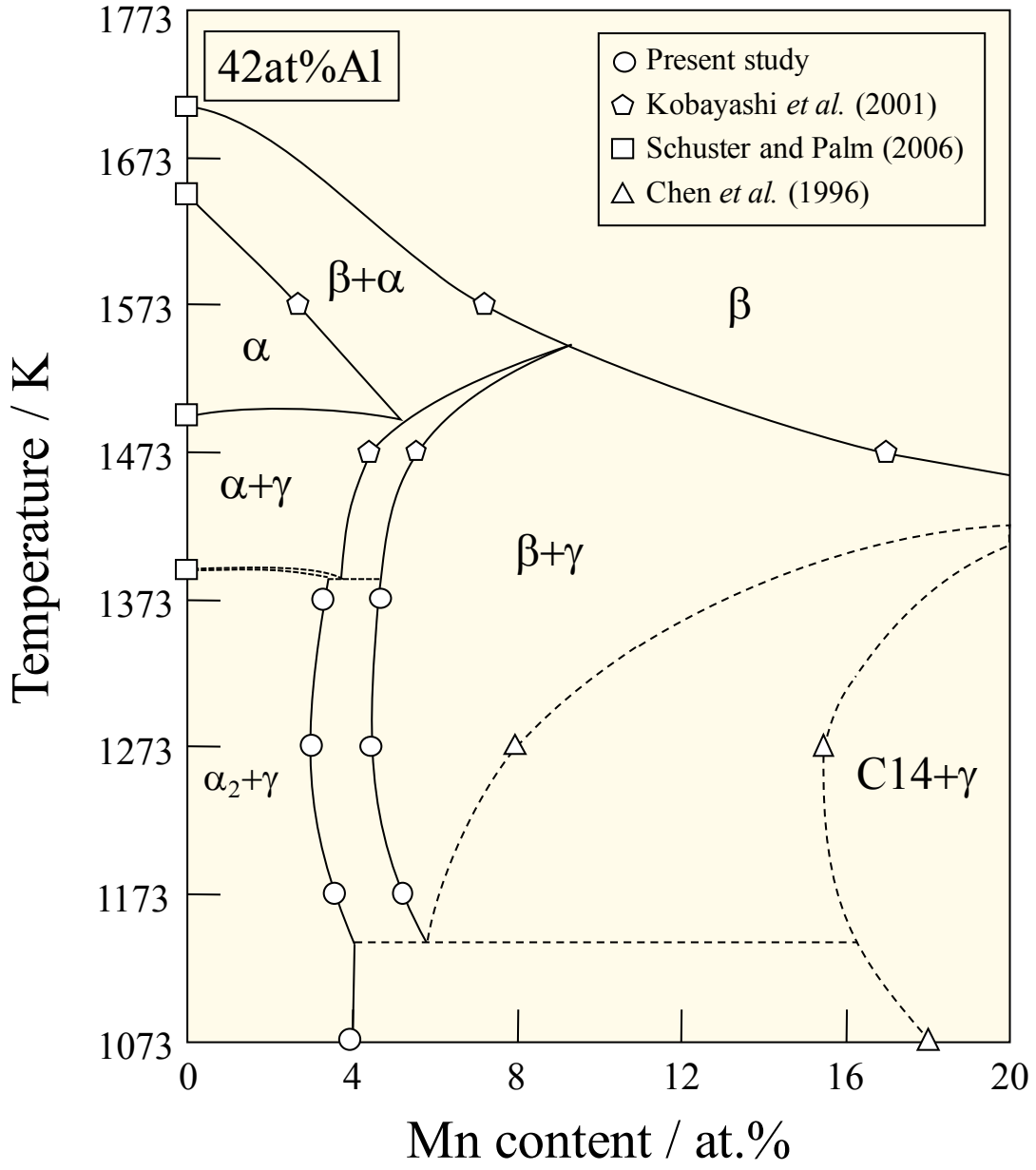

Fig. A-7. Vertical section in Ti-Al-Mn ternary system at 42 at%Al based on the present study along with reported data [2, 3, 5].

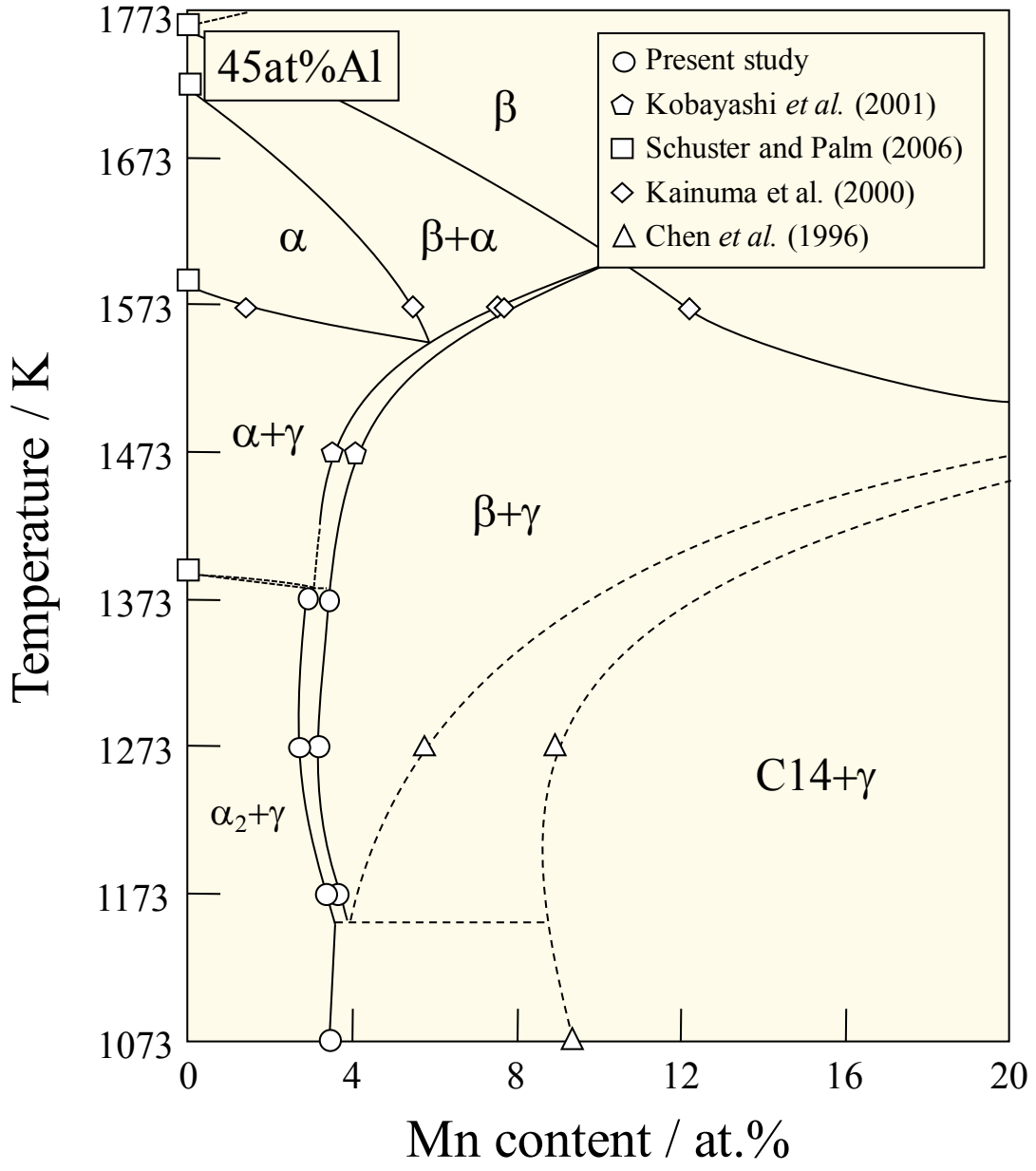

Fig. A-8. Vertical section in Ti-Al-Mn ternary system at 45 at%Al based on the present study along with reported data [2, 3, 5, 6].

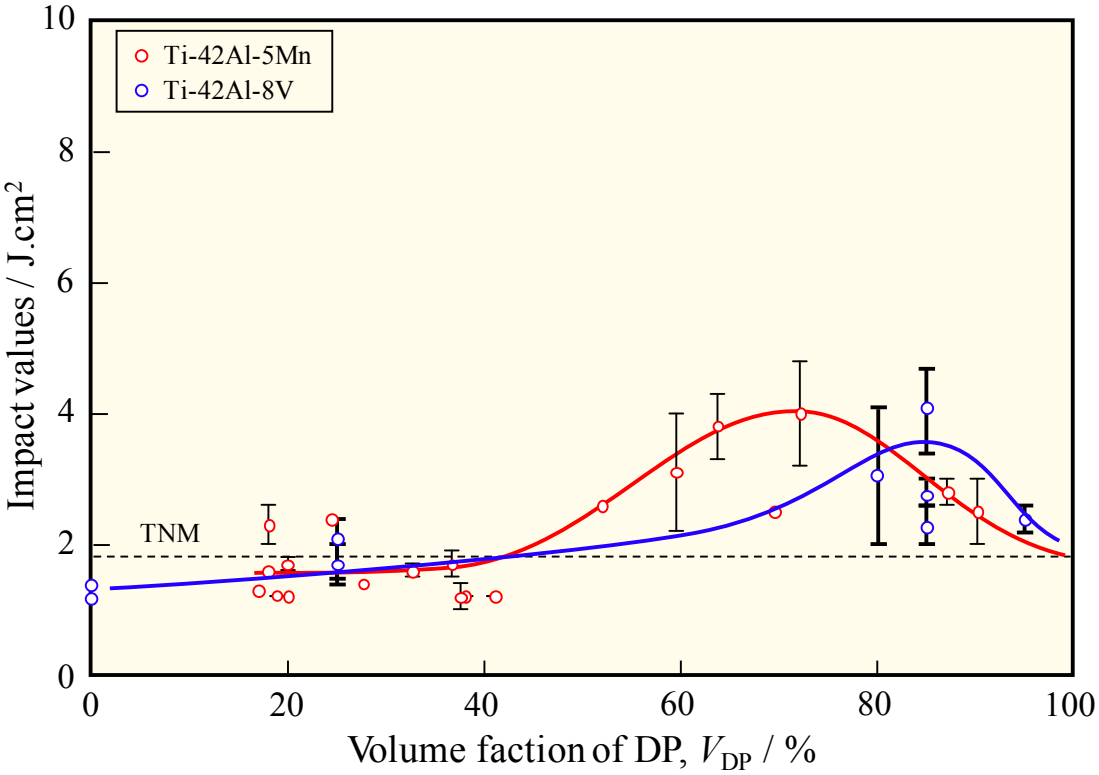

Fig. A-9. Effect of β/γ volume fraction on resilience.

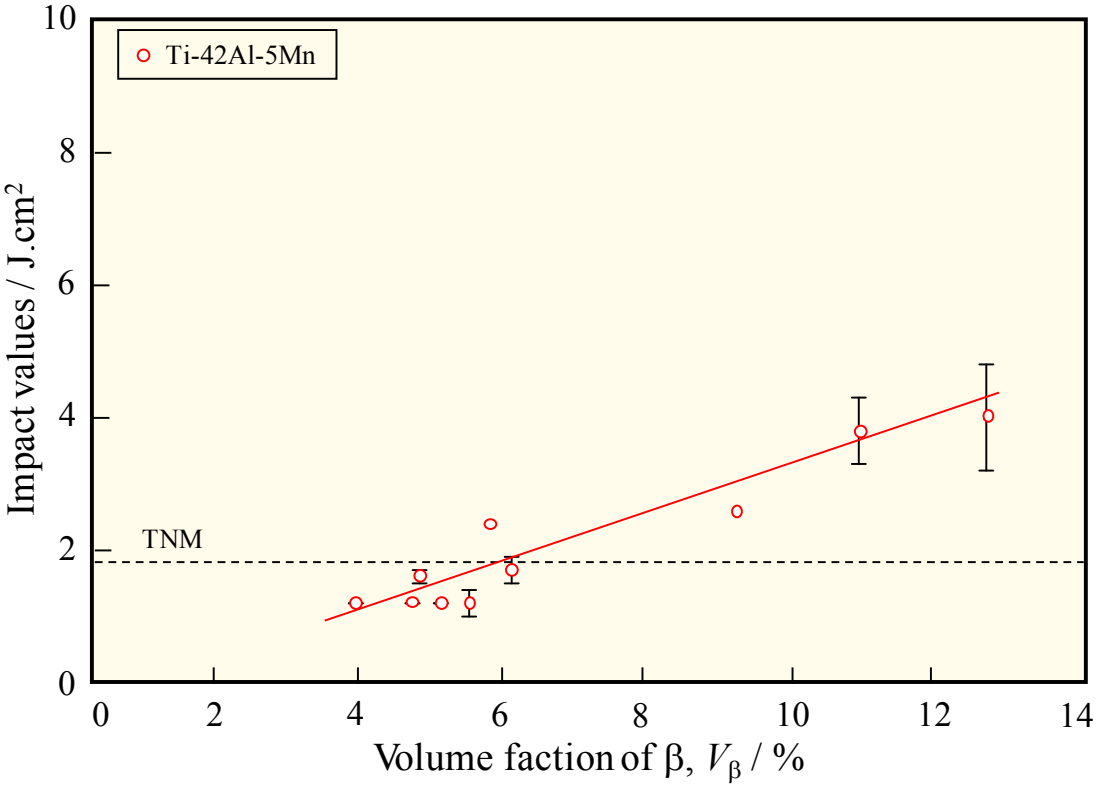

Fig. A-10. Effect of β phase on resilience.

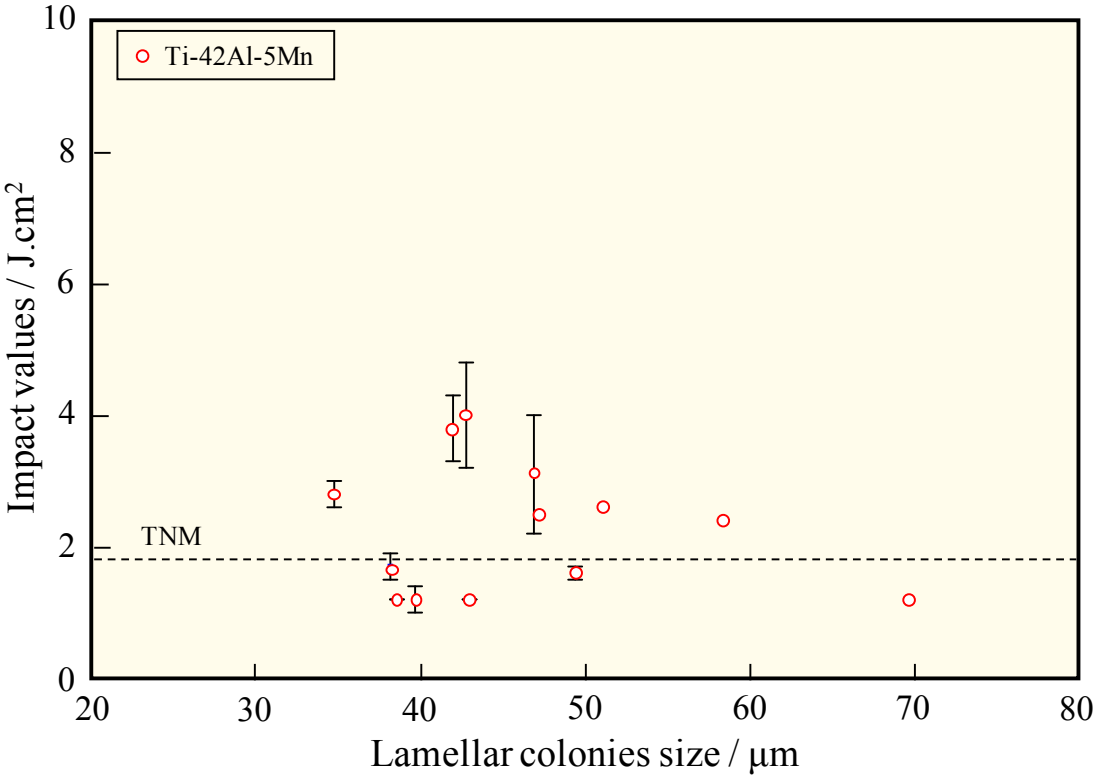

Fig. A-11. Effect of lamellar colonies size on resilience.

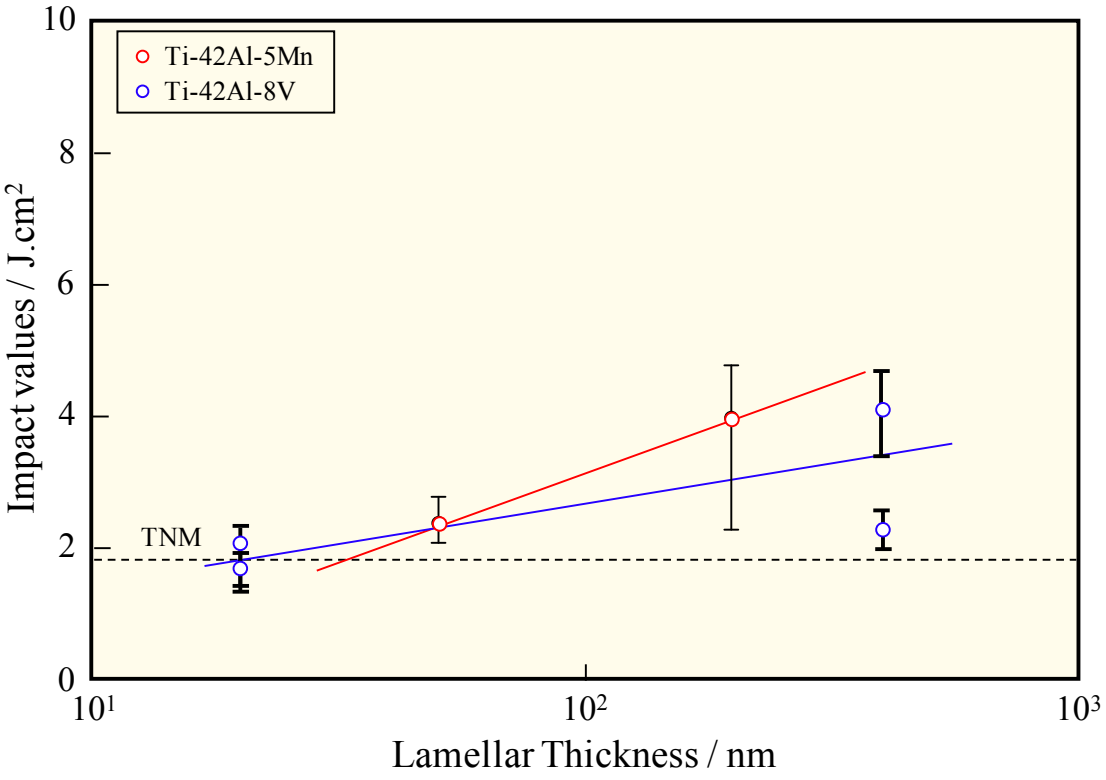

Fig. A-12. Effect of lamellar thickness on resilience.

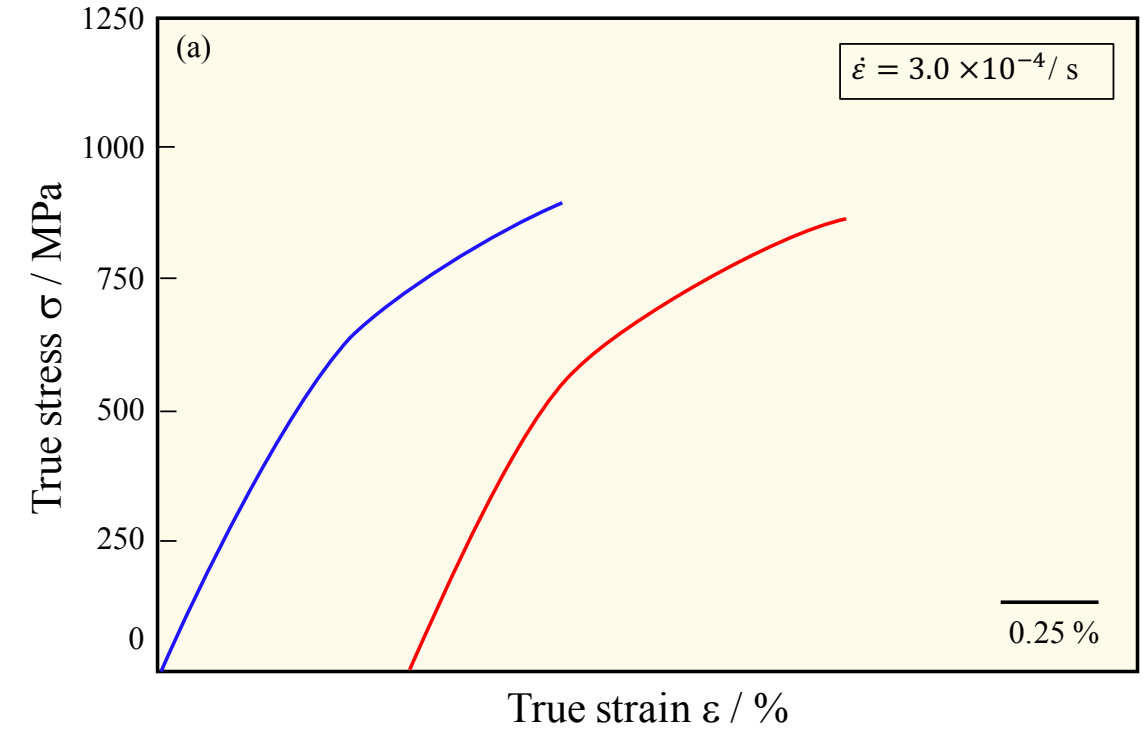

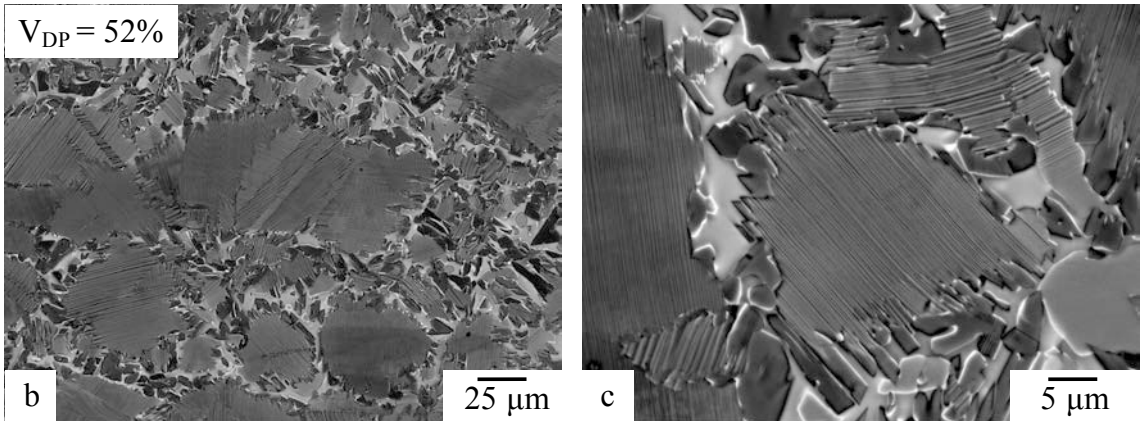

Sample	Yield stress σ_y / MPa	Fracture strength σ_m / MPa	Young's Modulus E / GPa	Elongation / %
42-5Mn-T1	400	872	153	0.56
42-5Mn-T2	480	903	147	0.36
Average	**440**	**888**	**150**	**0.46**

Fig. A-13. Tensile properties of Ti-42Al-5Mn: (a) stress-strain curve, (b, c) SEM images of the microstructure and (d) summarized table of the as-forged (AF) microstructure.

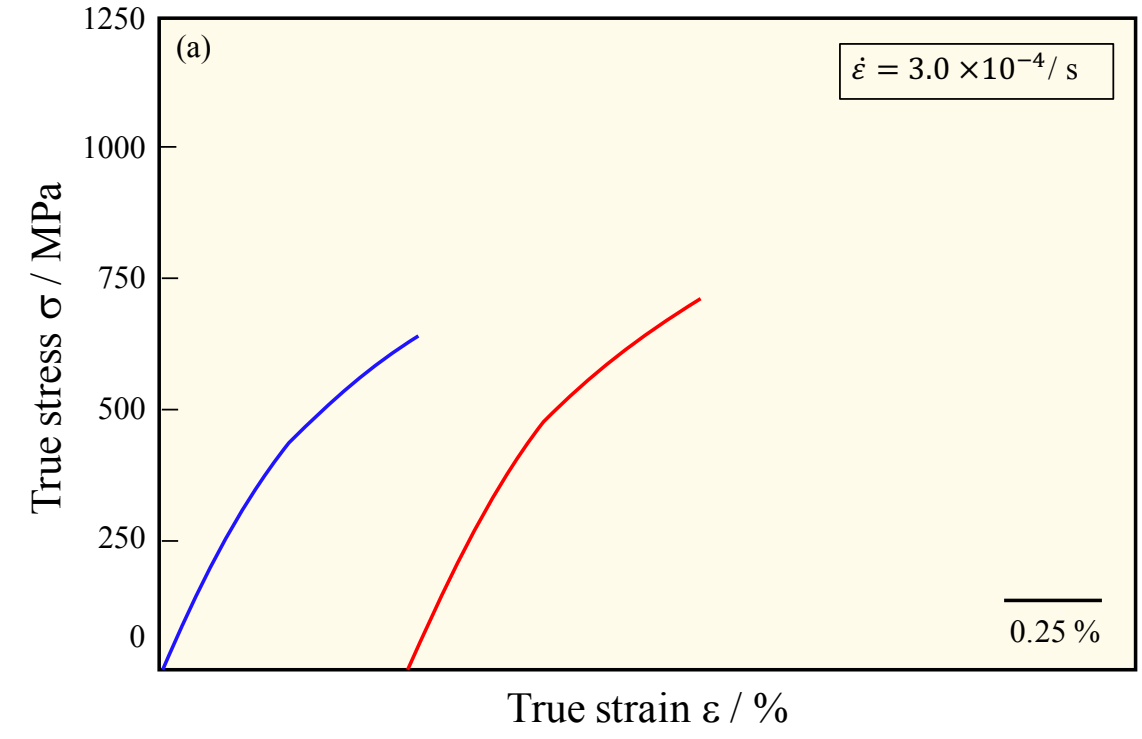

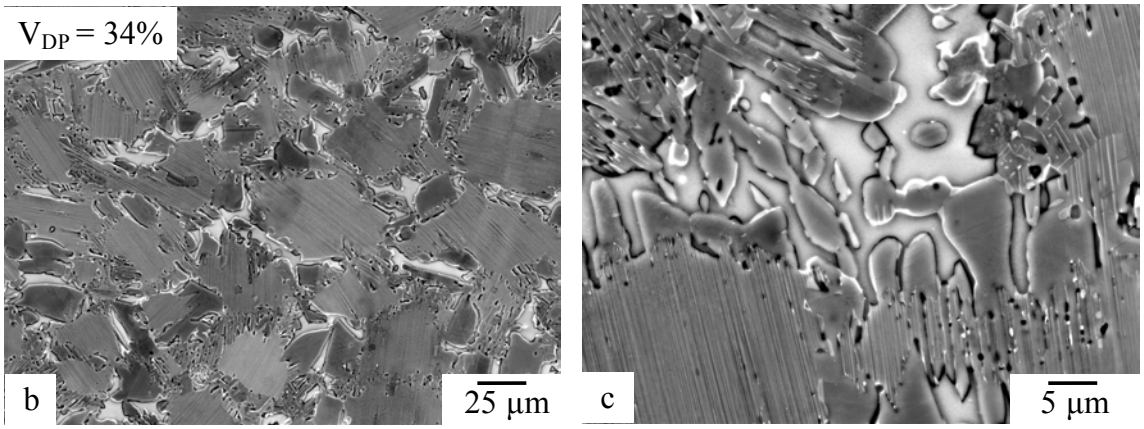

Sample	Yield stress σ_y / MPa	Fracture strength σ_m / MPa	Young's Modulus E / GPa	Elongation / %
42-5Mn-T3	340	715	164	0.28
42-5Mn-T4	290	644	150	0.25
Average	**315**	**680**	**157**	**0.27**

Fig. A-14. Tensile properties of Ti-42Al-5Mn: (a) stress-strain curve, (b, c) SEM images of the microstructure and (d) summarized table of the Globular Triplex (GTL) microstructure.

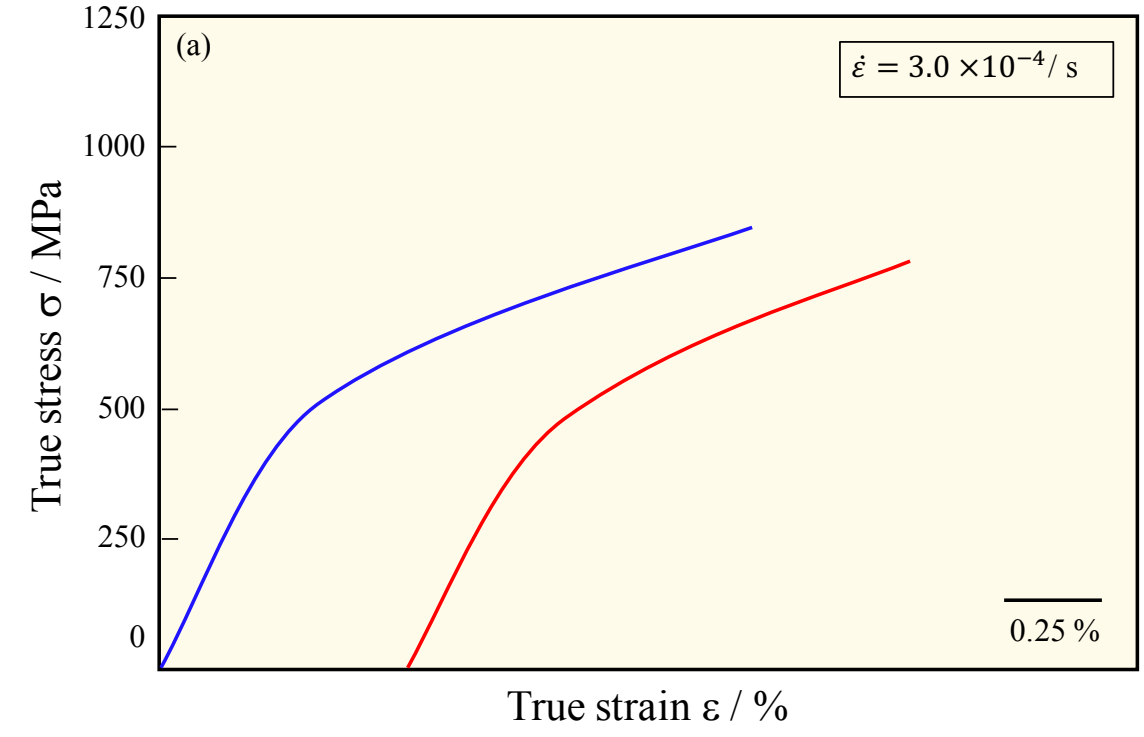

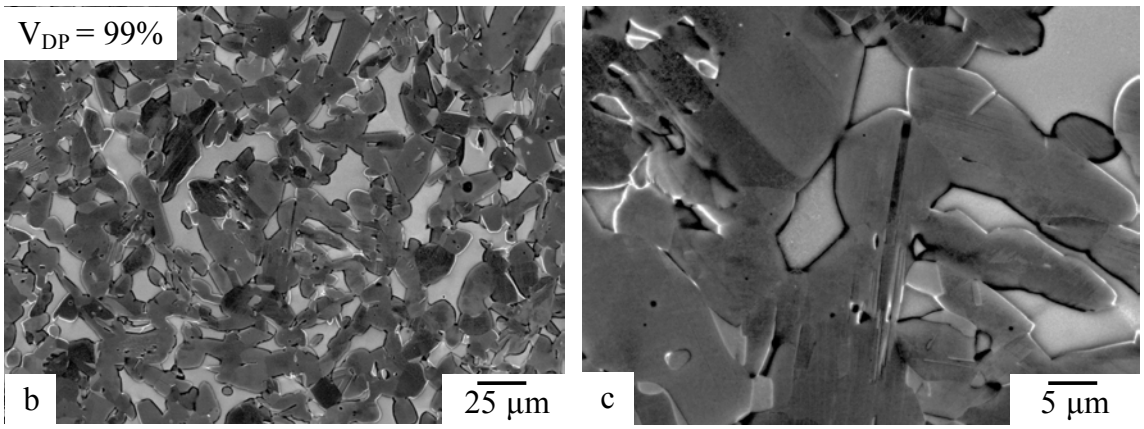

Sample	Yield stress σ_y / MPa	Fracture strength σ_m / MPa	Young's Modulus E / GPa	Elongation / %
043-5	400	776	146	0.78
043-8	350	847	150	0.97
Average	**375**	**812**	**148**	**0.89**

Fig. A-15. Tensile properties of Ti-42Al-5Mn: (a) stress-strain curve, (b, c) SEM images of the microstructure and (d) summarized table of the Nearly Globular β/γ Duplex (NGDP) microstructure.

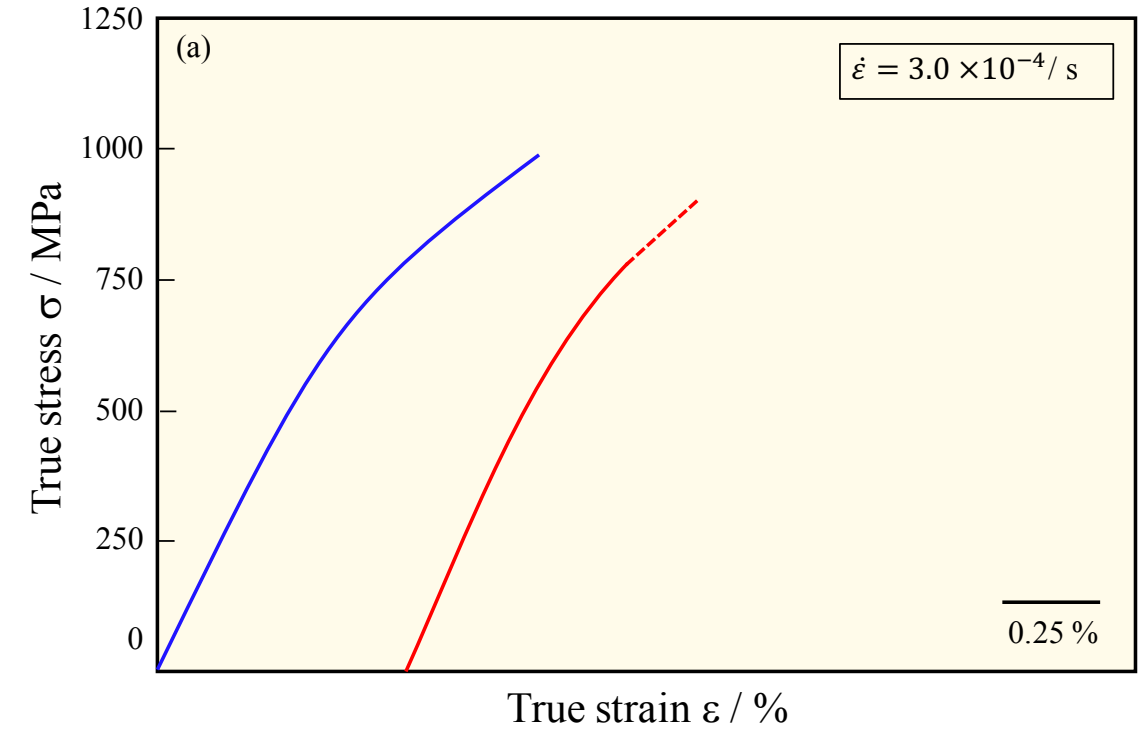

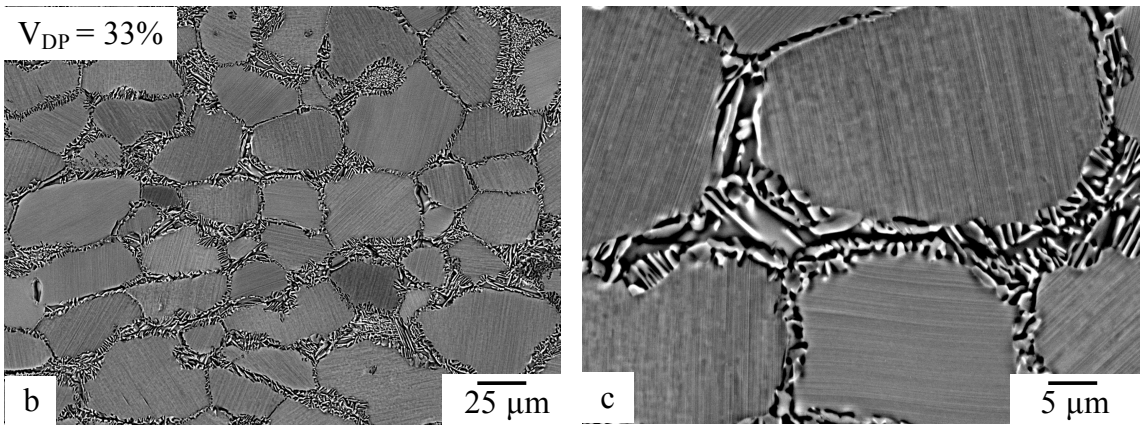

Sample	Yield stress σ_y / MPa	Fracture strength σ_m / MPa	Young's Modulus E / GPa	Elongation / %
KV4-7	410	898	172	–
KV4-8	530	1005	146	0.33
Average	**470**	**951**	**159**	**0.33**

Fig. A-16. Tensile properties of Ti-42Al-8V: (a) stress-strain curve, (b, c) SEM images of the microstructure and (d) summarized table of the Near γ Cellular Triplex (NCT) microstructure.

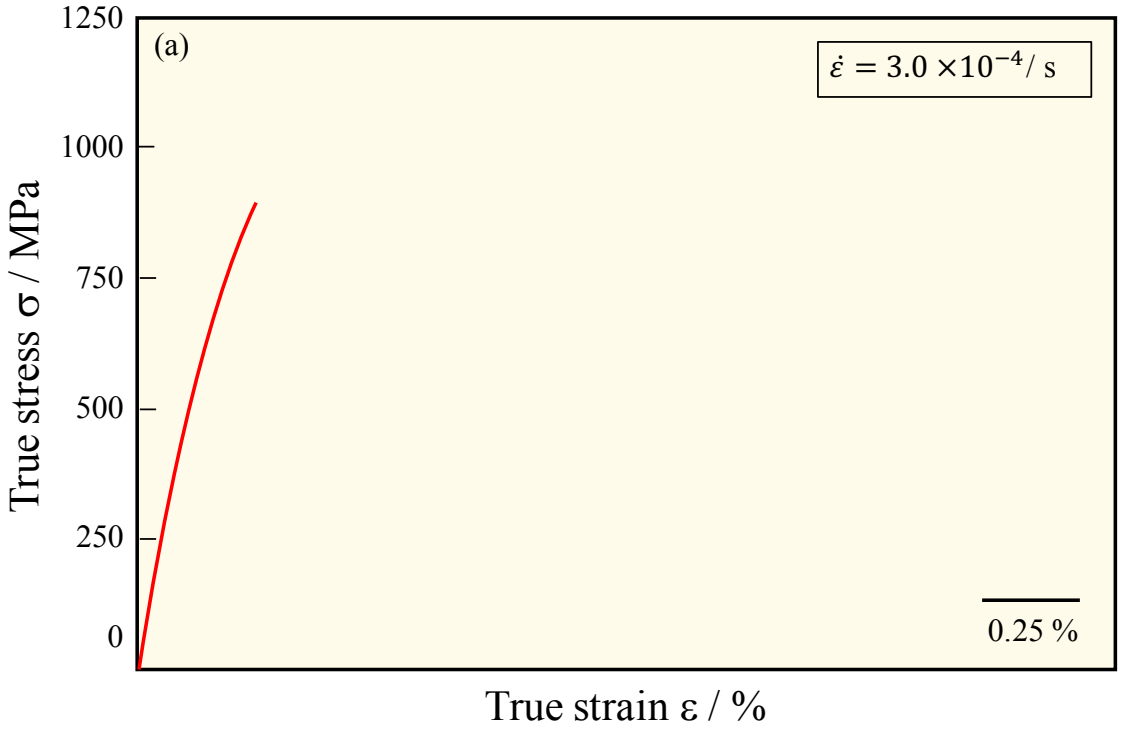

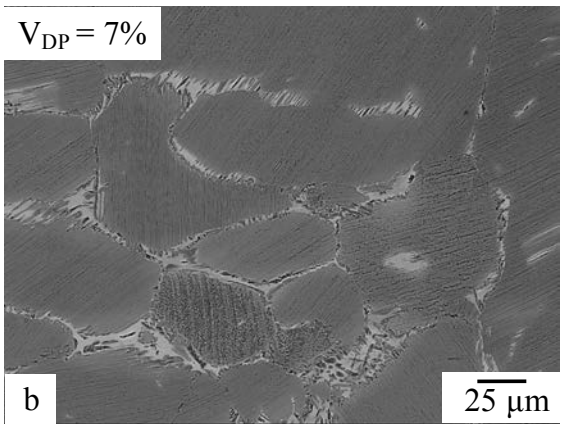

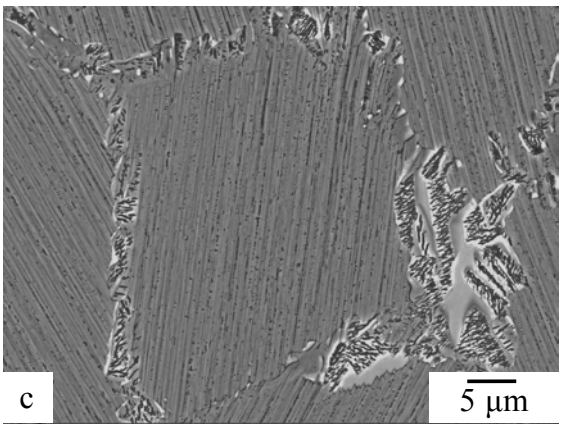

Sample	Yield stress σ_y / MPa	Fracture strength σ_m / MPa	Young's Modulus E / GPa	Elongation / %
ex-situ [8]	450	900	137	0.1
Average	**450**	**900**	**137**	**0.1**

Fig. A-17. Tensile properties of Ti-43Al-4Nb-5V: (a) stress-strain curve, (b, c) SEM images of the microstructure and (d) summarized table of the Nearly Lamellar (NL) microstructure determined by Usui et al. [8].

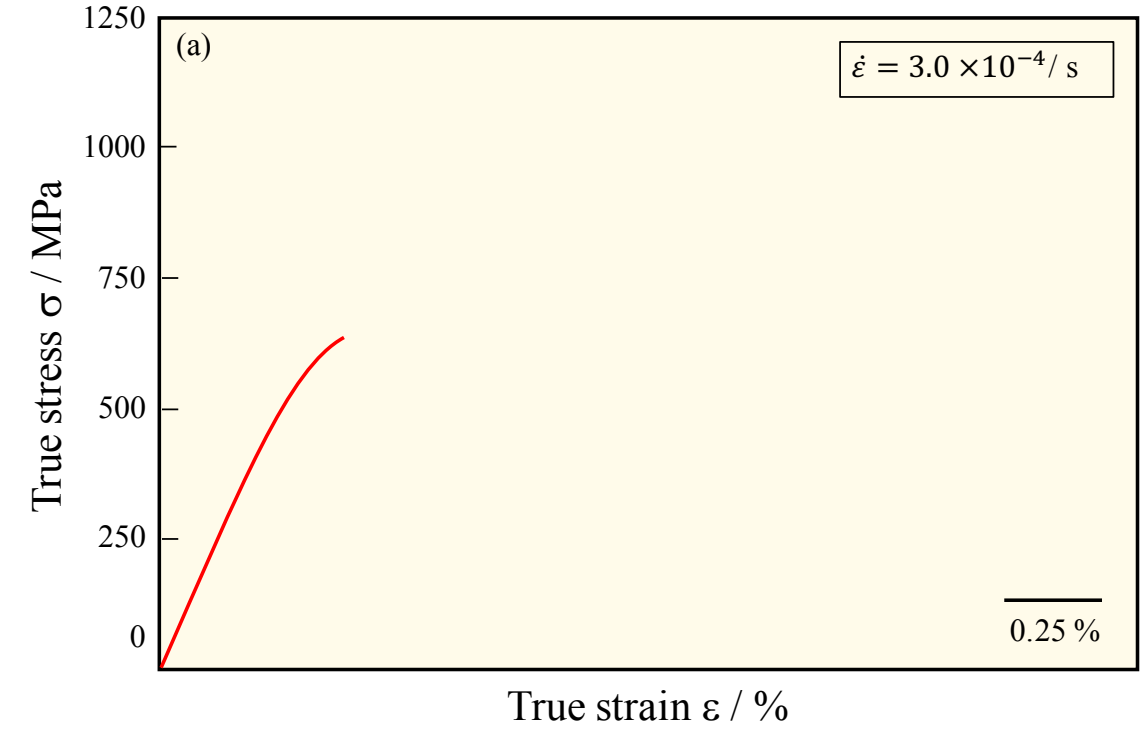

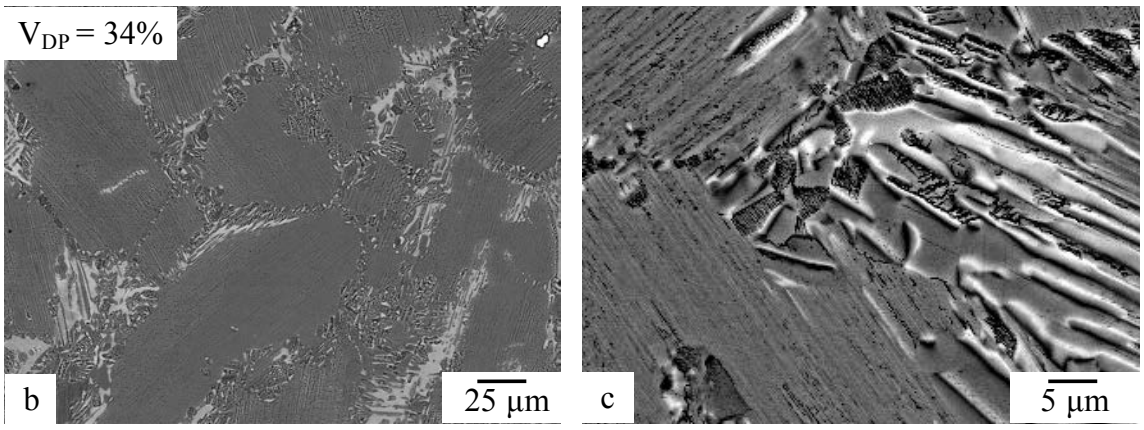

Sample	Yield stress σ_y / MPa	Fracture strength σ_m / MPa	Young's Modulus E / GPa	Elongation / %
43-4-5-T1	430	632	168	0.07
Average	**430**	**632**	**168**	**0.07**

Fig. A-18. Tensile properties of Ti-43Al-4Nb-5V: (a) stress-strain curve, (b, c) SEM images of the microstructure and (d) summarized table of the Lamellar Triplex (LTL) microstructure

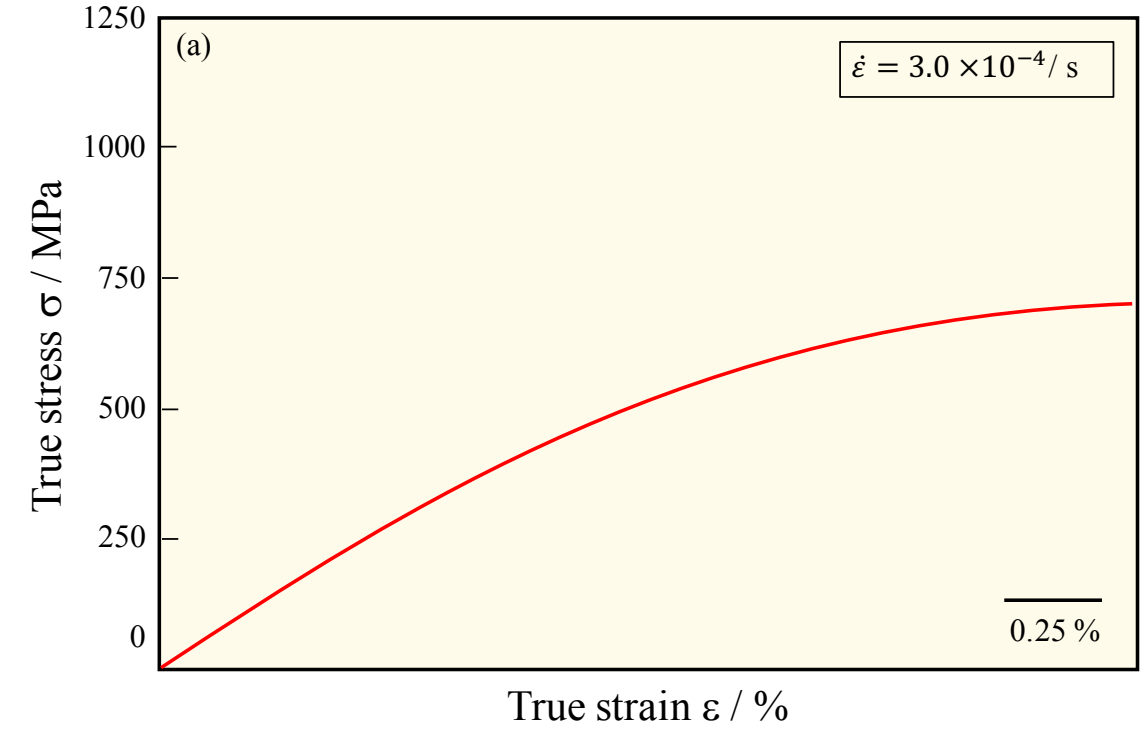

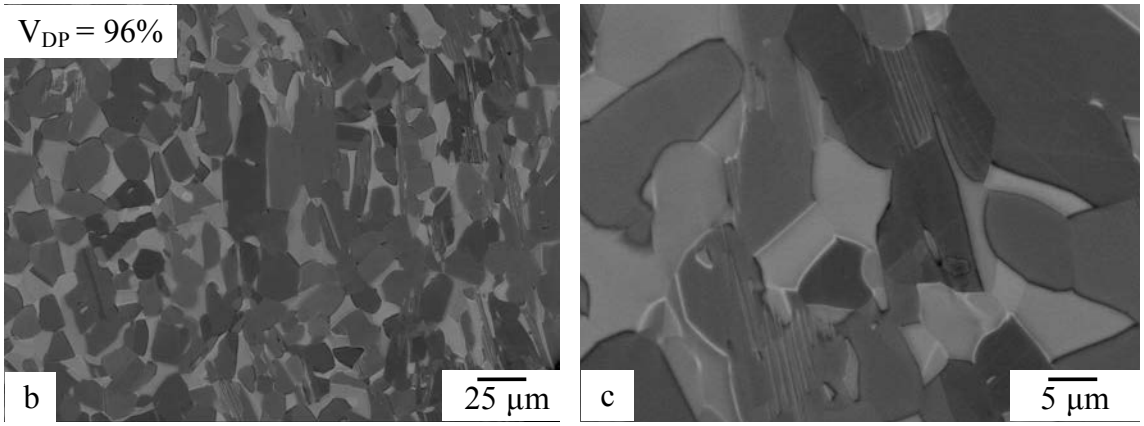

Sample	Yield stress σ_y / MPa	Fracture strength σ_m / MPa	Young's Modulus E / GPa	Elongation / %
in-situ [8]	495	775	47	2.31
Average	**495**	**775**	**47**	**2.31**

Fig. A-19. *In-situ* tensile properties of Ti-43Al-4Nb-5V: (a) stress-strain curve, (b, c) SEM images of the microstructure and (d) summarized table of the Nearly Globular β/γ Duplex (NGDP) microstructure determined by Nakamura et al. [8].

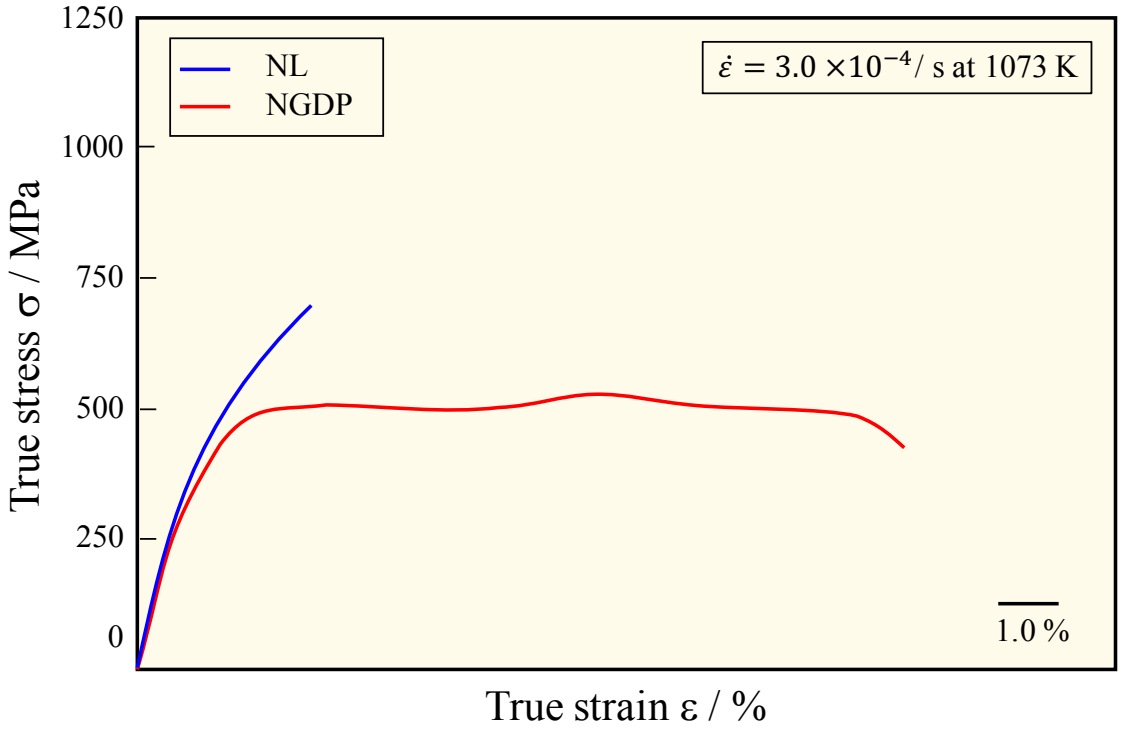

Fig. A-20. *in-situ* Tensile behaviour of Ti-43Al-4Nb-5V for NL and NGDP microstructure at 1073 K determined by Nakamura *et al.* [8].

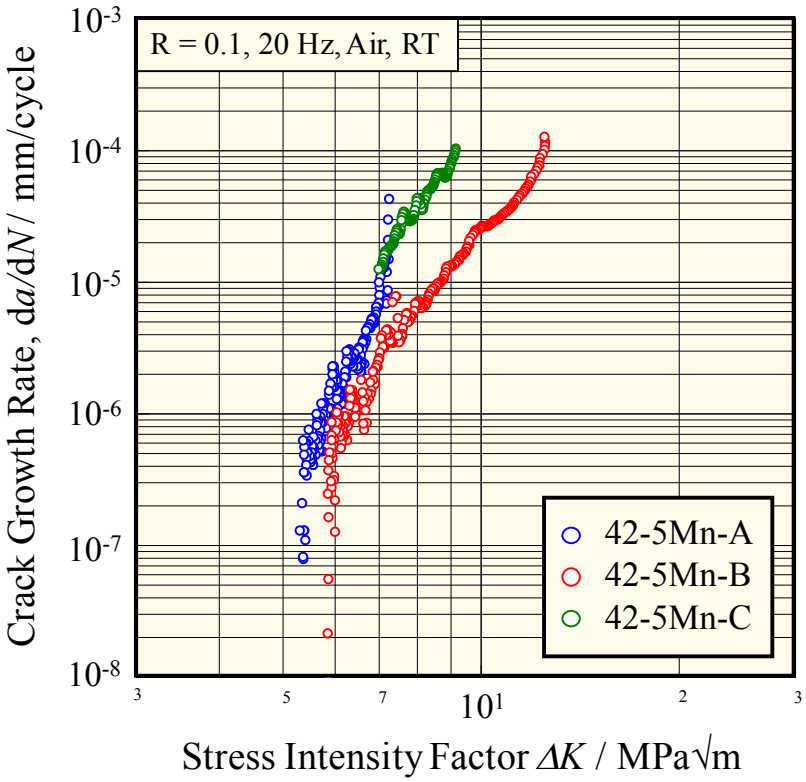

Fig. A-21. Fatigue crack growth curves of as-forged (AF) microstructure in 42-5Mn alloy.

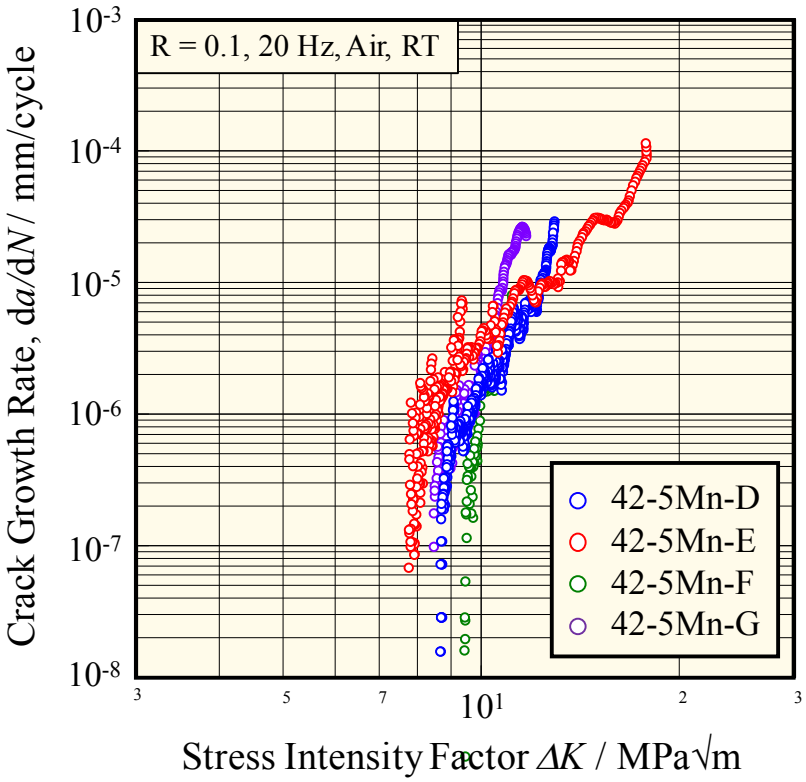

Fig. A-22. Fatigue crack growth curves of Globular Triplex (GTL) microstructure in 42-5Mn alloy.

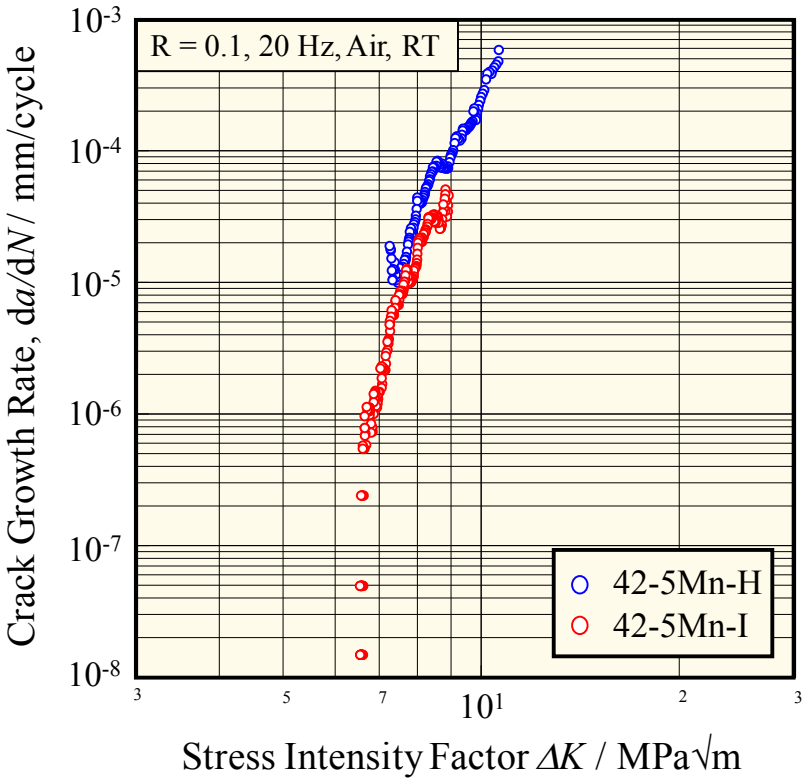

Fig. A-23. Fatigue crack growth curves of Nearly Globular β/γ Duplex (NGDP) microstructure in 42-5Mn alloy.

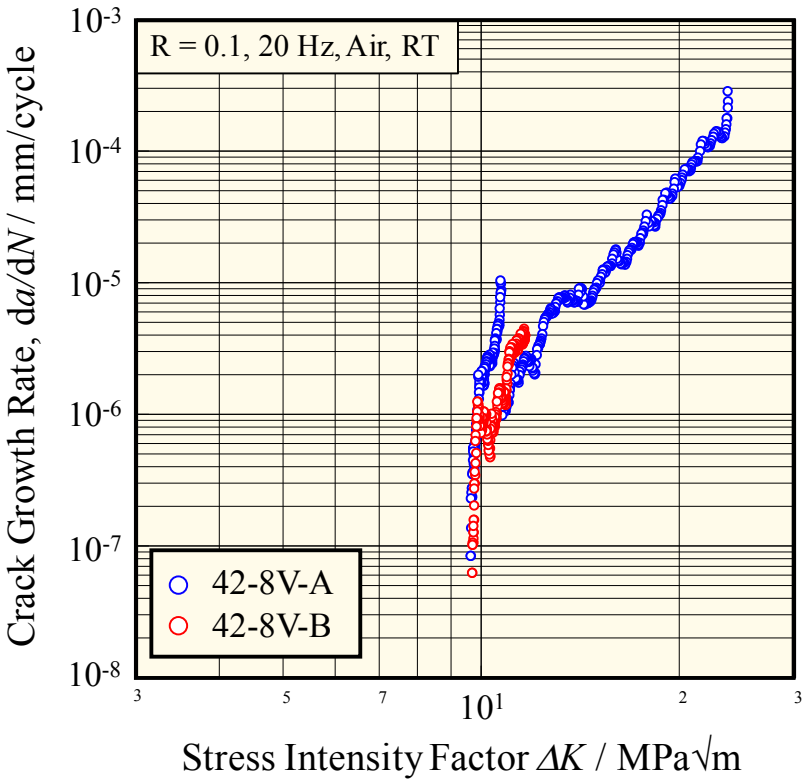

Fig. A-24. Fatigue crack growth curves of Near γ Cellular Triplex (NCT) microstructures in 42-8V alloy.

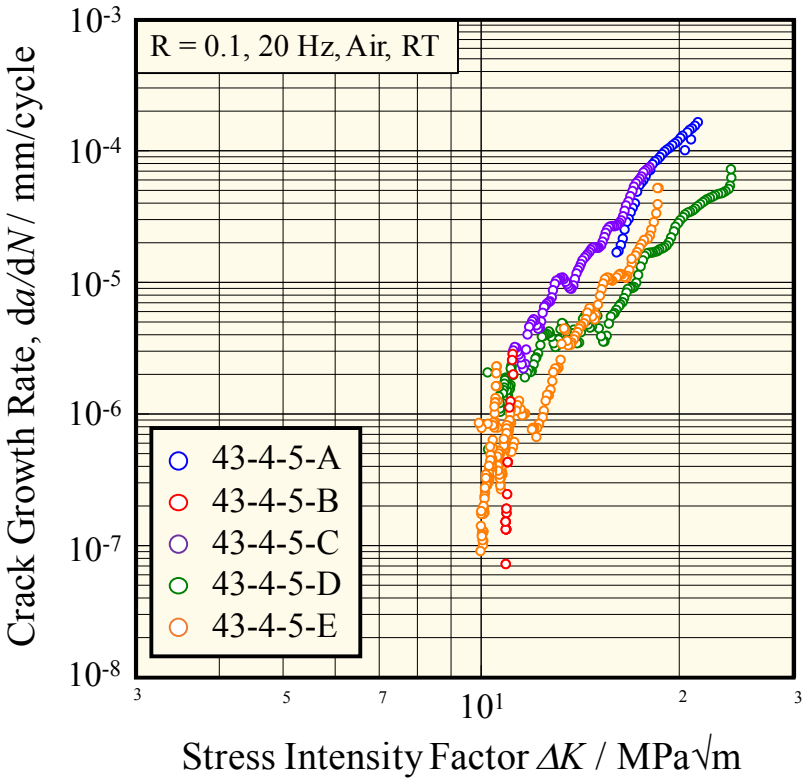

Fig. A-25. Fatigue crack growth curves of Nearly Lamellar (NL) microstructure in 43-4-5 alloy.

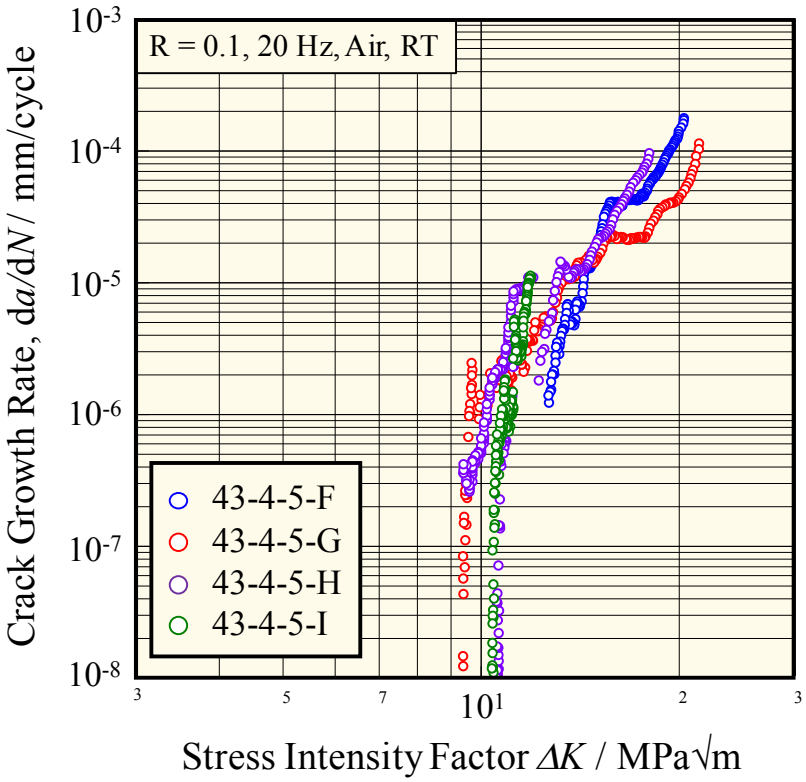

Fig. A-26. Fatigue crack growth curves of Lamellar Triplex (LTL) microstructures in 43-4-5 alloy.

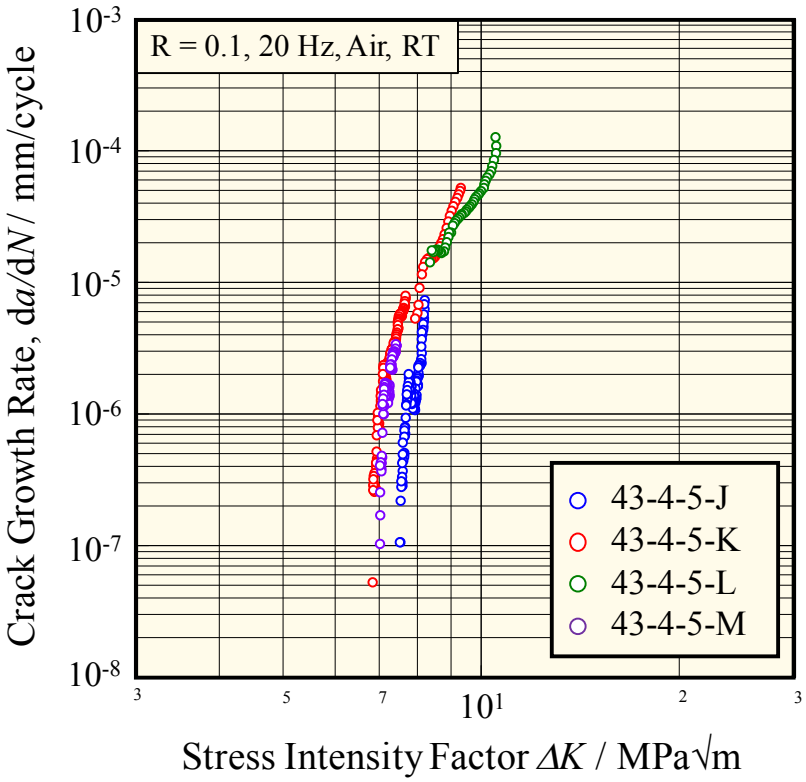

Fig. A-27. Fatigue crack growth curves of Nearly Globular β/γ Duplex (NGDP) microstructure in 43-4-5 alloy.

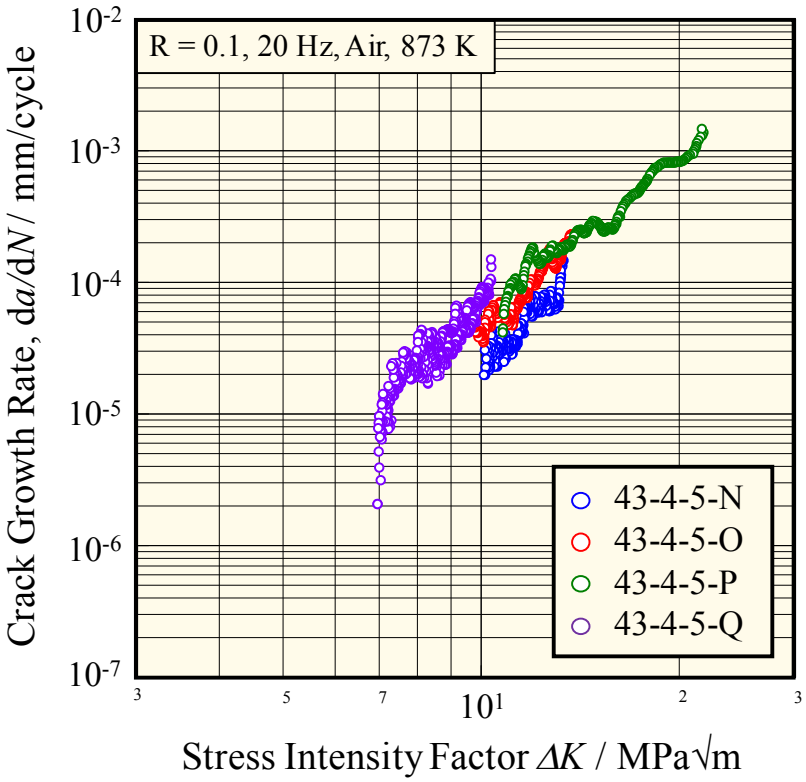

Fig. A-28. Fatigue crack growth curves of Nearly Lamellar (NL) microstructure in 43-4-5 alloy at 873 K.

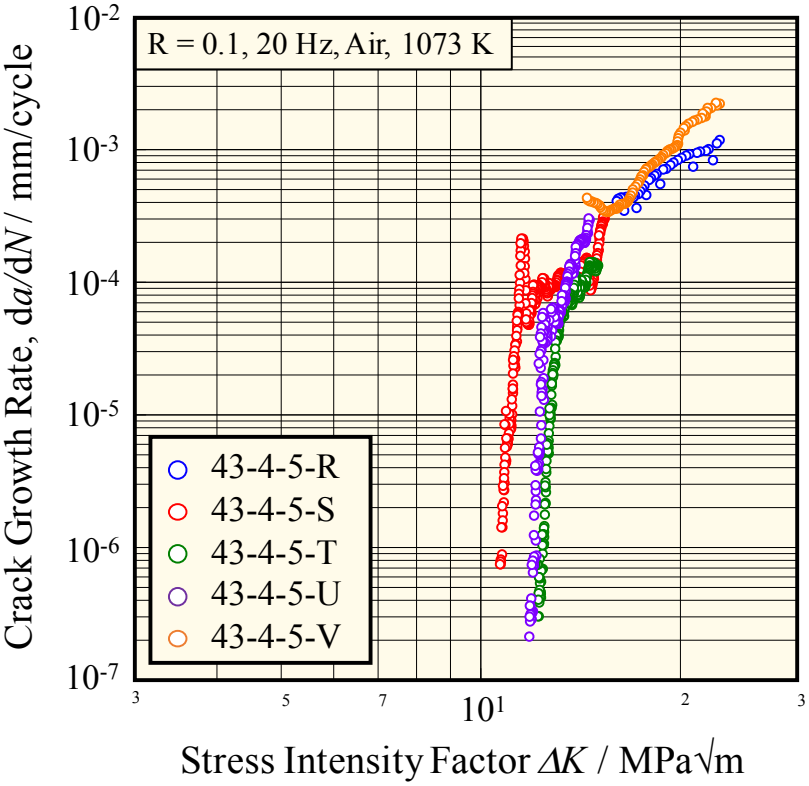

Fig. A-29. Fatigue crack growth curves of Nearly Lamellar (NL) microstructure in 43-4-5 alloy at 1073 K.

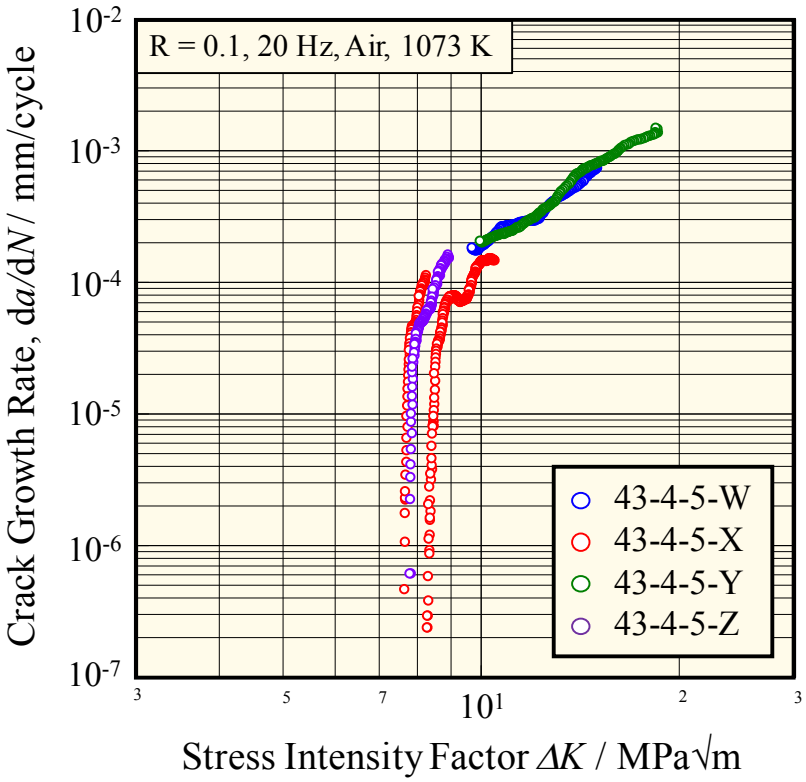

Fig. A-30. Fatigue crack growth curves of Nearly Globular β/γ Duplex (NGDP) microstructure in 43-4-5 alloy at 1073 K.

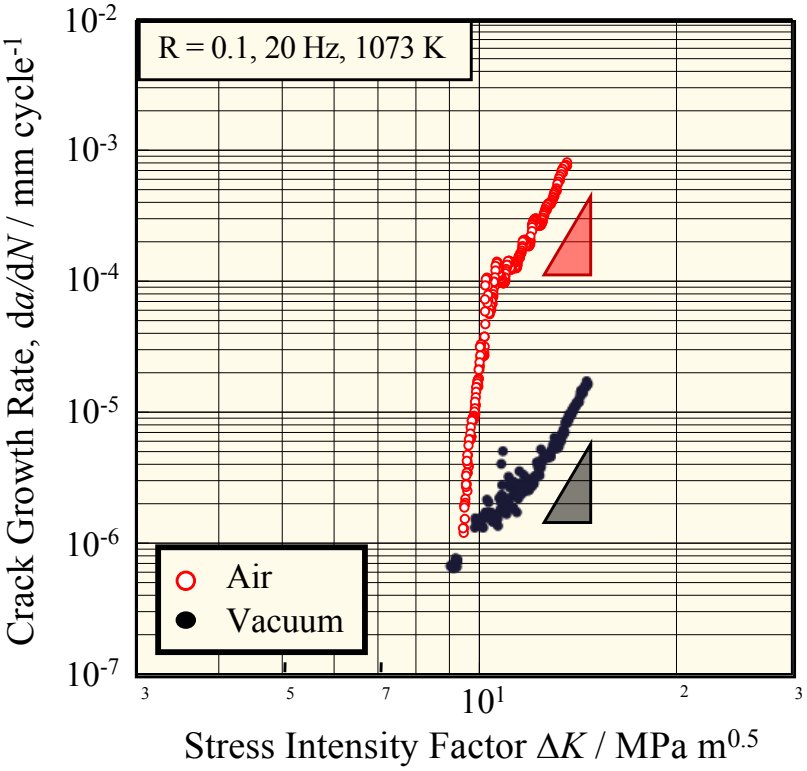

Fig. A-31. Effect of atmosphere on stress intensity during *K*-decreasing test near fatigue threshold on GTL microstructure (Ti-42Al-5Mn) in air and in vacuum (4.1×10^{-1} Pa) at 1073 K.

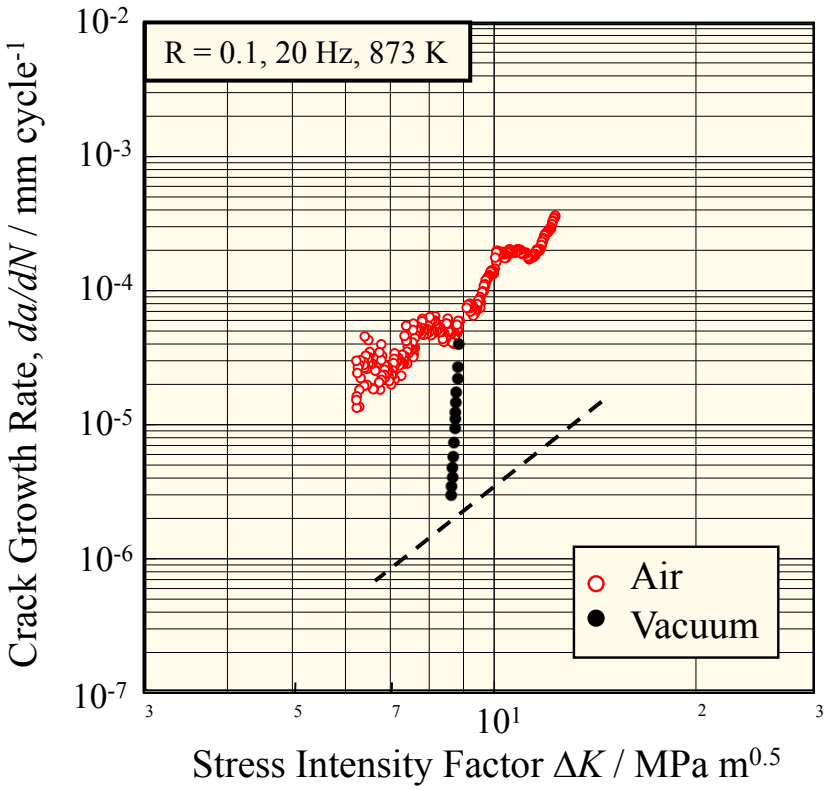

Fig. A-32. Effect of atmosphere on stress intensity during *K*-decreasing test near fatigue threshold on GTL microstructure (Ti-42Al-5Mn) in air and in vacuum (6.9×10^{-1} Pa) at 873 K.

Acknowledgment

Three long but filled years have gone. I had a great opportunity not only to learn metallurgy in the metallurgy and ceramics science department of the well-known Tokyo Institute of Technology but also to enjoy a different culture.

This thesis could not be done without two persons. First of all, I would like to thank my supervisor Prof. Takeyama, who has been taking care of me for 3 years. Despite you was often occupied, you always keep an eye of the progression of your students. I truly admire your passion on both research and education. Your discussions and advices were always precious and useful. Then, I do not know how thank Naka, without him I would not be here today. He inspired me to purse in doctorate after my engineering degree and introduced me to Prof. Takeyama. I know he followed my researches from France and also during his stays in Japan when he came to give lectures.

I would like to thank the examiners of this thesis. One again thank to Prof. Takeyama but also Prof. Nakamura, Prof. Fujii, Prof. Muraishi and Prof. Kobayashi. I hope your enjoyed this work as much I appreciated to do it.

To continue, I would like thank the laboratory staff who I enjoyed to work with. I thank again to Prof. Kobayashi and also to Prof. Nakashima for their availability and advices. They helped me a lot especially with phase equilibria. A big thank to Prof. Yamagata, for all about the fatigue crack growth tests. I really enjoyed our discussions and also thank for the help during the thesis writing. I would like thank Ali who share his experiences and who I enjoyed talking with. You helped me to take a different point of view on my researches. Our discussions were always welcome. Finally, but not least, thank you Ms. Taga for your kindness and your help with the university administration.

Thank also to the members of the titanium aluminides team who worked together with me. Thank to Wakabayashi, Yoshida, Nakamura, Kinouchi, Okada, Kimoto, Ikemura and Murata. Special thought for Nakamura, Okada and Murata who worked on the same theme with me and helped me a lot with experiment conducting.

Thanks to all laboratory members, current and graduated, for their kindness, for helping me to feel welcome when I arrived and for bringing joy every day at the laboratory, sometimes too much. I think in particular to Yoshihara, Mise, Kumagai, Satoshi, Nakumara, Kwak, Ohta and Ooki.

Thanks to Nagashima for always remember my birthday. Dear Oh, I am sorry it did not work. Thanks also to all the others that made this three years a wonderful time.

Special thanks to Ida for being such a nice tutor for me. You took care of me since I arrived in Japan until the end. Thank for helping me to move, with the Japanese administration and all the rest. I learned many things from you.

Thank also to my friends, those who stayed in France, those who came visiting Japan while I was here and also the news one I met in Japan.

I would like to thank obviouly my family who always supporting me all along this three years. Maman (and Vador), Papa, Solen, all grandparents, Fanny and all the others, Merci.

最後に，お世話してくださった英里香の家族に感謝致します.

And I kept the best for the end. Thank Erika, you illuminated all my days since I met you. I am glad we can finally start our life together.

May the Force be with you!

Loris SIGNORI